WILEY-VCH

Edited by Alberto Puga

Photocatalytic Hydrogen Production for Sustainable Energy

Photocatalytic Hydrogen Production for Sustainable Energy

Photocatalytic Hydrogen Production for Sustainable Energy

Edited by Alberto Puga

WILEY-VCH

Editor

Dr Alberto Puga
Universitat Rovira i Virgili
Department of Chemical Engineering
Av. Països Catalans 26
43007 Tarragona
Spain

Cover Images: © Larisa-K/Pixabay;
© akitada31/Pixabay

Library of Congress Card No.: applied for

British Library Cataloguing-in-Publication Data
A catalogue record for this book is available from the British Library.

Bibliographic information published by the Deutsche Nationalbibliothek The Deutsche Nationalbibliothek lists this publication in the Deutsche Nationalbibliografie; detailed bibliographic data are available on the Internet at <http://dnb.d-nb.de>.

Print ISBN: 978-3-527-34983-8
ePDF ISBN: 978-3-527-83541-6
ePub ISBN: 978-3-527-83543-0
oBook ISBN: 978-3-527-83542-3

Typesetting Straive, Chennai, India

Contents

Preface

One of the main motivations of science is to understand nature. Research is the tool to gain knowledge about its underlying principles, from the forces exerted by black holes to the puzzling properties of subatomic particles. In between, the arguably more fascinating and marvelous phenomenon we witness is the existence of life. Primarily, life on Earth is possible thanks to the astonishingly sophisticated machinery of natural photosynthesis, whereby sunlight photons are absorbed by a complex biochemical system in the thylakoids of chloroplasts, and their energy is effectively converted to chemical energy via an intricate bioelectrochemical process. The products of photosynthesis then serve as food, structural materials, and energy sources for a plethora of dependent species, including us human beings. The most striking beauty of natural photosynthesis lies in the fact that it takes place effectively, silently, mildly, selectively, and spontaneously, simply as the right structures are exposed to sunlight.

Strictly speaking, most forms of energy used by mankind today have their origins in sunlight. This includes fossil fuels, but they were generated, accumulated, and preserved by chance in limited amounts that will not last for too long at the pace we use them currently. Fuels are substances with a high density of chemical energy that can be transported and used as required. Therefore, mimicking nature with the aim to store solar energy into a fuel by a direct, convenient, straightforward and efficient fashion represents a fantastic solution to replace fossil, finite energy resources. This strategy is known as artificial photosynthesis. Giovanni Ciamician, a pioneer in the art of photocatalysis, at the beginning of the twentieth century, suggested that mastering photochemistry would enable the generation of solar fuels, among which hydrogen from water may hold a prevalent position. Today, we are starting to appreciate this as a perfectly suited approach to implement a sustainable energy scheme for future generations.

It is highly comforting to verify that the use of solar photocatalysis has greatly advanced in recent times, thanks to the efforts of many research teams worldwide. In particular, the relatively elementary hydrogen molecule, which despite its small size, carries a large amount of energy, can be formed by photocatalysis from water resources and only under the action of sunlight, by a range of diverse processes. This book aims at compiling the wealth of scientific knowledge on photocatalytic hydrogen production, ponder on the current status of the related technologies, and

foster further research. As the reader will note throughout its pages, the field of photocatalysis and its application in the context of sustainable energy is burgeoning. Year after year, smarter materials able to utilize wider portions of the solar spectrum at higher efficiencies are being discovered and reported. Hydrogen production by solar photocatalysis, which is enticing due to its simplicity regarding practical and technical aspects, is becoming more and more competitive. However, there is still a long way to go before this will become a reality. Energy security and threats to the environment require rapid action, and most likely solar photocatalytic hydrogen will not solve all issues on time, but it is not anymore unreasonable to take it seriously as one of the possible solutions.

Thanks to the renowned experts in the field that have contributed to this book, the reader holds a rich and valuable source of information, not only for the scientific research community, but for anyone interested in the fields of solar energy, hydrogen, environmental technologies, and water sciences. Prof. Ohtani and co-workers are gratefully acknowledged for explaining the basic principles of photocatalysis in an accessible and concise way. The chapter by Prof. Bahnemann's team thoroughly dissects the mechanistic pathways making photocatalytic hydrogen production possible. In addition to an overview on overall water splitting by myself, Prof. Farràs and coworkers describe the complementary photoelectrochemical approach, whereas Prof. Idriss's chapter focuses on the adoption of photovoltaic materials to obtain hydrogen from water. Dr. Albero and Prof. García have reviewed the development of disruptive metal–organic frameworks for hydrogen production, providing a fantastic example of the ample room for advancements in materials science. Prof. Fornasiero and co-workers draw our attention to the fruitful and rather unexplored field of photocatalytic organic synthesis, entailing hydrogen production. Regarding renewable feedstocks, Prof. Lee, Prof. Leem, and co-workers produced a comprehensive account on hydrogen from biomass. In a similar realm, the chapter by Prof. Kozlova's team reviews the use of sulfide photocatalysts with visible light activity. One particularly relevant photocatalytic hydrogen production process entails the use of wastewaters as a feedstock, as summarized and discussed in a sensibly analytical fashion by Prof. Contreras and Dr. Toledo Camacho. Finally, the outstanding experience of Prof. Malato and co-workers on solar plants is reflected in their chapter, providing a motivating perspective about the scale-up of photoreactors for the eventual mass production of solar hydrogen. The professionality and expertise of all authors is the cornerstone that makes this book a unique and authoritative reference. My most sincere gratitude goes to all of them.

Tarragona (Spain) *Alberto Puga*
27 October 2022

1

Photocatalytic Hydrogen Production in the Context of Sustainable Energy

Alberto Puga

Universitat Rovira i Virgili (URV), Department of Chemical Engineering, Av. Països Catalans 26, 43007 Tarragona, Spain

1.1 The Transition to Sustainable Energy

1.1.1 Trends in Primary Energy Production

The production of energy has not ceased to increase during the last two centuries [1]. This fact is rooted in the Industrial Revolution since the machinery representing its very heart was (and still is) powered by the exploitation of massive amounts of fossil carbon resources [2]. One key consequence of the industrial economy has been the improvement of living conditions, which, in turn, has resulted in sustained population growth worldwide. A greater population then needs more energy, leading to ever-increasing energy production. Therefore, it is not surprising that the general trend is still clearly upward for the last few decades (Figure 1.1).

Despite transient declines due to contingencies such as the credit crunch of 2007–2008 or the coronavirus pandemic in 2020, this steady and relentless increment in energy demand experienced in recent times is expected to continue for several more decades, in parallel to global demography. This is because world population growth might not reach a plateau until the end of this century, even if natural increase rates are slowing down. Although energy use is extraordinarily unequal across the planet, the overall current trend is also one of increasing energy demand in relative terms, that is, each generation consumes more energy per person than the previous one. In terms of sustainability, and considering that an excess of energy use above a certain threshold does not lead to improved living standards, an optimal and reasonable average annual per capita energy consumption at 2.8 tons of oil equivalent (toe) has been advocated [4]. Along these lines, global energy production would have to almost double up to almost 3×10^5 TWh in 2050. It is apparent that coping with demand from our near-future energy-hungry societies will represent a gigantic challenge. Therefore, energy security will also require judicious consumption and smart and efficient production, distribution, and use systems [5].

Photocatalytic Hydrogen Production for Sustainable Energy, First Edition. Edited by Alberto Puga.

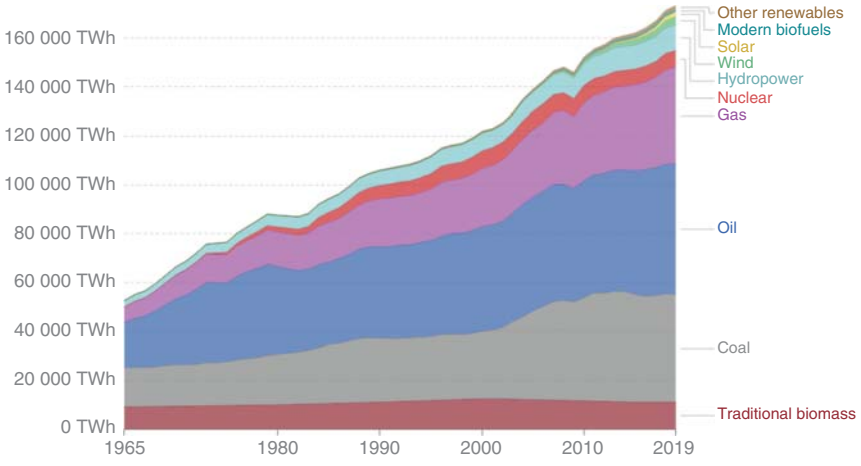

Figure 1.1 Global primary energy supply by source since 1965. Traditional biomass represents raw or gently processed solid fuels such as wood, peat, or charcoal. Modern biofuels include biomass-derived liquid fuels such as biodiesel or bioethanol. Source: OurWorldInData.org/energy, based on data from Refs. [1, 3]; Creative Commons 2022 Our World In Data.

Regarding the shares of different sources in our energy mix, it is striking to note that little has changed in the last half century besides the surge of nuclear power and the rather modest development of renewables. In fact, fossil fuels represented almost 80% of all primary energy supply in 2019 (Figure 1.1). This situation is evolving along a decarbonization pathway owing to the formidable improvement of solar and wind energy technologies, which are becoming cost-competitive at a rapid pace, motivated by the depletion of fossil fuels and the dreadful negative effects of CO_2 emissions on the global climate (see following sections). However, it is naive to assume that the enormous amounts of fossil fuel in use today (see Figure 1.1) will be easily replaced with renewables.

1.1.2 Fossil Reserves

The depletion of reserves of carbon-based fossil fuels, chiefly natural gas, crude oil, and coal, is proceeding at a rapid pace due to our obstinate dependence on them. Proponents of persisting on their mass extraction and exploitation argue that technological advances are constantly enabling new discoveries. Therefore, the so-called proven reserves – i.e. those accessible with current technologies – have been increasing, being hitherto able to meet demand in a satisfactory fashion. It should be noted, though, that most of the newly discovered oil and gas fields are nonconventional and/or extremely difficult to reach, such as extra heavy crude, tar sands, shale oil and gas, or deep offshore fields.

The data in Table 1.1 establish a comparison of reserves and consumption data. Proven reserves in present times are significant, but somewhat lower than total reserves by the end of last century. These numbers must be taken with care due

Table 1.1 Comparison of total reserves, proven reserves, and consumption of fossil fuels.

	Amounts of fossil fuels/Gt(C)			
	Total reserves[a)]	Proved reserves in 2020[b)]	1965–2020 Consumption[b)]	Reserves-to-production ratio[b)]/y
Gas	140	96	60	49
Oil	230	208	155	54
Coal	3510	752	162	139

a) According to geological inventories performed in the late twentieth century [6].
b) According to the BP Statistical Review of World Energy [3].

to the uncertainty in their estimation methods, but it is important to note that most of the existing oil and gas (coal is an exception) can be accessed using current means. What is even more relevant is assessing how much of the fossil fuel reserves have been already used and how much is still left. Only during the last 55 years, a significant proportion of all initially available crude oil and natural gas has been used by humanity (e.g. 155 and 60 Gt(C) equivalent, respectively, as compared to 208 and 96 Gt(C) in predicted reserves as of 2020, see Table 1.1). It should be emphasized that proven reserves are expected to be progressively more challenging for future extraction, and hence, less efficient and more expensive. Another matter of concern is their concentration in certain areas of the planet, creating dramatic geopolitical tensions and conflicts for the control of production [7, 8].

Data in Table 1.1 clearly reveal that almost half of our underground battery of stored fossil oil and gas energy is already gone, and for obvious reasons, it will not be replenished to any practically meaningful extent on a human timescale. An unavoidable question follows: how long can we still rely on fossil fuels? One straightforward way to calculate this is the reserves-to-production ratio based on current data, which points to only another half century until total depletion of oil and gas (54 and 49 years, respectively, Table 1.1), and somewhat longer for coal. Future events may of course alter such projections, but based on all the above data, it would not be surprising if production of fossil fuels will stop being able to cope with world energy demand at some not-so-distant point, probably within the next couple of generations.

1.1.3 Carbon Dioxide Emissions and Global Warming

The finite nature of fossil fuels should be a strong enough argument in itself to seriously and strategically plan our economies ahead of their inaccessibility or depletion. In addition to that, their mass consumption is noticeably affecting global carbon cycles, especially with regard to emissions, and consequent atmospheric accumulation, of carbon dioxide [6, 9]. As illustrated in Figure 1.2, anthropogenic emissions pump more CO_2 into the atmosphere than nature is able to fixate into biomass or to store into oceans (9 Gt(C) emitted, vs. 3 and 2 Gt(C) used by plants and algae to grow or absorbed by oceans, respectively, Figure 1.2).

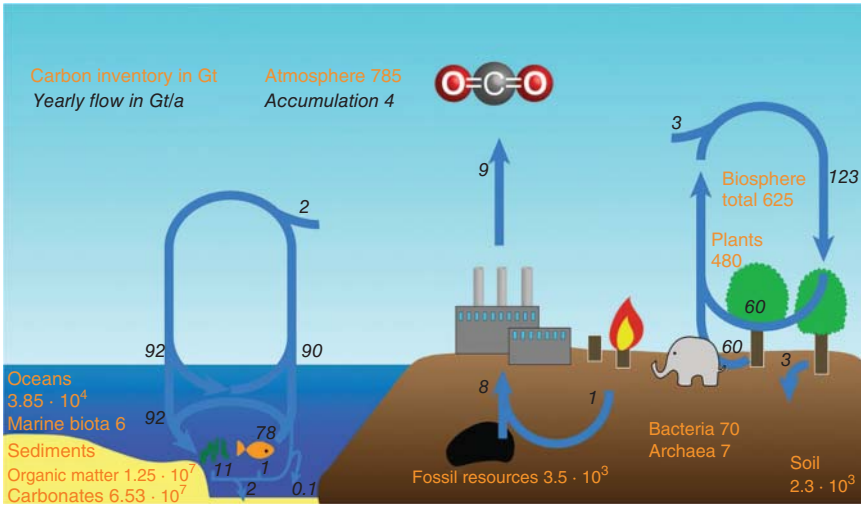

Figure 1.2 Global carbon inventories and flows on Earth, showing natural carbon cycle events and the influence of human activities. Source: P, Müller [9]/with permission of Royal Society of Chemistry.

Among the effects of CO_2 accumulation in the atmosphere, global warming is the most threatening and worrisome. The correlation of average temperatures with atmospheric CO_2 levels has been established even in a pre-industrial time frame with little influence from human activities, confirming its greenhouse effect [10]. Moreover, the extraordinary buildup of carbon dioxide in the Earth's atmosphere from burning fossil fuels in recent times is now completely out of doubt [6, 11]. The extent to which this will affect global climate is a matter of intense debate, but many different models predict a dangerous rise in temperatures, probably leading to other uncharted consequences such as extreme weather events.

1.1.4 Strategic Low-carbon Goals and Energy Sustainability

Both eventual shortages of fossil fuels and global warming due to the greenhouse effect of anthropogenically emitted CO_2 will sooner or later force humankind to a determined decarbonization. The sustainability of future energy schemes will thus largely depend on a successful transition from the current overexploitation of fossil fuels to the efficient and judicious use of renewable energy sources. Developing low-carbon, circular-carbon, or carbon-free energy sources are in principle valid options to strive on this ambitious goal.

The European Union has committed to become completely carbon-neutral, that is, to reduce its CO_2 emissions to net-zero, by 2050 [12]. In this context, the International Energy Agency has set out a comprehensive scrutiny of a range of technological options to effectively transition to decarbonized energy schemes within the same time span, emphasizing on the convenience of solar and wind electricity generation as key tools [13]. It should not be forgotten that containment of energy use to judicious per-capita amounts will be also crucial to achieve any

sustainability goals, albeit equality should also be ensured in fairness toward currently less favored communities, which require improvement of their living standards, as stressed in the United Nations' Sustainable Development Goals [14].

During such a challenging journey, the prevalence of natural gas over crude oil and coal as a low-carbon – yet still fossil – fuel and a renewed focus on nuclear power as an emissions-free way to produce electricity are also emerging as temporary means to maintain CO_2 emissions as low as possible.

Whatever the route chosen, a significant portion of energy demand that is currently met by fossil fuels will most likely require a shift toward electrification systems. This is a grand challenge considering that this amounts to more than 80% of global energy supply (Figure 1.1). Sectors such as transportation, especially by air and waterborne means, are extremely difficult to electrify. A more realistic option in this regard would be the use of nonfossil, low-carbon, storable chemical fuels of sustainable origin, among which, hydrogen is expected to play a major role.

1.2 Hydrogen as Renewable Energy Carrier

1.2.1 The Colors of Hydrogen: Toward Clean Hydrogen

Hydrogen is regarded as a versatile and potentially cost-competitive energy carrier, which may complement and even replace electrical grids and batteries for a number of final applications, especially in heavy industry and transportation sectors [15]. Not surprisingly, both public institutions and private corporations (alone or allied) are turning their efforts to consolidate hydrogen development projects. For example, the European Green Deal decidedly relies on decarbonization via its Hydrogen Strategy [16].

Most hydrogen currently produced is derived from fossil resources (*ca.* 95%), whereas some is obtained by electrolysis, historically as a by-product of the chlor-alkali process (*ca.* 5%) [7, 17]. This situation is rapidly evolving with the advent of a myriad of new green hydrogen projects. But what do we mean by green hydrogen? This term encompasses a set of technologies based on the production of hydrogen using renewable energy sources and involving zero-carbon or at least low-carbon emissions [15]. By contrast, hydrogen from fossil fuels has been given other color codes depending on its source and production process (Figure 1.3), such as:

- black hydrogen: from coal gasification,
- gray hydrogen: from natural gas reforming, or
- blue hydrogen: from natural gas reforming with carbon capture and storage.

Not further commented herein, other color codes have been proposed:

- brown hydrogen: by the gasification of lignite or other low-quality coal feedstocks,
- turquoise hydrogen: by thermal methane splitting (solid carbon as a by-product instead of CO_2),
- pink hydrogen: by water electrolysis using nuclear power, or
- yellow hydrogen: by water electrolysis using grid energy.

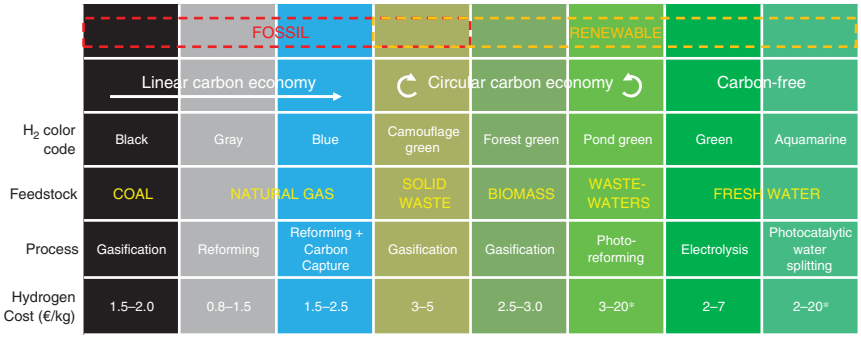

Figure 1.3 Comparative diagram summarizing different hydrogen production technologies according to the sustainability of the processes, defined by the H_2 color codes. Sustainability increases from left to right. The feedstocks used as hydrogen precursors range from fossil to waste, biomass, and ultimately pure water, representing the paradigm of green hydrogen. Costs of hydrogen have been collected from Refs. [15, 18–22]; asterisks indicate estimates based on techno-economic assessments.

Genuinely, green hydrogen refers to hydrogen that is produced by water electrolysis using renewable electricity, chiefly derived from solar or wind energy. Other renewable hydrogen production processes have not been unambiguously categorized. It is herein proposed (see Figure 1.3) to code them as follows:

- forest green hydrogen: from biomass gasification,
- camouflage green hydrogen: from the gasification of solid waste (e.g. mixed plastic, unrecyclable fraction of municipal solid waste, food waste, or dried sludge),
- pond green hydrogen: produced by the photoreforming of wastewaters, and
- aquamarine hydrogen: produced by photocatalytic water splitting.

1.2.2 Costs of Hydrogen Production

Prices of green hydrogen are in the range of €3–7/kg(H_2) in most common cases, whereas hydrogen from fossil fuels is still somewhat cheaper, with levelized costs as low as *ca.* €0.8–1.5/kg(H_2) for production by steam reforming of natural gas, and less than €2/kg(H_2) for coal gasification (Figure 1.3). So-called blue hydrogen, that is, produced by steam reforming of natural gas coupled with carbon dioxide capture and sequestration, is around or slightly above €2/kg(H_2) [15]. It is convenient to remark here that, as global prices of fossil fuel raw energy materials are sharply rising as this book is being written, the estimated costs of black, gray, and blue hydrogen listed in Figure 1.3 are also expected to increase significantly. This might well be a transient situation due to tensions in the geopolitical arena and, consequently, in the fossil fuel market, but the unavoidable scarcity of natural gas, crude oil, and coal in the mid-term future will most likely drive nonrenewable hydrogen costs to permanently uncompetitive levels.

Current green hydrogen costs are rapidly approaching an acceptable target for competitiveness as compared to processes fed with fossil fuels. With the

formidable development in and deployment of solar photovoltaics and wind turbines, renewable electricity is becoming cheaper than that obtained by power plants based on the combustion of fossil fuels. Moreover, continued electrolysis scale-up and optimization are bringing green hydrogen production costs down at an unprecedented pace. In favorable situations, renewable hydrogen can be even below €1.5/kg(H_2) [15]. This represents a change of paradigm toward green energy being more affordable than that produced from fossil fuels. Photocatalytic water splitting, whereby direct conversion of solar energy into hydrogen takes place, might represent a breakthrough in sustainable energy schemes given its simplicity. The technology is still immature, and efficiencies are rather low. For a typical solar-to-hydrogen efficiency at 0.75%, photocatalytic hydrogen would be expensive using state-of-the-art materials and reactors (€17/kg(H_2) [22]), but projections indicate encouraging reductions in costs if performance and durability issues can be overcome, especially in the case of photoelectrochemical approaches (Figure 1.3).

In an intermediate category of hydrogen production processes between fossil- and water-derived, a series of alternative emergent approaches can be considered. The most relevant examples are the gasification of either biomass or solid waste; some initiatives have achieved commercialization of such technologies. The reforming of organic matter, entailing its conversion into hydrogen and carbon dioxide under anaerobic conditions, is a milder catalytic route enabling energy recovery. Interestingly, the process can be activated by light in the presence of photocatalysts, as further commented below (Section 1.3.3). These waste valorization, circular-carbon, processes can result in remarkably competitive hydrogen production (below €3/kg(H_2), see Figure 1.3).

1.2.3 Solar Fuels and Synthetic Fuels

The production of solar hydrogen is a milestone of renewable green energy since it unifies the harnessing of solar light as a primary energy source and the use of a, theoretically, carbon-free fuel. Not only these sustainability credentials, but also the fact that the relentless reduction in photovoltaic electricity generation costs encourages investment, are resulting in a burgeoning wave of solar green hydrogen projects. Therefore, the production of hydrogen by photovoltaics-electrolysis represents a perfect embodiment of solar fuel technologies.

Photocatalysis offers the advantage of using and/or converting solar irradiation for the production of hydrogen in one step, that is, without the requirement of firstly generating electricity and transporting it to an electrochemical device. Unfortunately, overall efficiencies are still lower for photocatalytic hydrogen production than for the two-step photovoltaics–electrolysis process [22]. Hybrid photoelectrochemical systems are at a more advanced technology readiness level than purely photocatalytic counterparts, although engineering complexity and durability are still hurdles to overcome for their consolidation [23].

Other renewable solar fuel technologies are being investigated and on occasions tested on pilot plant demonstration levels. The most relevant examples are summarized herein. Thermosolar catalysis can be applied to water splitting and a range of

other processes leading to solar fuels [22, 24]. Carbon dioxide reduction is a truly sustainable option if performed from the artificial photosynthesis perspective [25]. The solar conversion of waste into fuels is an emerging field of research offering interesting energetic valorization and circular-carbon opportunities [26]. Finally, and obviously based on or inspired by natural photosynthesis, a myriad of sunlight-powered photobiological processes can be designed to produce fuels [22]. Not all these processes involve carbon-free hydrogen production, but most are aligned with a circular-carbon economy.

Green hydrogen is undeniably the cornerstone of decarbonization strategies. However, carbon-based solar fuels may also hold a prevalent position in future energy schemes. Circular-carbon strategies such as the capture and conversion of CO_2 into fuels, or waste-to-fuels valorization, will be useful to achieve sustainability goals. Moreover, the use of green hydrogen for the production of synthetic fuels and chemicals (e.g. methane, methanol, liquid hydrocarbon fuels, olefins, or ammonia) is gaining ground with the advent of affordable renewable energy. The hydrogenation of CO_2 is reminiscent of Fischer–Tropsch processes and readily leads to recycled carbon substances that can be stored more easily than hydrogen itself [27–29]. For example, synthetic methane or methanol produced via this route can thus be directly distributed by existing infrastructure such as pipelines and tankers, and eventually utilized by chemical sites, other industries, or even households [30].

1.3 The Opportunity for Photocatalytic Hydrogen

Hydrogen production by photocatalysis was completely unknown 50 years ago. Today, research activity in this area is burgeoning, as evidenced by an exponential growth in the number of publications year-over-year [22]. This has been motivated by the frantically and eagerly pursued goal of achieving the direct conversion of solar energy into a chemical fuel using only water as the feedstock, that is, overall water splitting [8, 31]. Hundreds, if not thousands, of new materials have been synthesized and tested for such a purpose. Remarkably high photocatalytic hydrogen production efficiencies have been attained for many different systems, yet most often using reducible substances as electron donors, thus impairing the elusive oxidation half-reaction to generate O_2 as the by-product. Conversely, overall photocatalytic water splitting represents a grand challenge requiring sophisticated materials and engineering design and/or activation by highly energetic photons (mostly in the UV frequencies), which represent a relatively small fraction of solar radiation energy. In view of this, the scientific community is striving to advance on two fronts: one is to more decidedly investigate the feasibility of photocatalytic hydrogen from water (aquamarine hydrogen, as defined herein, see Figure 1.3), and the other to re-invent and re-define advantageous processes that produce hydrogen from different feedstocks using light. The following subsections briefly introduce such approaches, whereas the different chapters in this book delve into specific examples on different areas.

1.3.1 Photoelectrocatalytic Water Splitting

The electrolysis of aqueous solutions has been known and practiced widely, mostly for the production of chlorine and caustic soda, since the end of the eighteenth century [32]. A renaissance in electrolysis technologies is currently taking place in the context of green hydrogen generation from pure water (see Section 1.2.1 above). The use of light to assist the electrolytic dissociation of water was firstly discovered by Fujishima and Honda in the early 1970s, who succeeded in producing O_2 from TiO_2 photoelectrodes under UV-visible irradiation at potentials remarkably less positive (i.e. milder) than the standard potential [33]. Figure 1.4 shows the original diagram of the photoelectrochemical cell designed, showing how a typical electrolysis cell was adapted for irradiation of the photoanode through a suitably transparent window, whereas the rest of the design was essentially unchanged. This pioneering discovery marked the start of a formidably active field of research based on the promoting effect of light (and electricity) for hydrogen production via photo(electro)catalytic processes using mostly inorganic active catalytic materials.

Multiple variations of the photoelectrochemical cell shown in Figure 1.4, on occasions entailing a high degree of sophistication, have been reported [22]. The use of double light-activation (i.e. photocathode–photoanode systems) may lead to effective unassisted photoelectrochemical water splitting, and this has encouraged intense investigation. A detailed account of such systems is presented in Chapters 5 and 6 of this book.

A breakthrough in photoelectrochemical systems is the integration of photovoltaic materials with electrocatalysts [23]. The former absorb light and enable separation of photogenerated charge carriers, whereas the latter provide kinetically feasible pathways for charge transfer to water and the subsequent hydrogen and oxygen evolutions. Integration of multijunction photovoltaics in photoanodes and electrical connection to cathodes has generally led to superior activities, although other combinations are also possible. Moreover, electrodes can be connected either

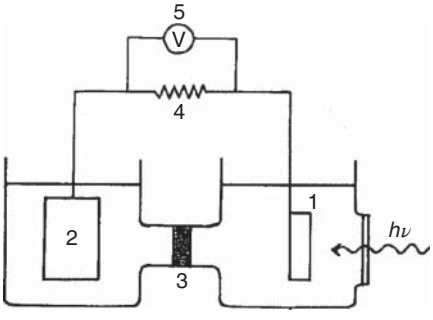

Figure 1.4 Scheme of the cell in the original article by Fujishima and Honda reporting the first photoelectrochemical process for overall water splitting. Irradiation of a TiO_2 photoanode (1) facilitated oxygen gas evolution, whereas a platinum black cathode (2) was used for hydrogen evolution in the dark; a compartment separator (3) was used for ionic transport; and an electrical circuit (4, 5) allowed electron transport from photoanode to cathode. Source: Fujishima A, Honda K. [33]/with permission of Nature Publishing Group.

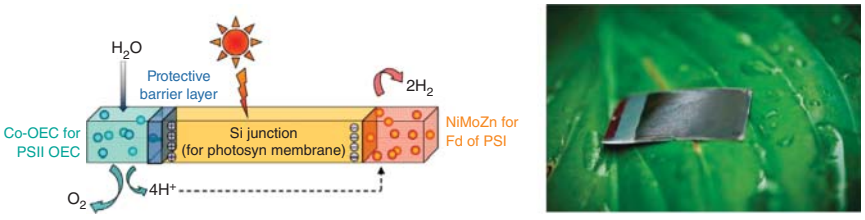

Figure 1.5 Left: Diagram of a wireless photoelectrochemical cell constructed by a back-to-back assembly of a triple junction amorphous silicon photovoltaic membrane as the light-absorbing material, and cobalt-based oxygen evolution and Ni–Mo–Zn hydrogen evolution catalysts (OEC and HEC, respectively). The OEC and HEC are inspired by photosystem II and photosystem I structures, respectively, found in natural photosynthetic organisms. Right: An aspect of an artificial leaf based on the wireless photoelectrochemical design. Source: Nocera DG. [34]/with permission of American Chemical Society.

externally (wired configuration) or in an integrated fashion (wireless configuration) [23]. A notable example of the wireless design is the artificial leaf developed by Nocera and co-workers, whereby triple junction amorphous silicon semiconductors were interfaced with appropriate Earth-abundant electrocatalysts, namely, a self-healing cobalt-based oxygen evolution catalyst and a Ni–Mo–Zn hydrogen evolution catalyst [34, 35]. The wireless photoelectrochemical cell design and an artificial leaf based on such a concept are shown in Figure 1.5. Importantly, these photoelectrocatalytic leaves split water with no electrical energy input or circuit, and can be considered closer to photocatalytic systems in practical terms.

1.3.2 Photocatalytic Water Splitting

The photocatalytic approach is presumably a distinct possibility to harness solar irradiation by directly using it to activate chemical reactions. On the other hand, overall water splitting is a convenient and clean way to store energy in a chemical fashion. For these reasons, photocatalytic water splitting is fiercely sought after as a sustainable and clean pathway to store solar energy [36–38]. The downside of this approach is that combining all efficiency requirements in a single photocatalytic material is an elusive goal [39].

The simplest possible photocatalyst configuration consists of a particulate semiconductor furnished with redox active sites for hydrogen and oxygen evolution, most commonly as deposited co-catalysts (see Figure 1.6). A clear limitation to this is related to energy levels and thermodynamics, since valence and conduction bands should lie more positive and more negative than the O_2/H_2O and H_2O/H_2 redox potentials, respectively. Moreover, overpotentials are generally required for efficiency, and hence, photon energy must be higher than that of the free energy change for water splitting plus those additional potentials. In practice, the band gaps of photocatalysts tend to be large (>3 eV), thus limiting the portion of the usable solar spectrum mostly to the UV region. An alternative solution is the combination of two semiconductors in a Z-scheme configuration inspired by the biochemical machinery of photosynthetic organisms [40]. One of the semiconductors may have lower-lying energy levels than the other, so that they are appropriately aligned with

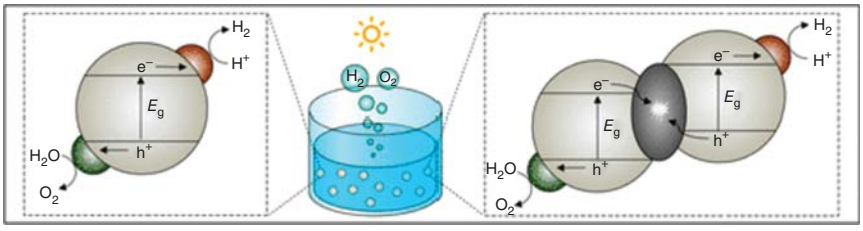

Figure 1.6 Representation of single semiconductor (left) and double-semiconductor Z-scheme (right) designs for overall water splitting photocatalysts incorporating dedicated co-catalysts for H_2 and O_2 evolution. Reproduced with permission from Ref. [22]; Creative Commons 2022 American Chemical Society.

oxygen and hydrogen evolution redox potentials, respectively, and the band gaps may be smaller, in theory enhancing visible light activation.

Excellence in photocatalytic materials has led to impressive progress in water splitting for both single particle and Z-scheme designs [41]. Record-breaking solar-to-hydrogen efficiencies exceeding 1% are being reported in recent years [22], motivating further research and development to improve performances. This is still far away from the arbitrary 10% solar-to-hydrogen energy conversion target for cost competitiveness [18], but a more reasonable medium-term goal at 5% might not be so distant provided new disruptive knowledge on photocatalytic materials and cost reductions upon scale-up can be attained.

1.3.3 Photocatalytic Hydrogen from Various Feedstocks by Photoreforming

Beyond overall water splitting, other substrates can be transformed by photocatalysis to generate hydrogen and other products. A recurring example is that of aqueous halides, which can be also split into elemental hydrogen and halogen, the latter being also a valuable commodity [42–44]. This is the case for chlorine and hypochlorite typically produced by the electrolytic chlor-alkali process, as mentioned above (see Sections 1.2.1 and 1.3.1).

In addition to halogens, nitrogen compounds are relevant since they are ubiquitous in water effluents from domestic, agricultural, and farming activities. Photocatalytic decomposition of urea or even urine [45–47], ammonia [48], and ultimately amino acids, proteins, or their metabolites [46] has been explored, also aiming at selective transformation into elemental nitrogen and hydrogen gases. Importantly, the reverse reduction of N_2 to NH_3 has also been observed [46, 49, 50]. Reduced sulfur species such as sulfides can be also used as substrates for the photocatalytic production of hydrogen [26]. Recovery of solid elemental sulfur has been proposed as a convenient way to deal with waste streams containing sulfide [51].

Needless to say, employing alternatives to water (maybe more correctly, additional substrates) as the electron donors in the overall redox reaction must be the result of a sensible choice leading to advantageous outcomes. However, many reports on photocatalytic production of hydrogen have relied on the use of sacrificial electron

donors to accelerate hydrogen production rates (otherwise limited by the generally sluggish kinetics of O_2 evolution) without caring about their fate or recyclability [52]. Examples include sulfides/sulfites and a range of model organic substances such as alcohols or saccharides, most of which are too valuable *per se* to justify their conversion into hydrogen. Notwithstanding this, if they constitute low-value streams of challenging valorization, transformation into hydrogen might be a profitable approach.

The photocatalytic production of hydrogen from organic substances under anaerobic conditions can be categorized into the so-called photoreforming processes [53, 54]. Ultimately, the organic carbon may be mineralized into CO_2. Oxidation of most organics is both thermodynamically and kinetically more favorable and straightforward than oxygen evolution from water. Early discoveries in this field using semiconductor photocatalysts were reported by Kawai, Sakata, and coworkers from the late 1970s onward. They succeeded in generating hydrogen from aqueous solutions of a range of organic compounds, and most surprisingly, also from insoluble lipids or organic solids such as fats, carbon, cellulose, synthetic polymers, algae, plants, and insects [46, 55, 56]. Photocatalysis appeared to be a powerful tool to generate hydrogen from recalcitrant organic matter of diverse origins, and under remarkably mild, nearly ambient, conditions.

Photoreforming of wastewaters [26], solid waste including plastics [19], raw biomass [57], or biomass derivatives in a biorefinery concept [53, 58, 59] is currently and increasingly considered as valorization options for otherwise challenging streams. Chapters 9 and 10 in this book deal with the photocatalytic conversion of biomass derivatives for hydrogen production, whereas Chapter 11 focuses on the photoreforming of wastewaters. Projections suggesting room for commercial opportunity are stimulating decided initiatives to develop photocatalytic waste-to-hydrogen processes from a laboratory curiosity to real technology. Teams such as those in the solar platform of Almeria (Spain) led by Malato and co-workers have paved the way by adopting their concentrating sunlight reactors for hydrogen production [60, 61]. Reisner and co-workers performed a techno-economic assessment for the photoreforming of solid plastic waste and hinted at what a solar hydrogen production plant based on such a process might look like (Figure 1.7). Finally, opportunities for photocatalytic organic synthesis giving rise to hydrogen as a co-product from diverse substrates have the incentive of generating high-value substances by a sustainable and atom-economic process [62]. Chapter 8 by Fornasiero and co-workers delves into this topic.

The preceding paragraphs outline several useful classes of photocatalytic transformations involving hydrogen production from tremendously variate substrates. The solar option is the preferred activation mode given the virtually free energetic cost, albeit the use of artificial light might prove useful or necessary in some instances. Whatever the irradiation source, a benefit must be ensured regarding the oxidation half-reaction, be it the degradation of an inconvenient waste or the generation of a valuable co-product.

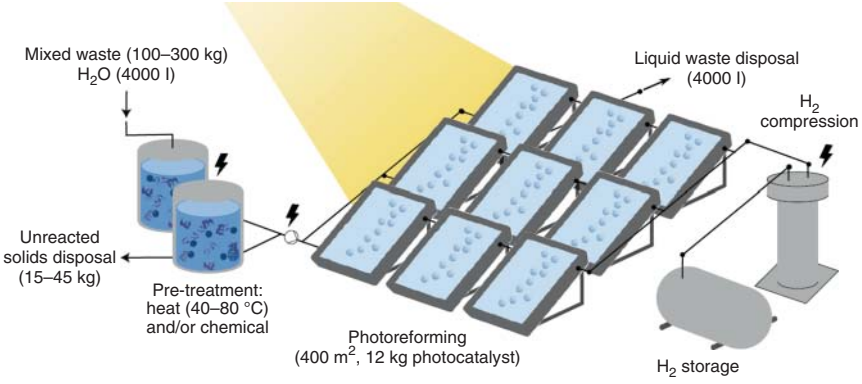

Figure 1.7 Illustration of a projected solar pilot plant for the production of hydrogen by photoreforming of solid waste in water. Source: Uekert et al. [19]/with permission of Springer Nature Limited.

1.3.4 Photobiocatalytic Hydrogen

The term photocatalysis in its broadest dimension comprises any biological transformations promoted by light, mostly sunlight, since these involve the absorption of photons, their use to generate charge carriers, and the eventual catalytic action of enzymes, thanks to an incredibly complex biochemical machinery [63]. Natural photosynthesis is probably the most sublime example of photocatalysis, and maybe also of solar energy use, allowing the creation of life on Earth. Compared with it, even state-of-the-art artificial photosynthetic processes can be viewed as rather rudimentary.

As a hybrid between photobiological and artificial photocatalytic systems, the combination of synthetic materials and reaction setups with microorganisms is a worthwhile and exciting field of research in its own right. The biological part might play a role in absorbing light, promoting chemical reactions, or both. At a lower degree of biotechnological implications, the coupling of enzymes or biomimetic synthetic organometallic substances as co-catalysts into inorganic photocatalysts has attracted significant attention [64, 65]. A typical example is the use of hydrogenases to provide active sites for the hydrogen evolution reaction.

Photobiocatalysis is a relatively unexplored technology as compared to its other photocatalytic counterparts [22, 23]. Curiously, the discovery of photobiological hydrogen production by algae in a light-promoted fermentative process was the first ever reported photocatalytic technology for the purpose, dating back to 1942 [66]. Two main approaches have been adopted: (i) biophotolysis, as a biochemical embodiment of overall water splitting; and (ii) photofermentation, whereby microorganisms thrive under sunlight irradiation in the presence of biomass-based feed, enabling the evolution of hydrogen under anaerobic conditions.

The singularity of photobiological hydrogen production deserves attention from the scientific community, although unfortunately, it is not further accounted for in this book. It would be good news should an explosion in this fascinating field of research be witnessed by future generations.

1.4 Outlook

Photocatalysis requires essentially a source of light and an appropriate redox photoactive material. On a fundamental level, electromagnetic energy is absorbed, channeled, and harnessed to drive chemical reactions. Energy can be only utilized for the activation of thermodynamically spontaneous processes (e.g. aerobic oxidation of organics) or also stored in chemical products of endergonic ones (e.g. overall water splitting or natural photosynthesis). The complexity of the photocatalytic system may vary greatly depending on the specific transformation taking place, but in general terms, activation by light proceeds under near-ambient conditions. Additional energy might be also applied in the form of, *inter alia*, electricity or heat, but mild operation conditions are a clear advantage of photocatalytic processes over their classical thermocatalytic counterparts.

Generating hydrogen by photocatalysis is certainly possible in a formidable variety of systems. However, an assessment of each process must be undertaken to ensure its merits, be they economic, environmental, or energetic. Considering a specific case, the production of hydrogen by the photoreforming of alcohols might proceed rapidly and at an outstanding quantum efficiency close to 100%, but it may be meaningless to do so since the value of the starting alcohols might be even higher than that of the produced hydrogen. Notwithstanding this, one could consider a process of this kind still useful if a simple alcohol such as methanol is used as a high volumetric energy density carrier of hydrogen for eventual use in fuel cells. From a different perspective, the photoreforming of a range of organic (or inorganic) substances can make sense for the energetic valorization of waste streams or in high-added-value synthetic processes.

The most popular and intensely sought objective of photocatalysis is the storage of solar energy into chemical energy by artificial photosynthetic processes, namely overall water splitting and carbon dioxide reduction. The former is seen as the quintessence of renewable and sustainable energy schemes, since it goes beyond the green credentials of hydrogen produced by photovoltaics followed by electrolysis, due to its presumably enhanced simplicity and affordability. Photocatalytic hydrogen by overall water splitting has been given here aquamarine as a color code denoting extreme cleanliness. The bad news lies in the fact that efficiencies using state-of-the-art systems are still far from the desirable threshold (5%) for consolidation of the technology in terms of competitiveness. Surpassing this landmark in the near future would be a game-changer, provided the environmental and societal impact of mining and supplying materials for the required photocatalysts on a gigantic scale globally to meet energy demand can be kept within reasonable levels. We should not be surprised if, in addition to technological advancements, our exorbitant thirst for energy will have to be restrained to some extent to maintain a peaceful balance with energy production. Ultimately, humankind must assume that our planet has its limits.

Acknowledgments

A.P. thanks the Spanish Ministry of Science and Innovation, the Spanish Research State Agency, (MCIN/AEI/10.13039/501100011033) and the European Social Fund for a "Ramón y Cajal" contract (RYC-2017-22849).

References

1 Smil, V. (2016). *Energy Transitions: Global and National Perspectives*, 2nd ed. Praeger.
2 Hudson, P. (2014). *The Industrial Revolution*. London: Hodder Arnold.
3 (2021). *Statistical Review of World Energy 2021*, 7th ed. BP.
4 Armaroli, N. and Balzani, V. (2016). Solar electricity and solar fuels: status and perspectives in the context of the energy transition. *Chem. Eur. J.* 22 (1): 32–57.
5 IEA (2020). *Key World Energy Statistics 2020*. Paris: International Energy Agency https://www.iea.org/reports/key-world-energy-statistics-2020.
6 Falkowski, P., Scholes, R.J., Boyle, E. et al. (2000). The global carbon cycle: a test of our knowledge of Earth as a system. *Science* 290 (5490): 291–296.
7 Armaroli, N. and Balzani, V. (2010). *Energy for a Sustainable World: From the Oil Age to a Sun-Powered Future*. Wiley.
8 Armaroli, N. and Balzani, V. (2007). The future of energy supply: challenges and opportunities. *Angew. Chem. Int. Ed.* 46 (1+2): 52–66.
9 Tomkins, P. and Müller, T.E. (2019). Evaluating the carbon inventory, carbon fluxes and carbon cycles for a long-term sustainable world. *Green Chem.* 21 (15): 3994–4013.
10 Lüthi, D., Le Floch, M., Bereiter, B. et al. (2008). High-resolution carbon dioxide concentration record 650,000–800,000 years before present. *Nature* 453 (7193): 379–382.
11 Keeling, R.F. (2008). Recording Earth's vital signs. *Science* 319 (5871): 1771.
12 Directorate-General for Climate Action (2019). *Going climate-neutral by 2050: a strategic long-term vision for a prosperous, modern, competitive and climate-neutral EU economy*. European Commission.
13 Bouckaert, S., Pales, A.F., McGlade, C. et al. (2021). *Net Zero by 2050, A Rodmap for the Global Energy sector*. Paris: International Energy Agency.
14 (2020). *The Sustainable Development Goals Report*. United Nations.
15 Gielen, D., Taibi, E., and Miranda, R. (2019). *Hydrogen: A Renewable Energy Perspective*. International Renewable Energy Agency (IRENA).
16 Directorate-General for Research and Innovation (2020). Research & Innovation key driver of the hydrogen strategy. European Commission.
17 Armaroli, N. and Balzani, V. (2011). The hydrogen issue. *ChemSusChem* 4 (1): 21–36.

18 Shaner, M.R., Atwater, H.A., Lewis, N.S., and McFarland, E.W. (2016). A comparative technoeconomic analysis of renewable hydrogen production using solar energy. *Energy Environ. Sci.* 9 (7): 2354–2371.

19 Uekert, T., Pichler, C.M., Schubert, T., and Reisner, E. (2020). Solar-driven reforming of solid waste for a sustainable future. *Nat. Sustainability* 4 (5): 383–391.

20 Navarro, R.M., Sánchez-Sánchez, M.C., Alvarez-Galvan, M.C. et al. (2009). Hydrogen production from renewable sources: biomass and photocatalytic opportunities. *Energy Environ. Sci.* 2: 35–54.

21 Pinaud, B.A., Benck, J.D., Seitz, L.C. et al. (2013). Technical and economic feasibility of centralized facilities for solar hydrogen production via photocatalysis and photoelectrochemistry. *Energy Environ. Sci.* 6 (7): 1983–2002.

22 Song, H., Luo, S., Huang, H. et al. (2022). Solar-driven hydrogen production: recent advances, challenges, and future perspectives. *ACS Energy Lett.* 7 (3): 1043–1065.

23 Liu, G., Sheng, Y., Ager, J.W. et al. (2019). Research advances towards large-scale solar hydrogen production from water. *EnergyChem* 1 (2): 100014.

24 Mateo, D., Cerrillo, J.L., Durini, S., and Gascon, J. (2021). Fundamentals and applications of photo-thermal catalysis. *Chem. Soc. Rev.* 50 (3): 2173–2210.

25 Li, K., Peng, B., and Peng, T. (2016). Recent advances in heterogeneous photocatalytic CO_2 conversion to solar fuels. *ACS Catal.* 6 (11): 7485–7527.

26 Jeon, T.H., Koo, M.S., Kim, H., and Choi, W. (2018). Dual-functional photocatalytic and photoelectrocatalytic systems for energy- and resource-recovering water treatment. *ACS Catal.* 8 (12): 11542–11563.

27 Centi, G., Quadrelli, E.A., and Perathoner, S. (2013). Catalysis for CO_2 conversion: a key technology for rapid introduction of renewable energy in the value chain of chemical industries. *Energy Environ. Sci.* 6 (6): 1711–1731.

28 Puga, A.V. (2018). On the nature of active phases and sites in CO or CO_2 hydrogenation catalysts. *Catal. Sci. Technol.* 8: 5681–5707.

29 Aresta, M., Dibenedetto, A., and Angelini, A. (2014). Catalysis for the valorization of exhaust carbon: from CO_2 to chemicals, materials, and fuels. Technological use of CO_2. *Chem. Rev.* 114 (3): 1709–1742.

30 Olah, G.A., Goeppert, A., and Prakash, G.K.S. (2009). *Beyond Oil and Gas: The Methanol Economy*, 2e. Wiley-VCH Verlag.

31 Balzani, V., Credi, A., and Venturi, M. (2008). Photochemical conversion of solar energy. *ChemSusChem* 1 (1-2): 26–58.

32 Bommaraju, T.V., Lüke, B., O'Brien, T.F., and Blackburn, M.C. Chlorine. In: *Kirk-Othmer Encyclopedia of Chemical Technology*. (Ed.), https://doi.org/10.1002/0471238961.0308121503211812.a01.pub2.

33 Fujishima, A. and Honda, K. (1972). Electrochemical photolysis of water at a semiconductor electrode. *Nature* 238: 37–38.

34 Nocera, D.G. (2012). The artificial leaf. *Acc. Chem. Res.* 45: 767–776.

35 Reece, S.Y., Hamel, J.A., Sung, K. et al. (2011). Wireless solar water splitting using silicon-based semiconductors and earth-abundant catalysts. *Science* 334: 645–648.

36 Takanabe, K. (2017). Photocatalytic water splitting: quantitative approaches toward photocatalyst by design. *ACS Catal.* 7 (11): 8006–8022.

37 Kim, J.H., Hansora, D., Sharma, P. et al. (2019). Toward practical solar hydrogen production – an artificial photosynthetic leaf-to-farm challenge. *Chem. Soc. Rev.* 48 (7): 1908–1971.

38 Chen, S., Takata, T., and Domen, K. (2017). Particulate photocatalysts for overall water splitting. *Nat. Rev. Mater.* 2 (10): 17050.

39 Idriss, H. (2020). The elusive photocatalytic water splitting reaction using sunlight on suspended nanoparticles: is there a way forward? *Catal. Sci. Technol.* 10 (2): 304–310.

40 Wang, Y., Suzuki, H., Xie, J. et al. (2018). Mimicking natural photosynthesis: solar to renewable H_2 fuel synthesis by Z-scheme water splitting systems. *Chem. Rev.* 118 (10): 5201–5241.

41 Hisatomi, T. and Domen, K. (2019). Reaction systems for solar hydrogen production via water splitting with particulate semiconductor photocatalysts. *Nat. Catal.* 2 (5): 387–399.

42 Bard, A.J. and Fox, M.A. (1995). Artificial photosynthesis – solar splitting of water to hydrogen and oxygen. *Acc. Chem. Res.* 28 (3): 141–145.

43 Teets, T.S. and Nocera, D.G. (2011). Photocatalytic hydrogen production. *Chem. Commun.* 47 (33): 9268–9274.

44 Antonietti, M. and Savateev, A. (2018). Splitting water by electrochemistry and artificial photosynthesis: excellent science but a nightmare of translation? *Chem. Rec.* 18 (7-8): 969–972.

45 Wang, G., Ling, Y., Lu, X. et al. (2012). Solar driven hydrogen releasing from urea and human urine. *Energy Environ. Sci.* 5 (8): 8215–8219.

46 Kawai, T. and Sakata, T. (1981). Photocatalytic hydrogen production from water by the decomposition of poly(vinyl chloride), protein, algae, dead insects, and excrement. *Chem. Lett.* 81–84.

47 Kim, J., Monllor-Satoca, D., and Choi, W. (2012). Simultaneous production of hydrogen with the degradation of organic pollutants using TiO_2 photocatalyst modified with dual surface components. *Energy Environ. Sci.* 5 (6): 7647–7656.

48 Yuzawa, H., Mori, T., Itoh, H., and Yoshida, H. (2012). Reaction mechanism of ammonia decomposition to nitrogen and hydrogen over metal loaded titanium oxide photocatalyst. *J. Phys. Chem. C* 116 (6): 4126–4136.

49 Schrauzer, G.N. and Guth, T.D. (1977). Photolysis of water and photoreduction of nitrogen on titanium dioxide. *J. Am. Chem. Soc.* 99 (22): 7189–7193.

50 Sakata, T. (1985). Photocatalysis of irradiated semiconductor surfaces – its application to water splitting and some organic-reactions. *J. Photochem.* 29 (1-2): 205–215.

51 Gonell, F., Puga, A.V., Julián-López, B. et al. (2016). Copper-doped titania photocatalysts for simultaneous reduction of CO_2 and production of H_2 from aqueous sulfide. *Appl. Catal., B* 180: 263–270.

52 Kamat, P.V. and Jin, S. (2018). Semiconductor photocatalysis: "tell us the complete story!". *ACS Energy Lett.* 3 (3): 622–623.

53 Puga, A.V. (2016). Photocatalytic production of hydrogen from biomass-derived feedstocks. *Coord. Chem. Rev.* 315: 1–66.

54 Christoforidis, K.C. and Fornasiero, P. (2017). Photocatalytic hydrogen production: a rift into the future energy supply. *ChemCatChem* 9 (9): 1523–1544.
55 Kawai, T. and Sakata, T. (1980). Conversion of carbohydrate into hydrogen fuel by a photocatalytic process. *Nature* 286 (5772): 474–476.
56 Kawai, T. and Sakata, T. (1979). Hydrogen evolution from water using solid carbon and light energy. *Nature* 282: 283–284.
57 Kuehnel, M. and Reisner, E. (2018). Solar hydrogen generation from lignocellulose. *Angew. Chem. Int. Ed.* 57 (13): 3290–3296.
58 Davis, K.A., Yoo, S., Shuler, E.W. et al. (2021). Photocatalytic hydrogen evolution from biomass conversion. *Nano Convergence* 8 (1): 6.
59 Granone, L.I., Sieland, F., Zheng, N. et al. (2018). Photocatalytic conversion of biomass into valuable products: a meaningful approach? *Green Chem.* 20 (6): 1169–1192.
60 Maldonado, M.I., López-Martín, A., Colón, G. et al. (2018). Solar pilot plant scale hydrogen generation by irradiation of Cu/TiO_2 composites in presence of sacrificial electron donors. *Appl. Catal., B* 229: 15–23.
61 Arzate Salgado, S.Y., Ramírez Zamora, R.M., Zanella, R. et al. (2016). Photocatalytic hydrogen production in a solar pilot plant using a Au/TiO_2 photo catalyst. *Int. J. Hydrogen Energy* 41 (28): 11933–11940.
62 Friedmann, D., Hakki, A., Kim, H. et al. (2016). Heterogeneous photocatalytic organic synthesis: state-of-the-art and future perspectives. *Green Chem.* 18 (20): 5391–5411.
63 Blankenship, R.E. (2002). *Molecular Mechanisms of Photosynthesis*. Wiley.
64 Wen, F. and Li, C. (2013). Hybrid artificial photosynthetic systems comprising semiconductors as light harvesters and biomimetic complexes as molecular cocatalysts. *Acc. Chem. Res.* 46 (11): 2355–2364.
65 Hennessey, S. and Farràs, P. (2018). Production of solar chemicals: gaining selectivity with hybrid molecule/semiconductor assemblies. *Chem. Commun.* 54 (50): 6662–6680.
66 Gaffron, H. and Rubin, J. (1942). Fermentative and photochemical production of hydrogen in algae. *J. Gen. Physiol.* 26 (2): 219–240.

2

Fundamentals and Concepts of Photocatalytic Hydrogen Evolution

Bunsho Ohtani[1], Fitri R. Amalia[2], Mahbub A. Akanda[2], and Mai Takashima[3]

[1] *Nonprofitable Organization touche NPO, 1-6-414, North 4, West 14, Sapporo 060-0004, Japan*
[2] *Hokkaido University, Institute for Catalysis, Sapporo 001-0021, Japan*
[3] *Graduate School of Engineering, Nagoya University, Furo-cho, Nagoya 464-8603, Japan*

2.1 Heterogeneous Photocatalysis

In this chapter, the authors are intending to describe the fundamentals of hydrogen evolution through heterogeneous photocatalysis, which can be defined as the reactions proceeding at the interface of a photoirradiated solid photocatalyst and gas or liquid phase (therefore a term "heterogeneous" is included). In a strict scientific sense, the requisites for heterogeneous photocatalysis (hereafter "photocatalysis") are (a) no (or not detectable) change in the structure of the photocatalyst by the reaction and (b) that the reaction is initiated by photoabsorption of the photocatalyst.

The well-known principle (or mechanism) of photocatalysis includes (i) photoexcitation of electron from the filled electronic state to the vacant electronic state, (ii) transfer of excited electron to a surface-adsorbed substrate to result in its reduction as well as transfer of positive hole, i.e. from the vacant electronic state, to a surface-adsorbed substrate to result in its oxidation, otherwise (iii) deexcitation to the original state, i.e. recombination of the excited electron and the positive hole occurs to give no chemical reaction. When a semiconductor is used as a photocatalyst, bandgap excitation from its filled valence band to its vacant conduction band happens upon photoirradiation of light of energy higher than the bandgap, but photocatalysis is not limited to the reaction through bandgap excitation. As long as a given reaction with a solid satisfies the requisites (a) and (b), the reaction can be called as photocatalysis [1–3].

2.2 Thermodynamic Description

As a general description, photocatalytic reaction through (i) reduction of a substrate adsorbed on the surface by photoexcited electron, i.e. a conduction-band electron, and (ii) oxidation of another (or same) substrate adsorbed on the surface by transferring an electron from the substrate to a photocatalyst, i.e. valence-band

Photocatalytic Hydrogen Production for Sustainable Energy, First Edition. Edited by Alberto Puga.

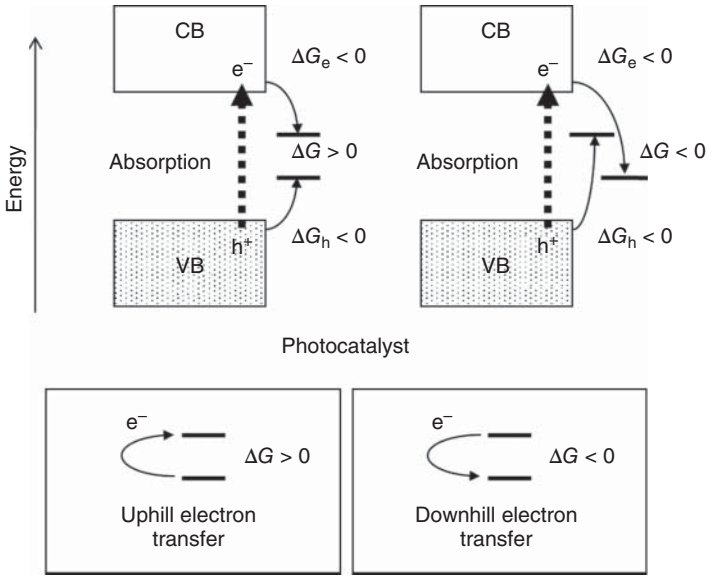

Figure 2.1 Thermodynamic principle, i.e. Gibbs-energy change, of photocatalysis by semiconducting materials. Photoexcited-electron (conduction band = CB) transfer and positive-hole (valence band = VB) transfer proceed if partial Gibbs-energy change, ΔG_e and ΔG_h, respectively, is negative, even if overall Gibbs-energy change (ΔG) is positive, i.e. uphill (energy-storing) electron transfer.

positive-hole transfer from a photocatalyst. For semiconductors (or insulators, similar to semiconductors in electronic band structure), electrons in the conduction band are relaxed to the bottom of the conduction band and positive holes in the valence band to the top of the valence band, losing their energy even if electrons in the middle energy part of the valence band are excited to the middle energy part of the conduction band (Figure 2.1).

Then, the requisites are only two in thermodynamics: the energy of the conduction-band bottom is higher than the standard electrode potential (SEP) for a substrate to be reduced and the energy of the valence-band top is lower than the SEP of a substrate to be oxidized.

Therefore, the SEP for reduction can be energetically higher than the SEP for oxidation, i.e. even positive Gibbs energy-change reactions such as water photolysis to hydrogen and oxygen can be driven by photoirradiation in the thermodynamic sense. This is the reason why the famous paper published in 1972 in Nature [4] has attracted much attention of scientists since solar energy can be converted into chemical energy, hydrogen. In the chapter, titanium(IV) oxide (titania) single crystal, rutile, was used as a photoanode and platinum as a counter cathode, and thereby this system is not photocatalysis; an external circuit cannot be introduced in the abovementioned photocatalytic-reaction systems. However, people, at that time, noticed the probability of water splitting using photocatalysts, such as titania. An important point is that the abovementioned Nature paper clearly claimed [5] as the experimental results, though not explicitly, that bias application, electrically or chemically (by differentiating the pH of two chambers), is necessary even though the band position was expected to drive water splitting. In other words, a titania

particle loaded with platinum, i.e. a short-circuited electrochemical cell composed of a titania anode and a platinum cathode, does not work to drive water photolysis.

What does it mean? A possible explanation is that the photocatalytic water splitting is governed kinetically, but not thermodynamically, and the fast recombination of electrons and positive holes retards the reaction. So many papers have been published claiming that a photocatalyst can drive hydrogen or oxygen evolution from water in the reaction system by including electron donor, i.e. reductant or electron acceptor, i.e. oxidant, respectively, but no water splitting to produce hydrogen and oxygen simultaneously proceeds without those sacrificial agents. However, a limited number of photocatalysts have been reported to be able to drive water splitting. Such a difference in activity has been interpreted with the difference in the rate of electron-positive hole recombination, though the recombination rate cannot be measured directly. In other words, nobody knows the true reason that enables the photocatalytic water splitting, and yet there is a possibility that a hidden thermodynamic principle is there in the mechanism of photocatalytic water splitting. It should be remembered that in the early stages of photocatalysis studies, the electric field inside the semiconductor photocatalyst was assumed to be the "space-charge (depletion) layer" since the transfer of electrons in donor levels in n-type semiconductors to the electrolyte is expected and the resultant electric field (potential slope) might separate charge carriers, i.e. electron and positive hole [6], though in ordinary metal-oxide particles the donor density seems negligible to form the space-charge layer (Figure 2.2).

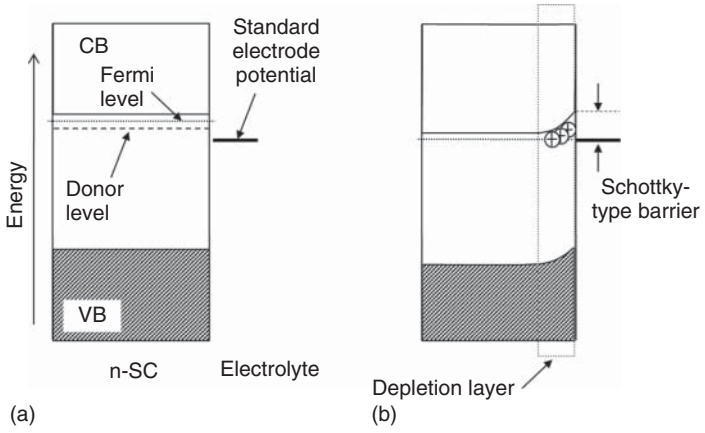

Figure 2.2 Schottky-type barrier created at the interface of n-type semiconductor (n-SC) with donor levels and electrolyte (a) before and (b) after their contact to make the Fermi level (the energy level at which the probability of taking that energy by electrons becomes half, showing that electronic states below the Fermi level are filled with electrons; in general, for n-type semiconductors, the Fermi level is located between the conduction-band bottom and a donor level) of the semiconductor and the standard electrode potential of an electrolyte to be the same. Electric field is formed inside of the semiconductor electrode (material), and that part is called the depletion layer, where donor electrons are transferred to the electrolyte. If light is absorbed in the depletion layer, an electron-positive hole pair is separated spontaneously by the electric field in the layer. For n-type semiconductor materials with low donor density, the depth of the depletion layer must be larger than the size, i.e. such depletion layer cannot be presumed.

2.3 Standard Electrode Potential

As is well-known, standard hydrogen electrode (SHE), so-called "redox potential" for hydrogen evolution, is 0 V in its definition, and the other SEPs are shown in reference to SHE. Here, the meaning of "standard" is the activity (concentration) of all the species included in the equation,

$$H^+ + e^- = 1/2\,H_2 \tag{2.1}$$

protons and hydrogen, have activities of unity, while the activity of electrons is defined as 1. It should be noted that the process of Eq. (2.1) seems to be a one-electron process (electrochemical equilibrium shown by "=") and different from the two-electron process as,

$$2H^+ + 2e^- = H_2 \tag{2.2}$$

but both equations give the same SHE, 0 V. In practice, a one-electron process produces hydrogen atom, as

$$H^+ + e^- = H\cdot \tag{2.3}$$

is not defined; if defined, its SEP should be higher (more negative/cathodic) due to the energy of H_2 formation from two hydrogen atoms (H·s). Then, for hydrogen evolution, we assume a two-electron process anytime. This is contrastive with water oxidation reactions in one-, two-, or four-electron processes to produce hydroxyl radical, hydrogen peroxide, or oxygen, respectively, as follows (it should be noted that an electron must be on the left side in an equation of electrochemical equilibrium):

$$H^+ + OH\cdot + e^- = H_2O \tag{2.4}$$

$$2H^+ + 2e^- + H_2O_2 = 2H_2O \tag{2.5}$$

$$4H^+ + 4e^- + O_2 = 2H_2O \tag{2.6}$$

with SEP of 2.8, 1.77, and 1.23 V (vs. SHE [7]), respectively (Figure 2.3).

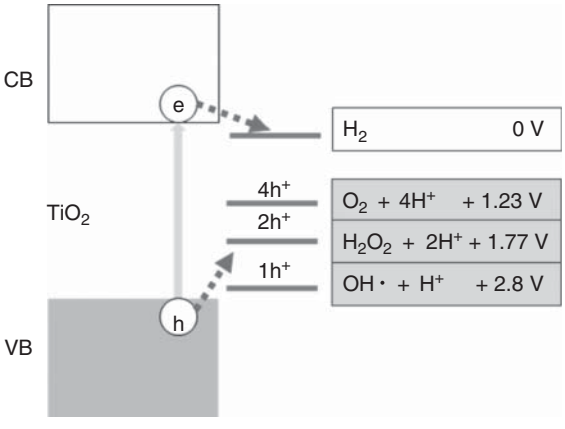

Figure 2.3 Standard electrode potential (SEP) for various redox couples related to water oxidation, as well as SEP of hydrogen evolution (0 V). For titania and other metal oxides, valence-band (VB) top energy may be deep (more positive) enough to drive any reaction, one, two, or four-electron process for water oxidation may proceed, and thermodynamically no rule for the choice.

In general, SEPs for further oxidation of hydroxyl radical and hydrogen peroxide to produce oxygen are higher (more negative/cathodic), i.e. once those intermediate species are produced, further oxidation into oxygen occurs spontaneously at that electrode potential. In the discussion of photocatalysis by particulate photocatalysts using SEPs, it should be noted that the number of electrons to be transferred from one particle is limited depending on the light flux incident in the reaction system and on the size of photocatalyst particles. Therefore, as is discussed later, for multielectron processes such as oxygen production, the higher the number of transferred electrons in a step, the easier it is to drive the reaction. In other words, even if low-number electron transfer is difficult, high-number electron transfer can proceed, as observed for oxygen reduction in photocatalytic organic decomposition reactions [8]. On the other hand, for hydrogen evolution, no such situation is assumed; the SEP to be compared to the conduction-bottom energy is always that of SHE.

2.4 Photocatalysts for Hydrogen Evolution

Then, what kind of photocatalysts can produce hydrogen under photoirradiation? For metal oxides, the answer has been already reported in 1980 [9], though this paper has been almost neglected [5], as shown in Figure 2.4.

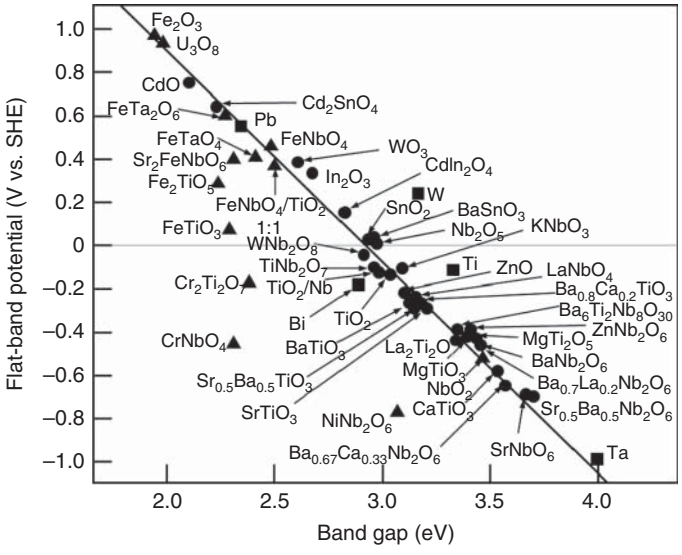

Figure 2.4 Scaife's plot reproduced from the original figure (Figure 2.3) in his original paper: Source: Scaife [9], (Fig. 3)/with permission of Elsevier. Almost linear relation with the slope of −1 suggests that only flat-band potential (potential at which no band bending is there by applying external bias potential and the same as the Fermi level), almost the same as conduction-band bottom energy, shifts upward with the increase in bandgap energy, keeping the valence-band (VB) top position unchanged, probably due to that VB is composed mainly of oxygen 2p orbitals.

Except for several outliers, flat-band potential (FBP; in the unit of V; see the caption of Figure 2.4), almost the same as the conduction-band bottom energy, was reduced, i.e. the potential was shifted negatively along with the increase in bandgap energy (in the unit of eV), indicating that the valence-band top position of those metal oxides is almost the same and only the conduction-band position is shifted by the change in bandgap. The FBP of titania (rutile) is a little higher (more negative) than SHE, and thereby titania and the other metal oxides of bandgap larger than c. 3 eV have potential to drive hydrogen evolution from water, while the narrow bandgap (<3 eV) metal oxides, which can be excited by visible light, cannot. It should be reminded that the FBPs in the plot were measured (or calibrated) in the electrolyte solution of pH 0, i.e. concentration of proton (H^+) to be 1 mol l^{-1} (if activity coefficient is assumed to be unity) and the band position is shifted to negative (cathodic) side by changing the pH of the aqueous electrolyte solution by c. 60 mV for 1 pH unit (Nernst's law) [7] for metal oxides and sulfides (with surface oxide layer), but the actual electrode potential for Eq. (2.1) is also shifted similarly [7].

Therefore, getting a metal-oxide photocatalyst for hydrogen evolution under visible-light irradiation seems challenging. One possible strategy is doping of heteroatoms to raise the position of the valence-band top, keeping the conduction-band bottom energy higher than SHE (for example, [10]), though it seems that there were no reports showing the valence-band position of doped metal oxides was raised even when the absorption-edge wavelength corresponding to the bandgap was shifted to the visible range [2]. Another strategy is the combination of two types of photocatalysts for hydrogen and oxygen evolutions, i.e. Z-scheme photocatalytic-reaction systems (for example, [11, 12]), but this is also not straightforward [2] and not discussed in this chapter.

If the scope is not limited to metal oxides, the probability of getting better photocatalysts for hydrogen evolution increases since valence-band position can be changed for non-oxides; metal sulfides and nitrides (or oxynitrides) may have higher valence-band positions while keeping their conduction-band positions. Therefore, cadmium sulfide (CdS) was used instead of metal oxides; the color of cadmium oxide (CdO), which is white, is changed to yellow, blue color absorbing, with CdS. Actually, as described in Section 2.6, CdS can be used for photocatalytic hydrogen evolution in the presence of a strong electron donor such as methanol. However, nonmetal oxides for hydrogen evolution are stable only in the presence of strong electron donors and tend to be oxidized, at least partly, in their absence.

2.5 Co-catalysts for Hydrogen Evolution

In almost all the cases, photocatalysts having conduction-band top position higher than SHE cannot produce hydrogen even in the presence of strong electron donors such as methanol when used without co-catalyst loading. In the early stages of photocatalysis studies in the 1970s and 1980s, the mechanism was understood by assuming semiconductor photocatalyst particles to be micronized short-circuited

electrochemical cells composed of semiconductor, titania in almost all the cases, and platinum electrodes [13]. Therefore, loading of platinum or other noble metals seems to be a requisite for photocatalysis. However, since bare semiconductor photocatalysts were found to be able to drive oxidative decomposition of organic compounds in the presence of air (oxygen) without noble-metal loading, platinum is not an essential requisite for photocatalysis. Consequently, the loaded noble-metal deposits have been recognized as a co-catalyst only for hydrogen evolution. Since those noble metals have quite low or negligible hydrogen overpotential, i.e. the bias potential required for actual hydrogen evolution in reference to SHE.

Then, why metal oxides (having conduction-band bottom higher than RHE) cannot liberate hydrogen or show high hydrogen overpotential even though it is thermodynamically possible to liberate hydrogen? For titania, it has been known that titanium(IV) ions in the lattice are converted into titanium(III) (Ti^{3+}) ions upon reduction, and a proton (H^+) is inserted to compensate for the reduced positive charge to show blue-gray color by absorbing visible-near infrared light. For example, measurements using double-beam photoacoustic spectroscopy (DB-PAS) [14] revealed that ultra-bandgap ultraviolet irradiation onto commercial titania powers under the methanol-saturated nitrogen atmosphere turned the color from white to gray and absorption (photoacoustic signal intensity) at 530 nm was increased with the time of irradiation, as shown in Figure 2.5.

The absorption increase was negligible under air even when methanol as a hole scavenger was included in the atmosphere, suggesting that photoexcited electrons

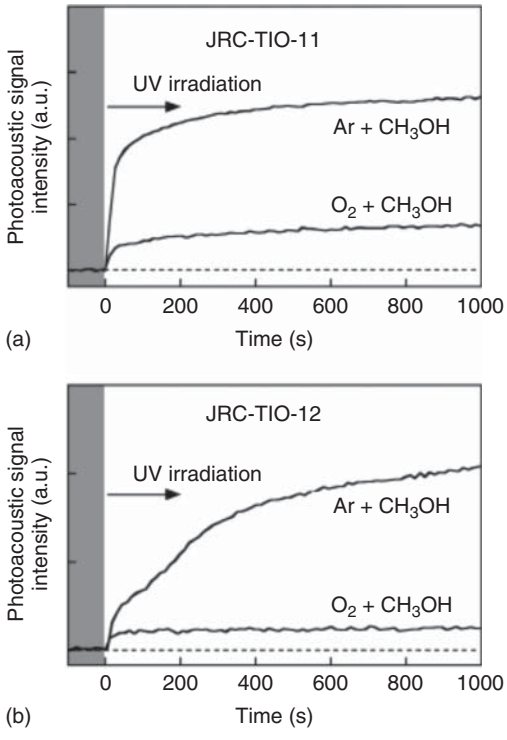

Figure 2.5 Change in photoacoustic-signal intensity, i.e. photoabsorption, at 530 nm by photoirradiation of two commercial titania samples ((a) JRC-TIO-11 and (b) JRC-TIO-12) under methanol saturated argon or oxygen atmosphere. Source: Murakami et al. [14], (Fig. 9)/with permission of American Chemical Society.

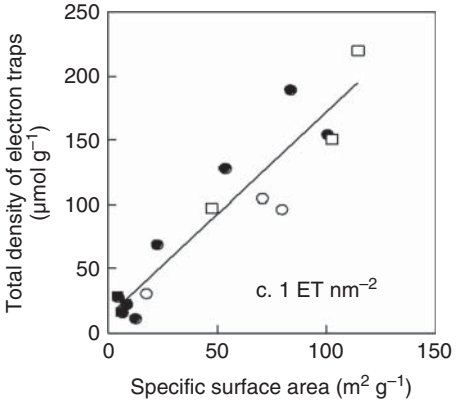

Figure 2.6 Correlation between total density of ETs and specific surface area of representative titania samples. Open circles and squares denote anatase and retile samples, respectively, and closed circles and squares denote anatase-rich and rutile-rich samples, respectively. Rough estimation from the slope of this plot suggests the surface density of electron traps (ETs) to be c. 1 ET nm^{-2}. Source: Nitta et al. [16], (Fig. S3)/Royal Society of Chemistry/CC BY-3.0.

can reduce titania itself to lead to the visible-light absorption in the presence of a hole scavenger but in the absence of electron acceptors such as oxygen; water or proton adsorbed on the surface of titania seems not to accept electrons. Since the absorption increase was saturated by the prolonged irradiation, the number (density) of titanium(IV) ions to be reduced may be limited. In other words, electrons are captured by certain electronic states, "electron traps (ETs)," in/on the titania samples and their number (density) seems limited. Recent results obtained using newly developed reversed double-beam photoacoustic spectroscopy (RDB-PAS), modified DB-PAS to fill up ETs with electrons excited directly from the valence band, indicate that the measured ETs of titania samples are mainly located on the surface with similar area density [15], as shown in Figure 2.6.

A significant finding is that the abovementioned electron-trap filling by photoirradiation becomes negligible when platinum is loaded on the surface of titania samples, suggesting that platinum efficiently captures electrons and promotes molecular-hydrogen (H_2) production.

2.6 Role of Platinum

Can loaded platinum produce hydrogen anytime? The answer might be "No." It has been reported that platinum-loaded metal oxides with conduction-band bottom position lower than SHE, such as tungsten(VI) oxide (WO_3) [17] and bismuth tungstate (Bi_2WO_6) [8] cannot liberate hydrogen even though the photoexcited electrons could be transferred to platinum; those platinum-deposited metal oxides, WO_3 and Bi_2WO_6, cannot induce photocatalytic hydrogen evolution but can drive oxidative decomposition of organic compounds with reduction of oxygen in more feasible two-electron mode (Eq. (2.7); 0.68 V vs. SHE) but not in one-electron mode (Eq. (2.8); –0.13 V vs. SHE) with the aid of platinum.

$$O_2 + 2e^- + 2H^+ = H_2O_2 \tag{2.7}$$

$$O_2 + e^- + H^+ = HO_2 \tag{2.8}$$

The abovementioned results suggest that the (electrochemical) potential of platinum is governed by the conduction-band bottom position of metal oxides in contact with platinum. Therefore, one possible explanation for the role of platinum (and probably the other noble metals) is storing electrons to drive a two-electron process of hydrogen evolution (Eqs. (2.1) and (2.2)).

While photocatalytic hydrogen evolution by bare titania is negligible [18], cadmium sulfide (CdS) has been reported to liberate hydrogen even without loaded noble metals [19] (photocatalytic activity enhancement was also observed by noble-metal loading), probably due to the conduction-band bottom position being higher than that of titania. It was also reported that capture of photoexcited electrons by cadmium(II) ions, i.e. electron traps, leads to metallic cadmium deposits, and the higher the density of ETs increases, the higher the photocatalytic activity becomes [20]. If the hydrogen evolution from cadmium sulfide is assumed to occur on those cadmium-metal deposits, the role of deposited metals for hydrogen evolution may be to store electrons, keeping their energy to be used in the two-electron hydrogen-evolution process, but not an electrocatalyst reducing the activation energy for hydrogen evolution, though this is not supported directly by any experimental evidence.

Then, how much amount of platinum is necessary to optimize the hydrogen evolution by titania? Generally speaking, platinum-amount dependence of the photocatalytic hydrogen-evolution rate is (i) increased almost linearly with small-amount platinum deposition, (ii) saturated at a certain amount of deposition, and (iii) slightly decreases by further deposition. For example, photocatalytic hydrogen evolution from aqueous 2-propanol by titania platinum-loaded through an ex situ impregnation-hydrogen reduction scheme [21] is shown in Figure 2.7, as the dependence of the rate as a function of the estimated surface area of platinum.

In this paper, the number of platinum deposits on a titania (Degussa (presently Evonik) P25; c. 30 nm in size) particle was estimated and suggested that only one platinum deposit of size c. 2 nm is necessary for hydrogen evolution and excess loading might reduce the activity due to shading light against titania photoabsorption. The reason for the rate decrease might be still open, assuming the role of platinum for the two-electron process; an excess number of platinum deposits may decrease the

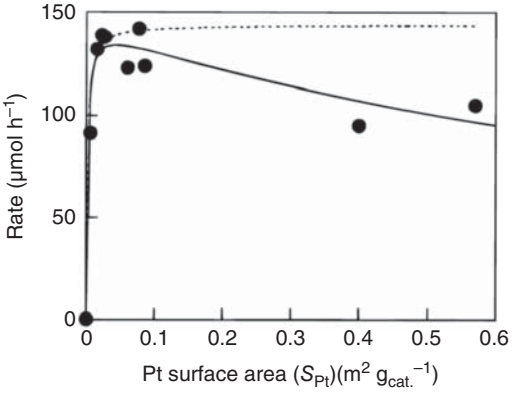

Figure 2.7 Rate of photocatalytic hydrogen evolution from aqueous 2-propanol as function of platinum surface area (S_{Pt}) estimated from the size of platinum deposits seen in the transmission electron microscopic images. Source: Ohtani et al. [21], (Fig. 7)/with permission of American Chemical Society.

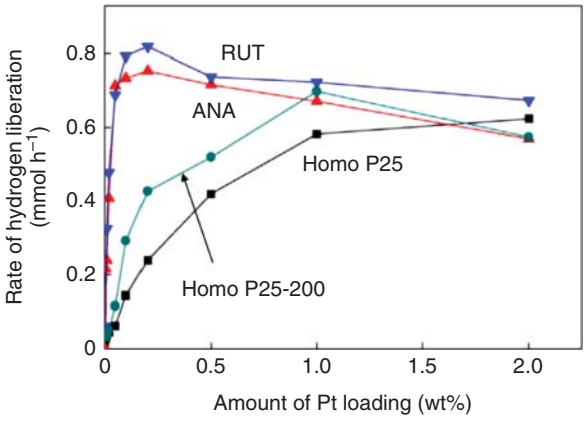

Figure 2.8 Dependence of photocatalytic activity (rate of hydrogen evolution from aqueous 50 vol% methanol) on the amount of platinum loading. Source: Wang et al. [23], (Fig. 3(A)/with permission of Elsevier.

probability of storing a second electron for a one-electron bearing platinum deposit (a similar negative effect of excess deposits has been suggested for photocatalytic oxygen evolution through multielectron process [22]). It may be true that one a few nanometer-sized platinum deposit can accept electrons produced anywhere in a contacting (at least) a few 10 nm-sized titania.

Recent results on the photocatalytic activity of Evonik P25 and the samples prepared from P25 showed a significant suggestion on the platinum-amount dependence of the photocatalytic hydrogen-evolution rate (A topic on the comparison of anatase and rutile crystallites in P25 will be discussed in the next section.) [23], as shown in Figure 2.8.

Platinum-amount dependences of anatase and rutile particles (ANA and RUT, respectively) isolated from P25 [24, 25], P25 homogenized by freeze drying (Homo P25), and Homo P25 calcined in air at 473K (Homo P25-200) were similar to the previous dependence, as shown in Figure 2.7. However, the rate-saturation amount was significantly different; ANA and RUT showed very low (<0.1%), while Homo P25 showed high saturation amount of c. 1%. Taking into account that ANA and RUT underwent annealing (calcination) in air at 473 K of wet precipitates, their particles were aggregated to give secondary particles through interparticle dehydration of surface hydroxyl groups. On the other hand, original P25 is prepared in a gas-phase dry process and aggregation of particles seems negligible as P25 gives fume (smoke) and Homo P25 was prepared by suspending P25 in water, stirring and freeze drying, i.e. without heat treatment inducing aggregation. Consequently, the abovementioned difference in the rate-saturation amount can be interpreted by the assumption that a platinum deposit can accept electrons produced in any particle of an aggregate, i.e. interparticle electron transfer occurs in the aggregated particles. Calcination at 473 K of Homo P25 (Homo P25-200) led to a steeper increase in the rate compared with that of Homo P25, though not the same as those of ANA and RUT; calcination of dry particles may give less aggregated particles.

For the practical application of photocatalysis, it should be noted that those hydrogen evolution co-catalysts such as platinum can also enhance the reduction of oxidation product, for example, oxygen as an oxidation product of water splitting (see Section 2.8).

2.7 Anatase and Rutile

One of the myths in photocatalysis studies is that the photocatalytic activity of anatase particles is much higher than that of rutile particles. Another myth is that the anatase–rutile mixture shows much higher activity due to the transfer of charge carriers between them. However, as was clearly shown in Figure 2.8, ANA, RUT, and P25 (Homo P25 and Homo 25-200) showed almost the same activity for hydrogen evolution from aqueous methanol, i.e. when comparing the activity of particles of similar size, a few ten nanometers, the activity might not be dependent on the crystalline structure.

In the general liquid-phase manufacturing processes, anatase particles have been prepared at relatively low temperature, and rutile particles have been prepared at higher temperature, since anatase is converted into rutile upon heating; it is so difficult to prepare large-sized, e.g. >500 nm, non-aggregated anatase particles and to prepare small-sized, e.g. <10 nm, rutile particles. The reason why it is believed that rutile is less active compared to anatase for photocatalytic hydrogen evolution is that rutile samples used in those tests might be large, i.e. low specific surface area. It has been suggested that hydrogen evolution reaction requires the properties of titania photocatalysts of sufficiently large surface area while both anatase and rutile give comparable influence on the basis of the results of statistical analysis [26]. On the other hand, similar statistical analysis for the oxidative decomposition of organic compounds in water or in air showed that the presence of anatase is required, while particle size or specific surface area does not so significantly affect the activity [26]. One of the possible explanations of such crystalline-structure dependence is that anatase has a slightly higher conduction-bottom energy suitable for reduction of oxygen in the one-electron process (Eq. (2.8)) [27], while rutile cannot reduce oxygen due to the possibly lower conduction-bottom position. In practice, platinum loading enhances the rutile activity for organic decomposition, and the enhancement ratio is far higher than that of anatase (data not shown = unpublished results), presumably due to the two-electron process of oxygen reduction (Eq. (2.7)) on platinum. Since rutile activity is comparable to anatase activity for hydrogen evolution, both anatase and rutile crystallites satisfy the thermodynamic requirement for hydrogen evolution, i.e. conduction-bottom position higher than SHE.

Then, what happens when those anatase and rutile crystallites are mixed? P25 is a mixture of anatase and rutile as well as an amorphous phase (though their composition seems not constant even in one package) [25]. In the ordinary test reactions for photocatalytic hydrogen evolution, platinum loading is performed by photodeposition; a precursor, e.g. chloroplatinic acid (H_2PtCl_6), in its aqueous solution containing an electron donor, such as methanol, is irradiated. Since the bandgap of anatase is a little wider than that of rutile, the absorption (longer) edge wavelength of anatase is shorter than that of rutile. Therefore, the wavelength dependence of photoreaction (including photocatalysis), i.e. the action spectrum, may indicate the crystalline phase, anatase and rutile, which works in the photocatalysis [28, 29]. For photocatalytic hydrogen evolution from aqueous methanol (50%) including H_2PtCl_6 (corresponding to 2 wt% loading), $\lambda_{1/2}$, wavelength giving value

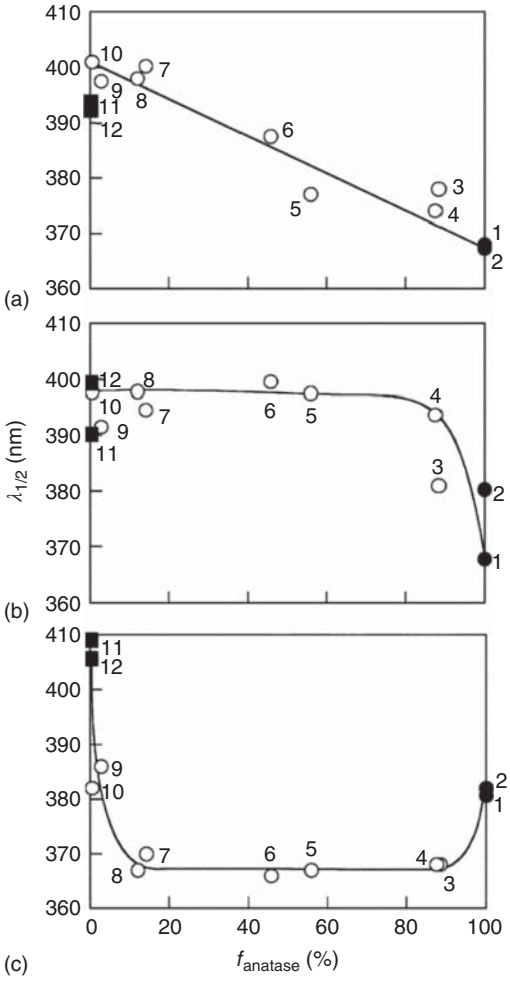

Figure 2.9 Wavelength giving half value of rate at 350 nm ($\lambda_{1/2}$) for three kinds of photocatalytic reactions, (a) hydrogen evolution from aqueous methanol (50 vol%) with deposited platinum under deaerated conditions, (b) oxygen evolution from a deaerated aqueous silver salt solution and (c) carbon dioxide evolution from aqueous acetic acid (5 vol%) under aerobic conditions, plotted against the content of anatase ($f_{anatase}$) in commercial titania samples. Sample numbers; 1: Merck, 2: JRC (Japan Reference Catalyst)-TIO-3, 3: Wako (anatase), 4: Degussa (presently Evonik) P25, 5: Merck + Ishihara CR-EL, 6: Wako (anatase) + Ishihara CR-EL, 7: Aldrich (rutile), 8: JRC-TIO-5, 9: Wako (rutile), 10: Ishihara CR-EL, 11: Ishihara CR-EL calcined in air at 1473 K and 12: Degussa (presently Evonik) P25 calcined in air at 1473 K. Source: Torimoto et al. [28], (Fig. 3)/with permission of Royal Society of Chemistry.

(normalized apparent quantum efficiency) half of that at 350 nm, was shifted almost linearly with the content of anatase (or rutile) as shown in Figure 2.9.

Here, (true) quantum efficiency is defined as the ratio of number (rate) of electrons (or positive holes) transferred to a substrate with number (rate) of photons absorbed by a photocatalyst. To estimate the number of transferred electrons (positive holes) from the substrate consumption or product liberation amount, it is necessary to assume the number of electrons/holes required for one mole of substrate consumption or product liberation. For example, for water splitting into hydrogen and oxygen, two and four moles of electrons/holes are required to produce one mole of hydrogen and oxygen, respectively. Practically speaking, it is rather difficult to measure the molar amount of photons absorbed by a photocatalyst due to the reflection and scattering of light by the photocatalyst (this is completely different from the estimation of photon absorption by molecules in a solvent or in the gas phase). Therefore, "apparent" quantum efficiency, a ratio of number (rate) of electrons (or positive

holes) transferred to a substrate with number (rate) of photons "incident" upon a photocatalytic system, is used, and the plot of apparent quantum efficiency as a function of irradiation-light wavelength reflects the photoabsorption spectrum for the photocatalysis [1–3]. The relation shown in Figure 2.9 suggests that anatase and rutile in their mixture show comparable activity for hydrogen evolution as discussed above. On the other hand, $\lambda_{1/2}$ for oxidative decomposition of acetic acid to yield carbon dioxide by anatase–rutile mixtures without platinum loading was even shorter (c. 370 nm) than $\lambda_{1/2}$ of pure anatase samples (c. 380 nm) except for the mixture of rutile content > c. 90%, indicating that only anatase works as a photocatalyst and rutile absorbing longer-wavelength light induces the shift $\lambda_{1/2}$ to shorter wavelength by c. 10 nm (inner filter effect), consistent with the abovementioned anatase priority for organic decomposition.

An interesting result has been obtained using P25 by reducing the amount of platinum loading (unpublished data). When a sufficient amount (2 wt%) of platinum was loaded, the action spectrum for hydrogen evolution from aqueous methanol (50%) was similar to the diffuse reflectance spectrum, indicating that both anatase and rutile worked. However, when the amount of photodeposited platinum was reduced to 0.2 wt%, the action spectrum was shifted to a longer wavelength and became similar to the action spectrum of a mixture of 2 wt% platinum-loaded isolated rutile (RUT) and bare (i.e. inactive) isolated anatase (ANA) (similar results have been reported in another paper [23]). This suggests that rutile crystallites are preferentially loaded with platinum, keeping anatase particles unloaded. Thus, the discussion on the photocatalytic activities for crystalline mixtures seems not to be straightforward.

2.8 Outlooks on Photocatalytic Hydrogen Evolution

As described above, photocatalytic hydrogen evolution can be driven by a photocatalyst having a conduction-band bottom position, i.e. reduction ability, higher than SHE in the thermodynamic sense, and SHE (as a two-electron process) is the sole SEP to be compared with the conduction-band bottom position of a photocatalyst. This is contrastive contrasted to the reduction of oxygen where one-, two-, or four-electron processes can be chosen. On the other hand, in the sense of kinetics (also related to thermodynamics), loading of noble metals such as platinum is essential to store photoexcited electrons (probably in the form of adsorbed hydrogen atoms) and liberate hydrogen in a two-electron process.

It should be noted that the above explanation is limited only to the hydrogen evolution reaction as a half reaction driven by photoexcited electrons, and even if hydrogen evolution is observed by a photocatalyst in the presence of strong electron donors, only "latent" ability of hydrogen evolution of the photocatalyst is suggested. If the other half of the reaction driven by positive holes, for example, oxygen evolution, can proceed negligibly, the overall photocatalytic reaction including hydrogen evolution cannot be observed. Then, if both half reactions with positive Gibbs-energy change for the overall reaction (energy-storing reaction such as water

splitting) proceed efficiently, the possible challenge is to avoid backward reaction of generated products, especially on a co-catalyst for hydrogen evolution. An example of a successful solution is covering the co-catalyst surface with a thin layer of metal oxides allowing only protons, not oxygen, to reach the inner surface of the co-catalyst [30].

References

1 Ohtani, B. (2008). Preparing articles on photocatalysis—Beyond the illusions, misconceptions, and speculation. *Chem. Lett.* 37 (3): 217–229. https://doi.org/10.1246/cl.2008.216.

2 Ohtani, B. (2010). Photocatalysis A to Z—What we know and what we don't know. *J. Photochem. Photobiol. C Photochem. Rev.* 11 (4): 157–178. https://doi.org/10.1016/j.jphotochemrev.2011.02.001.

3 Ohtani, B. (2014). Revisiting the fundamental physical chemistry in heterogeneous photocatalysis: its thermodynamics and kinetics. *Phys. Chem. Chem. Phys.* 16 (5): 1788–1797. https://doi.org/10.1039/c3cp53653j.

4 Fujishima, A. and Honda, K. (1972). Electrochemical photolysis of water at a semiconductor electrode. *Nature* 238: 37–38. https://doi.org/10.1038/238037a0.

5 Ohtani, B. (2014). Revisiting the original works related to titania photocatalysis: a review of papers in the early stage of photocatalysis studies. *Electrochemistry* 82 (6): 414–425. https://doi.org/10.5796/electrochemistry.82.414.

6 Ohtani, B. (2018). Physicochemical mechanistic studies on photocatalysis–extension of semiconductor photoelectrochemistry concept beyond its limitation. *Electrochemistry* 86 (6): 273–280. https://doi.org/10.5796/electrochemistry.18-6-E2667.

7 Bard, A.J., Parsons, R., and Jordan, J. (ed.) *Standard Potentials in Aqueous Solution*. New York: Marcel Dekker.

8 Hori, H., Takashima, M., Takase, M. et al. (2018). Multielectron reduction of molecular oxygen in photocatalytic decomposition of organic compounds by bismuth tungstate particles without cocatalyst loading. *Catal. Today* 303: 341–349. https://doi.org/https://doi.org/10.1016/j.cattod.2017.08.045.

9 Scaife, D.E. (1980). Oxide semiconductors in photoelectrochemical conversion of solar energy. *Solar Energy* 25: 42–54. https://doi.org/10.1016/0038-092X(80)90405-3.

10 Ashahi, R., Morikawa, T., Ohwaki, T. et al. (2001). Visible-light photocatalysis in nitrogen-doped titanium oxides. *Science* 293 (5528): 269–271. https://doi.org/10.1126/science.1061051.

11 Sayama, K., Mukasa, K., Abe, R. et al. (2001). Stoichiometric water splitting into H_2 and O_2 using a mixture of two different photocatalysts and an IO_3^-/I^- shuttle redox mediator under visible light irradiation. *Chem. Commun.* 2416–2417. https://doi.org/10.1039/B107673F.

12 Abe, R., Shinmei, K., Hara, K., and Ohtani, B. (2009). Robust dye-sensitized overall water splitting system with two-step photoexcitation of coumarindyes and

metal oxide semiconductors. *Chem. Commun.* 45 (24): 3577–3579. https://doi.org/10.1039/b905935k.

13 Bard, A.J. (1979). Photoelectrochemistry and heterogeneous photo-catalysis at semiconductors. *J. Photochem.* 10 (1): 59–75. https://doi.org/10.1016/0047-2670(79)80037-4.

14 Murakami, N., Prieto-Mahaney, O.-O., Abe, R. et al. (2007). Double-beam photoacoustic spectroscopic studies on transient absorption of titanium(IV) oxide photocatalyst powders. *J. Phys. Chem. C* 111 (32): 11927–11935. https://doi.org/10.1021/jp071362x.

15 Nitta, A., Takashima, M., Murakami, N. et al. (2018). Reversed double-beam photoacoustic spectroscopy of metal-oxide powders for estimation of their energy-resolved distribution of electron traps and electronic-band structure. *Electrochim. Acta* 264: 83–90. https://doi.org/10.1016/j.electacta.2017.12.160.

16 Nitta, A., Takase, M., Takashima, M. et al. (2016). A fingerprint of metal-oxide powders: energy-resolved distribution of electron traps. *Chem. Commun.* 52 (81): 12096–12099. https://doi.org/10.1039/C6CC04999K.

17 Abe, R., Takami, H., Murakami, N., and Ohtani, B. (2008). Pristine simple oxide photocatalysts as visible light driven photocatalysts: highly efficient decomposition of organic compounds over platinum-loaded tungsten oxide. *J. Am. Chem. Soc.* 130 (25): 7780–7781. https://doi.org/10.1021/ja800835q.

18 Nishimoto, S.-I., Ohtani, B., and Kagiya, T. (1985). Photocatalytic dehydrogenation of aliphatic alcohols by aqueous suspensions of platinized titanium dioxide. *J. Chem. Soc., Faraday Trans.* 1, 81 (10): 2467–2474. https://doi.org/10.1039/F19858102467.

19 Ohtani, B., Kawaguchi, J.-I., Kozawa, M. et al. (1995). Effect of platinum loading on the photocatalytic activity of cadmium(II) sulfide particles suspended in aqueous amino acid solutions. *J. Photochem. Photobiol. A: Chem.* 90 (1): 75–80. https://doi.org/10.1016/1010-6030(95)04084-S.

20 Ohtani, B., Kusakabe, S., Okada, K. et al. (2001). Photocatalytic stereoselective N-cyclization of 2,6-diaminopimelic acid into piperidine-2,6-dicarboxylic acid by an aqueous suspension of activated cadmium(II) sulfide particles. *J. Chem. Soc., Perkin Trans.* 2, 2: 201–209. https://doi.org/10.1039/b006967l.

21 Ohtani, B., Iwai, K., Nishimoto, S.-I., and Sato, S. (1997). Role of platinum deposits on titanium(IV) oxide particles: structural and kinetic analyses of photocatalytic reaction in aqueous alcohol and amino acid solutions. *J. Phys. Chem. B.* 101 (17): 3349–3359. https://doi.org/10.1021/jp962060q.

22 Ketwong, P., Yoshihara, S., Takeuchi, S. et al. (2020). Light intensity-dependence studies on the role of surface deposits for titania-photocatalyzed oxygen evolution: are they really cocatalysts? *J. Chem. Phys.* 153: 124709. https://doi.org/10.1063/5.0014913.

23 Wang, K., Wei, Z., Ohtani, B., and Kowalska, E. (2018). Interparticle electron transfer in methanol dehydrogenation on platinum-loaded titania particles prepared from P25. *Catal. Today* 303: 327–333. https://doi.org/10.1016/j.cattod.2017.08.046.

24 Ohtani, B., Azuma, Y., Li, D. et al. (2007). Isolation of anatase crystallites from anatase-rutile mixed particles by dissolution with aqueous hydrogen peroxide and ammonia. *Trans. Mater. Res. Soc. Jpn.* 32 (2): 401–404.

25 Ohtani, B., Prieto-Mahaney, O.-O., Li, D., and Abe, R. (2010). What is Degussa (Evonik) P25? Crystal composition analysis, reconstruction from isolated pure particles, and photocatalytic activity test. *J. Photochem. Photobiol. A Chem.* 216 (2-3): 179–182. https://doi.org/10.1016/j.jphotochem.2010.07.024.

26 Ohtani, B., Prieto-Mahaney, O.-O., Amano, F. et al. (2010). What are titania photocatalysts?—An exploratory correlation of photocatalytic activity with structural and physical properties. *J. Adv. Oxid. Technol.* 13 (3): 247–261. https://doi.org/10.1515/jaots-2010-0303.

27 Kavan, L., Graetzel, M., Gilbert, S.E. et al. (1996). Electrochemical and photoelectrochemical investigation of single-crystal anatase. *J. Am. Chem. Soc.* 118 (28): 6716–6723. https://doi.org/10.1021/ja954172l.

28 Torimoto, T., Nakamura, N., Ikeda, S., and Ohtani, B. (2002). Discrimination of active crystalline phases in anatase-rutile mixed titanium(IV) oxide photocatalysts through action spectrum analyses. *Phys. Chem. Chem. Phys.* 4 (23): 5910–5914. https://doi.org/10.1039/b207448f.

29 Torimoto, T., Aburakawa, Y., Kawahara, Y. et al. (2004). Light intensity dependence of the action spectra of photocatalytic reactions with anatase titanium(IV) oxide. *Chem. Phys. Lett.* 392 (1-3): 220–224. https://doi.org/10.1016/j.cplett.2004.05.077.

30 Maeda, K., Teramura, K., Lu, D. et al. (2006). Noble-metal/Cr_2O_3 core/shell nanoparticles as a cocatalyst for photocatalytic overall water splitting. *Angew. Chem.* 118: 7970–7973. https://doi.org/10.1002/ange.200602473.

3

Isotopic Substitution to Unravel the Mechanisms of Photocatalytic Hydrogen Production

Mariano Curti[1], Yamen AlSalka[2], Osama Al-Madanat[3], and Detlef W. Bahnemann[4,5]

[1] Institute of Chemical Research of Catalonia (ICIQ), Barcelona Institute of Science and Technology (BIST), Avda. Països Catalans 16, 43007 Tarragona, Spain
[2] Institute für Nanophotonik Göttingen e. V., Photonic Sensor Technology, Hans-Adolf-Krebs-Weg 1, 37077 Göttingen, Germany
[3] Mutah University, Chemistry Department, Faculty of Science, Mutah, 61710 Al-Karak, Jordan
[4] Institut für Technische Chemie, Gottfried Wilhelm Leibniz Universität Hannover, Callinstrasse 3, 30167 Hannover, Germany
[5] Saint-Petersburg State University, Laboratory "Photoactive Nanocomposite Materials,", Ulyanovskaya str. 1, Peterhof, 198504 Saint Petersburg, Russia

3.1 Introduction

The 1972 report by Fujishima and Honda, demonstrating photoelectrochemical water splitting over a TiO_2 electrode, led to an explosion in heterogeneous photocatalysis research [1]. In addition to the importance of the discovery by itself, the oil crisis of 1973 was undoubtedly an important contributor to such an explosion [2], setting photocatalytic hydrogen production as a prime candidate to solve humanity's ever-increasing power hunger. It is remarkable that, almost 50 years later, heterogeneous photocatalysis is still seen as a promising candidate, and yet has not reached widespread commercial deployment. Akin to the oil crisis of 1973, the context now is very pressing: we have finally accepted that anthropogenic climate change poses a serious risk to the survival of our species, and thus we need to devise clean energy sources more desperately than ever.

The complexity of heterogeneous photocatalytic processes is probably the main reason for their delayed application. Light absorption and scattering, charge separation, charge-carrier diffusion and transport, catalytic efficiency, and mass transport all play a large role in determining the efficiency [3]. Similarly, there is no single tool capable of revealing all the mechanistic details needed to increase efficiency. Instead, researchers have resorted to a large collection of techniques to slowly gather pieces of the puzzle. These include steady-state [4] and time-resolved spectroscopy [5]; materials characterization tools such as XRD [6]; and photoelectrochemical analyses [7], among many others [8].

Photocatalytic Hydrogen Production for Sustainable Energy, First Edition. Edited by Alberto Puga.

In this chapter, we focus on one such technique, isotopic substitution, that, despite being very powerful, has perhaps not seen much adoption. The basic idea is very simple: it involves using isotopically labeled compounds, which could be any of those involved in the process: the photocatalyst itself, the solvent, or a substrate taking part in the photocatalytic reaction. First, this allows pinpointing the route of individual atoms. For instance, by using ^{18}O-labeled TiO_2 and an unlabeled aqueous solution of an organic compound, it can be demonstrated that some of the O atoms initially in the photocatalyst will be part of the CO_2 evolved as photooxidation proceeds (i.e. $C^{16}O^{18}O$ and $C^{18}O_2$ can be detected in the gas phase) [9, 10]. Second, the analysis of the kinetics upon isotopic substitution allows to evaluate rate-determining steps in a mechanism. For example, a comparison of the degradation rates of isopropanol in H_2O or D_2O over TiO_2 allowed to propose the photogeneration of hydroxyl radicals as the rate-determining step of the process [11]. And third, the use of certain isotopes may allow the application of some techniques that would otherwise be unusable. A prime example of this is magnetic resonance techniques, where naturally abundant isotopes might not yield any signal at all, while others could be readily detected. This is illustrated by the use of ^{17}O in electron paramagnetic resonance (EPR) by Giamello et al., which provided rich information on TiO_2 that would be otherwise unobtainable with the (magnetically inactive and most abundant) isotope ^{16}O [12].

It is noteworthy that the analysis of photocatalytic processes often entails conditions that are not representative of the operative ones. For instance, time-resolved spectroscopies often employ laser irradiation at irradiances much larger than those used for photocatalytic reactions, and thus the results may be difficult to extrapolate. In the case of isotopic substitution, the system is only slightly perturbed. In particular, the mass difference between H and D may yield a significant change in kinetics that must be considered; for other substitutions, such as ^{16}O to ^{18}O, or ^{44}Ti to ^{47}Ti, the changes in kinetics are negligible.

We note that several studies described in this chapter do not specifically involve hydrogen evolution but are instead mechanistic studies on photocatalytic processes or materials. However, although undoubtedly there are peculiarities in the mechanisms of hydrogen evolution, we believe those studies are largely relevant when trying to understand (and, ultimately, optimize) hydrogen production. We also believe those studies can inspire new avenues for the investigation of photocatalytic hydrogen generation processes.

3.2 Isotopic Substitution on the Solvent or Substrate

3.2.1 Water

Although, ideally, water would be the only source of molecular hydrogen, photocatalytic water splitting is a very challenging reaction due to both thermodynamic and kinetic issues [8]. It is thus common to employ sacrificial electron donors, which readily scavenge holes, thus extending photogenerated electron lifetimes and significantly increasing hydrogen production efficiency. When studying the involved

mechanisms in such systems, isotopic substitution has been employed both in the organic substrates and in the solvent (generally water). However, in this section, we restrict ourselves to works targeting true water splitting, and leave studies employing water isotopologues together with sacrificial electron donors for the latter sections.

Before going into specific examples, we briefly describe the kinetic isotope effect (KIE). This is the effect that performing isotopic substitution has on the rate of a reaction. Most commonly, the involved isotopes are H and D. For a given reaction, if the rates (strictly speaking, rate constants) are given by k_H and k_D when using H and D, respectively, then the KIE is:

$$\mathrm{KIE} = \frac{k_H}{k_D} \tag{3.1}$$

A KIE of 1 indicates that the rate-determining step does not involve a bond with the atoms being substituted [13]. On the contrary, larger values mean that these atoms are involved in a bond that changes during the rate-limiting step. This change can be a cleavage ("primary KIE"), or less abrupt, such as a different hybridization ("secondary KIE"); the KIE values are normally higher in the first case. Ultimately, the origin of the KIE is the difference in the zero-point energy of the molecule under study between the reactant and the transition state [14]. This difference becomes higher as the mass difference between the isotopes increases; H and D, then, give the largest KIEs among the commonly employed isotopes.

The group of Domen provides good early examples of isotopic substitution applied to photocatalytic water splitting [15, 16]. In one of these, the material under study was Zn-doped Ga_2O_3 modified with a $Rh_{2-y}Cr_yO_3$ co-catalyst [16]. The authors analyzed the KIE when using either H_2O or D_2O for water splitting, and found a maximum value of 1.9, i.e. relatively small. It also showed a strong dependence on light intensity and amount of photocatalyst: when these parameters were low, they became the limiting factor of the reaction, and thus the isotopes had no effect (rates were insensitive to H_2O/D_2O bond cleavage reactions). On the other hand, a reduced co-catalyst loading (or high light intensity) created a bottleneck on H_2 evolution that led to a higher steady-state concentration of photogenerated carriers available for surface reactions; this resulted in larger KIEs. It was also highlighted that, in electrochemical water splitting, the external voltage guarantees a steady supply of charge carriers, thus rendering surface reaction steps as rate-determining and resulting in strong KIEs.

In recent years, several materials have shown great promise for the water-splitting reaction; isotopic substitution has provided an important tool to understand the processes behind this complex reaction [17–21]. For instance, Zhao et al. prepared carbon nitride nanosheets with varying levels of boron dopants and nitrogen defects; this allowed them to serve as either H_2- or O_2-evolving photocatalysts [18]. These two types were then coupled together, and with Pt and $Co(OH)_2$ co-catalysts, to produce composites with a Z-scheme electronic structure and remarkable efficiencies. The use of $H_2{}^{18}O$ led exclusively to $^{18}O_2$ evolution, confirming water oxidation as its source. A similar application of isotope labeling was done in another recent work, which achieved full water splitting on CdS nanorods that included Pt nanoparticles and a Ru-based dye as co-catalysts [19].

3.2.2 Alcohols

Methanol is frequently employed in photocatalytic systems as a sacrificial electron donor to improve H_2 production. Its reaction with photogenerated holes in the ps to ns range reduces charge carrier recombination [8], and also produces $^{\cdot}CH_2OH$ radicals, which can inject electrons in the photocatalyst's conduction band [22], further improving efficiency.

Chiarello, Ferri, and Selli performed a detailed mechanistic study on methanol photoreforming in the gas phase [23]. Quantitative monitoring of the main stable intermediates (formaldehyde and formic acid) and products (carbon dioxide and molecular hydrogen) at different methanol : water molar fractions provided abundant mechanistic information (Figure 3.1). In particular, it allowed to propose and fit a kinetic scheme that considered three different oxidation pathways: an indirect $^{\cdot}OH$ radical-mediated path, a hole-mediated direct path, or a direct water-assisted path.

It is important to mention that the role of $^{\cdot}OH$ radicals has been a hotly debated topic in the photocatalytic community. Although the production of $^{\cdot}OH_{free}$ from water photooxidation over TiO_2 has been strongly challenged [24], it can be safely assumed that the semiconductor surface can indeed provide trap states for holes (for instance, at two-fold coordinated bridging oxygen atoms), which can then be subsequently transferred to organic molecules. As a separate pathway, free valence band holes can also be directly transferred to the organic substrates [25]. One or both mechanisms could be operative, depending on the identity of the molecule: while weakly interacting species favor an indirect pathway (e.g. benzene), those that show a strong electronic interaction with the surface (i.e. are strongly chemisorbed, such as formic acid) generally react with holes in a direct way [25].

The mechanism proposed by Chiarello et al. considers a special oxidation path as well, occurring far from the hydrogen-evolving co-catalyst. In such a case, protons produced from the direct oxidation of methanol (see Eq. (3.7)) are initially far from the co-catalyst, and thus need to be transferred through neighboring hydroxyl groups to the noble metal particles. It is thus described as "water-assisted" oxidation. Kinetic

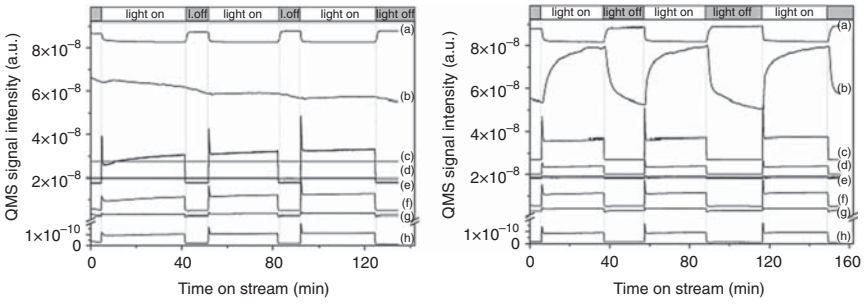

Figure 3.1 Quadrupole MS signals recorded during the gas-phase photocatalytic reforming of methanol over Pt-TiO_2, with H_2O (left) and D_2O (right), and a methanol molar fraction of 0.045, in three consecutive irradiation cycles. The registered traces correspond to: (a) the $^{+}CH_2 = OH$ fragment of methanol, (b) HDO, (c) D_2, (d) HD, (e) H_2, (f) CO_2, (g) CO, and (h) HCOOH. Source: Chiarello [23]/with permission of Elsevier.

fitting allowed the authors to determine that this pathway strongly contributed in the oxidation of methanol and formaldehyde at most methanol : water molar fractions.

To differentiate between the direct and indirect oxidation pathways, the authors resorted to isotopic labeling. They reasoned that, when employing CH_3OH–D_2O mixtures, two D_2 molecules and four HDO molecules would be produced from indirect oxidation (Eqs. (3.2)–(3.6)).

$$D_2O + h^+_{vb} \rightarrow \dot{O}D + D^+ \tag{3.2}$$

$$CH_3OH + 2\dot{O}D \rightarrow CH_2O + 2HDO \tag{3.3}$$

$$CH_2O + 2\dot{O}D \rightarrow HCOOD + HDO \tag{3.4}$$

$$HCOOD + 2\dot{O}D \rightarrow CO_2 + HDO + D_2O \tag{3.5}$$

$$2D^+ + 2e^-_{CB} \rightarrow D_2 \tag{3.6}$$

In contrast, if considering only the direct oxidation mechanism (Eqs. (3.7)–(3.10)), H_2, HD, and D_2 production would be expected, without any HDO. Based on the reaction stoichiometry, the formed gases (H_2, HD, and D_2) would contain 33.3% of D atoms and 66.7% of H atoms.

$$CH_3OH + 2h^+_{vb} \rightarrow CH_2O + 2H^+ \tag{3.7}$$

$$CH_2O + D_2O + 2h^+_{vb} \rightarrow HCOOH + D^+ + H^+ \tag{3.8}$$

$$HCOOH + 2h^+_{vb} \rightarrow CO_2 + D^+ + H^+ \tag{3.9}$$

$$2D^+ + 4H^+ + 6e^-_{CB} \rightarrow zHD + (1-z)D_2 + (2-z)H_2 \quad (\text{with } 0 \le z \le 1) \tag{3.10}$$

Moreover, in the water-assisted direct oxidation path that considers proton diffusion on the photocatalyst surface, isotopic exchange between H^+ and D^+ is expected to occur (Eq. (3.11)), increasing the D content in the evolved gases. Therefore, considering that the reaction proceeds through the three paths simultaneously, HDO is expected to be produced, alongside HD, D_2, and H_2, with a D atom content greater than 33.3%, and the exact value determined by the contribution of each reaction path.

$$D_2O + H^+ \rightarrow DHO + D^+ \tag{3.11}$$

We reproduce the mass spectrometry (MS) signals for a set of experiments on two different photocatalysts (Pt-TiO_2 and Au-TiO_2) and using three different methanol molar fractions (x = 0.0045, 0.10, or 0.64) in Figure 3.2. The main result is that the fraction of D-atoms in the evolved gas significantly decreased with increasing x, being 86%, 75%, and 26%, respectively for the aforementioned molar fractions in the Pt-TiO_2 system. In addition, HDO is produced only at the two lowest methanol molar fractions. This indicates that, at low x, the indirect pathway prevails, as shown

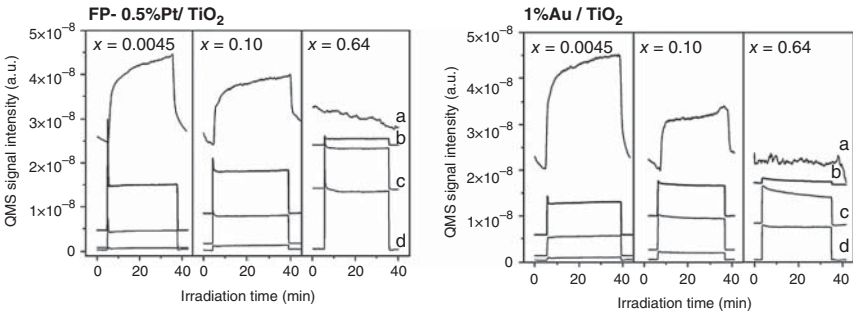

Figure 3.2 Quadrupole MS signals recorded during the photoreforming of D_2O/CH_3OH vapors in Ar for three different methanol molar fractions ($x = 0.0045$, 0.10, and 0.64) over Pt-TiO_2 and Au-TiO_2. The traces correspond to: (a) HDO, (b) D_2, (c) HD, and (d) H_2. Source: Chiarello [23]/with permission of Elsevier.

by HDO formation and D_2 being the main product; contrarily, at high *x,* the direct path is favored, with H_2 as the main product and no HDO formation.

In addition, the amount of produced CO_2 was independent of the water isotopologues, implying that the overall photoactivity was not affected by substituting H_2O for D_2O.

More common are studies of photocatalytic processes in suspension. Kandiel et al. [26] studied the photocatalytic reforming of aqueous methanol for long irradiation periods over platinized TiO_2 employing MS. They detected H_2 and CO_2 as the sole products. After the complete consumption of methanol in the system, the calculated ratio of evolved H_2 to CO_2 was close to 3 : 1, that is, the stoichiometric ratio for the complete reforming of methanol (Eq. (3.12)).

$$CH_3OH + H_2O \xrightarrow{Pt-TiO_2, h\nu} 3H_2 + CO_2 \tag{3.12}$$

Since the evolved amount of H_2 did not exceed the expected one for this reaction, the possibility of simultaneous (or subsequent) water splitting was excluded. Moreover, to identify the origin of the photocatalytically evolved hydrogen, the authors performed a series of experiments employing different methanol and water isotopologues: (a) CH_3OH/H_2O, (b) CD_3OD/D_2O, (c) CD_3OD/H_2O, and (d) $CH_3OH–D_2O$. As expected, only H_2 and D_2 were formed in cases (a) and (b), respectively. In case (c), the evolved gas was mainly H_2, suggesting water as the origin of molecular hydrogen. Interestingly, in case (d), the main product was D_2, although significant quantities of HD and H_2 were also detected. To account for the results of cases (c) and (d), the authors explain that the isotope present in water is in a 925 : 1 ratio to that in methanol, thus for statistical reasons, and given the possibility of proton exchange, the main molecular hydrogen isotopologue will match that of water. However, since H^+ reduction is favored in comparison to that of D^+, significant amounts of H_2 and HD are evolved from the $CH_3OH–D_2O$ system, even though H atoms are present in a much lower amount than D.

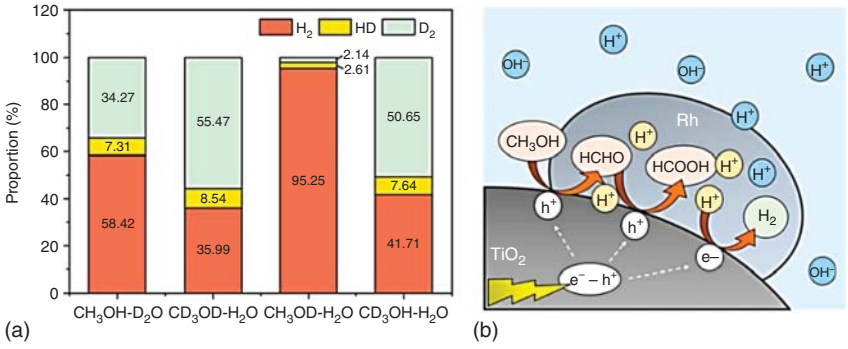

Figure 3.3 (a) Proportions of H_2, HD, and D_2 obtained from the photocatalytic reforming of methanol over Rh-loaded TiO_2, using different isotopologues for methanol and water. (b) Scheme of the proposed mechanism. Source: Fang et al. [27]/with permission of Elsevier.

It is noteworthy that the possibility of H (D) atoms originating from H_2O (D_2O) does not imply that water splitting is being observed. In fact, molecular hydrogen formation completely halts once methanol is depleted, illustrating that neither pristine nor Pt-modified TiO_2 can photocatalytically split water at appreciable rates.

A recent study from Fang et al. [27] led to different conclusions. These authors employed Rh-TiO_2 and evaluated hydrogen production in CH_3OH–H_2O mixtures with different isotopic compositions. In a CH_3OH–D_2O mixture, the main product was H_2; the total fraction of H in the evolved gas was 62%, vs. 38% for D (Figure 3.3a). Similarly, a CD_3OD–H_2O mixture led to a 60% : 40% D to H ratio. Moreover, hydrogen formation showed a solvent KIE of ~1.6 (k_{H2O}/k_{D2O}), and KIEs of 1.91 and 1.07 for CH_3OH/CH_3OD and CH_3OH/CD_3OH, respectively. This highlights the role of the O—H bond breakage in the process. Based on these results, the authors proposed a reaction mechanism (Figure 3.3b).

3.2.3 Carbonyl Compounds

Acetic acid has been shown to be a good hole scavenger in photocatalytic hydrogen production systems. However, the photocatalytic conversion of aqueous acetic acid not only produces H_2 and CO_2 but also hydrocarbons [28, 29] and oxygenated compounds [30, 31]. This introduces an important complexity: each of those products can partake in further oxidation and reduction reactions. Hence, isotopic labeling investigations are helpful to disentangle the reaction mechanism [32].

In an aqueous system containing Pt/TiO_2 as the photocatalyst, acetic acid can directly react with the photogenerated holes, eventually producing methyl radicals $^{\cdot}CH_3$ via a photo-Kolbe reaction mechanism (Eqs. (3.14) and (3.15)) [33]. In turn, these readily react with other radicals in the system, i.e. either with another methyl radical to produce ethane C_2H_6, or with a hydrogen atom $^{\cdot}H$ on the surface of Pt nanoparticles to form methane CH_4 (Eqs. (3.16) and (3.17)) [32]. Production of methane is preferred over dimerization, as evidenced by the formation of higher amounts of this compound with respect to ethane [29].

In addition, it has been postulated that $^{\cdot}OH$ radicals can form upon oxidation of water over the TiO_2 surface (Eq. (3.13)), and then can react with acetic acid via the abstraction of a hydrogen atom to produce $^{\cdot}CH_2COOH$ (Eq. (3.18)); these radicals can then react with e.g. $^{\cdot}CH_3$, $^{\cdot}OH$, or $^{\cdot}CH_2COOH$ to form several organic products [31]. In acidic media, however, the direct reaction between holes and acetic acid is dominant over the oxidation pathway involving $^{\cdot}OH$ radicals [30].

$$TiO_2(h^+) + H_2O \rightarrow TiO_2 + {}^{\cdot}OH + H^+ \tag{3.13}$$

$$TiO2(h^+) + CH_3COOH \rightarrow TiO_2 + CH_3COO^{\cdot} + H^+ \tag{3.14}$$

$$CH_3COO^{\cdot} \rightarrow {}^{\cdot}CH_3 + CO_2 \tag{3.15}$$

$$^{\cdot}CH_3 + {}^{\cdot}CH_3 \rightarrow C_2H_6 \tag{3.16}$$

$$^{\cdot}CH_3 + {}^{\cdot}H_{ads(Pt)} \rightarrow CH_4 \tag{3.17}$$

$$^{\cdot}OH + CH_3COOH \rightarrow H_2O + {}^{\cdot}CH_2COOH \tag{3.18}$$

The use of different isotopic mixtures in the photocatalytic system, i.e. (i) $CD_3COOD–H_2O$, (ii) $CH_3COOD–H_2O$, (iii) $CD_3COOD–D_2O$, (iv) $CH_3COOH–D_2O$, and (v) $CH_3COOD–D_2O$, strongly influences the reaction rates, as studied for Pt/TiO_2. Photoreforming of CD_3COOD produces 1.3–1.5 times larger amounts of CO_2 compared to CH_3COOH (in either H_2O or D_2O) [32]. When H_2O is used as a solvent, a rapid exchange of acidic protons occurs [34] (Eq. (3.19)), making CO_2 evolution from CH_3COOD and CH_3COOH very close to each other. The evolved amounts of CO_2 from a specific organic substrate (either $CH_3COOH(D)$ or $CD_3COOD(H)$) are independent of the solvent used (H_2O or D_2O), because $CD_3COOD(H)$ is more readily oxidized than $CH_3COOH(D)$ [32].

$$CH_3COO–D + H–O–H \leftrightarrow CH_3COO–H + H–O–D \tag{3.19}$$

As mentioned above, the H-isotopologues of carboxylic acids produce various by-products upon their light-induced decomposition, whilst fewer by-products are generated from the D-isotopologues [35]. However, the reaction rate of the decarboxylation of acetic acid is independent of the employed solvent. Contrarily, the evolved molecular hydrogen isotopologue is directly related to the solvent used: while H_2 is the main product in the case of $CD_3COOD–H_2O$, D_2 is dominant for $CH_3COOH–D_2O$ [32].

Eqs. (3.20)–(3.26) describe the mechanism of H_2, D_2, and HD formation in the $CD_3COOD–H_2O$ system. It is expected that in H/D mixed reaction systems like $CD_3COOD–H_2O$, $CH_3COOD–H_2O$, $CH_3COOH–D_2O$, and $CH_3COOD–D_2O$, a fast proton exchange reaction occurs [34] as can be seen in Eq. (3.19). At the same time, since the number of substrate molecules is negligible compared to the number of solvent molecules present in the system, the reduction of protons originating from the solvent decomposition is highly favored. This prevents a definite determination of the source of the protons that are eventually reduced to produce hydrogen [32].

$$TiO_2(h^+) + D_2O \rightarrow TiO_2 + {}^{\cdot}OD + D^+ \quad (3.20)$$

$$H_2O + D^+ \rightarrow HDO + H^+ \quad (3.21)$$

$$CD_3COO^{\cdot} \rightarrow {}^{\cdot}CD_3 + CO_2 \quad (3.22)$$

$$TiO_2(e^-) + D^+{}_{ads(Pt)} \rightarrow TiO_2 + {}^{\cdot}D_{ads(Pt)} \quad (3.23)$$

$$TiO_2(e^-) + H^+{}_{ads(Pt)} \rightarrow TiO_2 + {}^{\cdot}H_{ads(Pt)} \quad (3.24)$$

$${}^{\cdot}D_{ads(Pt)} + {}^{\cdot}D_{ads(Pt)} \rightarrow D_2 \quad (3.25)$$

$${}^{\cdot}D_{ads(Pt)} + {}^{\cdot}H_{ads(Pt)} \rightarrow HD \quad (3.26)$$

Oxalic acid is a compound that, despite its strong adsorption to TiO_2, has not been used very often as a hole scavenger in photocatalytic H_2 production. We speculate this may be related to the absence of C—H neighboring to the carboxylate group, often seen as a prerequisite for H-abstraction [36, 37]. Nevertheless, oxalic acid photoreforming yields a higher H_2 production rate than formic acid and formaldehyde over TiO_2 [36, 38].

The source of H_2 evolved from the photocatalytic reforming of oxalic acid over Pt/TiO_2 has been studied using several D_2O–H_2O mixtures as solvent. As shown in Figure 3.4, upon increasing the D_2O fraction, both the rate of production and total yield of H_2 and CO_2 gases gradually decreased. In particular, the amount of CO_2 was ~1.5 times lower in the case of $C_2H_2O_4$–D_2O than in the case of $C_2H_2O_4$–H_2O [39]. In line with the results described above for acetic acid, no H_2 or HD was detected when using D_2O as the solvent, while HD, H_2, and D_2 were evolved from the photoreforming of $C_2H_2O_4$ dissolved in D_2O–H_2O mixtures. The isotopic composition of the evolved molecular hydrogen was in all cases similar to that of the solvent, suggesting at first glance that the latter may be the source of the atoms in the gas [39]. However, as discussed throughout this chapter, the fact that the solvent is in a much larger concentration than oxalic acid, together with the fast proton exchange reaction rate, could very well mask the real origin of the atoms.

The use of D_2O as a solvent lowers the CO_2 and H_2 evolution rates with respect to H_2O. Such a phenomenon has been also noticed in the case of Pt/TiO_2 photocatalytic reforming of formaldehyde [40], methanol, and benzene [41]. In those cases, the decrease in the reaction rate has been explained by a hindrance in ${}^{\cdot}OH$ (${}^{\cdot}OD$) radical generation. However, in the case of oxalic acid, a direct reaction with the photogenerated holes at the surface is the dominant mechanism (Eqs. (3.27) and (3.28)). Therefore, the isotopic effect on kinetics could be related to the proton reduction step, which is considered the rate-determining step [42, 43]. Moreover, only H_2 and HD could be detected when the D_2O content in the solvent was lower than 50%, a fact related to the preferential protium reduction [42].

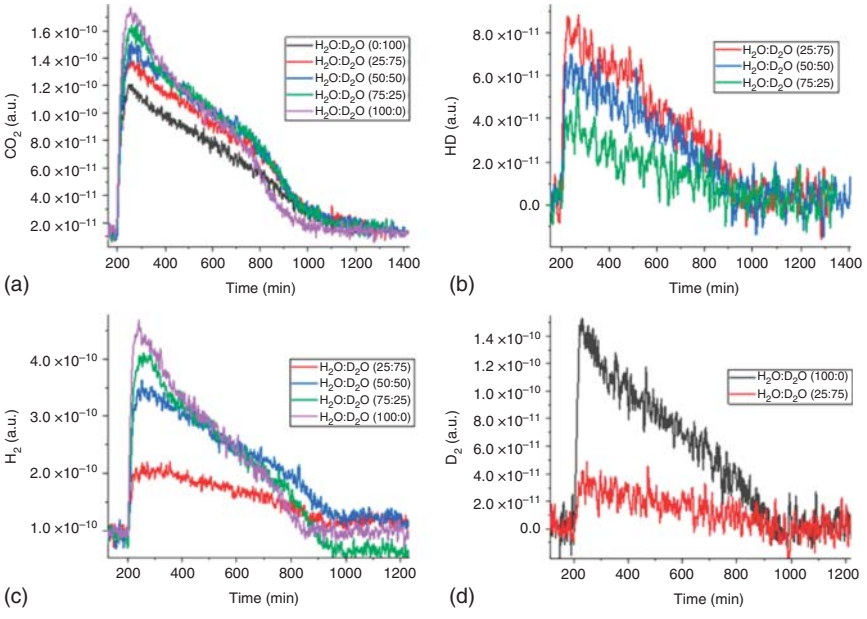

Figure 3.4 Quadrupole mass spectrometry (QMS) signals for the generated CO_2 (a), HD (b), H_2 (c), and D_2 (d) using different H_2O/D_2O mixtures over Pt/TiO_2 during the photocatalytic reforming of oxalic acid. Source: AlSalka et al. [39]/MDPI/CC BY 4.0.

$$HC_2O_4^- + TiO_2(h^+) \rightarrow HC_2O_4^{\cdot} + TiO_2 \tag{3.27}$$

$$HC_2O_4^{\cdot} \rightarrow CO_2 + HCO_2^{\cdot} \rightleftharpoons {}^{\cdot}CO_2^- + H^+ \tag{3.28}$$

Formic acid is considered one of the most promising hydrogen storage materials because of its high hydrogen content ($43.8\,g\,H_2\ kg^{-1}$) [44]. Although it can be readily dehydrogenated via different (electro-)chemical processes, these are usually accompanied by undesired side-reactions such as CO production [45]. Alternatively, Stucky and coworkers have studied its photoreforming over AgPd supported on g-C_3N_4 photocatalysts and employed H/D isotope labeling to analyze the mechanism [46]. Under visible light irradiation and using D_2O as a solvent, the D content in the evolved gas was around 65%; however, an 87% D content was detected in the product when white light (i.e. with a UV component) was used, suggesting a wavelength-dependent mechanism. Furthermore, the hemi-reactions of the photocatalytic process occur at different components of the photocatalyst. While AgPd serves as the water reduction site, g-C_3N_4 acts as the formic acid oxidation site [47, 48].

Formaldehyde has been studied as a hole scavenger using Pt/TiO_2 under irradiation in oxygen-free conditions [49]. The global equation for its photocatalytic reforming is shown in Eq. (3.29).

$$HCHO + H_2O\,(Pt/TiO_2) \rightarrow CO_2 + 2H_2 \tag{3.29}$$

Qualitative analysis of isotopic exchange using MS and H_2O or D_2O as solvent revealed the evolution of different molecular hydrogen isotopologues [49]. In line with the results described above for other substrates, the evolved isotopologues followed those of the solvent. Moreover, the rate of CO_2 production was highest in the system containing pure water as the solvent, while it decreased linearly as the fraction of D_2O increased. This behavior was explained based on the oxidation potential of $^{\cdot}OD$ radicals, which is lower compared to the oxidation potential of $^{\cdot}OH$ radicals. This explanation thus assumes that oxidation proceeds through the intermediate formation of these radicals.

Attenuated total reflection–Fourier-transform infrared (ATR–FTIR) investigations showed as well that formaldehyde gradually converts to deuterated formic acid on the surface of irradiated Pt/TiO_2 in D_2O, as confirmed by the shifting of different bands in FTIR spectra [49]. Formic acid then undergoes direct oxidation in a photo-Kolbe reaction. Moreover, it was suggested that the presence of D_2O in the solvent can perturb the structure of adsorbed intermediates, as illustrated by the transformation of formate from a bidentate structure to a monodentate one (Figure 3.5) [50]. This information allowed the authors to propose a complete mechanism for the photoreforming of formaldehyde, shown in Figure 3.6.

3.2.4 Aromatic Compounds

Yang et al. [51] studied the photoelectrocatalytic degradation of 4-chlorophenol over TiO_2 electrodes under UV illumination. The isotopic tracer experiments with $H_2{}^{18}O$ indicate that most of the $^{\cdot}OH$ radicals that formed the primary hydroxylated intermediates were derived from the oxidation of adsorbed H_2O or OH^- by photogenerated holes. Several studies have reported this process as the rate-determining step of the photocatalytic degradation of aromatic compounds [52].

More recently, Al-Madanat et al. studied the photocatalytic reforming of naphthalene isotopologues in suspensions with variable H_2O–D_2O compositions over $Pt\text{-}TiO_2$, by means of MS [42]. The authors found that the isotopic composition of the evolved hydrogen matched that of the solvent and not that of naphthalene. Analyzing the reaction rates revealed that only water is apparently involved in the rate-determining step of the reaction. The decrease in the total amount of evolved gases (H_2, HD, and D_2) as the D_2O fraction increases (Figure 3.7) indicates a reduction in the reaction rate. Similar behavior has been observed for the

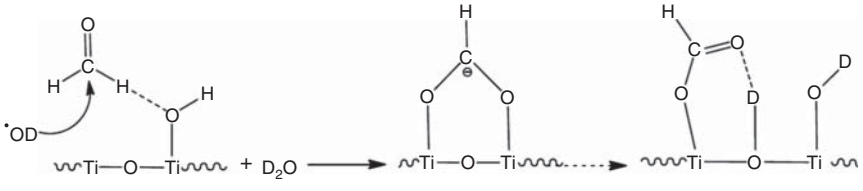

Figure 3.5 Photocatalytic formaldehyde oxidation in the presence of D_2O over Pt/TiO_2. Formate is formed, and its adsorption mode changed in presence of D_2O. Source: Reproduced with permission from Belhadj [50].

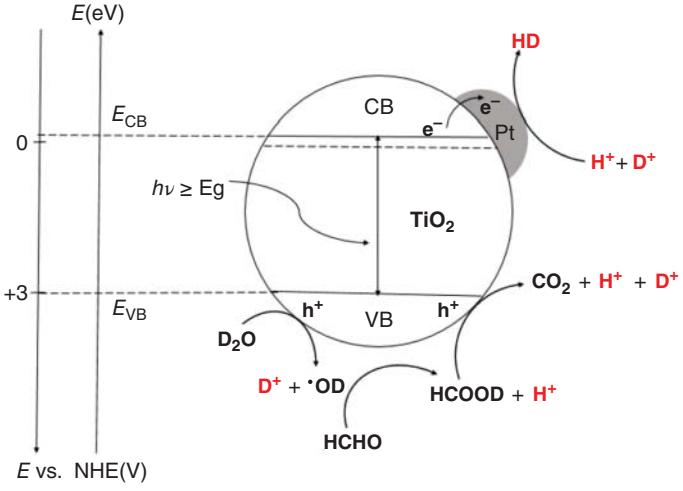

Figure 3.6 Proposed mechanism of the photocatalytic reforming of formaldehyde in D_2O. Source: Reproduced with permission from Belhadj [50].

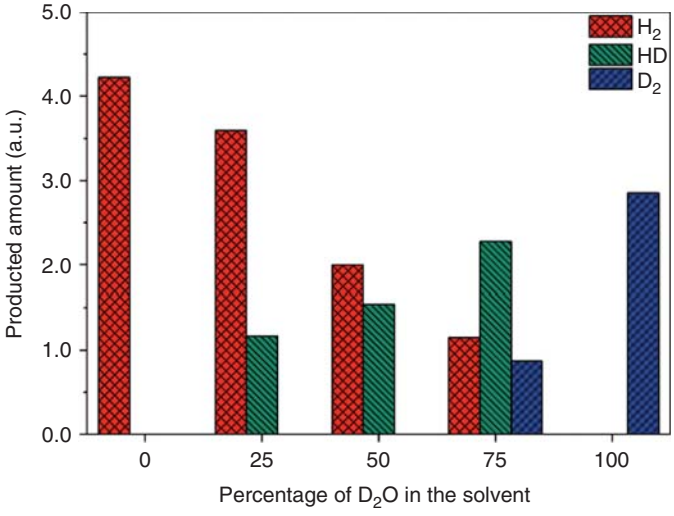

Figure 3.7 Evolved gases (H_2, HD, and D_2) during the photocatalytic reforming of aqueous naphthalene over Pt-UV100 employing different D_2O/H_2O compositions. Source: Al-Madanat, et al. [42]/with permission of American Chemical Society.

photocatalytic reforming of benzene over platinized TiO_2 and is interpreted by the hindered production of $^{\cdot}OH$ radicals when using D_2O [53]. In the naphthalene study, however, these radicals were not considered to play an important role on the basis of EPR spin-trapping experiments [42]. Moreover, Post and Hiskey [40] have reported that the overvoltage for molecular hydrogen evolution from D_2O is 50–87 mV greater than in H_2O. Therefore, the observed KIE (k_H/k_D) of 1.3 could respond to a rate-determining step related to proton reduction.

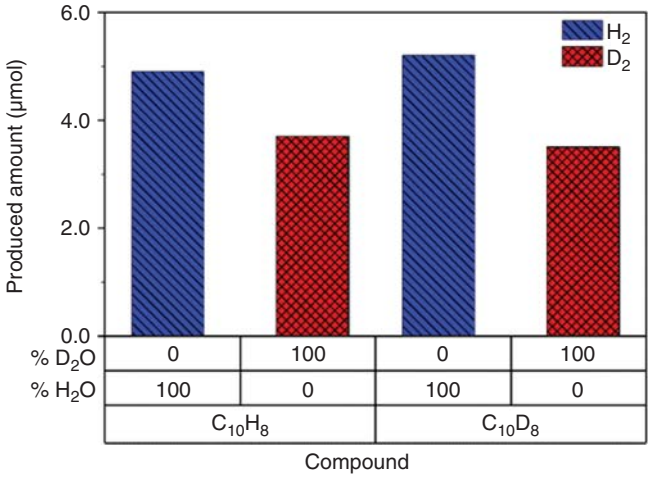

Figure 3.8 Isotopic distribution of the evolved gases (H_2 and D_2) from the photocatalytic reforming of aqueous natural or deuterated naphthalene, over Pt-UV100 employing D_2O or H_2O. Source: Al-Madanat, et al. [42]/with permission of American Chemical Society.

The use of either natural-composition or deuterated naphthalene leads to very similar amounts of evolved hydrogen, when accounting for the solvent effect (H_2O or D_2O, Figure 3.8). This suggests that, in contrast with water, hydrogen abstraction from naphthalene is not involved in the rate-determining step of the reaction. Similar conclusions have been reported for the photocatalytic reforming of aqueous benzene over platinized TiO_2 [53].

3.3 Isotopic Substitution on the Photocatalyst

Previous sections have dealt with isotopic substitution in either the solvent or the substrate molecules involved in the photocatalytic reaction. An alternative way in which isotopic substitution can be applied to unravel photocatalytic mechanisms is on the photocatalyst itself. This significantly broadens the scope of experimental techniques that can be used to characterize the materials and photoinduced reactions, as we illustrate below.

3.3.1 Ti Substitution

Given the popularity of TiO_2-based materials, it is not surprising that most studies of this type were performed on this photocatalyst. We can initially divide them by the isotopically substituted element, that is, Ti or O. In the former's case, there is a relatively small number of examples, mostly dealing with the structural properties of the materials. For instance, Henderson et al. have analyzed defect diffusion in single-crystalline anatase [54] and rutile [55] TiO_2 surfaces. Using ^{46}Ti- or

^{18}O-enriched samples and static secondary ion mass spectrometry (SSIMS), these authors demonstrated differential behavior between anatase and rutile. While in anatase both Ti and O ions diffuse from the surface into the bulk under vacuum reduction (or vice versa during oxidation), only Ti ions do so in rutile. The relevance of these studies, besides the understanding of the processes themselves, resides in the great promise that defect engineering presents for highly efficient hydrogen evolving materials, as exemplified by the so-called "black TiO_2" [56] or other partially reduced TiO_2-based materials that show photoinduced hydrogen evolution without the need for noble metal co-catalysts [57].

Titanium isotopes are also relevant for nuclear magnetic resonance (NMR) studies on photocatalytic materials. Two of the five stable Ti isotopes are magnetically active: ^{47}Ti and ^{49}Ti, with a natural abundance of 7.4% and 5.4%, respectively [58]. These low values, together with other problematic properties such as their quadrupole moment, render them challenging for solid-state NMR. However, relatively recent advances in NMR have enabled studying these species. Indeed, a recent book chapter by Lucier and Huang provides a comprehensive account of NMR applications on Ti-based systems [58]. Early work by Kolem and Kanert, using some of these advances in NMR, has carefully monitored the motion of defects in rutile under different temperatures and oxygen partial pressures [59]. More recently, Toberer et al. employed NMR to study changes in the local environment of Ti as a Zn_2TiO_4 precursor progressively formed a hierarchically porous rutile TiO_2 material [60]. Interestingly, chemical reduction using H_2 led to signals that, being accompanied by a dark blue coloration, were ascribed to Ti^{3+} centers (Figure 3.9). Although these signals were relatively weak, they may provide a unique way to characterize partially reduced TiO_2 samples.

Other studies exploited the fact that the local Ti environment (and thus NMR response) is different for anatase, rutile, and brookite to study crystallinity and phase distribution in TiO_2 nanoparticles. Although XRD can, in principle, be used to quantify crystalline phases (e.g. via Rietveld refinement [61]), the typically broad

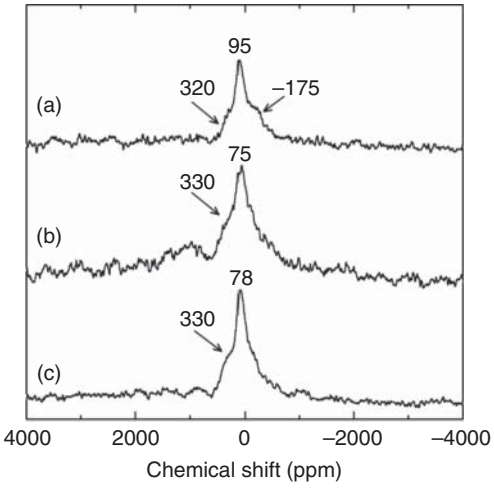

Figure 3.9 Spin-echo ^{47,49}Ti NMR spectra of (a) macroporous Zn_2TiO_4 after acid leaching and (b, c) of the same sample after subsequent reduction in flowing 5%H_2/N_2 at 1023 K for (b) 1 and (c) 12 hours. The positions of the main signals (in ppm) are highlighted. The feature at 330 ppm is assigned to Ti^{3+} species. Spectra were collected at room temperature and in a magnetic field of 19.6 T. Source: Toberer [60]/with permission of American Chemical Society.

reflections from nanoparticulated materials can complicate such analysis. The work by Gervais et al. nicely shows how XRD estimations can be independently supported by solid-state NMR to obtain reliable phase compositions in different samples [62]. Quantitative XRD measurements can also be complicated by the presence of amorphous phases [63]. On the other hand, a comprehensive study on ^{17}O- and ^{49}Ti-enriched titania–silica glasses across a range of Ti:Si ratios provides an example where amorphous and anatase phases could be well differentiated by combining neutron diffraction with solid-state NMR [64]. This study determined that, at low Ti : Si ratios (8 : 92), Ti simply substituted Si in a tetrahedral coordination environment, while higher ratios (18 : 82) led to phase separation (i.e. TiO_2 formation), to which ^{17}O NMR is very sensitive [64].

Very recently, a novel NMR approach to monitor quadrupolar nuclei has been developed and applied to TiO_2-supported MoO_3 [65]. This technique has allowed the observation of ^{49}Ti surface sites and notably, the preferential location of the amorphous TiO_2 phase at the surface of the particles. In addition, the authors have demonstrated its application on Al-doped ZnO nanoparticles, which also have potential applications as a photocatalytic material [65].

3.3.2 O Substitution

More abundant are studies in which isotopic substitution was performed on the oxygen atoms of TiO_2. In fact, a review by Zhao et al. provides a summary of photocatalytic studies employing ^{18}O [66], while the same topic was also covered in a recent review by some of us [67].

To follow the historical timeline, we start with studies in which labeled O was initially not part of the TiO_2 lattice, but was instead incorporated by a photoinduced exchange with molecular $^{18}O_2$. In the early 70s, Formenti, Courbon, et al. observed for the first time that the irradiation of anatase powders in the presence of $^{18}O_2$ led to the production of $^{16}O^{18}O$ and $^{16}O_2$ in the gas phase [68, 69]. Moreover, the fact that the concentration of $^{16}O^{18}O$ rapidly increased upon starting irradiation helped them in determining that the operative mechanism involved one surface oxygen atom at a time [69].

Additionally, the analysis of the oxygen exchange activity and photocatalytic oxidation rate over different oxides (including ZnO, TiO_2, ZrO_2, SnO_2, and V_2O_5) [69–73] found a strong correlation between the two, pointing to the requirement of labile surface O atoms for efficient photooxidation [70]. In a more recent article, Pichat et al. used the oxygen isotopic exchange technique to assess the accessibility of the TiO_2 surface when deposited together with a non-active material [70], which is of relevance for commercial formulations of cost-effective photocatalysts [74].

It is noteworthy that, although most studies of this type have employed labeled O_2, incorporation of oxygen atoms from other gases such as $N^{18}O$ and $S^{18}O_2$ has also been observed [75, 76]. Furthermore, Lin et al. performed revealing work on photoinduced oxygen exchange over TiO_2 by combining $^{18}O_2$ with CO, CO_2, carbonate, and formate, observing that CO does not exchange O with O_2, but the remaining compounds do [77]. This highlights a possible limitation of the technique: the more

complex the system under study, the harder it may become to unravel the mechanism by isotopic exchange since several dark and light-initiated processes may contribute to it. Another common source for labeled O has been through ^{18}O-enriched water. Indeed, several works have demonstrated the incorporation of this isotope as surficial hydroxyl groups in TiO_2 materials [67, 78].

Besides the photoinduced oxygen exchange, other works have explored oxidation mechanisms via ^{18}O-labeling the TiO_2 surface itself. Early work in this direction used the natural isotopologue of TiO_2, and then performed a surface enrichment in ^{18}O by promoting exchange with molecular $^{18}O_2$ at 750 K or electrochemically in $H_2{}^{18}O$ [79–81]. A shortcoming of this approach is that the enrichment of the surface is not complete; for instance, Henderson observed a 2.5 : 1 ratio of surficial ^{18}O to ^{16}O [80]. He utilized these samples to evaluate the temperature-dependent decomposition of formic acid over rutile (100) [80] and (110) [79] single-crystals, and in both cases, the incorporation of ^{18}O into oxidation products was confirmed.

Later on, Kavan et al. devised a synthetic procedure that yielded isotopically pure $Ti^{18}O_2$ [82], which paved the way for a number of studies on this material [9, 10, 21, 82–84]. The synthesis procedure was relatively straightforward, using $H_2{}^{17/18}O$ to hydrolyze a TiO_2 halide precursor (e.g. $TiCl_4$) [9, 82]. We should note, however, that isotopically substituted reagents tend to be expensive, and this may constrain the available synthesis pathways. For instance, syntheses in aqueous media, such as the amply used hydrothermal methods [85], may not be accessible due to the need for a large amount of isotopically substituted water.

In simultaneous with developing the synthetic procedure, Kavan et al. studied the isotope exchange between $Ti^{18}O_2$ and CO_2 both in the dark [82] and under irradiation [83]. In the dark, the exchange depended upon sample history: while a sample heated to a low temperature (473 K) did not display oxygen exchange, a sample annealed in vacuum at 723 K readily underwent exchange. This was explained by the oxygen vacancies that were introduced during high-temperature heating that acted as traps for CO_2 molecules [82]. Under irradiation conditions, although the pre-treatments did have a similar effect, both samples exhibited exchange [83]. An FTIR investigation also allowed us to propose a mechanism for the exchange [83]. Soon after, the same group performed a study using the same $Ti^{18}O_2$ with formic acid and found that all oxidation products (CO_2, CO, and H_2O) contained lattice oxygen atoms [10]. On the other hand, formic acid itself did not exchange oxygen atoms with the lattice, neither in the dark nor under illumination, and even prevented isotopic incorporation in the oxidation products when it was preadsorbed to the surface [10]. This was ascribed to a blocking effect from formic acid, which was also displayed by adsorbed water.

Employing a similarly synthesized $Ti^{18}O_2$ material, Montoya et al. performed a series of studies on aqueous and organic media, in which the authors tackled the role of bridging oxygen atoms on TiO_2 anaerobic photooxidations [9, 21, 84]. Using water, aqueous benzene, and benzene, phenol, and benzaldehyde in acetonitrile, led in all cases to the incorporation of lattice oxygen atoms to the photooxidation products. This was taken as a confirmation of the so-called "redox photooxidation

mechanism." [86] These studies, although in anaerobic conditions, employed silver salts as electron scavengers, and thus no hydrogen was evolved.

In addition to ^{18}O as mentioned above, the ^{17}O isotope has also seen applications through NMR studies of TiO_2 materials. This nucleus is amenable to NMR thanks to its small quadrupolar moment and large chemical shift range, but suffers from a very low natural abundance (0.037%), and thus requires enriching the samples [62, 87]. A good example is that by Bastow et al., who produced ^{17}O-labeled TiO_2 by hydrolyzing titanium isopropoxide with isotopically enriched $H_2{}^{17}O$ [87]. Magic-angle spinning NMR allowed to follow the crystallization process and changes in the Ti environment well beyond the capabilities of XRD (hindered by small crystallite sizes) [87].

This isotope has also been cleverly exploited for mechanistic studies by means of EPR spectroscopy. Giamello's group, in particular, performed a series of very interesting studies based on the inclusion of ^{17}O on the three main polymorphs of TiO_2: anatase [88], rutile [12], and brookite [89]. The nuclear spin of this isotope, $I = 5/2$, yields hyperfine interactions that can be detected using highly sensitive pulsed EPR, in contrast with ^{16}O, which has $I = 0$. These experiments allowed the description of the coordination sphere around Ti^{3+} centers. Moreover, the use of selective isotopic enrichment made it possible to discriminate between electrons trapped as Ti^{3+} species either in the bulk or at the surface.

3.3.3 H Substitution

Superficially, to say that binary oxides (such as TiO_2) are composed of two elements is a tautology. However, under common operating conditions, it is accepted that water is strongly adsorbed on their surfaces, thus constituting an integral part of the material [90]. We thus consider here studies in which isotopic substitution was performed on hydrogen atoms at the surface of the semiconductor.

Exploiting the fact that H and D have very different masses, most of these works employ vibrational spectroscopy, a very powerful technique to investigate photocatalytic surfaces. A recent book chapter by Hadjiivanov et al. summarizes important insights that can be obtained from this technique coupled with isotopic substitution [91]. The basic principle is easy to grasp: assuming that a vibration involving two atoms with masses M_A and M_B can be approximated as a harmonic oscillator, the stretching frequency ν depends on the reduced mass of the pair μ:

$$\nu = \frac{1}{2\pi}\sqrt{\frac{k}{\mu}} \tag{3.30}$$

where k is the force constant and the reduced mass is given by:

$$\mu = \frac{M_A M_B}{M_A + M_B} \tag{3.31}$$

Thus, upon performing isotopic substitution (e.g. from isotope A to A′), the vibrational frequencies will shift accordingly. To quantify this shift, one can define an isotopic shift factor i:

$$i = \frac{\nu_{AB}}{\nu_{A'B}} = \sqrt{\frac{\mu_{A'B}}{\mu_{AB}}} \tag{3.32}$$

As mentioned, due to the large mass difference between H and D, this substitution will lead to large shifts in the bands, while other substitutions, such as ^{12}C to ^{13}C, will produce more modest (but still measurable) band shifts. For instance, the expected isotopic shift factor when going from ^{12}C—H to ^{12}C—D is 1.362, while it is just 1.003 when going from ^{12}C—H to ^{13}C—H [91].

Grassian's group has explored this type of technique in various studies of catalytically relevant systems [92–94]. An interesting example is the study of SO_2 adsorption and photooxidation over TiO_2 [92]. The adsorption was shown to intimately involve surficial OH groups: the reaction of one OH with SO_2 led to adsorbed bisulfite, while the reaction of two OH groups with SO_2 yielded sulfite and water. Isotopic labeling was instrumental in uncovering the overlapping bands in the Ti—OH (Ti—OD) region around 3600 cm^{-1} (2700 cm^{-1}), as illustrated in Figure 3.10.

The dependence of the isotopic shift factor on the identity of the atoms can be exploited to determine which ones are involved in a given vibrational mode. To give an example, the expected i for the Zn–H/Zn–D substitution is 1.403. Experiments on ZnO surfaces exposed to either H_2 or D_2 have shown a band located at 1708 or 1233 cm^{-1}, respectively, yielding $i = 1.385$ [95]. On the other hand, the observed i is 1.3556 for the O—H/O—D pair [96]. Comparing these values thus allows assigning the bands to vibrations involving Zn and H atoms. It must also be noted that the experimental i values often differ from the expected values, as a result of partially wrong assumptions made in the aforementioned equation (such as the harmonic behavior).

Another interesting combination of infrared (IR) spectroscopy combined with isotopic substitution is that by Panayatov and Yates, who produced n-type TiO_2 by irradiating pristine TiO_2 with atomic H or D [97]. Remarkably, they observed the production of electron-hole pairs as a result of the H-atom irradiation. A broad spectral

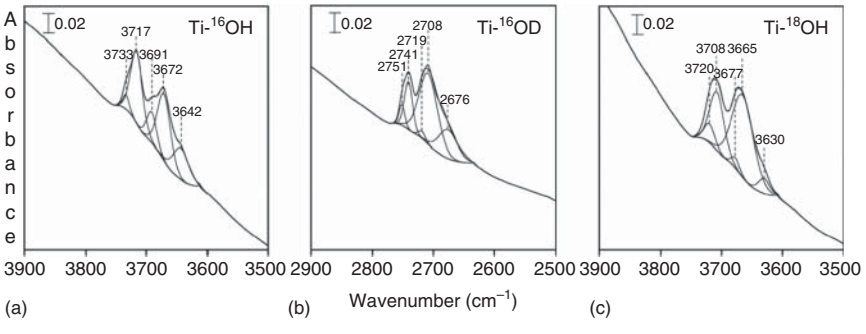

Figure 3.10 Fourier-Transform Infrared (FTIR) spectra in the OH or OD stretching regions for (a) unlabeled TiO_2, (b) deuterated TiO_2, and (c) ^{18}O-labeled TiO_2. Peak fittings are included, and positions are indicated in each plot. Source: Nanayakkara et al. [92]/with permission of Royal Society of Chemistry.

feature that appeared at ~2000 cm^{-1} was evaluated to be not related to vibrational modes involving H, since isotopic substitution to D did not yield any shift or change in the band. Instead, it was determined to be a trap state for charge carriers [97].

3.3.4 Substitution in Materials Other than TiO_2

Albeit less frequently than for TiO_2, mechanistic studies employing isotopic substitution have also been performed using other photocatalytic materials. Most of them, however, employ isotopically labeled substrates (not the photocatalysts themselves), and are therefore described in the preceding sections.

Continuing with the IR technique and H/D substitution, the work by Bocuzzi et al. mentioned above [95] helped to determine the specific interactions involved in the chemisorption of H_2/D_2 on ZnO, and to differentiate between dissociative and molecular adsorption on the semiconductor. More recent articles on ZnO using IR have explored water adsorption, where isotopic substitution allowed to determine that both molecular and dissociative adsorption take place, with a remarkable amount of detail regarding the specific ZnO facets involved [98].

Of great relevance for hydrogen production, which commonly involves a platinum co-catalyst, is the early work by Bewick and Russell [99] on electrochemical hydrogen production over Pt in aqueous systems. Employing IR in reflectance mode with either H_2O, D_2O, or mixtures of them, the authors concluded that hydrogen atoms weakly bound to platinum are at the same time strongly bound to distinctly oriented water molecules. Contrarily, for hydrogen atoms strongly bound to Pt, there is no significant perturbation of the structural arrangement of water molecules [99]. More recently, a study on well-defined Pt_{13} clusters was able to determine, upon gas-phase chemisorption of H_2 (or D_2), that H atoms bridge two Pt atoms across the edges of the metal clusters [100]. Although the specific properties of these clusters typically depend on their size [101], it is remarkable how IR in conjunction with isotopic substitution can offer a structural picture with rich atomistic details.

In a recent study, Huang et al. [102] provided an example of an increasingly important trend [103], that is, the use of organic polymers as photocatalytic materials for H_2 production. These authors employed heterostructures based on covalent triazine frameworks, where electron-withdrawing (benzothiadiazole) or electron-donating (thiophene) functionalities were cleverly incorporated to improve charge-carrier separation and thus decrease recombination, a common issue with organic materials. In this work, solid-state cross-polarization magic-angle-spinning ^{13}C-NMR was important to assess the actual incorporation of these functionalities, giving signals that are well-separated from the main polymer backbone. Isotopic enrichment was not necessary given the natural abundance of ^{13}C and the elemental composition of the materials.

Within the same broad class of materials, the group of Lotsch has provided an enlightening report on Pt-modified graphitic carbon nitride with remarkable efficiency toward H_2 production [104]. The key to this efficiency is a post-synthetic treatment (using a KSCN salt melt) that incorporates urea into the polymer network, providing a binding site for the Pt co-catalyst particles. As part of an extensive

characterization, the authors employed isotope-enriched $KS^{13}C^{15}N$, which helped confirm through FTIR and ^{13}C and ^{15}N NMR that urea was indeed incorporated into the material, and that it was involved in the binding to Pt particles, coordinating them through the oxygen atom. In addition, these experiments (that also included double correlation $^{1}H–^{15}N–^{13}C$ 2D NMR) provided structural information on the resulting polymers, such as an increased packing due to the urea modification [104].

3.4 Concluding Remarks

In this chapter we have tried to illustrate different use cases of isotopic substitution, and the mechanistic information that it allows to extract from heterogeneous photocatalytic systems. We did not attempt to cover all examples from the literature, but instead to provide a good overview of the range of possible applications – and the conclusions that each group of authors was able to derive.

Finally, we highlight a few rather obvious aspects involving isotopic labeling that were touched on in passing in the preceding sections. First and foremost, it must be mentioned that a limiting factor regarding isotopic labeling is the cost of the reagents that very much depends on the compound and isotopologues that one is interested in. As a simple example, D_2O can be acquired at a relatively low cost of $\sim$2 € g^{-1}; $H_2{}^{18}O$ can easily cost 200 times that, while the cost for $H_2{}^{17}O$ increases by a factor of 1000 (with decreasing isotopic purities, as well). Thus, isotopic substitution cannot be expected to become a widespread technique, especially in developing countries. On the bright side, the necessary equipment is normally of general use; as mentioned across this chapter, isotopologues are usually monitored via techniques such as MS, NMR, EPR, or FTIR, without the need for any special adaptation to consider the different isotopologues. In addition, the natural abundance of certain isotopes may render them detectable without the need for enrichment, as is the case for ^{13}C NMR, relevant e.g. when using sacrificial compounds for hydrogen production.

When analyzing the results, it is important to be aware of unexpected results. In particular, we highlight the possibility of hydrogen exchange when trying to ascertain the source of hydrogen atoms for H_2 production. For instance, several studies have analyzed the photoreforming of alcohols, employing different isotopologues for either the alcohol, water (the solvent), or both. In most cases, the isotopologues of the evolved hydrogen coincided with those of water (e.g. H_2 was produced from CD_3OD/D_2O, while D_2 was produced from CH_3OH/D_2O). However, alcohols generally exchange protons very fast with water [105]. Since the solvent is present in overwhelming majority, it is not surprising that the evolved molecular isotopologue matches that of the solvent. We note as well that some works have claimed the opposite result, with the H_2 isotopologue matching that of the alcohol [106]; this certainly provides proof on the origin of the atoms. This is the case, for instance, of the work by Zhao et al., who studied the photoreforming of different alcohols over Rh-doped $SrTiO_3$ [106], and proposed a concerted mechanism that could explain the absence of proton exchange with the solvent.

Regarding the KIE, we also highlight that, in some cases, it could be exploited to facilitate experimental analysis. For instance, H–D substitution could be employed to retard the decomposition of reaction intermediates, improving the chances of detection [67].

Acknowledgments

The studies performed in the laboratory "Photoactive nanocomposite materials" were supported by Saint-Petersburg State University (ID: 73032813).

References

1 Fujishima, A. and Honda, K. (1972). Electrochemical photolysis of water at a semiconductor electrode. *Nature* 238 (5358): 37–38.
2 Serpone, N.A. and Emeline, A.V. (2012). Semiconductor photocatalysis – past, present, and future outlook. *J. Phys. Chem. Lett.* 3 (5): 673–677.
3 Takanabe, K. (2017). Photocatalytic water splitting: quantitative approaches toward photocatalyst by design. *ACS Catal.* 7 (11): 8006–8022.
4 Nosaka, Y., Nishikawa, M., and Nosaka, A.Y. (2014). Spectroscopic investigation of the mechanism of photocatalysis. *Molecules* 19 (11): 18248–18267.
5 Günnemann, C., Curti, M., Schneider, J., and Bahnemann, D.W. (2020). Dynamics of photoinduced bulk and surface reactions involving semiconductors characterized by time resolved spectroscopy techniques (2015-2018). In: *Photochemistry*, vol. 47 (ed. A. Albini and S. Protti), 122–158. Royal Society of Chemistry.
6 Holder, C.F. and Schaak, R.E. (2019). Tutorial on powder X-ray diffraction for characterizing nanoscale materials. *ACS Nano* 13 (7): 7359–7365.
7 Rajeshwar, K. (2002). Fundamentals of semiconductor electrochemistry and photoelectrochemistry. In: *Encyclopedia of Electrochemistry* (ed. A.J. Bard). Wiley.
8 Schneider, J., Matsuoka, M., Takeuchi, M. et al. (2014). Understanding TiO_2 photocatalysis: mechanisms and materials. *Chem. Rev.* 114 (19): 9919–9986.
9 Montoya, J.F., Ivanova, I., Dillert, R. et al. (2013). Catalytic role of surface oxygens in TiO_2 photooxidation reactions: aqueous benzene photooxidation with $Ti^{18}O_2$ under anaerobic conditions. *J. Phys. Chem. Lett.* 4 (9): 1415–1422.
10 Civiš, S., Ferus, M., Zukalová, M. et al. (2012). Photochemistry and gas-phase FTIR spectroscopy of formic acid interaction with anatase $Ti^{18}O_2$ nanoparticles. *J. Phys. Chem. C* 116 (20): 11200–11205.
11 Cunningham, J. and Srijaranai, S. (1988). Isotope-effect evidence for hydroxyl radical involvement in alcohol photo-oxidation sensitized by TiO_2 in aqueous suspension. *J. Photochem. Photobiol., A* 43 (3): 329–335.
12 Livraghi, S., Maurelli, S., Paganini, M.C. et al. (2011). Probing the local environment of Ti^{3+} ions in TiO_2 (rutile) by ^{17}O HYSCORE. *Angew. Chem. Int. Ed.* 50 (35): 8038–8040.

13 Wolfsberg, M., Hook, W.A., Paneth, P., and Rebelo, L.P.N. (2009). *Isotope Effects*. Netherlands, Dordrecht: Springer.

14 Lin, Y., Deng, C., Wu, L. et al. (2020). Quantitative isotope measurements in heterogeneous photocatalysis and electrocatalysis. *Energy Environ. Sci.* 13 (9): 2602–2617.

15 Hisatomi, T., Maeda, K., Takanabe, K. et al. (2009). Aspects of the water splitting mechanism on $(Ga_{1-x}Zn_x)(N_{1-x}O_x)$ photocatalyst modified with $Rh_{2-y}Cr_yO_3$ cocatalyst. *J. Phys. Chem. C* 113 (51): 21458–21466.

16 Hisatomi, T., Miyazaki, K., Takanabe, K. et al. (2010). Isotopic and kinetic assessment of photocatalytic water splitting on Zn-added Ga_2O_3 photocatalyst loaded with $Rh_{2-y}Cr_yO_3$ cocatalyst. *Chem. Phys. Lett.* 486 (4–6): 144–146.

17 Sanwald, K.E., Berto, T.F., Jentys, A. et al. (2018). Kinetic coupling of water splitting and photoreforming on $SrTiO_3$-based photocatalysts. *ACS Catal.* 8 (4): 2902–2913.

18 Zhao, D., Wang, Y., Dong, C.-L. et al. (2021). Boron-doped nitrogen-deficient carbon nitride-based Z-scheme heterostructures for photocatalytic overall water splitting. *Nat. Energy* 6 (4): 388–397.

19 Wolff, C.M., Frischmann, P.D., Schulze, M. et al. (2018). All-in-one visible-light-driven water splitting by combining nanoparticulate and molecular co-catalysts on CdS nanorods. *Nat. Energy* 3 (10): 862–869.

20 Wang, Q., Nakabayashi, M., Hisatomi, T. et al. (2019). Oxysulfide photocatalyst for visible-light-driven overall water splitting. *Nat. Mater.* 18 (8): 827–832.

21 Montoya, J.F., Bahnemann, D.W., Salvador, P., and Peral, J. (2017). Catalytic role of bridging oxygens in TiO_2 liquid phase photocatalytic reactions: analysis of $H_2{}^{16}O$ photooxidation on labeled $Ti^{18}O_2$. *Catal. Sci. Technol.* 7 (4): 902–910.

22 Schneider, J. and Bahnemann, D.W. (2013). Undesired role of sacrificial reagents in photocatalysis. *J. Phys. Chem. Lett.* 4 (20): 3479–3483.

23 Chiarello, G.L., Ferri, D., and Selli, E. (2011). Effect of the CH_3OH/H_2O ratio on the mechanism of the gas-phase photocatalytic reforming of methanol on noble metal-modified TiO_2. *J. Catal.* 280 (2): 168–177.

24 Salvador, P. (2007). On the nature of photogenerated radical species active in the oxidative degradation of dissolved pollutants with TiO_2 aqueous suspensions: a revision in the light of the electronic structure of adsorbed water. *J. Phys. Chem. C* 111 (45): 17038–17043.

25 Montoya, J.F., Peral, J., and Salvador, P. (2014). Comprehensive kinetic and mechanistic analysis of TiO_2 photocatalytic reactions according to the direct–indirect model: (I) theoretical approach. *J. Phys. Chem. C* 118 (26): 14266–14275.

26 Kandiel, T.A., Ivanova, I., and Bahnemann, D.W. (2014). Long-term investigation of the photocatalytic hydrogen production on platinized TiO_2: an isotopic study. *Energy Environ. Sci.* 7 (4): 1420.

27 Fang, S., Liu, Y., Sun, Z. et al. (2020). Photocatalytic hydrogen production over Rh-loaded TiO_2: What is the origin of hydrogen and how to achieve hydrogen production from water? *Appl. Catal., B* 278: 119316.

28 Kawai, T. and Sakata, T. (1980). Photocatalytic decomposition of gaseous water over TiO_2 and TiO_2 – RuO_2 surfaces. *Chem. Phys. Lett.* 72 (1): 87–89.

29 Hamid, S., Dillert, R., and Bahnemann, D.W. (2018). Photocatalytic reforming of aqueous acetic acid into molecular hydrogen and hydrocarbons over co-catalyst-loaded TiO_2: shifting the product distribution. *J. Phys. Chem. C* 122 (24): 12792–12809.

30 Sakata, T., Kawai, T., and Hashimoto, K. (1984). Heterogeneous photocatalytic reactions of organic acids and water. New reaction paths besides the photo-Kolbe reaction. *J. Phys. Chem.* 88 (11): 2344–2350.

31 Hamid, S., Ivanova, I., Jeon, T.H. et al. (2017). Photocatalytic conversion of acetate into molecular hydrogen and hydrocarbons over Pt/TiO_2: pH dependent formation of Kolbe and Hofer-Moest products. *J. Catal.* 349: 128–135.

32 Hamid, S., Dillert, R., Schneider, J., and Bahnemann, D.W. (2018). Spectroscopic analysis of proton exchange during the photocatalytic decomposition of aqueous acetic acid: an isotopic study on the product distribution and reaction rate. *Catal. Sci. Technol.* 8 (22): 5886–5899.

33 Kraeutler, B., Jaeger, C.D., and Bard, A.J. (1978). Direct observation of radical intermediates in the photo-Kolbe reaction – heterogeneous photocatalytic radical formation by electron spin resonance. *J. Am. Chem. Soc.* 100 (15): 4903–4905.

34 Bonhoeffer, K.F. (1938). Deuteron transfer in solutions. *Trans. Faraday Soc.* 34: 252.

35 Singleton, D.L., Paraskevopoulos, G., and Irwin, R.S. (1989). Rates and mechanism of the reactions of hydroxyl radicals with acetic, deuterated acetic, and propionic acids in the gas phase. *J. Am. Chem. Soc.* 111 (14): 5248–5251.

36 AlSalka, Y., Al-Madanat, O., Curti, M. et al. (2020). Photocatalytic H_2 evolution from oxalic acid: effect of cocatalysts and carbon dioxide radical anion on the surface charge transfer mechanisms. *ACS Appl. Energy Mater.* 3 (7): 6678–6691.

37 AlSalka, Y., Hakki, A., Fleisch, M., and Bahnemann, D.W. (2018). Understanding the degradation pathways of oxalic acid in different photocatalytic systems: towards simultaneous photocatalytic hydrogen evolution. *J. Photochem. Photobiol., A* 366: 81–90.

38 Li, Y., Lu, G., and Li, S. (2001). Photocatalytic hydrogen generation and decomposition of oxalic acid over platinized TiO_2. *Appl. Catal., A* 214 (2): 179–185.

39 AlSalka, Y., Al-Madanat, O., Hakki, A., and Bahnemann, D.W. (2021). Boosting the H_2 production efficiency via photocatalytic organic reforming: the role of additional hole scavenging system. *Catalysts* 11 (12): 1423.

40 Post, B. and Hiskey, C.F. (1951). Electrokinetics of hydrogen evolution.[1,2] II. Deuterium overvoltage on mercury. *J. Am. Chem. Soc.* 73 (1): 161–164.

41 Yuzawa, H., Aoki, M., Itoh, H., and Yoshida, H. (2011). Adsorption and photoadsorption states of benzene derivatives on titanium oxide studied by NMR. *J. Phys. Chem. Lett.* 2 (15): 1868–1873.

42 Al-Madanat, O., AlSalka, Y., Curti, M. et al. (2020). Mechanistic insights into hydrogen evolution by photocatalytic reforming of naphthalene. *ACS Catal.* 10 (13): 7398–7412.

43 Yates, J.T. and McKee, D.W. (1981). Kinetic isotope effect in the heterogeneous reaction of graphite with H_2O (D_2O). *J. Chem. Phys.* 75 (6): 2711–2714.

44 Eppinger, J. and Huang, K.-W. (2017). Formic acid as a hydrogen energy carrier. *ACS Energy Lett.* 2 (1): 188–195.

45 Mori, K., Futamura, Y., Masuda, S. et al. (2019). Controlled release of hydrogen isotope compounds and tunneling effect in the heterogeneously-catalyzed formic acid dehydrogenation. *Nat. Commun.* 10 (1): 4094.

46 Xiao, L., Jun, Y.-S., Wu, B. et al. (2017). Carbon nitride supported AgPd alloy nanocatalysts for dehydrogenation of formic acid under visible light. *J. Mater. Chem. A* 5 (14): 6382–6387.

47 Wang, Y., Wang, X., and Antonietti, M. (2012). Polymeric graphitic carbon nitride as a heterogeneous organocatalyst: from photochemistry to multipurpose catalysis to sustainable chemistry. *Angew. Chem. Int. Ed.* 51 (1): 68–89.

48 Cao, S. and Yu, J. (2014). g-C_3N_4 -based photocatalysts for hydrogen generation. *J. Phys. Chem. Lett.* 5 (12): 2101–2107.

49 Belhadj, H., Hamid, S., Robertson, P.K.J., and Bahnemann, D.W. (2017). Mechanisms of simultaneous hydrogen production and formaldehyde oxidation in H_2O and D_2O over platinized TiO_2. *ACS Catal.* 7 (7): 4753–4758.

50 Belhadj, H. (2017) Solvent isotope effect (D_2O) in photocatalytic systems.

51 Yang, J., Dai, J., Chen, C., and Zhao, J. (2009). Effects of hydroxyl radicals and oxygen species on the 4-chlorophenol degradation by photoelectrocatalytic reactions with TiO_2-film electrodes. *J. Photochem. Photobiol., A* 208 (1): 66–77.

52 Li, Y., Wen, B., Yu, C. et al. (2012). Pathway of oxygen incorporation from O_2 in TiO_2 photocatalytic hydroxylation of aromatics: oxygen isotope labeling studies. *Chemistry* 18 (7): 2030–2039.

53 Yuzawa, H., Aoki, M., Otake, K. et al. (2012). Reaction mechanism of aromatic ring hydroxylation by water over platinum-loaded titanium oxide photocatalyst. *J. Phys. Chem. C* 116 (48): 25376–25387.

54 Herman, G.S., Zehr, R.T., and Henderson, M.A. (2013). Characterization of oxygen and titanium diffusion at the anatase TiO_2(001) surface. *Surf. Sci.* 612: L5–L8.

55 Henderson, M.A. (1999). A surface perspective on self-diffusion in rutile TiO_2. *Surf. Sci.* 419 (2–3): 174–187.

56 Naldoni, A., Altomare, M., Zoppellaro, G. et al. (2019). Photocatalysis with reduced TiO_2: from black TiO_2 to cocatalyst-free hydrogen production. *ACS Catal.* 9 (1): 345–364.

57 AlSalka, Y., Hakki, A., Schneider, J., and Bahnemann, D.W. (2018). Co-catalyst-free photocatalytic hydrogen evolution on TiO_2: synthesis of optimized photocatalyst through statistical material science. *Appl. Catal., B* 238: 422–433.

58 Lucier, B.E.G. and Huang, Y. (2016). Reviewing $^{47/49}$Ti solid-state NMR spectroscopy: from alloys and simple compounds to catalysts and porous materials. In: *Annual Reports on NMR Spectroscopy*, vol. 88, 1–78. Academic Press Inc.

59 Kolem, H. and Kanert, O. (1989). Nuclear magnetic resonance study of defect motion and cation diffusion in single crystal rutile (TiO_{2-x})/Kernmagnetische

Resonanz-Untersuchungen zur Defektbewegung und kationen-diffusion in einkristallinem rutil (TiO_{2-x}). *Int. J. Mater. Res.* 80 (4): 227–234.

60 Toberer, E.S., Epping, J.D., Chmelka, B.F., and Seshadri, R. (2006). Hierarchically porous rutile titania: harnessing spontaneous compositional change in mixed-metal oxides. *Chem. Mater.* 18 (26): 6345–6351.

61 Curti, M., Kirsch, A., Granone, L.I. et al. (2018). Visible-light photocatalysis with mullite-type $Bi_2(Al_{1-x}Fe_x)_4O_9$: striking the balance between bandgap narrowing and conduction band lowering. *ACS Catal.* 8 (9): 8844–8855.

62 Gervais, C., Smith, M.E., Pottier, A. et al. (2001). Solid-state ^{47,49}Ti MNR determination of the phase distribution of titania nanoparticles. *Chem. Mater.* 13 (2): 462–467.

63 Ohtani, B. (2010). Photocatalysis A to Z-What we know and what we do not know in a scientific sense. *J. Photochem. Photobiol., C* 11 (4): 157–178.

64 Pickup, D.M., Sowrey, F.E., Newport, R.J. et al. (2004). The structure of TiO_2-SiO_2 sol-gel glasses from neutron diffraction with isotopic substitution of titanium and ^{17}O and ^{49}Ti solid-state NMR with isotopic enrichment. *J. Phys. Chem. B* 108 (30): 10872–10880.

65 Nagashima, H., Trébosc, J., Trébosc, J. et al. (2020). Observation of low-γ quadrupolar nuclei by surface-enhanced NMR spectroscopy. *J. Am. Chem. Soc.* 142 (24): 10659–10672.

66 Pang, X., Chen, C., Ji, H. et al. (2014). Unraveling the photocatalytic mechanisms on TiO_2 surfaces using the oxygen-18 isotopic label technique. *Molecules* 19 (10): 16291–16311.

67 Günnemann, C., Bahnemann, D.W., and Robertson, P.K.J. (2021). Isotope effects in photocatalysis: an underexplored issue. *ACS Omega* 6 (17): 11113–11121.

68 Formenti, M., Courbon, H., Juillet, F. et al. (1972). Photointeraction between oxygen and nonporous particles of anatase. *J. Vac. Sci. Technol.* 9 (2): 947–952.

69 Courbon, H., Formenti, M., and Pichat, P. (1977). Study of oxygen isotopic exchange over ultraviolet irradiated anatase samples and comparison with the photooxidation of isobutane into acetone. *J. Phys. Chem.* 81 (6): 550–554.

70 Pichat, P., Courbon, H., Enriquez, R. et al. (2007). Light-induced isotopic exchange between O_2 and semiconductor oxides, a characterization method that deserves not to be overlooked. *Res. Chem. Intermed.* 33 (3–5): 239–250.

71 Sato, S. (1987). Photocatalytic activities of metal oxide semiconductors for oxygen isotope exchange and oxidation reactions. *J. Catal.* 106 (1): 295–300.

72 Sato, S., Kadowaki, T., and Yamaguti, K. (1984). Photocatalytic oxygen isotopic exchange between oxygen molecule and the lattice oxygen of titanium dioxide prepared from titanium hydroxide. *J. Phys. Chem.* 88 (14): 2930–2931.

73 Tanaka, K. and Miyahara, K. (1974). Intermediate oxygen species of homomolecular oxygen exchange and the oxidation of carbon monoxide over zinc oxide under illumination. *J. Phys. Chem.* 78 (22): 2303–2304.

74 Günnemann, C., Curti, M., Sieland, F., and Bahnemann, D.W. (2021). Charge carriers in commercial photocatalysts: fractal kinetics and effect of “inert” additives. *Top. Catal.* 64 (13–16): 737–747.

75 Yanagisawa, Y. (1997). Oxygen exchange between SO_2 adsorbate and TiO_2 surfaces. *Appl. Surf. Sci.* 115 (4): 377–380.

76 Courbon, H. and Pichat, P. (1984). Room-temperature interaction of $N^{18}O$ with ultraviolet-illuminated titanium dioxide. *J. Chem. Soc., Faraday Trans. 1* 80 (11): 3175.

77 Liao, L.F., Lien, C.F., Shieh, D.L. et al. (2002). FTIR study of adsorption and photoassisted oxygen isotopic exchange of carbon monoxide, carbon dioxide, carbonate, and formate on TiO_2. *J. Phys. Chem. B* 106 (43): 11240–11245.

78 Nakamura, R. and Nakato, Y. (2004). Primary intermediates of oxygen photoevolution reaction on TiO_2 (Rutile) particles, revealed by *in situ* FTIR absorption and photoluminescence measurements. *J. Am. Chem. Soc.* 126 (4): 1290–1298.

79 Henderson, M.A. (1997). Complexity in the decomposition of formic acid on the TiO_2 (110) surface. *J. Phys. Chem. B* 101 (2): 221–229.

80 Henderson, M.A. (1995). Formic acid decomposition on the {110}-microfaceted surface of TiO_2(100): insights derived from ^{18}O-labeling studies. *J. Phys. Chem.* 99 (41): 15253–15261.

81 Bogdanoff, P. and Alonso-Vante, N. (1994). A kinetic approach of competitive photoelectrooxidation of HCOOH and H_2O on TiO_2 anatase thin layers via on-line mass detection. *J. Electroanal. Chem.* 379 (1–2): 415–421.

82 Kavan, L., Zukalova, M., Ferus, M. et al. (2011). Oxygen-isotope labeled titania: $Ti^{18}O_2$. *Phys. Chem. Chem. Phys.* 13 (24): 11583–11586.

83 Civiš, S., Ferus, M., Kubát, P. et al. (2011). Oxygen-isotope exchange between CO_2 and solid $Ti^{18}O_2$. *J. Phys. Chem. C* 115 (22): 11156–11162.

84 Montoya, J.F., Bahnemann, D.W., Peral, J., and Salvador, P. (2014). Catalytic role of TiO_2 terminal oxygen atoms in liquid-phase photocatalytic reactions: oxidation of aromatic compounds in anhydrous acetonitrile. *ChemPhysChem*. 15 (11): 2311–2320.

85 Chen, X. and Mao, S.S. (2007). Titanium dioxide nanomaterials: synthesis, properties, modifications, and applications. *Chem. Rev.* 107 (7): 2891–2959.

86 Salvador, P. (2011). Mechanisms of water photooxidation at n-TiO_2 rutile single crystal oriented electrodes under UV illumination in competition with photocorrosion. *Prog. Surf. Sci.* 86 (1–2): 41–58.

87 Bastow, T.J., Moodie, A.F., Smith, M.E., and Whitfield, H.J. (1993). Characterisation of titania gels by ^{17}O nuclear magnetic resonance and electron diffraction. *J. Mater. Chem.* 3 (7): 697.

88 Livraghi, S., Chiesa, M., Paganini, M.C., and Giamello, E. (2011). On the nature of reduced states in titanium dioxide as monitored by electron paramagnetic resonance. I: The anatase case. *J. Phys. Chem. C* 115 (51): 25413–25421.

89 Livraghi, S., Rolando, M., Maurelli, S. et al. (2014). Nature of reduced states in titanium dioxide as monitored by electron paramagnetic resonance. II: Rutile and brookite cases. *J. Phys. Chem. C* 118 (38): 22141–22148.

90 Diebold, U. (2003). The surface science of titanium dioxide. *Surf. Sci. Rep.* 48 (5–8): 53–229.

91 Hadjiivanov, K., Mihaylov, M., Panayotov, D. et al. (2014). Isotopes in the FTIR investigations of solid surfaces. *Spectrosc. Prop. Inorg. Organomet. Compd.* 45: 43–78.

92 Nanayakkara, C.E., Pettibone, J., and Grassian, V.H. (2012). Sulfur dioxide adsorption and photooxidation on isotopically-labeled titanium dioxide nanoparticle surfaces: roles of surface hydroxyl groups and adsorbed water in the formation and stability of adsorbed sulfite and sulfate. *Phys. Chem. Chem. Phys.* 14 (19): 6957–6966.

93 Baltrusaitis, J., Jensen, J.H., and Grassian, V.H. (2006). FTIR spectroscopy combined with isotope labeling and quantum chemical calculations to investigate adsorbed bicarbonate formation following reaction of carbon dioxide with surface hydroxyl groups on Fe_2O_3 and Al_2O_3. *J. Phys. Chem. B* 110 (24): 12005–12016.

94 Li, G., Jones, C.A., Grassian, V.H., and Larsen, S.C. (2005). Selective catalytic reduction of NO_2 with urea in nanocrystalline NaY zeolite. *J. Catal.* 234 (2): 401–413.

95 Boccuzzi, F. (1978). Infrared study of ZnO surface properties I. Hydrogen and deuterium chemisorption at room temperature. *J. Catal.* 51 (2): 150–159.

96 Cheng, B.-M., Lee, Y.-P., and Ogilvie, J.F. (1988). The infrared absorption spectrum of hydroxyl radicals in solid argon. *Chem. Phys. Lett.* 151 (1–2): 109–115.

97 Panayotov, D.A. and Yates, J.T. (2007). n-Type doping of TiO_2 with atomic hydrogen-observation of the production of conduction band electrons by infrared spectroscopy. *Chem. Phys. Lett.* 436 (1–3): 204–208.

98 Noei, H., Qiu, H., Wang, Y. et al. (2008). The identification of hydroxyl groups on ZnO nanoparticles by infrared spectroscopy. *Phys. Chem. Chem. Phys.* 10 (47): 7092–7097.

99 Bewick, A. and Russell, J.W. (1982). Structural investigation by infra-red spectroscopy of adsorbed hydrogen on platinum. *J. Electroanal. Chem. Interfacial Electrochem.* 132: 329–344.

100 Keppeler, M. and Roduner, E. (2014). Platinum-hydrogen vibrations and low energy electronic excitations of 13-atom Pt nanoclusters. *Phys. Chem. Chem. Phys.* 16 (48): 26613–26616.

101 Tyo, E.C. and Vajda, S. (2015). Catalysis by clusters with precise numbers of atoms. *Nat. Nanotechnol.* 10 (7): 577–588.

102 Huang, W., He, Q., Hu, Y., and Li, Y. (2019). Molecular heterostructures of covalent triazine frameworks for enhanced photocatalytic hydrogen production. *Angew. Chem.* 131 (26): 8768–8772.

103 Banerjee, T., Podjaski, F., Kröger, J. et al. (2021). Polymer photocatalysts for solar-to-chemical energy conversion. *Nat. Rev. Mater.* 6 (2): 168–190.

104 Lau, V.W., Yu, V.W., Ehrat, F. et al. (2017). Urea-modified carbon nitrides: enhancing photocatalytic hydrogen evolution by rational defect engineering. *Adv. Energy Mater.* 7 (12): 1602251.

105 Tewari, K.C. and Li, N.C. (1970). Nuclear magnetic resonance study of proton exchange in the water – 2-propanol system. *Can. J. Chem.* 48 (10): 1616–1618.

106 Zhao, G., Busser, G.W., Froese, C. et al. (2019). Anaerobic alcohol conversion to carbonyl compounds over nanoscaled Rh-doped $SrTiO_3$ under visible light. *J. Phys. Chem. Lett.* 10 (9): 2075–2080.

4

Photocatalytic Overall Water Splitting and Related Processes for Strategic Energy Storage into Hydrogen

Alberto Puga

Universitat Rovira i Virgili (URV), Department of Chemical Engineering, Av. Països Catalans 26, 43007 Tarragona, Spain

4.1 Photocatalysis as a Water Splitting Technology Option

4.1.1 What Is (and What Is Not) Photocatalytic Overall Water Splitting?

Water splitting is the dissociative transformation of water into elemental hydrogen (i.e. dihydrogen, H_2) and oxygen (i.e. dioxygen, O_2). During water splitting, the two O—H bonds in water molecules must be cleaved and reorganized in such a manner that each atom eventually becomes bonded to another one, identical to itself [1–3]. This is a rather stringent definition, implying only one possible reaction stoichiometry, as written in Eq. (4.1), and is often reinforced with the epithet "overall", to avoid confusions and misconceptions. Overall water splitting thus means that only water is transformed during the process.

$$H_2O \rightarrow H_2 + \tfrac{1}{2}\, O_2 \tag{4.1}$$

However, and strictly speaking, the reaction defined in Eq. (4.1) is not the only possible overall water splitting reaction. Instead of O_2, other oxidation products such as ozone (seldom, if ever, produced by photocatalysis) or hydrogen peroxide (Eq. (4.2)), both useful oxidants and disinfectants, could be formed.

$$H_2O \rightarrow \tfrac{1}{2}\, H_2 + \tfrac{1}{2}\, H_2O_2 \tag{4.2}$$

The utility of water splitting transformations lies in the fact that hydrogen is produced. Overall water splitting, as defined in Eq. (4.1) (but also in Eq. (4.2)), requires an energy input, and the result is the storage of such energy in the formed products, especially hydrogen, which can be utilized as a versatile fuel (see Section 4.2.1). If the energy used is of renewable origin, the hydrogen obtained is a true paradigm of clean and sustainable fuels. Photocatalysis entails promotion of chemical reactions by the action of photonic energy – *i.e.* light – and in this context, it represents a strategic opportunity for harnessing sunlight and storing the incommensurate amount of energy it provides [4, 5].

Photocatalytic Hydrogen Production for Sustainable Energy, First Edition. Edited by Alberto Puga.

Even if water may appear as an abundant feedstock, overall water splitting generally requires purified water, and its supply in large amounts for energy applications cannot be taken for granted [6]. This is especially serious in scenarios of fresh water scarcity, which are unfortunately too frequent and widespread in low-income parts of the world. In this context, the production of hydrogen from impure waters or even seawater becomes enticing. Given the presence of a range of substances dissolved in these waters, other products might be expected. A clear example is that of brines, which may lead to the production of chlorine and sodium hydroxide (Eq. (4.3)), akin to the chloralkali process [3]. Albeit useful, this is clearly not overall water splitting. Section 4.6 provides an account of this area of research.

$$2\,H_2O + 2\,NaCl \rightarrow H_2 + 2\,NaOH + Cl_2 \tag{4.3}$$

In photocatalysis, the development of new materials for hydrogen production is an extraordinarily active research field [7–10]. A large number of examples rely on the use of sacrificial electron donors, generally organic substances, which are much more prone to oxidation than water itself, as substrates to boost the formation of H_2. Regrettably, some such reports keep using the term "water splitting" – incorrectly – to describe their findings, and what is worse, purified and valuable sacrificial feedstocks are often consumed and hence, unproductively destructed. For a process of this kind to be reasonable and sensible, the sacrificial material should be a low-grade feedstock, or even a waste, to be valorized [11–14]. Chapters 9 and 10 of this book deal with the valorization of biomass-derived products, whereas Chapter 11 is an account of the photocatalytic wastewater-to-hydrogen process.

This chapter presents a brief overview of photocatalytic water splitting and the history of its technological development for the last 50 years. The emerging alternative overall water splitting pathway leading to H_2O_2 as the coproduct and some elementary variants of water splitting involving the use of saline waters, ammonia, or other hydrogen-containing bulk chemicals are also examined.

4.1.2 Comparison to Competing Technologies: Photoelectrochemical and Photovoltaic-Electrochemical

The production of the so-called "green" hydrogen by the electrolysis (electrochemical splitting) of purified water using renewable electricity is a mature technology, currently experiencing a rapid growth in terms of installed capacity (see Chapter 1 and Ref. [15]). A significant proportion of these ongoing projects is based on photovoltaic electricity, and hence, the hydrogen produced is a clear embodiment of solar energy storage. In this scenario of increasingly available and affordable solar hydrogen, why developing photocatalytic water splitting technologies? The main motivation is simplicity. Solar photocatalysis only requires a light-absorbing material exhibiting activity for the desired transformation under irradiation, *i.e.* immersing an appropriate photocatalyst in water and exposing it to sunlight [4, 16–18].

Figure 4.1 illustrates the water splitting design differences between the photocatalytic, photoelectrochemical, and photovoltaic-electrochemical approaches. Photocatalysis occurs on the surface of discrete particles immersed in water in

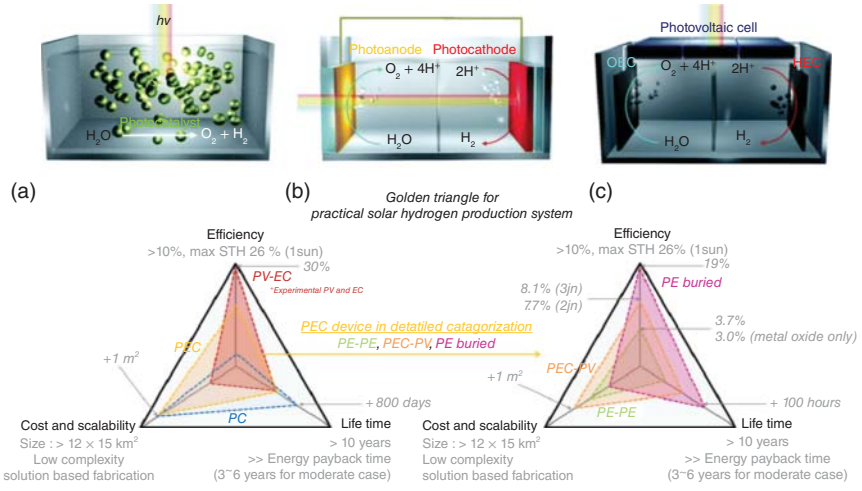

Figure 4.1 Comparison of light-activated overall water splitting systems. Top: Schemes of photocatalytic (a), photoelectrochemical (b), and photovoltaic-electrolytic (c) designs, showing the much simpler configuration of photocatalytic devices based on the direct irradiation of an active material immersed in water, as compared to the need for wired cells for the other two options. Bottom: triangle plots assessing the suitability of each technology on the grounds of efficiency, cost/scalability and durability as key performance parameters; PC, PEC, and PV-EC stand for photocatalytic, photoelectrochemical and photovoltaic-electrochemical, respectively, whereas the PEC approach is broken down into PE-PE, PE buried, and PEC-PV, designating dual photoelectrode, photovoltaics-based photoelectrode materials with buried double or triple junctions (2jn and 3jn, respectively), and hybrid photoelectrochemical-photovoltaic designs, respectively; STH stands for solar-to-hydrogen energy conversion efficiency. Source: Kim et al. [4]/with permission of Royal Society of Chemistry.

a single compartment, as further discussed below, and hence, does not require electrical connections. The disadvantage of this setup is that a mixture of H_2 and O_2 is generated, and downstream separation is necessary, implying technical issues and added cost. On the other hand, photovoltaic electricity must be transported to separate electrodes for hydrogen and oxygen evolution in a two-compartment electrolytic cell furnished with an ion-transport membrane, operating in the dark. Photoelectrochemical cells represent intermediate designs and may adopt a range of configurations.

Although the consolidated photovoltaic-electrolytic technology offers reasonable efficiencies close to the theoretical maximum, materials costs and lifetimes are yet to be improved. This is being challenged by advances in photoelectrochemical devices that do not require the two-step process of electricity generation and transportation to the electrochemical cell, for example by integrating multi-junction photovoltaic materials in photoelectrodes (Figure 4.1, top, b, and "PE buried," bottom, right panel). The downside of such sophisticated designs is their complexity. Chapters 5 of this book delve into photoelectrochemical water splitting, whereas chapter 6 examines the emerging option of junction photoelectrodes. The merit and potential of photocatalytic water splitting lie in its much lower cost and easier scalability and

reproducibility (Figure 4.1, bottom, left panel), due to its conceptual simplicity and straightforward cell construction and operation. Recent and impressive progress has demonstrated that scale-up to multi-square-meter solar plants can be readily achieved [19–21], as reported in chapter 12. Notwithstanding this, a real challenge remains to be tackled: solar-to-hydrogen efficiency must be drastically improved by actively researching on breakthrough materials.

4.2 Basics and Fundamentals of Photocatalytic Water Splitting

4.2.1 Water Splitting Thermodynamics, Energy Balance and Metrics

Water splitting requires energy to happen. In thermodynamic terms, the reaction is endergonic since its free energy change is positive ($\Delta G^0 = 237.1\ \mathrm{kJ\ mol^{-1}}$ at standard conditions for Eq. (4.1)). This is burdensome since the process must be forced by injecting (at least) that amount of energy into the system in an effective manner, though conversely, such energy is eventually stored in the hydrogen product [22]. Natural photosynthesis is the best example of such a phenomenon, whereby sunlight is utilized to produce complex biomass as the material supporting and powering life on Earth, and by resembling it, light-driven overall water splitting is considered as an artificial photosynthetic process. As in natural photosynthesis, photonic energy must be absorbed and channeled perfectly by means of an appropriate material.

Converting the free energy input mentioned above and considering that Eq. (4.1) involves the transfer of two electrons, photons of energy equal to or above 1.23 eV, i.e. wavelengths below *ca.* 1000 nm, are required. This equates to roughly the UV, visible, and near-infrared ranges of the solar spectrum. The remaining infrared fraction cannot promote the reaction. Therefore, the solar-to-hydrogen conversion efficiency (STH), defined as the ratio between the amount of chemical energy stored in the hydrogen produced and the amount of incident sunlight energy, has a theoretical limit of around 40%. In reality, it is highly ambitious to achieve even significantly lower STHs due to a series of events resulting in energy losses (see Sections 4.2.2 and 4.2.3). Apparent quantum efficiencies (AQY) as defined in Eq. (4.4)

$$\mathrm{AQY} = \frac{n(\mathrm{photons})}{2\,n(\mathrm{H_2})} \tag{4.4}$$

where n(photons) and $n(\mathrm{H_2})$ are the amounts of incident photons and hydrogen molecules (two is the factor reflecting the fact that two photons, subsequently generating two electrons, are involved to produce one hydrogen molecule, see Ref. [23]) are generally well below the ideal 100%. Even for perfectly performing photocatalysts, STH decreases dramatically if the usable solar spectrum is reduced, as shown in Figure 4.2.

Based on projections estimating a threshold STH of 10% for competitive hydrogen by photocatalytic water splitting [24–26], all the UV, blue, and green light should be harnessed (*ca.* <540 nm). More optimistic scenarios suggest that 3–5% STH might be economically competitive due to the affordability of photocatalysis [20, 27].

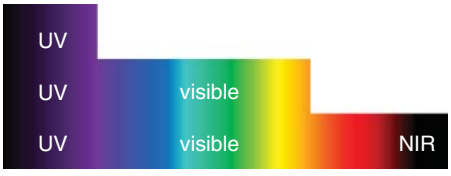

Wavelength range (λ/nm)	Minimum photon energy (eV)	Maximum efficiency (STH/%)
< 400	3.10	2
< 600	2.07	16
< 800	1.55	32

Figure 4.2 Theoretical maximum solar-to-hydrogen conversion efficiencies (STH), assuming all incident photons result in H_2 production (apparent quantum efficiencies of 100%), for ideal photocatalysts absorbing different fractions of the solar spectrum up to their absorption edge wavelength. Data taken from Ref. [24].

Unfortunately, the best photocatalytic overall water splitting systems reported today perform at STH values ranging 1–2%, and rarely absorb above 500 nm [18].

4.2.2 Photophysics of Heterogeneous Semiconductor Photocatalysts

The light-driven activity of photocatalysts primarily stems from the absorption of photons. Either a discrete molecular substance or a semiconductor may act as photocatalysts. In overall water splitting, the latter kind of photocatalysts are by far more common, and they operate in heterogeneous mode since they are solids, which, generally, do not dissolve in water. Upon photon absorption, the particular electronic structure of semiconductors is amenable to the promotion of an electron from the valence band to the conduction band of the material – importantly, the energy of the photon (see Figure 4.2) must overcome the difference between both bands, known as the bandgap. Appropriate semiconductors for water splitting photocatalysis include several metal oxides, sulfides or nitrides, and polymeric materials (see below). The photogenerated electrons and holes may then separate, migrate to appropriate active sites, and, once there, participate in the reduction and oxidation, respectively, of water. An illustration of this photophysical mechanism, typical for any semiconductor photocatalysis process, is shown in Figure 4.3.

All steps in this photocatalytic machinery must proceed smoothly to completion to attain high efficiencies (AQYs, and in turn, STHs). However, performances may be sluggish on many occasions, and it is tedious and cumbersome to identify which steps are more detrimentally affected [28]. A look at the timescales in Figure 4.3 (bottom) promptly reveals that, whilst photon absorption and subsequent generation of charge carriers are extremely rapid (femto-to-picoseconds), completion of a full photocatalytic cycle is orders of magnitude slower (milliseconds to seconds), and it is not surprising that charges may recombine (and hence, annihilate) along such a long journey. It is widely accepted that such recombination events severely undermine photocatalytic efficiency, leading to energy loss and low AQYs; in this regard, good semiconductor crystallinity and low-defect density minimize recombination probability. Another critical stage is the diffusion and transfer of charges to the active catalytic sites through their interfaces with the semiconductor, although photocatalysis

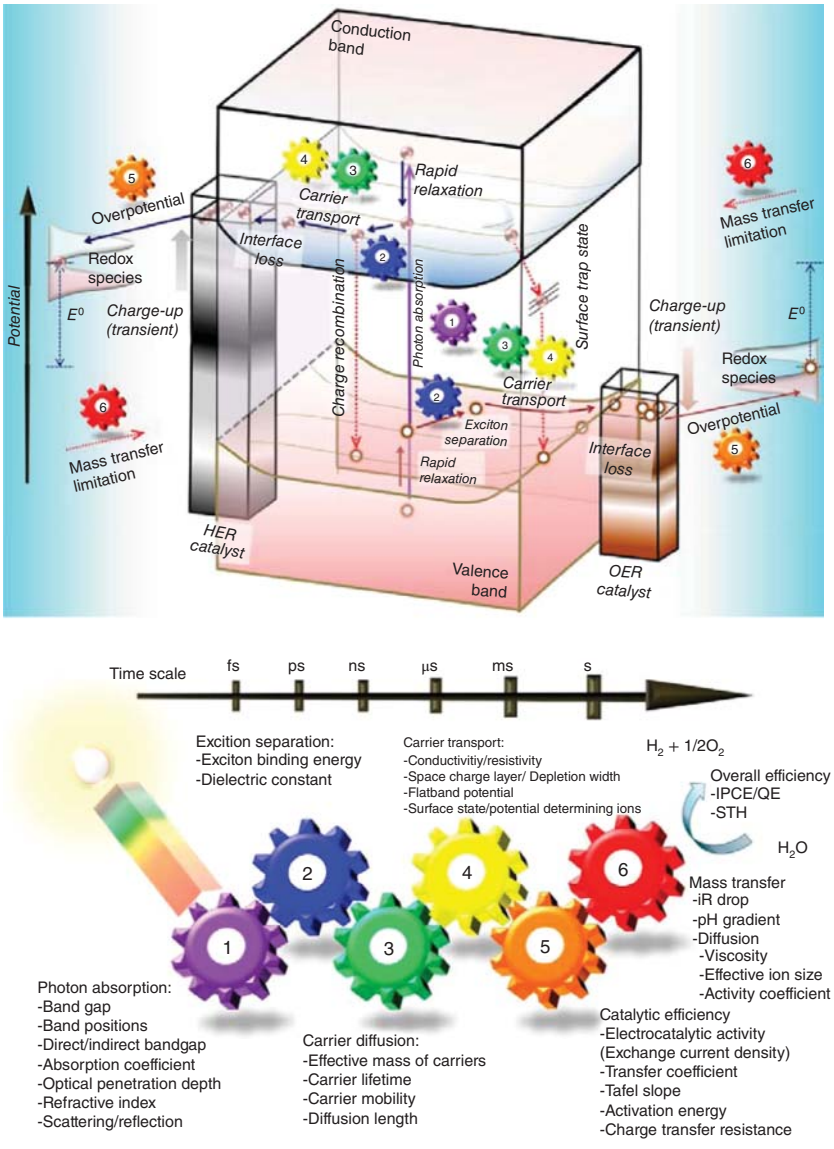

Figure 4.3 Top: A scheme showing the photophysical mechanistic steps taking place in a semiconductor-based photocatalyst, namely, 1: photon absorption and electron promotion from valence band to conduction band (across the bandgap), 2: exciton separation into electron-hole pairs (represented by filled and empty balls, respectively), 3: electron and hole (charge carriers) migration through conduction and valence bands, respectively, 4: charge carrier transport to surface active sites (HER and OER are the hydrogen and oxygen evolution reactions, respectively), 5: charge carrier transfer to reactants (in overall water splitting, H_2O molecules), and 6: diffusion of reactants (H_2O molecules and derived species) and products (H_2 and O_2 molecules); electron-hole recombination may happen directly or through trap states, thus resulting in energy loss. Bottom: Gear diagram showing timescales and main parameters affecting each one of the steps. Source: Takanabe [28]/with permission of American Chemical Society.

holds an advantage in this regard with respect to (photo)electrochemistry since the typically small size of semiconductor particles implies short diffusion paths and less relevant interface polarization [24].

4.2.3 The Challenging Kinetics of Water Splitting and Co-Catalyst Requirements

In addition to thermodynamic and photophysical constraints, overall water splitting suffers from a serious kinetic drawback related to the complex charge carrier transfer (step 5 in Figure 4.3). Two electrons must be transferred to two protons for hydrogen evolution, whereas oxygen formation is even more challenging since it requires the participation of four holes and the close interaction of two-oxygen species from two different water molecules. As a consequence, additional energy barriers must be overcome for both half-reactions. These are known as overpotentials, and although they are also relevant in (photo)electrochemical water splitting, the delicate photophysical machinery of photocatalysis is more susceptible to activity decrease due to the burden they impose on charge transfer across the material surface.

Most semiconductors alone do not contain appropriate active sites for hydrogen or oxygen evolution, and therefore, unsurmountable overpotentials severely hinder overall water splitting on them. An adequate solution to this issue is the incorporation of co-catalysts able to lower such overpotentials. Commonly, different, dedicated, and appropriately designed co-catalysts for either H_2 or O_2 evolution are deposited on the surface of the semiconductor, hosting and transferring electrons from its conduction band and holes from its valence band, respectively (Figure 4.3 and Refs. [9, 29]). Subsequently, they facilitate their transfer to the appropriate redox reactant species. Examples of hydrogen evolution co-catalysts are nanoparticles of noble metals or metal oxides, sulfides or phosphides, and biomimetic organometallic complexes, whereas the choice of oxygen evolution co-catalysts is somewhat more stringent, encompassing certain nanoparticles of metal oxides or complexes [9, 24, 26, 29–31]. On occasions, charge separation and accumulation in the co-catalysts prevents photocorrosion on some redox-unstable semiconductors [24].

4.2.4 Photoreactor Engineering and Process Conditions

The fact that solar photocatalysis may work by simply exposing an active material immersed in water to sunlight under ambient temperature and pressure conditions surely facilitates reaction engineering. However, the gigantic size of the endeavor for strategic solar energy storage by producing photocatalytic hydrogen leads to a key parameter of special significance: irradiation area. A projection by Maeda and Domen estimated that as much as ten thousand 5×5 km solar plants would be needed to meet one third of all energy consumption by 2050, assuming that breakthrough developments will ensure STH of at least 10% [25]. Therefore, maximization of light absorption and use of minimal photocatalyst amounts will dictate and probably constrain photoreactor design and construction. Another crucial

aspect is that the H_2/O_2 mixture produced must be promptly evacuated and separated.

Currently, most photocatalytic experiments reported in the literature have been performed in batch photoreactors containing a suspension of the photocatalyst in aqueous media. This configuration results in inefficient light absorption due to reflection and scattering of incident radiation by the multiple suspended particles, and oversized photocatalyst amounts given that light penetration will be restricted to the uppermost layer of suspension [22, 32]. Large-scale solar plants based on tubular photoreactors mounted on concentrators have been successfully constructed and

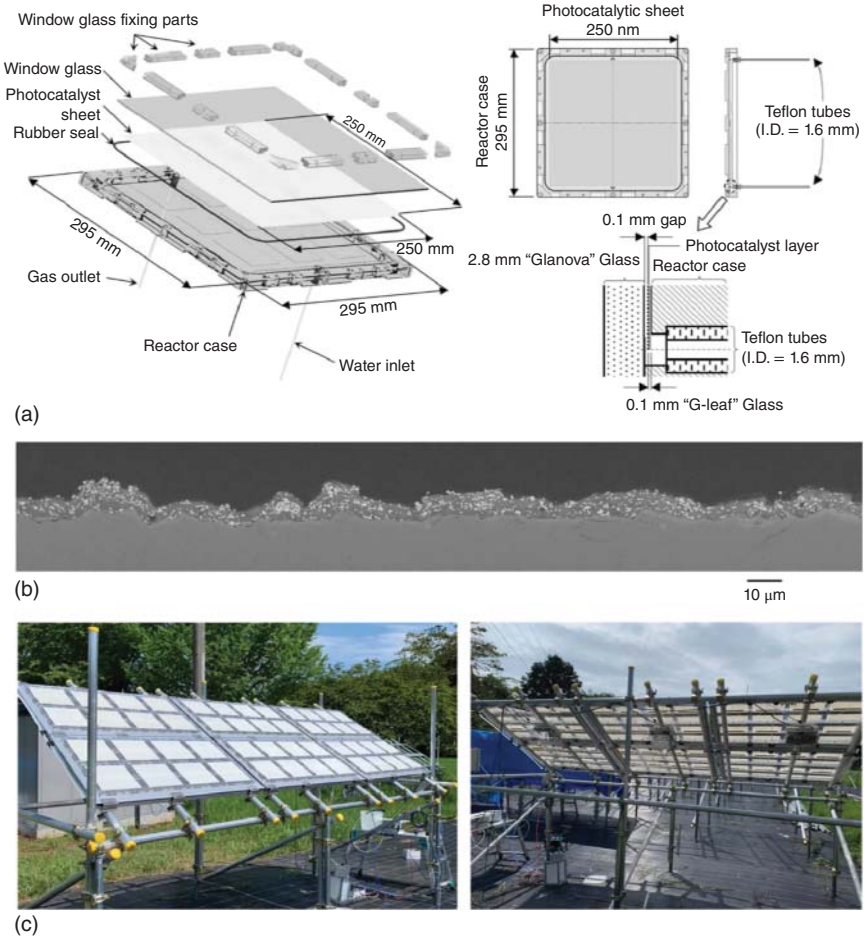

Figure 4.4 Large-scale photocatalytic overall water splitting flat panels based on immobilized photocatalyst sheets. Top, (a): Design of individual panel photoreactors (625 cm^2) in plastic casing made by injection molding. Middle, (b): Cross-section scanning electron microscope image of the thin photocatalyst layers immobilized on frosted glass sheets. Bottom, (c): Photographs of panel assemblies into larger units, showing that the technology is amenable and robust for scale-up into multi-square-meter solar water splitting plants. Source: Nishiyama et al. [19]/with permission of Nature Publishing Group.

tested [33], although they operate in suspension mode, and hence, photocatalyst sedimentation and oversizing problems are not solved. Recently, planar photoreactors whereby thin layers (down to 10 μm in thickness) of the photocatalyst are fixed and immobilized, and then submerged in shallow depths of water covered with transparent windows, have been developed [27]. Even a 100 m^2 plant has been built and operated successfully [19]. Details of the design of the individual, modular, flat panel reactors employed are shown in Figure 4.4. Such an impressive achievement demonstrates that affordable and replicable scale-up and implementation of photocatalytic overall water splitting systems is surely achievable.

4.3 Materials for Photocatalytic Overall Splitting of Pure Water into H_2 and O_2

One of the major obstacles in improving solar overall water splitting (*i.e.* STH) is the design and mass-production of photocatalysts exhibiting high photonic efficiency (*i.e.* AQY) for a wide fraction of the solar spectrum, including radiation wavelengths from the highly energetic UV range, and well into the visible. The simplest approach regarding materials design entails using one semiconductor having a bandgap energy (E_g) surmountable for the most visible range photons (around or smaller than 2 eV, Figure 4.2). Even if that condition is met and provided highly active sites (co-catalysts) are present, the potential of charge carriers (electrons in the conduction band and holes in the valence band) must be enough (more negative and more positive, respectively) to enable O_2 and H_2 formation, respectively, as hinted in Figure 4.3 [8, 24]. The approach based on only one semiconductor as light-absorbing photocatalyst component is convenient in terms of materials affordability, although it must meet these stringent energy constraints (Figure 4.5a). In addition, overpotentials force the band potentials to be even further away in energy to ensure activity, increasing the required bandgap, and thus narrowing the usable solar spectrum visible range. Nature has provided a smart solution to such a hurdle: constructing a photocatalytic system whereby two different absorbers may be excited, and hence generate charge carriers, by lower-energy photons, inspired by the photosystems in photosynthetic organisms [35]. Photosystems rely on pigments such as chlorophyll as light absorbers, linked to highly sophisticated metalloproteins acting as reactor centers. In "artificial" photocatalysis, semiconductors are used instead due to their availability and stability [24, 36]. Electrons photogenerated by one of the absorbers are used to form H_2, and holes photogenerated by the second one lead to O_2 formation. The unused charge carriers recombine internally in a Z-scheme by means of redox mediators, as shown in Figure 4.5. Redox mediators can be either dissolved in water, and thus, free to diffuse to and from the two different semiconductors, or solid components tightly bound to both semiconductors. In either case, it is critical to suppress the several backward, unproductive, electron transfer steps that are unfortunately more probable and favorable than water splitting in Z-scheme systems (dashed arrows in Figure 4.5).

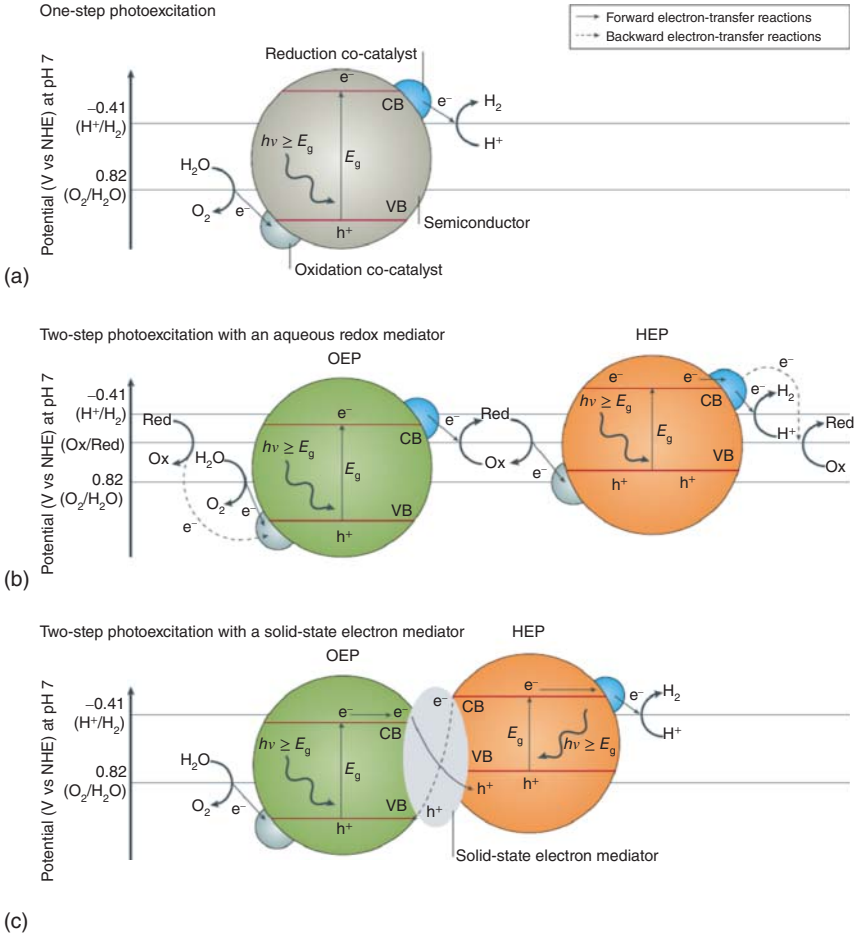

Figure 4.5 Energy diagrams in semiconductor-based photocatalytic overall water splitting. Top, (a): One – semiconductor configuration. Middle, (b): Two-semiconductor configuration with a redox mediator in aqueous solution. Bottom, (c): Two-semiconductor configuration with a solid-state mediator. CB, conduction band; E_g, semiconductor bandgap; HEP, hydrogen evolution photocatalyst; NHE, normal hydrogen electrode; OEP, oxygen evolution photocatalyst; Ox, oxidant; Red, reductant; VB, valence band. Blue and gray balls represent co-catalysts for H_2 and O_2 evolution, respectively. Note that two and four electrons (not specified for simplicity) are involved in the formation of H_2 and O_2 molecules, respectively. Source: Chen et al. [34]/with permission of Nature Publishing Group.

To summarize, one-semiconductor overall water splitting photocatalysts are simple to produce, yet they are only active under the most highly energetic fraction of sunlight, whereas two-semiconductors may exhibit activity for a larger portion of the lower-energy, visible solar spectrum, but are significantly more challenging to design and prepare. Another issue to remark is that the necessity for two absorbers in the latter means that twice the number of photons are required for a given transformation as compared to their one-absorber counterparts; therefore, four photons (two

per absorber) must be absorbed to split one molecule of water instead of two [24]. The following sections present a succinct overview of the main achievements in overall water splitting photocatalysis encompassing both configurations. It is not the goal of this chapter to provide a comprehensive review, but to highlight outstanding and disruptive examples of different kinds of successful materials.

4.3.1 Single Light Absorber Configuration Based on Metal Oxide Semiconductors

The discovery of the Fujishima–Honda effect, leading to light-induced water oxidation on TiO_2 semiconductor electrodes, was reported [37], initiated an exciting research race that continues today, as evidenced throughout this chapter. Several years later, the first example of overall splitting of water vapor adsorbed on TiO_2 and iron-modified TiO_2, under highly energetic UV light, was reported [38]. The amounts of H_2 and O_2 were small – yet measurable – and production rates tended to decrease with time after a few hours, and these facts stimulated further materials design to modify the photocatalyst or seek new appropriate semiconductors. Shortly afterward, Kawai and Sakata found that the sluggish activity exerted by TiO_2 could be improved by several orders of magnitude by incorporating RuO_2, a known water oxidation material, to the photocatalyst, achieving steady H_2/O_2 for several days [39]. Conversely, and contemporarily, Sato and White reported that the deposition of Pt or Rh as hydrogen evolution co-catalysts on TiO_2 also enhanced overall water splitting activity [40, 41]. Unfortunately, metallic (Pt^0, Rh^0) surfaces readily catalyze the reverse reaction, forming water again, severely affecting long-term activity [41–43]. This can be solved by tuning the oxidation state of surface platinum, *i.e.* by depositing PtO, which, is inactive for the back-reaction, instead of Pt^0 [44]. The action of UV irradiation can promote the reduction of surface platinum to Pt^0, ensuring the presence of H_2-evolution active sites to some extent [45]. This fact evidences the main drawback of TiO_2, which, although being inexpensive, abundant, and stable, is nevertheless hindered by the relatively high photonic energy required to activate it ($E_g \approx 3.0$–3.2 eV, Figure 4.2), restricting its theoretical maximum solar efficiency. Table 4.1 compares photocatalytic water splitting for representative examples of oxide semiconductors.

An obvious step forward is the search for oxide semiconductors with appropriate band potentials [28, 57]. One such example is Cu_2O, with a narrow bandgap ($E_g \approx 2.0$–2.2 eV, depending on preparation conditions, absorbing photons below *ca.* 600 nm) and suitable conduction and valence band redox ability for water splitting. Stable H_2/O_2 production was reported for Cu_2O, without any co-catalysts, immersed in liquid water under visible light for up to 1900 hours [47]. Low rates and photo-stability concerns have limited further development of photocatalytic overall water splitting using Cu_2O [22]. Another more recent yet similar example is that of CoO. Albeit its conduction band potential is not negative enough to favor H_2 formation, surprisingly efficient overall water splitting under simulated solar light has been reported for co-catalyst-free CoO nanoparticles (STH = 5%), although photocatalyst durability was poor [46]. Necessary elucidation of the

Table 4.1 Photocatalytic overall water splitting data for single light absorber materials.

Semiconductor	HEC	OEC	Reaction medium	Light source	Efficiency	References
TiO_2	Rh	—	Adsorbed water vapor	Hg lamp, 500 W, 250–400 nm	AQY = 29%	[41]
CoO	—	—	Pure liquid water	Solar simulator	STH = 5%	[46]
Cu_2O	—	—	Pure liquid water	Xe lamp, 300 W, >460 nm	AQY = 0.3% (550–600 nm)	[47]
$SrTiO_3$	NiO	—[a)]	Water vapor	Hg lamp, 450 W	AQY = 1% (365 nm)	[48]
$K_4Nb_6O_{17}$	NiO	—[a)]	Pure liquid water	Hg lamp, 450 W	AQY = 3.5% (330 nm)	[49]
$NaTaO_3$	NiO	—[a)]	Pure liquid water	Hg lamp, 400 W	AQY = 20% (270 nm)	[50]
Rh, Sb:$SrTiO_3$	IrO_x[b)]	IrO_2	Liquid water (pH = 3)	Xe lamp, 300 W, >440 nm	AQY = 0.1% (420 nm)	[51]
Al:$SrTiO_3$	CrO_x/Rh	CoOOH	Liquid water (pH = 3)	Xe lamp, 300 W, >440 nm	AQY ≈ 96% (350–360 nm) STH = 0.65%	[52]
$(Ga_{1-x}Zn_x)(N_{1-x}O_x)$	$RhCrO_x$	—	Liquid water (pH = 4.5)	Hg lamp, 300 W, >400 nm	AQY ≈ 2.5% (420–440 nm)	[53]
$Y_2Ti_2O_5S_2$	CrO_x/Rh	IrO_2	Liquid water (pH = 8.5)	Xe lamp, 300 W, >420 nm	AQY ≈ 5.3% (420–480 nm)	[54]
C_3N_4	Pt/PtO_x	CoO_x	Liquid water	Xe lamp, 300 W, >420 nm	AQY ≈ 0.3% (405 nm)	[55]
PTEPB[c)]	—	—	Liquid water	Xe lamp, 300 W, >420 nm	AQY ≈ 10.3% (420 nm) STH = 0.60%	[56]

a) Nickel oxide and nickel metal are probably the O_2 and H_2 evolution co-catalysts, respectively, according to follow-up studies.
b) Partly reduced iridium oxides are presumably the H_2 evolution co-catalysts.
c) PTEPB: a 2D conjugated microporous polymer formed by tri(ethynylphenyl)benzene units.

mechanism, independent validation of these results by other laboratories, and stability enhancement would take photocatalysis closer to practical and competitive implementation. Many other simple oxides are only active in the UV region, as for example ZrO_2 or Ga_2O_3, whereas the band potentials of most transition metal oxides absorbing visible light are misaligned for water splitting [8, 34].

Mixed metal oxides represent a distinct class including semiconductors with tunable electronic structure. Among these, titanates, niobates, and tantalate solids with perovskite structures have resulted in remarkable photocatalytic overall water splitting activities, yet their wide bandgaps limit the usable sunlight spectrum to the UV region. Early discoveries were centered on $SrTiO_3$, similar to TiO_2 in electronic band structure, which is still the focus of successful development today (see below). Long-term H_2/O_2 production was found for $NiO/SrTiO_3$, whereby deposited nickel oxide acted as a co-catalyst, suppressing the counterproductive reverse reaction [48, 58]. Niobates loaded with analogous nickel co-catalysts soon equaled or outperformed titanates [49, 59], as shown in Table 4.1. Tantalates were reported to split water under UV light even in the absence of co-catalysts, reflecting that their conduction bands are widely negative, and hence, they have a strong reducing potential. This kind of semiconductor can only be activated by UV photons of high energy, and their modification is vital for solar photocatalysis, as discussed in the next section.

4.3.2 Doped Metal Oxides Improve Single Absorber Photocatalysts

Tantalate structures were among the first to be doped [7, 8, 34], leading to greatly enhanced photocatalytic water splitting. Activity enhancement for sodium tantalate-doped with a series of lanthanides ($Ln:NaTaO_3$) was recorded, and ascribed to limited crystal growth during the high-temperature synthetic protocols employed, which in turn facilitated charge carrier diffusion through shorter paths and transfer to more abundant active sites due to increased surface area; AQY reached around 50% in the far UV region for $NiO/La:NaTaO_3$ [60]. Despite such encouraging results, doping did not improve visible-light activity to any apparent extent. The visible-activity milestone was achieved using strontium titanate co-doped with rhodium and antimony, using iridium oxide as a co-catalyst ($IrO_2/Rh, Sb:SrTiO_3$), owing to the narrowing of the bandgap by rhodium-based electronic levels above the valence band [51]. Nonetheless, the choice of doped oxide systems is rather limited, and visible-light efficiencies are impractically low (see Table 4.1).

Let aside the focus on visible activation, metal doping of $SrTiO_3$ is recently leading to outstanding enhancements of photocatalytic overall water splitting under UV and solar irradiations. An Earth-abundant metal such as aluminum, introduced simply by performing flux synthesis (*i.e.* in molten salt media) in alumina crucibles, exerted the beneficial effects of restricting crystal growth (small $Al:SrTiO_3$ particles are formed) and providing shallow states that trap and promptly transfer photogenerated electrons for H_2 formation [61]. Solar panels were constructed

based on this material, resulting in a remarkable STH of around 0.4% under outdoor operation [21]. The co-catalyst used, a mixed chromium-rhodium oxide, suffered from Cr^{6+} leaching after photo-oxidation, negatively affecting durability. A solution to this issue, whereby an appropriate cobalt O_2 evolution co-catalyst (CoOOH) helped trap and channel oxidizing holes effectively, was later formulated, resulting in remarkable stability for 1000 hours [62]. An impressive photon-to-hydrogen efficiency (AQY ≈ 96%) has been reported by sequentially photo-depositing each co-catalyst component on the adequate facets, that is, the H_2-evolving CrO_x/Rh and the O_2-evolving CoOOH on electron- and hole-enriched surfaces (see Figure 4.6 and Ref. [52]). Such successful and rapid development has recently culminated in the demonstration of a 100 m^2 solar water splitting plant, producing H_2 for several months in a row under natural sunlight and ambient conditions, by Domen's team (Figure 4.4, Ref. [19]). This is a breakthrough showing that single-semiconductor photocatalysts are suitable and affordable for the scale-up of real solar photocatalytic water splitting plants.

4.3.3 Modifications of Single Light Absorber Photocatalysts: (Oxy)nitrides, (Oxy)sulfides

As hinted above, the valence band levels of oxides tend to be relatively low in energy since they are formed by low-lying, stable, O 2p orbitals, and consequently, their bandgaps are too wide (>3 eV) for activation under visible light. Doping oxide structures with nitrogen or sulfur introduces new states above the valence band, with the contribution of N 2p or S 3p orbitals [63]. The most successful approach to achieve this has been the synthesis of solid oxynitride solutions, such as $(Ga_{1-x}Zn_x)(N_{1-x}O_x)$, a smart design since both GaN and ZnO have the same crystal structure, and hence, gallium and zinc on one side, and nitrogen and oxygen on the other, are mutually replaceable; by depositing nanoparticles of a rhodium-chromium co-catalyst, photocatalytic overall water splitting was observed under visible light for up to 35 hours [53, 64], see Table 4.1. Bandgap narrowing from the parent semiconductors (3.4 and 3.2 eV for GaN and ZnO, respectively) down to 2.6 eV for $(Ga_{1-x}Zn_x)(N_{1-x}O_x)$ enables activity up to *ca.* 500 nm, including blue light (see Figure 4.2). Other nitrides and oxynitrides, such as Ta_3N_5 or TaON, have shown further extension of the visible-light absorption range [4, 34, 65]. As their main downside, durability of these materials is somewhat limited due to the instability of nitride to oxidizing conditions, a phenomenon that deserves special consideration.

Whilst the photostability of sulfide and oxysulfide materials is equally problematic, given the tendency of sulfide to become oxidized, they bear an enormous potential to absorb a wide range of visible light [34]. A recent example is $Y_2Ti_2O_5S_2$, which has shown overall water splitting activity up to 640 nm when loaded with CrO_x/Rh and IrO_2 as co-catalysts; the iridium co-catalyst effectively traps and uses holes for O_2 evolution, thus suppressing the oxidation of S^{2-} [54].

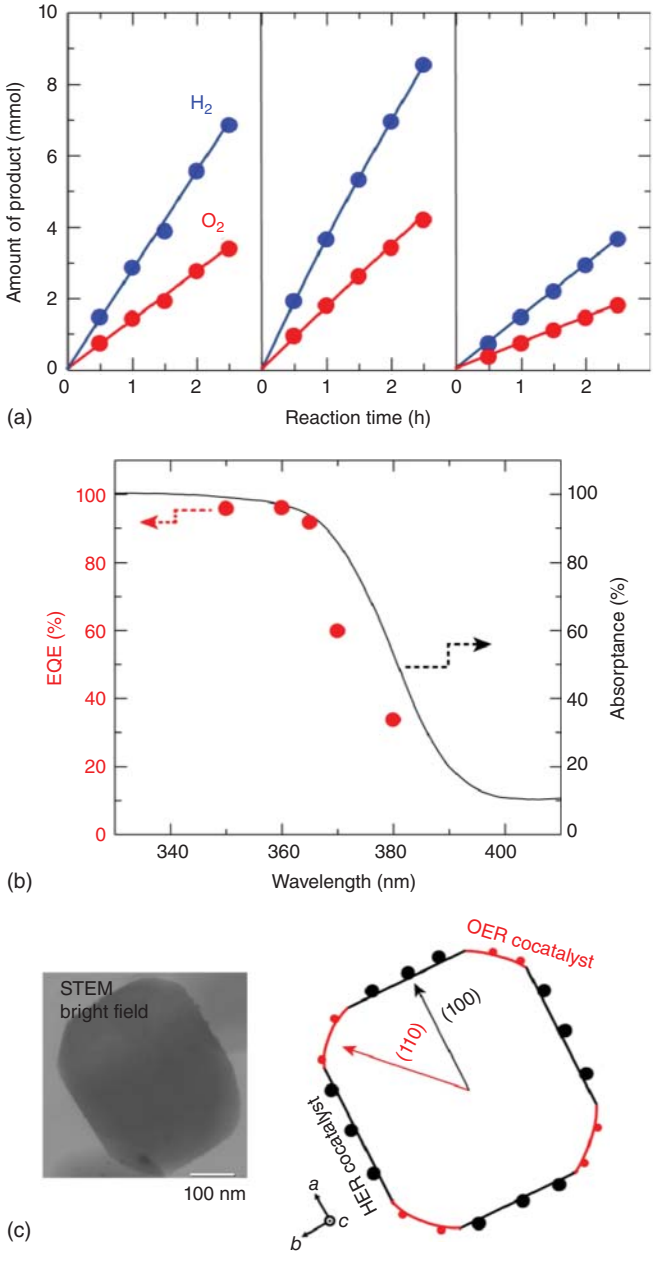

Figure 4.6 (a): Water splitting activity of CrO_x/Rh/Al:$SrTiO_3$ (left), sequentially photo-deposited CoOOH/CrO_x/Rh/Al:$SrTiO_3$ (middle) and co-impregnated CrO_x/Rh/Al:$SrTiO_3$ (right). (b): Diffuse reflectance spectrum of Al:$SrTiO_3$ and wavelength dependence of AQY (here designated as external quantum efficiency, EQE) for the photocatalytic overall water splitting on CoOOH/CrO_x/Rh/Al:$SrTiO_3$ (corresponding to: a, middle). (c): Scanning-transmission electron microscopy image of CoOOH/CrO_x/Rh/Al:$SrTiO_3$ alongside a model representation of its crystallite morphology and co-catalyst location. Source: Takata et al. [52]/with permission of Nature Publishing Group.

4.3.4 Organic or Metal–Organic Semiconductors for Photocatalytic Water Splitting

The majority of semiconductors used in photocatalysis and other light-activated technologies are inorganic, chiefly combinations of metals with oxygen and/or other non-metals [10], as outlined in the preceding sections. A completely different, and far less studied, class is that of organic semiconductors [66]. They tend to be less resistant and durable than their inorganic counterparts, albeit their structural tunability may potentially lead to myriad materials with compelling properties. Totally organic π-conjugated polymers, covalent-organic frameworks and metal-organic frameworks (MOFs) are the most promising types of materials for photocatalysis.

The most prominent example of π-conjugated polymer semiconductor is graphitic carbon nitride (C_3N_4), a 2D material. It can be readily prepared by thermal condensation and its band structure is adequately matched for overall water splitting [67]. As in the case of inorganic nitrides, C_3N_4 is prone to photo-degradation by oxidation, and the deposition of efficient co-catalysts is a requirement both for water splitting activity and protection of the material from highly oxidizing holes. In this regard, remarkable stability was achieved by depositing CoO_x and Pt-PtO_x as O_2 and H_2 evolution co-catalysts [55]. Previously, an impressive STH (2%) and long-term stability of up to 200 days was reported for a C_3N_4 photocatalyst only having carbon dots as a co-catalyst [68]. Mechanistic studies, and validation by independent laboratories, are still necessary to confirm the potential of graphitic C_3N_4 for photocatalytic water splitting.

Evolution of 2D π-conjugated polymers is flourishing into the field of covalent organic frameworks, whose structures contain channel-like micropores, in turn resulting in materials of large surface areas. Their semiconductor features in terms of light absorption can be adjusted by modifying their structures, as for aromatic cores of increasing size (benzene *vs.* triphenylbenzene) linked with ethynyl units, whereby the latter results in reduced bandgaps ($E_g = 2.85$ eV) and hence higher photocatalytic water splitting efficiency in the absence of any co-catalysts [56]. The versatility of organic polymers of structural design, and its impact on photocatalytic activity, has been shown by the production of poly(dibenzothiophene sulfone), having a 1D backbone, which reaches a steady H_2/O_2 production under visible light after 60 hours in the presence of deposited Pd and IrO_2 co-catalysts [69].

MOFs are generally 3D microporous structures having metal-based cores and organic linkers, which may exert semiconductor properties [70]. Despite the intense research activity around them, their application as photocatalysts for overall water splitting has been seldom studied, probably owing in part to their poor hydrolytic stability. The first publication, dating back only five years, reports a MOF formed by aluminum cores, aminoterephthalate linkers and nickel as co-catalyst, leading to H_2/O_2 production for a few hours [71]. Durability has been improved by a new class of robust titanium-squarate materials with platinum co-catalysts, which showed stable activity for up to ten days [72]. The highly sophisticated preparation of artificial chloroplasts based on MOFs encapsulated in liposomes, has also been described; this bioinspired Z-scheme system promoted water splitting under visible

light for three days [73]. The design possibilities of (metal-)organic semiconductors represent a stimulating horizon for photocatalysis, provided stability issues can be addressed.

4.3.5 Bioinspired Two-Absorber Z-Scheme Configurations toward Artificial Chloroplasts

The limited visible-light absorption of most single absorber photocatalysts can be overcome by combining two absorbers that complement each other, whilst each one of them becomes activated by lower energy photons (see Figure 4.5, discussion at the beginning of Section 4.3, and Refs. [16, 36]). This comes at the expense of material preparation complexity, since it relies on a sophisticated Z-scheme multi-component bioinspired approach, as in the artificial chloroplast mentioned above [73]. Simpler designs encompass the use of two inorganic semiconductors as light absorbers and a redox mediator that can be dissolved in the aqueous reaction medium or physically contact particles of both semiconductors in the solid state.

The first demonstration of a Z-scheme for overall water splitting used I^-/IO_3^- as the redox mediator pair and two TiO_2 particulate materials (see Figure 4.5b), i.e. one having an anatase structure and Pt as a co-catalyst for H_2 evolution and the other based on a rutile structure for O_2 evolution; the different components were simply mixed in water and water splitting proceeded for 100 hours under UV-visible light [74]. Unproductive electron transfer reactions cause short circuit in the process. This takes place to some extent in these systems given the free diffusion of the electron mediator in the solution, hampering efficiencies. Improvements can be achieved by an appropriate selection of components; for example, using Fe^{3+}/Fe^{2+} as the redox mediator and Rh:$SrTiO_3$ and $BiVO_4$ as light absorbers exerts activity below 500 nm, although efficiencies remain moderate [75]. Table 4.2 lists a series of Z-scheme photocatalytic systems for overall water splitting.

Strategies to avoid back and cross reactions include separating both components of the photocatalyst into different compartments connected through a membrane, or simply using no electron mediator at all. A demonstration of direct inter-particle electron transfer was possible employing the Ru/Rh:$SrTiO_3$ and $BiVO_4$ combination (see above) by carefully adjusting the pH of the solution to maximize the contact of the different semiconductors by aggregation [76]. Diffusion and the low probability of surface encounters still restrict efficiencies for suspension setups. Evolution of this into immobilized layers whereby the two photocatalyst component particles are closely contacting each other, prepared by either screen printing [80] or particle transfer techniques [81], has emerged in recent years [10, 27]. A particularly effective approach consists of using a solid-state, conducting, solid mediator enabling rapid electron transfer following the Z-scheme pathway (Figure 4.5c). Deposition of gold by electron beam evaporation produced sheets with high quality contacts between Ru/La,Rh:$SrTiO_3$ and RuO_x/Mo:$BiVO_4$ in an improved photocatalyst system, leading to an order of magnitude higher efficiency (see Table 4.2, Ref. [77]). As a cheaper alternative to gold, an amorphous graphitic carbon conductor was proposed and successfully deposited as a solid-state mediator, with comparable activity [78].

Table 4.2 Photocatalytic overall water splitting data for Z-scheme materials comprising two light absorbers.

HEPC[a)]	OEPC[b)]	Electron mediator	Reaction medium	Light source	Efficiency	References
$Ru/Rh:SrTiO_3$	$BiVO_4$	Fe^{3+}/Fe^{2+}	Water (H_2SO_4, pH = 2.4)	Xe lamp, 300 W (>420 nm) or solar simulator	AQY = 4.2% (420 nm) STH = 0.1%	[75]
$Ru/Rh:SrTiO_3$	$BiVO_4$	—	Water (H_2SO_4, pH = 3.5)	Xe lamp, 300 W (>420 nm) or solar simulator	AQY = 1.7% (420 nm) STH = 0.12%	[76]
CrO_x/Ru/La, $Rh:SrTiO_3$	RuO_x/Mo:$BiVO_4$	Au	Water, 10 kPa	Xe lamp, 300 W (>420 nm) or solar simulator	AQY = 33% (419 nm) STH = 1.1%	[77]
CrO_x/Ru/La, $Rh:SrTiO_3$	RuO_x/Mo:$BiVO_4$	C (graphitic, amorphous)	Water (H_2SO_4, pH = 3.5), 10 kPa	Xe lamp, 300 W (>420 nm) or solar simulator	AQY = 26% (419 nm) STH = 1.0%	[78]
CrO_x/Ru/La, $Rh:SrTiO_3$	RuO_x/Mo:$BiVO_4$	Indium tin oxide	Water (H_2SO_4, pH = 3.5), 10 kPa	Xe lamp, 300 W (>420 nm) or solar simulator	AQY = 10.2% (420 nm) STH = 0.4%	[79]

a) HEPC: H_2 evolution photocatalyst.
b) OEPC: O_2 evolution photocatalyst.

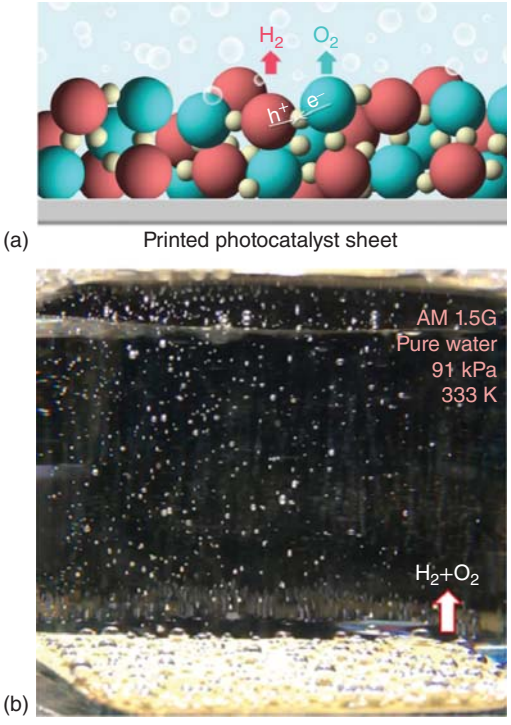

Figure 4.7 (a): Illustration of a printed layer of a Z-scheme photocatalyst composed of CrO_x/Rh/La, Rh:$SrTiO_3$ (red spheres), RuO_x/Mo:$BiVO_4$ (blue spheres) and indium tin oxide (yellow spheres) nanoparticles as the H_2 evolution, O_2 evolution, and solid electron mediator, respectively. Source: Reproduced with permission from Wang et al. [79]; copyright 2018 Elsevier. (b): Photograph of a 3 × 3 cm sheet based on the Z-scheme described above, irradiated using simulated sunlight (AM 1.5G) in water, showing the evolution of H_2/O_2 bubbles. Source: Wang and Domen [10]/with permission of American Chemical Society.

This technology was further improved by using a transparent conductor mediator, indium tin oxide (ITO), which is amenable to screen printing of large flat panels (see Figure 4.7, Ref. [79]).

Whilst the bioinspired Z-scheme approach entails a great challenge due to complexity in fabrication, it is an appealing technology for the design of artificial chloroplasts [73].

4.3.6 Artificial Leaves Based on Semiconductor Junctions

A step beyond in overall water splitting technologies only requiring the immersion of an appropriate material in irradiated water is that represented by artificial leaves [4, 82]. The difference with immobilized photocatalyst particle layers lies in the fact that artificial leaves are assemblies of a flat photovoltaic-type absorber interfaced with appropriate co-catalysts. The absorber is generally based on semiconductor junctions. Another way to define such artificial leaves is a wireless, compact, integrated photovoltaic-electrolysis system whereby H_2 and O_2 evolution sites are appropriately contacted on either side of the photovoltaic unit.

Among different attempts to construct efficient and stable artificial designs, the most prominent and successful examples were reported by Nocera and coworkers [82]. As a sunlight absorber, a triple-junction amorphous silicon material was used, and interfaced with ITO coated with a cobalt-phosphate O_2-evolving co-catalyst, and a stainless steel sheet coated with a nickel-molybdenum-zinc

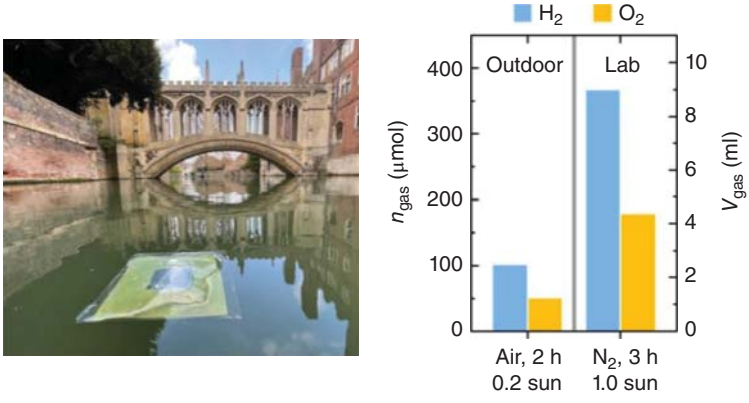

Figure 4.8 Left: Photograph of a floating artificial leaf comprising a $TiCoO_x/BiVO_4$ photoanode and Pt/perovskite photocathode under operation on the waters of river Cam (Bridge of Sighs, St. John's College, Cambridge, United Kingdom). Right: H_2/O_2 production from overall water splitting using the artificial leaves under natural sunlight on a cloudy day and ambient atmospheric conditions, or in a laboratory setup under simulated sunlight and inert atmosphere. Source: Andrei et al. [87]/with permission of Nature Publishing Group.

H_2-evolving co-catalyst, to achieve remarkable stability and STH of around 2.5% [83]. The O_2-evolving co-catalyst had been previously envisaged and then optimized as a self-healing dynamic material that is deposited in situ from Co^{2+} in a phosphate buffer solution at neutral pH, with a similar structure and mechanistic functionalities to the Mn_4O_4Ca cluster in natural photosystem II [84, 85]. The team founded a spin-off company, Sun Catalytix, to commercialize the artificial leaf, which was later purchased by a major aerospace technology corporation [5].

Phenomena hampering the efficiency of artificial leaves include long-charge carrier diffusion paths with multiple junctions, and the shadowing effect of deposited co-catalysts on the irradiation area. The selective and localized electrodeposition of a H_2 evolution co-catalyst (Pt) on the line shaped electrode of a commercial triple-junction photovoltaic cell (InGaP, GaAs, and Ge as semiconductors) was proposed as a solution to overcome such issues, resulting in an STH of around 11.2% [86]. It should be noted that photovoltaic-grade semiconductors are not water-stable, and the leaf must be rigorously sealed. Very recently, floating, flexible photoelectrochemical artificial leaves based on a combination of $TiCoO_x/BiVO_4$ photoanode and Pt/perovskite photocathode have been constructed and operated in open waters such as a river (Figure 4.8); a conductive graphite-epoxy resin was used as an electrical contactor and encapsulant [87]. Although the efficiency is lower than in laboratory experiments, the demonstration of a device that can autonomously perform solar water splitting outdoors on unpurified water is a major achievement.

4.4 Photocatalytic Splitting of Seawater

More than 97% of all water on Earth is in seas and oceans, whereas fresh water availability for human use (including industry, farming, and agriculture) is or

will soon become critical in many geographical locations [88, 89]. Moreover, current water-to-hydrogen technologies use purified water as the feedstock. Albeit previous desalination can be an option, the development of successful direct seawater splitting implies obvious advantages in terms of sustainability. Recent efforts in this regard have been devoted to the fields of electrolysis [6, 89] and photocatalysis [88, 89].

The presence of large amounts of salts – chiefly, sodium chloride – in seawater is a key factor influencing the efficiency and durability of water splitting systems. In particular, Cl^- may exert both positive and negative effects. The oxidation of Cl^- to chlorine (Cl_2) and hypochlorite (ClO^-) is hindered thermodynamically yet favored kinetically with respect to water oxidation to O_2 [88, 89]. Regardless of whether oxidation of chloride or water takes place, the reduction half reaction is invariably the generation of H_2 from water protons, provided no other sacrificial reagents are used. In practice, brine electrolysis is the basis of the industrial production of Cl_2 (Eq. (4.3)) or ClO^- for bleach and other disinfecting formulations [90]. Adaptation of such technology to hydrogen production can be beneficial [91].

Regarding photocatalysis, Lee and coworkers first reported photocatalytic H_2/O_2 production from filtered natural or model seawater employing suspended NiO/Ni/$La_2Ti_2O_7$ under UV light, observing some detrimental effect of most salts relative to pure water, and no formal oxidation of Cl^- [92]. This was later confirmed for artificial seawater splitting under visible light on $Rh_{2-y}Cr_yO_3/(Ga_{0.88}Zn_{0.12})(N_{0.88}O_{0.12})$, which underwent a diminution of activity to approximately half relative to pure water, and lack of stability due to degradation of the photocatalyst [93]. Some indication of chloride oxidation was hinted in this latter report, inhibiting O_2 evolution, but none of the expected useful co-products were formed in appreciable amounts. Effective production of H_2/O_2 was also reported on magnesium-doped GaN–InGaN nanowires having deposited Cr_2O_3/Rh and CoO_x as co-catalysts from aqueous NaCl solutions, with co-production of small amounts of Cl_2 and ClO^- (Figure 4.9); lower

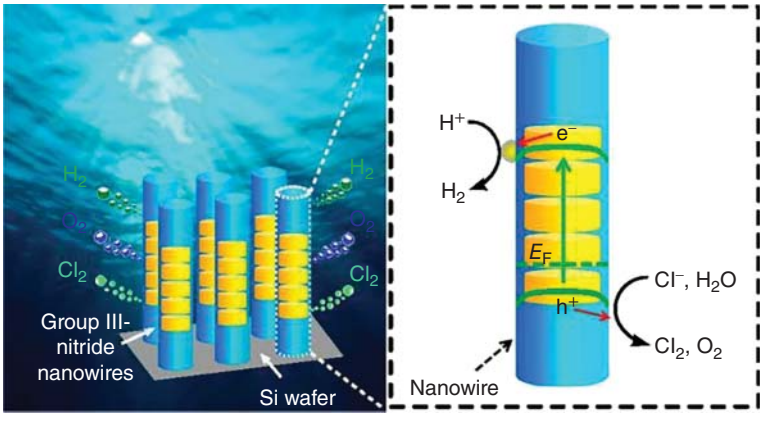

Figure 4.9 Artwork representation of a photocatalyst consisting of Cr_2O_3/Rh-CoO_x/GaN–InGaN nanowires on silicon wafers enabling the sunlight-promoted splitting of seawater, generating H_2/O_2 and traces of Cl_2 and ClO^-. Source: Guan et al. [94]/with permission of American Chemical Society.

activity was observed from simulated seawater owing to poor photocatalyst stability under its mild basicity (pH ≈ 8), and yet, remarkably high STH (1.9%) was achieved under concentrated sunlight [94].

Several other photocatalytic systems exhibiting tolerance to saline aqueous media and hydrogen production activity include some oxide materials. For example, hydrogen was evolved from WO_2-Na_xWO_3 composites under visible-infrared light, although neither O_2 nor oxidized chlorine products were detected; instead, the formation of hydroxide radicals and hydrogen peroxide (H_2O_2) by water oxidation was suggested [95]. The splitting of pure water or artificial seawater into H_2 and H_2O_2 was later demonstrated by using TiO_2 (brookite) nanoflutes with deposited platinum as a co-catalyst, both under UV-vis or natural sunlight [96]. Despite the limited number of reports, proof of concept of solar photocatalytic seawater splitting and the possibility to obtain peroxides (see next section) are enticing prospects.

4.5 Photocatalytic Overall Water Splitting into H_2O_2 and H_2

The preceding sections summarize the wealth of knowledge available on overall water splitting to H_2 and O_2 thanks to stupendous efforts and astonishing success in photocatalyst and co-catalyst design. On most occasions, the generation and reactivity of O_2 appear to be the bottleneck to even superior performance. Formation of an oxygen molecule takes place by a four-electron process (Eq. (4.1)) in several steps, and therefore, several burdens might hinder its completion. However, if it takes place half way by the transfer of two electrons, the alternative and useful water oxidation coproduct H_2O_2 can be produced (Eq. (4.2)). Early studies suggested this possibility, although it has been commonly regarded as a failure, and only recently its enhancement is beginning to be considered as a viable and worthwhile option [91, 97].

In 1980, the production of hydrogen from UV-irradiated suspensions of TiO_2 and ZnO photocatalysts was reported, but intriguingly, no oxygen could be detected, a fact that was ascribed to its conversion into H_2O_2 [98]. A thorough study by Kondarides and coworkers revealed that H_2O_2 is more rapidly produced by oxidation of surface hydroxyl groups typically present on oxide particles, and subsequent coupling to adsorbed peroxides; unfortunately, sustained water splitting on Pt/TiO_2 by this process could not be achieved [99]. It is commonly presumed that surface peroxides tend to poison the photocatalyst, hampering the recovery of H_2O_2. Some improvement in terms of productivity and durability has been reported using Pt-loaded brookite nanoflutes, also from seawater and under natural sunlight [96].

Carbon nitrides are another class of photocatalysts that can enable H_2/H_2O_2 production, importantly, also under visible light. Overall water splitting was reported for Pt/C_3N_4 with peroxide instead of oxygen formation; peroxide remained tightly adsorbed on the photocatalyst, and forced desorption by exhaustive venting was necessary to maintain multi-cycle efficiency [100]. Such serious poisoning of the carbon nitride surface by peroxide was solved by incorporating co-catalysts (carbon dots [68] or MnO_2 [101]), which decompose it to oxygen and water. Further development of

these systems has resulted in a phosphorus-doped C_3N_4 material with cobalt-nickel phosphide as a co-catalyst exhibiting high activity and selectivity under visible light [102]. Despite the prospects of H_2O_2 production by photocatalytic water splitting, the release and recovery of the product as a useful active oxygen substance must be solved.

4.6 Beyond Water Splitting: Photocatalytic Hydrogen from NH_3 or Other Binary Hydrogen Substances

Despite the photocatalytic overall water splitting efficiencies attained so far are relatively low, they represent a significant success given the energetic, mechanistic, and practical hurdles to overcome. By analogy, other simple binary hydrogen substances can also be in principle split. The most obvious example is ammonia (NH_3). It is massively produced in industry as a fertilizer precursor by the direct reaction of N_2 and H_2 (4.5), and can be considered as a hydrogen carrier if the reverse, endergonic – ammonia splitting – reaction (Eq. (4.5)) can be conducted [2, 103].

$$NH_3 \rightarrow {}^3/_2\, H_2 + {}^1/_2\, N_2 \tag{4.5}$$

Early studies revealing the photocatalytic activity of TiO_2 to generate NH_3 from gaseous N_2 in the presence of water [38] were followed by the incorporation of platinum as a hydrogen-evolving co-catalyst, resulting in the co-production of NH_3 and H_2, albeit at declining ammonia yields, a fact that was attributed to splitting according to Eq. (4.5) [104]. Production of H_2/N_2 in a nearly stoichiometric ratio ($\approx$3) by this process was performed in the vapor phase in continuous operation on Pt/TiO_2 photocatalysts, with enhanced productivity in the presence of water [105]. Interestingly, the reaction proceeds at higher rates in aqueous solution [104], and at basic pH [105, 106], with negligible formation of noxious nitrates/nitrites [106]. Ruthenium can effectively perform as an oxidation co-catalyst on ZnS for N_2 evolution in ammonia splitting under UV and simulated sunlight [107], but beyond these reports, and regrettably, little progress in this field has been made in recent years [108]. The prospects of the implementation of a hydrogen economy and the feasibility of ammonia as a carrier might (should) stimulate further research to explore photocatalysis as a splitting technology.

Other substrates for photocatalytic hydrogen production have been proposed. Nocera advocated a reversible energy storage cycle based on hydrogen halides as hydrogen carriers [109]. Hydrogen sulfide is another possible precursor involving a more facile oxidation half-reaction than water [110], although the multiple possible stable products obtained (sulfate, sulfite) hamper reversibility. Selectivity to elemental sulfur has been proposed by using Cu-doped TiO_2 photocatalysts as a viable solution [111]. The field is still immature and ample room for further progress might be ahead for sulfur-hydrogen systems. Finally, methane reforming (the prevalent route toward industrial hydrogen production currently) can be also performed under irradiation [112, 113]. The rich knowledge and future improvements in photocatalytic overall water splitting surely represent a valid asset for the development of these other hydrogen production technologies.

4.7 Outlook and Prospects

Whilst the generation of hydrogen and oxygen from water by electrochemical methods has been known for centuries, the realization of the simpler photocatalytic approach, whereby the dissociation of water takes place on the surface of an irradiated photo-active material, has been much more arduous to materialize. Nonetheless, the development of photocatalytic overall water splitting technologies has rapidly evolved during the last five decades. Initial demonstrations of UV-active semiconductor suspensions inspired a burgeoning wave of bold and dedicated research work. The burdens to overcome were chiefly low efficiencies, short durability, and scant visible-light response. Advances to overcome the former two burdens have relied on the design of co-catalysts promoting the key redox steps on water to generate hydrogen and oxygen while protecting the semiconductor from the accumulation of photogenerated charge carriers. The design of semiconductors with narrower bandgaps yet maintaining appropriate band potentials for water splitting has been successful in extending activity into the visible range of the solar spectrum. An alternative strategy to harness more such low-energy photons is the construction of bioinspired Z-scheme combinations of two semiconductors complementing each other. Moreover, multi-junction photovoltaic systems can be integrated into standalone wireless artificial leaves for water splitting, bridging the gap with photoelectrochemical technologies.

At the present stage, solar-to-hydrogen efficiencies of photocatalytic water splitting have achieved a few units on a percent basis. The competitive threshold for solar hydrogen is estimated to be somewhat higher, ideally around 10%, and consequently, continuation of the hitherto astonishing advancements in basic research is still required, both in photonic efficiency and in the utilization of visible photons. The possibility to use seawater or untreated surface water, or the promotion of other hydrogen production processes, such as those leading to hydrogen peroxide as the oxidation product, is enticing to expand on sustainability and viability dimensions. Direct solar energy storage into renewable hydrogen is, *per se*, an incredibly rewarding target to motivate further endeavors in the photocatalytic option.

Acknowledgments

A.P. thanks the Spanish Ministry of Science and Innovation, the Spanish Research State Agency, (MCIN/AEI/10.13039/501100011033) and the European Social Fund for a "Ramón y Cajal" contract (RYC-2017-22849).

References

1 Lewis, N.S. and Nocera, D.G. (2006). Powering the planet: chemical challenges in solar energy utilization. *Proc. Natl. Acad. Sci. U. S. A.* 103 (43): 15729–15735.

2 Armaroli, N. and Balzani, V. (2011). The hydrogen issue. *ChemSusChem* 4 (1): 21–36.

3 Bard, A.J. and Fox, M.A. (1995). Artificial photosynthesis: solar splitting of water to hydrogen and oxygen. *Acc. Chem. Res.* 28 (3): 141–145.

4 Kim, J.H., Hansora, D., Sharma, P. et al. (2019). Toward practical solar hydrogen production – an artificial photosynthetic leaf-to-farm challenge. *Chem. Soc. Rev.* 48 (7): 1908–1971.

5 Armaroli, N. and Balzani, V. (2016). Solar electricity and solar fuels: status and perspectives in the context of the energy transition. *Chem. Eur. J.* 22 (1): 32–57.

6 Tong, W., Forster, M., Dionigi, F. et al. (2020). Electrolysis of low-grade and saline surface water. *Nat. Energy* 5 (5): 367–377.

7 Chen, X.B., Shen, S.H., Guo, L.J., and Mao, S.S. (2010). Semiconductor-based photocatalytic hydrogen generation. *Chem. Rev.* 110 (11): 6503–6570.

8 Kudo, A. and Miseki, Y. (2009). Heterogeneous photocatalyst materials for water splitting. *Chem. Soc. Rev.* 38: 253–278.

9 Ran, J., Zhang, J., Yu, J. et al. (2014). Earth-abundant cocatalysts for semiconductor-based photocatalytic water splitting. *Chem. Soc. Rev.* 43 (22): 7787–7812.

10 Wang, Q. and Domen, K. (2020). Particulate photocatalysts for light-driven water splitting: mechanisms, challenges, and design strategies. *Chem. Rev.* 120 (2): 919–985.

11 Jeon, T.H., Koo, M.S., Kim, H., and Choi, W. (2018). Dual-functional photocatalytic and photoelectrocatalytic systems for energy- and resource-recovering water treatment. *ACS Catal.* 8 (12): 11542–11563.

12 Granone, L.I., Sieland, F., Zheng, N. et al. (2018). Photocatalytic conversion of biomass into valuable products: a meaningful approach? *Green Chem.* 20 (6): 1169–1192.

13 Kamat, P.V. and Jin, S. (2018). Semiconductor photocatalysis: "tell us the complete story!". *ACS Energy Lett.* 3 (3): 622–623.

14 Puga, A.V. (2016). Photocatalytic production of hydrogen from biomass-derived feedstocks. *Coord. Chem. Rev.* 315: 1–66.

15 IEA (2021. Global Hydrogen Review 2021, International Energy Agency, Paris https://www.iea.org/reports/global-hydrogen-review-2021.

16 Bard, A.J. (1979). Photoelectrochemistry and heterogeneous photocatalysis at semiconductors. *J. Photochem.* 10: 59–75.

17 Bard, A.J. (1980). Photoelectrochemistry. *Science* 207 (4427): 139–144.

18 Song, H., Luo, S., Huang, H. et al. (2022). Solar-driven hydrogen production: recent advances, challenges, and future perspectives. *ACS Energy Lett.* 7 (3): 1043–1065.

19 Nishiyama, H., Yamada, T., Nakabayashi, M. et al. (2021). Photocatalytic solar hydrogen production from water on a 100-m^2 scale. *Nature* 598 (7880): 304–307.

20 Liu, G., Sheng, Y., Ager, J.W. et al. (2019). Research advances towards large-scale solar hydrogen production from water. *EnergyChem* 1 (2): 100014.

21 Goto, Y., Hisatomi, T., Wang, Q. et al. (2018). A particulate photocatalyst water-splitting panel for large-scale solar hydrogen generation. *Joule* 2 (3): 509–520.

22 Fabian, D.M., Hu, S., Singh, N. et al. (2015). Particle suspension reactors and materials for solar-driven water splitting. *Energy Environ. Sci.* 8 (10): 2825–2850.

23 Kisch, H. and Bahnemann, D. (2015). Best practice in photocatalysis: comparing rates or apparent quantum yields? *J. Phys. Chem. Lett.* 6 (10): 1907–1910.

24 Hisatomi, T., Kubota, J., and Domen, K. (2014). Recent advances in semiconductors for photocatalytic and photoelectrochemical water splitting. *Chem. Soc. Rev.* 43 (22): 7520–7535.

25 Maeda, K. and Domen, K. (2010). Photocatalytic water splitting: recent progress and future challenges. *J. Phys. Chem. Lett.* 1 (18): 2655–2661.

26 Pinaud, B.A., Benck, J.D., Seitz, L.C. et al. (2013). Technical and economic feasibility of centralized facilities for solar hydrogen production via photocatalysis and photoelectrochemistry. *Energy Environ. Sci.* 6 (7): 1983–2002.

27 Gopinath, C.S. and Nalajala, N. (2021). A scalable and thin film approach for solar hydrogen generation: a review on enhanced photocatalytic water splitting. *J. Mater. Chem. A* 9 (3): 1353–1371.

28 Takanabe, K. (2017). Photocatalytic water splitting: quantitative approaches toward photocatalyst by design. *ACS Catal.* 7 (11): 8006–8022.

29 Yang, J., Wang, D., Han, H., and Li, C. (2013). Roles of cocatalysts in photocatalysis and photoelectrocatalysis. *Acc. Chem. Res.* 46 (8): 1900–1909.

30 Wen, F. and Li, C. (2013). Hybrid artificial photosynthetic systems comprising semiconductors as light harvesters and biomimetic complexes as molecular cocatalysts. *Acc. Chem. Res.* 46 (11): 2355–2364.

31 Kanan, M.W., Surendranath, Y., and Nocera, D.G. (2009). Cobalt–phosphate oxygen-evolving compound. *Chem. Soc. Rev.* 38 (1): 109–114.

32 Hisatomi, T. and Domen, K. (2019). Reaction systems for solar hydrogen production via water splitting with particulate semiconductor photocatalysts. *Nat. Catal.* 2 (5): 387–399.

33 Spasiano, D., Marotta, R., Malato, S. et al. (2015). Solar photocatalysis: materials, reactors, some commercial, and pre-industrialized applications. A comprehensive approach. *Appl. Catal., B* 170-171: 90–123.

34 Chen, S., Takata, T., and Domen, K. (2017). Particulate photocatalysts for overall water splitting. *Nat. Rev. Mater.* 2 (10): 17050.

35 Blankenship, R.E. (2002). *Molecular Mechanisms of Photosynthesis*. Wiley.

36 Wang, Y., Suzuki, H., Xie, J. et al. (2018). Mimicking natural photosynthesis: solar to renewable H_2 fuel synthesis by z-scheme water splitting systems. *Chem. Rev.* 118 (10): 5201–5241.

37 Fujishima, A. and Honda, K. (1972). Electrochemical photolysis of water at a semiconductor electrode. *Nature* 238: 37–38.

38 Schrauzer, G.N. and Guth, T.D. (1977). Photolysis of water and photoreduction of nitrogen on titanium dioxide. *J. Am. Chem. Soc.* 99 (22): 7189–7193.

39 Kawai, T. and Sakata, T. (1980). Photocatalytic decomposition of gaseous water over TiO_2 and TiO_2—RuO_2 surfaces. *Chem. Phys. Lett.* 72 (1): 87–89.

40 Sato, S. and White, J.M. (1980). Photodecomposition of water over platinum/titanium dioxide catalysts. *Chem. Phys. Lett.* 72 (1): 83–86.

41 Yamaguti, K. and Sato, S. (1985). Photolysis of water over metallized powdered titanium dioxide. *J. Chem. Soc., Faraday Trans. 1 F* 81 (5): 1237–1246.

42 Patsoura, A., Kondarides, D.I., and Verykios, X.E. (2007). Photocatalytic degradation of organic pollutants with simultaneous production of hydrogen. *Catal. Today* 124: 94–102.

43 Patsoura, A., Kondarides, D.I., and Verykios, X.E. (2006). Enhancement of photoinduced hydrogen production from irradiated Pt/TiO_2 suspensions with simultaneous degradation of azo-dyes. *Appl. Catal., B.* 64: 171–179.

44 Hang Li, Y., Xing, J., Jia Chen, Z. et al. (2013). Unidirectional suppression of hydrogen oxidation on oxidized platinum clusters. *Nat. Commun.* 4: 2500.

45 Liu, L., Meira, D.M., Arenal, R. et al. (2019). Determination of the evolution of heterogeneous single metal atoms and nanoclusters under reaction conditions: which are the working catalytic sites? *ACS Catal.* 9 (12): 10626–10639.

46 Liao, L., Zhang, Q., Su, Z. et al. (2014). Efficient solar water-splitting using a nanocrystalline CoO photocatalyst. *Nat. Nanotechnol.* 9 (1): 69–73.

47 Hara, M., Kondo, T., Komoda, M. et al. (1998). Cu_2O as a photocatalyst for overall water splitting under visible light irradiation. *Chem. Commun.* 3: 357–358.

48 Domen, K., Naito, S., Soma, M. et al. (1980). Photocatalytic decomposition of water vapour on an $NiO–SrTiO_3$ catalyst. *J. Chem. Soc., Chem. Commun.* 12: 543–544.

49 Kudo, A., Tanaka, A., Domen, K. et al. (1988). Photocatalytic decomposition of water over nickel oxide-potassium niobate ($NiO-K_4Nb_6O_{17}$) catalyst. *J. Catal.* 111: 67–76.

50 Kato, H. and Kudo, A. (1998). New tantalate photocatalysts for water decomposition into H_2 and O_2. *Chem. Phys. Lett.* 295 (5): 487–492.

51 Asai, R., Nemoto, H., Jia, Q. et al. (2014). A visible light responsive rhodium and antimony-codoped $SrTiO_3$ powdered photocatalyst loaded with an IrO_2 cocatalyst for solar water splitting. *Chem. Commun.* 50 (19): 2543–2546.

52 Takata, T., Jiang, J., Sakata, Y. et al. (2020). Photocatalytic water splitting with a quantum efficiency of almost unity. *Nature* 581 (7809): 411–414.

53 Maeda, K., Teramura, K., Lu, D. et al. (2006). Photocatalyst releasing hydrogen from water. *Nature* 440: 295.

54 Wang, Q., Nakabayashi, M., Hisatomi, T. et al. (2019). Oxysulfide photocatalyst for visible-light-driven overall water splitting. *Nat. Mater.* 18 (8): 827–832.

55 Zhang, G., Lan, Z.-A., Lin, L. et al. (2016). Overall water splitting by $Pt/g-C_3N_4$ photocatalysts without using sacrificial agents. *Chem. Sci.* 7 (5): 3062–3066.

56 Wang, L., Wan, Y., Ding, Y. et al. (2017). Conjugated microporous polymer nanosheets for overall water splitting using visible light. *Adv. Mater.* 29 (38): 1702428.

57 Xu, Y. and Schoonen, M.A.A. (2000). The absolute energy positions of conduction and valence bands of selected semiconducting minerals. *Am. Mineral.* 85: 543–556.

58 Domen, K., Kudo, A., and Onishi, T. (1986). Mechanism of photocatalytic decomposition of water into hydrogen and oxygen over nickel oxide-strontium titanate. *J. Catal.* 102: 92–98.

59 Domen, K., Kudo, A., Shinozaki, A. et al. (1986). Photodecomposition of water and hydrogen evolution from aqueous methanol solution over novel niobate photocatalysts. *J. Chem. Soc., Chem. Commun.* 4: 356–357.

60 Kudo, A. and Kato, H. (2000). Effect of lanthanide-doping into $NaTaO_3$ photocatalysts for efficient water splitting. *Chem. Phys. Lett.* 331 (5): 373–377.

61 Ham, Y., Hisatomi, T., Goto, Y. et al. (2016). Flux-mediated doping of SrTiO3 photocatalysts for efficient overall water splitting. *J. Mater. Chem. A* 4 (8): 3027–3033.

62 Lyu, H., Hisatomi, T., Goto, Y. et al. (2019). An Al-doped $SrTiO_3$ photocatalyst maintaining sunlight-driven overall water splitting activity for over 1000 h of constant illumination. *Chem. Sci.* 10 (11): 3196–3201.

63 Asahi, R., Morikawa, T., Irie, H., and Ohwaki, T. (2014). Nitrogen-doped titanium dioxide as visible-light-sensitive photocatalyst: designs, developments, and prospects. *Chem. Rev.* 114 (19): 9824–9852.

64 Maeda, K., Takata, T., Hara, M. et al. (2005). GaN:ZnO solid solution as a photocatalyst for visible-light-driven overall water splitting. *J. Am. Chem. Soc.* 127 (23): 8286–8287.

65 Wang, Z., Inoue, Y., Hisatomi, T. et al. (2018). Overall water splitting by Ta_3N_5 nanorod single crystals grown on the edges of $KTaO_3$ particles. *Nat. Catal.* 1 (10): 756–763.

66 Bai, Y., Hippalgaonkar, K., and Sprick, R.S. (2021). Organic materials as photocatalysts for water splitting. *J. Mater. Chem. A* 9 (30): 16222–16232.

67 Wang, X., Maeda, K., Thomas, A. et al. (2009). A metal-free polymeric photocatalyst for hydrogen production from water under visible light. *Nat. Mater.* 8 (1): 76–80.

68 Liu, J., Liu, Y., Liu, N. et al. (2015). Metal-free efficient photocatalyst for stable visible water splitting via a two-electron pathway. *Science* 347 (6225): 970–974.

69 Bai, Y., Li, C., Liu, L. et al. (2022). Photocatalytic overall water splitting under visible light enabled by a particulate conjugated polymer loaded with palladium and iridium. *Angew. Chem., Int. Ed.* 61: e202201299.

70 Silva, C.G., Corma, A., and García, H. (2010). Metal-organic frameworks as semiconductors. *J. Mater. Chem.* 20 (16): 3141–3156.

71 An, Y., Liu, Y., An, P. et al. (2017). Ni^{II} coordination to an Al-based metal–organic framework made from 2-aminoterephthalate for photocatalytic overall water splitting. *Angew. Chem., Int. Ed.* 56 (11): 3036–3040.

72 Salcedo-Abraira, P., Babaryk, A.A., Montero-Lanzuela, E. et al. (2021). A novel porous Ti-squarate as efficient photocatalyst in the overall water splitting reaction under simulated sunlight irradiation. *Adv. Mater.* 33 (52): 2106627.

73 Hu, H., Wang, Z., Cao, L. et al. (2021). Metal–organic frameworks embedded in a liposome facilitate overall photocatalytic water splitting. *Nat. Chem.* 13 (4): 358–366.

74 Abe, R., Sayama, K., Domen, K., and Arakawa, H. (2001). A new type of water splitting system composed of two different TiO_2 photocatalysts (anatase, rutile) and a IO_3^-/I^- shuttle redox mediator. *Chem. Phys. Lett.* 344 (3): 339–344.

75 Kato, H., Sasaki, Y., Shirakura, N., and Kudo, A. (2013). Synthesis of highly active rhodium-doped $SrTiO_3$ powders in Z-scheme systems for visible-light-driven photocatalytic overall water splitting. *J. Mater. Chem. A* 1 (39): 12327–12333.

76 Sasaki, Y., Nemoto, H., Saito, K., and Kudo, A. (2009). Solar water splitting using powdered photocatalysts driven by Z-schematic interparticle electron transfer without an electron mediator. *J. Phys. Chem. C* 113 (40): 17536–17542.

77 Wang, Q., Hisatomi, T., Jia, Q. et al. (2016). Scalable water splitting on particulate photocatalyst sheets with a solar-to-hydrogen energy conversion efficiency exceeding 1%. *Nat. Mater.* 15 (6): 611–615.

78 Wang, Q., Hisatomi, T., Suzuki, Y. et al. (2017). Particulate photocatalyst sheets based on carbon conductor layer for efficient Z-scheme pure-water splitting at ambient pressure. *J. Am. Chem. Soc.* 139 (4): 1675–1683.

79 Wang, Q., Okunaka, S., Tokudome, H. et al. (2018). Printable photocatalyst sheets incorporating a transparent conductive mediator for Z-scheme water splitting. *Joule* 2 (12): 2667–2680.

80 Okunaka, S., Tokudome, H., and Abe, R. (2016). Z-scheme water splitting into H_2 and O_2 under visible light over photocatalyst panels consisting of Rh-doped $SrTiO_3$ and $BiVO_4$ fine particles. *Chem. Lett.* 45 (1): 57–59.

81 Wang, Q., Li, Y., Hisatomi, T. et al. (2015). Z-scheme water splitting using particulate semiconductors immobilized onto metal layers for efficient electron relay. *J. Catal.* 328: 308–315.

82 Nocera, D.G. (2012). The artificial leaf. *Acc. Chem. Res.* 45: 767–776.

83 Reece, S.Y., Hamel, J.A., Sung, K. et al. (2011). Wireless solar water splitting using silicon-based semiconductors and Earth-abundant catalysts. *Science* 334: 645–648.

84 Surendranath, Y., Kanan, M.W., and Nocera, D.G. (2010). Mechanistic studies of the oxygen evolution reaction by a cobalt-phosphate catalyst at neutral pH. *J. Am. Chem. Soc.* 132 (46): 16501–16509.

85 Kanan, M.W. and Nocera, D.G. (2008). In situ formation of an oxygen-evolving catalyst in neutral water containing phosphate and Co^{2+}. *Science* 321 (5892): 1072–1075.

86 Okamoto, S., Deguchi, M., and Yotsuhashi, S. (2017). Modulated III–V triple-junction solar cell wireless device for efficient water splitting. *J. Phys. Chem. C* 121 (3): 1393–1398.

87 Andrei, V., Ucoski, G.M., Pornrungroj, C. et al. (2022). Floating perovskite-$BiVO_4$ devices for scalable solar fuel production. *Nature* 608 (7923): 518–522.

88 Zhang, J., Hu, W., Cao, S., and Piao, L. (2020). Recent progress for hydrogen production by photocatalytic natural or simulated seawater splitting. *Nano Res.* 13 (9): 2313–2322.

89 Dingenen, F. and Verbruggen, S.W. (2021). Tapping hydrogen fuel from the ocean: a review on photocatalytic, photoelectrochemical and electrolytic splitting of seawater. *Renewable Sustainable Energy Rev.* 142: 110866.

90 Bommaraju, T.V., Lüke, B., O'Brien, T.F., and Blackburn, M.C. (2002). Chlorine. In: *Kirk-Othmer Encyclopedia of Chemical Technology*. https://doi.org/10.1002/0471238961.0308121503211812.a01.pub2.

91 Antonietti, M. and Savateev, A. (2018). Splitting water by electrochemistry and artificial photosynthesis: excellent science but a nightmare of translation? *Chem. Rec.* 18 (7–8): 969–972.

92 Ji, S.M., Jun, H., Jang, J.S. et al. (2007). Photocatalytic hydrogen production from natural seawater. *J. Photochem. Photobiol., A* 189 (1): 141–144.

93 Maeda, K., Masuda, H., and Domen, K. (2009). Effect of electrolyte addition on activity of $(Ga_{1-x}Zn_x)(N_{1-x}O_x)$ photocatalyst for overall water splitting under visible light. *Catal. Today* 147 (3): 173–178.

94 Guan, X., Chowdhury, F.A., Pant, N. et al. (2018). Efficient unassisted overall photocatalytic seawater splitting on GaN-based nanowire arrays. *J. Phys. Chem. C* 122 (25): 13797–13802.

95 Cui, G., Wang, W., Ma, M. et al. (2015). IR-driven photocatalytic water splitting with WO_2–Na_xWO_3 hybrid conductor material. *Nano Lett.* 15 (11): 7199–7203.

96 Cao, S., Chan, T.-S., Lu, Y.-R. et al. (2020). Photocatalytic pure water splitting with high efficiency and value by Pt/porous brookite TiO_2 nanoflutes. *Nano Energy* 67: 104287.

97 Idriss, H. (2020). The elusive photocatalytic water splitting reaction using sunlight on suspended nanoparticles: is there a way forward? *Catal. Sci. Technol.* 10 (2): 304–310.

98 Rao, M.V., Rajeshwar, K., Verneker, V.R.P., and DuBow, J. (1980). Photosynthetic production of hydrogen and hydrogen peroxide on semiconducting oxide grains in aqueous solutions. *J. Phys. Chem.* 84 (15): 1987–1991.

99 Daskalaki, V.M., Panagiotopoulou, P., and Kondarides, D.I. (2011). Production of peroxide species in Pt/TiO_2 suspensions under conditions of photocatalytic water splitting and glycerol photoreforming. *Chem. Eng. J.* 170: 433–439.

100 Liu, J., Zhang, Y., Lu, L. et al. (2012). Self-regenerated solar-driven photocatalytic water-splitting by urea derived graphitic carbon nitride with platinum nanoparticles. *Chem. Commun.* 48 (70): 8826–8828.

101 Liu, J., Liu, N.Y., Li, H. et al. (2016). A critical study of the generality of the two step two electron pathway for water splitting by application of a C_3N_4/MnO_2 photocatalyst. *Nanoscale* 8 (23): 11956–11961.

102 Xue, F., Si, Y., Wang, M. et al. (2019). Toward efficient photocatalytic pure water splitting for simultaneous H_2 and H_2O_2 production. *Nano Energy* 62: 823–831.

103 Gielen D, Taibi E, and Miranda R (2019). Hydrogen: a renewable energy perspective. International Renewable Energy Agency (IRENA).

104 Qing-shui, L., Kazunari, D., Shuichi, N. et al. (1983). Photocatalytic synthesis and photodecomposition of ammonia over $SrTiO_3$ and $BaTiO_3$ based catalysts. *Chem. Lett.* 12 (3): 321–324.

105 Yuzawa, H., Mori, T., Itoh, H., and Yoshida, H. (2012). Reaction mechanism of ammonia decomposition to nitrogen and hydrogen over metal loaded titanium oxide photocatalyst. *J. Phys. Chem. C* 116 (6): 4126–4136.

106 Kominami, H., Nishimune, H., Ohta, Y. et al. (2012). Photocatalytic hydrogen formation from ammonia and methyl amine in an aqueous suspension of metal-loaded titanium(IV) oxide particles. *Appl. Catal., B* 111–112: 297–302.

107 Iwase, A., Ii, K., and Kudo, A. (2018). Decomposition of an aqueous ammonia solution as a photon energy conversion reaction using a Ru-loaded ZnS photocatalyst. *Chem. Commun.* 54 (48): 6117–6119.

108 Lucentini, I., Garcia, X., Vendrell, X., and Llorca, J. (2021). Review of the decomposition of ammonia to generate hydrogen. *Ind. Eng. Chem. Res.* 60 (51): 18560–18611.

109 Teets, T.S. and Nocera, D.G. (2011). Photocatalytic hydrogen production. *Chem. Commun.* 47 (33): 9268–9274.

110 Oladipo, H., Yusuf, A., Al Jitan, S., and Palmisano, G. (2021). Overview and challenges of the photolytic and photocatalytic splitting of H_2S. *Catal. Today* 380: 125–137.

111 Gonell, F., Puga, A.V., Julián-López, B. et al. (2016). Copper-doped titania photocatalysts for simultaneous reduction of CO_2 and production of H_2 from aqueous sulfide. *Appl. Catal., B* 180: 263–270.

112 Yoshida, H., Kato, S., Hirao, K. et al. (2007). Photocatalytic steam reforming of methane over platinum-loaded semiconductors for hydrogen production. *Chem. Lett.* 36: 430–431.

113 Yoshida, H., Hirao, K., Nishimoto, J.I. et al. (2008). Hydrogen production from methane and water on platinum loaded titanium oxide photocatalysts. *J. Phys. Chem. C* 112 (14): 5542–5551.

5

Photoelectrocatalytic H_2 Production

Levente Nagy, Roberto González-Gómez, Gunasekaran Kumaravel Dinesh, and Pau Farràs

University of Galway, Energy Research Centre, Ryan Institute, School of Chemical and Biological Sciences, University Road, Galway, H91 CF50, Ireland

5.1 Introduction

The over-exploitation of fossil fuels and the ever-increasing global energy demand have brought about extensive research in green energy strategies and sustainable development [1]. Low and zero-carbon technologies are proposed as potential solutions, however, despite great advancements in these areas, there is still a need to develop more efficient processes to simultaneously produce clean energy while reducing the global carbon footprint.

Sustainable H_2 production through photoelectrochemical (PEC) water splitting (also known as *golden hydrogen*) is considered a promising technology in green energy harvesting and long-term energy storage, in particular for distributed production in locations with poor electricity and/or gas networks. Since PEC H_2 production was first reported by Fujishima and Honda [2], the investigation of novel light-harvesting materials for use as photocatalysts in this reaction has garnered growing research attention.

The underlying principle behind PEC H_2 production is rather straightforward, however, the molecular basis and reaction mechanisms have yet to be fully understood [3]. A PEC cell consists of a semiconductor photoelectrode immersed in an electrolytic solution. When the device is irradiated, photons are absorbed by the light harvester, producing an electron excitation from the valence band to the conduction band, generating an electron–hole pair, which drives a chemical reaction (Figure 5.1). In order to produce H_2, a PEC system electrolyses water into H_2 through the hydrogen evolution reaction (HER) and O_2 *via* the oxygen evolution reaction (OER) [5]. If the photoelectrode is an *n*-type semiconductor, it functions as a photoanode and facilitates the OER. Conversely, a *p*-type semiconductor acts as a photocathode and carries out the HER [6].

Photocatalytic Hydrogen Production for Sustainable Energy, First Edition. Edited by Alberto Puga.

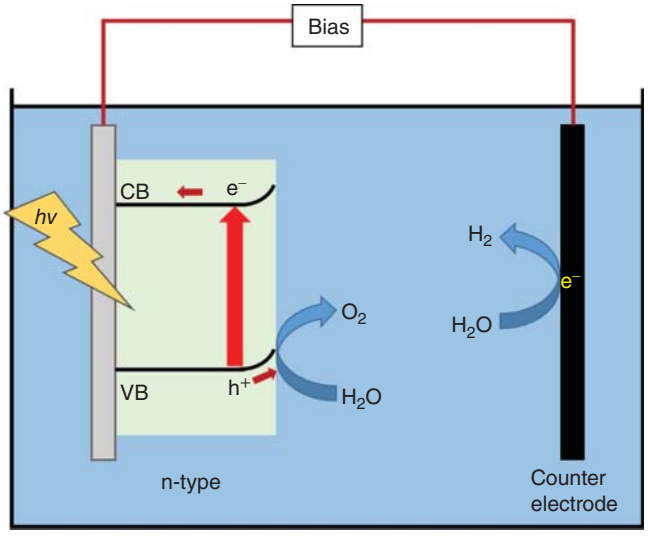

Figure 5.1 Simplified scheme representing the role of the photogenerated electron–hole pair in the PEC water splitting process. The electrode shown is a photoanode, facilitating the OER. Source: Kalanur et al. [4]/with permission of Springer Nature.

In this chapter, the principles of PEC H_2 production and the parameters that influence its efficiency are explored. Subsequently, PEC device design considerations, including photoelectrode materials and PEC cell configurations, are discussed. Finally, theoretical models of the photophysical and electrochemical phenomena involved in PEC H_2 production are briefly summarized.

5.2 Parameters Affecting PEC H_2 Production

The following section explores the factors that affect PEC performance and efficiency, namely, solar-to-H_2 (STH), incident photon to current efficiency (IPCE), photocurrent density, and reactor setup. The theoretical basis for these interdependent parameters is established, and novel strategies to enhance PEC performance are discussed.

5.2.1 Solar-to-H_2 Conversion Efficiency

Several solar-driven H_2 production methodologies have been developed with varying device complexities and efficiencies, however, practical PEC H_2 production using low-complexity devices with high efficiency still remains out of reach (Figure 5.2).

The STH conversion efficiency (η_{STH}) describes the ratio of input solar energy to the amount of H_2 generated. As such, it is a crucial parameter for comparing the efficiency and overall performance of PEC devices and benchmarking them against different solar technologies.

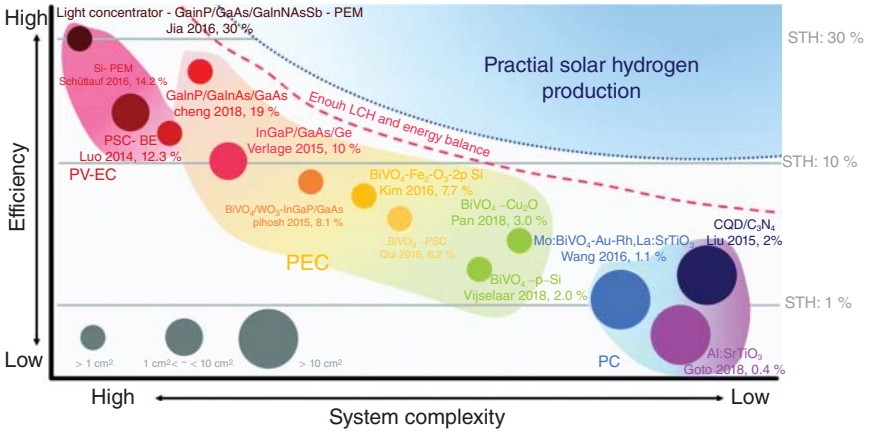

Figure 5.2 Technological map showing various solar-energy approaches for photon-driven H_2 production. Source: Kim et al. [7]/with permission of Royal Society of Chemistry.

The η_{STH} calculation is dependent on the configuration of the PEC cell. In a two-electrode PEC system, η_{STH} can be obtained by measuring the amount of H_2 produced under standard solar illumination conditions (AM 1.5G), as shown in Eq. (5.1) [8, 9].

$$\eta_{STH} = \left[\frac{\text{rate of } H_2 \text{ production} \times \Delta G}{P_{total} \times \text{illuminated area}}\right]_{AM1.5G} \tag{5.1}$$

where the rate of H_2 production is expressed in mol s^{-1}; ΔG corresponds to the Gibbs free energy required for water splitting, 237.2 kJ mol^{-1}; and P_{total} represents the total incident solar light intensity (W cm^{-2}). For example, AM 1.5G corresponds to 1 sun or 0.1 W cm^{-2}.

For a three-electrode PEC system, where the reference electrode allows for electrochemical measurements, η_{STH} can be determined using Eq. (5.2) [10].

$$\eta_{STH} = \left[\frac{|J_{sc}| \times E \times \eta_F}{P_{total}}\right]_{AM1.5G} \tag{5.2}$$

where, J_{sc} is the short-circuit photocurrent density (A cm^{-2}); E corresponds to the theoretical voltage required for the electrolysis of water, 1.23 V; and η_F is the Faradaic efficiency for hydrogen evolution, which is defined as the ratio of gas generated to the theoretical maximum gas evolution [11]. Different methodologies may be used to quantify the amount of gas produced, ranging from gas chromatography [12] to flow meters [13], water displacement systems [14], or in-line mass spectrometry [15]. In all cases, it is necessary to confirm that all the gas evolved corresponds to hydrogen before η_F can be calculated. These parameters are measured without any sacrificial reagents and without any pH variation or electrical bias between the working electrode and the counter electrode.

Since many photoelectrode materials provide insufficient voltage, an external bias is often necessary to drive the PEC water splitting reaction. In these cases, the applied

bias photon-to-voltage conversion efficiency, or ABPE, defined in Eq. (5.3), must be used instead of the η_{STH} equation [10].

$$\text{ABPE} = \left[\frac{|J_{photo}| \times (E - V_{bias})}{P_{total}}\right]_{AM1.5G} \tag{5.3}$$

where, V_{bias} corresponds to the applied external voltage, and J_{photo} is the photocurrent density (mA cm^{-2}) measured.

5.2.2 Incident Photon to Current Efficiency

The photocurrent produced by a number of incident photons of a given wavelength λ is known as the IPCE given by Eq. (5.4) [16]. It is a useful expression for determining the system's electrical sensitivity to light.

$$\text{IPCE}(\lambda) = \frac{n_h(\lambda)}{n_{ph}(\lambda)} = \frac{h \times c}{e} \times \frac{J_{photo}(\lambda)}{\lambda \times P_{total}(\lambda)} \tag{5.4}$$

where, n_h and n_{ph} correspond to the number of holes produced and incident photons, respectively. In the second expression, h is Planck's constant, c is the speed of light, and e is the charge of an electron [17].

Since IPCE is dependent on the light intensity and wavelength, it is closely linked to the optical properties of the photoelectrode. Incident photons are either absorbed, transmitted, or reflected by the semiconductor material. Light absorption efficiency (η_A), also known as light harvesting efficiency (LHE), describes the fraction of photons that the photoelectrode can harvest, and is given by Eq. (5.5) [18].

$$\eta_A = 1 - \eta_R - \eta_T \tag{5.5}$$

in which η_R and η_T are the light reflection and transmittance efficiencies, respectively. These parameters are conventionally determined using reflectance spectroscopy, which reveals the characteristics of the working electrode material.

5.2.3 Photocurrent Density

In a PEC system, in order to measure the current generated by the photoelectrode under light illumination, a voltage bias is applied between the working electrode and the counter/reference electrode. The difference between current under dark conditions and current generated under illumination is known as photocurrent.

Photocurrent density is a standard evaluation tool for understanding photoelectrode performance that can be obtained using a conventional three-electrode voltammetry cell setup. Figure 5.3 shows the anodic photocurrent density obtained in response to an applied electrode potential.

5.2.4 Reactor Setup

The PEC reactor, or photocell, consists of photoelectrodes connected *via* an electrolyte. A reference electrode could also be included, allowing voltametric determination of the photocell's performance. Although research focus on

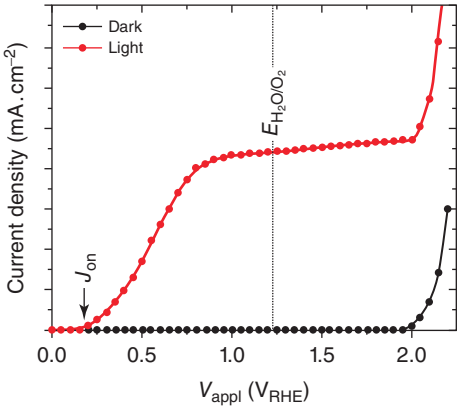

Figure 5.3 A generic photocurrent density measurement of a photoanode. The applied potential (*vs.* RHE) is swept from cathodic to anodic potentials in the dark (black curve) and light (red curve); J_{on} represents the onset of the photocurrent and E_{H_2O/O_2} represents the thermodynamic potential for water oxidation (1.23 V_{RHE}). Source: Moss et al. [19]/with permission of John Wiley & Sons.

photocell design has been limited, it is an important consideration for commercial and industrial-scale applications of PEC systems. A photocell setup can modify active surface illumination, fluid flow, and bubble formation, all of which are crucial for maximizing the efficiency of a reactor. Therefore, a description of different PEC reactors, variations in incident light, and photocell window materials are needed to construct an efficient reactor setup.

5.2.4.1 Type of Photocell

In general, photocells can be divided into two major categories: Open and H-type. Open photocells are basic configurations where the three electrodes are situated in a shared electrolyte chamber (Figure 5.4a). In this setup, the gases evolved during the reaction are mixed, thus, a method for gas separation, such as gas chromatography, is required. Conversely, an H-type photocell features separate chambers for each electrode, which allows for the straightforward collection of separated gases (Figure 5.4b). Note that lab-scale versions of these devices generally operate with the light source fixed at a certain distance from the working electrode to efficiently calculate the light intensity reaching the photoelectrode.

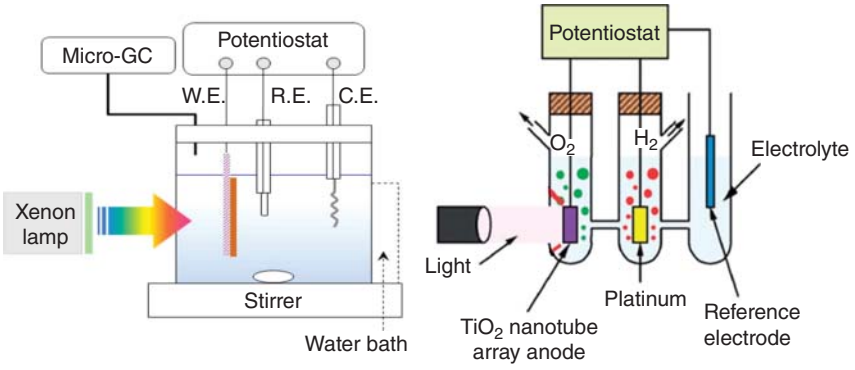

Figure 5.4 Schematic diagrams of (a) Open and (b) H-type photocells. Source: Xing et al. [20]/with permission of Elsevier.

5.2.4.2 Incident Light

Commercial and industrial applications of PEC reactors require direct illumination by natural sunlight. As such, the light intensity varies greatly depending on the weather, geographical location, and time of day. Furthermore, the geometric shape of the photoreactor can also influence the incident light intensity. Maximum H_2 production can be achieved by utilizing the full solar spectrum at an illumination intensity of at least 0.1 W cm^{-2}. Outdoor applications typically use concentrator lenses, which focus incident light onto photoactive surfaces to increase illumination intensity; by using these lenses, illumination of up to 47.4 W cm^{-2} (>400 suns) has been achieved [13]. For example, a hematite photoanode PEC system utilizing a dual-axis tracking system for outdoor operation was reported to achieve 0.5–2 mA cm^{-2} photocurrent density output (Figure 5.5) [19].

5.2.4.3 Photocell Window Material

Incident light must reach the photoelectrode of the photocell through the optical window, which should not reflect or absorb any of the desired operating wavelengths. To assess the effectiveness of window materials, Huang *et al.* [21] compared the H_2 production rate in a standard photoreactor cell while modifying the optical window material (Figure 5.6). Although these tests were performed in photocatalytic reactors instead of PEC cells, the results can shed light on some useful alternative materials for PEC reactor design. The results show that quartz windows facilitate the highest H_2 production, but their high cost rules them out for large-scale applications [20]. More cost-effective window materials are necessary to support commercial PEC applications. Polymer films such as Aclar™ and Mylar™ have emerged as promising alternative materials as they enable similar H_2 production rates to quartz at a lower cost [21, 22]. In addition, safety considerations need to be evaluated for industrial applications, as quartz or glass can pose a safety issue with reactions under pressure, while plastic-based materials offer a competitive advantage in this regard.

A detailed examination of photoreactor designs, including photocell types, window materials, and light concentrators, can be found in the 2013 review by Xing et al. [20].

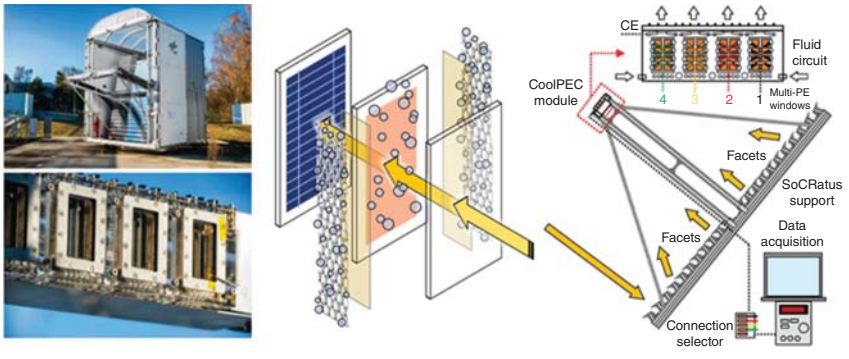

Figure 5.5 Large-scale, outdoor PEC system mounted on a dual-axis solar tracking system. Source: Moss et al. [19]/with permission of John Wiley & Sons.

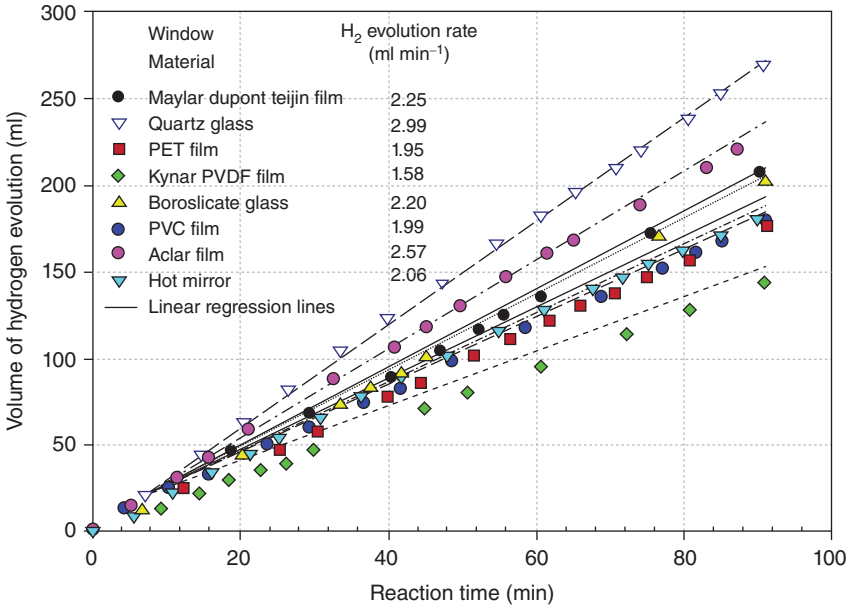

Figure 5.6 Comparison of the H_2 production rate for photocatalytic reactors utilizing different window materials. Source: Huang et al. [21]/with permission of Elsevier.

5.3 Photoelectrochemical Semiconductor Materials

High catalytic activity and stability are two important properties that an ideal solar-active semiconductor should have. Additionally, to increase the efficiency of the PEC water splitting reaction, the photoelectrode should have efficient charge carrier separation, and suitable bandgap energy and position, to maximize the absorption of useable photons [23].

The identification of viable photoelectrocatalysts for the HER and OER processes is a key stepping stone toward sustainable PEC H_2 production. For this reason, metal oxide photoelectrocatalysts have undergone extensive study owing to their high efficiency, stability, and cost-effectiveness. Furthermore, nanostructured metal oxides have the added benefit of increased surface area and quantum size effects, which can prove beneficial for PEC efficiency [24]. In this section, the influence of nanocatalyst morphology and electrode modification on the PEC activity and efficiency is explored.

5.3.1 Morphologies of Semiconductor Materials

State-of-the-art photoanode materials reported in the literature include TiO_2, Fe_2O_3, $BiVO_4$, and CdS, while Cu_2O and metal phosphides (M_xP_y) are typically used for photocathodes [23]. These photoelectrodes conventionally use bulk catalysts, however, nanostructured semiconductor materials have recently emerged as promising candidates to improve η_{STH} in PEC water splitting systems. Morphology,

pore structure, lattice impurity, and available redox-active sites have a central role in determining the conversion efficiency of these nanomaterials. The following section will focus on nanostructure morphology and how it affects PEC reactor performance.

The principal objective of semiconductor design is to improve charge separation and charge transport pathways, thereby enhancing HER and OER kinetics. Semiconductor morphology can be modulated by modifying the synthesis variables that control the nucleation and growth processes of the nanostructure. As a result, it is possible to optimize specific surface area, electrical conductivity, crystallinity, optical absorbance, and effective bandgap, which are bottlenecks for increasing photocurrent generation [25]. Recently, Lamers *et al.* [26] investigated the effect of annealing on $BiVO_4$ samples and reported increased crystallinity, improved charge transfer, and reduced bandgap in annealed samples. These effects facilitated an overall 50% increase under AM 1.5 illumination.

Nanomaterials have proven to be ideal candidates for rational semiconductor fabrication approaches. Recent studies have shown that semiconductor composition and nanostructure have a significant effect on photoelectrode performance, as shown in Table 5.1.

5.3.2 Photoelectrode Modification

Fast charge-recombination is a major hurdle that solar-active catalysts often face, leading to slow H_2 generation kinetics and low efficiency. The introduction of protective layers and co-catalysts has been shown to overcome this crucial drawback [34–36].

Heterostructures are obtained through doping of semiconductor materials, as a result, heterojunctions with suitable bandgaps are formed. These regions promote current flow and charge separation, supporting increased photocurrent, stability, and reaction kinetics. Promising heterostructured materials include $CuAlO_2$/$CuFeO_2$, CuO/CdS/TiO_2/Pt [37] photocathodes and In_2O_3/In_2S_3, CdS/Ti [38], $NiCo_2O_4$/TiO_2/$BiVO_4$, and $BiVO_4$/WO_3 [39] photoanodes.

Table 5.1 PEC performance of metal oxide nanostructures measured under AM 1.5G simulated solar light.

Materials	Nanostructure	Photocurrent density (mA cm^{-2}) *vs.* RHE	Electrolyte	Light source
$BiVO_4$ [27]	Microflower	5.66 at 0.9 V	0.5 M Na_2SO_4	Halogen
$BiVO_4$ [28]	Nanotextured pillar	1.95 at 0.9 V	0.5 M Na_2SO_4	Xenon
$CuWO_4$ [29]	Nanoflower	0.58 at 1.0 V	0.1 M NaH_2PO_4	Xenon
TiO_2 [30]	Nanosponge	0.06 at 0.8 V	0.1 M Na_2SO_4	Xenon
TiO_2 [31]	Nanoflower	0.75 at 0.2 V	1.0 M NaOH	Xenon
WO_3 ([32])	Nanoplate	1.00 at 1.6 V	0.5 M Na_2SO_4	Xenon
ZnO [33]	Nanowire	0.60 at 0.3 V	0.1 M NaOH	UV-LED

In the following sections, the main strategies used to modify photoelectrodes with metallic and non-metallic compounds will be explored; namely, bilayers, Z-scheme multilayers, co-catalyst doping, and surface passivation coating.

5.3.2.1 Bilayer Structure

Photoelectrodes comprised of two layers of thin-film semiconductors are referred to as bilayer set-ups. The incorporation of a secondary layer increases light-trapping capability, which results in a significant decrease in surface reflectance. Bilayers that employ both wide and narrow bandgaps exhibit directional charge transport, which leads to the formation of an internal electric field that inhibits charge recombination [40].

The bilayer arrangement has proven to increase photocurrent density significantly. For example, Kodan *et al.* [41] synthesized a $BiVO_4/MoO_3$ bilayer photoanode through radio-frequency sputtering, showing a sixfold improvement in photocurrent density compared to a bare $BiVO_4$ photoanode (0.03 to 0.22 mA cm^{-2} at 1.23 V *vs.* RHE).

The bilayer can also consist of two distinct phases of the same material. For instance, Park *et al.* [42] recently reported the fabrication of a bilayer photocathode that consists of vertical Sb_2Se_3 nanorods grown on top of a Sb_2Se_3 thin film (Figure 5.7). This configuration achieved close to 30 mA cm^{-2} at 0 V *vs.* RHE, a significant improvement compared to single Sb_2Se_3 layers that achieved 12.5 mA cm^{-2} at 0 V *vs.* RHE [43].

5.3.2.2 Z-Scheme Multilayer

Multilayer structures seek to improve the photocatalytic activity of the photoelectrode by mimicking natural photosynthetic systems. The well-known Z-scheme of

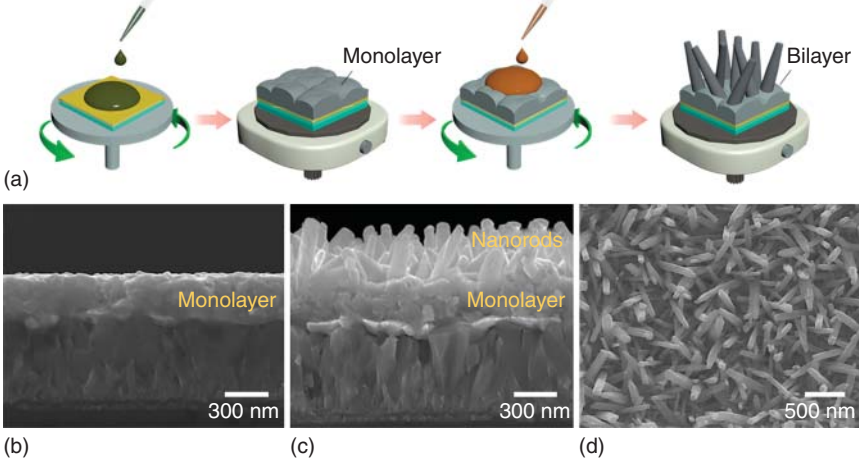

Figure 5.7 (a) Schematic diagram of fabrication procedure for Sb_2Se_3 nanorod-thin film bilayer; (b–d) SEM images depicting monolayer and bilayer electrodes, showing distinct structural separation. Source: Park et al. [42]/with permission of American Chemical Society.

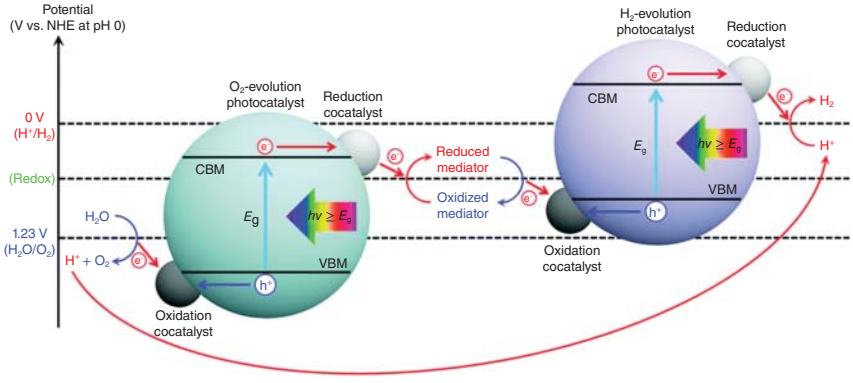

Figure 5.8 Schematic diagram illustrating the overall water splitting process in a Z-scheme pathway. CBM: conduction band minimum; VBM: valence band maximum. Source: Wang et al. [44]/with permission of Royal Society of Chemistry.

photosynthesis is characterized by two photoexcitation processes, which are coupled by electron transfer through the stepwise arrangement of energy levels (Figure 5.8). Similarly, a Z-scheme multilayer photoelectrode contains a photosystem I (PSI) and photosystem II (PSII). This multilayer approach reduces charge recombination and improves light harvesting considerably while maintaining ideal redox ability [45].

Recently, Liu *et al.* [46] reported the synthesis of a direct Z-scheme multilayer photocatalyst based on a black/red phosphorous heterojunction. The resulting photoelectrode exhibited a photocurrent density of 0.03 mA cm^{-2} at 0.1 V (*vs.* Ag/AgCl) in 0.5 M Na_2SO_4 electrolyte, more than triple the current density reached by black and red phosphorous alone under the same conditions.

The review by Wang *et al.* [47] contains an in-depth investigation of recent Z-scheme multilayer photoelectrode systems.

5.3.2.3 Co-Catalyst Layer

Recent reports have shown that the overpotential required for PEC water splitting can be decreased by incorporating a co-catalyst into the photoelectrode. The most efficient transition metal catalysts for electrochemical water splitting, namely IrO_x, CoO_x, and NiO_x, have demonstrated a notable reduction in onset potential when used as co-catalysts in a PEC system. In addition, these decorated photoelectrodes displayed considerable stability at the co-catalyst/photocatalyst interfaces [48, 49]. The enhanced PEC activity is attributed to additional reaction sites and improved charge separation. Oxidative co-catalysts can also reduce photogenerated holes from the light-harvesting semiconductor, thereby preventing photocorrosion and improving the stability of the photoelectrode.

A recent report by Fang *et al.* [50] described a $BiVO_4$ photoelectrode modified by NiFeOOH and Co-P_i co-catalysts, which featured increased charge transfer kinetics and process efficiency, when compared to a bare $BiVO_4$ photoelectrode.

The improved light-harvesting and charge separation capability of the Co-P_i photocatalyst promoted an almost six times increase in photocurrent density. Examples of photoelectrodes and their synergy with co-catalyst are presented in a review by Yang *et al.* [49], and the recent perspective on co-catalyst design by Saruyama *et al.* [51].

5.3.2.4 Surface Passivation Coating

Practical applications of PEC water splitting are hindered by the deterioration of photoelectrodes during the water oxidation process. Degradation can be avoided through the application of a thin passivation layer without a considerable impact on charge transfer. A layer as thin as 1–2 nm is sufficient to isolate the photoelectrode surface from the electrolyte and reduce photocorrosion [52]. Kim *et al.* [53] demonstrated that the lifespan and stability of a $BiVO_4$ photoelectrode can be increased significantly through the use of a TiO_2/ZnO passivation layer, resulting in more than two times higher current densities than bare $BiVO_4$. The role of passivation layers in photoelectrodes is discussed in detail by Liu *et al.* [52].

Examples of modified photoelectrodes using the abovementioned strategies are presented in Table 5.2 with their reported performance.

Table 5.2 Examples of heterostructured photoelectrodes for H_2 generation.

Material	Category and synthesis method	Photocurrent density (mA cm^{-2}) *vs.* RHE	Electrolyte	ηSTH (%)
$BiVO_4$/Fe_2O_3 [55]	Bilayer via metal–organic deposition	7.00 at 1.23 V	1.0 M $KHCO_3$	7.7
$BiVO_4$/Fe_2O_3 [56]	Bilayer via spin coating	1.63 at 1.23 V	0.1 M KH_2PO_4	—
In_2O_3/Bi_2WO_6 [57]	Bilayer via electrospray	1.03 at 0.90 V	1.0 M KOH	—
TiO_2/CdS/CdSe [58]	Tandem DSSC via electrodeposition	6.00 at 1.23 V	0.35 M Na_2SO_3 and 0.24 M Na_2S	2.1
Cu_2O/CdS/ZnO [59]	Heterojunction co-catalyst via electrodeposition	7.00 at 0.60 V	0.25 M Na_2SO_3 and 0.35 M Na_2S	2.8
TiO_2/Al_2O_3[60]	Surface coating via atomic layer deposition	0.90 at 0.70 V	1.0 M KOH	—
Fe_2O_3/IrO_x [61]	Surface coating via particle assisted deposition	3.00 at 1.23 V	1.0 M NaOH	—
ZnO/Au/Cu_2O [62]	Z-scheme system via hydrothermal procedure	0.206 at 0.45 V	0.5 M Na_2SO_4	—

5.4 Photoelectrochemical Reactor Configurations

Optimizing the design of PEC reactors is key to maximizing photon absorption per unit volume of the reactor, mitigating corrosion, and isolating products that might undergo reverse reactions. For solar-driven water splitting, a membrane is used to separate the H_2 and O_2 produced, and to prevent the crossover of ions between electrodes, which would lower overall process efficiency.

The spacing of the PEC reactor assembly must also be considered to reduce ionic potential losses in the electrolyte and achieve uniform potential and current distributions. Therefore, the inter-electrode distance and the gas separator-electrode spacing must be minimized.

In this section, the main classifications of PEC reactor configurations, namely, single- and tandem-photoelectrode cells, and dye-sensitized semiconductor cells (DSSCs), will be discussed. Figure 5.9 shows the relationship of these classifications to the overall field of PEC H_2 generation. A recent review by Ahmed and Dincer [63] provides a comprehensive discussion of reactor configurations.

5.4.1 Single Photoelectrochemical Cells

PEC reactors built with only one photoactive electrode, a photoanode or photocathode, are known as single PEC cells. A non-photoactive metallic counter electrode, generally made from platinum, is used to complete the cell (Figure 5.10a).

Single photoelectrode cells require the application of extra voltage, or bias, to drive the electrolysis process. In the case of wide-gap semiconductors, the introduction of a bias helps reduce electron–hole recombination. The added bias can be applied either externally as an electrical, chemical, or photovoltaic (PV) bias, or alternatively applied internally using a PEC-PV system [63].

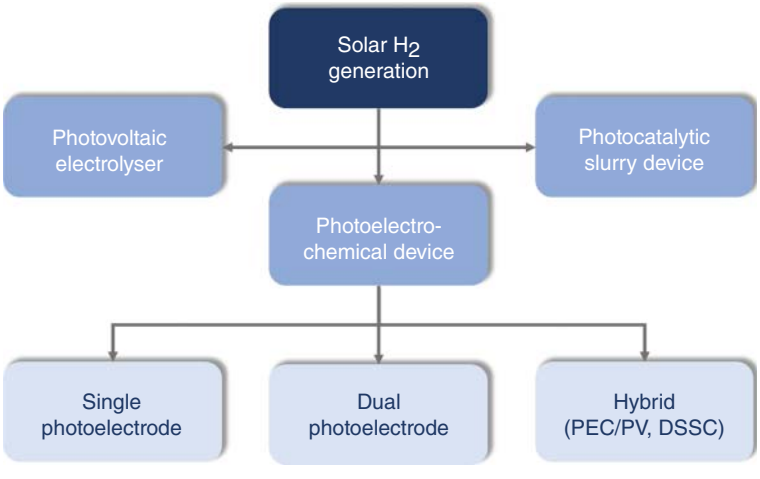

Figure 5.9 Main classification of PEC reactors within the larger family of PEC H_2 generation cells. Source: Ahmed and Dincer [63]/with permission of Elsevier.

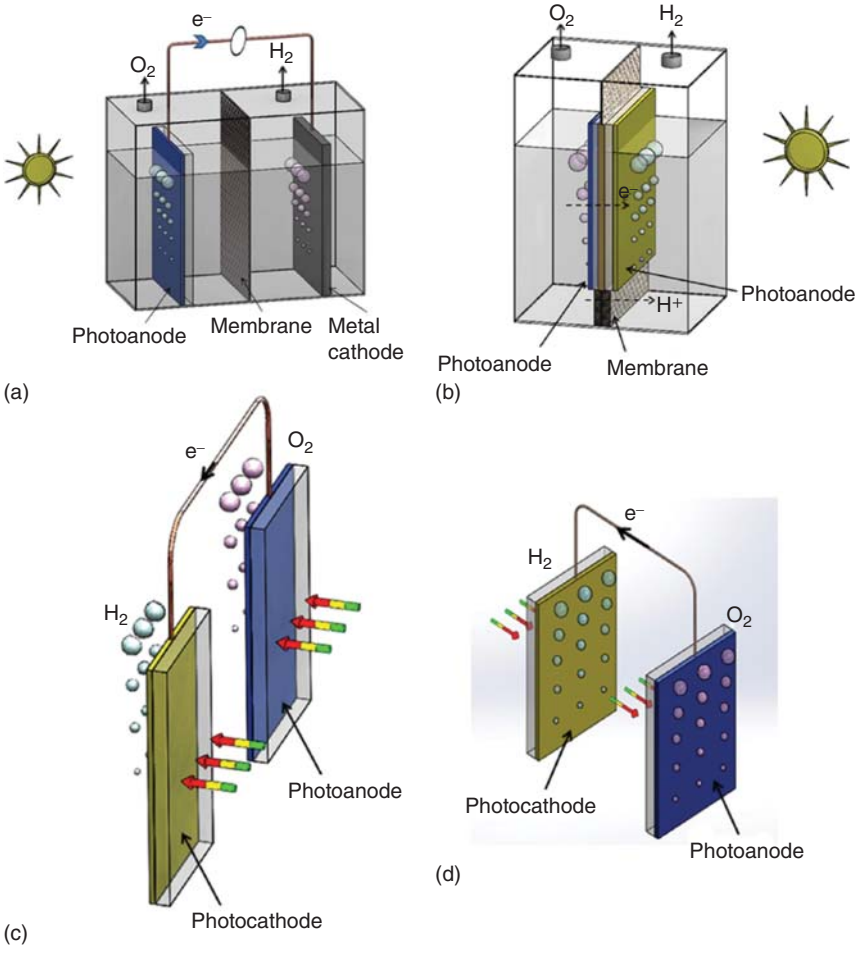

Figure 5.10 (a) Single photoelectrode cell. (b) Monolithic tandem photoelectrode cell. (c) Parallel tandem configuration. (d) Overlapping tandem configuration. Source: Ahmed and Dincer [63]/with permission of Elsevier.

Light absorption and photocurrent density in single PEC cells can be enhanced by utilizing several layers of semiconductors on the photoelectrode, however, an applied voltage is still necessary to drive the water splitting reaction.

5.4.2 Tandem Photoelectrochemical Cells

An approach to confer increased light absorption range and enhanced η_{STH} to the system is the incorporation of both high and low bandgap semiconductors. Since both electrodes in the cell are photoactive, this configuration is usually described as a dual or tandem PEC cell. In such a photocell, both photoelectrodes contribute a portion of the necessary voltage for water splitting [64].

The photocathode and photoanode can either be physically separated in a wired arrangement or merged into a monolithic cell (Figure 5.10b). In contrast to the metallic connections generally used in wired arrangements, monolithic assemblies use transparent conductive metal oxides to maintain maximum solar irradiation and achieve a solid ohmic contact between the semiconductors. The alignment of semiconductors in the tandem arrangement is crucial for maximizing light exposure for both photoelectrodes simultaneously, which is achieved by positioning them parallel or overlapping (Figure 5.10c,d). In an overlapping configuration, it is imperative to ensure that the wide bandgap semiconductor is positioned closer to the light source, so that the lower energy photons that pass through it can be absorbed by the low bandgap absorber [65].

Yin *et al.* [66] described an integrated PEC tandem cell without external bias using a FeOOH modified $TiO_2/BiVO_4$ photoanode and a *p*-Cu_2O photocathode. This system achieved a photoconversion efficiency of 0.46% and H_2 evolution of 2.36 μmol cm^{-2} over 2.5 hours. Further investigation of tandem cells can be found in a recent review by Chen *et al.* [67].

5.4.3 PEC-DSSC Systems

A molecular dye can be incorporated into a semiconductor to enhance the light-harvesting capabilities of the cell, creating a PEC dye sensitised semiconductor cell (PEC-DSSC). In a synergistic setup, the dye can be linked to a water oxidation co-catalyst, allowing the oxidized dye to be regenerated by an electron source, water (Figure 5.11). Although great strides have been made to enhance DSSC activity in this manner, there are still improvements to be made to enhance η_{STH}. An external

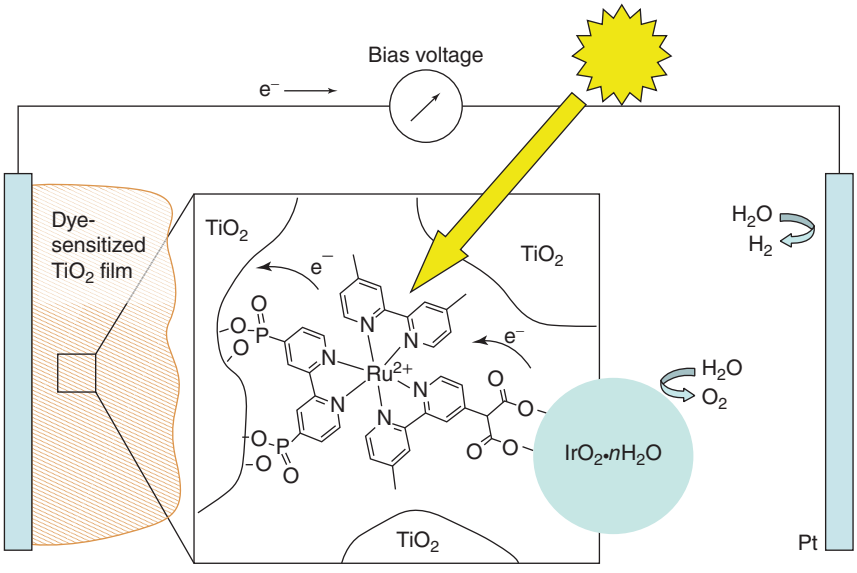

Figure 5.11 Schematic diagram of a PEC-DSSC system for the PEC water splitting process. Source: Youngblood et al. [68]/with permission of American Chemical Society.

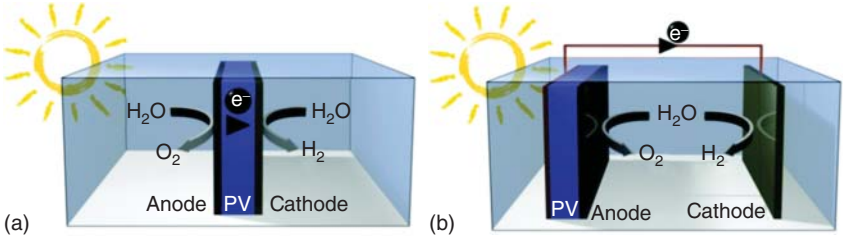

Figure 5.12 Schematic illustrations of integrated (a) and partially-integrated (b) PEC-PV systems. Source: Bonke et al. [73]/with permission of Royal Society of Chemistry.

bias is often still required, as the PV power generated by DSSCs is insufficient for the complete water splitting process [69], however, there are reports of unassisted PEC-DSSC systems [70]. Furthermore, PEC-DSSCs possess a promising advantage; they perform well under low-light settings, which makes them suitable for indoor or low-intensity conditions, as has been observed for pure DSSC systems.

Initial lab-scale prototypes of PEC-DSSCs involving simple one-step excitation systems such as the $Ru(bpy)_3^{2+}$ sensitized Pt, TiO_2, and RuO_2 were reported by Borgarello *et al.* [54, 71]. Recently, more complex designs involving ion shuttles in Z-scheme systems have also emerged, as described by Prabavathy *et al.* [72].

5.4.4 Integrated PEC Systems

A PV unit may be incorporated into a PEC water splitting device to create an integrated PEC-PV (IPEC) system (Figure 5.12). PV units absorb light and convert it into electrical bias, which can drive the PEC water splitting reaction, facilitating unassisted solar H_2 generation.

Hybrid PEC-PV systems offer some of the highest reported η_{STH} values, which have already fulfilled industrial H_2 production requirements [74]. Bonke *et al.* reported an integrated GaInP/GaAs/Ge cell with Ni electrodes achieved a η_{STH} of 22.4% [73]. Despite these achievements, H_2 production *via* petrochemical routes still remains economically more viable, as solar cells are complex and expensive to fabricate. As such, research attention in this field has focused on using earth-abundant materials, improving device stability, and increasing overall efficiency in order to overcome these economic barriers [75]. The advantages of integrated PEC devices have been explored by Modestino and Haussener in their 2015 review [75]. In addition, a report comparing pure PEC solar H_2 devices to integrated PEC systems was published by Wang *et al.* [76].

5.5 Design Considerations for Water Splitting

In order to make PEC water splitting economically feasible on a commercial and industrial scale, robust and efficient photoelectrodes with high photocurrent densities are desired. As a consequence, PEC cells should present low overpotentials while maximizing light absorption and maintaining minimal fabrication costs. Design considerations should rely on synergies found in related technologies such

as high- and low- temperature fuel cells, electrolyzers, PVs, microfluidic systems, or electrochemical industrial processes.

PEC systems are governed by more complex physical and chemical challenges than many other systems, such as purely photocatalytic devices, since they incorporate both photophysical and electrochemical processes working in tandem. In regards to electrochemistry, the ionic path length and the electrolyte conductivity within the system can be limiting factors, which necessitate rational design and optimization. For PEC device scale-up, one should also account for heat transfer due to radiation absorption; charge generation, separation, and transport; and the coupled mass transport of ions and products [77].

Pilot projects for emerging technologies such as PEC hydrogen generation should follow carefully laid out strategies to maximize their success rate. Figure 5.13 shows a hierarchical design structure for a PEC device, starting from the selection of materials for the device and finalizing with a scaled-up prototype.

The influence of materials, operating conditions, and device design should dictate the requirement for modeling frameworks and experimentation. The following section discusses the main factors that should be taken into account when designing PEC water splitting systems.

5.5.1 Theoretical Studies and Models

A PEC water splitting system involves a myriad of interconnected processes, such as light absorption, charge transport, interfacial interactions, OER, and HER

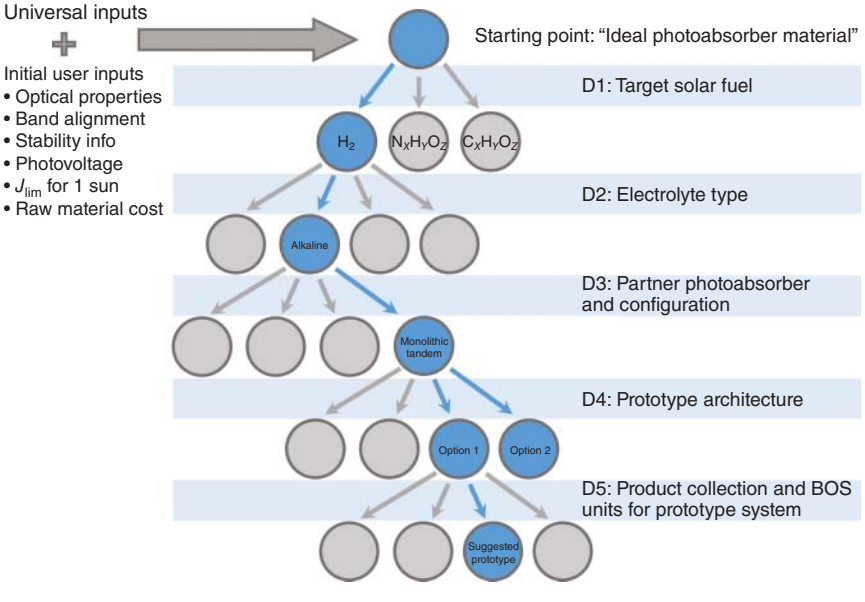

Figure 5.13 Example of a decision tree for the design of a PEC device for solar fuels production that starts its flow through decision points "D" with a novel photoabsorbing semiconductor and concludes with a prototype design. Source: Spitler et al. [77]/with permission of Royal Society of Chemistry.

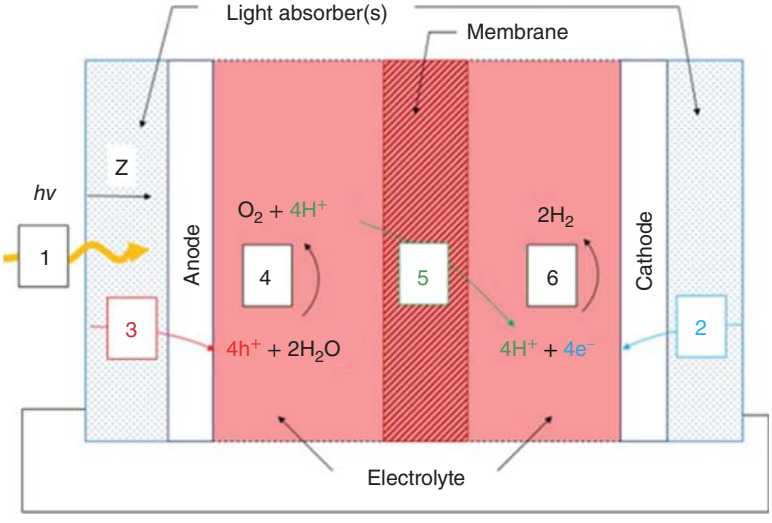

Figure 5.14 A representation of a PEC cell showing the processes involved in PEC water splitting. (1) Light absorption, (2,3) electron and hole transport, (4) OER, (5) proton transport, and (6) HER. Source: Berger and Newman [78]/with permission of IOP Publishing.

(Figure 5.14). Numerical and theoretical modeling of PEC systems can provide valuable insight into these processes, which would otherwise be unobtainable through experimental methods.

Many PEC models focus on specific relationships or phenomena. For instance, Haussener *et al.* proposed a numerical model concentrating on transport-related potential losses and product losses due to crossover and recombination events [79]. Meanwhile, physical models of charge transport have allowed for the numerical determination of band structures of PEC semiconductors in contact with the electrolyte [80].

More generalized studies have also emerged, which aim to account for all the aforementioned processes and their relationships and build a fully integrated model. Berger and Newman described a framework consisting of one-dimensional models for the light absorber and electrolyte. The light absorber and electrolyte can be coupled together through a charge transfer model to study the complete PEC water splitting system [78].

The rational design of photoelectrodes and PEC device components can be assisted by computational techniques and device modeling, which can be used to validate experimental results and provide predictive insights into device functionalization and performance. Different computational approaches may be used in conjunction to create a strong multiscale approach [81]. For an in-depth discussion of the theoretical modeling of PEC water splitting systems, and how it can guide device design, refer to the reviews by Xiang *et al.* [82] and Kemppainen *et al.* [83].

5.5.2 Temperature Effects

During the water electrolysis process in a parallel flow configuration, the temperature of the reactants and products fluctuates when traveling through the device, reaching its maximal temperature at the exit. Changes in ion conductivity cause thermal gradients across the device, which produce thermal stress and lead to the degradation and eventual failure of the cell.

Computational fluid dynamics can be used to investigate the thermomechanical behavior of the cell by computing the temperature gradient produced across the device. Results show that a maximum H_2 production rate of 65.25 mmol m^{-2} s^{-1} can be reached at a solar concentration of 170 suns, and a maximum η_{STH} of 9.24% at 150 suns. Figure 5.15 shows the H_2 flow rate and η_{STH} *vs.* solar concentration as described in the model. At high solar concentrations the model did not converge, which was associated with low photovoltage [84].

The operating temperature of PEC devices can have profound effects on operating voltage, production, and efficiency. At temperatures above 700 °C, the electrochemical equilibrium potential is reduced, and the efficiency of earth-abundant catalysts is drastically increased. Gutierrez and Haussener presented a nickel/yttria-stabilized-zirconia (Ni/YSZ) catalyst, which shows enhanced H_2 production at high temperatures. Further information and design guidelines for high-temperature PEC systems can also be found in this recent publication [84].

5.5.3 Semiconductor Features

Many challenges remain in the way of improving the η_{STH} of PEC water splitting devices, such as spectral responsive regions, recombination reactions, and low H_2 production under operating conditions. Recently, researchers have demonstrated

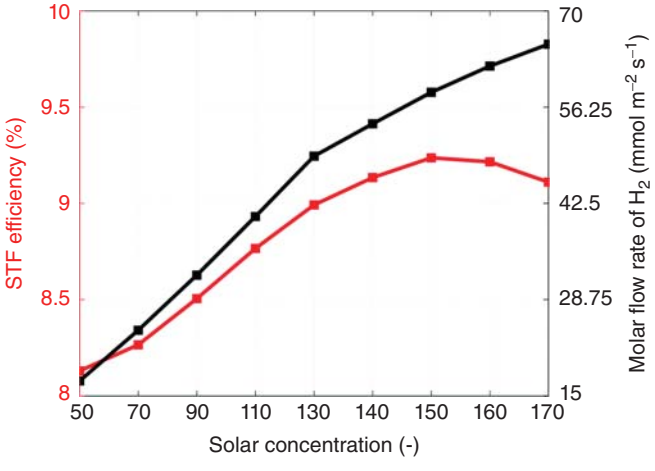

Figure 5.15 η_{STH} and molar H_2 flow rate at different levels of irradiation. Source: Gutierrez et al. [84]/with permission of Royal Society of Chemistry.

that tandem photoelectrode PEC systems are the most promising solution for achieving zero bias and decoupling PEC H_2 generation from conventional energy sources. However, the use of both photoanodes and photocathodes tailored for absorption in the visible spectrum and maximal η_{STH} entails the development of effective semiconductor materials [67].

- Strategies should be developed to extend the photoabsorption region of semiconductors to produce efficient, low-cost, stable, and light-responsive materials. Current candidates face obstacles including bandgap mismatch, low absorption coefficients, poor electrical conductivity, short charge carrier lifetime, and unsuitable diffusion length, which severely limit their performance. Surface engineering techniques such as adjusting the carrier diffusion distance toward the electrolyte could help overcome these limitations [23].
- The aqueous electrolyte required for PEC devices poses significant issues in the form of desorption, oxidation, and breakdown during photocatalytic reactions, which impact the stability of the electrodes. Molecules anchored onto semiconductors using passivation layers or multilayer composites can alleviate these problems [52, 85]. Physical separation between the semiconductor and the oxidized molecules, achieved through appropriate design based on dynamic equilibrium, could also serve as a viable solution to enhance device stability [86].

Material-based research in semiconductor photoelectrodes has taken various approaches:

- Investigation of non-abundant, high-efficiency materials aiming to set performance benchmarks and gain fundamental knowledge of PEC H_2 generation and device photocorrosion issues.
- Incorporation of earth-abundant materials as semiconductors to increase the cost-effectiveness of PEC devices.
- Utilization of co-catalysts to improve the light absorption capability of semiconductors and enhance reaction kinetics.
- Development of passivation layers or robust protective coatings to prevent photocorrosion and increase photoelectrode stability.

Several recent reviews have explored the utility and challenges related to these approaches [19, 23, 25].

5.5.4 Technical Challenges

Beyond system efficiency, technical challenges such as water supply and economic viability also stand in the way of industrial-scale utilization of PEC technologies. Several approaches have emerged to bypass these obstacles:

- Supplying water to PEC water splitting devices can pose a significant challenge in dry, hot areas that are the most ideal for light absorption. The use of water vapor directly from the air has been investigated as an alternative supply route to circumvent this concern [87, 88].

- PEC devices designed to generate H_2 directly from waste and brackish water pose a valuable opportunity regarding waste management and recycling. However, a greater understanding of the transport, thermodynamics, electrochemistry, system integration, and performance of these systems is required to produce economically viable versions of these PEC devices [89, 90]. In addition, the effects of impurities on the electrolyte are poorly understood and can lead to unexpected product formation, corrosion, and other side effects, decreasing the performance of the PEC.
- Organic oxidation and photoreforming are interesting alternative approaches to conventional water splitting that aim to increase the economic viability of PEC systems. In these approaches, the anodic potential is utilized to produce value-added products rather than O_2, while simultaneously producing H_2 at the cathode [91, 92]. This can become a very interesting approach if reaction selectivity is achieved, otherwise it is not possible to obtain value-added products.

5.6 Conclusion

The production of sustainable H_2 through PEC water splitting has garnered significant research interest in recent years. However, before this technology can reach industry standards, low η_{STH}, high operational expenses, and stability issues should be solved.

Researchers have employed various strategies to overcome these challenges. The optimization of semiconductor photoelectrodes through multilayer architectures, co-catalysts, and passivation coatings is an attractive approach. Furthermore, various PEC reactor configurations have emerged as candidates to bypass voltage limitations. In particular, integrated PEC-PV systems and unassisted tandem PEC cells show promise thanks to their high H_2 production rates and η_{STH}.

Several design considerations should be accounted for during the development of new prototype PEC technologies. Operating temperatures, semiconductor photoelectrode composition, and water supply are among the primary factors for economic viability and scale-up. These considerations can be guided by theoretical modeling and computational techniques.

PEC water splitting is gradually becoming a viable technology for the production of hydrogen. There are already commercial ventures that are starting to produce market-ready products, in particular for off-grid locations where hydrogen can be used as a feedstock for heating or cooking. We envisage that in the coming years, more PEC reactors will be available with improvements in the device components.

References

1 Züttel, A., (2008). Introduction, in: *Hydrogen as a Future Energy Carrier*. Wiley pp. 1–6. A. Züttel, A. Borgschulte and L. Schlapbachhttps://doi.org/10.1002/9783527622894.ch1

2 Fujishima, A. and Honda, K. (1971). Electrochemical evidence for the mechanism of the primary stage of photosynthesis. *Bull. Chem. Soc. Jpn.* 44: 1148–1150.

3 Li, Z., Luo, W., Zhang, M. et al. (2013). Photoelectrochemical cells for solar hydrogen production: current state of promising photoelectrodes, methods to improve their properties, and outlook. *Energy Environ. Sci.* 6: 347–370. https://doi.org/10.1039/C2EE22618A.

4 Kalanur, S.S., Duy, L.T., and Seo, H. (2018). Recent progress in photoelectrochemical water splitting activity of WO_3 photoanodes. *Top. Catal.* 61: 1043–1076. https://doi.org/10.1007/s11244-018-0950-1.

5 Marschall, R. (2021, 2021). 50 years of materials research for photocatalytic water splitting. *Eur. J. Inorg. Chem.* 2435–2441. https://doi.org/10.1002/ejic.202100264.

6 Hemmerling, J., Quinn, J., and Linic, S. (2020). Quantifying losses and assessing the photovoltage limits in metal–insulator–semiconductor water splitting systems. *Adv. Energy Mater.* 10: 1903354. https://doi.org/10.1002/aenm.201903354.

7 Kim, J.H., Hansora, D., Sharma, P. et al. (2019). Toward practical solar hydrogen production–an artificial photosynthetic leaf-to-farm challenge. *Chem. Soc. Rev.* 48: 1908–1971.

8 Liao, C.-H., Huang, C.-W., and Wu, J.C.S. (2012). Hydrogen production from semiconductor-based photocatalysis via water splitting. *Catalysts* 2: 490–516. https://doi.org/10.3390/catal2040490.

9 Varadhan, P., Fu, H.-C., Kao, Y.-C. et al. (2019). An efficient and stable photoelectrochemical system with 9% solar-to-hydrogen conversion efficiency via InGaP/GaAs double junction. *Nat. Commun.* 10: 5282. https://doi.org/10.1038/s41467-019-12977-x.

10 Dotan, H., Mathews, N., Hisatomi, T. et al. (2014). On the solar to hydrogen conversion efficiency of photoelectrodes for water splitting. *J. Phys. Chem. Lett.* 5 (19): 3330–3334.

11 Hu, Y., Chen, F., Ding, P. et al. (2018). Designing effective Si/Ag interface via controlled chemical etching for photoelectrochemical CO_2 reduction. *J. Mater. Chem. A* 6: 21906–21912.

12 Guo, M., Wang, L., Zhan, J. et al. (2020). A novel design of an electrolyser using a trifunctional (HER/OER/ORR) electrocatalyst for decoupled H_2/O_2 generation and solar to hydrogen conversion. *J. Mater. Chem. A* 8: 16609–16615.

13 Tembhurne, S., Nandjou, F., and Haussener, S. (2019). A thermally synergistic photo-electrochemical hydrogen generator operating under concentrated solar irradiation. *Nat. Energy* 4: 399–407. https://doi.org/10.1038/s41560-019-0373-7.

14 Ikram, A., Sahai, S., Rai, S. et al. (2016). Improved charge transportation at PbS QDs/TiO_2 interface for efficient PEC hydrogen generation. *Phys. Chem. Chem. Phys.* 18: 15815–15821. https://doi.org/10.1039/C6CP00854B.

15 Barawi, M., Ferrer, I.J., Ares, J.R., and Sánchez, C. (2014). Hydrogen evolution using palladium sulfide (PdS) nanocorals as photoanodes in aqueous solution. *ACS Appl. Mater. Interfaces* 6: 20544–20549. https://doi.org/10.1021/am5061504.

16 Ellis, D.S., Piekner, Y., Grave, D.A. et al. (2022). Considerations for the accurate measurement of incident photon to current efficiency in photoelectrochemical cells. *Front. Energy Res.* 9: 726069. https://doi.org/10.3389/fenrg.2021.726069

17 Chen, Z., Jaramillo, T.F., Deutsch, T.G. et al. (2010). Accelerating materials development for photoelectrochemical hydrogen production: standards for methods, definitions, and reporting protocols. *J. Mater. Res.* 25: 3–16.

18 Olascoaga, B., Mac Arthur, A., Atherton, J., and Porcar-Castell, A. (2016). A comparison of methods to estimate photosynthetic light absorption in leaves with contrasting morphology. *Tree Physiol.* 36: 368–379. https://doi.org/10.1093/treephys/tpv133.

19 Moss, B., Babacan, O., Kafizas, A., and Hankin, A. (2021). A review of inorganic photoelectrode developments and reactor scale-up challenges for solar hydrogen production. *Adv. Energy Mater.* 11: 2003286.

20 Xing, Z., Zong, X., Pan, J., and Wang, L. (2013). On the engineering part of solar hydrogen production from water splitting: photoreactor design. *Chem. Eng. Sci.* 104: 125–146.

21 Huang, C., Yao, W., Raissi, A.T., and Muradov, N. (2011). Development of efficient photoreactors for solar hydrogen production. *Sol. Energy* 85: 19–27. https://doi.org/10.1016/j.solener.2010.11.004.

22 Bosserez, T., Rongé, J., van Humbeeck, J. et al. (2015). Design of compact photoelectrochemical cells for water splitting. *Oil Gas Sci. Technol. – Rev. IFP Energies nouvelles* 70: 877–889.

23 Jiang, C., Moniz, S.J.A., Wang, A. et al. (2017). Photoelectrochemical devices for solar water splitting–materials and challenges. *Chem. Soc. Rev.* 46: 4645–4660.

24 Osterloh, F.E. (2013). Inorganic nanostructures for photoelectrochemical and photocatalytic water splitting. *Chem. Soc. Rev.* 42: 2294–2320. https://doi.org/10.1039/C2CS35266D.

25 Thakur, A., Ghosh, D., Devi, P. et al. (2020). Current progress and challenges in photoelectrode materials for the production of hydrogen. *Chem. Eng. J.* 397: 125415. https://doi.org/10.1016/j.cej.2020.125415.

26 Lamers, M., Fiechter, S., Friedrich, D. et al. (2018). Formation and suppression of defects during heat treatment of $BiVO_4$ photoanodes for solar water splitting. *J. Mater. Chem. A* 6: 18694–18700.

27 Samsudin, M.F.R., Bashiri, R., Mohamed, N.M. et al. (2020). Tailoring the morphological structure of $BiVO_4$ photocatalyst for enhanced photoelectrochemical solar hydrogen production from natural lake water. *Appl. Surf. Sci.* 504: 144417.

28 Yoon, H., Mali, M.G., Choi, J.Y. et al. (2015). Nanotextured pillars of electrosprayed bismuth vanadate for efficient photoelectrochemical water splitting. *Langmuir* 31: 3727–3737.

29 Zhou, M., Liu, Z., Li, X., and Liu, Z. (2018). Promising three-dimensional flowerlike $CuWO_4$ photoanode modified with CdS and FeOOH for efficient photoelectrochemical water splitting. *Ind. Eng. Chem. Res.* 57: 6210–6217.

30 Sánchez-Tovar, R., Fernández-Domene, R.M., García-García, D.M., and Garcia-Anton, J. (2015). Enhancement of photoelectrochemical activity for

water splitting by controlling hydrodynamic conditions on titanium anodization. *J. Power Sources* 286: 224–231.

31 Dong, W., Li, H., Xi, J. et al. (2017). Reduced TiO_2 nanoflower structured photoanodes for superior photoelectrochemical water splitting. *J. Alloys Compd.* 724: 280–286.

32 Zhou, J., Lin, S., Chen, Y., and Gaskov, A.M. (2017). Facile morphology control of WO_3 nanostructure arrays with enhanced photoelectrochemical performance. *Appl. Surf. Sci.* 403: 274–281.

33 Govatsi, K., Seferlis, A., Neophytides, S.G., and Yannopoulos, S.N. (2018). Influence of the morphology of ZnO nanowires on the photoelectrochemical water splitting efficiency. *Int. J. Hydrogen Energy* 43: 4866–4879.

34 Bhat, S.S.M., Lee, S.A., Lee, T.H. et al. (2020). All-solution-processed $BiVO_4$/TiO_2 photoanode with $NiCo_2O_4$ nanofiber cocatalyst for enhanced solar water oxidation. *ACS Appl. Energy Mater.* 3: 5646–5656.

35 Huang, M., Huang, Z., and Zhu, H. (2020). Excellent stability of molecular catalyst/$BiVO_4$ photoanode in borate buffer solution. *Nano Energy* 70: 104487.

36 Ye, W., Chen, F., Zhao, F. et al. (2016). $CuWO_4$ nanoflake array-based single-junction and heterojunction photoanodes for photoelectrochemical water oxidation. *ACS Appl. Mater. Interfaces* 8: 9211–9217.

37 Li, C., He, J., Xiao, Y. et al. (2020). Earth-abundant Cu-based metal oxide photocathodes for photoelectrochemical water splitting. *Energy Environ. Sci.* 13: 3269–3306. https://doi.org/10.1039/D0EE02397C.

38 Li, S., Xu, W., Meng, L. et al. (2022). Recent progress on semiconductor heterojunction-based photoanodes for photoelectrochemical water splitting. *Small Sci.* 2100112. https://doi.org/10.1002/smsc.202100112.

39 Yang, J.W., Ahn, S.H., and Jang, H.W. (2021). Crucial role of heterostructures in highly advanced water splitting photoelectrodes. *Curr. Opin. Green Sustainable Chem.* 29: 100454.

40 Choudhary, S., Upadhyay, S., Kumar, P. et al. (2012). Nanostructured bilayered thin films in photoelectrochemical water splitting–a review. *Int. J. Hydrogen Energy* 37: 18713–18730.

41 Kodan, N., Ahmad, M., and Mehta, B.R. (2021). Charge carrier separation and enhanced PEC properties of $BiVO_4$ based heterojunctions having ultrathin overlayers. *Int. J. Hydrogen Energy* 46: 189–196.

42 Park, J., Yang, W., Tan, J. et al. (2020). Hierarchal nanorod-derived bilayer strategy to enhance the photocurrent density of Sb_2Se_3 photocathodes for photoelectrochemical water splitting. *ACS Energy Lett.* 5: 136–145. https://doi.org/10.1021/acsenergylett.9b02486.

43 Yang, W., Ahn, J., Oh, Y. et al. (2018). Adjusting the anisotropy of 1D Sb_2Se_3 nanostructures for highly efficient photoelectrochemical water splitting. *Adv. Energy Mater.* 8: 1702888. https://doi.org/10.1002/aenm.201702888.

44 Wang, Z., Li, C., and Domen, K. (2019). Recent developments in heterogeneous photocatalysts for solar-driven overall water splitting. *Chem. Soc. Rev.* 48: 2109–2125. https://doi.org/10.1039/C8CS00542G.

45 Xia, X., Song, M., Wang, H. et al. (2019). Latest progress in constructing solid-state Z scheme photocatalysts for water splitting. *Nanoscale* 11: 11071–11082.

46 Liu, F., Shi, R., Wang, Z. et al. (2019). Direct Z-scheme hetero-phase junction of black/red phosphorus for photocatalytic water splitting. *Angew. Chem.* 131: 11917–11921.

47 Wang, Y., Suzuki, H., Xie, J. et al. (2018). Mimicking natural photosynthesis: solar to renewable H_2 fuel synthesis by Z-scheme water splitting systems. *Chem. Rev.* 118: 5201–5241.

48 Jian, J., Kumar, R., and Sun, J. (2020). Cu_2O/ZnO p–n junction decorated with NiO_x as a protective layer and cocatalyst for enhanced photoelectrochemical water splitting. *ACS Appl. Energy Mater.* 3: 10408–10414. https://doi.org/10.1021/acsaem.0c01198.

49 Yang, J., Wang, D., Han, H., and Li, C.A.N. (2013). Roles of cocatalysts in photocatalysis and photoelectrocatalysis. *Acc. Chem. Res.* 46: 1900–1909.

50 Fang, G., Liu, Z., and Han, C. (2020). Enhancing the PEC water splitting performance of $BiVO_4$ co-modifying with NiFeOOH and Co-Pi double layer cocatalysts. *Appl. Surf. Sci.* 515: 146095.

51 Saruyama, M., Pelicano, C.M., and Teranishi, T. (2022). Bridging electrocatalyst and cocatalyst studies for solar hydrogen production via water splitting. *Chem. Sci.* 13: 2824–2840. https://doi.org/10.1039/D1SC06015E.

52 Liu, R., Zheng, Z., Spurgeon, J., and Yang, X. (2014). Enhanced photoelectrochemical water-splitting performance of semiconductors by surface passivation layers. *Energy Environ. Sci.* 7: 2504–2517.

53 Kim, M.-W., Kim, K., Ohm, T.Y. et al. (2018). Electrosprayed $BiVO_4$ nanopillars coated with atomic-layer-deposited ZnO/TiO_2 as highly efficient photoanodes for solar water splitting. *Chem. Eng. J.* 333: 721–729.

54 Zhang, X., Peng, T., and Song, S. (2016). Recent advances in dye-sensitized semiconductor systems for photocatalytic hydrogen production. *J. Mater. Chem. A* 4: 2365–2402.

55 Kim, J.H., Jang, J.-W., Jo, Y.H. et al. (2016). Hetero-type dual photoanodes for unbiased solar water splitting with extended light harvesting. *Nat. Commun.* 7: 1–9.

56 Xia, L., Bai, J., Li, J. et al. (2017). High-performance $BiVO_4$ photoanodes cocatalyzed with an ultrathin α-Fe_2O_3 layer for photoelectrochemical application. *Appl. Catal. B: Environ.* 204: 127–133.

57 Joshi, B., Yoon, H., Kim, H. et al. (2015). Heterojunction photoanodes for solar water splitting using chemical-bath-deposited In_2O_3 micro-cubes and electro-sprayed Bi_2WO_6 textured nanopillars. *RSC Adv.* 5: 85323–85328.

58 Shin, K. and Park, J.H. (2015). Highly transparent dual-sensitized titanium dioxide nanotube arrays for spontaneous solar water splitting tandem configuration. *ACS Appl. Mater. Interfaces* 7: 18429–18434.

59 Chen, N., Hu, Y., Liu, X. et al. (2020). A dual-heterojunction Cu_2O/CdS/ZnO nanotube array photoanode for highly efficient photoelectrochemical

solar-driven hydrogen production with 2.8% efficiency. *J. Phys. Chem. C* 124: 21968–21977.

60 Gui, Q., Xu, Z., Zhang, H. et al. (2014). Enhanced photoelectrochemical water splitting performance of anodic TiO_2 nanotube arrays by surface passivation. *ACS Appl. Mater. Interfaces* 6: 17053–17058. https://doi.org/10.1021/am504662w.

61 Tilley, S.D., Cornuz, M., Sivula, K., and Grätzel, M. (2010). Light-induced water splitting with hematite: improved nanostructure and iridium oxide catalysis. *Angew. Chem. Int. Ed.* 49: 6405–6408. https://doi.org/10.1002/anie.201003110.

62 Yoon, J.-S., Lee, J.-W., and Sung, Y.-M. (2019). Enhanced photoelectrochemical properties of Z-scheme ZnO/p-n Cu_2O PV-PEC cells. *J. Alloys Compd.* 771: 869–876. https://doi.org/10.1016/j.jallcom.2018.09.021.

63 Ahmed, M. and Dincer, I. (2019). A review on photoelectrochemical hydrogen production systems: challenges and future directions. *Int. J. Hydrogen Energy* 44: 2474–2507.

64 Meng, F., Li, J., Cushing, S.K. et al. (2013). Solar hydrogen generation by nanoscale *p–n* junction of *p*-type molybdenum disulfide/*n*-type nitrogen-doped reduced graphene oxide. *J. Am. Chem. Soc.* 135: 10286–10289.

65 Bolink, H.J. (2018). Tandems in the thick of it. *Nat. Energy* 3: 1027–1028. https://doi.org/10.1038/s41560-018-0297-7.

66 Yin, X., Liu, Q., Yang, Y. et al. (2019). An efficient tandem photoelectrochemical cell composed of $FeOOH/TiO_2/BiVO_4$ and Cu_2O for self-driven solar water splitting. *Int. J. Hydrogen Energy* 44: 594–604.

67 Chen, Q., Fan, G., Fu, H. et al. (2018). Tandem photoelectrochemical cells for solar water splitting. *Adv. Phys.* 3: 1487267. https://doi.org/10.1080/23746149.2018.1487267.

68 Youngblood, W.J., Lee, S.-H.A., Kobayashi, Y. et al. (2009). Photoassisted overall water splitting in a visible light-absorbing dye-sensitized photoelectrochemical cell. *J. Am. Chem. Soc.* 131: 926–927. https://doi.org/10.1021/ja809108y.

69 Swierk, J.R. and Mallouk, T.E. (2013). Design and development of photoanodes for water-splitting dye-sensitized photoelectrochemical cells. *Chem. Soc. Rev.* 42: 2357–2387.

70 Shi, X., Jeong, H., Oh, S.J. et al. (2016). Unassisted photoelectrochemical water splitting exceeding 7% solar-to-hydrogen conversion efficiency using photon recycling. *Nat. Commun.* 7: 11943. https://doi.org/10.1038/ncomms11943.

71 Borgarello, E., Kiwi, J., Pelizzetti, E. et al. (1981). Photochemical cleavage of water by photocatalysis. *Nature* 289: 158–160.

72 Prabavathy, N., Shalini, S., Balasundaraprabhu, R. et al. (2017). Enhancement in the photostability of natural dyes for dye-sensitized solar cell (DSSC) applications: a review. *Int. J. Energy Res.* 41: 1372–1396.

73 Bonke, S.A., Wiechen, M., MacFarlane, D.R., and Spiccia, L. (2015). Renewable fuels from concentrated solar power: towards practical artificial photosynthesis. *Energy Environ. Sci.* 8: 2791–2796. https://doi.org/10.1039/C5EE02214B.

74 Li, R. (2017). Latest progress in hydrogen production from solar water splitting via photocatalysis, photoelectrochemical, and photovoltaic-photo-

electrochemical solutions. *Chin. J. Catal.* 38: 5–12. https://doi.org/10.1016/S1872-2067(16)62552-4.

75 Modestino, M.A. and Haussener, S. (2015). An integrated device view on photo-electrochemical solar-hydrogen generation. *Annu. Rev. Chem. Biomol. Eng.* 6: 13–34. https://doi.org/10.1146/annurev-chembioeng-061114-123357.

76 Wang, Z., Gu, Y., and Wang, L. (2021). Revisiting solar hydrogen production through photovoltaic-electrocatalytic and photoelectrochemical water splitting. *Front. Energy* 15: 596–599. https://doi.org/10.1007/s11708-021-0745-0.

77 Spitler, M.T., Modestino, M.A., Deutsch, T.G. et al. (2020). Practical challenges in the development of photoelectrochemical solar fuels production. *Sustainable Energy Fuels* 4: 985–995. https://doi.org/10.1039/C9SE00869A.

78 Berger, A. and Newman, J. (2014). An integrated 1-dimensional model of a photoelectrochemical cell for water splitting. *J. Electrochem. Soc.* 161: E3328.

79 Haussener, S., Xiang, C., Spurgeon, J.M. et al. (2012). Modeling, simulation, and design criteria for photoelectrochemical water-splitting systems. *Energy Environ. Sci.* 5: 9922–9935. https://doi.org/10.1039/C2EE23187E.

80 Cendula, P., Tilley, S.D., Gimenez, S. et al. (2014). Calculation of the energy band diagram of a photoelectrochemical water splitting cell. *J. Phys. Chem. C* 118: 29599–29607. https://doi.org/10.1021/jp509719d.

81 Gaudy, Y.K. and Haussener, S. (2016). Utilizing modeling, experiments, and statistics for the analysis of water-splitting photoelectrodes. *J. Mater. Chem. A* 4: 3100–3114. https://doi.org/10.1039/C5TA07328F.

82 Xiang, C., Weber, A.Z., Ardo, S. et al. (2016). Modeling, simulation, and implementation of solar-driven water-splitting devices. *Angew. Chem. Int. Ed.* 55: 12974–12988. https://doi.org/10.1002/anie.201510463.

83 Kemppainen, E., Halme, J., and Lund, P. (2015). Physical modeling of photoelectrochemical hydrogen production devices. *J. Phys. Chem. C* 119: 21747–21766.

84 Gutierrez, R.R. and Haussener, S. (2021). Modeling and design guidelines of high-temperature photoelectrochemical devices. *Sustainable Energy Fuels* 5: 2169–2180.

85 Li, F., Yang, H., Li, W., and Sun, L. (2018). Device fabrication for water oxidation, hydrogen generation, and CO_2 reduction via molecular engineering. *Joule* 2: 36–60. https://doi.org/10.1016/j.joule.2017.10.012.

86 Do Park, G., Lee, C.W., and Nam, K.T. (2018). Recent advances and perspectives of halide perovskite photocatalyst. *Curr. Opin. Electrochem.* 11: 98–104. https://doi.org/10.1016/j.coelec.2018.09.009.

87 Amano, F., Mukohara, H., Sato, H., and Ohno, T. (2019). Photoelectrochemical water vapor splitting using an ionomer-coated rutile TiO_2 thin layer on titanium microfiber felt as an oxygen-evolving photoanode. *Sustain. Energy Fuels* 3: 2048–2055. https://doi.org/10.1039/C9SE00292H.

88 Modestino, M.A., Dumortier, M., Hosseini Hashemi, S.M. et al. (2015). Vapor-fed microfluidic hydrogen generator. *Lab Chip* 15: 2287–2296. https://doi.org/10.1039/C5LC00259A.

89 Acar, C., Dincer, I., and Naterer, G.F. (2016). Clean hydrogen and power from impure water. *J. Power Sources* 331: 189–197. https://doi.org/10.1016/j.jpowsour.2016.09.026.

90 Zhou, Z., Wu, Z., Xu, Q., and Zhao, G. (2017). A solar-charged photoelectrochemical wastewater fuel cell for efficient and sustainable hydrogen production. *J. Mater. Chem. A* 5: 25450–25459. https://doi.org/10.1039/C7TA08112J.

91 Bhattacharjee, S., Andrei, V., Pornrungroj, C. et al. (2022). Reforming of soluble biomass and plastic derived waste using a bias-free $Cu_{30}Pd_{70}$|perovskite|Pt photoelectrochemical device. *Adv. Funct. Mater.* 32: 2109313. https://doi.org/10.1002/adfm.202109313.

92 Farràs, P., di Giovanni, C., Clifford, J.N. et al. (2016). Light driven styrene epoxidation and hydrogen generation using H_2O as an oxygen source in a photoelectrosynthesis cell. *Green Chem.* 18: 255–260. https://doi.org/10.1039/C5GC01589H.

6

Hydrogen Production from Water Using Thermal and Photo-Driven Systems. An Overview of Research Activity on Catalysts-Based Multi-junction Solar Cells

Hicham Idriss

Institute of Functional Interfaces (IFG), Karlsruhe Institute of Technology (KIT), Hermann-von-Helmholtz-Platz 1, 76344 Eggenstein-Leopoldshafen, Karlsruhe, Germany

6.1 Introduction

For a green economy to be possible in the near future, hydrogen production from H_2O is a sought-after alternative to fossil fuels. The present world annual production of hydrogen is about 70 million metric tons of which almost 50% is used to make ammonia, NH_3 (that is mostly used for fertilizers), and about 15% for other chemicals [1]. Hydrogen produced worldwide is largely made by steam CH_4 reforming (SMR), which is one of the most energy-intensive processes in the chemical industry [2]. Based on reaction stoichiometry, it releases 5.5 kg of CO_2 per 1 kg of H_2 ($CH_4 + 2H_2O \rightarrow CO_2 + 4H_2$). When the process itself is taken into account, in addition, the production [3] becomes about 9 kg of CO_2 per kg of H_2 and, this ratio can be as high as 12 [4]. This results in the production of about one billion tons/year of CO_2. The world's annual CO_2 emission from fossil fuels is, however, much larger. It is about 36 billion tons of which roughly 25% is emitted while generating electricity and heat, 20% due to transport activity, and 20% from other industrial processes. Because of the link between global warming and CO_2 emission, there is an increasing move toward finding alternative ways for energy vectors and their applications.

The amount of CO_2 released while producing hydrogen from fossil fuel represents 3–4% of its total emission. Making hydrogen from renewables to replace the present hydrogen, while very difficult, will not considerably change CO_2 emission. Actually, all chemicals (not fuel) consumed worldwide once burnt release about 3% of CO_2 globally. In other words, neither transforming CO_2 to chemicals, using H_2 from water, nor replacing SMR by electrolyzers (for example), will have a dramatic effect on CO_2 emission. The power of hydrogen and its important effect on cleaning the environment is when used as a fuel for transport, heat, and other energy applications, since they represent over 70% of CO_2 emission worldwide. This poses a much bigger problem for R&D, hydrogen needs to be made at a scale much larger than the present one and from water not from methane. This is a daunting task that is probably not fully appreciated nor given its level of importance. For that, global efforts

Photocatalytic Hydrogen Production for Sustainable Energy, First Edition. Edited by Alberto Puga.

to make hydrogen from water at the highest possible efficiency, safety, and process reliability should be the target. One cannot overemphasize the fact that transforming CO_2 to chemicals using hydrogen from water is itself irreverent worldwide, as numbers indicate that it would have a negligible effect on the environment; except when these chemicals are used as an energy vector, not as a commodity.

The present cost of hydrogen made by SMR with CO_2 sequestration is between US$1.3 and US$2.8 kg [5]. The cost of hydrogen from H_2O using energy from the sun will need to be competitive with this, or subsidized. At present, realistic numbers for the levelized cost of hydrogen (the minimum selling price of hydrogen without loss) production from water is about US$ 5–6/kg. The destructive effect on the environment of the carbon-based economy affecting marine life, and land (dryness) are increasingly observed, and will ultimately force continuous human and other living species displacements with the associated negative consequences. While there are a large number of methods for making hydrogen from water, the following three are so far the most promising; separately or together. Thermal, photocatalytic (PC), and electrocatalytic productions [6]. In the following, I address these three methods from the activities I have had on them in the last decade or so. They will be, albeit briefly, presented with emphasis on the concept, potential, and challenges of what might be needed in order to make a technology for hydrogen production from water possible.

6.1.1 Thermal Water Splitting Using Metal Oxides

6.1.1.1 Principle

This is a two-step reaction involving the reduction of an oxide material using heat, for simplicity in the case of a binary oxide, such as CeO_2, the reaction is as follows:

$$CeO_2 + \text{heat} \rightarrow CeO_{2-x} + x/2\, O_2 \tag{6.1}$$

$$CeO_{2-x} + H_2O \rightarrow CeO_2 + x\, H_2 \tag{6.2}$$

Reaction (6.1) requires an input of heat (endothermic) of around 1500 °C [7] in order to generate enough oxygen vacancies with a reasonable reaction rate. The diffusion of oxygen ions in CeO_2 at this temperature is typically between 10^{-5} and $10^{-4}\,cm^{-2}\,s^{-1}$ [8], and is therefore not critical at the reaction temperature. The second reaction (exothermic) occurs at temperatures around 1000 °C for practical (kinetic) reasons. There have been many prototype reactors, such as those given in reference [9].

Among the most studied binary metal oxides systems for redox reactions is CeO_2 (which is also used extensively as the support for automobile catalytic converters) [10]. This is because of its reducibility (Ce^{3+}/Ce^{4+} cations), stability, and the relatively fast kinetics of reduction and oxidation cycles when compared to many other oxides. The reduction of a fraction of Ce^{4+} cations (typically 10% or so) to Ce^{3+} in CeO_2 is associated with lattice expansion. The increase in size of Ce cations, Ce^{3+} (1.02 Å) larger than that of Ce^{4+} (0.87 Å) is often invoked as the cause of lattice expansion [11], although other interpretations have been reported [12]. The redox properties of CeO_2 can be monitored by X-ray photoelectron spectroscopy (XPS) when studied in situ or in operando conditions. For example, XPS Ce3d of CeO_2

before and after heating inside an ultra-high vacuum chamber (the spectrometer) at 1200 °C has been studied [13]. When the surface was exposed to water vapor at 100 K, clear evidence of Ce^{3+} consumption was seen (monitored by their XPS Ce3d lines); more details regarding the Ce^{4+} and Ce^{3+} XPS lines can be found elsewhere [14].

6.1.1.2 Application

In order to increase the number of active sites and obtain faster kinetics with CeO_2, doping with other metal cations has been conducted by many researchers. These can be grouped into three categories. (i) Compensation for lattice expansion, where Ce^{4+} cations are substituted by Zr^{4+} cations (much smaller: the size of Zr^{4+} cations is 0.59 Å while that of Ce^{4+} is 0.87 Å). Although, at high temperature needed for reduction considerable segregation occurs [15]. (ii) Additional charge transfer upon doping of CeO_2 by U^{4+} cations occurs, which results in increasing Ce^{3+} concentration. This is because UO_2 can accommodate nonstoichiometric amounts of oxygen anions up to $UO_{2.25}$ [16]. (iii) Aliovalent doping, where Fe^{3+} cations substitute Ce^{4+}, resulting in non-charged vacancies, which in turn cause lattice distortion [17].

As an example, Figure 6.1 presents the activity of reduced CeO_2 and reduced $Ce_{0.95}Fe_{0.05}O_{2-\delta}$ for thermal water splitting at 1200 °C, while Figure 6.2 presents the scanning transmission electron microscopy (STEM), energy dispersive X-ray (EDX) and electron energy loss spectroscopy (EELS) results of the $Ce_{0.95}Fe_{0.05}O_{2-\delta}$ oxide after the reaction. Prior to reaction, the oxides were heated to 1550 °C for 120 minutes. More details can be found in Refs [18, 19]. The following gives a brief description of the activity and properties of these oxides. The incorporation of Fe into CeO_2 has resulted in two main effects. The kinetic of the hydrogen production has increased and the total amount has almost doubled (per unit weight of oxide). This is in line with most studies pointing out to an increased reduction of CeO_2 due to the presence of Fe cations (up to a threshold level) [18, 20–25]. One can see this by the narrowing of the production peak of hydrogen where the full width half maximum (FWHM) decreased from c. 35 minutes to about 10 minutes (Figure 6.1a,b), which gives a simple observation on the kinetic effect. To further see the effect of Fe on the reduction kinetics, the decay parts of the peaks were fitted with an exponential decay function. Table 6.1 presents the different parameters of the decay for both oxides. The addition of Fe has increased the time constant (in min^{-1}) for water splitting by a factor of two when compared to CeO_2 alone. However, increasing the number of reduced sites should not reduce the decay time but mostly affect the amplitude (pre-factors A_1 and A_2) if these sites are all of similar nature and do not interact with each other. The decrease of the time constant by a factor of two in the case of the Fe-doped CeO_2 indicates that the reduced sites are more reactive than those of CeO_2 alone (see further discussion below). The ratio t_1/t_2 (or τ_2/τ_1) was found to be almost the same for both oxides. It is possible that the slowest (t_2) decay is due to events requiring additional energy than the first one; these can be, for example, due to defects' diffusion from the bulk to the surface. Initially, defects are statistically distributed in the bulk and on the surface. As the progress of the reaction increases, defects are healed, decreasing the statistical entropy of the system and increasing ΔG of the reaction, which in turn decreases

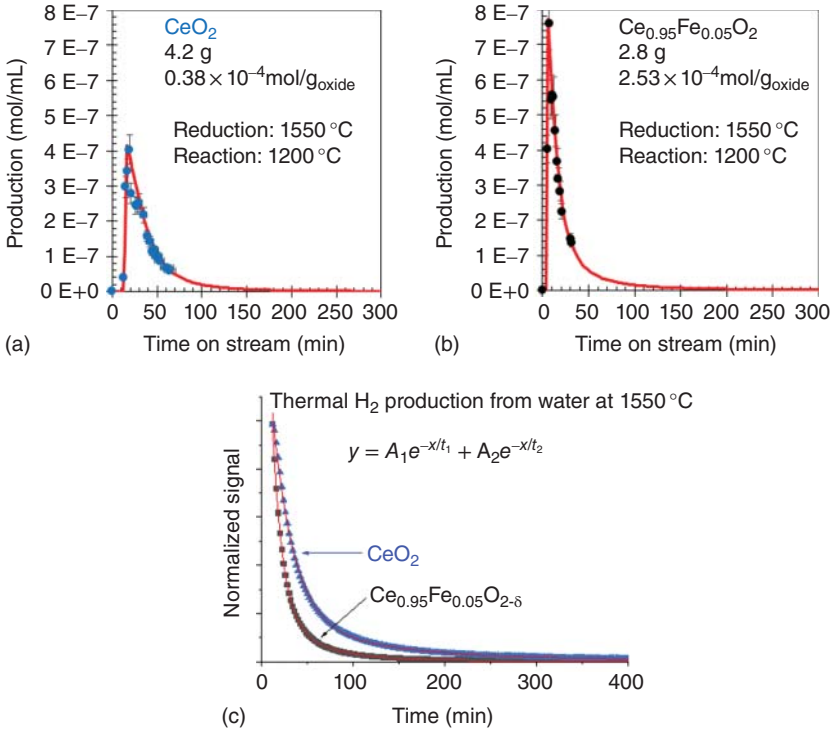

Figure 6.1 Thermo-chemical water splitting (TCWS) over CeO_2 (a) and $Ce_{0.95}Fe_{0.05}O_{2-\delta}$ (b) at 1200 °C, both were reduced under N_2 at 1550 °C for two-hour prior to use. The total amount of hydrogen from water per g of oxide is indicated. (c) Normalized fitting of the decay part of H_2 production using a bi-exponential function. Source: Al-Taweel et al. [18]/with permission of John Wiley & Sons, Inc.

the reaction rate because a defect site (or a bulk oxygen atom) would need to travel a longer distance to reach the surface.

Figure 6.2 shows, however, that the Fe-containing oxide is not stable. Initially, the as-prepared oxides contained (figures shown in Ref. [19]) Fe and Ce distributed in a homogeneous way, as evidenced by their TEM and X-ray diffraction (XRD) data (a solid solution). However, heating to the 1550 °C needed for reduction has resulted in considerable segregation of both cations. The segregation is gradual, with patches containing more distributed Fe cations than others, yet it is clear that a separated phase of iron suboxide has started to build up. This will eventually result in a decrease in the reaction rate to that observed with CeO_2 alone.

6.1.1.3 Limitation

Many other binary, tertiary, and higher mixed metal oxides are investigated with considerable knowledge gained at the materials, reaction and reactor design levels [20, 21]. Important issues still remain even if a reducible oxide system is found at a relatively low temperature, around 1000 °C. Among them are the following: (i) Deviation of the homogeneous distribution of metal cations in a mixed oxide

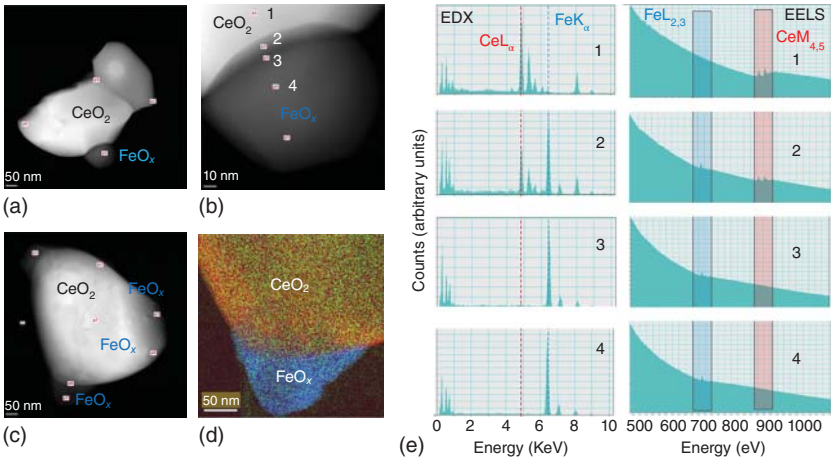

Figure 6.2 STEM, EDX, and EELS of $Ce_{0.95}Fe_{0.05}O_{2-\delta}$ after the reaction presented in Figure 6.1. A and B are for one particle, and C and D are for another particle. D. an elemental EELS map of the particle in C. The numbers one to four in E are those labeled in B. While clear segregation of iron to the edges of CeO_2 is seen, some iron is still present (EDX) within the crystallite (also note the presence of FeO_x on the large CeO_2 crystallite in C). The crystallite size as observed with TEM is close to 1 μm (an increase of almost 200 times when compared to that calcined at 500 °C). Yellow for cerium, blue for iron, and red for oxygen atoms. Based on elemental mapping, it seems that FeO_x is highly deficient in oxygen. Source: Al-Taweel et al. [18]/with permission of John Wiley & Sons, Inc.

Table 6.1 Fitting parameters for the decay part of the hydrogen production profile (at 1200 °C) from water shown in Figure 6.1.

Oxide	A_1 (mol/ml min)	t_1 (min)	τ $(\text{min})^{-1}$	A_2 (mol ml^{-1} min^{-1})	t_2 (min)	τ $(\text{min})^{-1}$	t_1/t_2
CeO_2	7.3×10^{-7}	22.5	0.044	9.7×10^{-8}	108.8	0.009	0.21
$Ce_{0.95}Fe_{0.05}O_2$	1.2×10^{-6}	10.7	0.093	1.3×10^{-7}	47.3	0.021	0.23

The time constant $\tau = 1/t$. $y = A_1e^{-x/t1} + A_2e^{-x/t2}$ is the exponential decay equation used.

material upon multiple redox cycles (segregation). (ii) The small extent of reduction requiring large reactors and materials. (iii) The high temperature needed for the process requires special materials for reactors/systems (heat concentration, corrosion, and resistance to temperature oscillations, among others). (iv) The input of energy (heat) using expensive optics. (v) The still slow kinetic of the reduction process (for the release of O_2). All these combined make this route unlikely in the near future. At present, the most recent techno-economy analysis (TEA) indicates that the levelized cost of H_2 (per kg) is at c. US$ 13 with the price lowered to US$ 6.5 for the best-case scenario [22]. One of the main advantages, however, is the utilization of a very large fraction of the sun light unlike most other methods. This method, once made possible and affordable, would be among the cleanest ones in making hydrogen and oxygen from water separately.

6.1.2 Electrocatalytic Water Splitting

Electrocatalytic water splitting is the most mature technology for making hydrogen from water, with many commercial systems available for small-and large-scale applications. With respect to making hydrogen from renewables, electrocatalysis is attractive because electricity can be generated from photovoltaic (PV) cells. At present, this system offers probably the least expensive method for making hydrogen with an estimated cost of between US$1.5 and US$2/kg_{H2} when electricity is provided at a cost of US$0.02/kWh, which is three to four times lower than the present cost [23]. Commercial electrolyzers work either at neutral pH, in this case using noble metals for both electrodes with a proton-exchange membrane (PEM), this is mostly for small-scale applications, or in alkaline environment for larger scale. In alkaline media, electrodes are made of mixed metal oxides based on Fe, Ni, and Co cations. Electrolysis is still a very active field of research, mostly focusing on two aspects. (i) To replace Pt cathodes by less expensive and less prone to poisoning metals such as NiMo [24] (CO on Pt has an adsorption energy of about 1.5 eV [25]). The fact that Pt has a very low overpotential (the amount of energy needed to drive the reaction in addition to that required to split water, which is less than 0.1 eV), makes its replacement by less noble metals a difficult task. Yet, for large-scale and wide-spread applications, Pt availability may become the bottleneck of the process if no replacement is found. (ii) The anode side, where losses of 0.3 eV or more occur; this is because of the four-electron requirement for molecular oxygen to form, among other factors. Many promising materials mostly Co- and Fe-based ones were and still are studied; for more information there is a large number of review articles on these materials [26–28].

6.1.3 Photocatalytic and Photoelectrocatalytic Water Splitting

6.1.3.1 Principle

Among the largest fractions of work on water splitting to molecular hydrogen and oxygen over the last two decades has been done on both PC and photoelectrocatalytic (PEC) systems. In that regard, one needs to make a few distinctions. PEC reactions require a bias, such as the one used by Fujishima and Honda in their seminal paper [29], or a connection between the anode and cathode. The most difficult part of the reaction is at the anode side in the case of PEC reaction or in the water oxidation side of unbiased particle-based systems, either dispersed in the medium or in the form of thin films. Light harvesting is at the essence of the PC systems. 1.23 eV (or about 1000 nm), the energy per electron needed to split water at room temperature, falls in the middle of the solar spectrum. In order to harvest sun light efficiently, one needs to make a photocatalyst that absorbs up to that energy (or about 50% of sun light).

6.1.3.2 Application

Many researchers, including my previous group, have studied a large number of concepts poised to improve the reaction efficiency. These studies include, synergism

of multiple phases of a semiconductor [30, 31], p–n junction for [32, 33], Z-scheme [34, 35], plasmonics [36], photonic bandgap materials [37, 38], up-conversion luminescence [39, 40], to name a few. While some progress was made, the overall efficiency of any of these studied systems fell below any promising direction for large-scale application. Moreover, because of the complexity of the water splitting reaction, research was focused on half of the reaction by using sacrificial agents. These include alcohols as electron donors (hole trapping) [41, 42] for H_2-production and metal cations as electron acceptors (electron trapping) [43, 44] for O_2-production. Electron donors result ultimately in the formation of CO_2 (a process called PC reforming) [45] while electron acceptors are deposited on the surface of the catalyst [46], a known structure-sensitive reaction for decades [47]. Economically, these systems are not sustainable for large-scale application. Some small applications might be suitable, such as the production of hydrogen from waste streams, which combined with environmental cleanup, can have some merits.

6.1.3.3 Limitation

At present, there is no reproducible work for pure water splitting on suspended stable powder materials (conceptually the least expensive method). Although reports have given 1% and 2% STH [48, 49]; these, even confirmed and found to be stable, are about 20 times lower than the needed reaction rate for practical applications. Most importantly, product separation is a major challenge. In order to separate H_2 from O_2, one needs to pressurize them, but because of flammability, these need to be diluted. We have looked into this in some details in the past [50, 51]. The cost of such a process, however, is very high at present [52]. This has motivated researchers to separate hydrogen and oxygen from the beginning. Some work has addressed these using, for example, a membrane in between two types of catalysts [53, 54], one for hydrogen and one for oxygen production, but the use of a redox system to close each loop is found to add further complications including, irreversible deposition of ions on the catalysts [55]. This last method might still be suitable for application, where hydrogen and oxygen are needed, if large land is not an issue, using replaceable "non-expensive" coated catalytic layers; more can be found in a recent review article [56].

6.2 A Case Study

Activities on a different system have started almost in parallel to photocatalysis, by other researchers, for decades [57, 58], on multi-junction GaAs-based solar cells (MJSCs), that have high efficiency in harvesting sun light [59]. These are based on epitaxial growth of semiconductors of different bandgaps extending to Ge (bandgap = 0.67 eV) [60]. Like any electronic device, they cannot function in an aqueous environment, so most of the work has focused on stabilizing them [61]. One of their important properties is that the charge carriers' density scales linearly with the photon flux, with simulation results up to 10 000 suns available [62].

Commercial systems are available with concentrations of about 1000 suns (http://www.sharp-world.com/corporate/news/130614.html).

Since a photocatalyst is a PV cell and an electrolyzer in one step, and since these MJSCs are already available, understanding, using, and mimicking them as the core catalyst would be a sensible approach. This is because they provide the needed voltage to electrolyze water. In particular, upon the realization that when it comes to charge carriers' transfer to make a catalytic reaction, one needs a perfect medium for their propagation, and this is provided by single crystals and not by particles with nano-dimension (where the high surface to bulk ratio inevitably increases the number of surface and near-surface defects). The present drawback of these cells is the generation of a voltage larger than that needed for the water splitting reaction (typically about 3 eV at one sun for triple-junction [3J] cells). This means a non-negligible fraction of the light harvested would be wasted. Yet with the manufacturing of four-junctions cells [63], the voltage can be increased enough to 3.5 eV or above making the use of two electrolyzers connected to one cell possible [64]. This has then the potential of getting a solar-to-hydrogen (STH) efficiency above 35%; probably the threshold for commercialization of the complete system to hydrogen from water.

6.2.1 Photoelectrocatalytic (PEC) Systems, Stability, and Performance

Unlike Si-based PV, MJSC provides the needed voltage for water electrolysis, per cell. This means that MJSC, as indicated above, are already tuned for charge carriers' generation and, therefore, it is more efficient to transfer these carriers to a metal (the cathode) and a metal oxide (the anode) to generate H_2 and O_2 directly and separately. This way, there will be no need to make large-scale electrolyzers. This comes with important constrains. Instead of large-scale electrolyzers, many thousands of MJSC on solar trackers would be mounted, each of them would be associated with the needed piping with H_2 and O_2 lines, and the whole system must be stable for over a decade.

Because PV cells corrode in an aqueous environment, both sides of the cell need protection [65–67].

Figure 6.3 presents a PEC reactor excited with light at 207 suns using a Fresnel lens of a system the group has developed over the course of the study. The PEC reactor is composed of a 3J GaInP/GaInAs/Ge PV cell ($5.0 \times 5.0\,mm^2$) from Azure Space as the photoabsorber. The back of the 3J PV cell is integrated to a 0.25 mm thick nickel foil. The nickel geometric area was ~4 cm^2 and the HER catalyst used was ~50 nm thick platinum sputtered onto both sides of a porous titanium mesh. An alkaline anion exchange membrane (Sustainion® 37–50, dioxide materials) was used for ion transfer and gas separation. The Ni foil in this case has three purposes: protection from corrosion, oxygen production catalyst, and heat dissipation. The electrolyte is a 5 M KOH solution. Also shown in the figure is the H_2/O_2 ratio and (STH) efficiency as a function of light concentration, the blue symbols represent the average STH of 13%, the red symbols represent the H_2 to O_2 stoichiometric ratio of two. It was found that a well-placed Ni foil connected to the backside protects it from

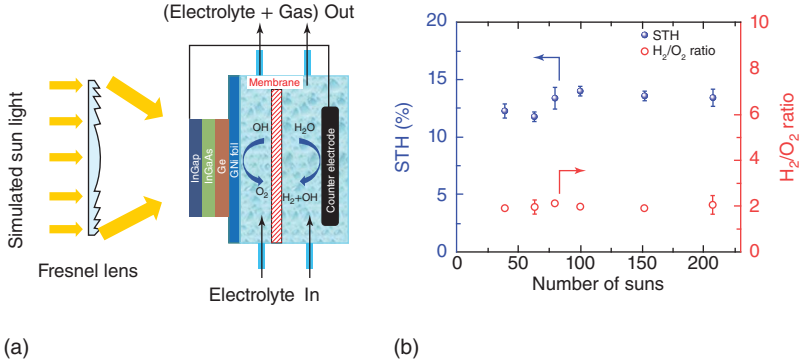

Figure 6.3 (a) A schematic of a photoelectrocatalytic reactor excited with light at 207 suns using a Fresnel lens. (b) H_2/O_2 ratio and solar-to-H_2 (solar-to-hydrogen [STH]) efficiency as a function of light concentration. Source: Khan et al. [68]/with permission of John Wiley & Sons.

corrosion and, depending on its thickness and extracted current, this can extend to many years); more details can be found [68]. At present, the practice is to protect the front side (the side receiving light) with a poly methyl methacrylate (PMMA) window and extract the generated electrons toward a cathode. In a pure PEC system, the front side should be directly making hydrogen. It is not clear if modifying the front side to directly make hydrogen is needed from an application perspective. There are emerging efforts to protect this front side (made of GaAs, GaInP, and similar III-V semiconductors) by epitaxy layers of a wider bandgap metal oxide with the conduction band edge (or defect states within its bandgap energy) suitable to extract excited electrons [69, 70]. This strategy, once successful, has further challenges. The deposition of metal nanoparticles on top of the protective oxide needs to be in the order of 0.01–0.05 monolayer to prevent light scattering and the formation of bubbles upon H_2 production at high light flux affect light penetration. Results from photocatalysis on nanoparticles indicate that small coverage by noble metals is sufficient [71–73] at one sun, but data with high light fluxes are not available.

So far, there are no TEA of such a system linking the projected drop in MJSC cost to H_2 production in a single step. Yet, a TEA of a simpler system in which these MJSC are connected to suitable electrolyzers to match the voltage has been conducted based on laboratory experimental results as well as on a larger scale demonstration unit. These are presented in Figures 6.4 and 6.5. Figure 6.4 shows that a stable hydrogen production is made possible with a high STH efficiency (average 18.7%), once power matching for both electrolyzers and PV cells is done without the use of electronics (DC–DC converters) [74]. Figure 6.5 shows a prototype made at the laboratory scale where two MJSC were connected in series to three electrolyzers (also connected in series) to match the power of the PV cells, again without the need for electronics in between (typically they decrease the performance because of increased resistance). The overall STH of this system was 28%.

Detailed TEA analysis has been used for similar systems, including power electronic costs. It indicates that the preset cost of producing hydrogen using this method

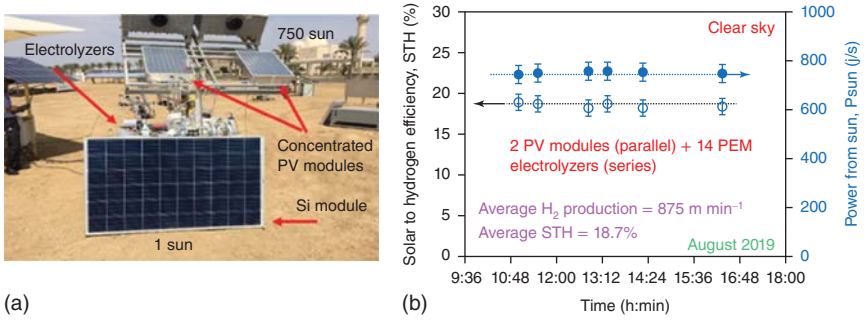

Figure 6.4 (a) Picture of outdoor PV-electrolysis experimental set up at SABIC Corporate Research and Development (CRD) center at KAUST – Thuwal, Saudi Arabia (22.3023 °N, 39.1231 °E). The power ratings of the concentrated PV module (from Ningbo Cinco Solar Co., Ltd., China) with 0.5 m^2 area and Si module (from Solar Tech Energy Corporation, Taiwan) with 1.5 m^2 are 145 and 270 W at a sun-light flux of 1000 W m^{-2}, respectively; (b) Data collected in August 2019 using an optimized system consisting of 14 PEM electrolyzers with the two concentrated PV modules, as shown in (a), without the use of power electronics. Source: Bashir et al. [75]/with permission of Elsevier.

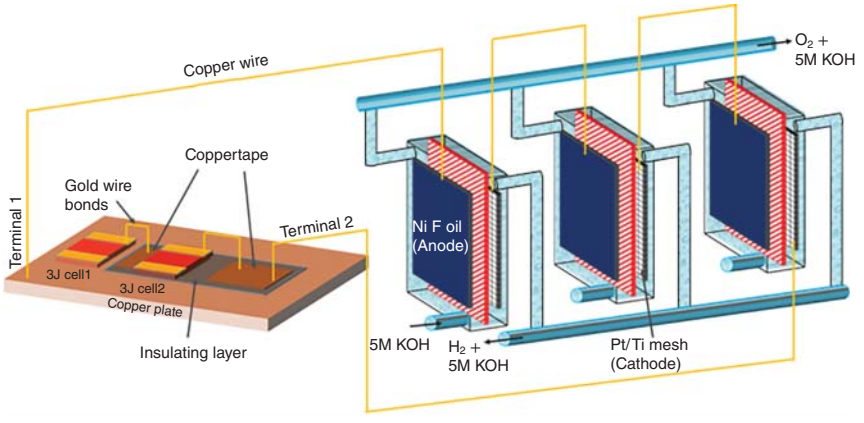

Figure 6.5 A PV-electrolysis setup consisting of two-triple-junction solar cells (each is composed of GaInP/GaInAs/Ge cells [3.0 × 3.0 mm^2]) connected in series to three alkaline electrolyzers, also connected in series. Each alkaline electrolyzer is composed of ca. 10 nm Pt particles deposited on both sides of a Ti mesh (Pt/Ti mesh) as the cathode and a $Ni(OH_2)$/Ni as the anode. The electrolyte (5 M KOH solution) is recirculated. Terminal 1: back side of the cells (+), and terminal 2: front side of the cell (–). Light at 41 suns concentration illuminated the cells, without the use of Fresnel lenses. Source: Khan et al. [75]/Royal Society of Chemistry/CC BY 3.0.

is about 20% more expensive than that of conventional PV-electrolysis (Table 6.2), yet it can become much cheaper when its production volume increases [75]. The main advantage is, as indicated above, sustaining very high light fluxes, which makes them ideal from a sustainability perspective because much less material is needed when compared to Si-based solar cells. Other advantages are the need for less land area because of their high efficiency, which at present is about 40% and theoretically can be over 80%; this is unlike Si-based solar cells that have reached near saturation

Table 6.2 Comparison between MJSC-based electrocatalytic system at 820-sun and a Si-PV cell for a similar electrocatalytic system at one sun.

	CPV	Silicon-PV
CAPEX		
Total PV cost (US$)	US$315 832 967.03	US$225 594 976.45
Total electrolyzer capital (US$)	US$156 193 758.24	US$156 193 758.24
Gas processing (US$)	US$4 143 572.97	US$4 143 572.97
Electrolyte processing (US$)	US$29 306.58	US$29 306.58
Land cost (US$)	US$381 375.86	US$977 275.64
Contingency (%)	US$94 858 545.11	US$77 387 777.97
Total CAPEX (US$)	US$571 439 525.79	US$464 326 667.85
OPEX		
Annual PV maintenance (US$/year)	US$18 662.86	
Compressor (US$/year)	US$393 477.73	
Water pump (US$/year)	US$20 755.22	
Annual water cost (US$/year)	US$216 450.00	
O&M of electrolyzer (US$/year)	US$4 183 761.38	
Annual electrolyzer replacement (US$/year)	US$2 342 906.37	
Annual electricity cost for utilities (US$/year)	US$134 032.50	
Annual staff cost (US$/year)	US$1 598 400.00	
Total OPEX (US$/year)	US$8 908 446.06	
Levelized cost of hydrogen (US$/kg)	US$5.9	US$4.9

CPV: concentrated photovoltaics. More details can be found in Khan et al. Ref. [75].
Source: Khan et al. [75]Royal Society of Chemistry/ CC BY 3.0.

from an efficiency perspective. The very small cell sizes when compared to Si-based solar cells has an additional advantage. This is related to heat management. Si-based PV cells absorb a large fraction of sun light as heat, this is poised to raise the local temperature where large installations are considered, in particular in hot countries, and seems to be largely overlooked at present, more details can be found in refs [76, 77]. Moreover, life cycle analysis puts MJSC less polluting than Si-based PV cells (22 gCO_2 per kWh for MJSC and 45.3 gCO_2 per kWh for monocrystalline Si-PV cells) [78, 79].

6.3 Conclusions

The following may summarize the presented research and development activity in this chapter. Today, solar thermal hydrogen production suffers from a very costly and complex reactor system (light harvesting and energy transfer) and slow kinetics.

A reducible and stable oxide material at practical temperatures of roughly 1000 °C is yet to be found. While electrocatalysis is a mature technology, it may become competitive when electricity from renewables and electrolyzers drops considerably in price. MJSCs, either as a source of electricity to electrolyzers or as a complete standalone one-step, unbiased PEC system, may compete with hydrogen from methane reforming once the process cost is dropped (in particular because of the cost of sun concentrators). While each method has its limitations, progress will be further accelerated with a worldwide committed support to take these research-based results to their next step.

Acknowledgments

Many thanks to the team who conducted most of the work presented in this chapter including: M. A. Khan, I. Al-Shankiti, A. Ziani, A. M. Nadeem, S. Al-Taweel, M. Al-Oufi, M. Al-Hakami, K. Mudiyanselege, and Y. Al-Salik, from SABIC Corporate Research Center at KAUST (Saudi Arabia).

References

1 Birol, F. (June 2019). The future of hydrogen, Seizing today's opportunities. Report prepared by the IEA for the G20, Japan, International Energy Agency.
2 Worrell, E., Phylipsen, D., Einstein, D., and Martin, N. (2000). Energy use and energy intensity of the U.S. Chemical Industry. Energy Analysis Department, Environmental Energy Technologies Division, Ernest Orlando Lawrence Berkeley National Laboratory, April 2000.
3 Sun, P. and Elgowainy, A. (2019). Updates of hydrogen production from SMR process in GREET. Systems Assessment Center, Energy Systems Division, Argonne National Laboratory. https://greet.es.anl.gov/publication-smr_h2_2019 (accessed July 2020).
4 Koch Blank, T. and Molly, P. (2020). Hydrogen's decarbonization impact for industry near-term challenges and long-term potential. Thomas Koch Blank, Patrick Molly, January, 2020. https://rmi.org/wp-content/uploads/2020/01/hydrogen_insight_brief.pdf (accessed January 2021).
5 Parkinson, B., Balcombe, P., Speirs, J.F. et al. (2019). Levelized cost of CO_2 mitigation from hydrogen production routes. *Energy Environ. Sci.* 12: 19–40; supporting information Tables S1 and S2.
6 Wang, M., Wang, G., Sun, Z. et al. (2019). *Global Energy Interconnect.* 2 (5): 43–44.
7 Chueh, W.C., Falter, C., Abbott, M. et al. (2010). High-flux solar-driven thermochemical dissociation of CO_2 and H_2O using nonstoichiometric ceria. *Science* 330: 1797–1801.
8 Ackermann, S., Scheffe, J.R., and Steinfeld, A. (2014). Thermodynamic analysis of cerium-based oxides for solar thermochemical fuel production. *J. Phys. Chem. C* 118: 5216–5225.

9 Abanades, S. (2019). Chem engineering, metal oxides applied to thermochemical water-splitting for hydrogen production using concentrated. *Sol. Energy* 3 (63): 1–28.

10 Trovarelli, A. (1996). Catalytic properties of ceria and CeO_2-containing materials. *Catal. Rev.* 38 (4): 439–520.

11 Hailstone, R.K., DiFrancesco, A.G., Leong, J.G. et al. (2009). A study of lattice expansion in CeO_2 nanoparticles by transmission electron microscopy. *J. Phys. Chem. C* 113: 15155–15159.

12 Muhich, C.L. (2017). Re-evaluating CeO_2 expansion upon reduction: noncounterpoised forces, not ionic radius effects, are the cause. *J. Phys. Chem. C* 121: 8052–8059.

13 Idriss, H. (2021). Towards large scale hydrogen production from water, what have we learned and what are the main hurdles to cross for commercialization. *Energy Technol.* 9: 2000843, 1-9.

14 Mullins, D.R., Overbury, S.H., and Huntley, D.R. (1998). Electron spectroscopy of single crystal and polycrystalline cerium oxide surfaces. *Surf. Sci.* 409: 307–319.

15 Grau-Crespo, R., De Leeuw, N.H., Hamad, S., and Waghmare, U.V. (2011). Phase separation and surface segregation in ceria–zirconia solid solutions. *Proc. R. Soc. A* 367: 1925–1938.

16 Scaranto, J. and Idriss, H. (2015). The effect of uranium cations on the redox properties of CeO_2 within the context of hydrogen production form water. *Top. Catal.* 58: 1443–1148.

17 Gupta, A., Waghmare, U.V., and Hegde, M.S. (2010). Correlation of oxygen storage capacity and structural distortion in transition-metal-, noble-metal-, and rare-Earth-ion-substituted CeO_2 from first principles calculation. *Chem. Mater.* 22: 5184–5198.

18 Al-Taweel, S., Nadeem, M.A., and Idriss, H. (2021). A study of $Ce_xFe_{1-x}O_2$ as a reducible oxide for the thermal hydrogen production from water. *Energy Technol.* 10: 2100491. (1–9).

19 Al-Shankiti, I., Choi, Y-M., Al-Otaibi, F., and H. Idriss. Catalysts for thermochemical water splitting. United States Of America Patents (12CHEM0009-US-PCT) was filed at the Patent Office on 24-07-2013 as Serial Number 14407335; and US Patents (12CHEM0009-US-CNT) on 02-05-2016 as Serial Number 15144476. Allowed, 16 June 2016, Granted 23-08-2016 as Patent No. 9421537, and Granted on 13-06-2017 as Patent No. 9675961.

20 Muhich, C.L., Ehrhart, B.D., Al-Shankiti, I. et al. (2016). A review and perspective of efficient hydrogen generation via solar thermal water splitting. *WIREs Energy Environ.* 5: 261–287.

21 Ehrhart, B.D., Muhich, C.L., Al-Shankiti, I., and Weimer, A.W. (2016). System efficiency for two-step metal oxide solar thermochemical hydrogen production – Part 2: Impact of gas heat recuperation and separation temperatures. *Int. J. Hydrogen Energy* 41: 19881–19893.

22 Moser, M., Pecchi, M., and Fend, T. (2019). Techno-economic assessment of solar hydrogen production by means of thermo-chemical cycles. *Energies* 12 (352): 1–17.

23 Quote from NEL Hydrogen to SABIC to make 200 tons of hydrogen at 200bar (February 2018).

24 Bau, J.A., Haspel, H., Ould-Chikh, S. et al. (2019). On the reconstruction of NiMo electrocatalysts by operando spectroscopy. *J. Mater. Chem. A* 7: 15031–15035.

25 Gunasooriya, G.K. and Saeys, M. (2018). CO adsorption on Pt(111): from isolated molecules to ordered high-coverage structures. *ACS Catal.* 8: 10225–10233.

26 Alsabban, M.M., Yang, X., Wahyudi, W. et al. (2019). Design and mechanistic study of highly-durable carbon coated cobalt diphosphide core-shell nanostructure electrocatalyst for the efficient and stable oxygen evolution reaction. *ACS Appl. Mater. Interfaces* 11: 20752–20761.

27 Song, J., Wei, C., Huang, Z.-F. et al. (2020). A review on fundamentals for designing oxygen evolution electrocatalysts. *Chem. Soc. Rev.* 49: 2196–2214.

28 Vazhayil, A., Vazhayal, L., Thomas, J., and Thomas., N. (2021). A comprehensive review on the recent developments in transition metal-based electrocatalysts for oxygen evolution reaction. *Appl. Surf. Sci. Adv.* 6: 100184.

29 Fujishima, A. and Honda, K. (1972). Electrochemical photolysis of water at a semiconductor electrode. *Nature* 238: 37–38.

30 Wahab, A.K., Ould-Chikh, S., Meyer, K., and Idriss, H. (2017). On the synergism of the different phases of TiO_2 in photo-catalysis for hydrogen production. *J. Catal.* 352: 657–671.

31 Connelly, K.A., Wahab, A.K., and Idriss, H. (2012). Photoreaction of Au/TiO_2 for hydrogen production from renewables: a review on the synergistic effect between anatase and rutile phases of TiO_2. *Mater. Renewable Sustainable Energy* 1 (3): 1–12.

32 Sinatra, L., LaGrow, A.P., Peng, W. et al. (2015). $Au/Cu_2O\text{-}TiO_2$ system for photo-catalytic hydrogen production. A pn-junction effect or a simple case of in situ reduction? *J. Catal.* 322: 109–117.

33 Khan, M.A., Al-Oufi, M., Toseef, A. et al. (2016). On the role of CoO in CoO_x/TiO_2 for the photocatalytic hydrogen production from water in the presence of glycerol. *Catal. Struct. React.* 192: 1–4.

34 Isimjan, T.T., Maity, P., Llorca, J. et al. (2017). Comprehensive study of all-solid-state Z-scheme photocatalytic system of ZnO/Pt/CdZnS. *ACS Omega* 2: 4828–4837.

35 Li, H., Tu, W., Zhou, Y., and Zou, Z. (2016). Z-scheme photocatalytic systems for promoting photocatalytic performance: recent progress and future challenges. *Adv. Sci.* 3: 1500389.

36 Khan, M.A., Al-Oufi, M., Sinatra, L. et al. (2017). Evidence of plasmonic induced photocatalytic hydrogen production on Pd/TiO_2 upon deposition on thin films of gold catalysis. *Catal. Lett.* 147: 811–820.

37 Jovic, V., Idriss, H., and Waterhouse, G.I. (2016). Slow photon amplification of gas-phase ethanol photo-oxidation in titania inverse opal photonic crystals. *Chem. Phys.* 479: 109–121.

38 Waterhouse, G.I.N., Wahab, A.K., Al-Oufi, M. et al. (2013). Hydrogen production by tuning the photonic band gap with the electronic band gap of TiO_2. *Sci. Rep.* 3: 2849.

39 Khan, M.A. and Idriss, H. (2017). A review on recent advances in plasmon enhanced upconversion and its possible effect on light harvesting for energy applications. *WIREs Energy Environ.* 6: 1–23.

40 AlGhamdi, H., Katsiev, B., Wahab, A.K. et al. (2017). Up-conversion luminescence coupled to plasmonic gold nanorods for light harvesting and hydrogen production. *Chem. Comm.* 53: 13051–13054.

41 Al-Azri, Z.H.N., Chan, A., Chen, W.-T. et al. (2015). On the role of metals and reaction media in photocatalysis for hydrogen production. Performance evaluation of M/TiO_2 photocatalysts (M = Pd, Pt, Au) for H_2 production in different alcohol-water mixtures. *J. Catal.* 329: 355–367.

42 Al-Azri, Z.H.N., Al-Oufi, M., Chan, A. et al. (2019). Metal particle size effects on the photocatalytic hydrogen ion reduction. *ACS Catal.* 9: 3946–3958.

43 Menendez, R.G., Bucci, A., Hutchinson, R. et al. (2016). Extremely active, tunable, and pH-responsive iridium water oxidation catalysts. *ACS Energy Lett.* 2: 105–110.

44 Pastori, G., Wahab, K.W., Bucci, A. et al. (2016). Heterogenized water oxidation catalysts prepared by immobilizing Klaüi-type organometallic precursors. *Chem. Eur. J.* 22: 1–6.

45 Bowker, M., Davies, P.R., and Al-Mazroai, L.S. (2009). Photocatalytic reforming of glycerol over gold and palladium as an alternative fuel source. *Catal. Lett.* 128: 253–255.

46 Khan, M.A., Nadeem, M.A., and Idriss, H. (2016). Ferroelectric polarization effect on semiconductor photo-catalytic activity: a review. *Surf. Sci. Rep.* 71: 1–31.

47 Lowekamp, J.B., Rohrer, G.S., Morris Hotsenpiller, P.A. et al. (1998). Anisotropic photochemical reactivity of bulk TiO_2 crystals. *J. Phys. Chem. B* 102: 7323–7327.

48 Wang, Q., Hisatomi, T., Jia, Q. et al. (2016). Scalable water splitting on particulate photocatalyst sheets with a solar-to-hydrogen energy conversion efficiency exceeding 1. *Nat. Mater.* 15: 611–615.

49 Liu, J., Liu, Y., Liu, N. et al. (2015). Metal-free efficient photocatalyst for stable visible water splitting via a two-electron pathway. *Science* 347: 970–974.

50 Al-Jodai, A.M., Haque, U.L., and Aldalaan, N.A. (2021). Process for separation of hydrogen and oxygen. Patent number: 10947115 (Sabic Global Technologies B.V.), filed 14 November 2016 and issued 16 March 2021.

51 Aldalaan, N.A., Al-Jodai, A.M., and Bashir, M.A. (2021). Process for separation of hydrogen and oxygen. Patent number: 10882742 (Sabic Global Technologies B.V.), filed 6 January 2017 and issued 5 January 2021.

52 Alsayegh, S., Johnson, J.R., Ohs, B. et al. (2017). Systematic optimization of H_2 recovery from water splitting process using membranes and N_2 diluent. *Int. J. Hydrogen Energy* 42: 6000–6011.

53 Vermaas, D.A., Sassenburg, M., and Smith, W.A. (2015). Photo-assisted water splitting with bipolar membrane induced pH gradients for practical solar fuel devices. *J. Mater. Chem. A* 3: 19556–19562.

54 Marino, T., Figoli, A., Molino, A. et al. (2019). Hydrogen and oxygen evolution in a membrane photoreactor using suspended nanosized Au/TiO_2 and Au/CeO_2. *Chem. Eng.* 3 (5): 1–12.

55 Yu, S.-C., Huang, C.-W., Liao, C.-H. et al. (2011). A novel membrane reactor for separating hydrogen and oxygen in photocatalytic water splitting. *J. Membr. Sci.* 382: 291–299.

56 Nadeem, M.A., Ziani, A.A., Khan, M.A., and Idriss, H. (2021). An overview of photocatalytic water splitting without sacrificial agents. *Catal.* 11 (1): 60.

57 Khaselev, O., Bansal, A., and Turner, J.A. (2001). High-efficiency integrated multi-junction photovoltaic/electrolysis systems for hydrogen production. *Int. J. Hydrogen Energy* 26: 127–132.

58 Döscher, H., Young, J.L., Geisz, J.F. et al. (2016). Solar-to-hydrogen efficiency: shining light on photoelectrochemical device performance. *Energy Environ. Sci.* 9: 74–80.

59 Young, J.L., Steiner, M.A., Döscher, H. et al. (2017) 17028). Direct solar-to-hydrogen conversion via inverted metamorphic multi-junction semiconductor architectures. *Nat. Energy* 2: 1–8.

60 Kittel, C. (1986). *Introduction to Solid State Physics*, 6e, 185. New York: Wiley.

61 Cheng, W.-H., Richter, M.H., May, M.M. et al. (2018). Monolithic photoelectrochemical device for 19% direct water splitting ACS. *Energy Lett.* 3: 1795–1800.

62 Zeitouny, J., Katz, E.A., Dollet, A., and Vossier, A. (2017) 1766). Band gap engineering of multi-junction solar cells: effects of series resistances and solar concentration. *Sci. Rep.* 7: 1–9.

63 Mathews, I., O'Mahony, D., Corbett, B., and Morrison, A.P. (2012). Theoretical performance of multi-junction solar cells combining III-V and Si materials. *Opt. Express* 20 (S5): A754–A764.

64 Jia, J., Seitz, L.C., Benck, J.D. et al. (2016). Solar water splitting by photovoltaic-electrolysis with a solar-to-hydrogen efficiency over 30%. *Nat. Commun.* 7: 13237.

65 Cheng, W.-H., Richter, M.H., May, M.M. et al. (2018). Monolithic photoelectrochemical device for direct water splitting with 19% efficiency. *ACS Energy Lett.* 3: 1795–1800.

66 Verlage, E., Hu, S., Liu, R. et al. (2015). A monolithically integrated, intrinsically safe, 10% efficient, solar-driven water-splitting system based on active, stable earth-abundant electrocatalysts in conjunction with tandem III–V light absorbers protected by amorphous TiO_2 films. *Energy Environ. Sci.* 8: 3166–3172.

67 Sun, K., Liu, R., Chen, Y. et al. (2016). A stabilized, intrinsically safe, 10% efficient, solar-driven water-splitting cell incorporating earth-abundant electrocatalysts with steady-state pH gradients and product separation enabled by a bipolar membrane. *Adv. Energy Mater.* 6: 1600379.

68 Khan, M.A., Al-Shankiti, I., Ziani, A. et al. (2020). A stable integrated photoelectrochemical reactor for H_2 production from water attains a solar-to-hydrogen efficiency of 18% at 15 suns and 13% at 207 suns. *Angew. Chem.* 59: 14802–14808.

69 Mudiyanselage, K., Nadeem, M.A., Raboui, H.A., and Idriss, H. (2020). Growth, and characterization, and stability testing of epitaxial MgO(100) on GaAs(100). *Surf. Sci.* 669: 121625.

70 Kornblum, L., Fenning, D.P., Faucher, J. et al. (2017). Solar hydrogen production using epitaxial $SrTiO_3$ on a GaAs photovoltaic. *Energy Environ. Sci.* 10: 377.

71 Bamwenda, G.R., Tsubota, S., Nakamura, T., and Haruta, M. (1995). Photoassisted hydrogen production from a water-ethanol solution: a comparison of activities of Au-TiO_2 and Pt-TiO_2. *J. Photochem. Photobiol. A* 89: 177–189.

72 Berr, M.J., Schweinberger, F.F., Döblinger, M. et al. (2012). Size-selected subnanometer cluster catalysts on semiconductor nanocrystal films for atomic scale insight into photocatalysis. *Nano Lett.* 12: 5903–5906.

73 Katsiev, K., Harrison, G., Thornton, G., and Idriss, H. (2019). Gold cluster coverage effect on H_2 production over rutile TiO_2(110). *ACS Catal.* 9: 8294–8305.

74 Bashir, S.M., Al-Oufi, M., Al-Hakami, M. et al. (2020). Comparison between the performance of high concentrated and non-concentrated PV-cells for hydrogen production using PEM water electrolyzers. *Sol. Energy* 205: 461–464.

75 Khan, M.A., Al-Shankiti, I., Ziani, A., and Idriss, H. (2021). Demonstration of 28% solar to hydrogen efficiency and evaluation of its economic importance. *Sustainable Energy Fuel* 5: 1085–1094.

76 Burg, B.R., Selviaridis, A., Paredes, S., and Michel, B. (2014). Ecological and economical advantages of efficient solar systems. *AIP Conf. Proc.* 1616: 317.

77 Burg, B.R., Ruch, P., Paredes, S., and Michel, B. (2015). Placement and efficiency effects on radiative forcing of solar installations. *AIP Conf. Proc.* 1679: 090001.

78 Fthenakis, V.M. and Kim, H.C. (2011). Photovoltaics: life-cycle analyses. *Sol. Energy* 85: 1609–1628.

79 Fthenakis, V.M. and Kim, H.C. (2021). Life cycle assessment of high-concentration photovoltaic systems. *Prog. Photovoltaics* 21: 379–388.

7

Photocatalytic Hydrogen Generation by Metal–Organic Frameworks

Josep Albero and Hermenegildo García

Instituto Universitario de Tecnología Química (CSIC-UPV), Universitat Politècnica de València, Avda. de los Narajos s/n, 46022 Valencia, Spain

7.1 Introduction

Due to the massive use of fossil fuels as a primary energy source, there has been a vast amount of CO_2 emissions into the atmosphere in the order of 30 gigatons per year. Periodic measurements of CO_2 concentration in air have shown a continuous increase from initial values below 300 ppm in the mid-fifties of the twentieth century to the current percentages above 400 ppm [1] Although, CO_2 was initially considered as an innocuous gas with little negative impact on the environment, detailed studies on atmospheric chemistry have convincingly shown that CO_2 and other gases absorbed in the infrared region are responsible for the so-called greenhouse effect [2, 3]. An obvious consequence of infrared radiation adsorption by CO_2, one of the main contributors of the greenhouse effect, is global Earth warming, with models predicting up to a 3 °C increase in the "average" global temperature of the planet and its corresponding influence on the climate [4]. These scientific evidences have led the international community to consider alternative sources to fossil fuels to provide the energy of the future.

In this context of revolutionary times in the supply of energy for industry, transportation, and domestic use, H_2 is considered an ideal energy vector for many applications [5, 6]. However, full implementation of the H_2 technology requires further scientific development regarding its production, storage, and use. Scheme 7.1 summarizes some key points that have been identified as bottle necks limiting full implementation of green H_2.

By the term green H_2 it means H_2 that has been obtained without a CO_2 foot-print. As indicated in Scheme 7.1, while H_2 is currently produced in massive amounts from hydrocarbons by steam reforming and used in many applications going from ammonia production, hydrocracking, methanol synthesis to the microchip industry and metallurgy, the process of gray hydrogen production emits CO_2 due to the oxidation of carbon atoms in the hydrocarbon [7, 8]. Therefore, new processes to produce H_2 have to be developed.

Photocatalytic Hydrogen Production for Sustainable Energy, First Edition. Edited by Alberto Puga.

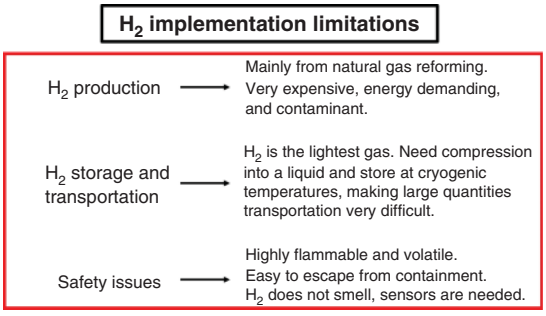

Scheme 7.1 Summary of the main drawbacks of H_2 as fuel.

To obtain green H_2, water is the evident feedstock. H_2 evolution from water requires a high energy input and can be achieved by thermal water splitting at temperatures above 1000 °C, electrochemically, or by the use of other primary, green energy sources [9]. The sunlight that has been responsible for the appearance of life on Earth is the greenest and abundant primary energy source. While sunlight can be used directly for thermosolar water splitting, the process requires a large capital investment for heliostatic mirrors, solar furnaces, and solar farms. This high investment limits the applicability of thermosolar H_2 production to large facilities in which large quantities of H_2 should be produced to make the process economically viable. Centralized H_2 production poses, however, the problem of H_2 transportation (Scheme 7.1). Since H_2 is a permanent gas and very difficult to pass into a liquid state, H_2 transportation to the consumption site can only be done at a reasonable cost through pipelines employing similar infrastructure as natural gas. In this context, it would be much more advisable to develop alternative technologies that could be applicable to remote places not connected to pipeline networks. This delocalized H_2 production is in principle very suited to the use of solar light as primary energy, since sunlight is a low power energy (1000 W m^{-2}) and, therefore, is more adequate for the production of small amounts of H_2 in different places. In this context, "photocatalysis" could become a competitive technology. Photocatalysis aims to mimic natural photosynthesis by green plants in which sunlight is converted into chemical energy in the form of glucose and ATP. In the present case, the aim of the photocatalytic process would be the production of H_2 from water.

7.2 Photocatalysis

The term catalysis was coined in the nineteenth century by Jöns Berzelius to denote materials not apparently involved in a chemical reaction, but able to promote and make feasible chemical processes by increasing their reaction rates [10]. In classical catalysis, the energy used to promote a reaction by accelerating its rate is heat. In comparison, the energy employed to activate a chemical reaction in photocatalysis is light. Solar photocatalysis refers to the case in which the light employed in the process is natural sunlight. Compared to artificial light from most common lamps,

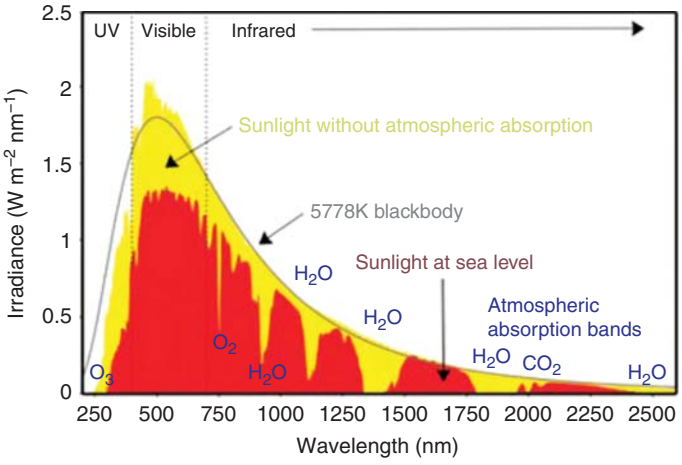

Figure 7.1 Spectrum of the incoming solar electromagnetic radiation before and after being filtered by the Earth's atmosphere. Source: Singh et al. [11]/With Permission of Elsevier.

natural sunlight has a characteristic spectral emission at the Earth's surface and much lesser intensity. Figure 7.1 shows a standardized emission spectrum of solar light after having been filtered by the planet's atmosphere.

In photocatalysis, the reaction is triggered by light absorption on a material acting as a catalyst. Therefore, a photocatalyst shares with catalysts common features like high surface area, substrate adsorption properties, and the presence of active sites. But in addition, photocatalysts should have specific features that include light absorption and an efficient mechanism through which the absorbed energy of a photon is converted into chemical energy. Scheme 7.2 illustrates the specific features that are wanted in a photocatalyst.

Heterogeneous photocatalysts features

- High surface area
- Single site structure
- Light harvesting in the solar spectrum
- Efficient charge separation
- Long-lived charge carriers
- High charge carrier mobility
- Selectivity towards target product

Scheme 7.2 Summary of the main features wanted in a heterogeneous photocatalysts.

The field of photocatalysis started with the seminal discovery by Fujishima and Honda that upon illumination with UV light TiO_2 electrodes submitted to an applied bias voltage, they were able to generate H_2 from water [12]. Photocatalysis developed in the eighties of last century together with a deep understanding of organic photochemistry. In initial stages, photocatalysis was focused on environmental remediation due to the ability of TiO_2 and other photocatalysts in contact with air and

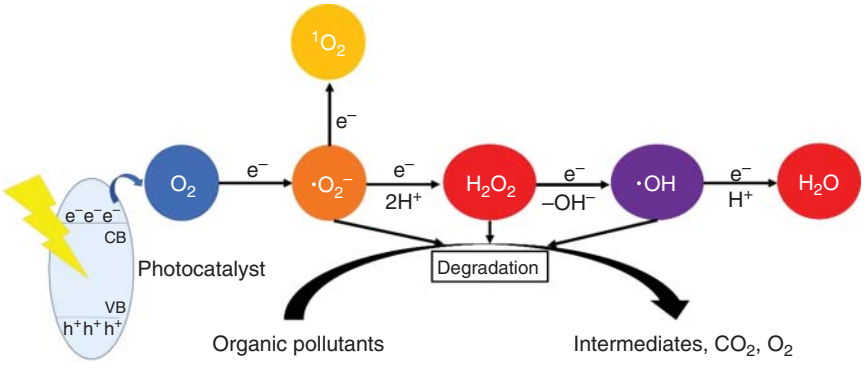

Scheme 7.3 Schematic illustration of the photocatalytic generation of reactive oxygen species that are able to promote aerobic pollutant degradation.

humidity to generate reactive oxygen species [13]. Scheme 7.3 illustrates the process of reactive oxygen species generation and their general activity to degrade organic molecules and toxic oxidized and reduced metal ions. Photocatalysis has shown general applicability for the treatment of air and polluted water containing a moderate pollutant concentration in the range of 1 to 10 ppm [14].

As the energy crisis was evolving at the beginning of the twentieth century, the target of photocatalysis moved from environmental remediation to provide alternative green and sustainable fuels by using solar light. Since fuels are supposed to deliver energy upon reaction with atmospheric oxygen, most of the fuels are reduced chemical compounds. Scheme 7.4 illustrates common solar fuels with an indication of the advantages and disadvantages and a summary of the current state of the art of their production by photocatalysis. As it can be seen in this scheme, H_2 is the solar fuel obtained with higher efficiency by photocatalysis. This efficiency is, however, still far from commercial application. To be economically competitive, H_2 obtained by photocatalysis has to achieve certain milestones regarding efficiency in the conversion of solar energy into hydrogen as well as photocatalyst durability and cost.

Regarding the efficiency in the conversion of sunlight into H_2, the current target values have been proposed following the successful performance of

Advantages	Solar fuels	Disadvantages
• Carbon-neutral energy source. • Reduced dependence on foreign oil and fossil fuels • Solar energy storage in chemical compounds	• H_2 • CH_4, CH_3OH, CO, etc. • Biomass	• High production cost • Low energy conversion rate

Scheme 7.4 Summary of the most common solar fuels and their advantages and disadvantages.

photovoltaic devices. As it will be commented later, photocatalysis shares many common elementary steps with photovoltaics. In a photovoltaic device, the energy of the photon is converted into electrical current at a given voltage. In most common cases, in photocatalysis, the photogenerated electrons, observed in photovoltaics, are used in the material to trigger a chemical reaction. Photovoltaics have succeeded in reaching the market with estimated solar-to-current efficiencies of about 20%. In photocatalysis, considering the low maturity of the technology, the target is to reach about 5% of solar light energy conversion into the water splitting reaction providing H_2. This 5% efficiency is also similar to the efficiency of natural photosynthesis, with remarkable differences regarding the starting materials and final products, as well as the much higher complexity of the biological machinery involved in the natural process.

Besides the target of 5% conversion, other economic considerations refer to the cost of the photocatalyst and the time that can be operated at high efficiency. A reasonable target would be a photocatalyst operating for one year (about 5000 hours) or longer and at a reasonable cost of 50 €/kg or lower.

Other issues are related to the quality of the water that should be employed in the process to avoid photocatalyst deactivation. The next section will discuss about possible photocatalysts for H_2 generation.

7.3 Photocatalysts

TiO_2 is by far the most widely used photocatalyst for H_2 generation. TiO_2 meets many desirable properties, such as abundance, low toxicity, affordable prices, and high chemical stability. In addition, TiO_2 shows high efficiency for H_2 evolution from water upon irradiation in the UV region. Unfortunately, as shown in Figure 7.1, natural sunlight does not contain radiation of the wavelength required to excite TiO_2. TiO_2, being a wide bandgap semiconductor (3.2 eV for the anatase phase), does not exhibit any photo-response under solar-light irradiation, for which the highest wavelength energy is about 3.1 eV going up to 1.5 eV. This lack of response of TiO_2 in the visible region has triggered intense research aimed at modification of TiO_2 by introducing mid-gap states to make possible the photo-response of modified TiO_2 in the visible region. Scheme 7.5 summarizes different strategies that have been reported to introduce visible light response in TiO_2.

Besides TiO_2, other inorganic semiconductors having a wide or moderate bandgap have also been tested for H_2 production. The list includes metal oxides and oxoanions, such as ZnO, Cu_2O, Fe_2O_3, WO_3, and $BiVO_4$, among others [15]. The overall conclusion is that these wide or moderate bandgap semiconductors do not exhibit significant advantages over the use of TiO_2 and much improvement is still needed to develop a suitable photocatalyst. The band alignment and suitable methods for band engineering to adapt the semiconductors to overall water splitting have become very difficult to achieve using these inorganic materials. Since overall water splitting is composed of two semi-reactions, namely hydrogen evolution reaction (HER) and oxygen evolution reaction (OER), each of them taking place

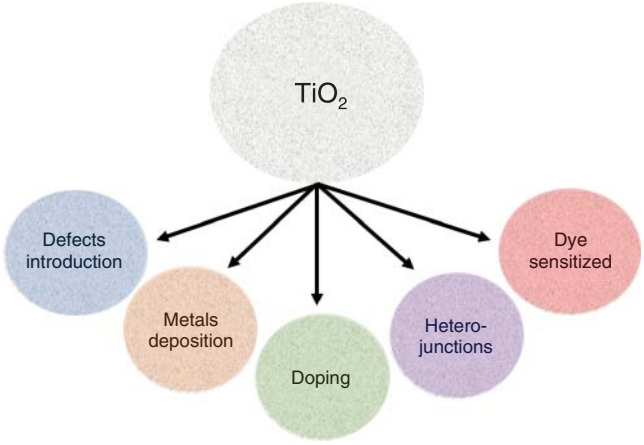

Scheme 7.5 Typical strategies to enhance TiO_2 light harvesting in the visible region.

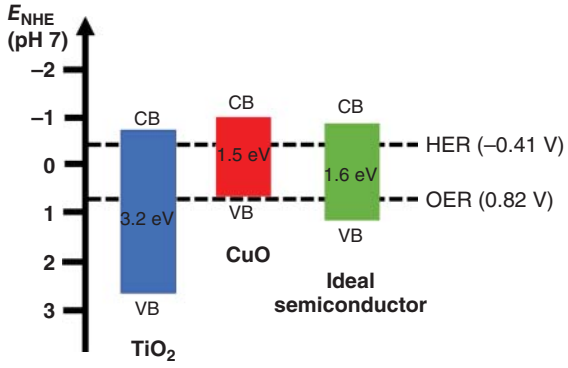

Scheme 7.6 Illustration of the HER and OER redox potentials at pH 7 and TiO_2, CuO, and ideal semiconductor band alignment.

below or above a certain potential depending on the pH, the conduction and valence band (CB and VB, respectively) of the semiconductor have to meet the required thermodynamic values. Scheme 7.6 depicts the redox potential for HER and OER and optimal alignment of CB and VB for overall water splitting at neutral pH. The ideal band alignment of semiconductors includes an overpotential with respect to the thermodynamic value to make the process kinetically possible at noticeable reaction rates.

Many other types of semiconductors have also been tested for overall water splitting and HER in the presence of sacrificial electron donors, but the previously commented target in the area regarding efficiency in solar energy to hydrogen conversion has not yet been achieved. Some of these photocatalysts have been summarized in Figure 7.2, including metal sulfides, nitrides, and phosphides as well as nonmetallic semiconductors, like graphitic carbon nitride and doped-graphenes. In all these cases, the presence of co-catalysts and/or the combination of two or

Photocatalysts

- Metal oxides: ZnO, CuO, WO_3, Fe_2O_3, NiO, $SrTiO_3$, $BiVO_4$, etc.
- Metal chalcogenides: CdSe, CdS, MoS_2, ZnS, etc.
- Metal nitrides: TaON, Ta_3N_5, BN, etc.
- Metal phosphides: Ni_2P, CoP, FeP, Cu_3P, Fe_2P, FeNiP, NiCoP, etc.
- Metal-free: g-C_3N_4, SiC, defective graphenes, organic polymers, etc.

Figure 7.2 Summary of the main materials employed for photocatalytic HER.

more semiconductors (heterojunctions) have appeared as generally valid strategies to enhance H_2 generation under photocatalyst irradiation.

7.4 Metal–Organic Frameworks (MOFs)

In the previous context of very difficult modification of inorganic oxides and semiconductors, in general, to align and adjust the valence and CB energies, one class of material that has shown a large degree of flexibility in composition and structure are MOFs. MOFs are porous crystalline solids whose structure is established by Coulombic and coordinative interactions between rigid bi- or multimodal-organic linkers and inorganic nodes constituted by one metal ion or a cluster of a few metal ions with or without oxo- or hydroxy-groups [16]. The directionality of the metal–ligand coordination bonds is responsible for the generation of an open lattice having a considerable proportion of empty space that can be as large as 50% of the total unit cell volume. In fact, MOFs are currently the record materials with the lowest framework density, meaning that the mass of the unit cell divided by its volume is the lowest among all reported materials. Framework density is a measure of how porous and empty a lattice is.

One of the most important features of MOFs is the flexibility in the composition that basically parallels the wide range of metal complexes that are known in chemistry. The number of MOFs structures known by now is over 90 000 and this number is continuously growing considering the intense research focused on the synthesis of new MOFs. It has been reported that MOFs of almost all transition metals, rare earth metals, as well as some alkaline earth and main group metals [17].

Regarding organic ligands, aromatic polycarboxylates such as terephthalate and 1,2,3-benzenetricarboxylate (BTC) are the most widely used for the synthesis of MOFs. Besides aromatic polycarboxylates, organic ligands having two or more N and P atoms have also been used. Particularly relevant is the case of 2-methylimidazolate, which is the common linker of the zeolitic imidazole framework (ZIF) series. Another feature of MOFs is the possibility to predict beforehand the resulting structure based on the consideration of the directionality of organic ligand binding and the structure of the inorganic nodes and their coordination geometry. A typical inorganic node is constituted by three metal cations sharing a central μ_3 oxygen atom, such as Cr_3-μ_3O that is present in MIL-100 and MIL-101 materials. The Cr_3-μ_3O cluster has seven positive charges that are compensated

by six carboxylate groups of two BTC (MIL100) or three terephthalates plus an additional anion (OH^- or F^-) from the synthesis. Other important metallic cluster that is common in most zirconium MOFs is $Zr_6O_4(OH_4)$. This cluster has an octahedral geometry in which Zr^{4+} ions are located at each of the six corners, and the eight octahedral faces have in the center an oxygen atom or an OH group in alternate positions. These clusters have an excess of 12 positive charges that, in the case of UiO-66 MOFs, are compensated by the Coulombic charge of twelve carboxylate groups of six terephthalates. Scheme 7.7 summarizes some of the advantages and disadvantages of MOF as compared to other porous materials.

Scheme 7.7 Some of the most relevant advantages and disadvantages of MOFs.

One major point of concern in MOFs is their poor structural stability upon heating or chemical stress. Due to the organic components, MOFs have a limited thermal stability, generally below 400 °C. This temperature is relatively low in comparison to other fully inorganic porous materials such as zeolites. Besides thermal stability and due to the properties of the coordinative bonds, the structure of MOFs can also be deteriorated in the presence of nucleophiles that can compete with carboxylate as ligands of the metallic clusters. For this reason, the stability of some MOFs in water at high temperature or at room temperature under extreme pH values is limited, and the solid may undergo collapse or dissolution under these conditions. Other solvents that can also solvate metal ions can behave similarly. One particular example of MOF structural instability is the case of MOF-5, one of the first MOFs ever prepared, initially reported by Yaghi [18]. Upon storage after preparation, MOF-5 changes the structure to other yet unknown material denoted as MOF-5′. Also, MOF-5′ is unstable in water and many other solvents. For all these reasons MOFs have gained a reputation as very unstable materials. While this instability can be found in many other cases due to the large diversity of compositions and structures, there are some other MOFs that have shown remarkable structural and chemical stability. This is the case of UiO-66 that can be heated above 450 °C without structural collapse [19]. It should be noted that this temperature is much higher than most of the temperatures employed in chemical reactions. In addition, these and other MOFs, particularly those of tetravalent or trivalent cations, are stable in very aggressive and corrosive media. This is the case not only of UiO-66, but also of MIL-100(Cr) and MIL-101(Cr) [20]. In the last case, the terephthalate ring can even be sulfonated using corrosive chlorosulfonic acid as a reagent in a post-synthetic treatment without damaging the crystal structure [21]. Figure 7.3 illustrates the structure of MIP-177, another Ti MOF with a remarkable thermal and chemical stability, showing the geometry of the metal node $Ti_{12}O_{15}$, and how its coordination with 5,5′-methylenediisophthalic acid (mdip) linker defines a network with monodirectional parallel hexagonal channels [22].

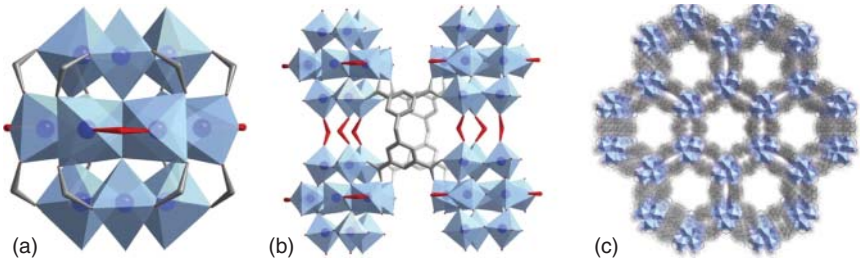

Figure 7.3 Schematic representation of (a) $Ti_{12}O_{15}$ cluster with 12 carboxylate groups from mdip linkers (in gray) and terminal formate groups (in red). (b) Adjacent $Ti_{12}O_{15}$ clusters with terminal and bridging formates (in red) connected by mdip linkers (in gray). (c) Nano-sized channels with a free diameter of 1.1 nm when viewed along the *c*-axis. Source: Wang et al. [22]/Springer Nature/CC BY 4.0.

A final consideration regarding stability is photostability, as many organic molecules undergo transformation upon exposure to light. The lack of photochemical stability is considered one of the major drawbacks of using organic molecules in photocatalysis, and since MOFs contain organic linkers, this point should be seriously addressed. For instance, aromatic carboxylic acids and carboxylates can undergo photodecarboxylation, evolving CO_2 and rendering the aromatic hydrocarbons. Since there are many carboxylate MOFs, the possibility to undergo photodecarboxylation has to be seriously considered. Obviously, the issue of photostability appears as the irradiation time increases for a period of times of months or longer. In fact, photodecarboxylation was observed to occur for several carboxylate MOF in a relative degree that depends on the composition of the metal node and the structure. Regarding photostability, it should be however commented that UV radiation is more damaging due to its higher energy than visible light. In addition, fast deactivation of excited states of organic linkers by efficient quenching also should diminish the tendency of decomposition.

7.5 MOFs as Photocatalysts

As commented in a previous section, it has been very difficult to tune and align the bandgap of TiO_2 and other inorganic metal oxides, the current situation being still unsatisfactory in spite of the considerable research in this area. In contrast, organic molecules can be easily modified and tuned to adapt their HOMO–LUMO bandgap for visible light absorption. By applying concepts of organic chemistry related to light absorption by chromophores and bond conjugation, it is possible to start with a parent molecule and introduce substituents that shift its light absorption toward the wanted wavelength region. One simple case is how the optical absorption spectrum of aromatic rings can be shifted by substituents that play a bathochromic (shift of the absorption λ_{max} to the red), auxochromic (intensification of molar absorption coefficient), and hypsochromic (shift of the absorption λ_{max} to the blue) effects. For instance, substitution of a benzene ring with an amino group causes,

according to Woodward–Hoffman rules, a shift in the absorption wavelength maximum of about 30 nm to the red (bathochromic group) [23]. Since MOFs combine organic and inorganic components, they can be easily modified by using as ligand an organic chromophore and, moreover, this organic chromophore can also be modified by appropriate substitution. Light absorption is the first pre-requisite in photocatalysis, as it has been commented before, and therefore, there are clear rules on how to modify the organic linkers to adapt them for solar light absorption and the positioning of the HOMO/LUMO frontier orbitals. Among the various MOFs containing chromophores as linkers, those having condensed polycyclic aromatic rings such as tetraphenyl porphyrin (PCN-222), pyrenyl (NU-1000), or even anthracenyl (MOF-74) or naphthyl (MOF-205) rings are very appropriate as starting chromophores for further tuning of their light absorption. Figure 7.4 shows some of the organic ligand structures with interesting optical absorption spectra regarding visible light photo-response.

At this point, it should be mentioned that since many MOFs contain transition metal ions with an incomplete d electron level, they can also exhibit light absorption

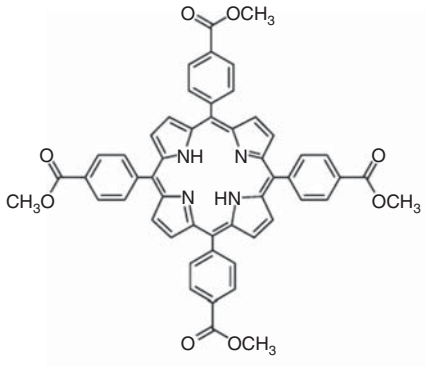

5,10,15,20-Tetrakis(4-methoxycarbonylphenyl)porphyrin

(a)

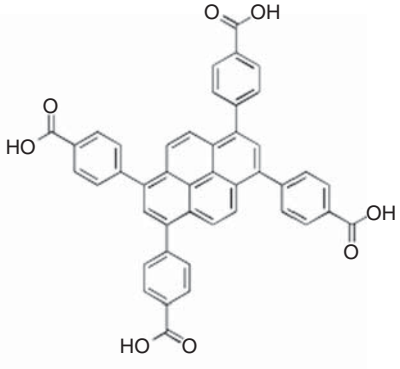

1,3,6,8-tetrakis(*p*-benzoic acid)pyrene

(b)

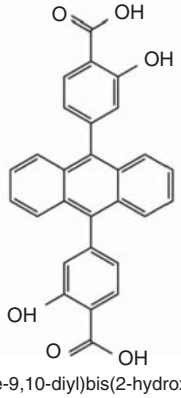

(c) 4,4‾-(anthracene-9,10-diyl)bis(2-hydroxybenzoic acid)

Figure 7.4 Chemical structure of the organic ligands of PCN-222 ligand (a), NU-1000 (b), and MOF-74 (c).

in the visible due to d–d electronic transitions. This is the case, for instance, of many MOFs containing Cu, Fe, Cr, or V. However, d–d transitions are, in general, not useful in photocatalysis since they are localized in a cation or atom and undergo very prompt relaxation to the initial ground state. As indicated earlier, photocatalysis requires charge separation, and d–d transitions do not allow, in general, charge separation. This point is, however, poorly investigated and certainly deserves much deeper attention in the future to see if somehow open-shell transition metal ions can be useful in photocatalysis. Scheme 7.8 illustrates why d–d transitions, even if they introduce coloration in the material are useless from the photocatalytic point of view, due to their failure to generate a charge separation state. For this reason, most of the most active MOF photocatalysts are based on transition metal ions having d^0 or d^{10} electronic configuration, such as those based on $Zr^{4+}(d^0)$, $Ti^{4+}(d^0)$, or $Zn^{2+}(d^{10})$, or $Cd^{2+}(d^{10})$.

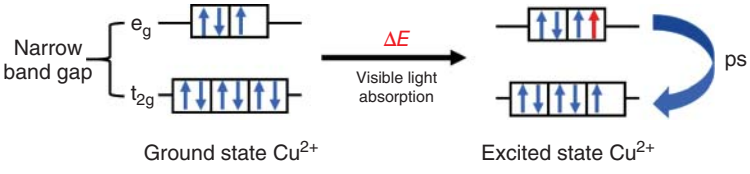

Scheme 7.8 Schematic illustration of the narrow bandgap in Cu^{2+} d ← d transitions indicating the fast recombination kinetics (in the picosecond time scale) of photoexcited electrons.

In this context, one seminal study by means of laser flash photolysis and transient absorption spectroscopy showed that upon excitation of the organic ligand, an electron transfer from the electron-rich ligand (consider that they are organic anions) to the electron-deficient metal node (consider that they are metal cations searching for electrons) can occur from the local ligand excited states (either singlet or triplet), giving rise to an efficient metal-to-ligand electron transition [24]. This type of ligand-to-metal charge transfer (LMCT) is well-known for molecular metal complexes, and MOFs will be a particular case in which the solid contains an infinite number of these metal complexes in a rigid environment defining an empty space. Scheme 7.9 illustrates the photochemical event after excitation of the organic ligand in a MOF. Similar electron transfer from the electronically excited ligand to metal-cation also happened in aqueous solution of the ligands in the presence of dissolved metal cations, but holding tight the linker and the metal ions with a defined spatial orientation in a rigid lattice favors considerably the efficiency of these electron transfer processes. Photoinduced electrons transfer can be considered as a charge separated state and after this event, several pathways can occur. One of them would be the reverse electron transfer, similar to the charge recombination event in semiconductors. Other pathway can be the migration of the charge carriers to neighboring linkers or metal nodes in the structure. This charge migration will result in a much longer lifetime of the charge separation, since annihilation by recombination becomes much less probable when the distance between electrons and holes increases. This charge migration is related to the semiconducting properties of a

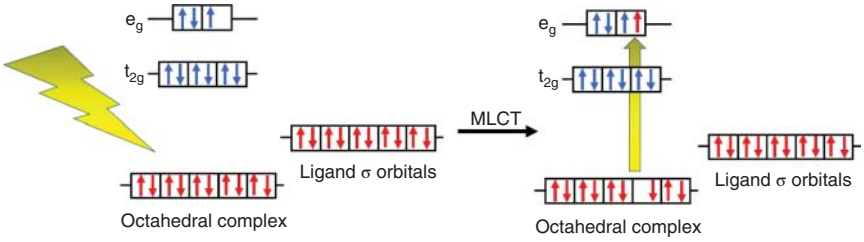

Scheme 7.9 Photoinduced ligand to metal charge transfer in MOFs.

material that requires a fast charge migration rate. Evidence by transient microwave spectroscopy monitoring the increase of electrical conductivity upon irradiation has shown that charge migration in MOFs is in general slower than in inorganic semiconductors. This slow charge migration has led to propose that the main migration mechanism in MOFs is by electron hopping between neighboring isoergonic sites [25].

In principle, slow charge migration, much slower than typical semiconductors in which one charge carrier moves fast, should be unfavorable from the point of view of the photocatalysis considering that substrates are adsorbed on the particle surface. In typical semiconductors, upon photoinduced charge separation, fast recombination of the geminate electron/hole pair prevails unless one of the charge carriers moves fast. However, in the case of the MOFs, it has to be considered that the special structure of these materials with positive metal ions and negative linkers favors charge separation and even geminate electron/hole can live much longer than typical lifetimes in semiconductors. This is just because MOFs already contain separated charges in their structure.

An additional point that has to be taken into account is porosity that makes accessible to substrates most of the internal void space of the particle. Thus, one can imagine that at the point where charge separation occurs, even in the interior of the MOF particle, substrates can quench and interact with these charge carriers. This is different than, for instance, nonporous TiO_2 particles, in which charge carriers must necessarily migrate to the external surface of the particle to become available for photocatalytic reactions. In the process of migration to the surface, random recombination events can also occur. However, it has to be said that certain indirect data suggest that also in the case of MOFs the external surface contributes more than expected to the photocatalytic process. For instance, comparing the photocatalytic degradation activity of MOF-5 for phenol and 2,6-di-*tert*-butylphenol (DTBP). DTBP is too large to be able to diffuse inside the MOF-5 pores. Therefore, the DTBP compound can only react on the external MOF-5 surface. However, DTBP becomes degraded photocatalytically much faster than phenol, which preferentially probes the internal surface of MOF-5 [26].

In the next sections, we will specifically discuss the use of MOFs as solar photocatalysts for H_2 generation, which is one of the most intensively researched photocatalytic reactions by MOFs.

7.6 MOFs as Photocatalysts for H_2 Generation

In the event of photon absorption and subsequent electron transfer, a pair electron/hole is generated. The electron can be consumed by protons or water, evolving H_2. In order for the process to be sustained with subsequent turnovers and closing catalytic cycles, the hole has also to be consumed at the same rate.

In the simplest approach, if H_2 is the target compound to be obtained, the rate of hole consumption is wanted to be as high as possible. In that way, the rate limiting step would be electron consumption, and H_2 formation would occur at the highest possible rate. These conditions for H_2 generation required then the presence of a good electron donor, whose role is the fast quenching of holes. Typical electron donors are organic compounds that have low oxidation potential, lower than that required for H_2O oxidation at neutral pH ($E_0^{Ph7} = +0.82\,V$). For this reason, the most typical electron donors are tertiary amines such as triethylamine (TEA) or triethanolamine (TEOA). The latter is preferred due to the less unpleasant smell found in amines due to its lesser volatility. Primary and secondary amines are more reactive than tertiary amines, and caution should be taken to confirm that MOF is stable in the presence of these tertiary amines. Since amines are good ligands of metal ions, they can compete with organic linkers and produce the partial or complete damage of the MOF structure. As previously commented, chemical stability is one of the major concerns that has to be addressed when using MOFs in catalysis. The problem of chemical stability is particularly relevant, since the proportion of the sacrificial amine used tends to be high. Other organic electron donors are alcohols, particularly ethanol and methanol. Although alcohols are worse electron donors than amines, they can also quench holes much faster than water. Scheme 7.10 illustrates the role of electron donors in H_2 generation.

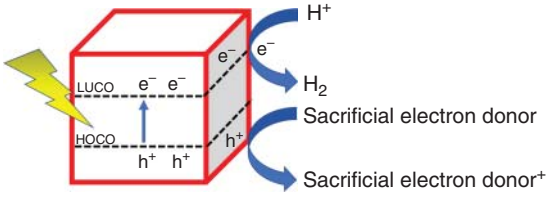

Scheme 7.10 Illustration of sacrificial electron donors in photocatalytic H_2 production.

It should be commented that when using electron donors, H_2 atoms can come from the decomposition of these sacrificial agents, even if water is the solvent. When the attention of the photocatalytic process is paid on the fate of the chemical compound used as a sacrificial electron donor, then the photocatalytic H_2 generation event is denoted as photoreforming since it parallels thermal catalytic processes in which H_2 is also formed from organic compounds. For instance, ethanol can become oxidized to acetaldehyde or acetic acid by simultaneously forming H_2. The process is summarized in Eqs. (7.1) and (7.2). Commenting on photoreforming, oxidation of

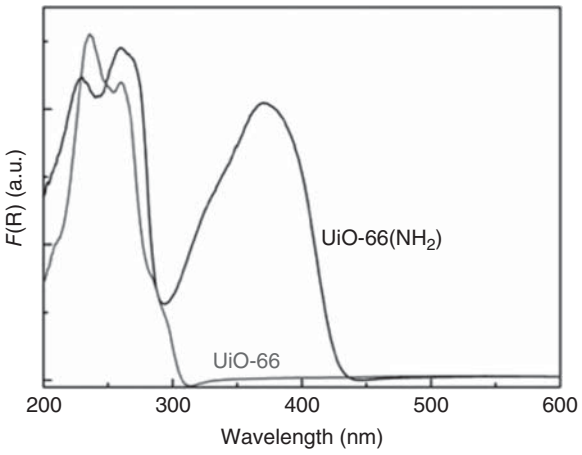

Figure 7.5 Diffuse reflectance UV–vis spectra of UiO-66 and UiO-66-NH_2. Source: Gomes et al. [27]/with permission of John Wiley & Sons.

benzyl alcohols to benzaldehydes and evolving simultaneously H_2 is one of the most studied photoreforming processes.

$$CH_3CH_2OH + {}^1/_2O_2 \rightarrow CH_3CHO + H_2O \tag{7.1}$$

$$CH_3CHO + {}^1/_2O_2 \rightarrow CH_3COOH \tag{7.2}$$

MOFs that have shown high activity in H_2 generation include UiO-66, MIL-100, and MIL-125, among others. In the first report of H_2 generation using MOFs from our group, it was shown that UiO-66 has poor photocatalytic activity under visible light irradiation, but *iso*-structural UiO-66 in which the linker contains an amino group significantly increases H_2 production in the presence of methanol upon visible-light irradiation [27]. Figure 7.5 summarizes the influence of the amino group on the photocatalytic process. As it can be seen in this figure, substitution of the benzyl ring by an amino group introduces a new electronic transition from the nitrogen lone pair to the antibonding π orbital, this electronic transition corresponding to a new absorption band with λ_{max} at 380 nm and extending into the visible region with onset beyond 400 nm. This new electronic $\pi^* \leftarrow$ n transition populates initially the antibonding π^* orbital of the aromatic ring, and subsequently the electron is transferred from the aminoterephthalate ligand to the $Zr_6O_4(OH_4)$ cluster, which is the site in which H_2 is supposed to evolve.

Photocatalysts can increase efficiency in different ways. Two of the most general ways are either by forming heterojunctions with other semiconductors or photocatalysts or by incorporating co-catalysts. Considering that charge separation produces electrons and holes, two co-catalysts, one for oxidation, and one for reduction, are in principle needed to accelerate the photocatalytic process. The most common photocatalyst for reductions, therefore, for the H_2 generation event are noble metals such as Pt, Rh, Au, Pd, but also Ni. Co-catalysts for oxidation include metal oxides such as RuO_2, MnO_2, and CuO_x. Among the various roles of co-catalysts, the most important ones are to store charge carriers and to promote the transfer of these charge carriers to the substrate.

In the particular case of H_2 generation, Pt nanoparticles act as a reservoir of electrons, and due to the high H_2 adsorption, these Pt nanoparticles transfer electrons to protons at a very high rate, favoring H_2 evolution. Also, in the case of MOFs, the presence of reduction co-catalysts has shown to increase the efficiency of the photocatalytic H_2 evolution. In general terms, the influence of co-catalysts in MOFs seems to be lower than in TiO_2 and other semiconductors. For instance, in the case of TiO_2, the position of Pt nanoparticles can increase the H_2 evolution rate by about two orders of magnitude, which is a remarkable enhancement. In the case of MOFs, the presence of co-catalysts typically increases the H_2 evolution rate by a factor of two, which is generally less than one order of magnitude. The lower influence of co-catalysts in the case of MOFs probably reflects the fact that these porous materials already contain transition metals at the nodes and that these metals can evolve H_2 much easily than TiO_2. For instance, in the previously commented case of UiO-66-NH_2, the Zr nodes containing hydroxyl-and oxo-groups can readily gain or lose one proton that can be converted into H_2 and, therefore, the influence of the presence of Pt is less relevant. Table 7.1 collects some of the MOFs that has been reported in the literature for H_2 generation as well as the sacrificial electron donors used, the nature of the co-catalyst and the production of H_2 that have been achieved. Considering the large number of studies on this H_2 evolution reaction in the presence of sacrificial reagents, Table 7.1 is by no means comprehensive and the reader could refer to the existing literature for a more exhaustive survey of MOFs, reagents, and conditions that have been tested as photocatalysts for H_2 evolution.

Table 7.1 Some relevant MOFs used as photocatalyst for HER in the presence of sacrificial electron donors.

Photocatalysts	H_2 production	Sacrificial agent	Co-catalyst	References
DLNU-M-CdS(H_2TD)	104.4 mmol g^{-1} in 4 h	TEOA	—	[28]
Pt@UiO-66-NH_2	257.38 μmol g^{-1}·h	TEOA	Pt nanoparticles	[29]
Co/NH_2-MIL-125(Ti)	0.8 h^{-1} TOF	TEA	Co cobaloxime	[30]
$Cd_{0.2}Zn_{0.8}S$@UiO-66-NH_2	5846.5 μmol g^{-1}·h	Na_2S/Na_2SO_3	$Cd_{0.2}Zn_{0.8}S$	[31]
Al-TCPP-Pt	35 h^{-1} TOF	TEOA	Pt single atom	[32]
Ni_2P@UiO-66-NH_2	378 μmol g^{-1}·h	Na_2SO_3	Ni_2P	[33]
1D Ti phosphonate-based MOF	2346 μmol g^{-1}·h	TEOA	—	[34]
MUV-10(Mn)	6500 μmol g^{-1} in 24 h	CH_3OH	—	[35]
Pt-MIL-125-$(SCH_3)_2$	3814 μmol g^{-1}·h	TEA	Pt	[36]
Cu_2O-MIL-125-NH_2	11 055.5 μmol g^{-1}·h	TEOA	Cu_2O	[37]

7.7 MOFs as Photocatalysts for Overall Water Splitting

Overall water splitting refers to the decomposition of H_2O into H_2 and O_2 in the corresponding stoichiometric amounts. Equations (7.3)–(7.5) illustrate the overall water splitting process that is the reverse of water formation. While in the previous section, when commenting on H_2 generation, we remarked the need of a sacrificial electron donor, the overall water splitting is a process running in the absence of any sacrificial agent. From the practical point of view, thinking about the feasibility of photocatalytic H_2 generation, sacrificial agents cannot be present since they are expensive chemicals that become necessarily degraded and decomposed when H_2 is generated.

$$\text{HER } 4H^+ + 4e^- \rightarrow 2H_2 \tag{7.3}$$

$$\text{OER } 2H_2O + 4h^+ \rightarrow O_2 + 4H^+ \tag{7.4}$$

$$\text{Overall } 2H_2O \rightarrow 2H_2 + O_2 \tag{7.5}$$

Overall water splitting is decomposed into two semi-reactions, one of them corresponding to H_2 generation (HER) as indicated in the previous section, but holes are consumed by water that should become oxidized to elemental oxygen (OER). The redox potential of the two semi-reactions depends on the pH of water. According to the Nerst equation (Eq. (7.6)), acid pH values favor H_2 production but make OER more difficult by increasing its oxidation potential. In contrast, basic pH values obviously disfavor H_2 evolution, but this condition is more favorable for the formation of O_2 by decreasing its oxidation potential. At this point, it should be reminded that the stability of MOFs under extreme pH conditions can be low, and it is more advisable to operate under neutral or quasi-neutral conditions. Scheme 7.11 illustrates the variation of the redox potential for H_2 and O_2 evolution at different pH.

$$E = E^0 - \frac{RT}{nF} \ln \frac{[\text{Ox}]}{[\text{Red}]} \tag{7.6}$$

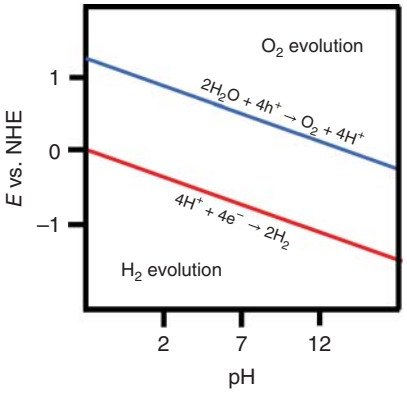

Scheme 7.11 Variation of water reduction and oxidation potentials as pH function.

As it can be seen in the diagram of Scheme 7.11, O_2 evolution is thermodynamically more demanding, requiring high oxidation potential at neutral or acid pH values than H_2 generation. For this reason, as commented in the previous section, sacrificial electron donors significantly increase H_2 evolution. In addition to thermodynamics consideration, also from the kinetic point of view, O_2 evolution reaction is more demanding and slower because it involves higher number of electrons and protons in the process. Kinetic reasons determine that an overpotential with respect to the thermodynamic values is necessary to observe overall water splitting at significant rates. As a rule of thumb, an overpotential of 0.3 V is necessary to overcome rate limitations.

Compared to H_2 generation in the presence of sacrificial electron donors and the previously commented kinetic limitations oxidation, co-catalysts are also needed to promote overall water splitting. One point that still needs to be addressed is how to locate the oxidation and reduction co-catalysts adequately in the lattice to avoid charge recombination and promote the oxidation and reduction steps of the overall water splitting [38].

In the current state of the art, it is important to comment that in comparison to the vast number of articles dealing with the use of MOFs for H_2 generation, the number of studies focusing on overall water splitting is much less, about 20 papers. It is clear that this number will experience dramatic growth in the very near future. The reason for this scarcity of studies on overall water splitting is not specific to MOFs, but common for other semiconductors and is the low rate of water oxidation, or even the insufficient oxidation potential of the VB maximum to promote this reaction. Not surprisingly, comparing the photocatalytic activity of a material for H_2 generation in the presence of sacrificial electron donors with the production of H_2 in overall water splitting notably decreases more than one order of magnitude. Even in some cases, the total absence of O_2 generation is observed. This situation has to be overcome by adequate band engineering of MOF materials that should locate VB maximum at oxidation potentials higher than +1 V vs. NHE without altering the CB potential minimum, which should be more negative than –0.6 V.

Probably the first report on overall water splitting appeared about four years ago and used a Ni complex as co-catalyst to favor overall water splitting [39]. Table 7.2 collects some of the MOFs that have been reported for overall water splitting as well as the reaction conditions, their productivity, and the stability of the materials. The next paragraphs intend to stress the flexibility that the MOF structure allows to further enhance the efficiency of photocatalytic overall water splitting.

Since MOFs are highly porous materials, co-catalysts can be located within the internal pores very near to the point in which charge separation occurs, thus, enhancing the photocatalytic activity, also for the particular case of photocatalytic overall water splitting. In one of the studies showing the influence of co-catalysts on the photocatalytic efficiency of simultaneous H_2 and O_2 evolution, it was observed that while the presence of a single co-catalysts increases the efficiency of overall water splitting in MIL-125(Ti)-NH_2, the presence simultaneously of two co-catalysts, for H_2 and O_2 evolution, respectively, increases the activity even

Table 7.2 Summary of some reported examples of MOF-based photocatalysts for overall water splitting including the light source conditions, productivity, and stability.

Photocatalysts	Reaction conditions	Photocatalytic activity	Stability	References
Al-ATA-Ni	300 W Xe lamp, 1 ml mg^{-1}	26.7 µmol g^{-1}·h H_2	2.5 h	[39]
Pt@NH_2-UiO-66@MnO_x	300 + UV arc lamp with a UV-cut off filter ($\lambda \geq 400$ nm)	20 µmol g^{-1}·h H_2 10 µmol g^{-1} h O_2	—	[40]
IEF-13	UV–vis 150 W Xe lamp	160 µmol g^{-1} H_2 46 µmol g^{-1} O_2	22 h	[41]
Pt and RuO_x, MIL-125(Ti)-NH_2	300 W Xenon lamp	218 and 85 µmol/ $g_{photocatalyst}$ at 24 h for H_2 and O_2, respectively	24 h	[42]
IEF-11	Simulated sunlight	672 µmol/$g_{catalyst}$ in 22 h of H_2	10 d	[43]
UiO-66(Zr/Ce/Ti)	Xenon lamp (150 mW cm^{-2})	230 and 110 µmol g^{-1} of H_2 and O_2, respectively, upon UV-light irradiation, and 210 and 70 µmol g^{-1} of H_2 and O_2, respectively, under visible-light irradiation	24 h	[44]
LP–MOFs assemblies	400 nm + 450 nm LEDs	836 µmol g^{-1} of H_2 and stoichiometric amounts of O_2	72 h	[45]
MIL-125(Ti)-CoPi-Pt	Xe lamp (300 W) 1 mg ml^{-1}	42 µl h^{-1} H_2 and 21 µl h^{-1} O_2	—	[46]

further [42]. However, as commented earlier, the effect of co-catalysts in MOFs for H_2 evolution is less than for other nonporous metal oxide semiconductors. In comparison, the influence of RuO_2 as an oxidation co-catalyst promoting O_2 evolution is larger. It was determined that co-catalysts can increase overall water splitting in MOFs by about one order of magnitude. With MIL-125(Ti)-NH_2 containing simultaneously both co-catalysts a productivity in overall water splitting using simulated sun light at 1 Sun power of about 200 µmol of H_2 perg was achieved at eight hours [42].

Besides co-catalysts and in line with the previously commented case of the influence of amino substitution at the linker, tuning metal nodes can be also a viable strategy to increase the photocatalytic overall water splitting efficiency. In one theoretical paper, Truhlar and coworkers, predicted that substitution of Zr^{4+} ions in UiO-66 by Ce^{4+} should modify the potential of the highest unoccupied crystal orbital (HOCO) and the lowest occupied crystal orbital (LUCO) [47]. In addition, although more difficult to predict, the kinetics of the generation of the charge separation state, depending particularly on the orbital overlap between organic linkers and metal nodes, should also favor photoinduced electron transfer

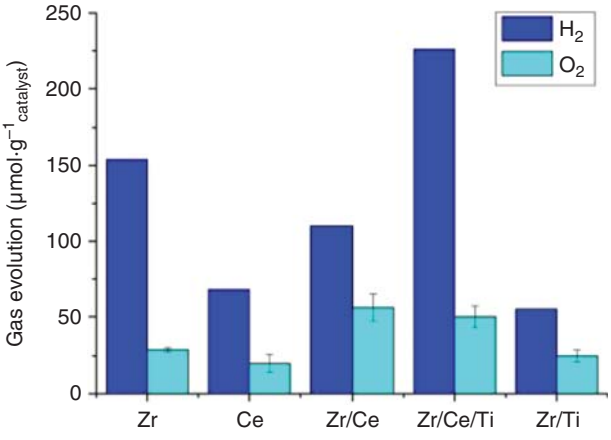

Figure 7.6 Photocatalytic gas evolution using different UiO-66 having as metal nodes a single metal (Zr or Ce) or a combination of two or three metals upon irradiation with UV–vis light. Source: Melillo et al. [44]/with permission of Elsevier.

over other deactivation pathways. These theoretical considerations led to the preparation of a series of bi- and trimetallic-UiO-66 materials in which one or more of the six Zr atoms on the $Zr_6(OH)_4O_4^{12+}$ nodes were replaced by Ce or Ti atoms. In agreement with the theoretical predictions the fully exchange UiO-66(Ce) has a strong absorption in the visible region, indicating that the bandgap has been significantly shorten compared to the pristine UiO-66(Zr) [44]. These bi- or trimetallic-UiO-66 exhibit enhanced photocatalytic activity for overall water splitting in the absence of any co-catalysts. The most active material was the one containing Zr, Ti, and Ce in the nodes, which exhibited a productivity under simulated sunlight at 1 Sun about 200 μmol g^{-1} at 24 hours [44]. Figure 7.6 shows the results reported for H_2 and O_2 evolution with the series of mixed metals UiO-66 studied. It would be interesting to combine the two approaches, i.e. node modification and the presence of suitable co-catalysts, particularly O_2 evolution co-catalysts.

It is evident that optimization of the photocatalytic activity of known materials has to be accompanied by the synthesis of other new MOFs with stronger absorption in the visible region. In this regard, porphyrin-based MOFs like, for instance, those of the series PCN are very promising. The porphyrin macroring allows to include a central metal in the porphyrin ring, without playing a structural role. This central metal can behave as a co-catalyst in the photocatalytic process. Recent data using a series of PCN-222(Zr) containing in the porphyrin ring Fe, Mn, Zn, and Co has shown that the central metal of the porphyrin ring plays a remarkable role in making possible overall water splitting [48]. Worth noting is that for some of the metals it was not possible to detect O_2, even using pure water without a sacrificial electron donor agent. This absence of oxygen detection indicates that some part of the photocatalytic system is undergoing oxidation, and probably this will result in the long term either in a decomposition of the MOF or in the observation of O_2 evolution after an induction period.

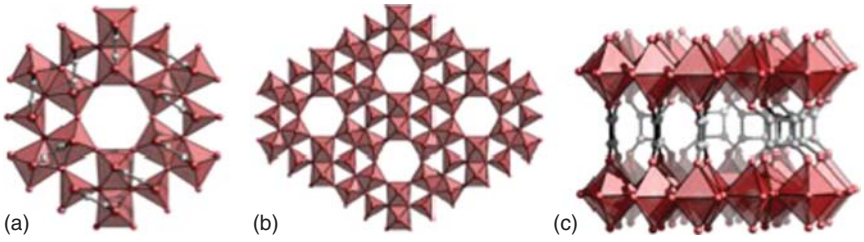

Figure 7.7 (a) IEF-11 structure, (b) Ti—O layer SBU, and (c) squarate linkers connecting the different Ti—O layers. Source: Salcedo et al. [43]/With permission of John Wiley & Sons.

In another example, the new MOF IEE-11(Ti) has shown very high activity for overall water splitting and very high photostability [43]. IEE-11 MOF contains Ti as nodal metal. Not surprisingly, in view of the photocatalytic activity of TiO_2 and other MOFs based on Ti, as in the case of MIL-125 and MIP-177, also IEF-11(Ti) exhibits photocatalytic activity. In IEEF-11, Ti^{4+} cations are octahedrally coordinated with oxygen sharing corners, forming like 2D layers of TiO_2. These TiO layers are held by squarate as pillars. Figure 7.7 illustrates the three different types of Ti coordination spheres present in IEF-11 and the position of squarate linkers perpendicular to the TiO layer. Squarate is a special case of non-benzenoid aromatic ring with a strong absorption in the visible at about 500 nm. Therefore, IEF-11(Ti) is suitable for visible light irradiation, thus being appropriate for solar light photocatalysis. In the absence of any co-catalysts or any other structural modification, IEF-11(Ti) gives a H_2 and O_2 productivity under simulated sunlight irradiation of about 672 $\mu mol/g_{catalyst}$ in 22 hours, which is probably the current record for photocatalytic overall water splitting. The IEF-11 structure allows again to propose an increase in efficiency through the design of related squarate linkers, doping of the metal layers, and the deposition of suitable co-catalysts [43].

In addition to photocatalytic systems based exclusively on MOFs and considering that heterojunction is a well-established methodology to enhance photocatalytic efficiency, it can also be foreseen that heterojunctions based on MOFs as components will also be developed in the future for photocatalytic overall water splitting. Taking into account that efficient heterojunctions require a high interfacial contact between the components, it appears that 2D MOFs or MOF with special morphology exposing a large surface area can be in principle more suitable in this strategy. This field of 2D MOFs with high aspect ratio and nanometric lateral dimensions will certainly grow in the near future and has promising applications in photocatalysis, particularly for establishing heterojunctions with other 2D materials.

7.8 Conclusions

This chapter has shown that MOFs can be considered as bridging the gap between inorganic semiconductors, which are structurally robust but difficult to modify, and organic molecules that are less photostable, but are simpler to be synthetized with

appropriate functionalization to maximize solar light absorption. In addition, MOFs have other positive features such as large surface area and high porosity, as well as synthesis by design and a wide range of chemical compositions that expand to almost all transition, rare earth, and main group metals.

It has been stressed that positioning of the organic ligand in intimate contact with metal ions, similar to metallic complexes, is very appropriate to trigger photoinduced electron transfer in an analogous way as it was already known for molecular metal complexes. This charge transfer is also favored by the Coulombic charges of electron-rich organic ligands and electron-deficient metal cations having empty orbitals.

An overall view of the current state of the art has shown that MOFs have gained a consolidated position as photocatalysts and that H_2 evolution in the presence of sacrificial electron donors has been one of the preferred photocatalytic reactions that have been evaluated for most of the MOFs. Simple rules such as adequate substitution of the organic linker, and incorporation of co-catalysts, such as platinum, have proved to apply for H_2 evolution in MOFs as well as for other semiconductors.

In contrast, it seems that photocatalytic oxygen evolution, required to achieve overall water splitting and a much more demanding reaction, has been much less studied. For this reason, studies in photocatalytic overall water splitting have started only about four years ago. However, considering its practical importance, it is clear that the interest of using MOFs as photocatalysts for overall water splitting will grow.

At the moment, the values of photocatalytic efficiency of MOFs for overall water splitting are still far, orders of magnitude, below what is needed for a commercial application. Industrial processes of photocatalytic H_2 generation require materials at an affordable cost and free from critical metals, operating continuously for more than one year under ambient conditions. The target efficiency in the conversion of solar energy into H_2 is set at about 5%, and the current systems based on MOFs are at the moment probably below 0.1%. However, the considerable interest in the topic and the large research effort in the field, allows predicting that much progress will be achieved in a few years.

References

1 Friedlingstein, P., Jones, M.W., O'Sullivan, M. et al. (2021). Global carbon budget 2021. *Earth Syst. Sci. Data Discuss.* 2021: 1–191.

2 Ramanathan, V. (1998). Trace-gas greenhouse effect and global warming: underlying principles and outstanding issues volvo environmental prize lecture-1997. *Ambio* 27: 187–197.

3 Crowley, T.J. and Berner, R.A. (2001). CO_2 and climate change. *Science* 292: 870–872.

4 Tollefson, J. (2021). IPCC climate report: Earth is warmer than it's been in 125,000 years. *Nature* 596: 171–172.

5 Schlapbach, L. and Züttel, A. (2001). Hydrogen-storage materials for mobile applications. *Nature* 414: 353–358.

6 Martín-García, Í., Rosales-Asensio, E., González-Martínez, A. et al. (2020). Hydrogen as an energy vector to optimize the energy exploitation of a self-consumption solar photovoltaic facility in a dwelling house. *Energy Rep.* 6: 155–166.

7 Zhang, B., Zhang, S.-X., Yao, R. et al. (2021). Progress and prospects of hydrogen production: opportunities and challenges. *J. Electron. Sci. Technol.* 19: 100080.

8 Stoffels, M.A., Klauck, F.J.R., Hamadi, T. et al. (2020). Technology trends of catalysts in hydrogenation reactions: a patent landscape analysis. *Adv. Synth. Catal.* 362: 1258–1274.

9 Dincer, I. (2012). Green methods for hydrogen production. *Int. J. Hydrogen Energy* 37: 1954–1971.

10 Smith, J.K. (2002). History of catalysis. In: *Encyclopedia of Catalysis* (ed. I.T. Horváth). Wiley.

11 Singh, V., Rayal, I., Sharma, H. et al. (2020). Chapter 1 – Solar radiation and light materials interaction. In: *Energy Saving Coating Materials* (ed. G.K. Dalapati and M. Sharma), 1–32. Elsevier.

12 Fujishima, A. and Honda, K. (1972). Electrochemical photolysis of water at a semiconductor electrode. *Nature* 238: 37–38.

13 Nosaka, Y. and Nosaka, A.Y. (2017). Generation and detection of reactive oxygen species in photocatalysis. *Chem. Rev.* 117: 11302–11336.

14 Hoffmann, M.R., Martin, S.T., Choi, W., and Bahnemann, D.W. (1995). Environmental applications of semiconductor photocatalysis. *Chem. Rev.* 95: 69–96.

15 Gaya, U.I. (2013). *Heterogeneous Photocatalysis Using Inorganic Semiconductor Solids*. Netherlands: Springer.

16 Zhou, H.C., Long, J.R., and Yaghi, O.M. (2012). Introduction to metal–organic frameworks. *Chem. Rev.* 112: 673–674.

17 Wang, Q. and Astruc, D. (2020). State of the art and prospects in metal–organic framework (MOF)-based and MOF-derived nanocatalysis. *Chem. Rev.* 120: 1438–1511.

18 Rosi, N.L., Eckert, J., Eddaoudi, M. et al. (2003). Hydrogen storage in microporous metal-organic frameworks. *Science* 300: 1127–1129.

19 Kandiah, M., Nilsen, M.H., Usseglio, S. et al. (2010). Synthesis and stability of tagged UiO-66 Zr-MOFs. *Chem. Mater.* 22: 6632–6640.

20 Serre, C., Millange, F., Surblé, S., and Férey, G. (2004). A route to the synthesis of trivalent transition-metal porous carboxylates with trimeric secondary building units. *Angew. Chem. Int. Ed.* 43: 6285–6289.

21 Saikia, M. and Saikia, L. (2016). Sulfonic acid-functionalized MIL-101(Cr) as a highly efficient heterogeneous catalyst for one-pot synthesis of 2-amino-4*H*-chromenes in aqueous medium. *RSC Adv.* 6: 15846–15853.

22 Wang, S., Kitao, T., Guillou, N. et al. (2018). A phase transformable ultrastable titanium-carboxylate framework for photoconduction. *Nat. Commun.* 9: 1660.

23 Horiuchi, Y., Toyao, T., Saito, M. et al. (2012). Visible-light-promoted photocatalytic hydrogen production by using an amino-functionalized Ti(IV) metal–organic framework. *J. Phys. Chem. C* 116: 20848–20853.

24 Silva, C.G., Corma, A., and García, H. (2010). Metal–organic frameworks as semiconductors. *J. Mater. Chem.* 20: 3141–3156.

25 di Nunzio, M.R., Caballero-Mancebo, E., Cohen, B., and Douhal, A. (2020). Photodynamical behaviour of MOFs and related composites: relevance to emerging photon-based science and applications. *J. Photochem. Photobiol. C Photochem. Rev.* 44: 100355.

26 Llabrés I Xamena, F.X., Corma, A., and Garcia, H. (2007). Applications for metal–organic frameworks (MOFs) as quantum dot semiconductors. *J. Phys. Chem. C* 111: 80–85.

27 Gomes Silva, C., Luz, I., Llabres I Xamena, F.X. et al. (2010). Water stable Zr–benzenedicarboxylate metal–organic frameworks as photocatalysts for hydrogen generation. *Chem. A – Eur. J.* 16: 11133–11138.

28 Dong, D., Yan, C., Huang, J. et al. (2019). An electron-donating strategy to guide the construction of MOF photocatalysts toward co-catalyst-free highly efficient photocatalytic H_2 evolution. *J. Mater. Chem. A* 7: 24180–24185.

29 Xiao, J.-D., Shang, Q., Xiong, Y. et al. (2016). Boosting photocatalytic hydrogen production of a metal–organic framework decorated with platinum nanoparticles: the platinum location matters. *Angew. Chem. Int. Ed.* 55: 9389–9393.

30 Nasalevich, M.A., Becker, R., Ramos-Fernandez, E.V. et al. (2015). Co@Nh_2-MIL-125(Ti): cobaloxime-derived metal–organic framework-based composite for light-driven H_2 production. *Energy Environ. Sci.* 8: 364–375.

31 Su, Y., Zhang, Z., Liu, H., and Wang, Y. (2017). $Cd_{0.2}Zn_{0.8}S$@UiO-66-Nh_2 nanocomposites as efficient and stable visible-light-driven photocatalyst for H_2 evolution and Co_2 reduction. *Appl. Catal. B* 200: 448–457.

32 Fang, X., Shang, Q., Wang, Y. et al. (2018). Single Pt atoms confined into a metal–organic framework for efficient photocatalysis. *Adv. Mater.* 30: 1705112.

33 Sun, K., Liu, M., Pei, J. et al. (2020). Incorporating transition-metal phosphides into metal-organic frameworks for enhanced photocatalysis. *Angew. Chem. Int. Ed.* 59: 22749–22755.

34 Zhu, Y.-P., Yin, J., Abou-Hamad, E. et al. (2020). Highly stable phosphonate-based MOFs with engineered bandgaps for efficient photocatalytic hydrogen production. *Adv. Mater.* 32: 1906368.

35 Castells-Gil, J., Padial, N.M., Almora-Barrios, N. et al. (2018). Chemical engineering of photoactivity in heterometallic titanium–organic frameworks by metal doping. *Angew. Chem.* 57: 8453–8457.

36 Han, S.-Y., Pan, D.-L., Chen, H. et al. (2018). A methylthio-functionalized-MOF photocatalyst with high performance for visible-light-driven H_2 evolution. *Angew. Chem. Int. Ed.* 57: 9864–9869.

37 Karthik, P., Balaraman, E., and Neppolian, B. (2018). Efficient solar light-driven H_2 production: post-synthetic encapsulation of a Cu_2O co-catalyst in a metal–organic framework (MOF) for boosting the effective charge carrier separation. *Catal. Sci. Technol.* 8: 3286–3294.

38 Leng, F., Liu, H., Ding, M. et al. (2018). Boosting photocatalytic hydrogen production of porphyrinic MOFs: the metal location in metalloporphyrin matters. *ACS Catal.* 8: 4583–4590.

39 An, Y., Liu, Y., An, P. et al. (2017). Ni^{II} coordination to an Al-based metal–organic framework made from 2-aminoterephthalate for photocatalytic overall water splitting. *Angew. Chem. Int. Ed.* 56: 3036–3040.

40 Zhang, J., Bai, T., Huang, H. et al. (2020). Metal–organic-framework-based photocatalysts optimized by spatially separated cocatalysts for overall water splitting. *Adv. Mater.* 32: 2004747.

41 Salcedo-Abraira, P., Vilela, S.M.F., Babaryk, A.A. et al. (2021). Nickel phosphonate MOF as efficient water splitting photocatalyst. *Nano Res.* 14: 450–457.

42 Remiro-Buenamañana, S., Cabrero-Antonino, M., Martínez-Guanter, M. et al. (2019). Influence of co-catalysts on the photocatalytic activity of MIL-125(Ti)-Nh_2 in the overall water splitting. *Appl. Catal. B: Environ.* 254: 677–684.

43 Salcedo-Abraira, P., Babaryk, A.A., Montero-Lanzuela, E. et al. A novel porous Ti-squarate as efficient photocatalyst in the overall water splitting reaction under simulated sunlight irradiation. *Adv. Mater.* 33 (52): 2106627.

44 Melillo, A., Cabrero-Antonino, M., Navalón, S. et al. (2020). Enhancing visible-light photocatalytic activity for overall water splitting in UiO-66 by controlling metal node composition. *Appl. Catal. B: Environ.* 278: 119345.

45 Hu, H., Wang, Z., Cao, L. et al. (2021). Metal–organic frameworks embedded in a liposome facilitate overall photocatalytic water splitting. *Nat. Chem.* 13: 358–366.

46 An, Y., Xu, B., Liu, Y. et al. (2017). Photocatalytic overall water splitting over MIL-125(Ti) upon CoPi and Pt co-catalyst deposition. *ChemistryOpen* 6: 701–705.

47 Wu, X.-P., Gagliardi, L., and Truhlar, D.G. (2018). Cerium metal–organic framework for photocatalysis. *J. Am. Chem. Soc.* 140: 7904–7912.

48 Feng, D., Gu, Z.-Y., Li, J.-R. et al. (2012). Zirconium-metalloporphyrin PCN-222: mesoporous metal–organic frameworks with ultrahigh stability as biomimetic catalysts. 51: 10307–10310.

8

Organic Transformations Involving Photocatalytic Hydrogen Release

Miriam Marchi, Michele Melchionna, and Paolo Fornasiero

University of Trieste, INSTM Trieste Research Unit and ICCOM-CNR Trieste Research Unit, Center for Energy, Environment and Transport Giacomo Ciamiciam, Department of Chemical and Pharmaceutical Sciences, L. Giorgieri 1, 34127, Trieste, Italy

8.1 Introduction

The demand for a low-carbon economy and sustainable energy sources has become increasingly important to minimize global dependence on finite and environmentally unfriendly fossil fuels. In the last decades, the use of hydrogen (H_2) as a zero-impact energy vector has often been considered as a key contributor in solving the global energy crisis [1] because its direct combustion does not in principle generate greenhouse gases or pollutants [2, 3].

In addition to its potential central role in the establishment of new clean energy schemes, currently H_2 is an important chemical reagent in many industrial processes, including the synthesis of ammonia and related fertilizers, the manufacture of methanol, petroleum refining hydrodesulfurization, hydrogenation, and many organic hydrogenation reactions in fine chemical synthesis [4]. Because of its industrial value, H_2 production has been the main focus of intense research in the last decades. Since H_2 is not a primary source as it is not naturally available, it has to be derived from other compounds that contain it [5]. Within this framework, it is today imperative that H_2 synthetic strategies will embrace the concept of sustainability and environmental friendliness while maintaining adequate efficiency. However, the current main approach for making H_2 still relies on energy-intensive and polluting methods, being mainly obtained by nonrenewable resources through processes that require high temperature and pressure: 95% of H_2 is extracted by thermal catalytic reforming of fossil fuels, mainly by steam reforming of methane (SMR). Greener approaches based on water electrolysis are being employed but still not achieving prominent market size, which is estimated at about 50 million metric tons yearly, while photocatalytic synthesis is yet to make a real industrial impact [6, 7]. Nevertheless, it is crucial to realize that hydrogen can also be produced through other processes and from a variety of primary sources other than fossil fuels, for example, biomass, wastes, or water [8].

Photocatalytic Hydrogen Production for Sustainable Energy, First Edition. Edited by Alberto Puga.

Solar energy has been widely recognized as one of the most green and bountiful renewable energy sources, which can be converted into chemical energy through photocatalysis [9, 10]. With the rapid development of photocatalysis in recent years, solar-driven hydrogen production has been gaining increasing attention. In 1972, Fujishima and Honda reported the first heterogeneous photo-assisted electrochemical H_2 production by water splitting (WS) [11]. Five years later, Lehn et al. published the first homogeneous photocatalytic H_2 production [12]. Since then, photocatalytic WS for hydrogen evolution has been the subject of intense research, becoming closely associated with the concept of solar energy and fossil fuel replacement [8]. However, pure photocatalytic WS is rather challenging as it suffers from several bottlenecks related to thermodynamics and kinetics [13]. The photocatalytic H_2 production from WS consists of two half-reactions: the proton reduction (called the hydrogen evolution reaction (HER)) and the four-electron water oxidation reaction (WOR), summarized below:

$2H^+ + 2e^- \rightarrow H_2$	Reduction (HER)
$2H_2O + 4\,h^+ \rightarrow O_2 + 4H^+$	Oxidation (WOR)
$2H_2O \rightarrow 2O_2 + 2H_2$	Overall water splitting (OWS)

Within this process, the oxidative half-reaction involving the use of holes to produce oxygen (O_2) needs to overcome a high thermodynamic barrier, requiring an energy superior to the standard potential of the water oxidation process of 1.23 V. An additional hurdle consists of the sluggish kinetics, which slows down the OWS process. Finally, since the thermodynamics of the WS process are largely disfavored ($\Delta G^0 = 238\,kJ\,mol^{-1}$), the reverse reaction, yielding water from the as-formed H_2 and O_2 strongly competes, further decreasing the efficiency of H_2 formation [14]. To overcome the issue related to energy-intensive oxidation reaction, the use of sacrificial agents, namely electron donor molecules that can react more easily with the photogenerated holes because of a lower oxidation potential, is one of the most common strategies for achieving higher H_2 evolution rates. Typical sacrificial agents include organic molecules such as formic acid, lactic acid, ascorbic acid, triethylamine, triethanolamine, ethanol, methanol, and so on, so that depending on their specific interaction with the catalyst surface (and that of the oxidation intermediates), the complete oxidation may in principle proceed, thus releasing CO_2 as the final product. However, other oxidation products are frequently observed in different amounts. This fact can be exploited for a double utility of the HER, in particular an interesting option is to pair the H_2 evolution with cooperative selective oxidative organic synthesis toward useful substrates [15]. This possibility critically hinges on the photocatalyst's structure and properties, so that rational design of the catalytic material to harness it with such a double functionality has become a very popular topic of research.

The present chapter will focus on developments in photocatalysis for selective organic transformations integrated with hydrogen production. The following sections will extensively discuss the recent developments in photoredox cooperative coupling constructions, analyzing the effects of using different organic substances and highlighting the main features of the employed photocatalysts.

8.2 Fundamental Principles of Photocatalytic Systems for H_2 Evolution

In order to meet sustainability guidelines, a very attractive way to produce hydrogen (which is almost established as a prerequisite for industrial appeal) is to perform the splitting of water into H_2 and O_2 by using renewable, abundant sunlight. In the last decades, various catalytic systems to achieve this ambitious goal have been investigated. The photocatalytic process is divided into three broad categories: homogeneous photocatalysis (the catalyst and the reagents are all in the same phase, generally all in liquid solution), heterogeneous photocatalysis (the phase of the catalyst is different from that of the reagents, generally the catalyst is present as a solid and the reagents are dissolved in solution), or dual-type photocatalysis (the reagents are in solution and the catalytic system is composed of one heterogeneous catalyst and one homogeneous catalyst working together).

The homogeneous type of photocatalysis usually involves the use of a metal complex, which is the catalytic species, and an organic/organometallic compound that functions as the photosensitizer (PS). In the case of the homogeneous photocatalytic H_2 production, the PS absorbs light and reaches an excited state that can be quenched through a reductive or an oxidative reaction pathway. The reductive quenching of the excited PS occurs through an electron transfer from an electron donor molecule to the PS, which is reduced, and subsequently returns to its ground state by transferring an electron to the catalyst. In the oxidative reaction pathway, the excited PS is oxidized by direct electron transfer to the catalyst, and then returns to its initial state by oxidizing a sacrificial agent. Hence, both mechanisms feature an electron transfer process between the catalyst and the PS. Once the catalyst has been activated following such an electron transfer, it can proceed with the first catalytic step. For H_2 evolution, the catalyst lowers the energy barrier for proton reduction, accelerating the desired process of hydrogen production. The thermodynamic requirements for this to occur are that the oxidation potential of the excited PS in the oxidative quenching (or the oxidation potential of the reduced PS in the reductive quenching) must be more negative than the reduction potential of the catalyst, while the reduction potential of the oxidized PS in the oxidative quenching (or the reduction potential of the excited PS in the reductive quenching) must be more positive than the oxidation potential of the electron donor (Figure 8.1).

The heterogeneous photocatalytic H_2 production employs a semiconductor (SC), which is an ideal light-absorbing material exhibiting a photoinduced separation of charges that depends primarily by the SC bandgap energy (E_g, representing the difference in energy between the valence band (VB) edge and the conduction band (CB) edge), with this energy that can vary from near-ultraviolet to visible light. The electronic band structure and the energies of photocatalysts are crucial in the chain of reaction steps Upon a light absorption of sufficient energy to overcome the E_g of the SC, electrons are excited from the occupied VB of the photocatalyst to the CB, thus creating electron (e^-)/hole (h^+) pairs. The photoexcited pairs are separated into free charge carriers, and they can migrate to the surface of the photocatalyst and be used to perform redox reactions. In the case of hydrogen production, electrons can reduce protons to H_2 if the photocatalyst CB potential is more negative than the

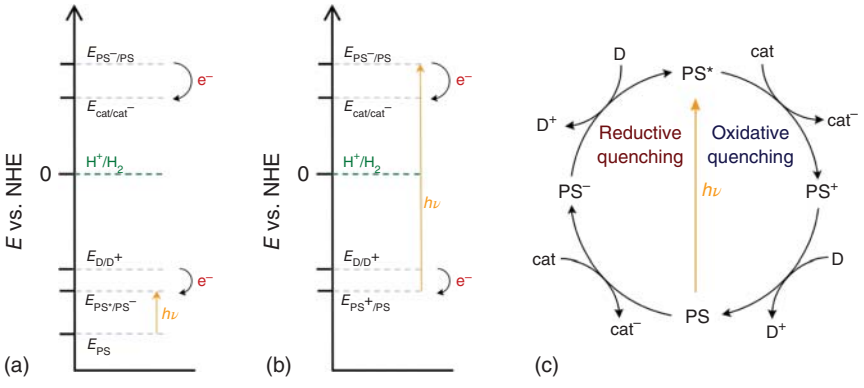

Figure 8.1 (a) Potential scheme of photocatalytic homogeneous system with reductive quenching. (b) Potential scheme of photocatalytic homogeneous system with oxidative quenching. (c) Schematic illustration of reductive and oxidative quenching.

H^+ to H_2 reduction potential (0 V vs. normal hydrogen electrode (NHE), pH 0.059). As mentioned above, the reduction of protons must proceed in concomitance with the photogenerated hole quenching by some electron donor species. If such a species is water (the ideal case to perform a pure WS), the top of the VB has to be more positive than the H_2O to O_2 oxidation potential (1.23 V vs. NHE, pH 0.059). Therefore, the theoretical bandgap of the SC required for WS must be 1.23 V (almost a wavelength of 1000 nm). In practice, however, the photocatalyst must have a bandgap larger than this thermodynamic-derived value, at least 1.7 V, due to the substantial additional overpotentials associated with the slow kinetic and energy losses of the reactions. Moreover, it is necessary to consider that carrying out the process at a pH greater than 0 implies that there will be lower availability of protons and that additional overpotential may be built up from several other contributions. Finally, the efficiency of the photocatalyst will be largely affected by the rate of recombination of the electrons and holes that have a strong tendency to reassociate [15, 16] (Figure 8.2).

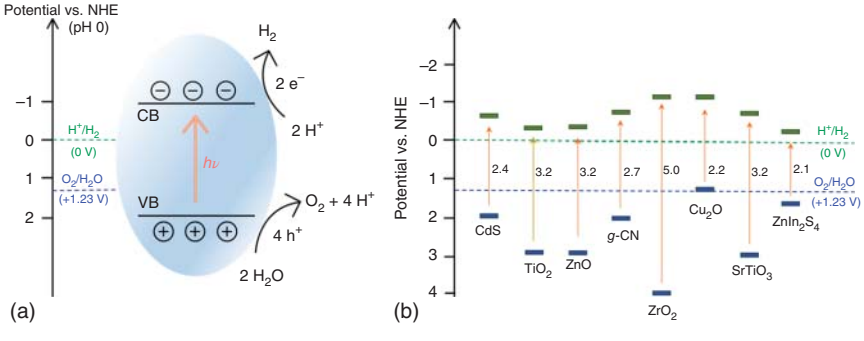

Figure 8.2 (a) Schematic illustration of photocatalytic water splitting to H_2 and O_2 on a semiconductor-based photocatalysts. NHE refers to normal hydrogen electrode. (b) Bandgap energies and band positions of some representative semiconductor photocatalysts.

The choice and the design of a catalyst for the WS process are therefore fundamental: high-performance heterogeneous catalysts are required to harvest light radiation efficiently and must possess long-term physicochemical stability, avoid a high rate of electron/hole recombination, allow fast diffusion of the charge carriers to the surface, and be cost-effective [17].

Very often, in addition to the SC photocatalyst, a co-catalyst is employed to promote the photocatalytic performance. The co-catalyst has diverse purposes: it inhibits the undesired recombination of the electron/hole pairs, as the electrons in the CB of the SC may be injected into the empty energy levels of the co-catalyst, thus being physically separated from the holes; it can provide additional reaction sites; and it may participate in the reaction mechanism. The most common co-catalysts are noble metal-based nanoparticles, especially based on Pt and Pd, which can guarantee excellent performances, but also non-precious transition metal-based (e.g. Co, Ni), carbon nanostructures (e.g. graphene, carbon nanotubes) and molecular-based (e.g. cabaloximes, $Mo_2S_{13}^{2-}$) co-catalysts have been successfully employed [18]. Enhancing charge separation is mostly obtained due to the formation of a Schottky barrier derived from the difference in Fermi levels of the co-catalyst and the SC.

More recently, photocatalysis for hydrogen production has also featured catalytic systems in which both homogeneous molecular catalysts and heterogeneous SCs as PS are used together.

As discussed earlier, OWS is still a highly demanding process for H_2 evolution in the wake of the challenging water oxidation, therefore sacrificial electron donors are frequently used to enhance H_2 evolution rates and also prolong the lifetime of the catalyst. Both inorganic and organic electron donor sacrificial agents are available for this purpose: inorganic compounds are generally not proton sources, and they are used only as hole scavengers to accelerate the hydrogen production. In addition, their oxidation products are often waste or even harmful substances. For instance, SO_3^{2-}, halogen anions (Cl^-, Br^-, I^-), CN^-, and Fe^{2+} are common inorganic sacrificial reagents, which can be oxidized by holes to, respectively, SO_4^{2-}, Cl_2, Br_2/Br_3^-, $I_2/I_3^-/IO_3^-$, OCN^-, and Fe^{3+} [19–21].

To avoid undesired waste, the use of organic compounds as sacrificial agents has gained significant attention. Carbon-containing compounds such as alcohols (e.g. methanol, glycerol), amines (e.g. triethylamine, triethanolamine), aldehydes (e.g. formaldehyde, acetaldehyde), sugars (e.g. glucose), and lignocellulose are efficient and of more appeal, especially when derived as byproducts from biomasses (in particular second generation biomasses), such as for instance, lignocellulosic biomass, bioethanol, or glycerol waste coming from biodiesel industry [22–24]. The photocatalytic H_2 production with organic sacrificial agents is often referred to as "photocatalytic reforming," and the general stoichiometric equation is:

$$C_xH_yO_z + (2x - z)\,H_2O \rightarrow xCO_2 + (2x - z + y)\,H_2$$

Methanol is the simplest choice for preliminary screening of catalysts because of its structure simplicity and a distribution of fewer oxidation products; its primary oxidation products, such as formaldehyde, can be further oxidized to formic acid and carbon dioxide.

A very attractive opportunity lies in the exploitation of the oxidation half-reaction to prepare added-value organic compounds, to double the utility of the photocatalytic process, and obtain simultaneously H_2 production and industrial-relevant chemicals.

For this purpose, research on dual-functional photocatalysis for H_2 evolution coupled with organic transformations has gained growing interest. A variety of organic transformations have been studied, such as the oxidation of alcohols and biomass-derived compounds, as well as C—C, C—N, S—S coupling reactions, degradations of pollutants, and plastics. In the next sections, we will discuss photoredox cooperative coupling of various organic synthesis and H_2 evolution categorized by organic reaction, with the aim to summarize the current state and progress in this emerging field.

8.3 Photocatalytic Organic Transformations Integrated with H_2 Generation

In photocatalytic organic reactions coupled with H_2 evolution reactions, typically used substrates include alcohols, ethers, amines, etc., able to replace water as proton sources and provide access to the synthesis of useful organic compounds parallel to hydrogen evolution. The use of solar energy for photoactivation is fundamental to allow the desired type of process, which is generally thermodynamically unfavorable. The rate-limiting step of concurrent organic synthesis and hydrogen production is the activation and cleavage of a X—H bonds (X = C, N, O, S) in the organic substrates. After this step, the protons obtained from the X—H bonds can interact with electrons in the CB of the photocatalyst and subsequently produce H_2, while the radical intermediates can participate in the organic reaction, thus leading to the formation of C—C/C—X bonds.

In 1985, Kisch and coworkers described chemoselective dehydrodimerization of cyclic ethers, such as tetrahydrofuran (THF), coupled with H_2 production with cubic n-ZnS to obtain both molecular H_2 and C—C coupled compounds under UV radiation [25].

After this first study, cooperative selective organic transformations and H_2 production have been an emerging line of research. The activation of C—H bonds, which are abundant in the natural world, to simultaneously obtain, under mild conditions, hydrogen evolution and the formation of C—X bonds is of great synthetic importance, and it represents a green and promising route in connection with sustainability requirements.

8.3.1 Photocatalytic Organic Oxidation Coupled with H_2 Production

8.3.1.1 Oxidation of Alcohols

Photocatalytic oxidation of alcohols leads to the formation of the corresponding carbonyls and C—C/C—O coupled compounds, which are useful building blocks for the synthesis of pharmaceutical intermediates and fine chemicals.

The photocatalytic approach guarantees a lower environmental impact in comparison with conventional methods, often involving toxic oxidants that generate undesired over-oxidized products such as MnO_4^- or CrO_3, and require high pressure and temperature [26].

In most instances of photocatalytic oxidation of alcohols, carbonyl compounds are the main products with SC-based photocatalysts (Scheme 8.1).

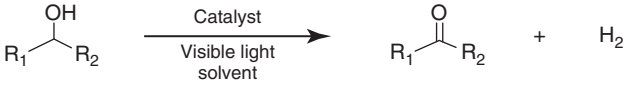

R_1, R_2 : alkyl, aryl, H, etc.

Scheme 8.1 Oxidation of alcohols to the corresponding carbonyl compounds integrated with hydrogen production.

In 2013, Higashimoto et al. described the first highly selective dehydrogenation of aromatic alcohols using visible light under unaerated and mild conditions. In particular, they described the oxidation of benzyl alcohol, which is an important platform reagent (that can be derived from biomass resources) to benzaldehyde coupled with H_2 evolution reaction with CdS–TiO_2 photocatalyst modified with Pd co-catalyst. Moreover, various derivatives of benzyl alcohol were tested, bearing either electron-donating or electron-withdrawing functional groups, with good conversions [27].

Few years later, Xu et al. reported the splitting of alcohols (methanol, ethanol…) into H_2 and corresponding carbonyl compounds in a stoichiometric manner using a Ni-modified CdS nanoparticle photocatalyst. The interface between CdS and Ni nanocrystals plays a key role in the proposed catalytic reaction mechanism. They presented that, at first, the alcohol can be absorbed on the Ni surface. After light irradiation, photoexcited electron and hole pairs are generated; the electron, localized from the CB of CdS to the Ni NPs, reacts with a proton extracted from the O—H group of the alcohol substrate, affording the generation of Ni—H hydride and an alkoxide anion. This anion is oxidized by the photoexcited hole, getting the corresponding carbonyl product and another Ni—H species, and two Ni—H hydrides are able to form one H_2. This catalytic system can work with both aliphatic and aromatic alcohols with high conversion and selectivity. Only long-chain aliphatic alcohols, such as 1-octanol, have shown low conversions, due to different C—H dissociation energies [28] (Figure 8.3).

After this work, noble-metal-free Ni-based co-catalysts have been widely applied in photocatalytic alcohol dehydrogenation [29, 30].

Besides CdS-based photocatalysts, various other SCs have been employed for selective alcohol oxidation, such as graphitic carbon nitride (*g*-CN) [29, 31], strontium titanate ($StTiO_3$) [32, 33] and $Zn_3In_2S_6$ [32].

Zhao et al. investigated a perovskite oxide, the Rh-doped strontium titanate with Pt nanoparticles deposited as a co-catalyst for alcohol dehydrogenation and reported

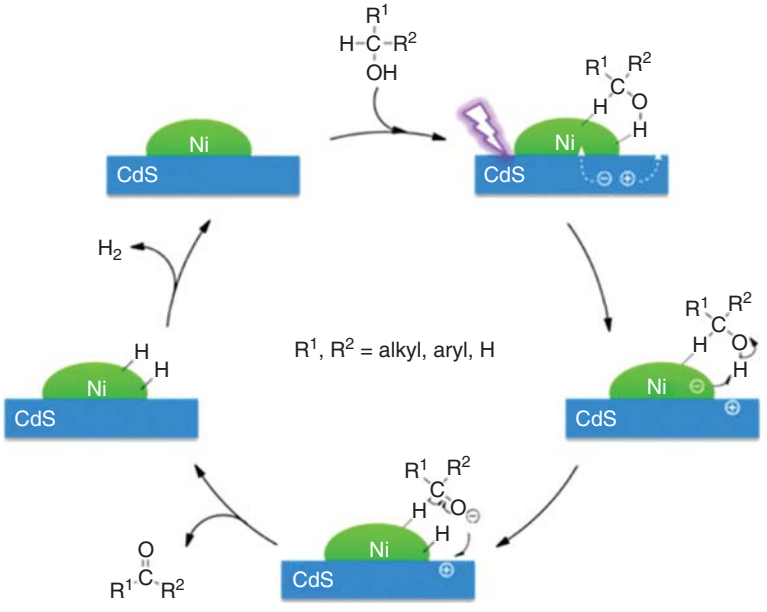

Figure 8.3 Proposed mechanism of the photooxidation of alcohols to the corresponding carbonyl compounds integrated with hydrogen production by Ni/CdS. Source: Chai et al. [28]/with permission of American Chemical Society.

a 70% conversion of benzyl alcohol to benzaldehyde [33]. Rh doping provides a suitable oxidation ability, and the catalytic performance was highly dependent on the abundance of surface oxygen defects generated with the doping process.

In the same year, a Fe-doped strontium titanate was also proposed as a photocatalyst for selective oxidation of alcohols to avoid the use of the expensive and less abundant Rh [32].

Wu et al. proposed a dehydrogenative method of alcohols to aldehydes/ketones with 3-mercaptopriopionic acid (MPA)-capped CdSe quantum dots (MPA-CdSe QDs) and Ni^{2+} ions as co-catalysts under visible light [26]. In this catalytic mechanism, the photoexcited hole migrates from the QDs to the absorbed thiolate anion or disulfide to produce the thiyl radical, which plays a key role by extracting hydrogen from the C—H bond of the alcohol, generating a carbon-centered radical as the C—H bond dissociation energy of the alcohol is lower than the dissociation energy of S—H. Subsequentially, the two carbon-centered radicals disproportionate, producing the desired product. Hydrogen atoms released as protons by equilibration of RSH with water are reduced to H_2 by the Ni^{2+} co-catalyst on Cd—Se QDs. This method leads to an efficient dehydrogenation of alcohols with excellent selectivity, employing water-soluble CdSe QDs as photocatalyst, Ni salt as co-catalyst for the hydrogen evolution, and MPA molecule and water as relay reagents.

Graphitic carbon nitride is an attractive metal-free SC, but it has to circumvent the limitations due to the low quantum efficiency and the high rate of recombination

of electron/hole pairs. Different strategies have been studied to optimize the performance of g-CN, such as heteroatom doping, nanostructured engineering, and heterostructure construction. The band edge positions make it feasible to promote diverse photocatalytic processes, including WS [34, 35].

Durrant, Reisner, and coworkers reported the dual function of H_2 production and the concomitant oxidation of benzyl alcohol under visible light by the combination of cyanamide functionalized carbon nitride ($^{NCN}CN_x$) photocatalyst and a molecular catalyst, Ni(II) diphosphine complexes (NiP), in purely aqueous solution. This process represents a closed redox system where the visible-light irradiation results in the formation of photoexcited states in the $^{NCN}CN_x$, in which the holes are quenched by benzyl alcohol, forming the corresponding aldehyde, and the photoexcited electrons are transferred from the $^{NCN}CN_x$ to the homogeneous catalyst NiP, producing H_2 [29].

In 2020, Zhang and coworkers combined the manipulation of morphology and electronic structure, realizing hierarchical P- and S-doped g-CN mesoporous spheres by a one-pot strategy. They achieved an outstanding H_2 and benzaldehyde production, with a much higher hydrogen generation than the bulk *g*-CN [31].

8.3.2 Oxidation of Biomass-Derived Intermediates

In the pursuit of green alternatives to replace petroleum-based fuels, the production of fuel and chemicals from biomass represents an attractive route. From biomass, key platform chemicals are produced and isolated, such as furfural alcohol and 5-hydroxymethylfurfurale (HMF) [36]. In the last years, photocatalytic upgrading of biomass-derived intermediate compounds to value-added products (aldehydes and acids) has attracted increasing attention, preferably with concomitant H_2 evolution [37, 38] (Scheme 8.2).

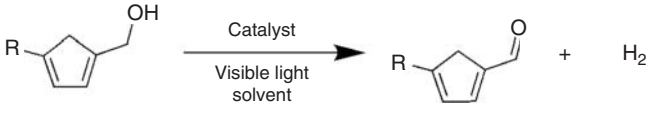

R : H, –CH_2OH, –CHO, –COOH

Scheme 8.2 Oxidation of biomass-derived intermediate compounds integrated with hydrogen production.

In 2017, Han and coworkers reported ultrathin two-dimensional Ni/CdS nanosheets for the transformation of HMF and furfural alcohol to their corresponding aldehydes and simultaneous H_2 production upon visible-light irradiation in neutral water. Ultrathin CdS nanosheets were loaded with controllable amount of Ni as co-catalyst by chemical reduction of $NiCl_2$ in the presence of CdS nanosheets. Computational studies demonstrated the ancillary role of the aldehyde group in the transformation of HMF, which prevalently adsorbs on the NiO(001) facets, promoting the oxidation of O—H group. Notably, the transformation rates of furfural

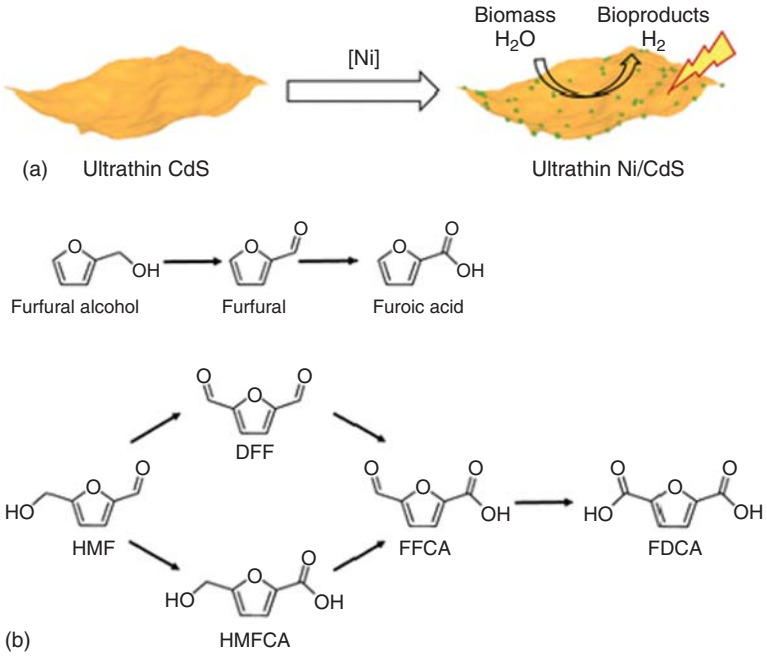

Figure 8.4 (a) Synthesis of ultrathin Ni/CdS nanosheets for integrated biomass valorization and H_2 production. (b) Schematic oxidation reactions of furfural alcohol and 5-hydroxymethylfurfurale to their corresponding aldehydes and acids. Source: Han et al. [39]/with permission of American Chemical Society.

alcohol in furfural exhibited a conversion of almost 100%, while the conversion for the transformation of HMF to 2,5-diformylfuran (DFF) was significantly lower due to the slightly stronger binding affinity of the aldehyde group in HMF to Ni/CdS. The use of alkaline conditions allowed instead to achieve complete transformation of both furfural alcohol and HMF to their corresponding carboxylates [39] (Figure 8.4).

Diaz and coworker employed melamine-derived g-CN for the photooxidation of HMF to the more valuable DFF in an aqueous medium. Interestingly, the degradation rate of HMF was faster than the formation rate of the desired product, suggesting the occurrence of alternative oxidation pathways. A post-synthetic modification of the original g-CN catalyst, consisting of a thermal exfoliation, tuned out to enhance the reaction rate and to eliminate from the photocatalyst surface uncondensed NH_2 sites, which were discovered to be detrimental for the reaction [40]. The valorization of biomass-derived HMF to DFF by porous graphitic carbon nitride (SGCN) under visible light in an aqueous medium has been recently explored. SGCN has an appropriate CB position to produce H_2 and a VB position to selectively oxidize –OH to –CHO groups without over-oxidation. A H_2 production rate of 12 μmol h^{-1} m^{-2} was achieved with a DFF yield of 13.8% and almost 100% of selectivity after six hours [41].

8.3.3 Photocatalytic Oxidative Coupling Reactions Integrated with H_2 Formation

8.3.3.1 Formation of C—C Coupled Products

Unimolecular oxidation is not the only way to hole consumption: photocatalytic bimolecular oxidative coupling reactions can also occur during H_2 evolution photocatalysis. Carbon–carbon coupling is a desirable alternative, which allows the formation of useful multi-carbon compounds with concomitant hydrogen production. In this type of reaction, the coupling reaction takes place with the simultaneous elimination of a proton from the C—H bonds, which is ultimately reduced to molecular H_2.

The dehydrogenative homocoupling reaction of alcohols is an ideal method for obtaining dihydric alcohols. The scheme below shows the general reaction of C—C coupling of alcohols (Scheme 8.3):

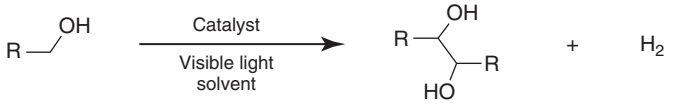

R : alkyl, aryl, H

Scheme 8.3 C—C coupling reaction of alcohols to dihydric alcohols integrated with hydrogen production.

This path poses several challenges: for instance, the conversion of methanol usually involves the activation of O—H or C—O bonds, while the C—H bond is unreactive. It is rare to find a method to preferentially activate the C—H bond instead of O—H bond and form the C—C bond. A photocatalyst based on MoS_2-foam-modified CdS nanorod is one of the few notable examples, which proved to be efficient for the dehydrogenative coupling of methanol into ethylene glycol (EG), in which preferential C—H bond activation occurs without affecting the O—H group. EG is a widely used chemical commodity, fundamental in the production of polyester such as poly(ethylene terephthalate) (PET), but in the current industry it is primarily produced from petroleum-derived ethylene via epoxidation and subsequent hydrolysis of ethylene oxide [42]. The dehydrogenative coupling of methanol is a promising nonpetroleum alternative, and the concomitant production of H_2 adds value to this synthetic strategy. The functioning of the hybrid CdS-based catalyst exploited in this work relies on the ability to allow the facile generation of $\cdot CH_2OH$ radical intermediate by using the photoexcited holes and the concerted proton–electron transfer (CPET) mechanism for subsequent C—C coupling, which occurs preferentially due to the weak adsorption of $\cdot CH_2OH$ and CH_3OH on the catalyst surface. The protons obtained from methanol are reduced to evolve to H_2 by the photoexcited electrons. In this study, CdS nanorods have been selected for their better performance in EG formation than other morphologies of this catalyst. To further increase the catalytic activity and selectivity, the addition of a co-catalyst has been investigated. CdS nanorods modified with MoS_2, and in particular MoS_2 nanofoam, have led not

only to an improvement in H_2 formation, but also to an increased selectivity for EG formation. MoS_2 nanofoam located on CdS has the ability to enhance the transfer of photogenerated electrons and holes, and it presents an increased intimate contact with CdS and more edge sites, which are H_2 evolution active sites, than MoS_2 nanosheet. Moreover, the mesoporous structure of MoS_2 foam facilitates the diffusion of $\cdot CH_2OH$ radicals into the mesopores, increasing the probability of the desired coupling. Due to the advantages described, the developed catalytic system led to an outstanding 90% selectivity for EG and high efficiency for H_2 evolution [43]. More recently, the same group reported a $CoP/Zn_2In_2S_5$ as a more environmentally friendly visible-light alternative strategy at ambient conditions, avoiding the use of the toxic CdS [44]. The $CoP/Zn_2In_2S_5$ showed the same high EG selectivity as in their previous work, although the activity decreased. They developed a few-layer $Zn_2In_2S_5$ nanosheets, synthesized by a simple hydrothermal and ultrasonication method, modified with CoP nanosheets as co-catalysts to increase the charge separation and to promote photocatalytic H_2 evolution, thereby enhancing the formation of EG. Moreover, they demonstrated the first dehydrogenative coupling of ethanol to 2,3-butanediol (2,3-BD) over $CoP/Zn_2In_2S_5$ catalyst, through the formation of $\cdot CH_2(OH)CH_3$ radical. The H_2 evolution occurs on the CoP surface, while $Zn_2In_2S_5$ is fundamental in the preferential activation of the C—H bond without affecting the O—H group, since the thiol groups (–S–H) on $Zn_2In_2S_5$ surface may trap holes, forming thiyl radicals, and then abstract hydrogen from C—H bond, generating the radical intermediates of alcohols.

Substituted aromatic alcohols are one class of important platform chemicals derivable from biomass sources. Besides the C—C bond formation of aliphatic alcohols, also aromatic alcohols such as benzyl alcohol have been investigated to produce useful value-added derivatives, such as hydrobenzoin (HB) and benzoin (BZ), which have application in chiral and synthetic chemistry [45]. In 2019, the first visible-light photocatalytic C—C coupling from benzyl alcohol to primarily HB on colloidal CdS quantum dots (QDs) has been reported. CdS QDs can lead to the proton-coupled oxidation of benzyl alcohol to either C—C coupled product or benzaldehyde. However, the presence of photodeposited Cd^0 on the surface of the QDs in situ, encouraged by the addition of a Cd^{2+} salt, promotes the back-reaction of benzaldehyde to the radical intermediate and, in this way, the C—C coupling reaction is favored with 91% selectivity [46].

In 2020, Luo et al. reported C—C coupling from benzyl alcohol to deoxybenzoin (DOB) with $ZnIn_2S_4$ as a photocatalyst coupled with H_2 coproduction under the irradiation of blue LEDs [47]. This transformation consists of a first step of dehydrocoupling of benzyl alcohol to intermediate HB, followed by either a second step of dehydration from HB to the desired product DOB through a redox-neutral process which consumes an electron–hole pair, or by a dehydrogenation to BZ. Ternary $ZnIn_2S_4$ is a kind of SC whose band structures can be tuned by modulating the ratio of zinc and indium contents, and this feature makes $ZnIn_2S_4$ a perfect candidate to alter selectivity toward DOB in this process. Indeed, the increase in Zn/In ratio allows to lower the CB bottom potential of the SC, facilitating the reductive cleavage of C—OH bond, and thus synthesizing preferentially the desired product DOB rather than BZ.

Xu and coworkers have reported a CdS/SiO_2 catalyst for the dehydrogenative C—C coupling of BA to HB with different substrate groups coupled with H_2 evolution [48]. In this catalytic system, CdS QDs are assembled on a spherical SiO_2 support, establishing an intimate connection: by this means, CdS QDs can simultaneously absorb the incident light and recycle the scattered light in the near-field of SiO_2, improving the light capturing capability and charge carrier generation over the composite. Thanks to the enhanced light-harvesting, the CdS/SiO_2 exhibited a significant increase in H_2 production rates than bare CdS QDs, and the system allows to achieve HB with an outstanding selectivity (96.4%). Moreover, the presence of SiO_2 facilitates the recovery and redispersion of CdS QDs from the reaction solvent (Figure 8.5).

Recently, $Mn_{0.3}Cd_{0.7}S$ nanorods modified with synergistic dual co-catalyst CoPi and Mo_2N proved to be highly competent for the visible-light-driven H_2 production with selective C—C coupling reaction of BA [49]. The catalytic system has been synthesized by electrostatic self-assembly and photodeposition methods. CoPi co-catalysts can serve as an oxidation active site to accumulate photogenerated holes and oxidize the C—H bond of BA, affording $\cdot CH_2(OH)Ph$ radical intermediate to subsequently form HB, while Mo_2N can capture and transport the photoexcited

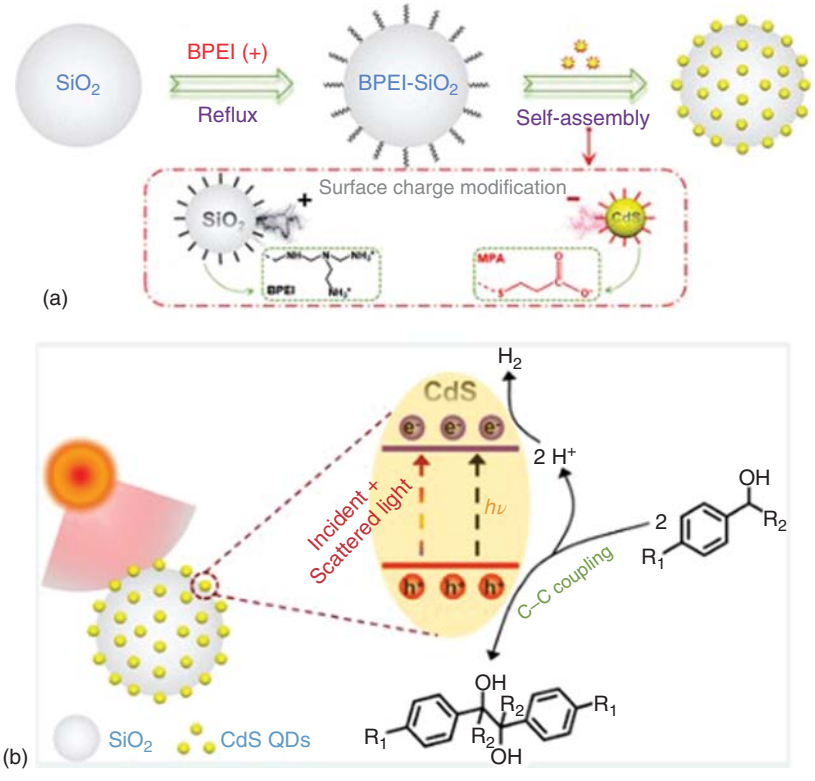

Figure 8.5 (a) Schematic preparation of CdS/SiO_2 composites. (b) Representation of dehydrogenative C—C coupling of BA over CdS/SiO_2 under visible light with concomitant H_2 evolution reaction. Source: Qi et al. [48]/with permission of American Chemical Society.

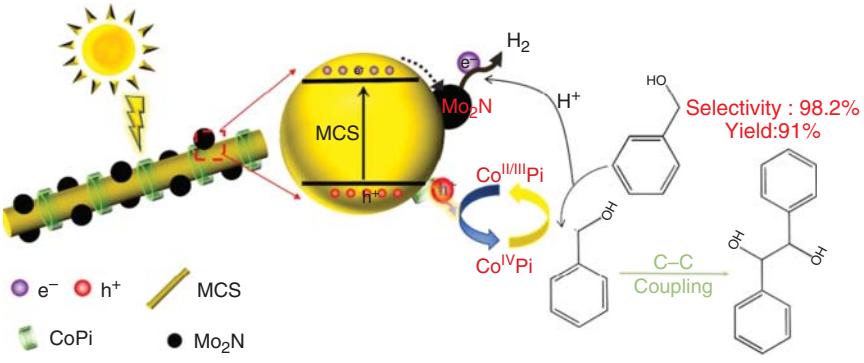

Figure 8.6 Illustrations of the visible-light-driven mechanism of selective C—C coupling of BA by $Mn_{0.3}Cd_{0.7}S$ nanorods with synergistic dual co-catalyst CoPi and Mo_2N with concomitant H_2 evolution reaction. Source: Wang et al. [49], with permission from Elsevier.

electrons and provide the active site for H_2 production. This catalytic system exhibits efficient charge separation, high performance for H_2 and tunable selectivity for the desired organic transformations. Mechanistic studies have suggested that the C—C bond formation occurs through a free radical mechanism. The synergistic effect of the dual co-catalysts represents the key to improve the charge separation efficiency, and thus enhancing the photocatalytic activity and tuning the selectivity for the organic transformation (Figure 8.6).

Besides C—C coupling reaction with alcohols, lignocellulose-derived furanics can also be converted to a variety of useful products. In particular, 2,5-dimethylfuran (2,5-DMF) and 2-methylfuran (2-MF) are attractive candidates for the production of diesel fuels [50]. To produce diesel fuel from these platforms, the carbon chain needs to be lengthened, preferably through a green strategy.

In 2019, Wang et al. investigated a Ru-doped $ZnIn_2S_4$, prepared by a one-pot hydrothermal method, for the coproduction of H_2 and diesel fuel precursors from MFs by visible-light-driven dehydrogenative C—C coupling [51]. The doping with Ru, which replaces the indium ions in the photocatalyst, improves the light harvesting and the charge separation efficiency. After excitation by visible light, the photogenerated holes of the catalyst oxidize the furfuryl C—H bond, affording protons and furfuryl radicals, which then undergo C—C coupling. By this mechanism, dimers are produced, and they react with 2,5-DMF/2-MF or with themselves, forming trimers and tetramers. In parallel with the production of diesel fuel precursors, the photoexcited electrons reduce the generated protons to H_2. In this work, a high selectivity (>96%) and a diesel fuel precursor production rate of 1.04 $g\,g_{catalyst}^{-1}\,h^{-1}$ were shown, as well as a hydrogen production rate of 6.0 $mmol\,g_{catalyst}^{-1}\,h^{-1}$. After chain lengthening, subsequent hydrodeoxygenation (HDO) of the coupling products of furanics converts oxygenated compounds into alkanes, leading to the straight- and branched-chain alkanes of diesel fuels [52] (Figure 8.7).

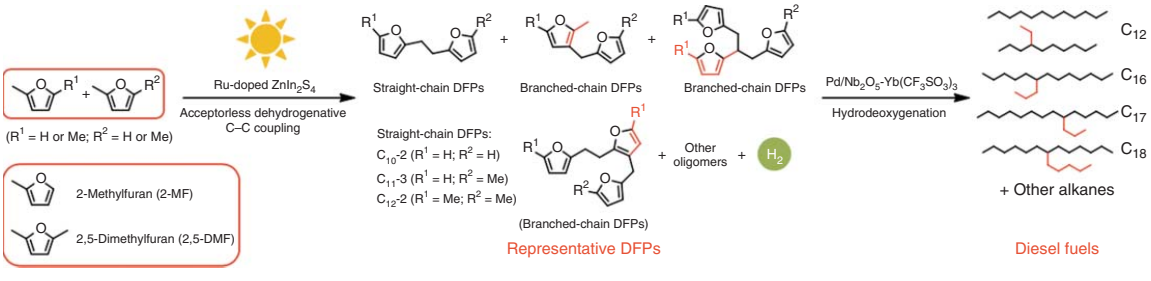

Figure 8.7 Illustration of the visible-light-driven chemical reactions involved in the conversion of 2,5-DMF and 2-MF into diesel fuel. Source: Montini et al. [51]/with permission from Elsevier.

8.3.3.2 Formation of C—N Coupled Products

The photocatalytic C—N homocoupling of amines integrated with H_2 formation has emerged in very recent years as a green strategy to prepare imines or imidazoles, which have various applications in agricultural, pharmaceutical, and synthetic chemistry [53] (Scheme 8.4).

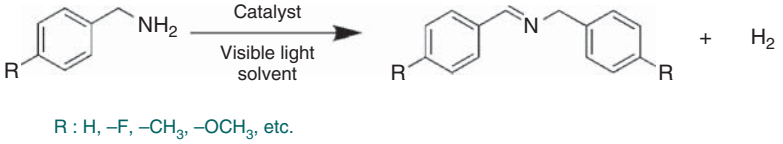

Scheme 8.4 C—N coupling reaction of amines to imines integrated with hydrogen production.

In 2018, Zhao and coworkers reported a recyclable, robust, and noble-metal-free photocatalytic system based on the integration of Ni and CdS that was able to achieve C–N coupling of diverse amines with coproduction of H_2 [54]. The results show that the photocatalytic activity of Ni/CdS NPs for both H_2 production and coupling of benzylamine increases by the efficient synergic effect between these two transformations; indeed, conversion of benzylamine to the corresponding imine exploits photoinduced holes, increasing H_2 production, and the consumption of photoinduced electrons for H_2 formation reduces charge carrier recombination, thus promoting hydrogen evolution and benzylamine coupling. Thanks to this integrating strategy, the photocatalytic results exhibit 99% conversion of benzylamine with a remarkable selectivity (97%) to the corresponding imine, an apparent quantum yield of 11.2% and an H_2 production rate increased by two orders of magnitude (up to 21.4 mmol g^{-1} h^{-1}) as compared to the use of hole scavengers like triethanolamine or Na_2S/Na_2SO_3 with the same Ni/CdS catalyst. The method was extended to a series of aryl amines, achieving excellent performances. The proposed mechanism consists of a first photoexcitation of electrons from the VB to the CB of CdS, with subsequent formation of holes in the VB; photoinduced electrons transfer to Ni NPs and reduce protons to H_2, while the carbon cationic species generated by the holes couple with the amine, forming the corresponding imine product.

Later, Zhang and colleagues developed in situ photodeposition of Ni clusters on ultrathin CdS nanosheets to produce imines with an improved photocatalytic activity [55]. The Ni clusters on the CdS promote the desorption of H_{ads} in the form of molecular H_2, thus liberating active sites on CdS and enhancing the kinetics of the production of imines. The photogenerated holes on CdS oxidize amines to aldimine intermediates, generating protons. Subsequently, another amine couples with the intermediate to form an imine and NH_3. They achieved an outstanding apparent quantum yield of 44% (Figure 8.8).

In addition to imines, the synthesis of substituted imidazoles via photocyclization of a wide range of amines at ambient conditions with blue LEDs over Mo-$ZnIn_2S_4$ has also been reported. [56] The reaction consists of the photoinduced C—C/C—N bond coupling and a subsequent dehydrogenation reaction. The Mo-doped $ZnIn_2S_4$

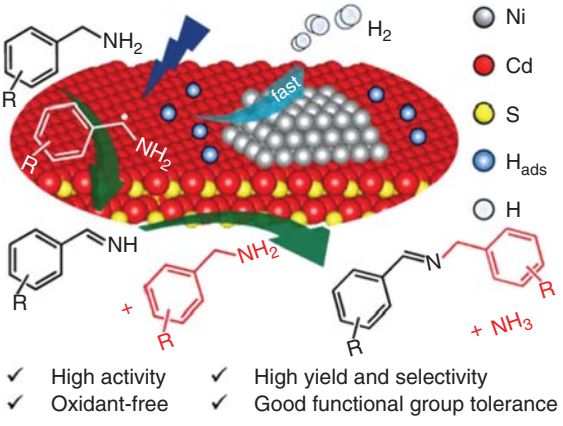

Figure 8.8 Schematic representation of C–N coupling of amines to produce simultaneously imines and H_2 over Ni decorated ultrathin CdS nanosheets. Source: Huang et al. [55]/with permission of American Chemical Society.

catalyst exhibited high activity and good reaction selectivity; the metal-doping of the SC allowed the tuning of the photocatalytic properties and favored the dehydrogenation reaction and the selectivity to imidazoles.

8.3.3.3 Formation of S–S Coupled Products

Disulfides are compounds of high interest in pharmaceuticals, synthetic chemistry, and material science. The common synthetic routes to produce disulfide from thiols suffer from limitations such as expensive reagents, over-oxidized byproducts (sulfoxides and sulfones), and complicated purification processes [57]. On the other hand, the photocatalytic oxidative coupling of thiols to disulfide is a valid alternative to avoid the abovementioned disadvantages of the commonly used synthetic methods (Scheme 8.5).

R : alkyl, aryl, etc.

Scheme 8.5 S–S coupling reaction of thiols to disulfides integrated with H_2 production.

In 2014, Wu and coworkers proposed a clean preparation of disulfides from thiols with coproduction of H_2 under visible-light irradiation over CdSe QDs with the addition of Ni(II) salts to the system. The dehydrocoupling of thiols occurs on the surface of CdSe QDs, and deprotonated thiols can bind to the photocatalyst surface through Cd—S bonds. With visible-light irradiation, the photoexcited holes are quenched by the bound thiolates, generating sulfur-centered radicals, which can undergo coupling reaction to form disulfides, while the presence of the Ni(II) ions absorbed on QDs promotes the photoexcited electrons to reduce protons into molecular H_2 [58].

In a recent work, Li and coworkers investigated the S—S coupling reaction with H_2 coproduction over Pt/$ZnIn_2S_4$ nanocomposite. The Pt NPs were obtained by

photoreduction of $[PtCl_6]^{2-}$ over hexagonal $ZnIn_2S_4$; the co-catalyst Pt significantly enhanced the catalytic performance, obtaining a complete conversion of thiols in six hours under visible-light irradiation and mild conditions [59].

8.3.4 Integration of H_2 Production with Oxidative Cross-Coupling

Oxidative cross-coupling is a powerful strategy in synthetic chemistry to obtain carbon–carbon and carbon–heteroatom bonds, which are useful to yield several types of value-added organic substrates [60]. In the following discussion, some of the most relevant examples of this strategy integrated with H_2 evolution reaction will be described.

Yoshida and coworkers investigated cross-coupling between benzene and ethers to give ether-substituted benzenes (α-arylated ethers) with Pd/TiO_2 catalyst. The Pd-loaded TiO_2 activated directly the sp^3 C—H bond at the α-carbon of ethers, and the Pd NPs promoted the subsequent C—C coupling between the benzene and the α-oxyalkyl radical. The high selectivity for the formation of α-substitution is mainly due to the lower bond cleavage energy of C—H bond at the α-carbon than that at the beta-position. Moreover, the catalytic system exhibited a very high conversion for the cross-coupling product instead of the homocoupling products [61].

Another example involving Pd/TiO_2 photocatalyst is the dehydrogenative cross-coupling between benzene and cyclohexane over Pd-modified TiO_2 photocatalyst under UV- and visible-light irradiation. In fact, both homocoupling to bicyclohexyl (BCH) and to biphenyl (BP) and cross-coupling reaction to phenylcyclohexane (PCH) can occur. With UV irradiation, photogenerated holes in TiO_2 react with benzene and cyclohexane to generate the corresponding radicals and, subsequently, the three corresponding possible products. Instead, with visible-light irradiation, a ligand-to-metal charge transfer (LMCT) complex of benzene adsorbed on TiO_2 induces an electron transfer from the benzene to the CB of TiO_2, and the resulting benzene radical cation selectively activates cyclohexane to generate cyclohexyl radical, thus forming PCH by the Pd-assisted addition-elimination route [62].

Recently, a selective cross-coupling reaction between toluene and acetone to produce ortho-substituted products over a metal-loaded TiO_2 was reported [63]. In this work, the selectivity for a product was tuned by the nature of the metal co-catalyst loaded on the TiO_2: Pd NPs promoted the formation of C—C bond between the aromatic ring of toluene and acetone to give ortho-substituted products such as 1-(*o*-tolyl)propan-2-one with high regioselectivity, while Pt promoted the cross-coupling reaction between the methyl group of toluene and acetone to give 4-phenylbutan-2-one. Thus, the cross-coupling reaction can follow two different pathways to the methyl substituted or the aromatic-substituted product depending on the metal co-catalyst. The Pd NP adsorbs and activates the aromatic ring of toluene to react with the acetonyl radical, following a radical addition-elimination mechanism, while with Pt NPs the mechanism occurs via radical–radical coupling.

Even for imines, the cross-coupling of primary alcohols and amines is a viable alternative to the more conventional homocoupling of amines (previously described

in Section 3.2.2). For instance, Kempe and coworkers reported the photocatalytic C—N multiple bond formation through dehydrogenation of alcohols and subsequent coupling with amines under mild conditions without the requirement of sacrificial electron donors. [64] The photocatalyst consists of a CdS/TiO_2 heterojunction assembled on a porous support decorated with Ni NPs. MIL-101 (Cr), a metal–organic framework (MOF), was chosen as support of the catalytic system for its large pore volume, which is optimal for the target catalytic activity. In this catalyst, charge carriers are distributed over three components, since the type II heterojunction between TiO_2 and CdS allows electron transfer between the CB of CdS and the CB of TiO_2, and Ni NPs favor charge separation. Therefore, the Ni/CdS/TiO2@MIL-101 photocatalyst has the ability to reduce the charge recombination rates, and metallic Ni can act as electron reservoirs and so as a co-catalyst for H_2 production. This reusable catalytic system has shown quantitative H_2 generation from alcohols and subsequentially coupling between the activated carbonyl compounds, obtained with hydrogen through the alcohols dehydrogenation, and amines with high selectivity.

Another relevant application of photocatalysts in tandem processes is the synthesis of benzimidazolic derivatives from nitro compounds. Benzimidazole and its derivatives are fundamental building blocks for pharmaceuticals and commonly employed in the synthesis of natural products, exhibiting biological activities as bactericides and anticarcinogens [65, 66]. The typical synthetic methods, such as condensation of *o*-aryldiamines with aldehydes, carboxylic acids, or their derivatives, usually suffer from low yields, drastic reaction conditions, several side reactions, and other limitations. Looking at more eco-friendly strategies, Shairashi et al. reported a one-pot multiple photocatalytic transformation from 1,2-phenylenediammines with aldehydes to produce benzimidazolic products over Pt/TiO_2 under UV–Vis irradiation, in which the key is the dehydrogenation of alcohols. Selvam et al. investigated a new acid- and oxidant-free strategy based on a one-pot synthesis of disubstituted benzimidazoles from N-substituted 2-nitroarenes exploiting the dehydrogenation of alcohol to reduce the NO_2 to $–NH_2$ and generate the aldehyde for the synthesis of the product, with Pt-TiO_2 and UV-light irradiation [67].

Recently, Fornasiero and coworkers developed a tandem one-pot synthesis of benzimidazoles from nitro compounds with visible light, which is more attractive than UV light. They used a TiO_2 co-doped with B and N in order to increase solar light harvesting, the lifetime of photogenerated charge carriers and the surface area, and loaded various metal co-catalysts (Pd, Pt, Ag, Cu). The proposed reaction mechanism starts with the dehydrogenation of alcohol, which leads to the production of hydrogen and aldehyde, followed by the reduction of the nitro compounds and thus the formation of phenylenediamine as an intermediate. Finally, this intermediate condenses with the aldehyde previously generated. The obtained imine compounds undergo cyclization, and at the end, a dehydrogenation leads to the desired product. The best catalytic performance was achieved with Pt/TiO_2-B, N due to the higher activity in H_2 production and to the low ability of Pt to hydrogenate C—X or C—O bonds in diverse precursors [68] (Figure 8.9).

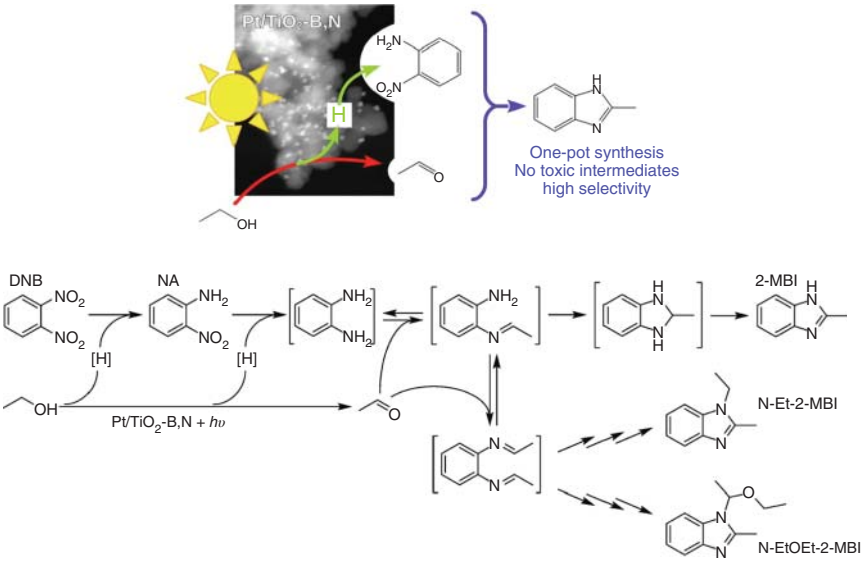

Figure 8.9 (a) Schematic illustration of photocatalytic one-pot synthesis of benzimidazoles over Pt/TiO_2 co-doped with B and N with plausible reaction mechanism. Source: Montini et al. [68]/with permission of Elsevier.

8.4 Conclusions and Perspectives

Cooperative photocatalytic organic transformations integrated with H_2 production represent a promising but still challenging opportunity for solar to chemical conversion, obtaining simultaneously clean H_2 fuel and industrial-relevant chemicals. In this chapter, we have discussed the basic concepts of photocatalysis for H_2 evolution and the principles of light-driven cooperative selective organic reactions with H_2 production for a better understanding of the topic. Moreover, the most significant advances have been presented, where H_2 production is coupled with the photocatalytic selective oxidation reactions to homocoupling and cross-coupling reactions. Available and suitable organic substrates, such as alcohols and amines, have been investigated as proton sources and hole scavengers to achieve the evolution of value-added chemicals.

The diversity of developed SC-based photocatalytic systems suggests that this topic of research in catalysis could be explored toward a wide scope of organic synthesis, thereby the economy of the overall process producing simultaneously two molecules of high interest (one of which is H_2) is potentially of extreme advantage. However, despite the many improvements in this field, several issues still need to be addressed. Firstly, the reported cooperative organic synthesis and H_2 production are still too little efficient, far yet from the ultimate goal of large-scale application. Research should be directed toward the development of sustainable catalysts with high selectivity, efficiency, and durability. For this purpose, it is of crucial importance to devote

special attention to approaches based on rational catalyst design with a bird-eye view to all implications. For example, metal sulfide-based SC, such as CdS and $ZnIn_2S_4$, are promising but usually suffer from photocorrosion due to the oxidation of sulfide anions and, moreover, cadmium exhibits significant toxicity. Therefore, considerable care must be given in the choice of sustainable catalysts of nontoxic nature.

Optimization of catalyst properties (such as surface area, light-harvesting properties, size, morphology, and energy band positions) is a process of particular relevance in the study of this type of application. Doping with foreign elements, using metal co-catalyst with a fine tuning of the nature of the metal, and forming heterostructures with suitable band structures and efficient charge carrier separation have been proven to be key strategies for this goal. This elaborate development of the photocatalytic system needs to be carried out for each type of organic reaction, to find the most efficient and selective photocatalyst for that specific transformation.

Mechanistic investigations of cooperative organic synthesis and H_2 evolution would be helpful to gain an understanding of the structure-performance relationship of photocatalytic systems, leading to faster material development. To this end, in situ techniques (such as XAS, NMR, and EPR spectroscopy) and theoretical DFT calculation could be fundamental to enhance the catalytic performance for a target reaction.

Lastly, the main goal, but still extremely far away, will be the practical applications in a large-scale industrial production driven by solar light. It represents a challenging scale-up, which requires not only optimizing the photocatalytic performance, but also a larger-scale photoreactor design, such as continuous flow reactors.

Acknowledgments

M.M. acknowledges the FRA2021 funded by the University of Trieste. It was also funded by a grant from the Italian Ministry of Foreign Affairs and International Cooperation – Project Italy–China no. CN19GR04 (Payment identification CUP J98D19000410001).

References

1 Armaroli, N. and Balzani, V. (2011). The hydrogen issue. *ChemSusChem* 4 (1): 21–36. https://doi.org/10.1002/cssc.201000182.

2 Rand, D.A.J. and Dell, R.M. (2007). *Hydrogen energy. R. Soc. Chem.* 2007: https://doi.org/10.1039/9781847558022.

3 Chen, D. and He, L. (2011). Towards an efficient hydrogen production from biomass: a review of processes and materials. *ChemCatChem* 3 (3): 490–511. https://doi.org/10.1002/cctc.201000345.

4 Ramachandran, R. and Menon, R.K. (1998). An overview of industrial uses of hydrogen. *Int. J. Hydrogen Energy* 23 (7): 593–598. https://doi.org/10.1016/S0360-3199(97)00112-2.

5 Mazloomi, K. and Gomes, C. (2012). Hydrogen as an energy carrier: prospects and challenges. *Renewable Sustainable Energy Rev.* 16: 3024–3033. https://doi.org/10.1016/j.rser.2012.02.028.

6 Conte, M., Mario, F., Agostino, I. et al. (2009). Hydrogen as future energy carrier: the ENEA point of view on technology and application prospects. *Energies* 2 (1): 150–179. https://doi.org/10.3390/en20100150.

7 Emonts, B. and Stolten, D. (2016). *Hydrogen Science and Engineering: Materials, Processes, Systems and Technology*. Wiley https://doi.org/10.1002/9783527674268.

8 Yao, Y., Gao, X., Li, Z. et al. (2020). Photocatalytic reforming for hydrogen evolution: a review. *Catalysts* 10 (3): 335. https://doi.org/10.3390/catal10030335.

9 Weinstein, L.A., Loomis, J., Bhatia, B. et al. (2015). Concentrating solar power. *Chem. Rev.* 115 (23): 12797–12838. https://doi.org/10.1021/acs.chemrev.5b00397.

10 Tang, J.H. and Sun, Y. (2020). Visible-light-driven organic transformations integrated with H_2 production on semiconductors. *Mater. Adv.* 1 (7): 2155–2162. https://doi.org/10.1039/D0MA00327A.

11 Fujishima, A. and Honda, K. (1972). Electrochemical photolysis of water at a semiconductor electrode. *Nature* 238 (5358): 37–38. https://doi.org/10.1038/238037a0.

12 Lehn, J.M. and Sauvage, J.P. (1977). Chemical storage of light energy. Catalytic generation of hydrogen by visible light or sunlight. Irradiation of neutral aqueous solutions. *Nouv. J. Chim.* 1 (6): 449–451.

13 Davis, K.A., Yoo, S., Shuler, E.W. et al. (2021). Photocatalytic hydrogen evolution from biomass conversion. *Nano Converg.* 8 (1): 6. https://doi.org/10.1186/s40580-021-00256-9.

14 Kubacka, A., Fernández-García, M., and Colón, G. (2012). Advanced nanoarchitectures for solar photocatalytic applications. *Chem. Rev.* 112 (3): 1555–1614. https://doi.org/10.1021/cr100454n.

15 Christoforidis, K.C. and Fornasiero, P. (2012). Photocatalytic hydrogen production: a rift into the future energy supply. *ChemCatChem* 9 (9): 1523–1544. https://doi.org/10.1002/cctc.201601659.

16 Friedmann, D., Hakki, A., Kim, H. et al. (2016). Heterogeneous photocatalytic organic synthesis: state-of-the-art and future perspectives. *Green Chem.* 18 (20): 5391–5411. https://doi.org/10.1039/C6GC01582D.

17 Wang, X., Maeda, K., Thomas, A. et al. (2009). A metal-free polymeric photocatalyst for hydrogen production from water under visible light. *Nat. Mater.* 8 (1): 76–80. https://doi.org/10.1038/nmat2317.

18 Kampouri, S. and Stylianou, K.C. (2019). Dual-functional photocatalysis for simultaneous hydrogen production and oxidation of organic substances. *ACS Catal.* 9 (5): 4247–4270. https://doi.org/10.1021/acscatal.9b00332.

19 Park, S., Chang, W.J., Lee, C.W. et al. (2016). Photocatalytic hydrogen generation from hydriodic acid using methylammonium lead iodide in dynamic equilibrium with aqueous solution. *Nat. Energy* 2: 16185. https://doi.org/10.1038/nenergy.2016.185.

20 Abe, R., Sayama, K., Domen, K. et al. (2001). A new type of water splitting system composed of two different TiO_2 photocatalysts (anatase, rutile) and a

IO_3^-/I^- shuttle redox mediator. *Chem. Phys. Lett.* 344 (3): 339–344. https://doi.org/10.1016/S0009-2614(01)00790-4.

21 Qi, M.Y., Conte, M., Anpo, M. et al. (2021). Cooperative coupling of oxidative organic synthesis and hydrogen production over semiconductor-based photocatalysts. *Chem. Rev.* 121 (21): 13051–13085. https://doi.org/10.1021/acs.chemrev.1c00197.

22 Zinoviev, S., Muller-Langer, F., Das, P. et al. (2010). Next-generation biofuels: survey of emerging technologies and sustainability issues. *ChemSusChem* 3 (10): 1106–1133. https://doi.org/10.1002/cssc.201000052.

23 Puga, A.V. (2016). Photocatalytic production of hydrogen from biomass-derived feedstocks. *Coord. Chem. Rev.* 315: 1–66. https://doi.org/10.1016/j.ccr.2015.12.009.

24 Puga, A.V., Forneli, A., García, H. et al. (2014). Production of H_2 by ethanol photoreforming on Au/TiO_2. *Adv. Funct. Mater.* 24 (2): 241–248. https://doi.org/10.1002/adfm.201301907.

25 Zeug, N., Buecheler, J., and Kisch, H. (1985). Catalytic formation of hydrogen and carbon-carbon bonds on illuminated zinc sulfide generated from zinc dithiolenes. *J. Am. Chem. Soc.* 107 (6): 1459–1465. https://doi.org/10.1021/ja00292a001.

26 Zhao, L.-M., Meng, Q.-Y., Fan, X.-B. et al. (2017). Photocatalysis with quantum dots and visible light: selective and efficient oxidation of alcohols to carbonyl compounds through a radical relay process in water. *Angew. Chem. Int. Ed.* 56 (11): 3020–3024. https://doi.org/10.1002/anie.201700243.

27 Higashimoto, S., Tanaka, Y., Ishikawa, R. et al. (2013). Selective dehydrogenation of aromatic alcohols photocatalyzed by Pd-deposited $CdS–TiO_2$ in aqueous solution using visible light. *Catal. Sci. Technol.* 3 (2): 400–403. https://doi.org/10.1039/C2CY20607B.

28 Chai, Z., Zeng, T.-T., Li, W. et al. (2016). Efficient visible light-driven splitting of alcohols into hydrogen and corresponding carbonyl compounds over a Ni-modified CdS photocatalyst. *J. Am. Chem. Soc.* 138 (32): 10128–10131. https://doi.org/10.1021/jacs.6b06860.

29 Kasap, H., Caputo, C., Martindale, B.C.M. et al. (2016). Solar-driven reduction of aqueous protons coupled to selective alcohol oxidation with a carbon nitride–molecular Ni catalyst system. *J. Am. Chem. Soc.* 138 (29): 9183–9192. https://doi.org/10.1021/jacs.6b04325.

30 Zhang, L., Jiang, D., Irfan, R.M. et al. (2019). Highly efficient and selective photocatalytic dehydrogenation of benzyl alcohol for simultaneous hydrogen and benzaldehyde production over Ni-decorated $Zn_{0.5}Cd_{0.5}S$ solid solution. *J. Energy Chem.* 30: 71–77. https://doi.org/10.1016/j.jechem.2018.03.014.

31 Zhang, F., Li, J., Wang, H. et al. (2020). Realizing synergistic effect of electronic modulation and nanostructure engineering over graphitic carbon nitride for highly efficient visible-light H_2 production coupled with benzyl alcohol oxidation. *Appl. Catal. B: Environ.* 269: 118772. https://doi.org/10.1016/j.apcatb.2020.118772.

32 Hu, Y., Zhao, G., Pan, Q. et al. (2019). Highly selective anaerobic oxidation of alcohols over Fe-doped $SrTiO_3$ under visible light. *ChemCatChem* 11 (20): 5139–5144. https://doi.org/10.1002/cctc.201901451.

33 Zhao, G., Busser, W., Froese, C. et al. (2019). Anaerobic alcohol conversion to carbonyl compounds over nanoscaled Rh-doped $SrTiO_3$ under visible light. *J. Phys. Chem. Lett.* 10 (9): 2075–2080. https://doi.org/10.1021/acs.jpclett.9b00621.

34 Martin, D.J., Reardon, P.J.T., Moniz, S.J.A. et al. (2014). Visible light-driven pure water splitting by a nature-inspired organic semiconductor-based system. *J. Am. Chem. Soc.* 136 (36): 12568–12571. https://doi.org/10.1021/ja506386e.

35 Liu, J., Liu, Y., Liu, N. et al. (2015). Metal-free efficient photocatalyst for stable visible water splitting via a two-electron pathway. *Science* 347 (6225): 970–974. https://doi.org/10.1126/science.aaa3145.

36 Xu, C., Paone, E., and Rodríguez-Padrón, D. (2020). Recent catalytic routes for the preparation and the upgrading of biomass derived furfural and 5-hydroxymethylfurfural. *Chem. Soc. Rev.* 49 (13): 4273–4306. https://doi.org/10.1039/D0CS00041H.

37 Nakagawa, Y., Tamura, M., and Tomishige, K. (2013). Catalytic reduction of biomass-derived furanic compounds with hydrogen. *ACS Catal.* 3 (12): 2655–2668. https://doi.org/10.1021/cs400616p.

38 Luo, H., Barrio, J., Sunny, N. et al. (2021). Progress and perspectives in photo- and electrochemical-oxidation of biomass for sustainable chemicals and hydrogen production. *Adv. Energy Mater.* 11 (43): 2101180. https://doi.org/10.1002/aenm.202101180.

39 Han, G., Jin, Y.-H., Burgess, R.A. et al. (2017). Visible-light-driven valorization of biomass intermediates integrated with H_2 production catalyzed by ultrathin Ni/CdS nanosheets. *J. Am. Chem. Soc.* 139 (44): 15584–15587. https://doi.org/10.1021/jacs.7b08657.

40 Krivtsov, I., Garcia-Lopez, E.I., Marcì, G. et al. (2017). Selective photocatalytic oxidation of 5-hydroxymethyl-2-furfural to 2,5-furandicarboxyaldehyde in aqueous suspension of g-C_3N_4. *Appl. Catal. B* 204: 430–439. https://doi.org/10.1016/j.apcatb.2016.11.049.

41 Battula, V.R., Jaryal, A., and Kailasam, K. (2019). Visible light-driven simultaneous H_2 production by water splitting coupled with selective oxidation of HMF to DFF catalyzed by porous carbon nitride. *J. Mater. Chem. A* 7 (10): 5643–5649. https://doi.org/10.1039/C8TA10926E.

42 Yue, H., Zhao, Y., Ma, X. et al. (2012). Ethylene glycol: properties, synthesis, and applications. *Chem. Soc. Rev.* 41 (11): 4218–4244. https://doi.org/10.1039/C2CS15359A.

43 Xie, S., Shen, Z., Deng, J. et al. (2018). Visible light-driven C–H activation and C–C coupling of methanol into ethylene glycol. *Nat. Commun.* 9 (1): 1181. https://doi.org/10.1038/s41467-018-03543-y.

44 Zhang, H., Xie, S., Hu, J. et al. (2020). C–H activations of methanol and ethanol and C–C couplings into diols by zinc–indium–sulfide under visible light. *Chem. Commun.* 56 (12): 1776–1779. https://doi.org/10.1039/C9CC09205F.

45 Wang, Y., Ren, P., Gu, X. et al. (2016). Probing the mechanism of benzaldehyde reduction to chiral hydrobenzoin on the CNT surface under

near-UV light irradiation. *Green Chem.* 18 (6): 1482–1487. https://doi.org/10.1039/C5GC02168E.

46 McClelland, K.P. and Weiss, E.A. (2019). Selective photocatalytic oxidation of benzyl alcohol to benzaldehyde or C–C coupled products by visible-light-absorbing quantum dots. *ACS Appl. Energy Mater.* 2 (1): 92–96. https://doi.org/10.1021/acsaem.8b01652.

47 Luo, N., Hou, T., Liu, S. et al. (2020). Photocatalytic coproduction of deoxybenzoin and H_2 through tandem redox reactions. *ACS Catal.* 10 (1): 762–769. https://doi.org/10.1021/acscatal.9b03651.

48 Qi, M.-Y., Li, Y.-H., Anpo, M. et al. (2020). Efficient photoredox-mediated C–C coupling organic synthesis and hydrogen production over engineered semiconductor quantum dots. *ACS Catal.* 10 (23): 14327–14335. https://doi.org/10.1021/acscatal.0c04237.

49 Wang, J., Qi, M.-Y., Wang, X., and Su, W. (2022). Cooperative hydrogen production and C−C coupling organic synthesis in one photoredox cycle. *Appl. Catal. B: Environ.* 302: 120812. https://doi.org/10.1016/j.apcatb.2021.120812.

50 Climent, M.J., Corma, A., and Iborra, S. (2014). Conversion of biomass platform molecules into fuel additives and liquid hydrocarbon fuels. *Green Chem.* 16 (2): 516–547. https://doi.org/10.1039/C3GC41492B.

51 Luo, N., Montini, T., Zhang, J. et al. (2019). Visible-light-driven coproduction of diesel precursors and hydrogen from lignocellulose-derived methylfurans. *Nat. Energy* 4 (7): 575–584. https://doi.org/10.1038/s41560-019-0403-5.

52 Luo, J., Hongseok, Y., Mironenko, A.V. et al. (2016). Mechanisms for high selectivity in the hydrodeoxygenation of 5-hydroxymethylfurfural over PtCo nanocrystals. *ACS Catal.* 6 (7): 4095–4104. https://doi.org/10.1021/acscatal.6b00750.

53 Lang, X., Ma, W., Zhao, Y. et al. (2012). Visible-light-induced selective photocatalytic aerobic oxidation of amines into imines on TiO_2. *Chem. A Eur. J.* 18 (9): 2624–2631. https://doi.org/10.1002/chem.201102779.

54 Yu, W., Zhang, D., Guo, X. et al. (2018). Enhanced visible light photocatalytic non-oxygen coupling of amines to imines integrated with hydrogen production over Ni/CdS nanoparticles. *Catal. Sci. Technol.* 8 (20): 5148–5154. https://doi.org/10.1039/C8CY01326H.

55 Huang, Y., Liu, C., Li, M. et al. (2020). Photoimmobilized Ni clusters boost photodehydrogenative coupling of amines to imines via enhanced hydrogen evolution kinetics. *ACS Catal.* 10 (6): 3904–3910. https://doi.org/10.1021/acscatal.0c00282.

56 Wang, M., Li, L., Lu, J. et al. (2017). Photocatalytic coupling of amines to imidazoles using a Mo–$ZnIn_2S_4$ catalyst. *Green Chem.* 19 (21): 5172–5177. https://doi.org/10.1039/C7GC01728F.

57 Almeida, A.M., Li, E., and Gellman, S.H. (2012). Parallel β-sheet secondary structure is stabilized and terminated by interstrand disulfide cross-linking. *J. Am. Chem. Soc.* 134 (1): 75–78. https://doi.org/10.1021/ja208856c.

58 Li, X.-B., Li, Z.-J., Gao, Y.-J. et al. (2014). Mechanistic insights into the interface-directed transformation of thiols into disulfides and molecular hydrogen

by visible-light irradiation of quantum dots. *Angew. Chem. Int. Ed.* 53 (8): 2085–2089. https://doi.org/10.1002/anie.201310249.

59 Xu, L., Deng, X., and Li, Z. (2018). Photocatalytic splitting of thiols to produce disulfides and hydrogen over $PtS/ZnIn_2S_4$ nanocomposites under visible light. *Appl. Catal. B Environ.* 234: 50–55. https://doi.org/10.1016/j.apcatb.2018.04.030.

60 Kozlowski, M.C. (2017). Oxidative coupling in complexity building transforms. *Acc. Chem. Res.* 50 (3): 638–643. https://doi.org/10.1021/acs.accounts.6b00637.

61 Tyagi, A., Matsumoto, T., Kato, T. et al. (2016). Direct C–H bond activation of ethers and successive C–C bond formation with benzene by a bifunctional palladium–titania photocatalyst. *Catal. Sci. Technol.* 6 (12): 4577–4583. https://doi.org/10.1039/C5CY02290H.

62 Yamamoto, A., Ohara, T., and Yoshida, H. (2018). Visible-light-induced photocatalytic benzene/cyclohexane cross-coupling utilizing a ligand-to-metal charge transfer benzene complex adsorbed on titanium oxides. *Catal. Sci. Technol.* 8 (8): 2046–2050. https://doi.org/10.1039/C7CY02566A.

63 Tyagi, A., Matsumoto, T., Yamamoto, A. et al. (2020). Metal cocatalyst directing photocatalytic acetonylation of toluene via dehydrogenative cross-coupling with acetone. *Catal. Lett.* 150 (1): 31–38. https://doi.org/10.1007/s10562-019-02923-3.

64 Tilgner, D., Klarner, M., Hammon, S. et al. (2019). H_2-generation from alcohols by the MOF-based noble metal-free photocatalyst $Ni/CdS/TiO_2$@MIL-101. *Aust. J. Chem.* 72 (10): 842–847. https://doi.org/10.1071/CH19255.

65 Charifson, P.S., Grillot, A.-L., Grossman, T.H. et al. (2008). Novel dual-targeting benzimidazole urea inhibitors of DNA gyrase and topoisomerase IV possessing potent antibacterial activity: intelligent design and evolution through the judicious use of structure-guided design and structure−activity relationships. *J. Med. Chem.* 51 (17): 5243–5263. https://doi.org/10.1021/jm800318d.

66 Boiani, M. and González, M. (2005). Imidazole and benzimidazole derivatives as chemotherapeutic agents. *Mini Rev. Med. Chem.* 5 (4): 409–424. https://doi.org/10.2174/1389557053544047.

67 Selvam, K. and Swaminathan, M. (2011). An easy one-step photocatalytic synthesis of 1-aryl-2-alkylbenzimidazoles by platinum loaded TiO_2 nanoparticles under UV and solar light. *Tetrahedron Lett.* 52 (26): 3386–3392. https://doi.org/10.1016/j.tetlet.2011.04.090.

68 Montini, T., Gombac, V., Delgado, J.J. et al. (2021). Sustainable photocatalytic synthesis of benzimidazoles. *Inorg. Chim. Acta* 520: 120289. https://doi.org/10.1016/j.ica.2021.120289.

9

Photocatalytic Hydrogen Production by Biomass Reforming

Thangjam I. Singh[1,2], Shuya Li[3], Gyu Leem[3,4], and Seunghyun Lee[1,2,4]

[1] *Hanyang University ERICA, Department of Chemical and Molecular Engineering, 55 Hanyangdeahak-ro, Sangnok-gu, Ansan, Gyeonggi-do, 15588, South Korea*
[2] *Hanyang University ERICA, Center for Bionano Intelligence Education and Research, 55 Hanyangdeahak-ro, Sangnok-gu, Ansan, Gyeonggi-do, 15588, South Korea*
[3] *State University of New York College of Environmental Science and Forestry, Department of Chemistry, 1 Forestry Drive, Syracuse, NY 13210, USA*
[4] *The Michael M. Szwarc Polymer Research Institute, 1 Forestry Drive, Syracuse, NY 13210, USA*

9.1 Introduction

Biomass is an abundant natural resource comprising various organic materials derived from living organisms, such as plant and animal waste, agricultural crop residue, algae, wood processing residue, and forestry residues [1]. Over the years, the accumulation of biomass has increased worldwide because of rapid agricultural and industrial activities, providing ample opportunities for the production of various renewable energy sources [2]. In the United States alone, the amount of biomass available is more than that required for food processing and animal feed; this biomass can be efficiently converted into biofuels [3, 4]. Biomass reforming can be used to produce various value-added chemicals, such as ethanol and bio-oils, which may potentially replace traditional petroleum chemicals [1]. Further, biomass-derived chemicals can be converted into alternative fuels such as hydrogen [5]. Hydrogen is considered a future energy carrier because of its high-energy-conversion efficiency, zero emissions of greenhouse gases, and large potential for utilization in various systems, including fuel cells and internal combustion engines. Presently, our economy largely relies on nonrenewable fossil fuels such as coal and petroleum; however, the continuous exhaustion of fossil reserves around the globe poses a serious threat to the world economy and may lead to an energy crisis in the future. Thus far, majority of the hydrogen produced from the steam reforming of methane feedstock meets approximately half the global hydrogen demand [6]. However, this method requires a substantial amount of energy, expensive equipment, and operation and maintenance costs; moreover, it produces greenhouse gases such as CO_2 and CO as byproducts [7, 8].

In this scenario, biomass reforming through natural light, commonly known as photocatalytic reforming, can minimize cost and generate clean hydrogen in

Photocatalytic Hydrogen Production for Sustainable Energy, First Edition. Edited by Alberto Puga.

an eco-friendly manner [9]. An alternative method for clean hydrogen production is electrochemical or photoelectrochemical water splitting [10, 11]. The photocatalytic conversion of biomass into hydrogen is energetically comparable to hydrogen production from water splitting. In the former, biomass is used instead of water; however, in the case of water splitting, water acts as the proton and electron source [12]. Photocatalytic hydrogen production from biomass requires only efficient and sustainable biomass materials as reaction materials, and naturally available sunlight is the only energy source required to initiate the process. Photo-biorefineries produce hydrogen in quantum yields above 70%. In contrast, the yield of hydrogen production through water splitting is only approximately 1.8%, owing to the high thermodynamic barrier and multi-electron-transfer process [7]. Photocatalytic hydrogen production from biomass not only cleanly generates hydrogen but also produces valuable byproducts for various industrial applications [7, 12, 13]. Thus, photocatalytic reforming of raw, partially derived, and unprocessed biomass is an emerging approach for renewable H_2 production in an affordable and eco-friendly manner. This chapter summarizes the general principles, common photocatalyst/co-catalyst systems, and their associated mechanism for the production of hydrogen, with special emphasis on the photocatalytic reforming of biomass.

9.2 General Principles of Photocatalysis

Honda and Fujishima observed the photocatalysis phenomenon in 1972 [14] and described it as a photoinduced catalytic reaction that can be broadly categorized into heterogeneous and homogeneous types [12, 15]. For example, in homogeneous photocatalysis, transition metal complexes such as iron and copper complexes act as photocatalysts. Under light irradiation, the metal complexes cause the central metal ions to undergo photoreduction to lower oxidation states and then re-oxidize them by molecular oxygen. In contrast, heterogeneous photocatalysis employs a typical semiconducting material as the photocatalyst and proceeds via three important steps: light absorption, photoexcited electron injection, and charge separation of the photoinduced holes and electrons. Subsequently, the redox reaction occurs on the photocatalyst surface. When the photocatalyst is illuminated by light with energy greater than its bandgap, an electron from the valence band (VB) of the catalyst is excited to the conduction band (CB), leaving behind a photogenerated hole and creating an electron–hole separation. The photoinduced electrons and holes move separately to the catalyst surface and undergo surface reactions with the adsorbed species on the surface to generate unstable free radicals, which include reactive oxygen species (ROS), such as hydroxyl radicals ($^{\bullet}OH$), superoxide anions ($^{\bullet}O_2-$), hydrogen peroxide (H_2O_2), and singlet oxygen ($^1O_2$) [12]. In general, photoinduced electrons and holes facilitate the reduction and oxidation of the species that are absorbed on the photocatalyst surface [12]. The ability of the generated electron–hole pair to initiate the required redox reaction (i.e. the oxidation of the biomass and reduction of hydrogen) solely depends on the VB/CB potential of the photocatalyst and the oxidation/reduction potential of the redox species in the system [7, 12].

9.3 Photocatalytic Reforming of Biomass

The photocatalytic reforming of biomass and its derivatives can be energetically compared to overall water splitting [8]. In photocatalytic biomass reforming, biomass acts as a proton and electron source, similar to water in the case of water splitting. The photogenerated holes in the photocatalyst oxidize biomass or its derivatives to generate various reactive free radicals, carbon dioxide, and protons via extractive electron transfer. However, the photoexcited electrons cause the reduction of available protons to generate molecular hydrogen gas.

In addition to earth-abundant and low-cost transition metal-based semiconductors serving as photocatalysts for hydrogen production through the reforming of nonedible biomass-derived materials, other factors, such as the reaction conditions, utilization of another co-catalyst, and solution identity, influence hydrogen production rates. In this chapter, hydrogen production by the photocatalytic reforming of biomass and its derivatives is broadly categorized based on the type of photocatalyst and substrate, viz. monomeric, polymeric, or pristine biomass. The main characteristics, mechanisms, and results of solar-driven heterogeneous photocatalysis for hydrogen production in such systems are briefly discussed below.

9.4 Metal-Based Photocatalytic Reforming of Biomass

9.4.1 TiO_2-Based Photocatalysts and Effect of Co-catalysts

TiO_2 is one of the most commonly used photocatalysts for photocatalytic applications, such as water splitting, dye degradation, and antibacterial applications, owing to its high chemical stability against corrosive environments, resistance to discoloration under UV irradiation, low cost, and low toxicity toward the environment [16]. However, it has a large bandgap of approximately 3.2 eV, making it sensitive to only UV radiation, which constitutes approximately 5% of the entire solar spectrum [16, 17]. Therefore, TiO_2 cannot be used effectively in the visible region of the spectrum. Accordingly, many efforts have been made to decrease the wide bandgap of TiO_2 and enhance its photocatalytic activity, which include metal doping, nonmetal doping, co-doping/tri-doping, nano-structuring, and immobilization [16, 18–20]. The dopants play different roles; they may act as electron traps, enhance electron–hole separation, redshift the bandgap absorption to visible light, and introduce new active sites for photocatalytic reactions. Thus, the deposition of metal nanoparticles on TiO_2 can promote its photocatalytic activity. The enhancement in the activity of TiO_2 can be ascribed to the transfer of photoinduced electrons from its CB to that of the deposited metal co-catalysts, enhanced electron–hole separation, and a longer lifetime of the charge carriers [21, 22]. However, the size of the metals, doping or loading percentage, and local structure significantly affect the overall photocatalytic performance of TiO_2 [21, 22]. In general, metal dopants improve charge carrier separation and the spectral response of pristine TiO_2 through various pathways, such as the electron trap

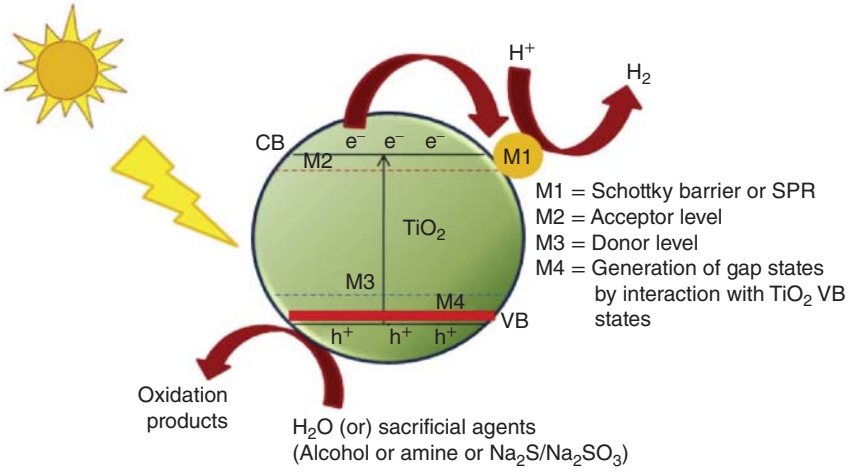

Figure 9.1 Schematic representation of the mechanism of metal dopants that enhance the charge separation and light absorption of TiO_2.

mechanism, surface plasmon resonance (SPR) effect, incorporation of new energy levels, and generation of gap states by interacting with the VB states of TiO_2. The plausible pathways for enhancing the charge carrier separation and light adsorption of TiO_2 by metal doping are illustrated in Figure 9.1.

9.4.1.1 Platinized TiO_2 (Pt/TiO_2) Photocatalysts

Platinum is considered a state-of-the-art catalyst for the hydrogen evolution reaction (HER) through electrochemical water splitting, owing to its low overpotential [23]. Introducing Pt into TiO_2 nanoparticles via Pt doping can suppress electron–hole recombination and enhance its photocatalytic activity for hydrogen generation [24–26]. For example, Yang's research group developed Pt-containing TiO_2 via a one-pot synthesis method and optimized the Pt loadings; this photocatalyst was employed for the photoreforming of methanol and showed high stability toward photocatalytic hydrogen production [26]. Notably, photocatalytic hydrogen production was unaffected by lignin as an inhibitor or a radical scavenger; in this reaction, alfalfa and rice husk were used as the biomass feedstock. This indicates that H_2 was solely generated from the reduction of water, which was caused by the oxidative degradation of the cellulosic fraction present in the biomass [27]. The amount of Pt required to obtain 1 g of H_2 was estimated at approximately 1.8 g, which indicates that approximately 33 l of H_2 per m^3 of water can be obtained using only 2 g of Pt. In contrast, the amount of Pt required to produce 1 g of H_2 through enzymatic conversion of cellulose is approximately 8.1 g [27]. Thus, the presence of cellulose or cellulose-containing biomass enhances photocatalytic hydrogen production.

The one-pot reforming of cellulosic biomass to produce hydrogen was also investigated using platinized TiO_2 combined with photocatalysis and acid hydrolysis [28]. Here, hydrogen production was accompanied by acid hydrolysis of the cellulose in the presence of 0.6 M sulfuric acid and Pt-TiO_2 as photocatalyst under

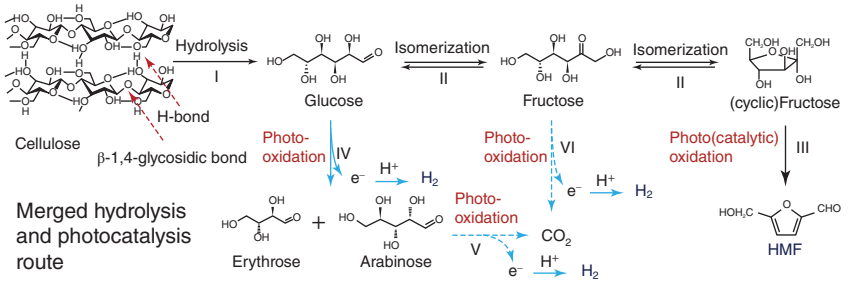

Figure 9.2 Schematic illustration of the proposed mechanism of cellulose decomposition through the combined effect of acid hydrolysis and photocatalysis.

light illumination at 403 K [28]. The acid hydrolysis of cellulose leads to the in situ generation of soluble carbohydrates, which serve as sacrificial electron donors owing to their low oxidation potentials. These soluble carbohydrates continuously supply electrons to the Pt-TiO_2 photocatalysts, which promotes the photocatalytic reduction of protons for hydrogen generation. The proposed mechanism of hydrogen production involves the formation of carbohydrates (glucose) through the acid hydrolysis of cellulose and subsequent oxidation of the in situ-generated carbohydrates, followed by proton reduction on the Pt-TiO_2 catalysts. This mechanism is illustrated in Figure 9.2.

When the amount of H_2SO_4 was increased from 0.1 to 0.6 M, the yields of hydrogen and glucose generated were 66% and 85%, respectively. The yield of hydrogen was lower than that of glucose, which implies that the rate of hydrolysis was higher than that of photocatalytic hydrogen evolution. This shows that the rate-limiting step in the overall system is proton reduction. Furthermore, hydrogen evolution was affected by the amount of cellulose present. Cellulose hydrolysis is crucial for generating the electron donors required for photocatalytic hydrogen evolution. Therefore, when a sufficient amount of cellulose is present in the system, the hydrogen production rate is mainly determined by photocatalysis. At approximately 12.5 mg of cellulose, the rate of hydrogen production was maximum, which resulted from the optimal balance between carbohydrate production through the hydrolysis of cellulose and photocatalytic water splitting. The presence of cellulose increases the hydrogen generation efficiency to approximately five times (c. 170 μmol) that in the absence of cellulose (c. 33 μmol), owing to the combined effect of acid hydrolysis and photocatalysis.

9.4.1.2 Pd/TiO_2 Photocatalysts

Although Pt is considered the best HER catalyst, the large-scale utilization of Pt or Pt-based catalysts for hydrogen production is not sustainable owing to its high cost and scarcity [29]. Pd is more sustainable than Pt because of its higher abundance and lower cost [24]. Pd-based photocatalysts such as Pd/TiO_2 have been investigated as viable alternatives to Pt-based catalysts, especially for biomass reforming and photocatalytic water splitting [18, 21, 30]. The hydrogen production rate of the Pd/TiO_2 photocatalysts for the photoreforming of methanol was highly dependent

on the size, loading, and local structure of the Pd nanoparticles [21]. The Pd/TiO_2 photocatalysts with 0.6% Pd loading and a diameter of 2.3 nm were found to exhibit the highest activity for hydrogen production; however, the activity decreased as the size of Pd increased further. A similar trend was also observed for higher Pd loading. Hydrogen production significantly decreased at Pd loading of 4% due to the agglomeration of nanoparticles, which altered the local structure of Pd metal and hampered the electronic charge-transfer process at the interface of the Pd-TiO_2 photocatalyst [21]. Furthermore, the molecular structure of biomass/biomass-derived liquids affects the photoreforming activity of Pd/TiO_2 [18]. Bahruji et al. studied the mechanism of the photocatalytic reforming of a variety of alcohols on a Pd/TiO_2 photocatalyst; they analyzed the effect of the molecular structures of alcohols on the rate of hydrogen generation [18]. This study laid down some simple rules to predict the relative rate of photocatalytic reforming. The presence of hydrogen at the α-position of the alcohol plays a significant role in this process, and primary alcohols undergoing decarbonylation to produce a CO_2 molecule, hydrogen, and an alkane (alkene in the case of methanol), as well as the complete oxidation of the in situ produced methylene groups generate CO_2 [18]. The hydrogen stoichiometry of the photoreforming of 1,3-propanediol, 1,2-propanediol, and ethylene glycol over the Pd/TiO_2 photocatalyst was found to be 8, 4, and 5, respectively, as shown in Eqs. (9.1)–(9.3), respectively [18]:

$$C_3H_8O_2 + 4H_2O \rightarrow 3CO_2 + 8H_2 \tag{9.1}$$

$$C_3H_8O_2 + 2H_2O \rightarrow CH_4 + 2CO_2 + 4H_2 \tag{9.2}$$

$$CH_2(OH)CH_2(OH) + 2H_2O \rightarrow 2CO_2 + 5H_2 \tag{9.3}$$

The mechanism of the photoreforming of primary alcohols over Pd/TiO_2 photocatalysts is schematically represented in Figure 9.3. This mechanism proposes that alcohol decomposes on the Pd sites of the Pd/TiO_2 photocatalyst initially and generates CO, which binds to the surface of the catalyst and causes surface poisoning [18, 31]. However, activated oxygen species resulting from light absorption convert CO to CO_2, thereby vacating the active sites for the absorption of additional oxygenated molecules to complete the cycle. In the proposed model, the rate of CO removal from the catalyst surface determines the rate of photoreforming.

9.4.1.3 Au/TiO_2 Photocatalysts

Au nanoparticles have been widely investigated for various photocatalytic applications owing to their strong SPR effect [32–35]. Therefore, using Au as a dopant can

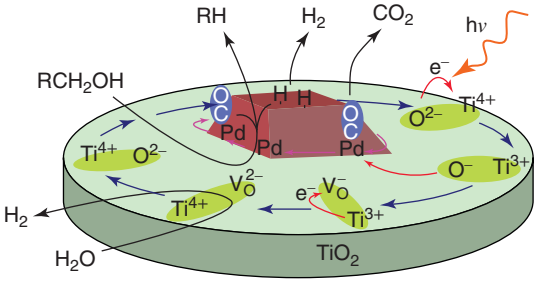

Figure 9.3 Simplified representation of the mechanism proposed for hydrogen production via photoreforming of primary alcohols over Pd-TiO_2 photocatalysts. Source: Bahruji et al. [18]/with permission of Elsevier.

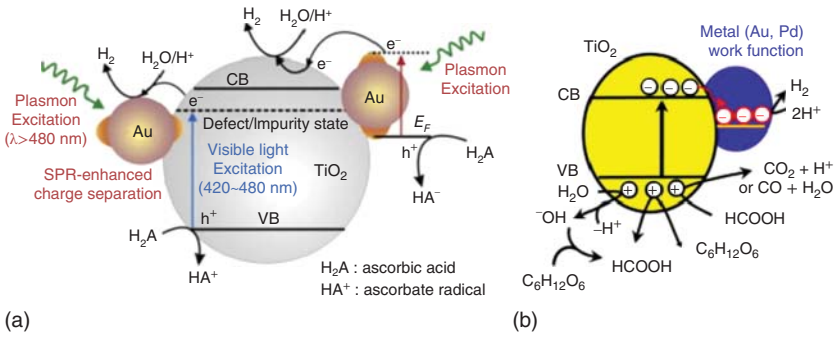

Figure 9.4 Schematic representation of the proposed mechanism for photocatalytic H_2 evolution over Au/TiO_2 photocatalysts under light illumination from (a) water reduction in the presence of ascorbic acid as the electron donor. Source: Fang et al. [36]/with permission of Elsevier and (b) from a glucose solution aided by the simultaneous deposition of Au on TiO_2. Source: Gomathisankar et al. [37]/with permission of Elsevier.

induce the SPR effect in Au/TiO_2 photocatalysts. The energy of the Au/TiO_2 system can be enhanced by tuning the position of the Fermi energy level with respect to the CB and depends on factors such as the size of the Au nanoparticles and degree of electron accumulation. Subramanian et al. investigated the effect of Au nanoparticles on the Fermi levels of Au/TiO_2 nanocomposites [36]. The Fermi level decreased with decreasing Au nanoparticle size [36]. This higher negative shift in the Fermi energy level indicates the more reductive nature of Au/TiO_2 [36]. Under visible-light irradiation, the efficiency of the hydrogen production reaction using Au/TiO_2 was found to be much higher than that using Pt/TiO_2. This difference in efficiency was attributed to the enhanced excitation of TiO_2 resulting from the strong localized electric field enabled by the plasmonic excitation of Au nanoparticles. Figure 9.4a shows a schematic representation of the proposed mechanism for photocatalytic hydrogen production using Au/TiO_2.

Gomathisankar et al. investigated a hydrogen production reaction from glucose by using an Au/TiO_2 photocatalyst [37]. Photocatalytic hydrogen evolution in the presence of Au nanoparticles was higher than that of bare TiO_2. This could be attributed to the improved electron–hole separation, which facilitates the charge-transfer process, and the Au nanoparticles function as co-photocatalysts (Figure 9.4b). In brief, TiO_2 creates electron–hole pairs under light irradiation. The photogenerated electrons then reduce Au^{3+} ions to Au (0), thereby forming the Au-TiO_2 interface and aligning the Fermi level accordingly. In contrast, the holes are quenched by glucose molecules in the solution. The water and glucose molecules continuously react with the photogenerated holes to produce CO, CO_2, hydroxyl radical species, and protons. During the process of glucose degradation over Au-TiO_2 photocatalysts, arabitol, glucaric acid, and gluconic acid were obtained as byproducts. The photocatalytic hydrogen production on Au/TiO_2 can be assumed to proceed via the following steps [37]:

$$TiO_2 + h\nu \rightarrow TiO_2\ \left(e^-_{CB} + h^+_{VB}\right)$$

$$Au^{3+} + 3e^-_{CB} \rightarrow TiO_2 - Au$$

$$h^{+}_{VB} + H_2O \rightarrow H^{+} + {}^{\bullet}OH$$

$$TiO_2 - Au + h\nu \rightarrow e^{-}_{CB}\,(Au) + h^{+}_{VB}\,(TiO_2)$$

$$2H^{+} + 2e^{-}_{CB}(Au) \rightarrow H_2$$

The visible-light irradiation of Au nanoparticles at an appropriate wavelength can boost the energy of the trapped electrons, owing to the SPR effect. Thus, when the Au nanoparticles on the TiO_2 surface were photo-excited, electrons were transferred to the CB of TiO_2 from Au, thereby generating holes in the Au nanoparticles and electrons in the CB of TiO_2 [38]. Thus, the density of photoexcited electrons around TiO_2 increases due to the resonance effect of Au under visible-light irradiation, which in turn boosts the photocatalytic hydrogen production of the Au-TiO_2 photocatalyst.

Several similar studies have reported photocatalytic hydrogen production by the reforming of biomass or biomass-derived feedstocks using Au/TiO_2 photocatalysts. For example, Fu et al. systematically investigated hydrogen evolution via the photocatalytic reforming of carbohydrates of different molecular weights, such as glucose, sucrose, and starch, using various noble metals, such as Au, Pd, Pt, and Ag, deposited on TiO_2 photocatalysts [39]. The effects of different carbohydrates, microwave pretreatment, concentration of carbohydrates, and different metal loadings on the hydrogen evolution rate were thoroughly investigated. The highest hydrogen production rate was observed for the photocatalytic reforming of glucose because of its higher effective molarity and faster diffusion in the solution [39]. Similarly, Murdoch et al. reported hydrogen production through the photoreforming of ethanol using Au/TiO_2 photocatalysts [40]. Au nanoparticles loaded onto anatase and rutile TiO_2 exhibited different hydrogen production rates. The hydrogen production rate of Au deposited on anatase TiO_2 was 2 orders of magnitude higher than that of Au deposited on rutile TiO_2. The higher hydrogen production rate of the anatase phase can be ascribed to the fact that its electron–hole recombination rate was lower than that of the rutile phase. This indicates that, although the presence of Au is essential, the nature of the support also plays an important role [40].

9.4.2 Non-precious Metals/TiO_2 Photocatalysts

Apart from precious metals such as Au, Pt, and Pd, which are expensive, non-precious transition metals such as Cu, Ni, W, Ag, Fe, Co, and Ce, which are inexpensive and relatively abundant in nature, have also been used as dopants to modify the optical and electrical properties of pristine TiO_2 for photocatalytic H_2 production [41–45]. For example, Hidalgo-Carrillo et al. reported the photocatalytic H_2 production from glycerol using Ni-doped TiO_2 under solar and UV irradiation [46]. Ni particles were incorporated into TiO_2 via the deposition–precipitation method. The photocatalytic activity of the TiO_2 catalyst containing approximately 0.5% Ni (by weight) was 15.5 times higher than that of Evonik P25 (TiO_2 nanoparticles); moreover, this Ni-doped TiO_2 catalyst generated approximately 2.6 mmol of H_2 per gram upon UV irradiation for six hours [46]. Figure 9.5a illustrates the plausible mechanism of H_2 production using Ni-doped TiO_2. Interestingly,

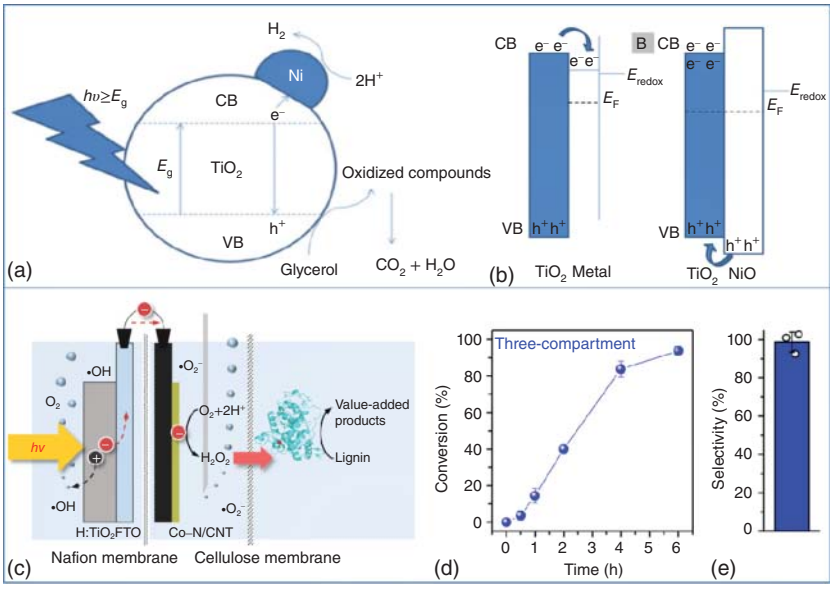

Figure 9.5 (a) Schematic representation of the activation of TiO_2 by Ni doping for photocatalytic hydrogen production from glycerol. Source: Hidalgo-Carrillo et al [46]/MDPI/CC BY 4.0, (b) energy levels of TiO_2 and NiO/TiO_2. Source: Bahruji et al. [47]/Elsevier/CC BY 4.0; (c) schematic for a three-compartment photo-electro-biochemical system, (d) depolymerization conversion efficiency, and (e) selectivity of lignin dimer in the three-compartment photo-electro-biochemical system. Source: Ko et al. [48]/Springer Nature/CC BY 4.0.

the oxidation state of the metal influences the photocatalytic activity. For example, the prereduction of solids results in the transfer of electrons from TiO_2 to Ni (0), while it is thermodynamically impeded in the case of NiO [47]. Thus, metals can help prevent electron–hole recombination by acting as electron traps, as shown in Figure 9.5b, and accordingly enhance the photocatalytic hydrogen production rate [47]. Similarly, Sadanandam et al. reported the photocatalytic H_2 production from a mixture of water and glycerol using cobalt-doped TiO_2 under solar irradiation [42]. The impregnation of Co^{2+} ions on the surface of TiO_2 expands its photo-response into the visible region and enhances hydrogen production. The photocatalytic H_2 production rate was higher in the glycerol: water mixture than in pure water. For example, the addition of 5% glycerol resulted in the maximum photocatalytic hydrogen production of 11 021 $\mu mol\, h^{-1}\, g^{-1}$ with 1 wt% Cobalt-doped TiO_2 as a photocatalyst, whereas in pure water, with 2 wt% Cobalt-doped TiO_2 as the photocatalyst, only about 220 $\mu mol\, h^{-1}\, g^{-1}$ of hydrogen was produced for the same duration of solar-light irradiation. In another report, Clarizia et al. studied a kinetic model to investigate hydrogen production using Cu-doped TiO_2 as the photocatalyst through the photoreforming of glycerol and methanol. A relationship between the hydrogen production rates and the concentration of methanol, glycerol, and catalysts was established experimentally [49]. Cu doping suppressed the electron–hole recombination rate (k_r) of Cu/TiO_2 by a factor of four compared to that of pristine TiO_2 and enhanced its quantum efficiency [49].

The efficiency of hydrogen production was also found to be influenced by the oxidation states of the transition metals [50–52]. For example, the hydrogen production efficiency of 5% wt% Mn-doped TiO_2 photocatalysts (1736 μmol h^{-1} g^{-1}) was approximately 6.5 times higher than that of TiO_2 (264 μmol h^{-1} g^{-1}); this difference was attributed to the high charge separation efficiency of different oxidation states (viz. Mn^{2+}, Mn^{3+}, and Mn^{4+}) of Mn dopants [50]. The Mn dopant in the Mn^{3+}/Mn^{4+} oxidation state acts as an electron trap to avoid the recombination of the charge carriers, thereby facilitating the accumulation of photogenerated electrons on the surface of the catalyst to enhance hydrogen production [50].

Co-doping with different transition metals has also been reported to effectively enhance the photocatalytic activity of TiO_2. Sun et al. reported Fe and Ni co-doped TiO_2 photocatalysts for hydrogen generation via photocatalytic water splitting [45]. The optimum molar ratios of Fe and Ni to Ti were found to be 5% and 4%, respectively. Co-doping with Fe and Ni improved the charge separation efficiency between the photogenerated electrons and holes and enhanced the absorption of visible light [45]. An average hydrogen evolution rate of 361.64 μ mol h^{-1} g^{-1} was achieved under visible-light irradiation for Fe and Ni co-doped TiO_2, which is much higher than that of individually metal-doped TiO_2. This demonstrated the advantages of bimetallic doping. Recently, Jang et al. reported the unique design of a three-compartment photo-electro-biochemical reactor that employed TiO_2 as the photocatalyst, cobalt-based electrocatalysts, and horseradish peroxidase/lignin peroxidase as biocatalysts. Each compartment was separated by cellulose and Nafion membranes to prevent the degradation of the biocatalyst by various elements such as light, gas bubbles, and reactive radicals, as schematically shown in Figure 9.5c [48]. The system enabled the unassisted, highly selective, and stable valorization of lignin upon solar-light irradiation without any input potential bias or any other sacrificial agents. The lignin dimer was chosen as the model compound for studying the specific cleavage of β-O-4 using lignin peroxidase isozyme H8 (LiPH8) as the biocatalyst in the presence of H_2O_2, which was photoelectrochemically generated. The fabricated three-compartment photo-electro-biochemical system demonstrated a maximum depolymerization conversion efficiency of 93.7% when operated for six hours and a high selectivity of ~98.7% for the lignin dimer in the presence of the biocatalyst (Figure 9.5d–e). However, the conversion efficiency and selectivity decreased in the absence of the LiPH8 biocatalysts, indicating that the presence of a biocatalyst is required for high selectivity of lignin valorization.

9.4.3 Nonmetals/TiO_2 Photocatalysts

Doping with nonmetals such as N, C, F, S, B, and I also enhances the photocatalytic activity of TiO_2 under visible-light irradiation [53–56]. Nonmetal doping is predicted to be more advantageous than metal doping as it avoids the formation and recombination of charge carrier centers, which is otherwise evident in metal doping [55, 56]. Studies based on theoretical calculations have shown that doping with nonmetals such as B, N, and C either tends to create energy states with unpaired electrons above the VB, thereby favoring defect creation, or favors the transfer of electrons with the

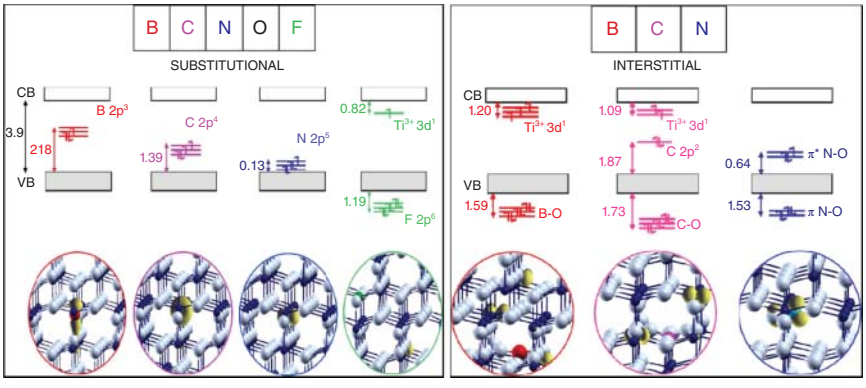

Figure 9.6 Schematic representation of Kohn–Sham one-electron states and spin density plots of nonmetals doping (a) substitutionally and (b) interstitially in anatase TiO_2. Source: Di Valentin [57]/with permission of Elsevier.

formation of O-heteroatom moieties, based on their location in the substitutional or interstitial sites (shown schematically in Figure 9.6a,b) [57]. Among the various nonmetals, nitrogen doping is popularly employed to enhance the photocatalytic properties of TiO_2 because the introduction of nitrogen into the TiO_2 crystal lattice reduces its bandgap energy owing to the hybridization of O 2p and N 2p orbitals[54–56] and improves the water-splitting efficiency [58]. An investigation to confirm nitrogen as the most appropriate nonmetal dopant for TiO_2 was experimentally carried out for the photodegradation of aldehydes [59]. The N-doped TiO_2 photocatalysts generated hydrogen at a rate of 28 μmol h^{-1}, which is significantly higher than that of pristine TiO_2 (2 μmol h^{-1}) under visible-light irradiation [54].

In addition to N doping, B and P doping were also investigated to enhance the photocatalytic activities of pristine TiO_2. For example, B-doped TiO_2 photocatalysts showed higher activity for ethanol reforming under UV-light irradiation than pristine TiO_2. This can be ascribed to the presence of oxygen-substituted B, which favors the exposure of highly photocatalytically active {200} planes [60]. Furthermore, Zhu et al. reported an enhanced HER rate of approximately 11.4 μmol h^{-1} for red phosphorous (RP)-doped TiO_2 (TiO_2/RP); in contrast, the HER rate of pristine TiO_2 was only 5.3 μmol h^{-1}. The improved HER activity of TiO_2/RP was ascribed to the extension of the optical absorption of TiO_2 to the visible region enabled by RP doping and the introduction of oxygen vacancies, which enhanced the charge carrier separation and transfer process [61, 62].

9.4.4 CdS-Based Photocatalysts and Co-catalyst Loading

Metal sulfides, especially CdS-based photocatalysts, have also been explored as potential visible-light-responsive photocatalysts for H_2 production because of their low bandgap (~2.4 eV) and high charge carrier transportation capacity [63, 64]. Accordingly, CdS and CdS-based co-catalysts have also been investigated for the

photoreforming of biomass and its derivatives to generate clean H_2 because of their excellent photocatalytic activity and outstanding response to visible light [65–68]. However, pristine CdS is not an efficient photocatalyst because of its fast charge recombination and self-photocorrosion [69, 70]. Hence, loading co-catalysts is an effective strategy to enhance the photocatalytic activity of CdS-based photocatalysts.

9.4.4.1 Au/CdS Photocatalysts

The photocatalytic H_2 production efficiency of pristine CdS photocatalysts is limited owing to their high charge recombination [69, 70]. Among the various techniques to overcome this limitation, loading novel metal co-catalyst onto CdS is an effective method to improve photocatalytic H_2 production, as novel metals are known to enhance the separation and transportation of photogenerated charge carriers [63]. For example, the reduction of Au^{3+} to metallic Au is easier than that of H^+ to H_2 [71]. Therefore, in the case of Au-loaded CdS (Au/CdS), Au^{3+} can be reduced by the photoinduced electrons transferred from CdS, while the holes created in the VB of CdS can be used to oxidize various biomass substrates and their derivatives to generate protons, thereby enhancing charge carrier separation. Furthermore, the Au/CdS heterojunction can serve as a Schottky junction, promoting the charge-transfer process [64]. Wang et al. reported photocatalytic H_2 production from a glucose solution using Au^{3+} doped on the surface of a CdS nanorod (Au/CdS-NRs) under visible-light irradiation, which yielded an H_2 evolution rate of 90 μmol g^{-1} h^{-1} [64].

9.4.4.2 Ni/CdS Photocatalyst

The charge recombination between photogenerated electrons and holes in light-absorbing photocatalysts such as CdS is in direct competition with the reduction of protons to H_2; therefore, decreasing the rate of the charge recombination process is highly critical. The introduction of sacrificial electron donors can accomplish this, but at the cost of reducing the oxidizing power of the photogenerated holes. Therefore, instead of using sacrificial electron donors, the use of metals such as Ni as co-catalysts can decrease the rate of the charge recombination process without compromising the oxidizing power of photogenerated holes. In this regard, Han et al. reported the photocatalytic upgrading of biomass derivatives such as furfural and 5-hydroxymethylfurfural (HMF) to more value-added products such as aldehydes and acids (i.e. 2,5-diformylfuran (DFF), 2,5-furandicarboxylic acid (FDCA), and furoic acid) using nickel-doped ultrathin CdS nanosheets (Ni/CdS) as photocatalysts [68]. This process converts simple biomass-derived materials into various value-added products and enables simultaneous H_2 production under light illumination.

9.4.4.3 NiS/CdS Photocatalyst

To overcome the limitations of CdS, transition metal sulfides such as NiS have also been explored as co-catalysts because of their low cost, good electrical conductivity, and p-type semiconductor nature. NiS loaded onto various host materials such as TiO_2 and graphitic carbon nitride (g-C_3N_4) has been widely used for photocatalytic H_2 production [72–74]. Li et al. reported photocatalytic hydrogen production

through the photoreforming of lignin and lactic acid in the presence of NiS/CdS photocatalysts under visible-light irradiation [74]. The presence of NiS can facilitate the charge carrier separation and transfer processes at the NiS/CdS interface, whereas lignin and lactic acid act as hole scavengers that enhance the separation of the charge carriers in CdS. Consequently, the photocatalytic H_2 production yield of NiS/CdS was much higher than that of pristine CdS. In fact, NiS/CdS with 20 mol% NiS was 5041 times more effective than pristine CdS in the presence of hole scavengers, resulting in apparent quantum efficiency (AQE) of 44.9% for H_2 evolution. Upon visible-light irradiation, electrons and holes are generated in CdS. Because the CB edge of CdS is more negative than the reduction potential of H^+/H_2, protons can be reduced to H_2. However, this H_2 reduction rate is very low owing to the fast recombination rate of the charge carriers in CdS. However, in the NiS/CdS photocatalyst, the photogenerated electrons, instead of taking part in the H^+/H_2 reduction directly, move to the NiS nanoparticles. This is because the CB of NiS is more negative than that of CdS. Moreover, the close NiS/CdS heterojunction also boosts electron transfer from CdS to the NiS nanoparticles. Because the unsaturated sulfide ions of NiS have a strong affinity for H^+ in the solution, they can serve as active sites for H^+ adsorption and ultimately enhance the photocatalytic H_2 production rate. This also minimizes electron–hole recombination and suppresses the self-photocorrosion of CdS, which would otherwise be observed in pristine CdS. This enhances the overall photocatalytic H_2 production efficiency.

9.4.5 Metal Sulfides Other than CdS

In addition to CdS-based photocatalysts, various metal sulfides, such as ZnS, and mixed sulfides, such as $ZnLn_2Sn_3$, have also been investigated for photocatalytic H_2 generation [75, 76]. Chen et al. reported the direct photogeneration of H_2 and 1,2-propanediol from an aqueous ethanol and methanol solution, with colloidal ZnS as the photocatalyst under light irradiation (125 W high-pressure Hg lamp) [75]. The H_2 and 1,2-propanediol yields increased with increasing pH and temperature. When the temperature was increased from 30 to 50 °C at pH = 10, the H_2 and 1,2-propanediol yields increased from 39 and 5.8 mmol to 45.6 mmol and 16.2 mmol, respectively [75]. In addition, Xitao et al. reported enhanced photocatalytic H_2 production through the photoreforming of an aqueous glycerol solution using an RGO/ZnO@ZnS-Bi_2S_3 nanocomposite as a photocatalyst [77]. The RGO/ZnO@ZnS-Bi_2S_3 nanocomposite exhibited excellent photocatalytic H_2 production from glycerol solution. The charge-transfer process in the nanocomposite is schematically represented in Figure 9.7. Under visible-light irradiation, Bi_2S_3 can be easily photoexcited to generate electron–hole pairs, which is not possible for ZnO and ZnS because of their larger bandgaps. The photogenerated electrons in the CB edge of Bi_2S_3 have a more negative potential than ZnS. Consequently, these electrons from Bi_2S_3 can be easily transferred to ZnO, ZnS, and RGO sequentially. The holes remain on the VB of Bi_2S_3, thereby separating the charge carriers efficiently. The electrons at the surface of RGO cause the reduction of water to generate hydrogen, whereas the holes created in the VB of Bi_2S_3 oxidize glycerol

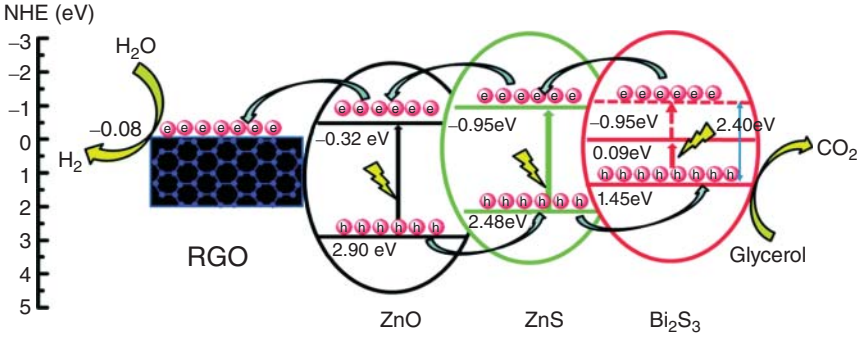

Figure 9.7 Schematic representation of the charge-transfer process in RGO/ZnO@ZnS-Bi_2S_3 for photocatalytic H_2 production through the photoreforming of an aqueous glycerol solution. Source: Xitao et al. [77]/with permission of Royal Society of Chemistry.

directly and generate CO_2 [77]. The RGO/ZnO@ZnS-Bi_2S_3 nanocomposite with an optimum Bi_2S_3/ZnS molar ratio generates the highest photocatalytic H_2 production rate of 310 μmol h^{-1} g^{-1}.

9.4.6 Metal Oxides Other than TiO_2-Based Photocatalysts

Apart from TiO_2, various simple metal oxides and mixed metal oxides have also been reported for photocatalytic H_2 production using various biomass and biomass-derived liquids [78–80]. Among the simple metal oxides, ZnO, WO_3, Cu_2O/CuO, Fe_2O_3, and Co_3O_4, have been used for various photocatalytic reactions [78–83]. A self-assembled 3D ZnO nanosphere was also reported to exhibit undiminished H_2 generation for a duration of approximately 24 hours upon light irradiation using a 300 W xenon lamp [78]. Gasparotto et al. studied Co_3O_4 and F-doped Co_3O_4 photocatalysts for H_2 production from a water/ethanol solution under UV-light irradiation. The hydrogen production rate of F-doped Co_3O_4 was approximately five times that of pristine Co_3O_4 under near-UV-light irradiation [79]. Although materials such as ZnO, WO_3, and Co_3O_4 show promising photocatalytic activities, their wider bandgaps limit the maximum utilization of visible light. In this regard, copper oxides, such as CuO and Cu_2O, have been found to exhibit high photocatalytic activities because of their significantly narrow bandgap suitable for visible-light irradiation, low cost, low toxicity, and abundant nature. For example, Zhang et al. reported photocatalytic H_2 generation via the photoreforming of glucose using Cu_2O photocatalysts with different morphologies and observed morphology-dependent H_2 evolution, as shown in Figure 9.8a–j [83]. Cu_2O with high-index planes showed higher H_2 production yields than cubic Cu_2O. This higher H_2 production on the high-index facets of Cu_2O can be attributed to the preferential accumulation of electrons on such facets. Similarly, Li et al. reported alkaline CuO-chitosan hybrid hydrogel (CuO@Cs-H) photocatalysts for the photocatalytic reforming of xylose to value-added products such as lactic acids under visible-light irradiation. CuO@Cs-H exhibited the highest lactic acid yield of 81.6% under mild

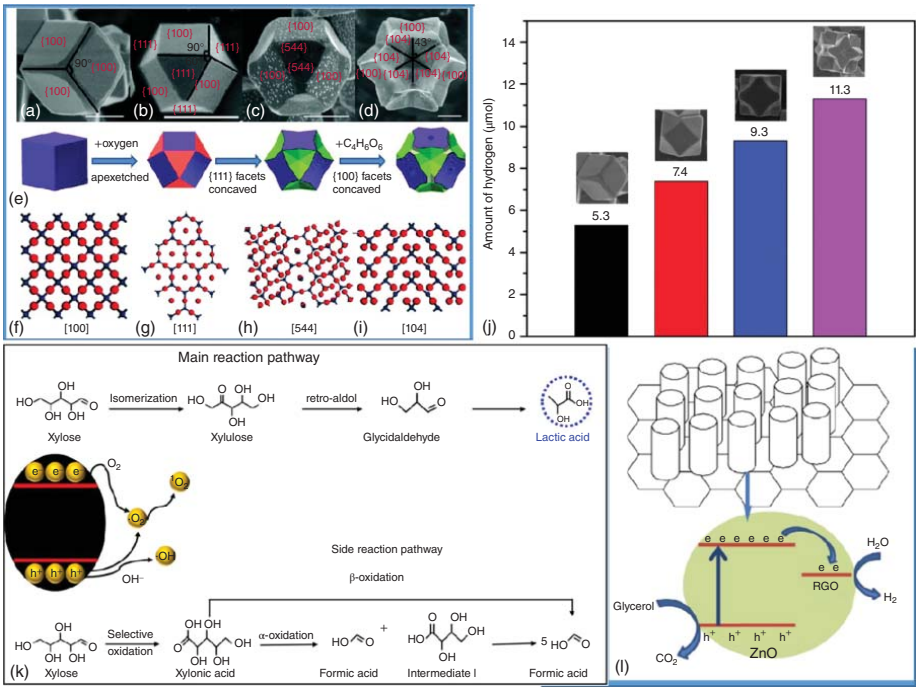

Figure 9.8 (a–d) Morphological evolution of Cu_2O under different reaction times, (e) schematic representation of Cu_2O synthesis, (f–i) various crystal facets: (f) [100] facet [83], (g) [111] facet [83], (h) [544] facet [83] and (i) [104] facet [83], (j) H_2 production enabled by Cu_2O with different morphologies under visible-light irradiation. Source: (a–j) Zhang et al. [83]/with permission of Royal Society of Chemistry; (k) schematic representation of the proposed reaction pathway for photocatalytic reforming of xylose using CuO@Cs-H photocatalysts under visible-light irradiation [82]; and (l) charge-transfer process of electrons in the ZnO nanorod/RGO photocatalyst for H_2 production. Source: Lv et al. [81]/with permission of Elsevier.

alkaline conditions, which was attributed to the synergistic effect between CuO and the alkaline chitosan hydrogel. The possible reaction pathways for CuO@Cs-H photocatalysts are schematically shown in Figure 9.8k. Under visible-light irradiation, $^1O_2$, h^+, $^\bullet OH$, and $^\bullet O_2^-$ are photogenerated. Subsequently, xylulose was obtained from xylose through isomerization under the influence of photogenerated radicals, followed by its conversion to glycidaldehyde, which was finally converted to lactic acid via the main reaction pathway. In the side-reaction pathways, xylose was converted into xylonic acid via selective oxidation, which was subsequently converted into formic acid through either α-oxidation or β-oxidation. Notably, the yield of lactic acid was much higher than that of glycidaldehyde, xylonic acid, and formic acid, indicating the high selectivity of the reaction toward lactic acid.

Lv et al. reported the use of ZnO nanorods grown on RGO for enhanced photocatalytic H_2 production from a glycerol solution [81]. Because the CB of ZnO is higher than the work function of RGO, it is expected that when the ZnO/RGO nanocomposite is formed, the electrons will move from the CB of ZnO to the surface of RGO upon light irradiation through Zn–O–C bonds. These photogenerated electrons are then captured by protons at the surface of the RGO and reduced to H_2, while the photogenerated holes in the VB of ZnO are trapped by the surface hydroxyl groups of water molecules, resulting in the formation of hydroxyl radicals ($^\bullet OH$). These highly reactive $^\bullet OH$ radicals will finally oxidize $C_3H_8O_3$ to CO_2, as schematically shown in Figure 9.8l.

9.5 Metal–Organic Framework (MOFs)-Based Photocatalysts

Metal–organic frameworks (MOFs) with semiconductor-like characteristics have recently attracted significant interest for photocatalysis [87–90]. Due to their unique physicochemical properties, MOFs offer several opportunities to combine light-harvesting and charge separation properties in a single structure with synergistic effects from various components for enhanced photocatalytic activities [88–90]. The highly porous nature of MOFs provides great exposure to the active sites required for catalysis, facilitates the movement of products or substrates, and even serves as a short migration path for charge carriers during photocatalytic activities. MOFs are structurally tunable and provide ample advantages for tuning their light response over a wide spectrum. Co-catalysts or photosensitizers can also be incorporated into MOFs to improve the electron–hole separation for better photocatalysis. Thus, MOFs can serve as efficient hosts to employ various strategic structural modifications to improve light-harvesting, boost electron–hole separation, and promote redox reactions, which are required for improving photocatalytic activities [88]. Li et al. reported a technique for the spatial charge separation in an MOF composite, Co(II) complex@MIL-125-NH_2 ($(Ti_8O_8(OH)_4(BDC\text{-}NH_2)_6)$), in which a Co(II) complex with a size larger than the pore opening of MIL-125-NH_2 was developed inside the cages of the MOF for enhanced photocatalytic H_2 production under visible-light irradiation [91]. The Co.(II) complex in the composite

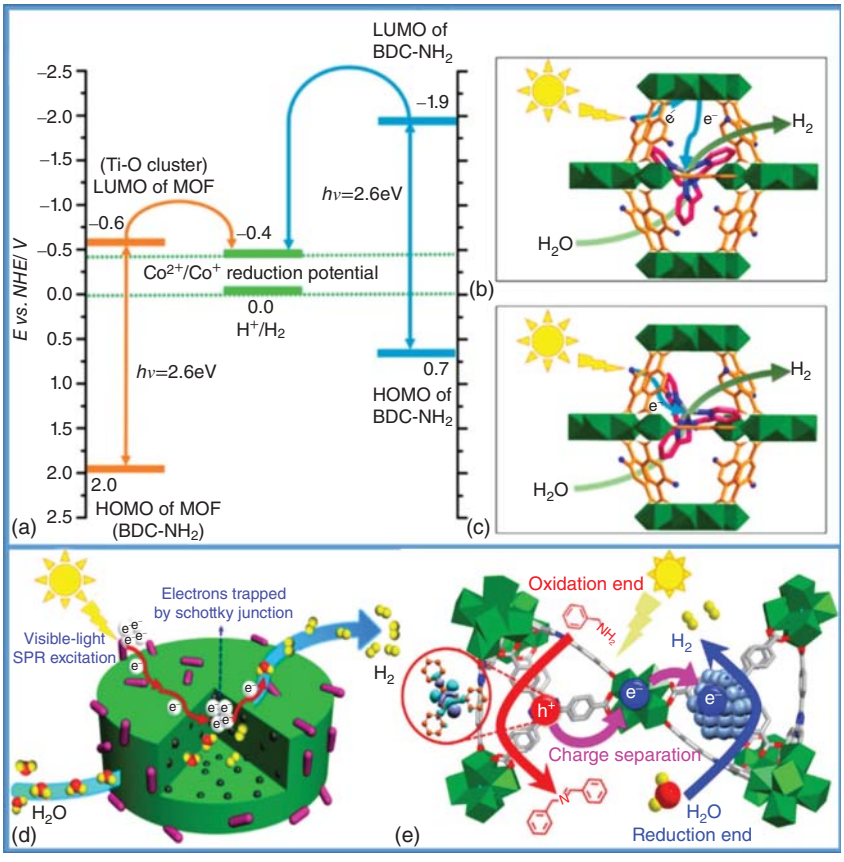

Figure 9.9 Schematic representation of the (a) redox potentials of the different species, (b, c) plausible mechanism of electron transfer between the Co (II) complex and (b) MIL-125-NH_2/ and (c) BDC-NH_2. Source: Li et al. [91]/with permission of American Chemical Society, (d) electron migration pathway and photocatalytic H_2 evolution over Pt@MIL-125/Au photocatalysts. Source: Xiao et al. [92]/with permission of John Wiley & Sons and (e) photocatalytic H_2 production and benzylamine oxidation over Pt/PCN-777. Source: Liu et al. [93]/with permission of John Wiley & Sons.

served as the active site to receive the electrons for H_2 production. Its potential is −0.4 V vs. NHE, which is between the LUMO energy level of MIL-125-NH_2 (also BDC-NH_2) and the $H^{+/}H_2$ reduction potential (Figure 9.9a). The electron-transfer process in the Co(II) complex@MIL-125-NH_2 composite can occur in either of the two ways shown schematically in Figure 9.9b, c. Briefly, the photogenerated electrons transfer from the ligand to the metal Ti-oxo cluster and finally to the Co(II) complex (Figure 9.9b). Then, the electrons transfer from the BDC-NH_2 ligand to the Co(II) complex directly facilitates the proton reduction (Figure 9.9c). In addition, Xiao et al. reported a Pt@MIL-125/Au composite photocatalyst for the efficient photocatalytic production of H_2 under visible-light irradiation, utilizing the advantages of plasmonic Au-MOFs and Pt-MOF Schottky junctions [92]. The interface of plasmonic Au nanoparticles and MOF generates plasmonic hot electrons in the LUMO of the MOFs upon light irradiation, while the other interface

of Pt and MOF establishes a Schottky junction, thereby initiating a unidirectional flow of electrons to be trapped at the Pt sites across the interfaces. This results in enhanced electron–hole separation, thereby boosting the overall H_2 production rate. The charge-transfer mechanism in Pt@MIL-125/Au is schematically represented in Figure 9.9d.

Liu et al. also explored the use of a platinum-loaded MOF composite (Pt/PCN-777) for photocatalytic H_2 production, along with the oxidation of benzylamine to *N*-benzylbenzaldimine [93]. The light absorption and charge separation in the Pt/PCN-777 composite was significantly extended by the elongated-conjugated ligand in the MOF (PCN-777). Thus, under light irradiation, the photogenerated protons can efficiently reduce H^+ to produce H_2, and the holes oxidize benzylamine to *N*-benzylbenzaldimine (Figure 9.9e). The Pt/PCN-777 composite with 2.3 wt% Pt showed superior photocatalytic activities in the coupled reactions than 2.4 wt% Pt/MOF-808. However, both MOFs exhibit the same topology and almost identical coordination environments as Zr-oxo clusters. Thus, the coupling of MOFs with various metallic nanoparticles, such as Au and Pt, shows promising photocatalytic activities for H_2 production.

In addition to metal nanoparticles, MOFs coupled with semiconducting materials, such as TiO_2, have also been investigated for various photocatalytic reactions. Martínez et al. reported H_2 production through the photoreforming of glycerol using a TiO_2/HKUST-1 composite under solar-light irradiation [94]. The TiO_2/HKUST-1 composite with TiO_2:HKUST-1 = 1 : 1 showed a higher H_2 production rate than pristine TiO_2 or HKUST-1, which is attributed to the synergistic effect resulting from each component prohibiting the electron–hole recombination. The proposed mechanism for the photoreforming of glycerol using the TiO_2/HKUST-1 composite photocatalyst is schematically shown in Figure 9.10. Upon light irradiation, the photogenerated electrons in the CB of TiO_2 cause the partial reduction of Cu^{2+} in HKUST-1 to Cu^+ to absorb visible light and finally contribute to proton reduction to generate H_2 (Figure 9.10).

The reversible generation of Cu^{2+}/Cu^{+1} moieties in the MOF composite was ascribed to the transfer of electrons from TiO_2 to HKUST-1, thereby generating

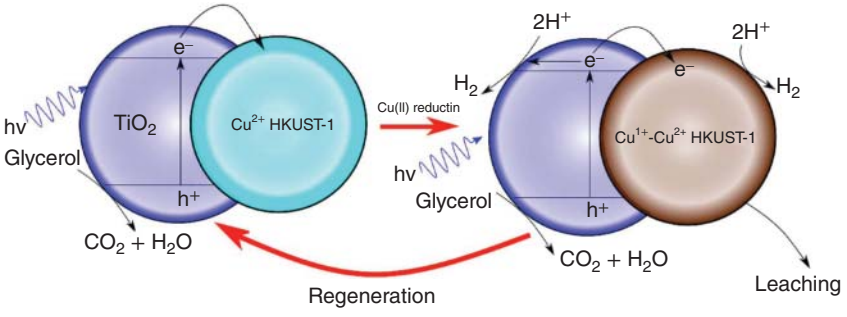

Figure 9.10 Schematic representation of the mechanism for the photoreforming of glycerol under solar-light irradiation using the TiO_2 P25/syn-HKUST-1 photocatalyst. Source: Martínez et al. [94]/MDPI/CC BY 4.0.

the Cu^{1+} and Cu^{2+} species in-situ in the MOF. The superior H_2 production rate of TiO_2/HKUST-1 can be attributed to the strong interactions between each component, which result from the synthesis of the composite through chemical methods compared to those of mixing or grinding methods. Thus, MOFs and their nanocomposites have been utilized as effective photocatalysts for various reactions. However, these studies are in the nascent stage and require further investigation to explore their applications.

9.6 Metal-Free Photocatalysts

To explore more cost-effective and stable photocatalysts than metal-based photocatalysts, various earth-abundant and low-cost nonmetals such as N, C, P, B, S, and Se, based on binary and ternary compounds (BC_3, B_4C, h-BN, C_xN_x, and BCN) and their heterojunctions, along with various organic-based photocatalysts. These photocatalysts, including covalent organic frameworks (COF), microporous polymers, and graphene oxides (GO), have also been explored as metal-free photocatalysts for various photocatalytic reactions such as H_2 production and biomass conversion [95–98]. For example, Liu et al. reported boron carbides ($B_{4.3}C$ and $B_{13}C_2$) as photocatalysts for H_2 production under visible-light irradiation [98]. $B_{4.3}C$ and $B_{13}C_2$ generated an H_2 yield of 2.9 and 0.9 μmol h^{-1}, respectively, from a 25% methanol aqueous solution under visible-light irradiation. In addition, Wang et al. explored the use of g-C_3N_4-based photocatalysts for photocatalytic H_2 production in the presence of a sacrificial donor under visible-light irradiation [99]. However, the efficiency of photocatalytic H_2 production for such g-C_3N_4-based photocatalysts was unsatisfactory because of their lower specific surface area (SSA), low light absorption, and high degree of electron–hole recombination [84, 99]. Therefore, to overcome their shortcomings, surface modification of the g-C_3N_4 photocatalysts has been employed via functionalization of the C—O functional group using an economical method [84]. The surface-modified g-C_3N_4 showed higher H_2 production than pristine unmodified g-C_3N_4, which is attributed to the enhancement in charge carrier separation, the extension of light absorption, and higher SSA. Kasap et al. reported the photoreforming of lignocellulose for H_2 production using cyanamide-functionalized carbon nitride ($^{NCN}CN_x$) with a molecular *bis*(diphosphine) Ni proton reduction co-catalyst under benign conditions [100]. Under alkaline conditions, approximately 2.62 μmol of H_2 was generated during four hours of AM 1.5G irradiation in a system containing 0.5 mg of $^{NCN}CN_x$ and 50 nmol of NiP, which is much larger than the H_2 yield of the pristine bulk $^{NCN}CN_x$. This higher photocatalytic activity of cyanamide-functionalized $^{NCN}CN_x$ was attributed to the enhanced transfer of photogenerated holes to electron-donating substrates enabled by cyanamide surface functionalization. Similarly, the photoreforming of xylan and lignin substrates was also explored using the same photocatalytic system. In this reaction, the H_2 production yield obtained from the photoreforming of xylan (~4.92 μmol) was higher than that of lignin (~0.20 μmol). This indicates that H_2 production is limited by the accessibility

of smaller substrate molecules that can quench the photogenerated holes on the surface of the photocatalyst. Using a raw and pristine biomass substrate such as sawdust, a H_2 production yield of ~202 μmol h^{-1} g_{cat}^{-1} was obtained. However, a decrease in the H_2 yield was observed for the Ni proton reduction co-catalysts after 24 hours; this yield was lower than those of other co-catalysts with slower kinetics, such as Pt and MoS_2, indicating its fragile molecular framework [100]. Recently, the oxidative depolymerization of various biomasses, especially lignin, was investigated for extracting electrons using phosphomolybdic acid (PMA) as a catalyst at a low energy input. Various value-added byproducts, such as vanillin and CO, were also generated in this process [101]. In this system, PMA acted as a catalyst and also as an electron mediator, while lignin was used as the electron source because of its high abundance and great potential for various applications. Unlike water splitting, which requires high energy input (~1.5–1.6 V vs. RHE) and costly OER electrocatalysts, the use of PMA enabled the extraction of electrons at a much lower energy (~0.95 V vs. RHE) from biomass and generated H_2 much more efficiently (Figure 9.11a) [101]. In addition to H_2 generation, PMA-enabled lignin oxidation generates various value-added products, such as CO and vanillin, from the depolymerization process (Figure 9.11b).

Another metal-free photocatalyst composed of 2D black phosphorus (BP) and carbon nitride (CN) nanohybrids was also investigated for H_2 evolution from an aqueous methanol solution under visible to near-infrared irradiation (NIR) [97]. Its photocatalytic activity is schematically shown in Figure 9.11c. The band structures of BP and CN show that a type 1 heterojunction can be formed at the BP/CN interface. Accordingly, upon visible light-irradiation, electron holes are generated in the CB and VB of CN, while the adjacent BP accepts the photogenerated electrons from the CN, thereby reducing the electron–hole recombination (Figure 9.11). The presence of a P—N coordinated bond at the BP/CN interface serves as an electron trap and facilitates H_2 production, while the photogenerated holes in BP are

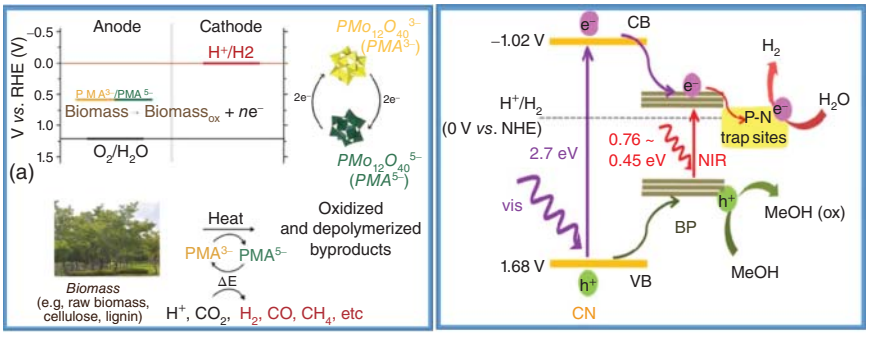

Figure 9.11 Schematic representation of (a, b) using biomass as an electron donor via oxidative depolymerization with phosphomolybdic acids (PMAs) in terms of energy efficiency and generation of value-added products. Source: Oh et al. [101]/with permission of American Chemical Society, and (c) mechanism of photocatalytic H_2 production using PB/CN under visible- and NIR-light irradiation. Source: Zhu et al. [97]/with permission of American Chemical Society.

quenched by methanol. Further, under visible-light irradiation, the photogenerated electrons in the CB of BP are trapped by the P—N coordinated bonds at the BP/CN interface, further enhancing H_2 production. Therefore, the interaction between P and N atoms at the BP/CN hybrid interface is important for enhancing H_2 production. In summary, the development of metal-free photocatalysts based on low-cost and earth-abundant elements for photocatalytic H_2 production from biomass or its derivatives has great potential for clean energy production and has attracted significant interest worldwide.

9.7 Dye-Sensitized TiO_2 Photocatalysts

Inspired by photosynthesis, a process that converts and stores solar energy into chemical fuels, hydrogen gas, or carbon-based fuels (e.g. methanol) using photoelectrochemical cells (PECs) has been developed [86, 102, 103]. Among PECs, a dye-sensitized photoelectrochemical cell (DSPEC) has been intensively explored for water oxidation and reduction by introducing a molecular chromophore-catalyst assembly on metal oxides (e.g. TiO_2, NiO) [104–106]. TiO_2 is the most common photosensitized semiconductor used as a photoanode with chromophore-catalyst molecular assembly [107]. Molecular chromophores used in DSPEC can be largely classified into two main groups: metal-free organic dyes[85, 108] and metal–ligand chromophores [109–111]. Especially, polypyridyl Ru(II)-based metal complexes have been widely used in DSPECs for water splitting and CO_2 reduction [112, 113]. Ruthenium (Ru) (II) tris-bipyridine (bpy), $[Ru(bpy)_3]^{2+}$, is commonly used in DSPECs as a photosensitizer or photocatalyst due to its wide light absorption range from near-UV to visible light, relatively high stability of the metal-to-ligand-charge-transfer (MLCT) excited state, and higher LUMO energy level for easier electron escape [110, 114–116].

Very recently, Li et al. reported the chemoselective oxidation of secondary benzylic alcohols in a lignin model compound, 2-phenoxy-1-phenylethanol (PP-ol), to 2-phenoxy-1-phenylethanone (PP-one) in the presence of nitroxyl mediator incorporated DSPEC [117, 118]. In the DSPEC, a carboxylic acid-functionalized polypyridyl Ru-based photocatalyst (RuC, ((bis-2,2′-bipyridine)(2,2′-bipyridine-4,4′-dicarboxylic acid) ruthenium(II)) was used as the photocatalyst by incorporating nitroxyl mediators (e.g. *N*-hydroxyphthalimide (NHPI) or acetamido-2,2,6,6-tetramethylpiperidine *N*-oxyl (ACT)). NHPI has been widely studied as an effective oxidizing mediator with the electro-induced generation of the N-oxyl radical, phthalimide *N*-oxyl (PINO), with a suitable O—H bond strength (BDE_{NHPI} = 86 kcal·mol^{-1}) for the electrocatalytic alcohol oxidation in lignin [119–121]. In the designed NHPI-mediated lignin oxidation in the DSPEC cell, H_2 gas is likely to be generated at the surface of the cathode via H^+ reduction [117]. The reaction mechanism of the photoinduced alcohol oxidation is shown in Figure 9.12a; the sequence of events is listed as follows: (1) photon absorption and excitation of photosensitizer, (2) electron injection into n-type TiO_2 semiconductor, (3) transport of the injected electron through the semiconductor to a transparent

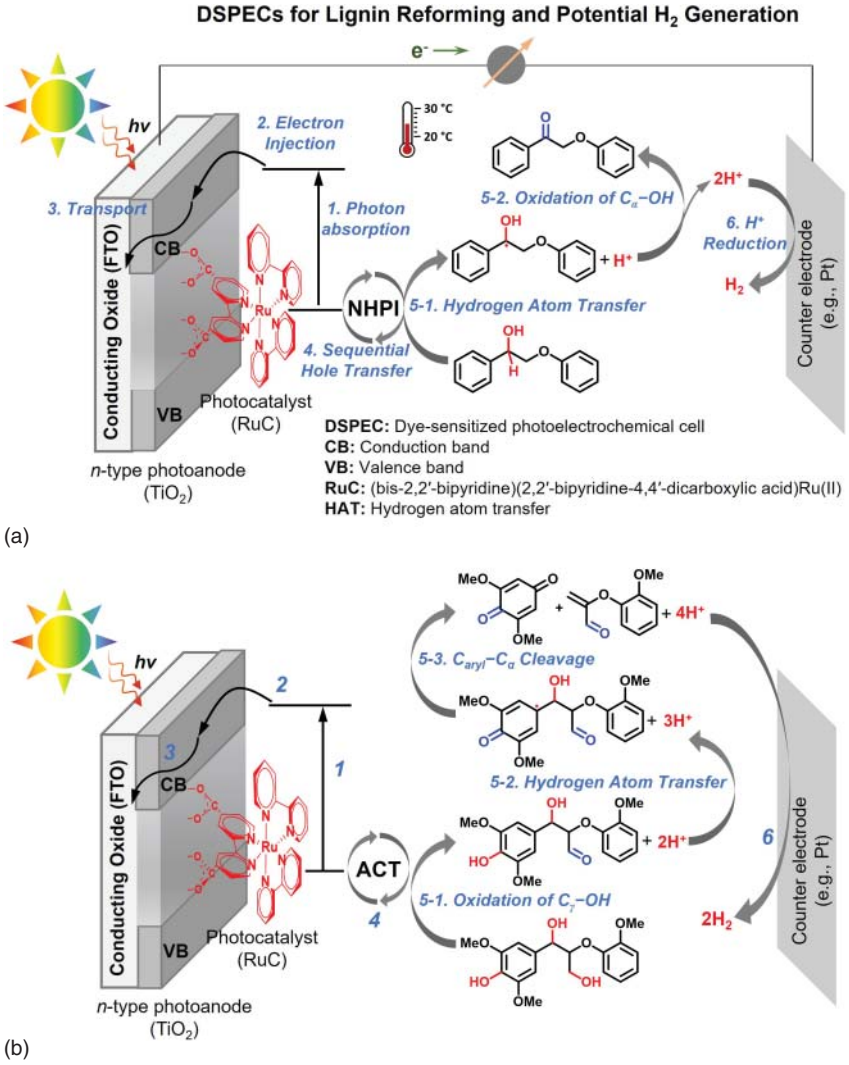

Figure 9.12 Schematic illustrations of photoinduced lignin reforming and potential H_2 generation in DSPEC cells. (a) Photocatalytic NHPI-mediated alcohol oxidation in the lignin model compound, 2-phenoxy-1-phenylethanol (PP-ol), to 2-phenoxy-1-phenylethanone (PP-one) at the interface of RuC coated TiO_2 photoanode and H_2 generation at the cathode surface (e.g. Pt). The proposed mechanism shows the following sequence of events: (1) chromophore light absorption; (2) charge injection into the CB of the semiconductor; (3) transport of the injected electron through the semiconductor to a transparent conducting oxide and its subsequent transfer to the anode; (4) hole transfer from the chromophore to the HAT mediator; (5) oxidation of secondary alcohol in PP-ol; and (6) H^+ reduction for the generation of H_2 gas. (b) C—C bond cleavage and H_2 generation from the lignin model compound, 1-(4-hydroxy-3,5-dimethoxyphenyl)-2-(2-methoxyphenoxy)propane-1,3-diol (HDMP-2ol), using an ACT-coupled DSPEC cell. The sequence of events is the same as that of the above DSPEC cell, except for step 5: C_{aryl}—C_α bond cleavage. (Source: Adapted from Refs. [117, 122].)

conducting oxide and its subsequent transfer to the photoanode, (4) hole transfer from the excited-state photosensitizer (RuC*) to NHPI, (5) HAT followed by C_α–OH oxidation, and (6) potential H_2 generation from H^+ reduction at the surface of cathode (i.e. Pt). As a result, the formation of the ketone product is shown, and the hydrogen atoms generated from step (5) are highly possible to form hydrogen gas at the cathode (step (6)). In this study of the HAT-coupled DSPEC cell for PP-ol oxidation, the combination of photocatalysis and electrocatalytic oxidation enables lignin oxidation with low applied bias at room temperature, providing a highly promising method for biomass reforming and hydrogen production.

Specific bond cleavage in the lignin model compound can also be performed using dye-sensitized TiO_2 photoanode [123], or the aforementioned HAT-coupled DSPEC cell [122], along with possible H_2 generation. C_{aryl}–C_α bond cleavage was achieved using a RuC-coated TiO_2 photoanode associated with the oxidizing mediator, ACT, in a DSPEC under solar illumination [122]. ACT has been widely studied as an efficient oxidizing mediator owing to the strong oxidizing ability of its oxoammonium form [124–126]. ACT-mediated chemoselective $C_{aryl} - C_\alpha$ bond cleavage in a lignin model compound 1-(4-hydroxy-3,5-dimethoxyphenyl)-2-(2-methoxyphenoxy)propane-1,3-diol occurred under mild conditions in a DSPEC. As shown in Figure 9.12b, following the first four photodynamic steps, the C_{aryl}–C_α bond is cleaved by the oxidation of the $C_\gamma - OH$ bond (step 5–1) and the HAT reaction for activating the phenolic hydroxyl groups (step 5-2). Similarly, H_2 can be generated at the surface of the cathode owing to H^+ reduction (step 6). In summary, these DSPEC are highly effective for the selective conversion of lignin and have potential applications in the generation of biofuels and H_2 gas.

9.8 Conclusion

Photocatalytic H_2 production from biomass offers a potential renewable energy source. Numerous photocatalysts for H_2 production from biomass have been developed because of the urgent demand to generate efficient, sustainable, and eco-friendly biofuels as renewable energy sources. Moreover, hydrogen gas may play an important role in the energy economy of humankind in the future. The photocatalytic production of H_2 from renewable biomass provides an efficient, economical, and environmentally friendly strategy that uses abundantly available solar energy. In particular, solar-driven photochemical reforming of earth-abundant biomass presents a possible solution for supplying H_2 in a sustainable way.

Acknowledgment

This work was supported by the National Research Foundation of Korea grant (2019R1C1C1009427) funded by the Ministry of Science and ICT, Republic of Korea, and the GRRC program of Gyeonggi province (GRRC 2020-B03). This work is also supported in part by the USDA National Institute of Food and Agriculture, McIntire Stennis project (No. 1026335).

References

1 Tursi, A. (2019). *Biofuel Res. J.* 6: 962.
2 Billi, U.S. (2011). *Ind. Biotechnol.* 7: 375.
3 Langholtz, M., Stokes, B., and Eaton, L. (2016). *Ind. Biotechnol.* 12: 282.
4 da Silva Veras, T., Mozer, T.S., da Costa Rubim Messeder dos Santos, D., and da Silva César, A. (2017). *Int. J. Hydrogen Energy* 42: 2018.
5 Puga, A.V. (2016). *Coord. Chem. Rev.* 315: 1.
6 Silva, C.G., Sampaio, M.J., Marques, R.R.N. et al. (2015). *Appl. Catal. B Environ.* 178: 82.
7 Davis, K.A., Yoo, S., Shuler, E.W. et al. (2021). *Nano Converg.* 8: 6.
8 Melo, M.D. and Silva, L.A. (2011). *J. Braz. Chem. Soc.* 22: 1399.
9 Rossetti, I. (2012). *ISRN Chem. Eng.* 2012: 1.
10 Wang, S., Lu, A., and Zhong, C.-J. (2021). *Nano Converg.* 8: 4.
11 Ros, C., Andreu, T., and Morante, J.R. (2020). *J. Mater. Chem. A* 8: 10625.
12 Huang, C.-W., Nguyen, B.-S., Wu, J.C.S., and Nguyen, V.-H. (2020). *Int. J. Hydrogen Energy* 45: 18144.
13 Hamelinck, C.N. and Faaij, A.P.C. (2002). *J. Power Sources* 111: 1.
14 Fujishima, A. and Honda, K. (1972). *Nature* 238: 37.
15 Fujishima, A., Rao, T.N., and Tryk, D.A. (2000). *J. Photochem. Photobiol. C Photochem. Rev.* 1: 1.
16 Lan, Y., Lu, Y., and Ren, Z. (2013). *Nano Energy* 2: 1031.
17 Lu, H., Zhao, J., Li, L. et al. (2011). *Energy Environ. Sci.* 4: 3384.
18 Bahruji, H., Bowker, M., Davies, P.R., and Pedrono, F. (2011). *Appl. Catal. B Environ.* 107: 205.
19 Luo, L., Zhang, T., Zhang, X. et al. (2020). *Catalysts* 10: 539.
20 Fujita, S., Kawamori, H., Honda, D. et al. (2016). *Appl. Catal. B Environ.* 181: 818.
21 Abdullah, N., Bahruji, H., Rogers, S.M. et al. (2019). *Phys. Chem. Chem. Phys.* 21: 16154.
22 Bloh, J.Z., Dillert, R., and Bahnemann, D.W. (2012). *J. Phys. Chem. C* 116: 25558.
23 Cheng, N., Stambula, S., Wang, D. et al. (2016). *Nat. Commun.* 7: 13638.
24 Colmenares, J.C., Magdziarz, A., Aramendia, M.A. et al. (2011). *Catal. Commun.* 16: 1.
25 Panagiotopoulou, P., Karamerou, E.E., and Kondarides, D.I. (2013). *Catal. Today* 209: 91.
26 Chung, Y.-H., Han, K., Lin, C.-Y. et al. (2020). *Catal. Today* 356: 95.
27 Speltini, A., Sturini, M., Dondi, D. et al. (2014). *Photochem. Photobiol. Sci.* 13: 1410.
28 Zou, J., Zhang, G., and Xu, X. (2018). *Appl. Catal. A Gen.* 563: 73.
29 Caravaca, A., Jones, W., Hardacre, C., and Bowker, M. (2016). *Proc. Math. Phys. Eng. Sci.* 472: 20160054.
30 Luna, A.L., Dragoe, D., Wang, K. et al. (2017). *J. Phys. Chem. C* 121: 14302.

31 Dickinson, A., James, D., Perkins, N. et al. (1999). *J. Mol. Catal. A Chem.* 146: 211.
32 Priebe, J.B., Radnik, J., Lennox, A.J.J. et al. (2015). *ACS Catal.* 5: 2137.
33 Serra, M., Albero, J., and García, H. (1842). *ChemPhysChem* 2015: 16.
34 Puga, A.V., Forneli, A., García, H., and Corma, A. (2014). *Adv. Funct. Mater.* 24: 241.
35 Kumaravel, V., Mathew, S., Bartlett, J., and Pillai, S.C. (2019). *Appl. Catal. B Environ.* 244: 1021.
36 Fang, J., Cao, S.W., Wang, Z. et al. (2012). *Int. J. Hydrogen Energy* 37: 17853.
37 Gomathisankar, P., Yamamoto, D., Katsumata, H. et al. (2013). *Int. J. Hydrogen Energy* 38: 5517.
38 Gomes Silva, C., Juárez, R., Marino, T. et al. (2011). *J. Am. Chem. Soc.* 133: 595.
39 Fu, X., Long, J., Wang, X. et al. (2008). *Int. J. Hydrogen Energy* 33: 6484.
40 Murdoch, M., Waterhouse, G.I.N., Nadeem, M.A. et al. (2011). *Nat. Chem.* 3: 489.
41 Fan, X., Wan, J., Liu, E. et al. (2015). *Ceram. Int.* 41: 5107.
42 Sadanandam, G., Lalitha, K., Kumari, V.D. et al. (2013). *Int. J. Hydrogen Energy* 38: 9655.
43 Liu, B., Su, S., Zhou, W. et al. (2017). *CrystEngComm* 19: 675.
44 Sun, T., Liu, E., Liang, X. et al. (2015). *Appl. Surf. Sci.* 347: 696.
45 Sun, T., Fan, J., Liu, E. et al. (2012). *Powder Technol.* 228: 210.
46 Hidalgo-Carrillo, J., Martín-Gómez, J., Morales, J. et al. (2019). *Energies* 12: 3351.
47 Bahruji, H., Bowker, M., Davies, P.R. et al. (2015). *Int. J. Hydrogen Energy* 40: 1465.
48 Ko, M., Pham, L.T.M., Sa, Y.J. et al. (2019). *Nat. Commun.* 10: 5123.
49 Clarizia, L., Di Somma, I., Onotri, L. et al. (2017). *Catal. Today* 281: 117.
50 Pérez-Larios, A., Hernández-Gordillo, A., Morales-Mendoza, G. et al. (2016). *Catal. Today* 266: 9.
51 Xu, Y., Lei, B., Guo, L. et al. (2008). *J. Hazard. Mater.* 160: 78.
52 Yan, X., Xue, C., Yang, B., and Yang, G. (2017). *Appl. Surf. Sci.* 394: 248.
53 Liu, G., Sun, C., Yan, X. et al. (2009). *J. Mater. Chem.* 19: 2822.
54 Babu, V.J., Kumar, M.K., Nair, A.S. et al. (2012). *Int. J. Hydrogen Energy* 37: 8897.
55 Fang, J., Wang, F., Qian, K. et al. (2008). *J. Phys. Chem. C* 112: 18150.
56 Zhang, G., Ding, X., Hu, Y. et al. (2008). *J. Phys. Chem. C* 112: 17994.
57 Di Valentin, C. and Pacchioni, G. (2013). *Catal. Today* 206: 12.
58 Preethi, L.K., Antony, R.P., Mathews, T. et al. (2017). *Sci. Rep.* 7: 14314.
59 Asahi, R., Morikawa, T., Ohwaki, T. et al. (2001). *Science* 293: 269.
60 Carmichael, P., Hazafy, D., Bhachu, D.S. et al. (2013). *Phys. Chem. Chem. Phys.* 15: 16788.
61 Zhu, Y., Li, J., Dong, C.-L. et al. (2019). *Appl. Catal. B* 255: 117764.
62 Wang, J., Zhang, D., Deng, J., and Chen, S. (2018). *J. Colloid Interface Sci.* 516: 215.

63 Cheng, L., Xiang, Q., Liao, Y., and Zhang, H. (2018). *Energy Environ. Sci.* 11: 1362.
64 Wang, X., Zheng, X., Han, H. et al. (2020). *J. Solid State Chem.* 289: 121495.
65 Ke, D., Liu, S., Dai, K. et al. (2009). *J. Phys. Chem. C* 113: 16021.
66 Quan, F., Zhang, J., Li, D. et al. (2018). *Chem. Eng.* 6: 14911.
67 Wakerley, D.W., Kuehnel, M.F., Orchard, K.L. et al. (2017). *Nat. Energy* 2: 17021.
68 Han, G., Jin, Y.H., Burgess, R.A. et al. (2017). *J. Am. Chem. Soc.* 139: 15584.
69 Chen, H., Sun, Z., Ye, S. et al. (2015). *J. Mater. Chem. A* 3: 15729.
70 Sun, Z., Chen, H., Zhang, L. et al. (2016). *J. Mater. Chem. A* 4: 13289.
71 Song, X., Liu, Y., Zheng, Y. et al. (2016). *Phys. Chem. Chem. Phys.* 18: 4577.
72 Zhang, L., Tian, B., Chen, F., and Zhang, J. (2012). *Int. J. Hydrogen Energy* 37: 17060.
73 Chen, Z., Sun, P., Fan, B. et al. (2014). *J. Phys. Chem. C* 118: 7801.
74 Li, C., Wang, H., Naghadeh, S.B. et al. (2018). *Appl. Catal. B Environ.* 227: 229.
75 Chen, L., Zhu, X., Wang, F., and Gu, W. (1993). *J. Photochem. Photobiol. A Chem.* 73: 217.
76 Peng, Y., Shang, L., Cao, Y. et al. (2015). *Appl. Surf. Sci.* 358: 485.
77 Xitao, W., Rong, L., and Kang, W. (2014). *J. Mater. Chem. A* 2: 8304.
78 Guo, S., Zhao, T., Jin, Z. et al. (2015). *J. Power Sources* 293: 17.
79 Gasparotto, A., Barreca, D., Bekermann, D. et al. (2011). *J. Am. Chem. Soc.* 133: 19362.
80 Tanaka, A., Hashimoto, K., and Kominami, H. (2014). *J. Am. Chem. Soc.* 136: 586.
81 Lv, R., Wang, X., Lv, W. et al. (2015). *J. Chem. Technol. Biotechnol.* 90: 550.
82 Li, Y., Ma, J., Jin, D. et al. (2021). *Appl. Catal. B* 291: 120123.
83 Zhang, L., Shi, J., Liu, M. et al. (2014). *Chem. Commun.* 50: 192.
84 Wang, C.-H., Qin, D.-D., Shan, D.-L. et al. (2017). *Phys. Chem. Chem. Phys.* 19: 4507.
85 Alibabaei, L., Dillon, R.J., Reilly, C.E. et al. (2017). *Mater. Interfaces* 9: 39018.
86 Umena, Y., Kawakami, K., Shen, J.-R., and Kamiya, N. (2011). *Nature* 473: 55.
87 Silva, C.G., Corma, A., and García, H. (2010). *J. Mater. Chem.* 20: 3141.
88 Xiao, J.-D. and Jiang, H.-L. (2019). *Acc. Chem. Res.* 52: 356.
89 Belousov, A.S. and Suleimanov, E.V. (2021). *Green Chem.* 23: 6172.
90 Toyao, T., Saito, M., Dohshi, S. et al. (2014). *Chem. Commun.* 50: 6779.
91 Li, Z., Xiao, J.-D., and Jiang, H.-L. (2016). *ACS Catal.* 6: 5359.
92 Xiao, J.-D., Han, L., Luo, J. et al. (2018). *Angew. Chem. Int. Ed.* 57: 1103.
93 Liu, H., Xu, C., Li, D., and Jiang, H.-L. (2018). *Angew. Chem. Int. Ed.* 57: 5379.
94 Martínez, F.M., Albiter, E., Alfaro, S. et al. (2019). *Catalysts* 9: 338.
95 Rahman, M.Z., Kibria, M.G., and Mullins, C.B. (1887). *Chem. Soc. Rev.* 2020: 49.
96 Li, C., Xu, Y., Tu, W. et al. (2017). *Green Chem.* 19: 882.
97 Zhu, M., Kim, S., Mao, L. et al. (2017). *J. Am. Chem. Soc.* 139: 13234.
98 Liao, Q., Wang, D., Ke, C. et al. (2021). *Appl. Catal. B* 298: 120548.
99 Wang, X., Maeda, K., Thomas, A. et al. (2009). *Nat. Mater.* 8: 76.

100 Kasap, H., Achilleos, D.S., Huang, A., and Reisner, E. (2018). *J. Am. Chem. Soc.* 140: 11604.

101 Oh, H., Choi, Y., Shin, C. et al. (2020). *ACS Catal.* 10: 2060.

102 Ferreira, K.N., Iverson, T.M., Maghlaoui, K. et al. (2004). *Science* 303: 1831.

103 Reece, S.Y., Hamel, J.A., Sung, K. et al. (2011). *Science* 334: 645.

104 Frischmann, P.D., Mahata, K., and Würthner, F. (1847). *Chem. Soc. Rev.* 2013: 42.

105 Grätzel, M. (2005). *Inorg. Chem.* 44: 6841.

106 Swierk, J.R. and Mallouk, T.E. (2013). *Chem. Soc. Rev.* 42: 2357.

107 Butburee, T., Chakthranont, P., Phawa, C., and Faungnawakij, K. (1873). *ChemCatChem* 2020: 12.

108 Wang, D., Eberhart, M.S., Sheridan, M.V. et al. (2018). *Proc. Natl. Acad. Sci.* 115: 8523.

109 Leem, G., Sherman, B.D., and Schanze, K.S. (2017). *Nano Converg.* 4: 1.

110 Sherman, B.D., Xie, Y., Sheridan, M.V. et al. (2017). *ACS Energy Lett.* 2: 124.

111 Zhu, Y., Wang, D., Huang, Q. et al. (2020). *Nat. Commun.* 11: 4610.

112 Brown, A.M., McCusker, C.E., and McCusker, J.K. (2014). *Dalt. Trans.* 43: 17635.

113 La Mazza, E., Puntoriero, F., Nastasi, F. et al. (2016). *Dalt. Trans.* 45: 19238.

114 Brennaman, M.K., Dillon, R.J., Alibabaei, L. et al. (2016). *J. Am. Chem. Soc.* 138: 13085.

115 Sherman, B.D., Sheridan, M.V., Wee, K.-R. et al. (2016). *J. Am. Chem. Soc.* 138: 16745.

116 Sheridan, M.V., Sherman, B.D., Coppo, R.L. et al. (2016). *ACS Energy Lett.* 1: 231.

117 Li, S., Li, Z.J., Yu, H. et al. (2020). *ACS Energy Lett.* 5: 777.

118 Li, S., Shuler, E.W., Willinger, D. et al. (2022). *ACS Appl. Mater. Interfaces* 14: 22799–22809.

119 Bosque, I., Magallanes, G., Rigoulet, M. et al. (2017). *ACS Cent. Sci.* 3: 621.

120 Shiraishi, T., Takano, T., Kamitakahara, H., and Nakatsubo, F. (2012). *Holzforschung* 66: 311.

121 Recupero, F. and Punta, C. (2007). *Chem. Rev.* 107: 3800.

122 Li, S., Kim, S., Davis, A.H. et al. (2021). *ACS Catal.* 11: 3771.

123 Li, S., Wijethunga, U.K., Davis, A.H. et al. (2022). *ACS Appl. Nano Mater.* 5: 948.

124 Rafiee, M., Alherech, M., Karlen, S.D., and Stahl, S.S. (2019). *J. Am. Chem. Soc.* 141: 15266.

125 Rafiee, M., Miles, K.C., and Stahl, S.S. (2015). *J. Am. Chem. Soc.* 137: 14751.

126 Rahimi, A., Azarpira, A., Kim, H. et al. (2013). *J. Am. Chem. Soc.* 135: 6415.

10

Photocatalytic Hydrogen Production from Aqueous Solutions of Organic Substances – Biomass Components – Over CdS-based Photocatalysts Under Visible Light

Anna Y. Kurenkova and Ekaterina A. Kozlova

Boreskov Institute of Catalysis, Department of Heterogeneous Catalysis, Ak. Lavrentieva Ave. 5, Novosibirsk 630090, Russian Federation

10.1 Introduction

Currently, particular attention is focused on the development of alternative energy sources to allow complete or partial rejection of traditional fossil fuels – oil, gas, and coal. Hydrogen is considered one of the most promising energy carriers of the future [1], since it releases only water as the combustion product and has a higher energy density as compared to traditional fuels [2]. The development of hydrogen energy will help to reduce greenhouse gas emissions into the atmosphere.

Hydrogen is one of the most abundant elements on Earth [3], but an overwhelming part of it presents in the bound state as a constituent of water, natural gas, and biomass. [4]. Numerous ways are available to produce hydrogen, but they typically release carbon oxides as byproducts [5]. The most common hydrogen producing process is steam reforming of natural gas (about 50% of the world's hydrogen production), followed by reforming of heavy oil fractions (30%) and coal gasification (18%) [6]. That is, fossil fuels are the main feedstock for industrial hydrogen production as of yet. Besides emitting undesirable byproducts, traditional hydrogen production processes proceed at high temperatures, which add considerable production costs.

Water splitting is assumed to be one of the most promising ways to produce hydrogen, provided that the required energy is obtained from renewable sources. If solar radiation serves as a source of energy, the process is called photocatalytic splitting of water. A clear advantage of photocatalysis is that the reaction proceeds at ambient temperature and atmospheric pressure [7]. Thus, photocatalytic hydrogen production possesses obvious advantages since it:

- releases pure hydrogen;
- uses available raw material – biomass;
- proceeds under benign reaction conditions (ambient temperature and atmospheric pressure).

Photocatalytic Hydrogen Production for Sustainable Energy, First Edition. Edited by Alberto Puga.

The phenomenon of photocatalytic decomposition of water under ultraviolet radiation in the presence of TiO_2 was discovered in 1972 [4]. Since that time, significant progress has been achieved in this research area, including the development of visible-light-driven photocatalysts [8]. One of the most promising photoactive materials operating under visible light is cadmium sulfide, owing to the suitable positions of its conduction and valence bands (CB and VB) [9]. However, this material is unstable and has low-quantum efficiency. Various methods are applied to improve the photocatalytic properties of CdS. The synthesis of solid solutions based on CdS and wider-gap semiconductors, for example, ZnS, attracts particular attention. This approach makes it possible to significantly improve the photocatalyst performance in the hydrogen evolution reaction [10–12]. The catalyst activity can be enhanced also by depositing the particles of transition metals or their compounds on the CdS surface [8]. Most of the research works reported in the literature on visible-light-driven photocatalysis are focused on hydrogen evolution from the solutions of inorganic electron donors, such as the Na_2S/Na_2SO_3 system. Much less studies are devoted to the use of aqueous solutions of sugars as organic electron donors, and only few works report the studies of photocatalytic hydrogen evolution from complex insoluble plant components such as starch, cellulose, and sawdust.

Organic biomass derivatives, as well as biomass components themselves, are of particular interest for using as electron donors, because they allow hydrogen production by using only renewable energy sources: water, solar radiation, and biomass [13]. Besides, biomass components belong to the carbon cycle (Figure 10.1a), i.e. the CO_2, which is formed as a byproduct of hydrogen evolution from biomass, can be again converted into biomass through photosynthesis in a fairly short time [14].

Thus, the CO_2 emissions from biomass processing add no negative impact on the environment, and the use of biomass for photocatalytic hydrogen evolution is consistent with the principles of sustainable development [16]. This chapter summarizes the data on the visible-light-driven photocatalytic production of hydrogen from plant biomass components. Particular attention will be focused on CdS-based photocatalysts, as they are highly active under the action of visible light.

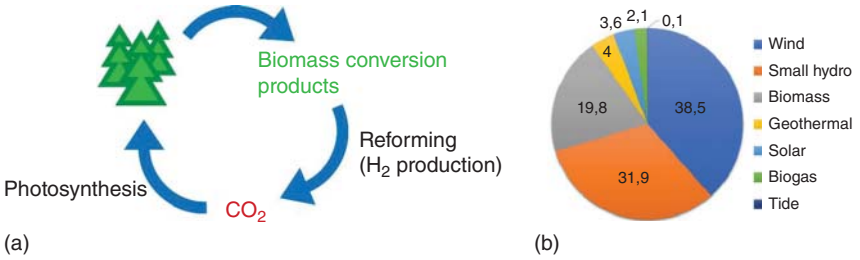

Figure 10.1 A carbon neutral cycle (a) according to [14]; the most widely used renewable sources of energy (b) according to [15]. Source: (a) Shimura and Yoshida [14]/with permission of Royal Society of Chemistry; (b) Muradov and Veziroğlu [15]/with permission of Elsevier.

10.2 Comparison of Various Biomass Processing Methods

Currently, biomass is widely used as a renewable energy source (Figure 10.1b), because this ubiquitous raw material is easily available on the planet [15]. For example, the United States produces about 1.3 billion tons of forest and agricultural waste annually, which would be sufficient for generating about 50% of the electricity consumed in the United States of America in 2014 [17]. Nevertheless, most biomass is used in direct combustion processes, and only a small part – in the production of chemical compounds. Presently, only about 1% of hydrogen is obtained from biomass [18]. The most common methods for producing hydrogen from biomass are divided into two categories, namely, thermochemical and biological ones.

Thermochemical processes include steam/oxygen gasification, pyrolysis, and gasification in supercritical water [13]. Besides hydrogen, these processes emit carbon oxides and volatile hydrocarbons [5, 13, 19]. At low temperatures, a large amount of tar and coke is also formed that causes catalyst deactivation [14, 20]. Hydrogen production from biomass under supercritical water conditions is accompanied by carbon dioxide emissions [13]. After cooling to ambient temperature, the gaseous products of biomass conversion are easily separated from the water phase.

The advantages of biological biomass conversion processes are benign reaction conditions, as they occur at ambient temperature and atmospheric pressure [21]. The shortcomings include low efficiency and high sensitivity to the process conditions [22, 23]. Thus, both thermochemical and biological processes have significant drawbacks. The search for the optimal process of biomass processing to obtain hydrogen seems vitally urgent.

10.3 Photocatalytic Hydrogen Production from Biomass Components

Photocatalytic hydrogen production from biomass is a promising method, since it uses only renewable energy sources and benign reaction conditions (ambient temperature and atmospheric pressure). Biomass photoreforming to produce hydrogen can be considered as an intermediate process between the decomposition of water and the oxidation of organic substances under aerobic conditions (Figure 10.2) [24]. The Gibbs free energy change for the reaction of complete decomposition of water is 237.1 kJ mol^{-1} (Eq. (10.1)), that of complete oxidation of ethanol under aerobic conditions is equal to −1325.4 kJ mol^{-1} (Eq. (10.2)). If ethanol oxidation is performed in the absence of oxygen, the photogenerated electrons reduce H^+ to H_2, $\Delta_r G^0 = 97.4$ kJ mol^{-1} (Eq. (10.3)).

$$2H_2O \rightleftharpoons 2H_2 + O_2 \tag{10.1}$$

$$C_2H_5OH + 3O_2 \rightleftharpoons 2CO_2 + 3H_2O \tag{10.2}$$

$$C_2H_5OH + 3H_2O \rightleftharpoons 2CO_2 + 6H_2 \tag{10.3}$$

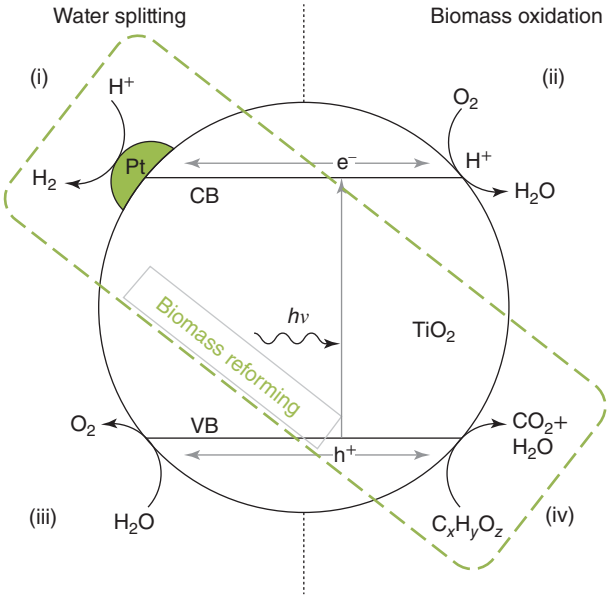

Figure 10.2 Schematic presentation of water splitting, organics oxidation, and biomass photocatalytic reforming according to [24]. Source: Puga [24]/with permission of Elsevier.

The pioneering work on hydrogen production from biomass components under light radiation appeared in 1980. The $Pt/RuO_2/TiO_2$ system functioning under ultraviolet radiation was used as a photocatalyst. The substrates were aqueous solutions of sugars, methanol, soluble starch, or cellulose suspension [25, 26]. Then the same research team proved possible the photocatalytic hydrogen evolution from amino acids, dead insects, and green algae [27]. The next important work was published in 1985; the authors, besides TiO_2-, used a CdS-based photocatalyst and lactic acid as an electron donor [28]. The sulfide-based photoactive materials allowed the expansion of the radiation spectrum, capable to induce hydrogen evolution, toward the visible light region. It was also shown in this work that CO_2 emissions in experiments with Pt/CdS were much less than in experiments with Pt/TiO_2. Analysis of the post-reaction aqueous solutions showed that in both cases, besides CO_2, some other carbonaceous products were formed depending on the catalyst type. Based on the data obtained, the authors proposed the following reaction routes for photocatalytic decomposition of lactic acid over catalysts Pt/TiO_2 (Eq. (10.4)) and Pt/CdS (Eq. (10.5)):

$$CH_3CH(OH)COOH \rightarrow H_2 + CO_2 + CH_3CHO \tag{10.4}$$

$$CH_3CH(OH)COOH \rightarrow H_2 + CH_3COCOOH \tag{10.5}$$

Thus, the process of photocatalytic hydrogen evolution from biomass components is accompanied by the formation of various byproduct organic compounds, with their distribution depending on the photocatalyst nature. Unfortunately, further works on the photocatalytic hydrogen evolution from biomass paid insufficient

attention to the studies of the oxidation products. Meanwhile, this issue is of particular interest, because photocatalytic reforming of biomass can yield some other valuable products, besides hydrogen.

Among biomass components and their derivatives, the most studied with regard to photocatalytic hydrogen production are alcohols, sugars, and some other highly water-soluble compounds. However, the studies are mainly limited to the use of TiO_2-based catalysts [29, 30], which have a wide bandgap, and therefore require exposure to ultraviolet radiation [29].

Let us consider the mechanism of alcohols oxidation on the photocatalyst surface, suggested in [31].

$$H_2O + e^- \rightleftharpoons H^{\cdot} + OH^- \tag{10.6}$$

$$2H^{\cdot} \rightleftharpoons H_2 \tag{10.7}$$

$$2\,h^+ + H_2O \rightleftharpoons H^+ + {}^{\cdot}OH \tag{10.8}$$

$$2\,h^+ + C_2H_5OH \rightleftharpoons 2H^+ + CH_3CHO \tag{10.9}$$

$$2\,h^+ + CH_3CHO + H_2O \rightleftharpoons 2H^+ + CH_3COOH \tag{10.10}$$

$$2\,h^+ + CH_3COOH \rightleftharpoons CO_2 + CH_4 \tag{10.11}$$

$$C_2H_5OH + 3H_2O \rightleftharpoons 2CO_2 + H_2 \tag{10.12}$$

$$C_2H_5OH + H_2O \rightleftharpoons CO_2 + 2H_2 + CH_4 \tag{10.13}$$

At the first step, a photoinduced formation of the electron and hole pairs occurs; the species migrate to the semiconductor surface, where electrons reduce water (Eqs. (10.6) and (10.7)), and holes react with water and ethanol molecules (Eqs. (10.8) and (10.9)) to produce protons, which then participate in the evolution of hydrogen and acetaldehyde and hydroxyl radicals, which interact with each other to form the final gaseous products. The overall process is described by Eqs. (10.12) and (10.13) for complete and incomplete photocatalytic oxidation of ethanol, respectively.

10.4 The Use of CdS-Based Photocatalysts for Hydrogen Evolution from Biomass Components

The studies on hydrogen evolution from alcohols and, to a lower extent, sugars in the presence of narrow bandgap semiconductor photocatalysts are also reported in the literature [32–34]. In [32], the process of photocatalytic evolution of H_2 from an ethanol solution over a Ni/CdS catalyst was studied in detail. It was shown that in a strong alkaline medium, holes on the CdS surface can react with hydroxide anions to form hydroxyl radicals, which migrate to the solution and oxidize ethanol to acetaldehyde or acetate. This process is called indirect oxidation of the substrate, because, unlike direct oxidation with holes, it occurs through an intermediate stage of hydroxyl radicals' formation. Oxidation of hydroxide ions by holes becomes

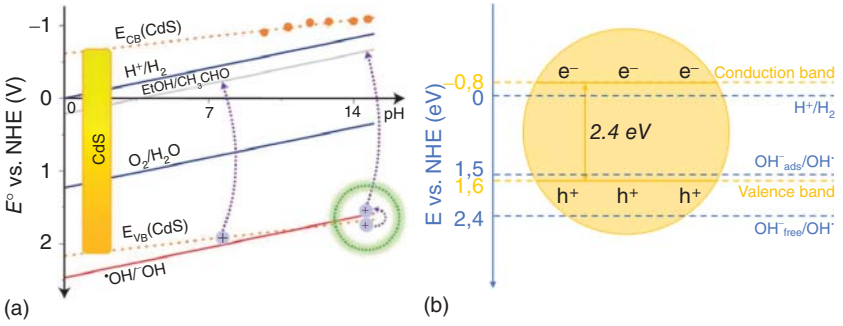

Figure 10.3 The effect of the solution pH on the redox potentials according to [32]. The green circle marks the region where the holes potential in CdS valence band is higher than the OH^- oxidation potential (a); OH^- oxidation potentials according to [35] relative to the CdS band structure (b) [36]. Source: (a) Simon et al. [32]/with permission of Springer Nature; (b) Adapted from Refs. [35, 36].

possible owing to the different influence of the solution pH on the CdS bandgap position and the OH^- oxidation potential.

The dependence of the oxidation potentials of ethanol and hydroxide ions obeys the Nernst equation: the slope of the straight line is $-59\,mV\,pH^{-1}$. The slope of the pH dependence of the CdS CB and VB position is $-33\,mV\,pH^{-1}$. Thus, at high pH values, the potential of holes in CdS exceeds the oxidation potential of OH^-. In highly alkaline solutions, ethanol is oxidized by hydroxyl radicals through a two-step mechanism, and in pH neutral solutions – by photogenerated holes directly (Figure 10.3a). This effect promoted considerably the rate of H_2 evolution from ethanol solutions at high pH.

A similar effect was observed for glycerol solutions in the presence of the $Pt/Cd_{0.5}Zn_{0.5}S$ photocatalyst [34]. Formate, glycolaldehyde, glycolate, glyceraldehyde, glycerol, and glycerate were found in the solution as oxidation products. Based on the data obtained, the following reaction mechanism was proposed:

$$Cd_{0.5}Zn_{0.5}S \rightarrow h^+ + e^- \tag{10.14}$$

$$h^+ + H_2O \rightleftharpoons {}^{\bullet}OH + H^+ \tag{10.15}$$

$$H^+ + e^- \rightleftharpoons 0,5H_2\ (\text{on Pt}) \tag{10.16}$$

$$CH_2(OH)CH(OH)CH_2OH + {}^{\bullet}OH \rightleftharpoons CH_2(OH)CH(OH)CHO + H_2O + H^{\bullet} \tag{10.17}$$

$$CH_2(OH)CH(OH)CHO + {}^{\bullet}OH \rightleftharpoons CH_2(OH)CH(OH)COOH + H^{\bullet} \tag{10.18}$$

$$CH_2(OH)CH(OH)COOH + OH \rightleftharpoons CH_2(OH)CHO + CO_2 + H_2O \tag{10.19}$$

$$CH_2(OH)CHO + {}^{\bullet}OH \rightleftharpoons CH_2(OH)COOH + H^{\bullet} \tag{10.20}$$

$$CH_2(OH)COOH \xrightarrow{{}^{\bullet}OH} HCOOH \xrightarrow{{}^{\bullet}OH} CO_2 + H_2O \tag{10.21}$$

High values of the hydrogen evolution rate (up to 74.6 mmol h^{-1} g^{-1}) from glycerol solutions were achieved with CdS modified with nickel particles deposited in situ from a $NiCl_2$ solution [35]. Mathematical modeling of the dependence between the reaction rate and the glycerol concentration was used to determine the rate constant of hydrogen evolution and the glycerol adsorption constant; the initial rate of hydrogen evolution was shown to obey the Langmuir–Hinshelwood dependence.

A study on the effect of the aqueous ethanol solution pH on the hydrogen evolution rate is reported in [37]. It was found that thermal treatment facilitated the formation of CdO on the CdS surface; in aqueous solutions, CdO gets covered with hydroxide ions to form a layer of CdS–CdO–$Cd(OH)_2$; platinum particles are then deposited on this layer. For this catalyst, the dependence of the H_2 evolution rate on the solution pH passes through a minimum corresponding to the catalyst isoelectric point (8–9).

Different types of dissociation can occur on the catalyst surface depending on the pH value:

$$Cd(OH)_2(s) + H^+ \rightleftharpoons Cd(OH)^+ \cdot H_2O \ (pH < pI) \tag{10.22}$$

$$Cd(OH)_2(s) + OH^- \rightleftharpoons CdO(OH)^- \cdot H_2O \ (pH > pI) \tag{10.23}$$

$Cd(OH)^+ \cdot H_2O$ and $CdO(OH)^- \cdot H_2O$ serve as active sites that accept photogenerated holes h^+ and form hydroxyl radicals $^{\cdot}OH$. Then the $^{\cdot}OH$ radicals react with the ethanol molecules:

$$^{\cdot}OH + C_2H_5OH \rightleftharpoons CH_3CH(OH)^{\cdot} + H_2O \tag{10.24}$$

Acetaldehyde CH_3CHO and H^+ are formed as ethanol oxidation products; then the generated protons are reduced to H_2 by electrons from the CdS CB. Besides, this work has demonstrated that the rate of hydrogen evolution is close to zero at ethanol concentrations of 0% and 95%. These data confirm that the water must be present in the reaction system to provide efficient trapping of photogenerated holes.

Similar results were reported in [35], where only trace amounts of hydrogen were detected at photocatalytic hydrogen evolution using pure glycerol. Since the oxidation potential of OH-groups on the catalyst surface is less than that of free OH^- ions (Figure 10.3b), OH-groups can be oxidized by the holes of the CdS VB. The formed hydroxyl radicals then react with glycerol molecules as discussed above. Thus, the mechanisms of hydrogen evolution from ethanol and glycerol aqueous solutions are entirely similar and seem to have been studied in sufficient detail.

It was shown that, similarly to aqueous alcohol solutions, glucose is oxidized by hydroxyl radicals through an indirect mechanism with the formation of gluconic acid as the main product [38]:

$$C_6H_{12}O_6 + 2\,^{\cdot}OH \rightleftharpoons C_6H_{12}O_7 + H_2O \tag{10.25}$$

Carboxylic acids can also be used as electron donors for hydrogen evolution in the presence of CdS-based photocatalysts [39–43]. Lactic, formic, and acetic acids are the most commonly used acid substrates. It is assumed that carboxylic acids are oxidized directly by photoinduced holes rather than hydroxyl radicals [39]. Researches in this

area are focused mainly on the photocatalyst structure and the effect of co-catalysts (Pt, MoS_2, Ga_2O_3, In_2O_3) on the hydrogen evolution rate; the peculiarities of the hydrogen evolution reaction in solutions of carboxylic acids attract less attention.

The studies on the use of low soluble biomass components, such as cellulose, lignin, starch, and sawdust, as a substrate for hydrogen evolution, have rarely been reported in the literature [44]. More than 90% of plant biomass is represented by lignocellulose, which comprises cellulose, lignin, and hemicellulose [45]. It is known that acidic and alkaline media are used for lignocellulose processing [46]. Scarce data is available in the literature on the photoreforming of insoluble biomass components under visible light radiation [44]. According to [45], the rate of hydrogen evolution increases with increasing pH in experiments with such substrates as wood flour, paper, or bagasse and the CdS/CdO_x photocatalyst. The authors attribute this effect to the formation of a thin shell of CdO_x on the surface of CdS in a strong alkaline medium. The shells block the CdS surface sites that promote charge-carrier recombination [47], but they are sufficiently thin to allow tunneling of electrons and holes from the core-shell interface to the catalyst surface [48].

The effect of the cobalt co-catalyst $Co(OH)_2$/Co(O)OH on the reaction rate was also studied in [49]. The limiting stage in the photoreforming of cellulose and hemicelluloses was the substrate oxidation; the addition of the Co co-catalyst caused no significant acceleration of the hydrogen evolution, since it only promoted the reduction of protons. In experiments with glucose, the Co-modified catalyst allowed significant increase in hydrogen evolution rate. This observation indicates that the soluble substrates are much easier-oxidizable than insoluble ones. This work is the only one that studies the photoreforming of low-soluble plant biomass components to hydrogen under visible radiation. Actually, photocatalytic hydrogen evolution from low-soluble biomass components is rarely studied in detail, even with TiO_2-based catalysts [24]. However, utilization of such biomass components as, for example, cellulose and starch, for hydrogen evolution seems to be highly profitable from an economic point of view, since it lacks the stages of depolymerization and isolation of soluble components.

10.5 The Synthesis of Novel Photocatalysts $Cd_{1-x}Zn_xS$-$Cd_{1-y}Zn_yS$ for Photocatalytic Hydrogen Evolution from Biomass Components

As mentioned above, most studies in the field of photocatalytic hydrogen production are focused on the use of biomass processing products (alcohols, sugars), although untreated biomass seems very attractive from a practical point of view. The most extensively studied semiconductor materials for photocatalytic hydrogen evolution are TiO_2, which is active under ultraviolet radiation, and CdS, which is active under visible light. Since single-phase sulfide catalysts provide a relatively low hydrogen evolution rate and suffer rapid deactivation, intensive research and development works are performed to improve their activity and stability, including the following methods: addition of wider-gap semiconductors, deposition of metals or their

compounds on the CdS surface, deposition of CdS on porous materials with a high specific surface area, heat treatment. Although the CdS-based catalysts are widely used, the data on their application for hydrogen evolution from biomass and its derivatives is limited; more extensive studies on this issue are obviously needed.

Our research group proposed approaches to create a highly active and stable photocatalyst, based on cadmium and zinc sulfide solid solutions, for hydrogen evolution under visible light radiation (450 nm) using a 0.1 M Na_2S/0.1 M Na_2SO_3 model system as an electron donor [50–53]. The synthesis of photocatalyst for hydrogen evolution from organic substrates was based on the results reported in [52], i.e. using CdS hydrothermal treatment followed by metal depositing.

Preliminary experiments were performed to study the effect of the deposited metal (Au, Pt) on the rate of hydrogen evolution from ethanol solutions (as the simplest organic substrate). According to the literature data, platinum particles on the catalyst surface improve considerably the adsorption of organic compounds as compared to unmodified catalysts [54, 55]. The results of kinetic experiments proved that the Pt-modified sample exhibited much higher activity in the reaction of hydrogen evolution from both ethanol and glucose solutions than the Au-doped one (Figure 10.4). So, the process of hydrogen evolution from organic substrates was studied using a $Pt/Cd_{1-x}Zn_xS$ catalyst. The temperature of sulfide hydrothermal treatment was varied from 100 to 140 °C, the mass content of platinum – from 0 to 1.5 wt%.

The catalysts' activity was tested in the reaction of hydrogen evolution under visible radiation (450 nm) [56]; aqueous solutions of the most common plant tissue monomers [57] – glucose and xylose – were used as substrates.

It has been shown that, similarly to the systems with inorganic electron donors, hydrothermal treatment leads to an increase in the photocatalyst activity (Figure 10.5a). The highest hydrogen evolution rate of 0.44 μmol min^{-1} was achieved with a catalyst aged in an autoclave at 120 °C (labeled as CdZnS 120).

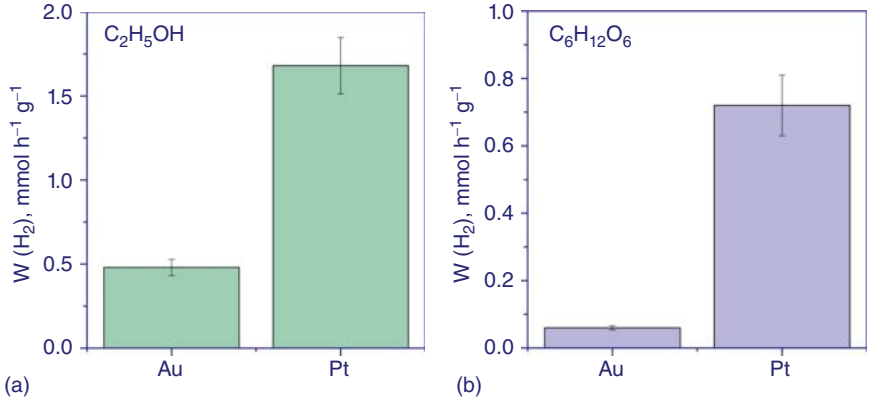

Figure 10.4 Hydrogen evolution rate on photocatalysts 1% Au/CdZnS T120 and 1% Pt/CdZnS T120 in aqueous solutions of ethanol (a) and glucose (b). Conditions: $C_0(C_2H_5OH) = 10\%$, $C_0(C_6H_{12}O_6) = 16$ mM, C(cat) = 2.5 g l^{-1}, $V = 100$ ml, $\lambda = 450$ nm. Source: (a) Kurenkova et al. [56]/with permission of Elsevier.

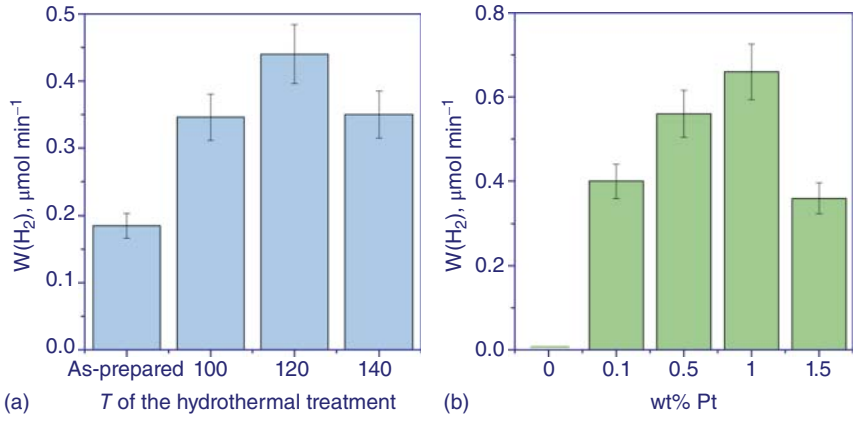

Figure 10.5 Hydrogen evolution rate depending on the temperature of hydrothermal treatment (a) and on the Pt loading (b). Conditions: C(cat) = 0.5 g l^{-1}, C_0(glucose) = 22 mM, C_0(NaOH) = 0.1 M, λ = 450 nm.

The study of the effect of platinum loading on the photocatalyst activity showed that the rate of hydrogen evolution first increases with increasing Pt content, reaches maximum at 1 wt% Pt, and then decreases (Figure 10.5b). Such a dependence results from a combination of two factors. On the one hand, increasing metal content promotes the number of both adsorption sites for organic molecules [54, 55] and metal–semiconductor contacts, which provides longer lifetime of the photogenerated charge carriers [58]. Besides, the platinum particles deposited on the sulfide surface facilitate more efficient charge separation owing to the formation of a Schottky barrier at the metal–semiconductor contact [26]. Photogenerated electrons migrate from the sulfide surface to platinum particles, and become available for reducing protons to produce hydrogen molecules [59]. Thus, a spatial separation of the photogenerated charge carriers occurs, and their lifetime becomes longer. On the other hand, as the metal loading increases, a part of the sulfide surface becomes inaccessible for light absorption and unable to generate electron–hole pairs. It should be noted that the rate of hydrogen evolution with the platinum-free CdZnS 120 sample appeared to be almost zero.

Photocatalyst 1%Pt/CdZnS was used in further experiments. This sample, as well as the initial solid solution of cadmium and zinc sulfides, was characterized by a set of physicochemical methods. According to the XRD (Figure 10.6a) and TEM (Figure 10.7) data, the hydrothermal treatment of the $Cd_{0.3}Zn_{0.7}S$ solid solution resulted in the formation of a two-phase photocatalyst $Cd_{0.6}Zn_{0.4}S/Cd_{0.1}Zn_{0.9}S$. The Rietveld method was used to decompose the peaks in the XRD pattern of CdZnS 120 in the range $2\theta = 40°–65°$. It is seen that the calculated and experimental XRD patterns practically coincide (Figure 10.6b).

$Cd_{0.6}Zn_{0.4}S$ has a disordered structure consisting of cubic and hexagonal lattices, while $Cd_{0.1}Zn_{0.9}S$ has a cubic structure. EDX analysis (Figure 10.7) allowed the mapping of each solid solution phase. ZnS particles are observed as well, but in minor amounts, and therefore they are not detected by XRD.

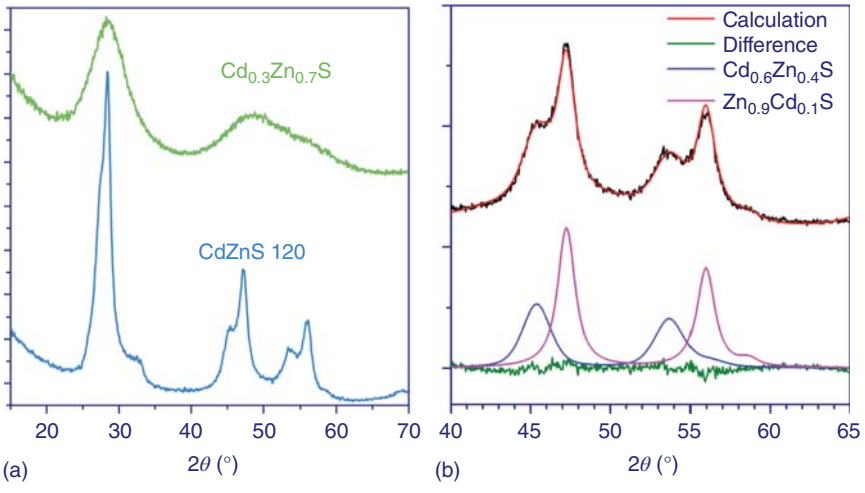

Figure 10.6 XRD patterns of photocatalysts CdZnS и CdZnS 120 (a); decomposition of the last two peaks in the CdZnS 120 XRD pattern by the Rietveld method (b). Source: Kurenkova et al. [56]/with permission of Elsevier.

Figure 10.8 illustrates the effect of the initial concentrations of substrate (glucose or xylose) and alkali on the hydrogen evolution rate. The reaction rate increases sharply with the sugar concentration increasing to 0.02 M and then remains practically constant. Such a curve is typical for the reactions mediated by the adsorbed substrate species on the catalyst surface, and is consistent with the Langmuir–Hinshelwood model [60, 61]. At low substrate concentrations, the rate of the photocatalytic reaction is limited by mass transfer from the solution to the catalyst surface.

At higher substrate concentrations, the adsorption saturation occurs, and the rate of hydrogen evolution is determined by interphase reactions on the catalyst surface [62]. Note that the dependencies for both sugars are similar, which indicates the same hydrogen photoevolution mechanism. An equation was proposed to describe the rate of hydrogen evolution from aqueous solutions of sugars (glucose and xylose) with an account for the substrate and alkali concentrations:

$$W = \frac{k_1 \times K_{ads} \times C(\text{sub}^-) + k_2 \times K_{ads} \times C(\text{sub}^-) \times C(\text{NaOH})}{1 + K_{ads} \times C(\text{sub}^-)} \quad (10.26)$$

where W – the initial H_2 production rate, $C(\text{sub}^-)$ – equilibrium concentration of anion ($C_6H_{11}O_6^-$ or $C_5H_9O_5^-$), $C(\text{NaOH})$ – initial concentration of NaOH, k_1, k_2 – reaction rate constants, K_{ads} – substrate adsorption constant.

This equation accounts for the following hydrogen photoevolution specific features: monomolecular adsorption of sugars on the photocatalyst surface; linear dependence of the reaction rate on the alkali concentration; higher reactivity of sugar anions as compared to sugar molecules. The activity of the 1% Pt/CdZnS 120 photocatalyst in hydrogen evolution from glucose solution (C_0 (NaOH) = 5 M) was 3.1–3.4 mmol H_2 g^{-1} h^{-1}, with AQE = 16.8% at 450 nm, exceeding respective reported data for similar systems [63, 64].

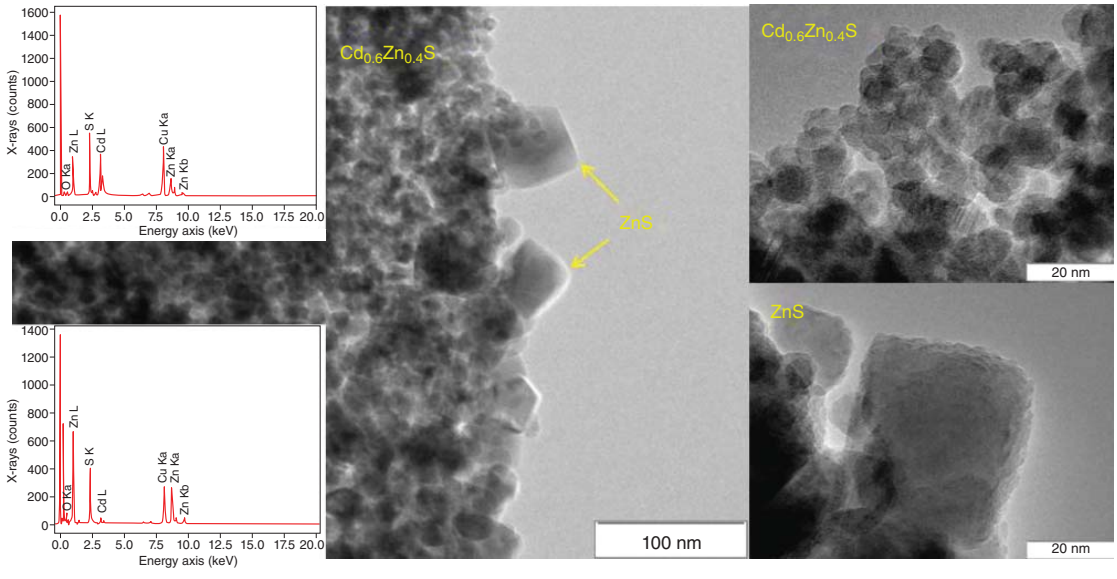

Figure 10.7 TEM images and EDX spectra of $Cd_{0.6}Zn_{0.4}S/Cd_{0.1}Zn_{0.9}S$. Source: Kurenkova, et al. [56]/with permission of Elsevier.

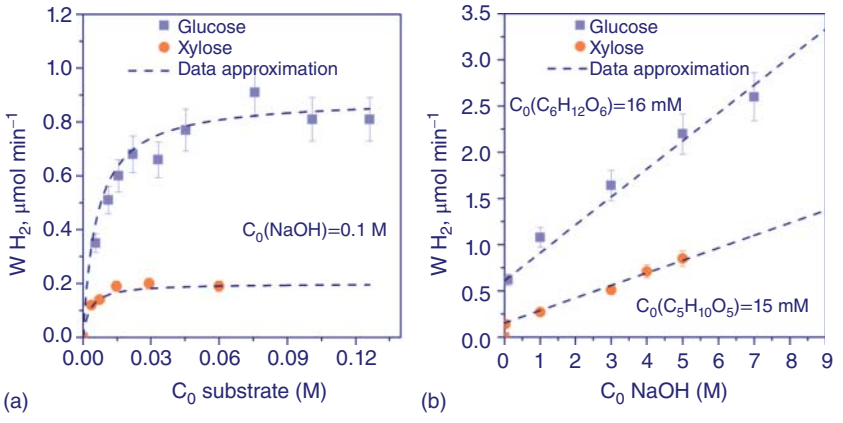

Figure 10.8 The rate of photocatalytic hydrogen evolution from aqueous solutions of glucose and xylose as a function of the substrate (a) and NaOH (b) concentrations. The data approximated by Eq. (10.26) are presented. Conditions: catalyst 1%Pt/CdZnS 120, C(cat) = 0.5 g l^{-1}, T = 20 °C, V = 100 ml, λ = 450 nm. Source: Kurenkova et al. [56]/with permission of Elsevier.

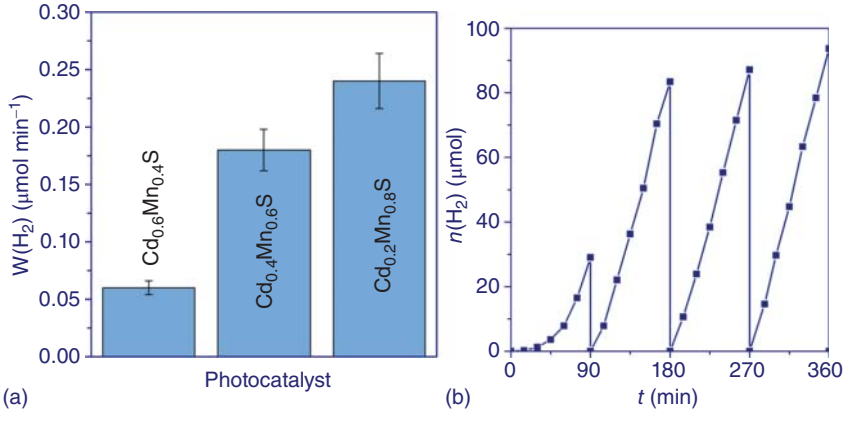

Figure 10.9 a) The rate of H_2 evolution on $Cd_{1-x}Mn_xS$ catalysts (x = 0.4–0.8) (a); the amount of H_2 evolution on the 1% $Pt/Cd_{0.2}Mn_{0.8}S$ catalyst during a cyclic experiment (b). Conditions: C (cat.) = 0.5 g l^{-1}, C_0(glucose) = 22 mM, C_0(NaOH) = 0.1 M, λ = 450 nm.

At present, attention is drawn to solid solutions based on cadmium and manganese sulfides. In our group, photocatalysts based on $Cd_{1-x}Mn_xS$ modified with platinum were synthesized. The synthesis was carried out similarly to the synthesis of CdZnS 120 samples. The activity of the obtained samples was tested in a glucose solution (Figure 10.9). It is worth noting the rather high activity of unmodified samples. The deposition of platinum made it possible to increase the rate of hydrogen evolution to 1.0 μmol min^{-1}. It is shown that these photocatalysts have a sufficiently high rate and stability in the reaction of hydrogen evolution from sugar solutions, which makes this topic promising for further research.

10.5.1 Hydrogen Evolution from Low-soluble Biomass Components

Since hydrogen photoproduction from glucose substrate demonstrated a high reaction rate and quantum yield values, it seems interesting to check the process performance using natural glucose polymers – cellulose and starch. From a practical point of view, the use of lightly processed biomass components makes the process of hydrogen production cheaper. It should be noted that the studies on low-soluble biomass components are much less frequent in the literature compared with, for example, sugars [24, 44].

10.5.1.1 Photocatalytic Hydrogen Evolution from Cellulose Aqueous Suspensions

In [65], the process of photocatalytic hydrogen production from an aqueous suspension of cellulose was studied, and the optimum reaction conditions to reach the highest process performance were determined. Similarly to the experiments with sugar solutions, the Pt depositing on the CdZnS surface provided a considerable increase in the reaction rate (Figure 10.10a). The catalyst containing 0.5 wt% Pt showed the maximum activity.

It should be noted that the most active photocatalyst for hydrogen evolution from aqueous cellulose suspensions differs in composition from that in experiments with aqueous solutions of Na_2S/Na_2SO_3 and sugars. The photocatalyst 0.5% $Pt/Cd_{1-x}Zn_xS$ (without hydrothermal treatment) (Figure 10.10b) was the most active in the case of

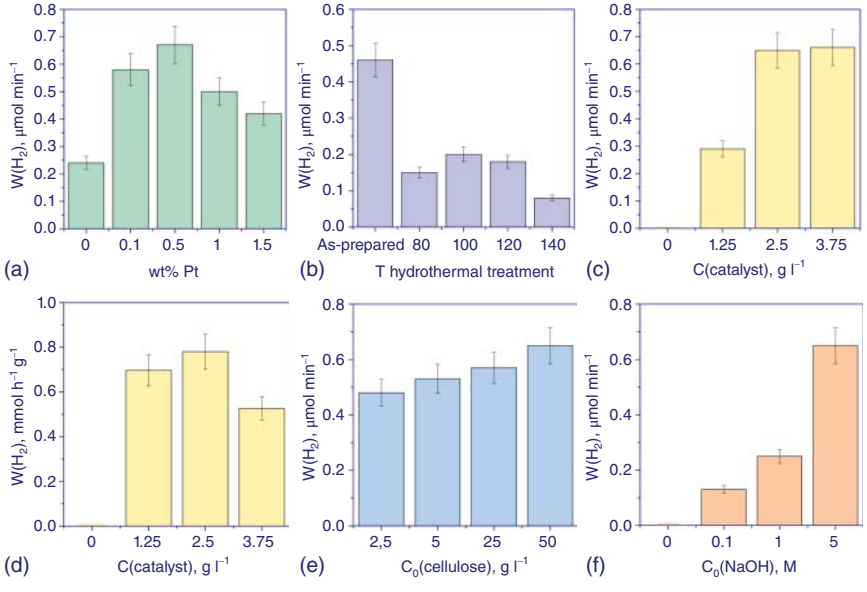

Figure 10.10 The rate of photocatalytic hydrogen evolution from aqueous cellulose suspension as a function of (a) pretreatment temperature; (b) calculated Pt loading; (c, d) photocatalyst concentration; (e) cellulose concentration; (f) NaOH concentration. Conditions: C_0(cellulose) = 50 g l^{-1}, C_0(NaOH) = 5 M, C(cat) = 2.5 g $^{-1}$, V = 20 ml, λ = 450 nm, t = 120 minutes (unless otherwise indicated).

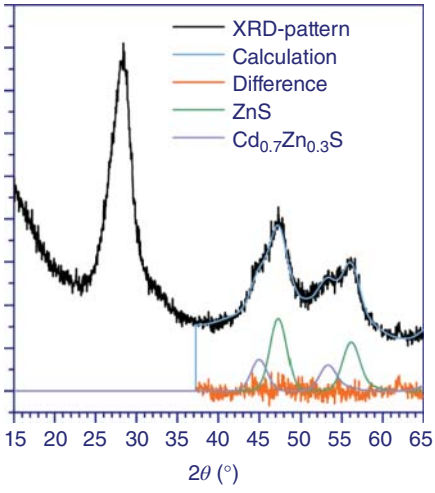

Figure 10.11 XRD pattern of the photocatalysts $Cd_{1-x}Zn_xS$ with the simulations of phase content.

cellulose, while 1%Pt/CdZnS T120 – in the case of soluble electron donors. Let us focus on the physicochemical properties of the 0.5% Pt/$Cd_{1-x}Zn_xS$ photocatalyst.

Figure 10.11 presents the XRD pattern of the $Cd_{1-x}Zn_xS$ photocatalyst. It contains three broad peaks attributed to cadmium and zinc sulfides. The last two peaks were simulated by the Rietveld method assuming two phases: $Cd_{0.7}Zn_{0.3}S$ and ZnS. The calculated and experimental XRD patterns practically coincide. Both phases comprise particles of 3.8 nm in size. Hereinafter, the $Cd_{0.7}Zn_{0.3}S$/ZnS mixed structure is designated as CdZnS.

The platinized sample was characterized by TEM (Figure 10.12) and dark field TEM (Figure 10.13) techniques. It should be noted that platinum nanoparticles are hardly visible in TEM images due to their small size (about 0.8 nm).

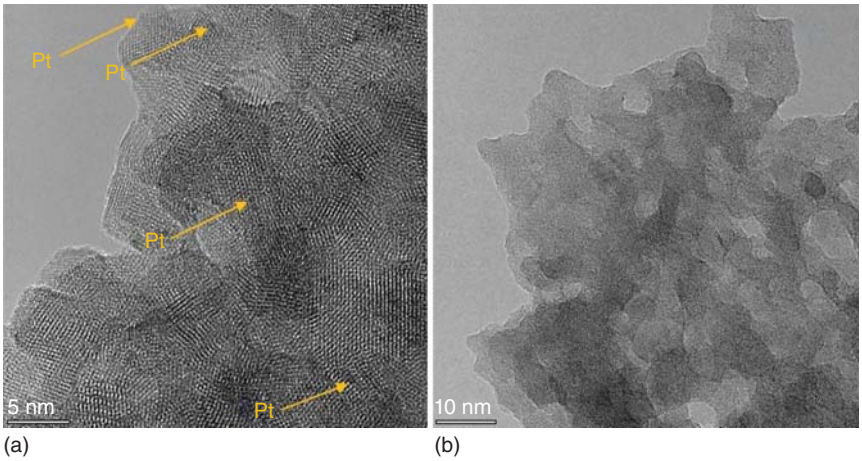

Figure 10.12 HRTEM images of the photocatalyst 0.5% Pt/CdZnS prepared without hydrothermal treatment.

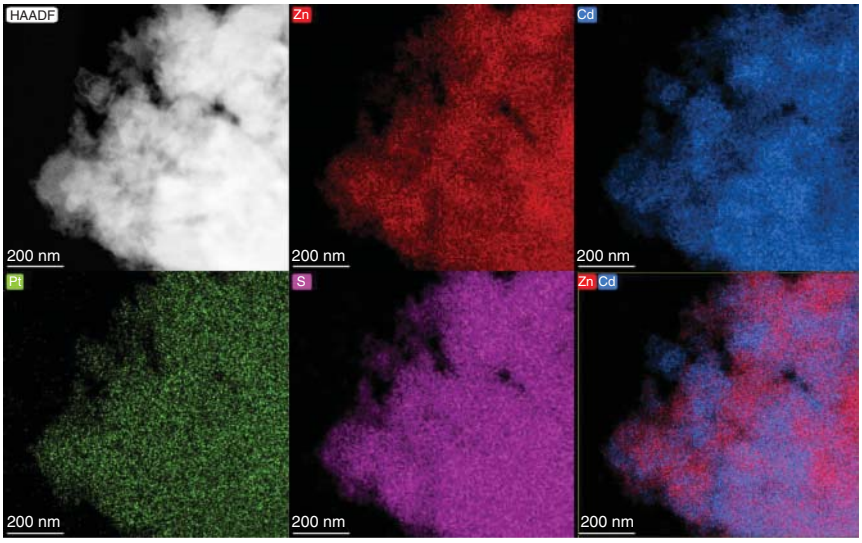

Figure 10.13 HAADF TEM imaging and elemental mapping of the photocatalyst 0.5% Pt/CdZnS prepared without hydrothermal treatment.

However, the elemental mapping image (Figure 10.13) clearly shows the presence of platinum species evenly distributed over the sample surface. The cadmium and zinc elemental distribution proves the formation of a 100–500 nm aggregates of Cd- and Zn-enriched phases. The aggregates are in close contact that facilitates the formation of interfacial heterojunctions and thus promotes the photocatalyst activity. The results obtained allow the conclusion that the synthesis of sulfide photocatalysts by the two-stage method without hydrothermal treatment yields two-phase systems possessing high photocatalytic activity. The difference in the activities of the obtained photocatalysts in sugar solutions and cellulose suspensions is most likely associated with different limiting stages of the processes of hydrogen evolution from soluble and low-soluble substrates.

The study of the effect of the photocatalyst concentration on the hydrogen evolution rate showed that the reaction rate increased with increasing photocatalyst concentration to 2.5 g l^{-1} and then remained constant (Figure 10.10c,d). Such a dependence is a result of two interacting factors. On the one hand, increasing photocatalyst concentration in the reaction mixture provides an increase in the number of active sites, and, consequently, in the number of adsorbed substrate molecules and absorbed light quanta. On the other hand, increasing the content the photocatalyst particles in the reactor impedes the light quanta to penetrate deeply into the suspension, which causes uneven illumination of the photocatalyst particles [66]. Thus, the optimum photocatalyst concentration is determined by the reactor geometry and the position of the light source.

A 20-fold increase in the substrate initial concentration – from 2.5 to 50 g l^{-1} – allowed only a 35% increase in the hydrogen evolution rate (Figure 10.10e). As the NaOH initial concentration was increased from 0.1 to 5 M, the reaction

rate increased by a factor of five (Figure 10.10f). According to the literature data, plant biomass undergoes partial depolymerization in an alkaline medium. Soluble organic species can be easily adsorbed on the photocatalyst surface and then react with photogenerated charge carriers [67]. Taking into account the strong dependence of the reaction rate on the NaOH concentration and the weak dependence on the cellulose concentration, it can be assumed that cellulose in the reaction suspension undergoes partial hydrolysis depending on the alkali concentration. The cellulose hydrolysis yields soluble compounds, which then serve as electron donors and react with photogenerated holes.

Thus, the optimized conditions for photocatalytic hydrogen evolution from cellulose suspension enabled considerable acceleration of the reaction: the maximum hydrogen evolution rate attained 0.8 mmol h^{-1} g^{-1}, the apparent quantum efficiency was 2.2%.

10.5.1.2 Photocatalytic Hydrogen Evolution from Starch Aqueous Suspensions

The use of starch as a sacrificial agent was aimed to reveal the general regularities of the reaction of photocatalytic hydrogen evolution from low-soluble biomass components. In [68], a series of experiments were carried out using insoluble starch. In the first stage, the effect of the substrate concentration on the reaction rate was studied using two types of starch: rice and corn (Sigma–Aldrich). The dependence of the hydrogen yield on the substrate concentration has a slight maximum of 51 ± 5 μmol H_2 at a starch concentration of 5 g l^{-1} (Figure 10.14a) and declines with further increase in starch concentration, most likely, due to decreasing transparency of the reaction mixture, as described above. For further studies, corn starch was chosen.

In experiments with starch substrate, the maximum reaction rate was achieved at a catalyst concentration of 3.75 g l^{-1} (Figure 10.14b), slightly exceeding respective value in experiments with cellulose. This difference most likely results from the different interactions of water with the used substrate. It seems reasonable to conclude that the photocatalyst concentration providing the maximum reaction rate is determined not only by the reactor type, but by the substrate nature as well. Specific photocatalytic activity has the maximum value at the lowest catalyst concentration because light quanta can easily reach the particle surface. Similarly to experiments with cellulose, the hydrogen evolution rate in starch suspensions increases considerably with increasing NaOH concentration (Figure 10.15a). The highest activity was achieved in a 5 M NaOH solution and was equal to 535 ± 50 μmol h^{-1} g^{-1}; the quantum efficiency was 1.4%. Note that the kinetic curve reaches a plateau after two hours of the experiment. It can be assumed that starch undergoes partial hydrolysis in the alkaline medium; the use of highly concentrated alkali solutions is unable to provide long-lasting hydrogen evolution.

Another method for starch pretreatment, described in the literature, consists of the heating of starch aqueous suspensions [69]. The next series of our kinetic experiments was devoted to the effect of preliminary alkaline hydrolysis of starch under heating on the rate of hydrogen evolution. The hydrolysis was carried out in the temperature range of 70–140 °C for one hour. The NaOH concentrations were 0.1,

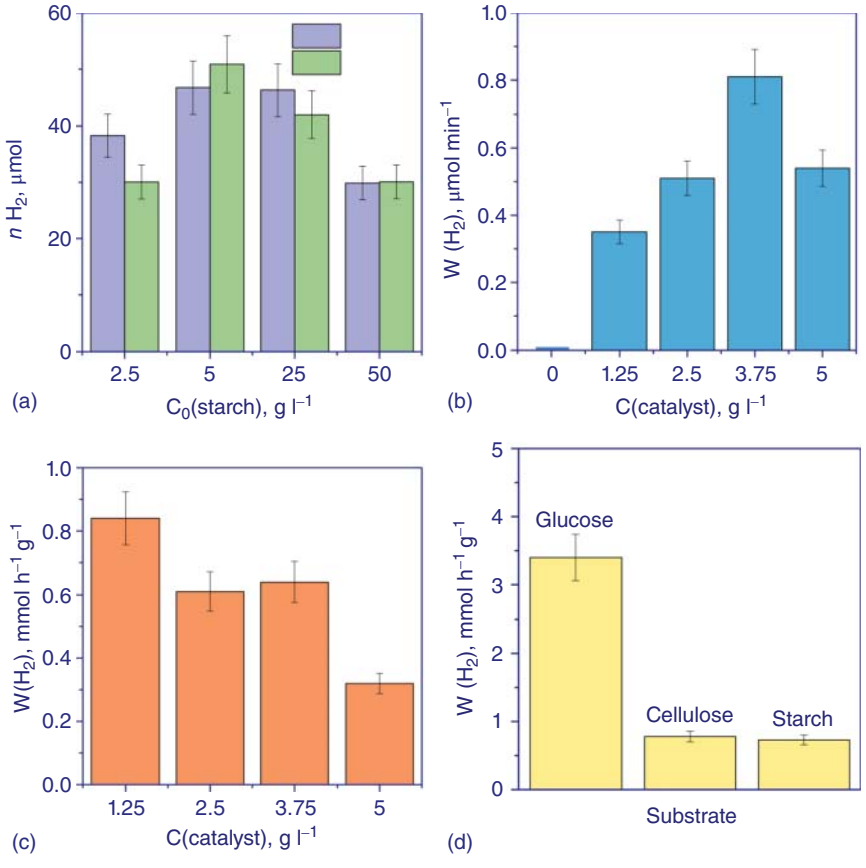

Figure 10.14 Photocatalytic hydrogen evolution from starch aqueous colloids: hydrogen yield as a function of starch concentration (a); hydrogen evolution rate as a function of catalyst concentration (b); specific catalytic activity as a function of catalyst concentration (c); the rates of hydrogen evolution from various biomass components (d). Conditions: C_0(NaOH) = 5 M, C_0(starch) = 5 g^{-1}, C(cat) = 2.5 g^{-1} (unless otherwise indicated), V = 20 ml, λ = 450 nm, T = 20 °C, t(reaction) = 120 minutes.

1, and 5 M. After cooling to room temperature, the obtained mixture was used for photocatalytic hydrogen evolution. Figure 10.15a demonstrates the kinetic curves of hydrogen evolution in two series of experiments – without preheating of starch aqueous suspension and with preheating at 70 °C. When a higher temperature was used for starch hydrolysis (105 and 140 °C), the H_2 yield was only a few μmol after six hours of the reaction suspension irradiation. The combination of highly concentrated NaOH and starch suspension preheated at 70 °C enabled a considerable increase in the hydrogen evolution rate. Note that the kinetic curve of H_2 evolution from preheated at 70 °C starch suspension in 5 M NaOH does not reach a plateau even after six hours on-stream. The rate of hydrogen evolution in the first two hours was 730 ± 73 μmol h^{-1} g^{-1}, quantum efficiency AQE = 1.8%; these values are sufficiently high, and are close to the respective values for other systems using insoluble biomass components [24]. The present work is one of the first to study the process

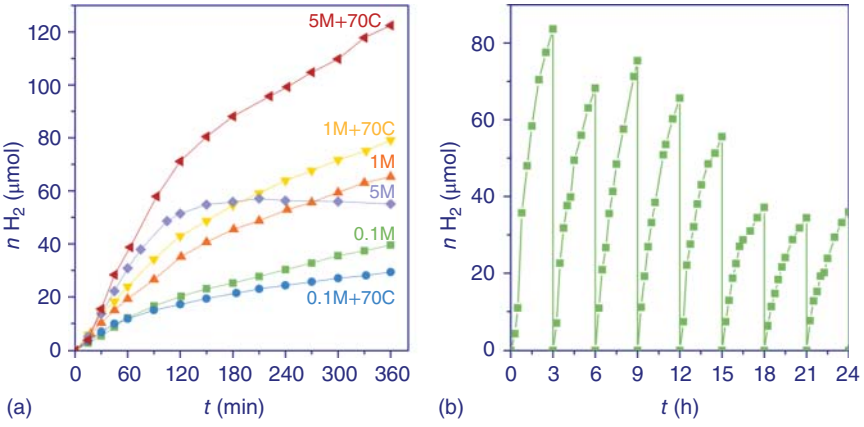

Figure 10.15 Photocatalytic hydrogen evolution from starch aqueous colloids: hydrogen yield depending on NaOH concentration and hydrolysis temperature (a); hydrogen production during 24 hours (b). Conditions: C_0(starch) = 5 g $^{-1}$, C(cat) = 2.5 g $^{-1}$, V = 20 ml, λ = 450 nm, T = 20 °C; T(pretreatment) = 20 °C (not indicated) or 70 °C (indicated as "70C").

of hydrogen evolution from insoluble starch. Figure 10.14d compares the activities of the synthesized photocatalyst Pt/CdZnS in systems with various sacrificial agents (glucose, cellulose, and starch) under the same reaction conditions. It is seen that the rate of H_2 evolution from natural glucose polymers – cellulose and starch – is the same, and 3.5 times as high in the glucose solution. This difference is obviously explained by the high solubility of glucose in water. Nevertheless, despite the fact that cellulose and starch are much more complex substrates, the synthesized photocatalyst exhibited sufficient activity in the hydrogen evolution reaction using these systems.

Figure 10.15b presents the results of the photocatalyst stability testing. The time dependence of the hydrogen yield is rather complex that is likely related to the substrate nature. However, the reaction rate remains sufficiently high during the first 18 hours, then gradually decreases, and finally reaches a constant value. The total amount of hydrogen evolved after a 24 hours photocatalytic reaction was 460 μmol or 11 ml. The results of kinetic experiments allow the suggestion that the combination of alkaline hydrolysis and heat treatment promotes efficient hydrolysis of starch with the formation of soluble organic compounds, which act as electron donors in the photocatalytic process, and react with photogenerated holes to yield the oxidation products [70]. Note, however, that the dependence of the hydrogen evolution rate on the starch hydrolysis temperature reaches a maximum at 70 °C. At higher temperatures, starch hydrolysates are formed, which appear to be efficient electron donors.

10.6 Concluding Remark and Outlook

Our study has demonstrated that photocatalysts based on cadmium sulfides and their solid solutions are active in the process of producing hydrogen under the action

of visible light from organic substrates - components of plant biomass. The activity of sulfide photocatalysts 0.5–1.5% $Pt/Cd_{1-x}Zn_xS$ was studied in the reaction of photocatalytic hydrogen evolution under visible light (450 nm) from aqueous solutions, suspensions, and colloids of biomass components (glucose, xylose, cellulose, and starch). It was shown that a strongly alkaline environment leads to the highest rate of hydrogen evolution for all studied substrates.

The highest rate of hydrogen evolution from glucose solutions was achieved in the presence of the 1% $Pt/Cd_{0.6}Zn_{0.4}S/Cd_{0.1}Zn_{0.9}S$ photocatalyst and amounted to 3.4 mmol h^{-1} g^{-1} with an apparent quantum efficiency of 8.4%. A mathematical model was proposed that describes the dependence of the hydrogen evolution rate on the initial concentrations of sugar and alkali, taking into account monomolecular reactions on the photocatalyst surface with the participation of adsorbed sugars, the linear dependence of the reaction rate on the NaOH content, and the higher reactivity of sugar anions compared to their molecular form. The features of the process of hydrogen evolution from poorly soluble biomass components, such as cellulose and corn starch, were studied. The highest activity in this series of experiments was shown by the 0.5% $Pt/Cd_{0.7}Zn_{0.3}S/ZnS$ photocatalyst. The maximum value of the rate of hydrogen evolution from the cellulose suspension was 0.8 mmol h^{-1} g^{-1}, AQE = 1.1%.

It turned out that for the production of hydrogen from aqueous starch suspensions, pretreatment of the substrate is of fundamental importance. It is shown that the alkaline hydrolysis of starch at 70 °C leads to the formation of a solution most suitable for efficient photocatalytic hydrogen evolution. The highest rate of hydrogen evolution from aqueous starch colloid was 0.7 mmol h^{-1} g^{-1}, AQE = 0.9%. It should be noted that the direct hydrolysis of starch under the conditions of a photocatalytic reaction requires a smaller number of stages and at lower temperatures than traditional processing methods, which makes it attractive from a practical point of view. Therefore, photocatalytic reforming of plant biomass components, accompanied by hydrogen evolution, is a promising direction for further research.

Acknowledgment

This work was supported by the Russian Science Foundation (RSF grant 21-13-00314; https://rscf.ru/en/project/21-13-00314/).

References

1 Nowotny, J., Sorrell, C.C., Sheppard, L.R., and Bak, T. (2005). Solar-hydrogen: environmentally safe fuel for the future. *Int. J. Hydrogen Energy* 30 (5): 521–544.

2 Huang, C.W., Nguyen, B.S., Wu, J.C.S., and Nguyen, V.H. (2020). A current perspective for photocatalysis towards the hydrogen production from biomass-derived organic substances and water. *Int. J. Hydrogen Energy* 45 (36): 18144–18159.

3 Møller, K.T., Jensen, T.R., Akiba, E., and Li, H.W. (2017). Hydrogen – a sustainable energy carrier. *Prog. Nat. Sci. Mater. Int.* 27 (1): 34–40.

4 Fujishima, A. and Honda, K. (1972). Electrochemical photolysis of water at a semiconductor electrode. *Nature* 238 (5358): 37–38.

5 Nikolaidis, P. and Poullikkas, A. (2017). A comparative overview of hydrogen production processes. *Renewable Sustainable Energy Rev.* 67: 597–611.

6 Dincer, I. and Acar, C. (2015). Review and evaluation of hydrogen production methods for better sustainability. *Int. J. Hydrogen Energy* 40 (34): 11094–11111.

7 Kondarides, D.I., Daskalaki, V.M., Patsoura, A., and Verykios, X.E. (2008). Hydrogen production by photo-induced reforming of biomass components and derivatives at ambient conditions. *Catal. Lett.* 122 (1–2): 26–32.

8 Chen, X., Shen, S., Guo, L., and Mao, S.S. (2010). Semiconductor-based photocatalytic hydrogen generation. *Chem. Rev.* 110 (11): 6503–6570.

9 Li, Z., Ma, T., Zhang, X., and Wang, Z. (2021). In_2Se_3/CdS nanocomposites as high efficiency photocatalysts for hydrogen production under visible light irradiation. *Int. J. Hydrogen Energy* 46 (29): 15539–15549.

10 Youn, H.-C., Baral, S., and Fendler, J.H. (1988). Dihexadecyl phosphate, vesicle-stabilized and in situ generated mixed CdS and ZnS semiconductor particles. Preparation and utilization for photosensitized charge separation and hydrogen generation. *J. Phys. Chem.* 92.

11 Zhang, K., Jing, D., Xing, C., and Guo, L. (2007). Significantly improved photocatalytic hydrogen production activity over $Cd_{1-x}Zn_xS$ photocatalysts prepared by a novel thermal sulfuration method. *Int. J. Hydrogen Energy* 32 (18): 4685–4691.

12 Chan, C.C., Chang, C.C., Hsu, C.H. et al. (2014). Efficient and stable photocatalytic hydrogen production from water splitting over $Zn_xCd_{1-x}S$ solid solutions under visible light irradiation. *Int. J. Hydrogen Energy* 39 (4): 1630–1639.

13 Navarro, R.M., Sánchez-Sánchez, M.C., Alvarez-Galvan, M.C. et al. (2009). Hydrogen production from renewable sources: biomass and photocatalytic opportunities. *Energy Environ. Sci.* 2 (1): 35–54.

14 Shimura, K. and Yoshida, H. (2011). Heterogeneous photocatalytic hydrogen production from water and biomass derivatives. *Energy Environ. Sci.* 4 (7): 2467–2481.

15 Muradov, N.Z. and Veziroğlu, T.N. (2008). "Green" path from fossil-based to hydrogen economy: an overview of carbon-neutral technologies. *Int. J. Hydrogen Energy* 33 (23): 6804–6839.

16 IUCN, UNEP, and WWF (1980). *World conservation strategy*, International Union for Conservation of Nature and Natural Resources UNEP World Wide Fund for Nature, UNEP, World Wide Fund for Nature, Gland, Switzerland.

17 Liu, W., Liu, C., Gogoi, P., and Deng, Y. (2020). Overview of biomass conversion to electricity and hydrogen and recent developments in low-temperature electrochemical approaches. *Engineering* 6 (12): 1351–1363.

18 Das, D., Khanna, N., and Nejat Vezirogğlu, T. (2008). Recent developments in biological hydrogen production processes. *Chem. Ind. Chem. Eng. Q.* 14 (2): 57–67.

19 Hisatomi, T., Takanabe, K., and Domen, K. (2015). Photocatalytic water-splitting reaction from catalytic and kinetic perspectives. *Catal. Lett.* 145 (1): 95–108.

20 Inaba, M., Murata, K., Saito, M., and Takahara, I. (2006). Hydrogen production by gasification of cellulose over Ni catalysts supported on zeolites. *Energy Fuels* 20 (2): 432–438.

21 Singh, L. and Wahid, Z.A. (2015). Methods for enhancing bio-hydrogen production from biological process: a review. *J. Ind. Eng. Chem.* 21: 70–80.

22 Hosseini, S.E., Wahid, M.A., Jamil, M.M. et al. (2015). A review on biomass-based hydrogen production for renewable energy supply. *Int. J. Energy Res.* 39 (12): 1597–1615.

23 Khanna, N. and Das, D. (2013). Biohydrogen production by dark fermentation. *Wiley Interdiscip. Rev. Energy Environ.* 2 (4): 401–421.

24 Puga, A.V. (2016). Photocatalytic production of hydrogen from biomass-derived feedstocks. *Coord. Chem. Rev.* 315: 1–66.

25 Kawai, T. and Sakata, T. (1980). Conversion of carbohydrate into hydrogen fuel by a photocatalytic process. *Nature* 286 (5772): 474–476.

26 Kawai, T. and Sakata, T. (1980). Photocatalytic hydrogen production from liquid methanol and water. *J. Chem. Soc. Chem. Commun.* 15: 694–695.

27 Tomoji, K. and Tadayoshi, S. (1981). Photocatalytic hydrogen production from water by the decomposition of poly-vinylchloride, protein, algae, dead insects, and excrement. *Catal. Lett.* 10 (1): 81–84.

28 Harada, H., Sakata, T., and Ueda, T. (1985). Effect of semiconductor on photocatalytic decomposition of lactic acid. *J. Am. Chem. Soc.* 107 (6): 1773–1774.

29 Cargnello, M., Gasparotto, A., Gombac, V. et al. (2011, 2011). Photocatalytic H_2 and added-value by-products-the role of metal oxide systems in their synthesis from oxygenates. *Eur. J. Inorg. Chem.* 28: 4309–4323.

30 Yasuda, M., Matsumoto, T., and Yamashita, T. (2018). Sacrificial hydrogen production over TiO_2-based photocatalysts: polyols, carboxylic acids, and saccharides. *Renewable Sustainable Energy Rev.* 81: 1627–1635.

31 Bamwenda, G.R., Tsubota, S., Nakamura, T., and Haruta, M. (1995). Photoassisted hydrogen production from a water-ethanol solution: a comparison of activities of Au/TiO_2 and Pt/TiO_2. *J. Photochem. Photobiol., A* 89 (2): 177–189.

32 Simon, T., Bouchonville, N., Berr, M.J. et al. (2014). Redox shuttle mechanism enhances photocatalytic H_2 generation on Ni-decorated CdS nanorods. *Nat. Mater.* 13 (11): 1013–1018.

33 Peng, S.Q., Peng, Y.J., Li, Y.X. et al. (2009). Photocatalytic hydrogen generation using glucose as electron donor over $Pt/Cd_xZn_{1-x}S$ solid solutions. *Res. Chem. Intermed.* 35 (6–7): 739–749.

34 Peng, S., Ding, M., Yi, T. et al. (2016). Photocatalytic hydrogen evolution and decomposition of glycerol over $Cd_{0.5}Zn_{0.5}S$ solid solution under visible light irradiation. *Environ. Prog. Sustainable Energy* 35 (1): 141–148.

35 Wang, J.-J., Li, Z.-J., Li, X.-B. et al. (2014). Photocatalytic hydrogen evolution from glycerol and water over nickel-hybrid cadmium sulfide quantum dots under visible-light irradiation. *ChemSusChem* 7 (5): 1468–1475.

36 Kudo, A. and Miseki, Y. (2009). Heterogeneous photocatalyst materials for water splitting. *Chem. Soc. Rev.* 38 (1): 253–278.

37 Jin, Z., Li, Q., Zheng, X. et al. (1993). Surface properties of PtCdS and mechanism of photocatalytic dehydrogenation of aqueous alcohol. *J. Photochem. Photobiol., A* 71 (1): 85–96.

38 Zhao, H., Ding, X., Zhang, B. et al. (2017). Enhanced photocatalytic hydrogen evolution along with byproducts suppressing over Z-scheme $Cd_xZn_{1-x}S$/Au/g-C_3N_4 photocatalysts under visible light. *Sci. Bull.* 62 (9): 602–609.

39 Jiang, S., Hu, Q., Xu, M. et al. (2020). Crystalline CdS/MoS_2 shape-controlled by a bacterial cellulose scaffold for enhanced photocatalytic hydrogen evolution. *Carbohydr. Polym.* 250: 116909.

40 Pan, Y., Zhuang, H., Hong, J. et al. (2014). Cadmium sulfide quantum dots supported on gallium and indium oxide for visible-light-driven hydrogen evolution from water. *ChemSusChem* 7 (9): 2537–2544.

41 Li, Y., Hu, Y., Peng, S. et al. (2009). Synthesis of CdS nanorods by an ethylenediamine assisted hydrothermal method for photocatalytic hydrogen evolution. *J. Phys. Chem. C* 113 (21): 9352–9358.

42 Li, Y., Du, J., Peng, S. et al. (2008). Enhancement of photocatalytic activity of cadmium sulfide for hydrogen evolution by photoetching. *Int. J. Hydrogen Energy* 33 (8): 2007–2013.

43 Harada, H., Sakata, T., and Ueda, T. (1989). Semiconductor effect on the selective photocatalytic reaction of. alpha.-hydroxycarboxylic acids. *J. Phys. Chem.* 93 (4): 1542–1548.

44 Kuehnel, M.F. and Reisner, E. (2018). Solar hydrogen generation from lignocellulose. *Angew. Chem. Int. Ed.* 57 (13): 3290–3296.

45 Wu, X., Fan, X., Xie, S. et al. (2018). Solar energy-driven lignin-first approach to full utilization of lignocellulosic biomass under mild conditions. *Nat. Catal.* 1 (10): 772–780.

46 Kumar, P., Barrett, D.M., Delwiche, M.J., and Stroeve, P. (2009). Methods for pretreatment of lignocellulosic biomass for efficient hydrolysis and biofuel production. *Ind. Eng. Chem. Res.* 48 (8): 3713–3729.

47 Spanhel, L., Haase, M., Weller, H., and Henglein, A. (1987). Photochemistry of colloidal semiconductors. 20. Surface modification and stability of strong luminescing CdS particles. *J. Am. Chem. Soc.* 109 (19): 5649–5655.

48 Dworak, L., Matylitsky, V.V., Breus, V.V. et al. (2011). Ultrafast charge separation at the CdSe/CdS Core/Shell quantum dot/methylviologen interface: implications for nanocrystal solar cells. *J. Phys. Chem. C* 115 (10): 3949–3955.

49 Wakerley, D.W., Kuehnel, M.F., Orchard, K.L. et al. (2017). Solar-driven reforming of lignocellulose to H_2 with a CdS/CdO_x photocatalyst. *Nat. Energy* 2 (4): 17021.

50 Kozlova, E.A., Kurenkova, A.Y., Semeykina, V.S. et al. (2015). Effect of titania regular macroporosity on the photocatalytic hydrogen evolution on $Cd_{1-x}Zn_xS/TiO_2$ catalysts under visible light. *ChemCatChem* 7 (24): 4108–4117.

51 Kozlova, E.A., Kurenkova, A.Y., Kolinko, P.A. et al. (2017). Photocatalytic hydrogen production using Me/$Cd_{0.3}Zn_{0.7}S$ (Me = Au, Pt, Pd) catalysts: transformation of the metallic catalyst under the action of the reaction medium. *Kinet. Catal.* 58 (4): 431–440.

52 Kozlova, E.A., Gribov, E.N., Kurenkova, A.Y. et al. (2019). Synthesis of multiphase Au/$Cd_{0.6}Zn_{0.4}S$/ZnS photocatalysts for improved photocatalytic performance. *Int. J. Hydrogen Energy* 44 (42): 23589–23599.

53 Markovskaya, D.V., Cherepanova, S.V., Saraev, A.A. et al. (2015). Photocatalytic hydrogen evolution from aqueous solutions of Na_2S/Na_2SO_3 under visible light irradiation on CuS/$Cd_{0.3}Zn_{0.7}S$ and Niz$Cd_{0.3}Zn_{0.7}S_1$+z. *Chem. Eng. J.* 262: 146–155.

54 Vorontsov, A.V., Stoyanova, I.V., Kozlov, D.V. et al. (2000). Kinetics of the photocatalytic oxidation of gaseous acetone over platinized titanium dioxide. *J. Catal.* 189 (2): 360–369.

55 Lam, S.W., Chiang, K., Lim, T.M. et al. (2007). The effect of platinum and silver deposits in the photocatalytic oxidation of resorcinol. *Appl. Catal., B* 72 (3–4): 363–372.

56 Kurenkova, A.Y., Markovskaya, D.V., Gerasimov, E.Y. et al. (2020). New insights into the mechanism of photocatalytic hydrogen evolution from aqueous solutions of saccharides over CdS-based photocatalysts under visible light. *Int. J. Hydrogen Energy* 45 (55): 30165–30177.

57 Hilpmann, G., Steudler, S., Ayubi, M.M. et al. (2018). Combining chemical and biological catalysis for the conversion of hemicelluloses: hydrolytic hydrogenation of xylan to xylitol. *Catal. Lett.* 149 (1): 69–76.

58 Kozlova, E.A. and Parmon, V.N. (2017). Heterogeneous semiconductor photocatalysts for hydrogen production from aqueous solutions of electron donors. *Russ. Chem. Rev.* 86 (9): 870–906.

59 Bao, N., Shen, L., Takata, T., and Domen, K. (2008). Self-templated synthesis of nanoporous CdS nanostructures for highly efficient photocatalytic hydrogen production under visible light. *Chem. Mater.* 20 (1): 110–117.

60 Zhang, X. (2014). Synthesis of Ni doped $InVO_4$ for enhanced photocatalytic hydrogen evolution using glucose as electron donor. *Catal. Lett.* 144 (7): 1253–1257.

61 Li, Y., Wang, J., Peng, S. et al. (2010). Photocatalytic hydrogen generation in the presence of glucose over ZnS-coated $ZnIn_2S_4$ under visible light irradiation. *Int. J. Hydrogen Energy* 35 (13): 7116–7126.

62 Markovskaya, D.V., Kozlova, E.A., Gerasimov, E.Y. et al. (2018). New photocatalysts based on $Cd_{0.3}Zn_{0.7}S$ and $Ni(OH)_2$ for hydrogen production from ethanol aqueous solutions under visible light. *Appl. Catal., A* 563: 170–176.

63 Nguyen, V.-C., Ke, N.-J., Nam, L.D. et al. (2019). Photocatalytic reforming of sugar and glucose into H_2 over functionalized graphene dots. *J. Mater. Chem. A* 7: 8384–8393.

64 Wei, Z., Liu, J., Fang, W. et al. (2018). Enhanced photocatalytic hydrogen evolution using a novel in situ heterojunction yttrium-doped $Bi_4NbO_8C_l$@Nb_2O_5. *Int. J. Hydrogen Energy* 43 (31): 14281–14292.

65 Kurenkova, A.Y. and Kozlova, E.A. (2020). CdS-based photocatalyst for hydrogen evolution from the cellulose aqueous suspension. *AIP Conf. Proc.* 2313 (1): 060009.

66 Lyubina, T.P. and Kozlova, E.A. (2012). New photocatalysts based on cadmium and zinc sulfides for hydrogen evolution from aqueous Na_2S-Na_2SO_3 solutions under irradiation with visible light. *Kinet. Catal.* 53 (2): 188–196.

67 Awatani, T., Dobson, K.D., McQuillan, A.J. et al. (1998). In situ infrared spectroscopic studies of adsorption of lactic acid and related compounds on the TiO_2 and CdS semiconductor photocatalyst surfaces from aqueous solutions. *Chem. Lett.* 8: 849–850.

68 Kurenkova, A.Y., Medvedeva, T.B., Gromov, N.V. et al. (2021). Sustainable hydrogen production from starch aqueous suspensions over a $Cd_{0.7}Zn_{0.3}S$-based photocatalyst. *Catalysts* 11 (7): 870.

69 Speltini, A., Gualco, F., Maraschi, F. et al. (2019). Photocatalytic hydrogen evolution assisted by aqueous (waste)biomass under simulated solar light: oxidized g-C_3N_4 vs. P25 titanium dioxide. *Int. J. Hydrogen Energy* 44 (8): 4072–4078.

70 Fu, X., Long, J., Wang, X. et al. (2008). Photocatalytic reforming of biomass: a systematic study of hydrogen evolution from glucose solution. *Int. J. Hydrogen Energy* 33 (22): 6484–6491.

11

Photocatalytic Hydrogen Production from Waste

Sandra Y. Toledo-Camacho[1] *and Sandra Contreras Iglesias*[2]

[1] *Universitat Rovira i Virgili, Departament d' Enginyeria Química, Av. Països Catalans, 26, Tarragona 43007, Spain*
[2] *Universitat Rovira i Virgili, Departament d' Enginyeria Química, Av. Països Catalans, 26, Tarragona 43007, Spain*

11.1 Introduction

Nowadays, "*waste-to-energy*" (WtE) seems to be the main slogan of many diverse scientific studies where the major motivation of the researchers is to find efficient routes for energy source production by economically, socially, and environmentally sustainable methods [1–3]. Although the Degrowth (equitable downscaling – smaller or negative growth rate – to balance global ecological conditions and economic system) is still quite controversial inside the political and economic global decisions – even for ordinary citizens, who enjoy a modern wasteful energy lifestyle – Circular Economy (an economic system with a circular production where waste turn into a resource) and Green Growth (economic growth that cares for – or try to restore – the environment) are, currently, the most acceptable approaches for sustainable development [4–6].

Regarding photocatalytic hydrogen (H_2) production from waste, in general, it is a technology that fits perfectly within the framework of sustainable development commented above, with three important approaches: (i) waste as a resource, which is generated vastly all over the world, (ii) H_2 as a clean energy carrier, when it comes from renewable feedstock, and (iii) photocatalysis, a technology that uses the most plentiful energy source on Earth – the sun – to promote chemical reactions. These three approaches embrace the Circular Economy and Green Growth, and, although nonconventional methods for H_2 generation like photocatalysis still present low efficiencies and their development means, nowadays, a technological challenge [7–9], at present prevails a lively enthusiasm for exploring new methods – or improving those that already exist – to make the photocatalytic H_2 generation scalable and as economically competitive as fossil fuel.

It is important to highlight that in between "*waste*" and "*energy*," there is a vast and complex network (a simplification in Figure 11.1) that combines, globally, levels such as: waste phase state, source, category [10], transformation method

Photocatalytic Hydrogen Production for Sustainable Energy, First Edition. Edited by Alberto Puga.

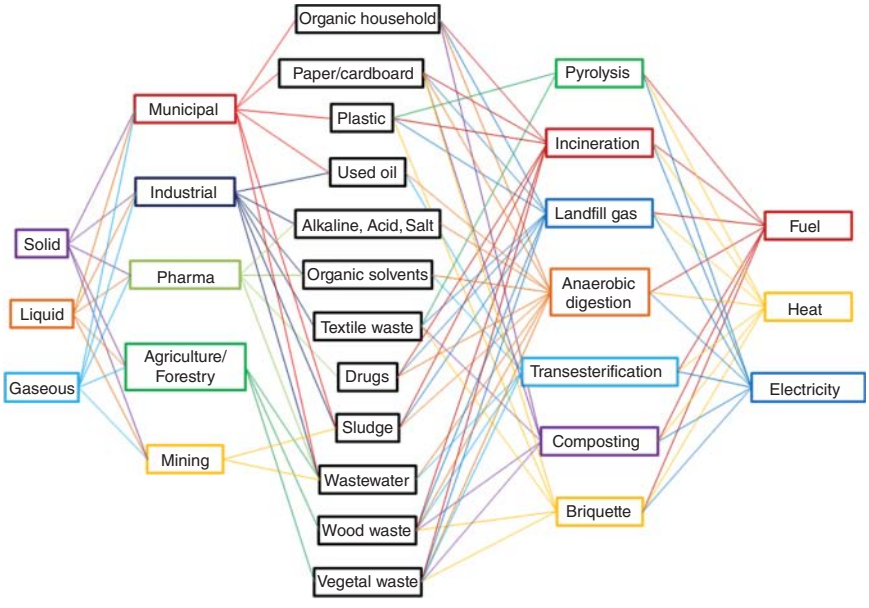

Figure 11.1 WtE network. Source: Adapted from Refs. [1, 3, 6, 10–13].

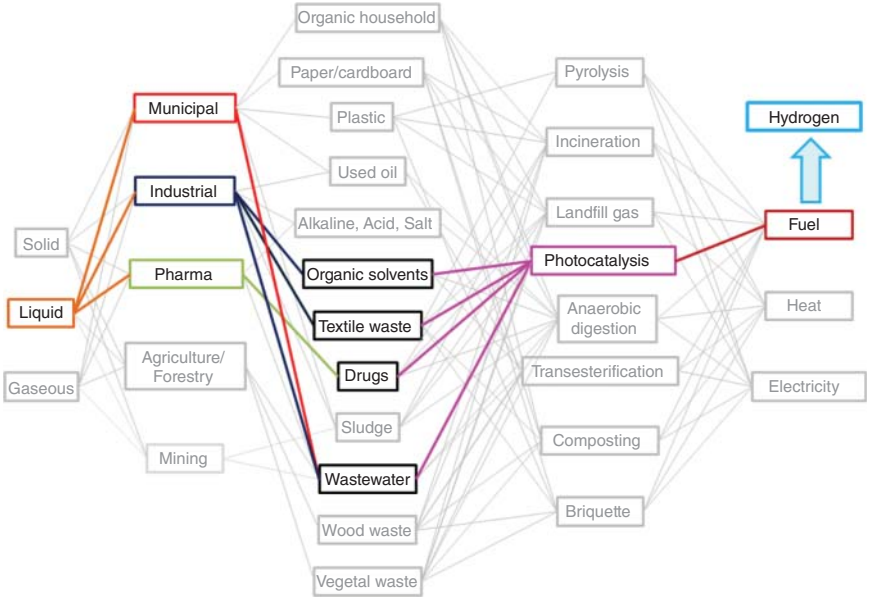

Figure 11.2 Photocatalytic H_2 generation contextualization inside the WtE network.

[1, 3, 13], and the final energy source (fuel – methane, diesel, methanol, petrol, hydrogen –, heat and electricity). Although the photocatalysis, applied for waste treatment or the H_2 generation from wastewater (WW) or any kind of waste, is still an emerging, immature technology and it does not figure yet in the WtE framework with enough competitive efficiencies (compared to incineration, gasification, pyrolysis, or anaerobic digestion – waste transformation methods widely studied and already implemented in WtE plants) [2, 3, 11, 14, 15], the increasing number of publications about H_2 photogeneration [16, 17] or waste photodegradation [18–20] seems to encourage continued investigation into this research line.

In this chapter, a review on the valorization of diverse chemical compounds present in different types of WW toward photocatalysis for H_2 production is presented. The development of the chapter follows Figure 11.2, which is a map that pretends to contextualize the photocatalytic H_2 generation inside the WtE network (Figure 11.1). This chapter is completed by Chapter 9, which presents the valorization of biomass residues to obtain hydrogen. Firstly, we focus on studies related to the photocatalyst for H_2 generation from MWW.

11.2 Municipal Wastewater (MWW)

In general, the WW are waters containing impurities of many different natures, and one of their classifications is by the source from which those waters come from. According to the European Environmental Agency, MWW is a combination of residual waters produced in households, commercial establishments and industries. It can be understood that its composition is complex, and depending on where it is generated (sector, locality, city, country), some of its WW characterization parameters change. For instance, color: gray to black or given as platinum–cobalt units −1200 U Pt—Co at the grit removal chamber influent [21], odor, content of chemical compounds of diverse nature (such as proteins, carbohydrates, fatties, oils, surfactant agents, heavy metals, nutrients, and microorganisms) measured as chemical oxygen demand (COD), dissolved organic carbon (DOC), biochemical oxygen demand (BOD), total organic carbon (TOC), and oil and grease (O&G). Other parameters are total suspended solid (TSS), total dissolved solid (TDS) and dissolved oxygen (DO).

Table 11.1 summarizes some of these parameters for MWW characterization for WW before grit removal chamber and secondary treatment. DOC and TOC values are probably, the main parameters that define the availability of any WW to be used as a sacrificial agent in photocatalytic processes. In view of the WtE framework and looking at Table 11.1, MWW can be considered as a proper source of valuable compounds for H_2 photogeneration. In addition, due to the inefficient degradation of some organic matter in WW treatment plants, photocatalysis might be a good beneficial support to reach a further degradation of persistent organic contaminants [16, 28] that could be an additional step to the biological treatment. Next, some discussion on photocatalytic H_2 generation research from MWW is presented.

Table 11.1 Characterization parameters of MWW.

Turbidity (UNT)	TSS (mg l^{-1})	PH	COD (mg l^{-1})	DOC (mg l^{-1})	BOD (mg l^{-1})	TOC (mg l^{-1})	References
260–400	377–825	7–8.2	430–800	—	—	—	[22] a)
88–355	110–380	7.1–7.8	120–280	—	—	—	[21] a)
270	—	—	506	50	—	—	[23] a)
80–300	12–550	—	100–600	49.6	80–305	37–160	[24] a)
—	—	—	250–800	—	110–350	80–260	[25] a)
—	—	7.6	—	—	—	250	[26] b)
—	7.4–14.3	—	23.4–38.9	—	5.7–12.2	—	[27] b)
—	—	7	45	9.3	—	9.8	[28] c)
—	—	7.5	—	—	—	109.2	[29] b)
—	—	3	—	100	—	—	[30] d)
—	—	3	348.3	—	—	97.7	[31] d)

a) Grit removal chamber influent.
b) Secondary treatment influent.
c) Secondary treatment effluent.
d) Secondary treatment influent, with adjusted pH.

Almomani et al. [26] studied Co/TiO_2 composites for the H_2 evolution from MWW (total nitrogen (TN): 23 mg-N/l, total phosphorous (TP): 9 mg-P/l, 34 mg-Cl^{-1}/l, 66 mg-$SO_4{}^{2-}$/l, alkalinity 110 mg-$CaCO_3$/l). Additional information on WWs characterization can be found in Table 11.1, and for H_2 operation conditions in Table 11.2. In this study, H_2 evolution on Co (5 wt%)/TiO_2 was 1.37×10^{-1} mmol $g_{cat}{}^{-1}$ h^{-1} and by decreasing organic matter in MWW (TOC reduction by 25%), they found H_2 increased. Interestingly, authors mentioned the concept of an optimal organic matter content, at which the organic matter captures more photons, donating e^- to the water splitting and further to the H_2 production. In different studies is exposed the fact of an optimal organic matter load, but more related to the capacity of the organic compounds as hole (h^+) scavenger, showing that at lower and higher organic matter content than an optimal, the electron/hole (e^-/h^+) pair recombination probability is higher [30, 33–35].

Another well-known challenge in using WW in photocatalysis for H_2 production is the presence of some components, such as chloride and sulfate ions at high concentration, in the medium. They act as e^- scavengers and block the charge transfer, specifically e^-, leading to a poor photocatalytic H_2 evolution [26]. For instance, Zhang et al. (2012) reported the strong adsorption of $HPO_4{}^{2-}$ ions to the TiO_2 surface by surface OH groups from TiO_2, inhibiting in a long-term the photocatalytic activity, likely, due to the reactive oxygen species (ROS) combination with the ions, becoming in radical anions with lower oxidation potential (more difficult to oxidize). However, interestingly, at lower than 0.1 mmol l^{-1} concentration of phosphate and $HCO_3{}^{-1}$ ions than 0.2 mmol l^{-1}, contaminant activity removal and

Table 11.2 Comparison of H_2 evolution on different photocatalysts from MWW.

Catalyst	Operating conditions	H_2 evolution (original unit)	H_2 evolution mmol g_{cat}^{-1} h^{-1}	References
Co/TiO_2 Co: 5 wt%	32 l, 0.15 g_{Cat} l^{-1}, 6 h, SL	123 μmol l^{-1}	1.37×10^{-1}	[26]
P-TiO_2/Pt	Deaerated. 5.65 l, 0.8 g_{Cat} l^{-1}, 5 h, SSL: 450 W Xe lamp ($\lambda > 400$ nm)	10.5 μmol	7.43×10^{-4}	[28]
	Aerated (DO: 6.5 mg l^{-1})	13.5 μmol	9.56×10^{-4}	
TiO_2-Au/ZnO	*E-coli* inactivation: 0.01 l, 0.2 g l^{-1}, 4 h, SSL: 300 W Xe lamp ($\lambda > 420$ nm). H_2 test: Na_2S 0.25 mol l^{-1} + Na_2SO_3 0.35 mol l^{-1}	273.5 μmol g_{cat}^{-1} h^{-1}	2.7×10^{-1}	[32]
TiO_2/ZnO		45 μmol g_{cat}^{-1} h^{-1}	4.50×10^{-2}	
Pd/P25 Pd: 0.25 wt%	25 L, 0.2 g_{cat} l^{-1}, 6 h, SL	3.0×10^{-1} ml g_{cat}^{-1} h^{-1}	1.34×10^{-4}	[29]
Au/TiO_2 Au: 0.5 wt%	2 mS cm^{-1}, 25 l, 0.2 g_{Cat} l^{-1}, 5 h, SL	22 μmol l^{-1}	2.20×10^{-2}	[30]
	3.5 mS cm^{-1}, 25 l, 0.2 g_{cat} l^{-1}, 5 h, SL	10 μmol l^{-1}	1.00×10^{-2}	
	5.4 mS cm^{-1}, 25 l, 0.2 g_{cat} l^{-1}, 5 h, SL	2 μmol l^{-1}	2.00×10^{-3}	
Pt/CdS-ZnS	25 l, 0.2 g_{cat} l^{-1}, 6 h, SL	209.3 μmol l^{-1}	1.74×10^{-1}	[31]

SSL: Simulated solar light
SL: Natural solar light

H_2 evolution were improved. Small amount of phosphates might delay the e^-/h^+ recombination.

With reference to the presence/absence of oxygen, there is a general understanding that photocatalytic H_2 evolution is more efficient under deaerated conditions [29, 36]. H_2 and O_2 compete for e^- in the conduction band (CB), so less e^- is available for H^+ reduction, and further, lower will be the H_2 generation. Zhang et al. [28] explained that, in the H_2 evolution process under aerated conditions, there might be two steps: (i) DO consumption by oxidation of complex organic molecules to simpler ones, with carbonyl and carboxylic functionalities (formaldehyde, acetaldehyde, acetate, and format), which are easily oxidizable; then, a higher probability of obtaining H^+ cations to (ii) the H_2 evolution. As the reaction between oxygen and e^- is slower than between h^+ and $^\bullet OH$ -or H_2O- species, the rate-controlling process is the e^- transfer rate from TiO_2 toward oxygen. From the results, authors observed that the higher the initial DO of the secondary effluent, the faster the endocrine activity removal and, interestingly, contrary to the general understanding, H_2 evolution was also higher than under anoxic conditions. In this study, hydrogen precursors seem to come, mainly, from hydrophilic substances (soluble microbial byproducts: humic/fulvic acids) > hydrophobic acids > hydrophobic neutral and > hydrophobic bases of the effluent organic matter.

Zhang et al. [28] studied a P-TiO_2/Pt microsphere catalyst for H_2 production with simultaneous estrogenic activity removal from MWW (estrogenic activity of 64.5 ng-E2 equivalents/l, 0.9 mg-TP/l, 4.1 mg-N/l, ammonia mg-N/l). When the reaction was carried out under aerated conditions, H_2 started to form, only, when estrogenic activity in the reaction was completely removed (>100 minutes), being even higher than under deaerated environment at the end of the experiment (five hours), 9.56×10^{-4} vs. 7.43×10^{-4} mmol $g_{cat}{}^{-1}h^{-1}$. The estrogenic activity removal under a deaerated atmosphere was 30.2% (attributed to OH oxidation), whilst under aerated conditions (initial DO 6.5 mg l^{-1}), it was completely removed in 100 minutes – likely due to ROS such as superoxide radicals ($^\bullet O_2{}^-$) and $^\bullet OH^-$.

Under deaerated conditions, complete mineralization is a complex process as $^\bullet OH$ radicals or h^+ are not, usually, selective for the complete oxidative reaction [37], but some researchers on H_2 production from the photoreforming or organic pollutants [16, 37] have considered the combination of both photocatalytic processes: aerobic – for organic WW treatment – and anaerobic – for H_2 generation. Some literature and brief discussion on this regard is presented in Section 11.2.

Regarding the best stage in a WW treatment plant for more efficient H_2 photogeneration, Zhang et al. [28] explained that photocatalytic oxidation – up to mineralization – of large molecular organic compounds is more efficient than smaller molecules. According to this, water in primary treatment or before secondary treatment might be a qualified H_2 source.

Several studies on H_2 photogeneration from MWW on TiO_2-based catalysts are found, basically, by doping or loading them with metal or semiconductor materials. For instance: 8.03×10^{-4} mmol $g_{cat}{}^{-1}h^{-1}$ on Pd(0.25 wt%)/P25 photocatalyst from MWW from the secondary treatment influent (262 mg-Na^+/l, 100 mg-NH^{4+}/l, 29 mg-K^+/l, 50 mg-Mg^{2+}/l, 96 mg-Ca^{2+}/l, 421 mg-Cl^-/l, 2.5 mg-Br^-/l, 11

mg-PO_4^{3-}/l, 91 mg-SO_4^{2-}/l) [29], where it was concluded that the lower H_2 photogeneration – with low TOC removal (8.7%) – compared to the ideal conditions in lab experiments, was, partially, caused by the high content of different impurities, such as dissolved ions (Na^+, NH_4^+, K^+, Mg^{2+}, Ca^{2+}, Cl^-, Br^-, PO_4^{3-}, SO_4^{2}). After the photoreaction, was observed a lower concentration of most of the ions, which was attributed to their adsorption on the catalyst.

Arzate Salgado and collaborators [30] obtained 2.20×10^{-2} mmol $g_{cat}^{-1}h^{-1}$ of H_2 over Au(0.5 wt%)/TiO_2 from MWW from secondary treatment influent with adjusted pH (2 mS cm^{-1}, 425 mg-Cl^-/l, 123 mg-SO_4^{2-}/l), and different to TiO_2. In Villa et al. [31] study, 1.74×10^{-1} mmol $g_{cat}^{-1}h^{-1}$ of H_2 were photogenerated on Pt/CdS-ZnS from MWW before secondary treatment. Arzate Salgado et al. [30] did mention on (i) the optimal co-catalyst loading, suggesting the existence of a surface plasmon resonance (SPR) effect on Au nanoparticles, where visible photon absorption promote e^- availability on the CB for H^+ reduction to H_2, and (ii) an optimal catalyst concentration, explaining that a high amount of catalytic nanoparticles suspended in solution would create a photon scattering effect. Villa et al. [31] reached the same conclusion for Pt/TiO_2-N and Pt/CdS-ZnS catalysts.

Concerning efficiencies, Arzate Salgado et al. [30] mentioned that, although H_2 evolution efficiencies from MWW are low, production of H_2 is maintained longer in time. Low rates are caused by the presence of many impurities, such as inorganic ions, which can poison the catalyst. Conducting tests varying the conductivity of MWW by adding inorganic salts (NaCl and Na_2SO_4), the authors found that high conductivity (5.44 mS cm^{-1}) did affect in a detrimental way the H_2 production (2×10^{-3} mmol $g_{cat}^{-1}h^{-1}$). Moreover, at lower values (3.5 and 2 mS cm^{-1}), it was higher (1.00×10^{-2} and 2.2×10^{-2} mmol $g_{cat}^{-1}h^{-1}$). It suggests photocatalytic H_2 evolution might be affected mainly by the nature of the sacrificial agents.

11.3 Industrial Wastewater (IWW)

IWW is the aqueous disposal of a wide diversity of pollutants coming from commercial or industrial processes, like textile, paper, printing and dying industry, chemical manufacturing, power plant, glass and cement industry, among others. Such pollutants are organic (acids, formaldehydes, hydrocarbons, phenols, etc.) and inorganic compounds (ammonia, nitrites, nitrates, phosphorus, sulfides, sulfates, etc.), volatile organic compounds (VOC) (benzene, toluene, xylenes, dichloromethane, trichloroethane, and trichloroethylene) and heavy metals – which are, either suspended or dissolved in sewage – (chromium, cadmium, lead, mercury, iron, copper, zinc, and cobalt).

IWW content depends on the source it comes from; then, the range of COD, BOD, and TSS parameters also varies and such a range can be so wide that their values might be close to the MWW parameter but also, they can be much higher, depending on the type of industry originating them: distilleries (85 000–110 000 mg-COD/l, 25 000–35 000 mg-BOD/l, 85 000–11 000 mg-TDS/l and pH 4–4.6), pulp and paper (1124–39 800 mg-COD/l, 568–13 300 mg-BOD/l, 50–28 270 mg-TDS/l and

pH 2.5–10.5), or petroleum petrochemical industry (1000–15 000 mg-COD/l, 110–148 mg-BOD/l, 19 600–42 000 mg-TDS/l and pH 8.3–10.2) [38]. IWW is also a potential e^- donor for the H_2 generation due to their high content of many different sacrificial agents, but specifically, of organic compounds. In this section is summarized the photocatalytic H_2 production from different industrial organic and inorganic chemicals in aqueous matrix, as well as the effect of oxic/anoxic conditions on the H_2 generation and organic pollutants' photodegradation. Several publications about photocatalytic materials for dye photodegradation and the H_2 evolution from inorganic sacrificial agents are also presented herein. Table 11.3 shows the operating conditions for H_2 evolution in the literature commented herein.

11.3.1 Effect of Oxic or Anoxic Conditions and Hydrogen Precursor

Starting from an oxic or anoxic condition in the photoreaction for H_2 production from organic compounds, there are some interesting studies discussing how the combination of both, O_2 presence and absence, affects both the photocatalytic H_2 evolution and photodegradation of organic compounds.

For instance, [37] carried out a study on a F-TiO_2/Pt photocatalyst for the anoxic H_2 evolution and, later, the oxic photodegradation of different organic compounds in aqueous solution, such as 4-chlorophenol (4-CP) and bisphenol A (BPA). In a previous work by same authors [43], it was shown that the simultaneous fluorination and platinization of the TiO_2 surface works well for anoxic degradation of organic molecules. When authors tested this catalyst for the anoxic photodegradation, 4-CP was near to 100% removed in around 30 minutes, while BPA required 90 minutes for around 80% of removal, and H_2 evolution was 2.40×10^{-6} and 7.00×10^{-6} mmol h^{-1} (information about the amount of catalyst is missing in the publication), respectively. Although removal of 4-CP was high, its mineralization in anoxic environment proceeded slowly (decreasing TOC by 50% in 50 hours), generating a set of intermediate products, such as hydroquinone, benzoquinone, 4-chlorocatechol, 4-chlororesorcinol, hydroxyl-hydroquinone, and different organic acids. Under oxic conditions, TOC was quickly removed.

Interestingly, in this publication, the authors proposed, by experiments using deuterated phenol and BPA (little D_2O), that the H_2 source was mainly water and not the organic compound. Organic compounds work as h^+ scavenger, whose adsorption on the catalyst (surface-bond OH radicals) is suppressed by fluorides deposited on the catalytic surface, but it does not block the formation of $^\bullet$OH, which oxidizes organic pollutants off the catalyst; then, more surface and e^- on the catalyst are available for water reduction – on the CB – and H_2 generation. On the opposite, in another study [44], results of H_2 photogeneration from the photoreforming of organic compound with D_2O showed the organic molecules as the main H_2 resource. From the available literature, this feature – only water or organic molecules as a source of H_2 in photocatalytic reactions – is not completely clear yet. It might depend on the reactivity or adsorption energies of the catalyst

Table 11.3 Comparison of H_2 evolution on different photocatalysts from compounds present in IWW.

Catalyst	Operating conditions	H_2 evolution (original units)	H_2 evolution mmol g_{cat}^{-1} h^{-1}	References
F-TiO_2/Pt	30 ml, 5 h, incident light intensity: 3×10^{-3} E_{in}/min l.	12 mmol	[a]) 2.40×10^{-3}	[37]
	4-CP: 300 μM			
	BPA: 300 μM	35 mmol	[a]) 7.00×10^{-3}	
Pd/TiO_2 Pd: 0.5 wt%	100 ml, 0.2 g Cat, 3 h,	9 ml	6.62×10^{-1}	[39]
	400 W Xe arc lamp.			
	Methanol (0.024 M)			
	Ethylene glycol (0.024 M)	12.3 ml	9.05×10^{-1}	
	Erythritol (0.024 M)	17 ml	1.25	
	Xylitol (0.024 M)	21.3 ml	1.57	
Pt/TiO_2 Pt: 1 wt%	Anoxic H_2 photogeneration 50 ml, 1 g_{cat} l^{-1}, 6 h. Oxic photodegradation: TiO_2, pH adjusted (0.01 M HCl + 0.01 M NaOH). UVA LED irradiation (6.04 Mw cm^{-2}). Humic acid.	81.2 mmol	1.62	[16]
Ni_2P/MIL-125-NH_2 Ni_2P: 9.2 wt%	17 ml, 17 mg Cat, 8 h, visible light ($\lambda \geq 420$ nm, 300 W Xe lamp), CH_3CN: TEA: H_2O (79 : 16 : 5 vol.%)	1230 μmol g_{cat}^{-1} h^{-1}	1.23	[40]
NiO/MIL-125-NH_2 NiO: 8.65 wt%		1084 μmol g_{cat}^{-1} h^{-1}	1.08	
CoP/MIL-125-NH_2 CoP: 8.8 wt%		828 μmol g_{cat}^{-1} h^{-1}	8.28×10^{-1}	
Co_3O_4/MIL-125-NH_2 Co_3O_4: 7.9 wt%		828 μmol g_{cat}^{-1} h^{-1}	8.28×10^{-1}	
Fe_2O_3/MIL-125-NH_2 Fe_2O_3: 10.2 wt%		435 μmol g_{cat}^{-1} h^{-1}	4.35×10^{-1}	
CuO/MIL-125-NH_2 CuO: 7.9 wt%		139 μmol g_{cat}^{-1} h^{-1}	1.39×10^{-1}	
Ni_2P/MIL-125-NH_2 Ni_2P: 9.2 wt%	CH_3CN: ascorbic acid: H_2O (79 : 16 : 5 vol.%)	0 μmol g_{cat}^{-1} h^{-1}	0	
	CH_3CN: methanol: H_2O (79 : 16 : 5 vol.%)	38 μmol g_{cat}^{-1} h^{-1}	3.80×10^{-2}	
	CH_3CN: ethanol: H_2O (79 : 16 : 5 vol.%)	26 μmol g_{cat}^{-1} h^{-1}	2.60×10^{-2}	

(Continued)

Table 11.3 (Continued)

Catalyst	Operating conditions	H_2 evolution (original units)	H_2 evolution mmol g_{cat}^{-1} h^{-1}	References
	CH_3CN: TEOA: H_2O (79 : 16 : 5 vol.%)	215 mol g_{cat}^{-1} h^{-1}	2.15×10^{-1}	
	17 ml, CH_3CN: H_2O (5vol.%) solution with RhB (1.2 ppm).	335 μmol g_{cat}^{-1} h^{-1}	3.35×10^{-1}	
Dyes and sulfides				
Ba titanate nanostructure	30 ml, 0.2 g_{cat}, 5 h, UVA light (Hg lamp $\lambda_{max} = 440$ nm), Na_2S/Na_2SO_3. Photodegradation test: 100 ml, Eriochrome black-T and potassium dichromate.	26 μmol g^{-1}	5.20×10^{-6}	[41]
Pt/SnS_2 nanoplates Pt: 1 wt% (200 °C, 24 h)	30 ml, 20 mg Cat, 4 h.	522.4 μmol g_{cat}^{-1} h^{-1}	1.31	[42]
Pt/SnS_2 nanoplates Pt: 1 wt% (180 °C, 24 h)	400 W Hg lamp.	222 μmol g_{cat}^{-1} h^{-1}	5.55×10^{-1}	
Pt/SnS_2 nanoplates Pt: 1 wt% (200 °C, 18 h)	Aqueous methanol solution (17 vol.%) + 0.1 M Na_2S and 0.1 M $NaSO_3$	175 μmol g_{cat}^{-1} h^{-1}	4.38×10^{-1}	
Pt/SnS_2 nanoplates Pt: 1 wt% (200 °C, 6 h)		75 μmol g_{cat}^{-1} h^{-1}	1.75×10^{-1}	
Co/TiO_2 Co: 5 wt%	32 l, 0.15 g_{cat} l, 6 h, generic IWW[c] (450 mg-TOC/l, SL	80 μmol l^{-1}	8.89×10^{-2}	[26]
	Formic acid (0.08 M)	5100 μmol l^{-1}	5.67	
Au/TiO_2 Au: 0.5 wt%	25 l, 0.2 g_{cat} l^{-1}, 5 h. IWW[c] (600 mg-DOC/l)	11.25 μmol l^{-1}	9.38×10^{-3}	[30]
	Formic acid (0.05 M)	6500 μmol l^{-1}	5.42	
	Methanol (0.05 M)	500 μmol l^{-1}	4.17×10^{-1}	
Co/TiO_2 Co: 5 wt%	32 l, 0.15 g_{cat} l^{-1}, 6 h, IWW[c] 450 mg-TOC/L, SL	80 μmol l^{-1}	8.89×10^{-2}	[26]

SL: Natural solar light; SSL: Solar simulated light; *Photoelectrocatalysis

a) H_2 evolution units in mmol/h (missing amount of catalyst, not given in the publication).

b) H_2 evolution on an electrode, then, units are mmol/h*cm^2.

c) Generic IWW, with no more information than the given herein.

surface, the nature of the catalyst and co-catalysts, and probably reaction conditions also exert a pressure on how the catalyst surface interacts with functional organic groups or water molecules. There are some studies focused on surface science that intend to clarify this point.

For instance, Kennedy et al. [39] suggested that alcohol molecules as sacrificial agents in the water splitting contribute as well to the H_2 generation – a confusing description, as some authors talk about water splitting, but a sacrificial agent is added in the photocatalytic H_2 test. It is described that the hydrogen in the alpha position of the carbon hydroxyl in oxygenate compounds dehydrogenates on a metal co-catalyst surface as gaseous H_2. The authors worked with Pd(0.5 wt%)/TiO_2 catalysts for H_2 evolution from the photoreforming of different water–alcohol (0.024 M) solutions: 6.62×10^{-1}, 9.05×10^{-1}, 1.25 and 1.57 mmol g_{cat}^{-1} h^{-1} of H_2 from methanol, ethylene glycol, erythritol, and xylitol. The higher the number of hydroxyl groups, the higher the H_2 evolved. When organic molecules are adsorbed on the metallic co-catalyst surface, they are decarbonylated and CO and gaseous H_2 stay adsorbed on the metal (Michael [45]). The catalyst is cleaned when TiO_2 is irradiated, the e^-/h^+ pair is formed, then h^+ attacks CO adsorbed. All in all, it seems H_2 is produced, not only from the alcohol dehydrogenation, but also from the decarbonylation. More details on this reaction mechanism can be found in these references [46–49].

Connecting back to the oxic or anoxic conditions for photocatalytic H_2 generation, G. Huang et al. [50] explored a similar but a little different strategy, switching the sequence proposed by [37]. So, first, the oxic treatment for the organic pollutant degradation – herein, purified humic acid (HA) (15.4 mg-TOC/l) – to benefit the second anoxic process, the H_2 generation – feed it with intermediate product from initial oxic photodegradation. HA can be used in WW to eliminate toxic metals and their ions. Hence, in the first step, HA oxic photodegradation on TiO_2 went from around 15 to 9 mg-TOC/l in eight hours (two, four, and six hours were also evaluated), where organic pollutants are first transformed to simpler intermediates in the initial oxic part with highly oxidant $^{\bullet}OH$ – formed from $^{\bullet}O_2^-$ (relatively low reactivity). For the photocatalytic H_2 generation test, the reaction solution consisted of the previous oxidized HA solution filtered to separate TiO_2 catalyst. Later, H_2 reaction was carried out on Pt(1 wt%)/TiO_2 catalyst.

The pre-oxidized solution during six hours showed a higher H_2 evolution (1.62 mmol g_{cat}^{-1} h^{-1}) compared to eight hours (4.5×10^{-1} mmol g_{cat}^{-1} h^{-1}), which can be explained by the TOC values before the H_2 evolution tests: 12.4 vs. 9.0 mg-TOC/l at eight and six hours, respectively. It might corroborate – once again – an optimal organic compound load, where, for the reaction system in this study [16], 9 mg-TOC/l is the optimal organic load that promotes a higher H_2 evolution. Comparing both H_2 evolution outcomes ([16, 37], 2.40×10^{-3} vs. 1.62 mmol g_{cat}^{-1} h^{-1}, respectively, it seems of considerable importance to take into account both steps, oxic and anoxic conditions – in this order – for an enhanced H_2 evolution by the photoreforming of WW.

11.3.2 Dyes-containing Wastewaters

About dyes, nowadays, textile, food, medical, agricultural, leather, and engineering industries use them intensively, where around 20% of dye is lost in the process; thus, they are discharged into the WW. The sewage of some of these industries, mainly the textile industry, is therefore colored, affecting importantly the living organisms in aquatic environments, as these compounds are designed with high biodegradation resistance. Among the different technologies for dyes removal from water (ozonation, membrane filtration, bio-adsorption, ion exchange removal, adsorption, biological/aerobic treatment, coagulation, catalytic reduction [51], photocatalysis has become a popular technology to confront this colored problem. Some studies dealing with simultaneous dyes photodegradation and photocatalytic H_2 generation are summarized in this section. In some of them, other sacrificial agents are also present in the water matrix. This information is also included in Table 11.3, within the dyes photodegradation section.

Kampouri et al. [40] reported the use of MIL-125-NH_2 catalyst loaded with different transition metal-based co-catalysts (Ni_2P, NiO, Co_3O_4, CoP, Fe_2O_3, and CuO) for concurrent photocatalytic H_2 generation and Rodhamine B (RhB) degradation. MIL-125-NH_2 is a metal–organic frameworks (MOFs) catalyst – porous materials containing metal ions with organic ligands. When RhB was tested for H_2 production in 17 ml of CH_3CN/water (5 vol%) solution, varying RhB concentration was found to have an optimal value on the dye amount in solution (1.2 ppm) at which H_2 evolution was the highest (3.35×10^{-1} mmol g_{cat}^{-1} h^{-1}). Below 1.2 ppm, the higher the dye concentration, the higher the H_2 generation, but above 1.2 ppm, the higher the dye concentration, the lower the H_2 production. Probably, at lower RhB concentration, photogenerated h^+ are easterly accessible to dye molecules, but at higher concentration than 1.2 ppm, a portion of the incident light is blocked. The RhB degradation efficiency was 45.8%, and the authors confirmed the presence of h^+ and $^{\bullet}OH$ radicals, where the RhB dye scavenges h^+ to promote H_2 photogeneration.

When H_2 evolution was studied from a mixture of acetonitrile (CH_3CN): triethylamine TEA: water (see Table 11.3 for more specific reaction conditions). The photocatalytic H_2 evolution was ranked in the following order of co-catalysts used: $Ni_2P > NiO > CoP = Co_3O_4 > Fe_2O_3 > CuO$ with following H_2 generation values: 1.23, 1.08, 8.28×10^{-1}, 8.28×10^{-1}, 4.35×10^{-1} and 1.39×10^{-1} mmol g_{cat}^{-1} h^{-1}, respectively. Testing different sacrificial agents on Ni_2P/MIL-125-NH_2, the decreasing order for H_2 evolution was TEA > triethanolamine (TEOA) > ethanol > methanol, 1.23, 2.15×10^{-1}, 2.60×10^{-2}, 3.8×10^{-2} mmol g_{cat}^{-1} h^{-1}.

Concerning inorganic compounds present in these WW, anions of sulfur, such as Na_2S and Na_2SO_3, are widely tested as sacrificial agents in photocatalytic H_2 studies. On the one hand, due to sulfide WWs are highly produced from different industries, as leather, pulp, and paper industry, but also from chemical plant in oil dehydrogenation and gas desulfurization processes [52, 53]. In addition, sulfur dyes are vastly used in the textile industry for cellulosic fibers staining [54]. On the other hand, sulfides and sulfites own lower splitting energy compared to water splitting;

then, obtaining H_2 from these compounds by photocatalytic processes is very attractive [52].

Karthik et al. [41] studied barium titanate nanostructures for photodegradation of an organic (Eriochrome black-T dye) and an inorganic (potassium dichromate mordent) pollutant, but the H_2 test was from Na_2S and Na_2SO_3 aqueous solution. More studies of this nature can be found in Ref. [55, 56].

In the study [41], H_2 production on barium titanate nanostructures was 5.20×10^{-6} mmol H_2 g_{cat}^{-1} h^{-1}. For dye photodegradation, the higher the Eriochrome black-T dye and potassium dichromate dye concentrations (from 10 to 40 ppm), the worse the degradation efficiencies. At more acidic initial pH (2–4), the dyes photodegradation efficiencies were higher than at basic pH (8, 10, 11, and 13). It seems, dye photodegradation efficiencies are closely related to the solution pH by the dye adsorption capacity, which might affect further the final H_2 evolution from dyes. Therefore, it is important to ensure a good interaction between dye molecules and the catalyst surface in order to improve the probability toward the H_2 generation. For instance, MO dye, which contains sulfonate groups charged negatively, at acid pH, its adsorption is easier on a – more – positively charged catalyst surface, but, for a cationic dye like MB, at low pH, a positive charged pollutant is not easily adsorbed on the positive charged catalytic surface; then, a high pH in the solution is required for the adsorption of MB – cationic dye – on the catalyst surface, that, at these basic conditions, acquires a negative charge vs. the pH of the solution [54].

Concerning pH, Arzate Salgado et al. [30] adjusted pH at 3 in their photocatalytic H_2 tests on Au(0.5 wt%)/TiO_2 catalyst. pH is modified under the premise that acid conditions provide more protons available for H_2 generation. However, when they performed H_2 tests at an alkaline pH (pH 8), H_2 evolution was the highest among the more basic pH values evaluated. They attributed it to a change in the catalytic surface charge, then, when the amount of H^+ protons changed, its e^- transfer capacity is modified, so H_2 generation is benefited. Importantly, the authors observed that pH became more acid along the reaction evolution, probably because of a H^+ removal or by generation of other organic acids [28]. pH was also found to change slightly over the reaction time in Ref. [57].

In [42], three different sacrificial agents were treated: an organic solvent (methanol), and two inorganic compounds (sulfides and sulfates) for H_2 generation and a dye (MB) for photodegradation tests. The two-dimensional (2D) hexagonal SnS_2 nanostructure catalysts were prepared under different conditions of temperature (150, 180, and 200 °C) and time (6, 12, 18, and 24 hours), and they were loaded with Pt (1 wt%). From the first set of experiments, where the reactant solution containing methanol (17 vol.%), Na_2S (0.1 M) and Na_2SO_3 (0.1 M), Pt(1 wt%)/SnS_2 catalyst (200 °C, 24 hours) showed the highest H_2 evolution, 1.31 mmol g_{cat}^{-1} h^{-1}. The second-best performing was Pt(1 wt%)/SnS_2 catalyst (180 °C, 24 hours), 5.55×10^{-1} mmol g_{cat}^{-1} h^{-1}, and the worst (200 °C, 6 hours), 1.75×10^{-1} mmol g_{cat}^{-1} h^{-1}.

In regard to how the catalysis synthesis conditions affect the final H_2 generation, herein, [42] explained that it might be due to (i) the morphology of the

catalyst – they found a lower thickness of the SnS_2 nanostructures seems to create a favorable pathway for an efficient e^-/h^+ separation – and (ii) the crystallinity, which associates a higher photoexcited charge recombination to more surface defects on the catalyst.

11.3.3 Biodiesel Production-derived Wastewater

Biodiesel is generally produced by a transesterification process, involving the conversion of triglycerides (oil) to a mixture of fatty esters (e.g. methyl esters, biodiesel) and byproduct (glycerol), in the presence of alcohol (e.g. methanol) and catalyst (e.g. NaOH). Traditionally, the main source of biodiesel has been vegetable oil. After separation of biodiesel and glycerol, and alcohol recovery, the biodiesel produced has to undergo a purification step (washing).

Biodiesel WW is mainly produced in this washing process, and therefore, is characterized by containing soap, free glycerol, residual methanol, catalyst, free fatty acids (oil), involving then high contents of COD and BOD. A characterization of these effluents is presented in the study by Daud et al. [58], and references herein. The main processes applied to biodiesel WW for their treatment are coagulation, electrocoagulation, biological processes, adsorption, and combinations of them.

Crude glycerol is the major byproduct in biodiesel production. Due to the large amount of impurities that contains (methanol, water, catalyst residue, free fatty acids, unreacted triglycerides, methyl esters, and other organic compounds), its direct usage in industries is hindered unless it is refined. However, purification processes involve a significant energy input, high chemical consumption, and high production costs. Therefore, alternatives for its valorization are being considered [59].

The characteristics of the biodiesel production effluents presented below make them suitable candidates to be considered for assessing the production of H_2 by photoreforming, besides their treatment for organic matter removal. Organic contaminants present there can be used as sacrificial e^- donors, as well as a source of H^+ for H_2 production. Different studies have been based on modifications of the commercial P25 TiO_2 catalyst to enhance H_2 production. In these studies, TiO_2 has been doped with metal and nonmetal elements to promote extension of the light absorption toward the visible region, but also alternatives to TiO_2 as a semiconductor material have been considered. Some of the more remarkable results found in the literature, together with information about the photocatalyst and operating conditions used, can be found in Table 11.4. Details about the synthesis of the tested materials can be found in the cited references.

Jandam et al. [61] studied different nonmetal-doped TiO_2 (phosphorous, carbon, silicon) in the treatment of a biodiesel WW. Among the tested nonmetals, P presented the best performance, considered to be thanks to its shorter bandgap energy, the presence of appropriate VB and CB positions, and a lower PZC (point of zero charge) value. The maximum H_2 production was obtained with the catalyst containing P (7 wt%), reaching 1.6 mmol H_2 g_{cat}^{-1} h^{-1} and 50.6% of COD removal. However, when this catalyst was tested for reuse, H_2 production decreased from

Table 11.4 Comparison of H_2 evolution on different photocatalysts from biodiesel production WW.

Catalyst	Operating conditions	H_2 evolution (original units)	H_2 evolution mmol g_{cat}^{-1} h^{-1}	References
Pt/TiO_2 Pt: 1 wt% (400 °C)	Biodiesel WW pretreated at pH 2.5 diluted 3.3 fold	115 mmol h^{-1}	287.5	[60]
Pd/TiO_2 Pd: 3 wt%	100 ml, 4 g l^{-1} cat., 5.93 mW cm^{-2} high pressure Hg lamp, 4 h	135 mmol h^{-1}	337.5	
P/TiO_2 P : 1 wt%	Biodiesel WW pretreated at pH 2	6.43 mmol g_{Cat}^{-1}	1.6	[61]
P/TiO_2 P : 7 wt%	4 g/L cat., 5.93 mW.cm^{-2} high pressure Hg lamp, 4 h	8.34 mmol/g	2.1	
ZnS/NiO core-shell	Crude glycerol (10 vol.%)		9.3	[62]
	180 ml, 10 mg cat., simulated solar light			
	Crude glycerol (10 vol.%)		18.5	
	1500 ml, natural sunlight			
Electrospun Bi/TiO_2 nanofibers	Glycerol (5 vol.%)		4.50	[63]
Bi: 3% mol (450°C)	0.5 g l^{-1} cat., 400 W high pressure Hg lamp, 3 h			
Pt/TiO_2 Pt: 0.5 wt%	Glycerol (1 mol l^{-1})	0.3	3.75	[64]
	1.33 g l^{-1} cat., 300 W Xe arc lamp,			
Pd/TiO_2 Pd: 0.5 wt%	Glycerol (0.1 vol.%)	15.5 ml	1.15	[65]
Au/TiO_2 Au: 2 wt%	2 g l^{-1} cat., 400 W Xe arc lamp, 3 h	8.6 ml	0.64	
TiO_2 + CuO mixture (10 : 1 wt%)	Biodiesel WW (diluted to a TOC = 1300 mg l^{-1})	13 kmol kJ^{-1}	0.8	[57]
	0.2 g l^{-1} cat., CPC[a] reactor, pilot plant, 14.25 l irradiated, 6 h, pH 5.5–6.5			
TiO_2 + CuO mixture (10 : 1 wt%/wt%)	Glycerol 0.05 mol l^{-1}	45.8 kmol kJ^{-1}	2.7 3.4 (at pH 9)	
	0.2 g l^{-1} cat., CPC reactor, pilot plant, 14.25 irradiated, 6 h, pH 5–6			
Au/TiO_2 Au: 0.5 wt%	Glycerol (0.05 M)	11.25 µmol l^{-1}	9.38×10^{-3}	[30]
	25 l, 0.2 g_{Cat} l^{-1}, 5 h.			

a) CPC: Parabolic solar collector compound.

1.61 to 1.35 mmol g_{cat}^{-1} h^{-1} from the first to the fourth use, and COD removal from 50.6% to 16.2%, even though this performance was higher than the bare support (calcined TiO_2 at 400 °C) itself. The same research group modified the same support, doping it with different metal nanoparticles (NPs) (Ni, Au, Pd, Pt). With these materials, H_2 production significantly increased up to 337.5 mmol H_2 g_{cat}^{-1} h^{-1} on Pd(3 wt%)/TiO_2.

Among the different metal NPs tested with 1 wt%, Pt showed the highest H_2 production, up to 287 mmol H_2 g_{cat}^{-1} h^{-1} with 29% of COD removal (compared to parent TiO_2 calcined at 400 °C, which achieved negligible H_2 production and similar COD removal). The photocatalytic H_2 production was ranked in the following order: $Pt_1/TiO_2 > Pd_1/TiO_2 > Au_1/TiO_2 > Ni_1/TiO_2$. Nevertheless, this performance could not be correlated with their characterization (BET surface area, size of metal NPs, bandgap, content of metallic state). However, the authors correlated it with the differences in the work function (minimum energy to extract an e^- from a metal) between the metal NPs and the parent TiO_2: the larger the difference in the work function, the higher the Schottky barrier at the metal-TiO_2 interface, inducing an efficient e^-/h^+ separation and lower recombination. Although the best results were achieved with Pt, as Pd reached close performance and considering the economic point of view, the authors studied the effect of different amount of metal NPs with the Pd/TiO_2 catalyst. When the amount of Pd was increased from 1 to 3 wt%, H_2 production rate increased from 275 to 337.5 mmol g_{cat}^{-1} h^{-1}, although a decrease was observed at 4 wt%. Metal NPs can serve as e^- sink, trapping photogenerated e^- and reducing the e^-/h^+ recombination. However, an excess of metal content, according to the authors, can prevent the absorption capacity of the parent TiO_2 and scatter the incident light [60].

Alternative materials to TiO_2 have also been developed. In the study presented by Rao et al. [62], ZnS/NiO core-shell nanostructures were synthesized and tested in the H_2 production from an industrial waste crude glycerol effluent. Tests were performed in two different reactor sizes (180 ml and 1.5 l) and with simulated and natural solar light, reaching 9.3 mmol g_{cat}^{-1} h^{-1} under simulated solar light and 18.5 mmol H_2 g_{cat}^{-1} h^{-1} under natural solar light irradiation with a 10 vol.% crude glycerol solution. Larger contents of crude glycerol demonstrated a lower yield of H_2 production. The ZnS/NiO core-shell nanostructures presented a better performance than the parent ZnS and NiO (6.2 and 2.1 mmol g_{cat}^{-1} h^{-1}, respectively), and good stability after five cycles. According to the PL studies performed by the authors, they state that NiO acts as a shell, protecting the core ZnS from photocorrosion, and as a co-catalyst minimizing charge carrier recombination.

H_2 production from photoreforming of pure glycerol has also been widely studied. Lee et al. [63] tested Bi/TiO_2 composite nanofibers with a 5 vol.% solution. Different calcination temperatures (450–850 °C) and Bi amount (3–9% mol) were studied, and Bi was incorporated by electrospinning process. The presence of Bi extended the light absorption to the visible region (narrower bandgap energy) and lower e^-/h^+ recombination owing to the well-dispersed and uniform TiO_2 and Bi_2O_3 heterojunctions. The material containing Bi(3 wt%)/TiO_2 calcined at 450 °C produced an amount of H_2 four times higher than bare TiO_2 (4.5 vs. 1.3 mmol g_{cat}^{-1} h^{-1}). Higher

contents of Bi were translated into lower H_2 production. According to the authors, this could be related to lower surface area and the possible formation of Bi clusters that could act as e^-/h^+ recombination sites. Together with the production of H_2, a reduction of 8% of TOC was achieved, whereas with bare TiO_2 nanofibers, negligible TOC reduction was observed.

Bowker et al. [65] compared Pd and Au-supported TiO_2, concluding that the production of H_2 was 1.7 faster over Pd(0.5 wt%)/TiO_2 than over Au(2 wt%)/TiO_2. They also proposed a mechanism for the photoreforming of glycerol. The production of H_2 achieved by the Pd(0.5 wt%)/TiO_2 is slightly higher than the maximum one obtained by [64] with Pt(0.5 wt%)/TiO_2 when similar operating conditions are compared. In this study, they also reported a quantum yield higher than 70% when a black light lamp was used with a 1 mol l^{-1} glycerol solution. Studies in a solar pilot plant were performed by Maldonado et al. [57] with a diluted biodiesel WW and glycerol (0.05 M). The production of H_2 was observed to be higher with glycerol, and the increase in pH was observed to have a beneficial effect on production rate, even though pH was not maintained constant throughout the experiments. Nevertheless, the production rate was lower than that obtained from formic acid under the same operating conditions. In the experiments performed with the biodiesel WW, it was observed that the production rate depended on the initial organic content, giving rise to an optimum one.

The identification of degradation products after the photocatalytic treatment has not been the general focus of those studies. However, in the works performed with pure glycerol and Pt/TiO_2, Pt-Au/TiO_2 and Cu/TiO_2 by Ref. [66–68], respectively, they identified aldehydes, 1,3-dihydroxypropanone, methanol, and acetic acid as the predominant intermediate byproducts in the liquid phase, besides H_2 and CO_2 in the gas phase.

11.4 Pharmaceutical Wastewater (PWW)

11.4.1 Pharmaceutical Compounds

Pharmaceutical compounds own unique biological and physicochemical properties, which, in addition to modern societies – highly dependent on drugs – pharma wastes have progressively become a big ghost in WW treatment plants. Traditional WW treatments are not so efficient in the biodegradation of some specific active pharma compounds. Hence, some of the pharma wastes – in an increasing amount – go through the treatment plant without any transformation to less toxic molecules, generating loss of soil fertility, contamination of groundwater and indirectly to freshwater, which further affect harmfully to human health and the ecosystem [69, 70].

The composition of PWW is so complex that classifying its components is not an easy task. For example, within them are found a high content and diversity of organic materials, antibiotics, hormones, vitamins, amino acids, acids [69, 71, 72] and their influent physicochemical properties to the WW treatment plant depend on the locality or country they are produced (because not all countries own the same

culture – in terms of life-style, for instance) and social economic power – no money, no meds – and this latest also changes inside the same country, as in third world countries, where there are poorer and less poor cities in a same country.

PWW is characterized by an elevated COD ($\approx$30 000 mg l^{-1}), BOD_5 ($\approx$10 000 mg l^{-1}) and a high organic content with a low biodegradability, high content of sulfates, chlorides, nitrates and nitrites, as well as, high content of TSS [73]. For more pharma waste characterization, see some values reported in: [38, 74, 75]. Concerning solvent-vehicle for drug products, water is commonly used, but organic solvents, such as alcohols, glycol ketones, oils, and cyclodextrins, are also used [76]. About active substances, information related to their concentration ranges in PWW can be found somewhere: [77, 78].

The characteristics commented above make PWW suitable candidates for the photocatalytic H_2 generation, not only due to the high number of different organic solvents, but also for the attractiveness of using solar energy to treat pharma wastes. However, the current literature available, related to pharma waste and photocatalysis, is mainly focused on: (i) only drug photodegradation, or, (ii) if H_2 evolution is tested from pharma products, they do not use real PWW – maybe in very few cases – but model compounds in aqueous solutions, or (iii) H_2 evolution is a kind of secondary interest in some publications, then, not much information is available on the photocatalytic H_2 evolution directly from the pharma waste degradation. Consequently, the studies presented in this section are related to pharma compounds treatment by photodegradation, where photocatalytic H_2 is produced, either from synthesized PWW, or, from organic (generic or drug-solvent) or inorganic aqueous solution (with no further explanation on why they use those sacrificial agents or their concentration).

The TiO_2 composites were studied in the design of hetero-structures with MoS_2 [79], which included the introduction of oxygen vacancies (OVs) and sulfide-defects sites for the H_2 photogeneration on MoS_2@TiO_2 catalyst from simulated pharmaceutical WW and photodegradation of different organic compounds. When TiO_2-OVs and MoS_{2-x}@TiO_2-OVs catalysts were tested in natural seawater – probably to see the effect of alkali cations, such as Na^+ and K^+, on the H_2 evolution – vs. deionized water. H_2 evolution was higher in natural seawater than in deionized water solutions and attributed it that alkali cations could coordinate with TEOA by means of electrostatic attraction and improve the separation rate of photogenerated carriers with TEOA. H_2 evolution on TiO_2-OVs was 4.53×10^{-1} mmol g_{cat}^{-1} h^{-1} (hierarchical microsphere TiO_2 only produced 3.15×10^{-4} mmol g_{cat}^{-1} h^{-1}), whereas 25%MoS_{2-x}@TiO_2-OVs displayed 2.99 mmol g_{cat}^{-1} h^{-1}. Such improvement was attributed to a correlation effect between the activity of OVs sites – favoring the H_2O splitting, which forms $^{\bullet}OH$ on the h^+ and oxidizes organic pollutants – and unsaturated S defects – enhancing the e^- transfer.

For the photocatalytic H_2 evolution on 25%MoS_{2-x}@TiO_2-OVs from simulated pharmaceutical WW of enrofloxacin (ENR), ofloxacin (OXF), ciprofloxacin (CIP) in water (see Table 11.5 for more detailed experimental conditions information), which are antibiotics, BPA – a chemical to fabricate plastics – H_2 generation

Table 11.5 Comparison of H_2 evolution on different photocatalysts from compounds in PWW.

Catalyst	Operating conditions	H_2 evolution (original unit)	H_2 evolution mmol g cat^{-1} h^{-1}	References
25%MoS_{2-x}@TiO_2-OVs	100 ml, 0.15 g l^{-1}, SSL Xenon Lamp ($\lambda > 400$ nm), TEOA (0.2 vol.%) in seawater	2985 µmol g_{cat}^{-1} h^{-1}	2.99	[79]
TiO_2-OVs		452.6 µmol g_{cat}^{-1} h^{-1}	4.53×10^{-1}	
TiO_2		315.2 µmol g_{cat}^{-1} h^{-1}	3.15×10^{-1}	
25%MoS_{2-x}@TiO_2-OVs	ENR: 20 mg l^{-1} in water	41.59 µmol g_{cat}^{-1} h^{-1}	4.16×10^{-2}	
	OXF: 20 mg l^{-1} in water	36.82 µmol g_{cat}^{-1} h^{-1}	3.68×10^{-2}	
	CIP: 20 mg l^{-1} in water	30.26 µmol g_{cat}^{-1} h^{-1}	3.03×10^{-2}	
	BPA: 20 mg l^{-1} in water	4.5 µmol g_{cat}^{-1} h^{-1}	4.50×10^{-3}	
BA3 TiO_2	5 ml, 10 g l^{-1}, SSL: UV-A ($\lambda_{max} > 365$ nm), methanol (50 vol.%) in water	190 µmol h^{-1}	3.8	[80]
Pure B TiO_2		47.6 µmol h^{-1}	9.52×10^{-1}	
Pure A TiO_2		44.8 µmol h^{-1}	8.96×10^{-1}	
P25		97.6 µmol h^{-1}	1.95	
Pt(2 wt%)/SFC-3	Solar light ($\lambda > 420$ nm) TEOA (10 vol.%) in water	4200 µmol $g_{cat}^{-1}h^{-1}$	4.20	[81]
SFC-3		2008 µmol g_{cat}^{-1} h^{-1}	2.01	
$SrTiO_3$/(30 wt% g-C_3N_4)		600 µmol g_{cat}^{-1} h^{-1}	6.00×10^{-1}	
$SrTiO_3$		25 µmol g_{cat}^{-1} h^{-1}	2.50×10^{-2}	
g-C_3N_4		148 µmol g_{cat}^{-1} h^{-1}	1.48×10^{-1}	
Pt(2 wt%)/SFC-3	TMA: 0.1 vol.% in water	1012 µmol g_{cat}^{-1} h^{-1}	1.01	
	DMF: 0.1 vol.% in water	302 µmol g_{cat}^{-1} h^{-1}	3.02×10^{-1}	
	AA: 0.1 vol.% in water	48 µmol g_{cat}^{-1} h^{-1}	4.80×10^{-2}	
	EG: 0.1 vol.% in water	42 µmol g_{cat}^{-1} h^{-1}	4.20×10^{-2}	
	LA: 0.1 vol.% in water	40 µmol g_{cat}^{-1} h^{-1}	4.00×10^{-2}	
Bi(2 wt%)/C_3N_4	100 ml, 0.5 g l, SSL Xenon Lamp ($\lambda > 420$ nm), amoxicilina (0.1 g l^{-1}) in water	718 µmol g_{cat}^{-1} h^{-1}	7.18E−01	[82]
C_3N_4		260 µmol g_{cat}^{-1} h^{-1}	2.60E−01	

was importantly lower than in the TEOA. In ENR, OXF, CIP, and BPA, H_2 was 4.16×10^{-2}, 3.68×10^{-2}, 3.03×10^{-2} and $\approx 4.5 \times 10^{-3}$ mmol g_{cat}^{-1} h^{-1}, respectively, and photodegradation efficiencies were – high: 95.6, 95.3, 72.1, and ≈ 42% for ENR, OXF, CIP, and BPA, respectively. The authors attributed this good degradation to the photogenerated e^-/h^+ pair separation, promoted by the OVs: h^+ oxidizes $^\bullet$OH from pollutants to form more $^\bullet$OH and react at the same time with pollutants.

In the study carried out by [80], different TiO_2 binary-phase BA (B: brookite and A: metastable anatase) catalysts were tested for photodegradation of diclofenac (DCF) and H_2 evolution from a water–methanol (50 vol.%) solution. The optimized material, BA3 TiO_2 catalyst (B : 38.2% and A : 61.8%) produced 3.8 mmol g_{cat}^{-1} h^{-1} of H_2, while, pure B and A phase, and P25 – as reference – generated only 9.52×10^{-1}, 8.96×10^{-1}, and 1.95 mmol g_{cat}^{-1} h^{-1}, respectively. The highest activity of B is possibly by a more negative CB level of B phase, conferring to the catalyst a larger ability to reduce protons. For the photodegradation of DCF under UV-A, BA3 TiO_2 catalyst adsorbed 25% of DCF and removed it from water by photodegradation in 2 h, with complete mineralization occurring in three hours. B and A catalysts presented a removal of around 50% and 70%, and this higher photodegradation on A, is attributed to its more positive VB level, therefore, a larger oxidation capacity.

In the last few years, g-C_3N_4 materials have awoken the interest as photocatalyst due to their light absorption capacity in the visible region, non-toxicity, photostability and simple synthesis [82, 83]. Moreover, though the fact that its CB level meets the required position for the H_2 evolution, g-C_3N_4 also require some help for a more efficient response, either in the H_2 photogeneration or pollutants photodegradation, for example, to correct the rapid e^-/h^+ recombination [84].

Moving onto more complex catalytic system, Kumar et al. [81] studied ternaries $SrTiO_3$/Ag/Fe_3O_4/(30 wt% g-C_3N_4) nanostructures (SFC-3) for H_2 evolution from aqueous solution of different organic compounds, such as trimethylamine (TMA), ascorbic acid (AA), lactic acid (LA), ethylene glycol (EG) and dimethylformamide (DMF), and the photodegradation of levofloxacin (LFC) – an antibiotic of the quinolones drug class – which break away from microbial and biological oxidation in the WW treatment plant due to its biological resistance.

The H_2 evolution in TMA (10 vol.%) over the ternary heterojunction SFC-3 loaded in situ with Pt(2 wt%) and without Pt presented important differences: 4.2 and 2.01 mmol g_{cat}^{-1} h^{-1}, respectively. Over the individual structures, $SrTiO_3$ and pure g-C_3N_4 showed lower H_2 evolution, 2.50×10^{-2} and 1.48×10^{-1} mmol g_{cat}^{-1} h^{-1}, respectively, caused, probably, by the wide bandgap of $SrTiO_3$ (vacancies in the crystal), narrow visible light absorption of g-C_3N_4, its low specific area, and poor charge transport. However, combining both structures, H_2 evolution was higher, 6.00×10^{-1} mmol g_{cat}^{-1} h^{-1}. This enhancement was attributed to a facile e^- movement from g-C_3N_4 toward the $SrTiO_3$ CB, improving the e^- availability for reduction of hydrogen cations (H^+) and the e^-/h^+ pair separation efficiency.

Incorporating Ag/Fe_3O_4 as first co-catalysts to the $SrTiO_3$/(30 wt% g-C_3N_4) structure, catalytic activity was significantly increased up to 2.01 mmol g_{cat}^{-1} h^{-1}, ascribed to the SPR of metallic Ag. Varying Ag/Fe_3O_4 content, after an

optimal value, the higher the Ag/Fe_3O_4 content, the higher the recombination response – co-catalyst sites might turn it into recombination centers –. The addition in situ of Pt promotes an e^- pumping from the g-C_3N_4 core to the Pt surface, increasing further the H_2 evolution. Finally, H_2 generation on SFC-3 catalyst using different sacrificial agents showed the next evolution, TMA 1.01, DMF: 3.02×10^{-1}, AA: 4.8×10^{-2}, EG: 4.2×10^{-2}, and LA: 4.0×10^{-2} mmol g_{cat}^{-1} h^{-1}. It seems that the solitary pair of e^- from amines is more susceptible to be oxidized by h^+ in the VB of the SFC-3 heterojunction. For LFC photodegradation, the ternary heterojunction showed a degradation rate of 55% in 90 minutes. By varying the catalyst concentration, authors [81] found an optimal value – specific for every photocatalytic system –, indicating that the higher the catalyst concentration, the higher the photon scattering. According to Almomani et al. [26], under natural solar light, the lower H_2 evolution at a higher e^- donor concentration than the optimal in each study, is because the energy reaching to the photosystem is not enough to oxidize more organic molecules.

In [82] studied the H_2 evolution on g-C_3N_4 catalyst doped with Bi spheres, from amoxicillin ($0.1\ gl^{-1}$) photodegradation. Bi seems to own a similar SPE to Au, Ag, and Cu [58]. Pure g-C_3N_4 catalyst generated only 2.6×10^{-1} mmol g_{cat}^{-1} h^{-1}, while Bi(2 wt%)/C_3N_4 catalyst showed the highest H_2 evolution (7.18×10^{-1} mmol g_{cat}^{-1} h^{-1}) with a degradation efficiency of around 5.3% in four hours. Photoluminescence (PL) spectra evidenced the beneficial effect of metallic Bi, due to the PL signal that was as weak as the Bi(2 wt%)/C_3N_4 loaded with Pt(1 wt%) —Pt, as co-catalyst, promotes a good e^- pumping toward its surface, then, better is the e^-/h^+ separation-. The enhanced H_2 evolution was attributed to hot e^- transferred from metallic Bi toward CB of the g-C_3N_4. Compared to previous studies, H_2 evolution from amoxicillin degradation is quite low for both applications, which at the same time, exposed the challenge for the photocatalytic H_2 generation from pharmaceutical compounds. For more studies related to the photocatalytic H_2 generation and photodegradation of pharmaceutical WW, the following references can be reviewed: [82, 85–88].

11.5 Conclusions

The photocatalytic H_2 generation from WW fits very well into the WtE approach, and H_2 has shown up, since some decades ago, as a promising alternative to fossil fuel. The high organic and inorganic content of some WW makes them a good option to reach a photofuel –H_2– generation plus environmental remediation at once. However, by their same complex nature, achieving efficiencies minimally competitive with other technologies for H_2 generation means a big challenge. From different studies, it was found that the existence of an optimal organic load for higher H_2 evolution, where below and above this value, the e^-/h^+ recombination probability is higher. As for catalyst concentration, it was also observed that an optimal value, where high concentrations entail to a shielding or shadow effect, and then, photonic energy is scattered. With reference to photocatalytic materials, TiO_2 is widely

studied, also assessing the incorporation into its structure or surface deposition of co-catalytic materials, such as precious noble metals Pt, Ag, Au, and some other metals (Cu, Co, Bi). g-C_3N_4 photocatalyst lately has also appeared as a promising catalytic support, but it also needs some extra help of co-catalysts. Different authors commented, as well, the importance of finding an optimal co-catalyst load to avoid the scattering of the incident light.

Assessing a MWW treatment plant and considering which influent/effluent could be more suitable for the photocatalytic H_2 production, the best stage could be the water influent to the secondary treatment (or before any biologic treatment). Primary treatment influent, for instance, contains an elevated concentration of suspended solids, obstructing the photon trip until the catalyst surface; the water inside the primary treatment stage contains high concentrations of compounds such as nitrogen, phosphorous, chlorides, sulfates, which act as h^+ scavengers, converting oxidant compounds to less reactive species, or poison the surface by adsorption; and in the case of secondary treatment effluents, their low organic content might not be enough to avoid the e^-/h^+ pair recombination. These outcomes could be also extended to the IWW depending on their composition.

Concerning global WW nature, biodiesel production-derived WW seems to present the highest efficiencies toward H_2. However, it is imperative to highlight that the efficiency values of the different studies shown in this chapter are not normalized to the operating conditions (reactor volume, catalyst and sacrificial agent concentration, irradiation, etc.), so as to make a proper comparison – they affect significantly the performance of the catalyst –. Moreover, as regards of the nature of pollutants, alcohol molecules are widely identified as the best sacrificial agents, giving the highest photocatalytic H_2 generation, for instance, methanol, ethanol, and glycerol, which is the main component of biodiesel.

Concerning oxic/anoxic conditions, taking into account that the influent WW (for both municipal and industrial WW) to the secondary treatment might contain O_2, plus, that the photodegradation requires oxic conditions (O_2 produces more selective and powerful oxidants as $^{\bullet}OH$ and $^{\bullet}O_2^-$), a more natural process to incorporate a photocatalytic H_2 generation stage in a WW treatment plant, according to the literature, might be by combining both photocatalytic processes: a first step for aerobic photodegradation of organic pollutants, then a second step for anaerobic H_2 photogeneration.

Due to the complexity of WW's and the high sensitivity of the photocatalytic materials toward any change in the reaction conditions, pretreatment methods for raw WW's have also been studied to get an extra enhancement in the photocatalytic H_2 formation (physical, microwave heat, acid/alkaline, ozonization, fungal, enzymatic, and ultrasonication pretreatment) [89], which can be a practical way to standardize the WW of different sources for H_2 evolution on a photocatalytic material.

Currently, the existing literature related to the use of real WW for photocatalytic H_2 generation is still short. Although lots of scientific publications with main title calling for the utilization of different WW for H_2 generation can be found, the truth is that the attention is mostly focused only on some common organic (methanol, formic acid, or triethanolamines) and inorganic (Na_2S and Na_2SO_3) sacrificial

agents. In such publications, the photodegradation is generally studied with real WW, but the photocatalytic H_2 tests are carried out using synthetic sacrificial agent solutions.

With all these considerations, it seems a good strategy for future research studies, for finding higher photocatalytic efficiencies toward H_2 generation from real WW at a larger scale than lab-scale, to look for a proper combination of the following three variables: (i) catalyst nature, not only the use of a well-known catalytic support (good photocatalytic activity and easy synthesis) as TiO_2, but also a co-catalyst (cheap and widely available in nature, besides an easy incorporation method to the support), (ii) sacrificial agent nature and its availability in real WW, and (iii) a (more realistic) photocatalytic system configuration. All this without forgetting that a proper WW pretreatment for photocatalytic H_2 generation might also favor final efficiencies toward H_2.

References

1 Boloy, R.A., da Cunha Reis, A., Rios, E.M. et al. (2021). Waste-to-energy technologies towards circular economy: a systematic literature review and bibliometric analysis. *Water Air Soil Pollut.* 232 (7): 306.

2 Pan, X., Wang, Y., and Chin, K.S. (2021). A large-scale group decision-making method for site selection of waste to energy project under interval type-2 fuzzy environment. *Sustainable Cities Soc.* 71 (May). Elsevier Ltd: 103003.

3 Wienchol, P., Szlęk, A., and Ditaranto, M. (2020). Waste-to-energy technology integrated with carbon capture – challenges and opportunities. *Energy* 198.

4 Belmonte-Ureña, L.J., Plaza-Úbeda, J.A., Vazquez-Brust, D., and Yakovleva, N. (2021). Circular economy, degrowth and green growth as pathways for research on sustainable development goals: a global analysis and future agenda. *Ecol. Econ.* 185 (March): 107050.

5 Hankammer, S., Kleer, R., Mühl, L., and Euler, J. (2021). Principles for organizations striving for sustainable degrowth: framework development and application to four B corps. *J. Cleaner Prod.* 300. Elsevier Ltd: 126818.

6 Krpan, D. and Basso, F. (2021). Keep degrowth or go rebirth? Regulatory focus theory and the support for a sustainable downscaling of production and consumption. *J. Environ. Psychol.* 74 (March).

7 Dincer, I. and Acar, C. (2015). Review and evaluation of hydrogen production methods for better sustainability. *Int. J. Hydrogen Energy* 40 (34). Elsevier Ltd: 11094–11111.

8 Lakhera, S.K., Rajan, A., Rugma, T.P., and Bernaurdshaw, N. (2021). A review on particulate photocatalytic hydrogen production system: progress made in achieving high energy conversion efficiency and key challenges ahead. *Renewable Sustainable Energy Rev.* 152 (April). Elsevier Ltd: 111694.

9 Sagir, M., Tahir, M.B., Waheed, U., and Akram, J. (2022). Role of photocatalysis in green energy production. In: *Encyclopedia of Smart Materials* (ed. A.-G. Olabi), 590–596. Elsevier.

10 Environmental and Forestry Statistics (2010). Guidance on classification of waste according to EWC-stat categories. Eurostat 2150/2002 (2): 82.

11 Khan, I. and Kabir, Z. (2020). Waste-to-energy generation technologies and the developing economies: a multi-criteria analysis for sustainability assessment. *Renewable Energy* 150. Elsevier Ltd: 320–333.

12 Parrodi, J.C., Hernández, D.H., and Pomberger, R. (2018). Potential and main technological challenges for material and energy recovery from fine fractions of landfill mining: a critical review. *Detritus* 3 (September): 19–29.

13 Seltenrich, N. (2016). Emerging waste-to-energy technologies: solid waste solution or dead end? *Environ. Health Perspect.* 124 (6): A106–A111.

14 Nikoobakht, A., Aghaei, J., Shafie-khah, M., and Catalão, J.P.S. (2020). Co-operation of electricity and natural gas systems including electric vehicles and variable renewable energy sources based on a continuous-time model approach. *Energy* 200.

15 Tsui, T.H. and Wong, J.W. (2019). A critical review: emerging bioeconomy and waste-to-energy technologies for sustainable municipal solid waste management. *Waste Disposal Sustainable Energy* 1 (3). Springer Singapore: 151–167.

16 Huang, C.W., Nguyen, B.S., Wu, J.C.S., and Nguyen, V.H. (2020). A current perspective for photocatalysis towards the hydrogen production from biomass-derived organic substances and water. *Int. J. Hydrogen Energy* 45 (36). Elsevier Ltd: 18144–18159.

17 Sridhar, A., Ponnuchamy, M., Kumar, P.S. et al. (2021). Progress in the production of hydrogen energy from food waste: a bibliometric analysis. *Int. J. Hydrogen Energy* 47 (62): 26326–26354.

18 Boyjoo, Y., Sun, H., Liu, J. et al. (2017). A review on photocatalysis for air treatment: from catalyst development to reactor design. *Chem. Eng. J.* 310. Elsevier B.V.: 537–559.

19 Long, Z., Li, Q., Wei, T. et al. (2020). Historical development and prospects of photocatalysts for pollutant removal in water. *J. Hazard. Mater.* 395: (January). Elsevier: 122599.

20 Singh, P. and Borthakur, A. (2018). A review on biodegradation and photocatalytic degradation of organic pollutants: a bibliometric and comparative analysis. *J. Cleaner Prod.* 196. Elsevier Ltd: 1669–1680.

21 Lorenzo, V., Eliet, J.G., Ocaña, L. et al. (2010). Evaluación de La Eficiencia de Los Procesos de Coagulación-Floculación Y Ozonización a Escala de Laboratorio En El Tratamiento de Aguas Residuales Municipales. *Revista CENIC. Ciencias Químicas* 41 (1): 49–56.

22 Al Bazedi, G.A. and Abdel-Fatah, M.A. (2020). Correlation between operating parameters and removal efficiency for chemically enhanced primary treatment system of wastewater. *Bull. Natl. Res. Cent.* 44 (1).

23 Tao, C., Parker, W., and Bérubé, P. (2021). Characterization and modelling of soluble microbial products in activated sludge systems treating municipal wastewater with special emphasis on temperature effect. *Sci. Total Environ.* 779.

24 Yang, L., Shin, H.-S., and Hur, J. (2014). Estimating the concentration and biodegradability of organic matter in 22 wastewater treatment plants using fluorescence excitation emission matrices and parallel factor analysis. *Sensors* 14: 1771–1786.

25 Kiepper, Brian (University of Georgia/Biological & Agricultural Engineering and Poultry Science Department). 2013. "Understanding Laboratory Wastewater Tests."

26 Almomani, F., Al-Jaml, K.L., and Bhosale, R.R. (2021). Solar photo-catalytic production of hydrogen by irradiation of cobalt co-doped TiO_2. *Int. J. Hydrogen Energy* 46 (22). Elsevier Ltd: 12068–12081.

27 Sun, Y., Chen, Z., Wu, G. et al. (2016). Characteristics of water quality of municipal wastewater treatment plants in China: implications for resources utilization and management. *J. Cleaner Prod.* 131. Elsevier Ltd: 1–9.

28 Zhang, W., Li, Y., Wang, C. et al. (2013). Mechanisms of simultaneous hydrogen production and estrogenic activity removal from secondary effluent though solar Photocatalysis. *Water Res.* 47 (9): 3173–3182.

29 Toledo-Camacho, S.Y., Rey, A., Maldonado, M.I. et al. (2021). Photocatalytic hydrogen production from water-methanol and -glycerol mixtures using $Pd/TiO_2(-WO_3)$ catalysts and validation in a solar pilot plant. *Int. J. Hydrogen Energy* 46 (73). Elsevier Ltd: 36152–36166.

30 Salgado, A., Yazmin, S., Zamora, R.M.R. et al. (2016). Photocatalytic hydrogen production in a solar pilot plant using a Au/TiO_2 photo catalyst. *Int. J. Hydrogen Energy* 41 (28): 11933–11940.

31 Villa, K., Domènech, X., Malato, S. et al. (2013). Heterogeneous photocatalytic hydrogen generation in a solar pilot plant. *Int. J. Hydrogen Energy* 38 (29): 12718–12724.

32 Liang, Y., Li, W., Wang, X. et al. (2021). TiO_2–ZnO/Au ternary heterojunction nanocomposite: excellent antibacterial property and visible-light photocatalytic hydrogen production efficiency. *Ceram. Int.* 48 (2). Elsevier Ltd: 2826–2832.

33 Ismael, M. (2021). Latest progress on the key operating parameters affecting the photocatalytic activity of TiO_2-based photocatalysts for hydrogen fuel production: a comprehensive review. *Fuel* 303 (June). Elsevier Ltd: 121207.

34 Romão, J., Salata, R., Park, S.Y., and Mul, G. (2016). Photocatalytic methanol assisted production of hydrogen with simultaneous degradation of methyl orange. *Appl. Catal., A* 518. Elsevier B.V.: 206–212.

35 Camacho, S.Y., Rey, A., Hernández-Alonso, M.D. et al. (2018). Pd/TiO_2-WO_3 photocatalysts for hydrogen generation from water-methanol mixtures. *Appl. Surf. Sci.* 455 (April). Elsevier: 570–580.

36 Rioja-Cabanillas, A., Valdesueiro, D., Fernández-Ibáñez, P., and Byrne, J.A. (2021). Hydrogen from wastewater by photocatalytic and photoelectrochemical treatment. *J. Phys. Energy* 3: 1–22.

37 Kim, J. and Choi, W. (2010). Hydrogen producing water treatment through solar photocatalysis. *Energy Environ. Sci.* 3 (8): 1042–1045.

38 Aydin, M.I. and Dincer, I. (2022). An assessment study on various clean hydrogen production methods. *Energy* 245. Elsevier Ltd: 123090.

39 Kennedy, J., Bahruji, H., Bowker, M. et al. (2018). Hydrogen generation by photocatalytic reforming of potential biofuels: polyols, cyclic alcohols, and saccharides. *J. Photochem. Photobiol., A* 356. Elsevier B.V.: 451–456.

40 Kampouri, S., Nguyen, T.N., Spodaryk, M. et al. (2018). Concurrent photocatalytic hydrogen generation and dye degradation using MIL-125-NH_2 under visible light irradiation. *Adv. Funct. Mater.* 28 (52): 1–9.

41 Karthik, K.V., Reddy, C., Reddy, K.R. et al. (2019). Barium titanate nanostructures for photocatalytic hydrogen generation and photodegradation of chemical pollutants. *J. Mater. Sci.: Mater. Electron.* 30 (23). Springer US: 20646–20653.

42 Damkale, S.R., Arbuj, S.S., Umarji, G.G. et al. (2019). Two-dimensional hexagonal SnS_2 nanostructures for photocatalytic hydrogen generation and dye degradation. *Sustainable Energy Fuels* 3 (12). Royal Society of Chemistry: 3406–3414.

43 Kim, J., Lee, J., and Choi, W. (2008). Synergic effect of simultaneous fluorination and platinization of TiO_2 surface on anoxic photocatalytic degradation of organic compounds. *Chem. Commun.* 1 (6): 756–758.

44 Fujita, S.I., Kawamori, H., Honda, D. et al. (2016). Photocatalytic hydrogen production from aqueous glycerol solution using NiO/TiO_2 catalysts: effects of preparation and reaction conditions. *Appl. Catal., B* 181. Elsevier B.V.: 818–824.

45 Bowker, M., Morton, C., Kennedy, J. et al. (2014). Hydrogen production by photoreforming of biofuels using Au, Pd and Au-Pd/TiO_2 photocatalysts. *J. Catal.* 310. Elsevier Inc.: 10–15.

46 Bahruji, H., Bowker, M., Brookes, C. et al. (2013). The adsorption and reaction of alcohols on TiO_2 and Pd/TiO_2 catalysts. *Appl. Catal., A* 454. Elsevier B.V.: 66–73.

47 Bahruji, H., Bowker, M., Davies, P.R. et al. (2015). The importance of metal reducibility for the Photoreforming of methanol on transition metal-TiO_2 photocatalysts and the use of non-precious metals. *Int. J. Hydrogen Energy* 40 (3). Elsevier Ltd: 1465–1471.

48 Bowker, M., Bahruji, H., Kennedy, J. et al. (2014). The photocatalytic window: photo-reforming of organics and water splitting for sustainable hydrogen production. *Catal. Lett.* 214–219.

49 Kennedy, J., Jones, W., Morgan, D.J. et al. (2015). Photocatalytic hydrogen production by reforming of methanol using Au/TiO_2, Ag/TiO_2 and Au-Ag/TiO_2 catalysts. *Catal. Struct. React.* 1 (1): 35–43.

50 Huang, G., Xiao, Z., Zhen, W. et al. (2020). Hydrogen production from natural organic matter via cascading oxic-anoxic photocatalytic processes: an energy recovering water purification technology. *Water Res.* 175. Elsevier Ltd: 115684.

51 Liu, Q. (2020). Pollution and treatment of dye waste-water. *IOP Conf. Ser.: Earth Environ. Sci.* 514 (5): 052001.

52 Gomathisankar, P., Hachisuka, K., Katsumata, H. et al. (2013). Photocatalytic hydrogen production from aqueous Na_2SO_3+ Na_2S solution with B/CuO/ZnO under visible light irradiation. *RSC Adv.* 3 (43): 20429–20436.

53 Koca, A. and Sahin, M. (2002). Photocatalytic hydrogen production by direct Sun light from sulfide/sulfite solution. *Int. J. Hydrogen Energy* 27 (4): 363–367.

54 Nguyen, T.A. and Juang, R.S. (2013). Treatment of waters and wastewaters containing sulfur dyes: a review. *Chem. Eng. J.* 219: 109–117.

55 Khan, Z., Chetia, T.R., Vardhaman, A.K. et al. (2012). Visible light assisted photocatalytic hydrogen generation and organic dye degradation by CdS-metal oxide hybrids in presence of graphene oxide. *RSC Adv.* 2 (32): 12122–12128.

56 Rafiq, A., Muhammad Ikram, S., Ali, F.N. et al. (2021). Photocatalytic degradation of dyes using semiconductor photocatalysts to clean industrial water pollution. *J. Ind. Eng. Chem.* 97: 111–128.

57 Maldonado, M.I., Saggioro, E., Peral, J. et al. (2019). Hydrogen generation by irradiation of commercial CuO + TiO_2 mixtures at solar pilot plant scale and in presence of organic electron donors. *Appl. Catal., B* 257 (February). Elsevier: 117890.

58 Dong, F., Zhao, Z., Sun, Y. et al. (2015). An advanced semimetal-organic Bi spheres-G-C_3N_4 Nanohybrid with SPR-enhanced visible-light photocatalytic performance for NO purification. *Environ. Sci. Technol.* 49 (20): 12432–12440.

59 Bart, J.C.J., Palmeri, N., and Cavallaro, S. (2010). Valorisation of the glycerol by-product from biodiesel production. In: *Biodiesel Science and Technology*, 571–624. Woodhead Publising.

60 Prayoonpunratn, P., Jedsukontorn, T., and Hunsom, M. (2021). Photocatalytic activity of metal nanoparticle-decorated titanium dioxide for simultaneous H_2 production and biodiesel wastewater remediation. *Chin. J. Chem. Eng.* 36. Elsevier B.V.: 86–100.

61 Jandam, N., Serivalsatit, K., Hunsom, M., and Pruksathorn, K. (2021). Ultrasound-assisted synthesis of nonmetal-doped titanium dioxide photocatalysts for simultaneous H_2 Production and chemical oxygen demand removal from industrial wastewater. *ACS Omegas* 6: 24709–24719.

62 Rao, N., Vempuluru, V.P., Bhargav, U. et al. (2021). Gram-scale synthesis of ZnS/NiO Core-Shell hierarchical nanostructures and their enhanced H_2 production in crude glycerol and sulphide wastewater. *Environ. Res.* 199 (February). Elsevier Inc.: 111323.

63 Lee, S.S., Bai, H., Chua, S.C. et al. (2021). Electrospun Bi_3^+/TiO_2 nanofibers for concurrent photocatalytic H_2 and clean water production from glycerol under solar irradiation: a systematic study. *J. Cleaner Prod.* 298: Elsevier Ltd: 126671.

64 Kondarides, D.I., Daskalaki, V.M., Patsoura, A., and Verykios, X.E. (2008). Hydrogen production by photo-induced reforming of biomass components and derivatives at ambient conditions. *Catal. Lett.* 122: 26–32.

65 Bowker, M., Davies, P.R., and Al-Mazroai, L.S. (2009). Photocatalytic reforming of glycerol over gold and palladium as an alternative fuel source. *Catal. Lett.* 128 (3–4): 253.

66 Daskalaki, V.M. and Kondarides, D.I. (2009). Efficient production of hydrogen by photo-induced reforming of glycerol at ambient conditions. *Catal. Today* 144 (1–2): 75–80.

67 Gallo, A., Montini, T., Marelli, M. et al. (2012). H_2 production by renewables photoreforming on Pt-Au/TiO_2 catalysts activated by reduction. *ChemSusChem* 5 (9): 1800–1811.

68 Montini, T., Gombac, V., Sordelli, L. et al. (2011). Nanostructured Cu/TiO_2 photocatalysts for H_2 production from ethanol and glycerol aqueous solutions. *ChemCatChem* 3 (3): 574–577.

69 Guo, Y., Qi, P.S., and Liu, Y.Z. (2017). A review on advanced treatment of pharmaceutical wastewater. *IOP Conf. Ser.: Earth Environ. Sci.* 63 (1): 012025.

70 Santos, J.L., Aparicio, I., Callejón, M., and Alonso, E. (2009). Occurrence of pharmaceutically active compounds during 1-year period in wastewaters from four wastewater treatment plants in Seville (Spain). *J. Hazard. Mater.* 164 (2–3): 1509–1516.

71 Meinzinger, F. and Oldenburg, M. (2009). Characteristics of source-separated household wastewater flows: a statistical assessment. *Water Sci. Technol.* 59 (9): 1785–1791.

72 Morais, S.A., Delerue-Matos, C., and Gabarrell, X. (2014). An uncertainty and sensitivity analysis applied to the prioritisation of pharmaceuticals as surface water contaminants from wastewater treatment plant direct emissions. *Sci. Total Environ.* 490. Elsevier B.V.: 342–350.

73 CETENMA – Centro Tecnológico de la Energía y del Medio Ambiente (2019). "Informe VIGILANCIA TECNOLÓGICA Tratamiento de Aguas Residuales Del Sector Farmacéutico."

74 Chen, Z., Wang, Y., Li, K., and Zhou, H. (2014). Effects of increasing organic loading rate on performance and microbial community shift of an up-flow anaerobic sludge blanket reactor treating diluted pharmaceutical wastewater. *J. Biosci. Bioeng.* 118 (3). Elsevier Ltd: 284–288.

75 Kumari, V. and Tripathi, A.K. (2019). Characterization of pharmaceuticals industrial effluent using GC–MS and FT-IR analyses and defining its toxicity. *Appl. Water Sci.* 9 (8). Springer International Publishing: 1–8.

76 Papadakis, E., Tula, A.K., and Gani, R. (2016). Solvent selection methodology for pharmaceutical processes: solvent swap. *Chem. Eng. Res. Des.* 115. Institution of Chemical Engineers: 443–461.

77 Kostich, M.S., Batt, A.L., and Lazorchak, J.M. (2014). Concentrations of prioritized pharmaceuticals in effluents from 50 large wastewater treatment plants in the US and implications for risk estimation. *Environ. Pollut.* 184. Elsevier Ltd: 354–359.

78 Monteiro, S.C. and Boxall, A.B.A. (2010). Occurrence and fate of human pharmaceuticals in the environment. *Rev. Environ. Contam. Toxicol.* 202.

79 Wu, Y., Chen, X., Cao, J. et al. (2021). Photocatalytically recovering hydrogen energy from wastewater treatment using MoS_2@TiO_2 with sulfur/oxygen dual-defect. *Appl. Catal., B* 303 (October 2021). Elsevier B.V.: 120878.

80 Khedr, T.M., El-Sheikh, S.M., Kowalska, E., and Abdeldayem, H.M. (2021). The synergistic effect of anatase and brookite for photocatalytic generation of hydrogen and diclofenac degradation. *J. Environ. Chem. Eng.* 9 (6). Elsevier Ltd: 106566.

81 Kumar, A., Rana, A., Sharma, G. et al. (2018). High-performance photocatalytic hydrogen production and degradation of levofloxacin by wide Spectrum-responsive Ag/Fe_3O_4 bridged $SrTiO_3$/g-C_3N_4 plasmonic nanojunctions: joint effect of Ag and Fe_3O_4. *ACS Appl. Mater. Interfaces* 10 (47): 40474–40490.

82 Wei, Z., Liu, J., Fang, W. et al. (2019). Photocatalytic hydrogen evolution with simultaneous antibiotic wastewater degradation via the visible-light-responsive bismuth spheres-G-C_3N_4 nanohybrid: waste to energy insight. *Chem. Eng. J.* 358 (September 2018). Elsevier: 944–954.

83 Jin, C., Kang, J., Li, Z. et al. (2020). Enhanced visible light photocatalytic degradation of tetracycline by MoS_2/Ag/g-C_3N_4 Z-scheme composites with peroxymonosulfate. *Appl. Surf. Sci.* 514 (March). Elsevier: 146076.

84 Wu, X., Chen, F., Wang, X., and Huogen, Y. (2018). In situ one-step hydrothermal synthesis of oxygen-containing groups-modified G-C_3N_4 for the improved photocatalytic H_2-evolution performance. *Appl. Surf. Sci.* 427. Elsevier B.V.: 645–653.

85 Abou-Elela, S.I. and El-Khateeb, M.A. (2015). Performance evaluation of activated sludge process for treating pharmaceutical wastewater contaminated with β-lactam antibiotics. *J. Ind. Pollut. Control* 31 (1): 1–5.

86 Cao, D., Wang, Q., Yue, W. et al. (2020). Solvothermal synthesis and enhanced photocatalytic hydrogen production of bi/Bi_2MoO_6 Co-sensitized TiO_2 nanotube arrays. *Sep. Purif. Technol.* 250 (May). Elsevier: 117132.

87 Chen, W., He, Z.C., Huang, G.B. et al. (2019). Direct Z-scheme 2D/2D $MnIn_2S_4$/g-C_3N_4 architectures with highly efficient photocatalytic activities towards treatment of pharmaceutical wastewater and hydrogen evolution. *Chem. Eng. J.* 359 (November 2018). Elsevier: 244–253.

88 Shinde, Y., Wadhai, S., Ponkshe, A. et al. (2018). Decoration of Pt on the metal free RGO-TiO_2 composite Photocatalyst for the enhanced photocatalytic hydrogen evolution and photocatalytic degradation of pharmaceutical pollutant B blocker. *Int. J. Hydrogen Energy* 43 (8). Elsevier Ltd: 4015–4027.

89 Sharmila, V., Godvin, J., Banu, R. et al. (2020). A review on evaluation of applied pretreatment methods of wastewater towards sustainable H_2 generation: energy efficiency analysis. *Int. J. Hydrogen Energy* 45 (15). Elsevier Ltd: 8329–8345.

12

Catalysts and Photoreactors for Photocatalytic Solar Hydrogen Production: Fundamentals and Recent Developments at Pilot Scale

Alba R. Aguirre[1], Alejandro C. Reina[2], José P. Pérez[3], Gerardo Colon[4], and Sixto Malato[1]

[1]CIEMAT – Plataforma Solar de Almería, Ctra. De Senés s/n, 04200 Tabernas, Almería, Spain
[2]Universidad Tecnológica Metropolitana, Programa Institucional de Fomento a la Investigación, Desarrollo e Innovación (PIDi), Ignacio Valdivieso, San Joaquín, Santiago, 2409, Chile
[3]Universitat Autònoma de Barcelona, Departament de Química, Edifici Cn, 08193, Bellaterra, Cerdanyola del Vallés, Spain
[4]Centro mixto Universidad de Sevilla-CSIC, Instituto de Ciencia de Materiales de Sevilla, Américo Vespucio 49, 41092 Sevilla, Spain

12.1 Materials for Solar Photocatalytic Hydrogen Production

"W*ater will be the coal of the future*…" was the visionary prediction of Jules Verne in early 1874 in his science fantasy fiction novel "The Mysterious Island" [1]. Indeed, producing energy from water still seems like a "mysterious island" in science. Since Fujishima and Honda stated that water could be split into H_2 and O_2 by photocatalysis in the lab [2], an enormous amount of research has been published pursuing the development of a material able to produce hydrogen with the aid of light. In spite of this extensive research, refining the process and making it more industrially feasible over the years, there is still no system that is both efficient and inexpensive enough to produce sufficient hydrogen to use as a clean-burning fuel on roads, in industry, and in the home. For hydrogen to make a significant contribution to the clean energy transition, it must be adopted in sectors where it is now almost completely absent, such as transportation, buildings, and power generation.

Today, particulate photocatalyst systems have very low solar-to-hydrogen (STH) conversion rates of around 1% at most [3], and any improvement in photocatalyst performance might be enough to make such systems feasible and allow their simplicity and scalability to be utilized.

12.1.1 General Considerations on the H_2 Production Reaction

Before any discussion of photocatalytic materials, a clear overview of the H_2 catalytic reaction pathway is necessary. From a thermodynamic point of view, water splitting

Photocatalytic Hydrogen Production for Sustainable Energy, First Edition. Edited by Alberto Puga.

is energetically disfavored and requires the standard Gibbs free energy change of 237 kJ mol^{-1}.

$2H^+ + 2e^- \rightarrow H_2$	Hydrogen evolution half-reaction
$2OH^- + 2h^+ \rightarrow ½O_2 + H_2O$	Oxygen evolution half-reaction
$H_2O \rightarrow H_2 + ½O_2$	Overall water splitting

It is evident that the redox potentials for the half reactions involved in the overall process determine the possible candidate photocatalysts. The positions of the valence and conduction bands (CB and VB) therefore become a necessary constraint and strongly limit the range of possible photocatalysts. Briefly, both the reduction and oxidation potentials of water should lie within the photocatalyst band gap. Thus, candidate photocatalysts for solar water splitting must meet two important requirements: (i) The bandgap must be 1.23 eV $< E_g <$ 3.26 eV, and (ii) the band edge positions at the bottom of the CB must be more negative than the redox potential of H+/H_2 (0 V vs. NHE), while the top edge of the VB must be more positive than the redox potential of O_2/H_2O (1.23 V). Any materials satisfying these conditions would be thermodynamically suitable for the photoinduced water splitting reaction (Figure 12.1).

The overall photocatalytic water splitting reaction is an endothermic reaction. This means that higher energy photons are required to overcome that energy barrier. In spite of the great number of photoactive semiconductors reported in the literature, TiO_2 appears to be the most efficient [4]. However, recombination of photogenerated pairs, the occurrence of fast competitive backward reaction, and the failure to absorb visible light photons hinder process efficiency, and STH rates drop drastically. Several approaches have therefore been proposed to overcome these strong handicaps.

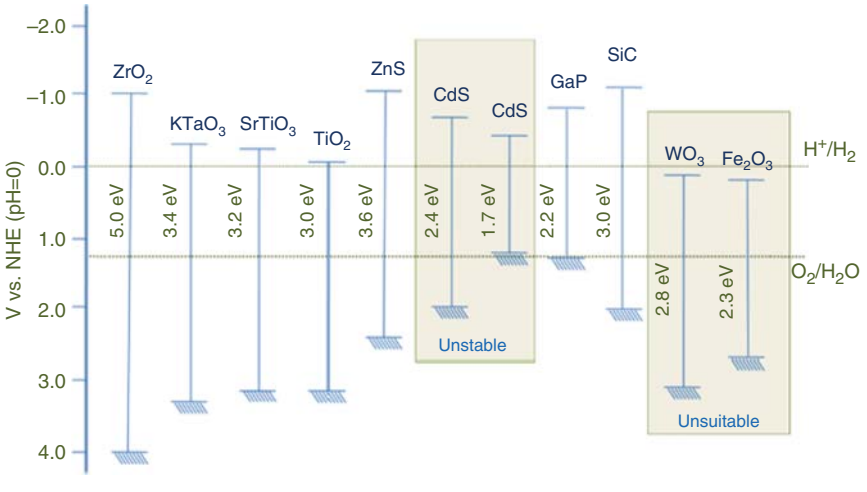

Figure 12.1 Bandgaps and band edge positions of selected semiconductors in relation to the redox potentials for the water splitting reaction.

The recombination of photogenerated charge carriers has been well-studied, since early research focused mainly on TiO_2-based catalysts [5]. Indeed, nonradiative recombination appears to be the main de-excitation channel of pure TiO_2 anatase-based nanosystems, and is generally accepted as the major drawback of this material. Solutions for morphological structural defects directly related to size, shape, secondary particle size, and porosity are therefore considered essential to be able to control light-matter interactions. Studies in this vein have included doping with metal or nonmetal elements [6], controlling the structure and facets [7], and introducing defects into nanocrystals [8].

In order to suppress the reverse reaction, a physical separation between the corresponding photoactive sites on the surface of the photocatalyst has been proposed. Such a physical separation of active sites would not only avoid the reverse reaction but also improve photonic efficiency by hindering recombination. The two approaches commonly used for attaining this surface separation of photogenerated electrons and holes are the use of a specific co-catalyst that would act as a specific electron or hole sink [9], or tailored heterostructures that would separate charges by band engineering [10] (Figure 12.2).

It is widely known that the water splitting reaction on TiO_2 as the model semiconductor is still very inefficient. As discussed above, oxidation of water to produce O_2 is more thermodynamically feasible than the formation of peroxo and hydroxyl compounds. Nevertheless, the slow kinetics of the O_2 reaction dramatically favors the formation of such alternative compounds that become kinetically competitive with O_2 production. Therefore, sacrificial agents are used to improve hydrogen productivity. The oxidation of such sacrificial organic compounds by these highly reactive compounds instead of water would enhance the performance of the reduction half-reaction. Thus, the photogenerated holes are continuously withdrawn from the catalyst, hampering the unwanted recombination of holes and electrons. Most of these would be organic, since organic molecules can be completely mineralized into such innocuous products as CO_2 and H_2O, although there may also be inorganic sacrificial agents. In any case, complex and high-added-value reagents are systematically avoided for this, and so far, the most appealing possibility has been the use of

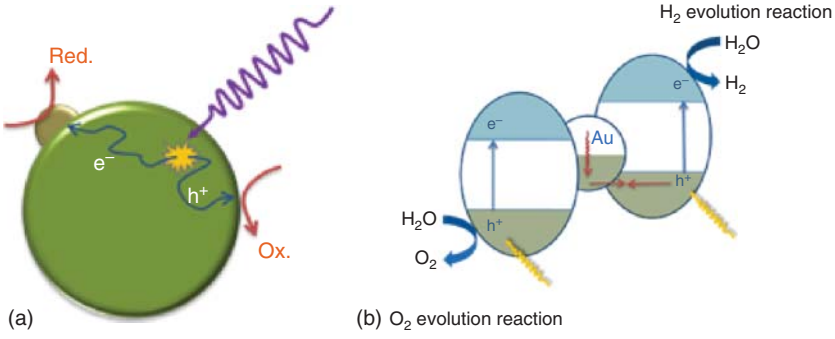

Figure 12.2 Photogenerated charge separation: (a) With a specific co-catalyst; (b) With a tailored heterostructure forming a Z-scheme system.

aqueous organic pollutants. This is a smart strategy that tackles two different problems at once: energy production and wastewater treatment.

12.1.2 Photoreforming

As discussed above, hydrogen production by photoreforming shows two clear advantages for the overall water splitting reaction. A sacrificial agent that could be easily oxidized, and therefore, assist in the reduction half-reaction, clearly affects reaction performance. It is evident that these combined processes represent an environmentally friendly, cost-effective method for industrial byproducts or wastewater treatment, with simultaneous production of energy.

During photoreforming, instead of water, organic compounds can act as photoinduced holes and photogenerated oxygen scavengers, thereby retarding electron–hole recombination as well as hydrogen–oxygen backward reaction. This would enhance the resulting hydrogen production rates. As would be expected, in this case, when complete oxidation of the sacrificial agent is achieved, the rate of hydrogen production would drop to values comparable to those with pure water. Therefore, and as mentioned above, the use of biomass-derived compounds is gaining increasing interest as an abundant, renewable, and clean feedstock for hydrogen production [11–13].

The Kondarides group, one of the first to study the systematic use of organic sacrificial agents, has published a large body of studies [14–16] in which many of those molecules were tested (alcohols, saccharides, azo dyes, organic acids, etc.) with excellent results for hydrogen generation. They are the team that coined the term "photoreforming" as an elegant way of describing the overall process, with the formation of hydrogen and transformation of the organic molecule all the way to CO_2, which very much resembles the classical reforming of methanol to CO_2:

Because of their simplicity and availability, small alcohols like methanol and ethanol are among the most tested sacrificial agents. In general, those molecules have been proven to support hydrogen production very effectively by photoreforming [17–19]. The photoreforming of alcohols is also especially efficient because the alpha-hydroxy radicals generated in the first oxidation step can then donate electrons into the CB of most of the semiconductors, thereby creating "current doubling" in which absorption of one UV photon by the photocatalyst creates two CB electrons, and thus one molecule of H_2 [20]. Nevertheless, since the availability of large concentrations of those two alcohols in wastewater (concentrations of the sacrificial agent must be large enough to produce sufficient quantities of hydrogen) is not as common as might be expected, the focus of research is now on glycerol. This polyalcohol is as or even more reactive than methanol or ethanol and can be found in large quantities in wastewater from the biodiesel industry. Indeed, biodiesel is produced by transesterification, which converts biomass triglycerides into methyl esters (the actual biodiesel) and the glycerol byproduct (in $g\,l^{-1}$ concentrations). Thus, a cheap and abundant source of glycerol exists, and can be taken advantage of as a sacrificial agent for hydrogen production. Also, as mentioned above, glycerol reactivity may be even higher than the smaller alcohols due to the presence of five α-H atoms, which take part in the formation of the highly reactive alpha-hydroxy radicals, and in turn, facilitate the production of H_2. There are many studies in

the literature demonstrating the highly advantageous role of glycerol. Many of those studies used aqueous synthetic glycerol solutions [21–23], but some others have already shown the usefulness of real biodiesel wastewater containing high concentrations of glycerol [24, 25].

Apart from alcohols, other organic molecules have proven to be successful sacrificial agents for the photocatalytic generation of hydrogen, such as glucose [12] and several other sugars [19, 26, 27], acetic acid [19, 28], lactic acid [29], phenolic compounds [30], EDTA [31], lignocellulosic biomass compounds [32, 33], solid waste [34] and mixtures of organic compounds found in real olive mill wastewater [35], biomass-derived feedstocks [36], swine sewage [37], and electroplating waste liquids [38]. Kawai et al. first demonstrated the possibility of converting carbohydrates (sugar, starch, or cellulose) in the presence of water and $RuO_2/TiO_2/Pt$ into hydrogen [39]. From this first result, many other attempts have been made with various target molecules and catalysts. In this sense, as a general trend, the complex molecular structure of carbohydrates leads to lower productivity than simple alcohols (methanol or ethanol).Therefore, the degradation of carbohydrates still requires further study for its improvement.

Another possibility arises from the use of different oxygenated substrates, non-derived in this case from biomass, such as waste pollutants, plastic wastes, or even methane. The possibility of the assembly of two interesting processes, hydrogen formation and pollutant degradation, appears of great relevance [40]. Thus, a wide variety of organic pollutants in water, such as pesticides or antibiotics, have been photoreformed, achieving, in all cases to complete mineralization simultaneously to the production of H_2 [41, 42]. From this approach, it can be found in the literature interesting examples including degradation of dyes, aldehydes [43], and even solid wastes, such as plastics or food [13]. As previously anticipated, as the molecule is simpler, the efficiency of the H_2 evolution is higher.

Inorganic compounds, like chloride [44], mixtures of Na_2S and Na_2SO_3 [45], and real sea water [46] have been shown to be excellent sacrificial agents. Sea water is of especial interest, since it is used as process water in many chemical processes and wastewater with high saline content is widely available. However, the activity of the photocatalyst is suppressed, and severe photocorrosion leads to a decrease in stability. recommend Therefore, further exploration of highly efficient, very stable photocatalysts is still required for seawater hydrogen production.

In spite of the large number of studies on hydrogen production by photoreforming, the productivity in each case is quite difficult to compare due to the high variety of operating conditions (reactor type, flow rates, lamp types and power, etc.). This points out the strong need to standardize results by providing the photonic efficiency [47].

12.2 Factors that Influence Photocatalyst Activity

Apart from the choice of photocatalytic materials and the possibility of composite structures that might be especially well-suited for harvesting visible light and promoting photocatalytic processes, including hydrogen generation, several other

factors clearly influence the performance of photocatalytic systems for hydrogen generation. It should first be emphasized that, although direct water splitting and hydrogen production without the use of sacrificial compound oxidation is possible, it is normally so difficult that we do not consider it viable, and therefore, concentrate here on hydrogen generation using sacrificial agents, mainly organic molecules. This section describes the factors affecting performance, that is, the structure and morphology of the catalyst in the reactor, light intensity, temperature, and pH.

12.2.1 Catalyst Structure and Morphology

A wide variety of catalyst morphologies, material combinations, surface areas, and crystal structures have been used for hydrogen generation. Although many of the materials that have successfully produced photocatalytic hydrogen at laboratory scale would fail in real applications for very simple reasons, like the difficulty in keeping very small particles in suspension when their point of zero charge (PZC) values are less than optimum, or on the contrary, of removing very small nanoparticles from an aqueous medium after reaction completion. Some of those structural features are briefly described below.

Nanopowder, nanofiber, nanotube, nanorod, flower-like and forest-like morphologies, nanoflakes, nanosheets, and three-dimensional ordered macroporous materials [45] have been tested with fairly good hydrogen production rates. Since the use of composites and heterojunctions (preferentially, Type II, Z-scheme, and S-scheme heterojunctions), interesting morphologies like core-shell particles [48] and core-shell nanofibers [49] have also been used as a very good strategy for efficiently increasing particulate photocatalyst activity.

The final goals of this wide variety of nano-oriented morphologies are to increase the surface area, which almost always increases the activity associated with a heterogeneous surface-driven process, and to avoid photogenerated charge recombination.

Nanoparticles and suspended nanostructures are the usual photocatalytic platforms, but hydrogen could also be produced by photoelectrocatalysis or photoelectrochemical reactors. Although as far as we know, there are still no pilot-plant scale photoelectrochemical reactors for hydrogen production, this possibility cannot be ruled out, since laboratory experiments have consistently proven the potential of such configurations for an efficient, sustained supply of hydrogen. Thus, a coating of photocatalytic material deposited on top of an inert conducting electrode (usually conducting glass) has been the prevailing choice of laboratory-scale studies. Several different photoactive material deposition techniques have been used, usually sol–gel coatings due to their simplicity. Growth of nanotubes and nanorods on the surface of conducting glass is another thoroughly studied possibility rendering excellent hydrogen generation rates. This is because of the dramatic increase in the surface reaction and the shorter distance that photogenerated charges have to travel to reach the reaction centers at the photocatalyst surface. One of the materials that has been recurrently used in those photoelectrochemical configurations, especially for the growth of nanorods, is MoS_2 (and its closely related Mo_3S_4 form) due to its convenient CB energy position and suitability for proton reduction and hydrogen

generation [50]. Nevertheless, photoelectrochemical configurations, as they are based on the use of macroscopic electrodes, could very easily be affected by energy and mass transfer limitations [51], which would have to be scrutinized in close detail before scale-up.

12.2.2 Light Intensity

The obvious and only cheap and sustainable source of photons available for real-scale hydrogen production reactors is sunlight. This involves direct irradiation of the reactor without concentration, i.e. light entering the reactor with an intensity of around one sun (standard illumination at AM1.5, or $1\,kW\,m^{-2}$), or irradiation with concentrated sunlight by using a solar collector with a light concentration ratio of over one. It is well known that an intensity above one sun causes no remarkable increase in photoactivity in many photocatalytic materials, since excess photons are lost as heat by photogenerated charge recombination [51], and therefore, the use of concentrating reactors with such materials makes no sense. In fact, the most widely used photocatalytic reactor configuration is based on compound parabolic collectors (CPC), which, although they make use of mirrors to take advantage of light coming from any direction (both direct and diffuse), involve no light concentration. However, this simple (with no mobile parts), economical reactor has an inherent limit to the amount of light that can be used by it, which may be viewed as an obstacle to further development (see Figure 12.3).

Better use of sunlight in solar concentrating photoreactors could therefore be a way of improving overall hydrogen generation efficiency. Several recent publications on the behavior of irradiation inside photocatalytic reactors for hydrogen production and the perspective for improving photon energy exploitation [52] have reported that the angles and intensity of the incident rays significantly affect radiation distribution (Figure 12.4). They also found that the equilibrium radiation distribution has a close relationship with the density distribution of the photocatalysts. The simulated results are expected to be helpful for obtaining the optimal operating parameters for solar photocatalytic hydrogen production.

Other examples of solar photocatalytic reactor pilot plants for hydrogen generation found in the literature are discussed in detail in the following sections. The effects of such experimental parameters as reactor configuration, type and concentration of sacrificial agent, photocatalyst load, pH, and temperature, are described. The feasibility of scale-up is explored, and further improvements in reaction yields are suggested.

Finally, it is worth mentioning that many studies published have demonstrated the photocatalytic generation of hydrogen using artificial sources of light. As this is out of the scope of this chapter, we only mention that the most frequently used artificial light setup is based on a 300 W Xenon arc lamp with UV (420 nm) cut-off filters. Obviously, such an experimental setup attempts to reproduce a scenario close to real sunlight irradiation. Other frequently used artificial light sources are based on UVA lamps and light emitting diode (LED) arrays emitting in the visible region. Some more exotic illumination sources, like the one described by Skillen et al. [53],

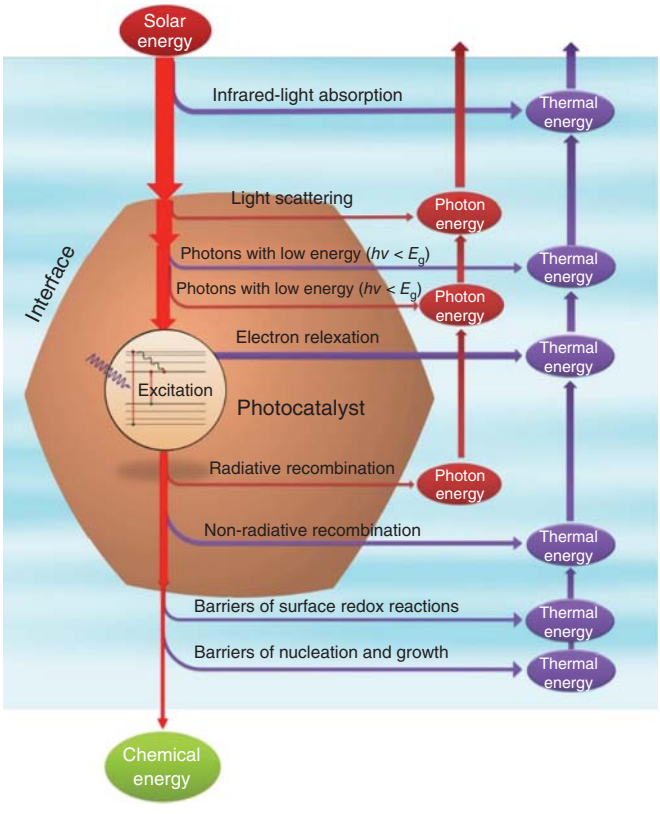

Figure 12.3 Schematic diagram of energy losses involved in photocatalytic water splitting. Source: Guo et al. [51]/with permission of Elsevier.

where light is delivered by a series of angled mirrors and the illumination shafts of a solar telescope, have also been used.

12.2.3 Temperature

In general, heterogeneous photocatalytic reactions are hardly affected by temperature. As these reactions are triggered by photon absorption and make use of photocatalyst materials with bandgaps that make thermal electron excitation to the CB impossible at "reasonable" temperatures, the study of this experimental variable is often neglected in their description. Nevertheless, several steps that are always connected to the photocatalytic reaction itself, like reagent and product adsorption–desorption equilibrium, solubility of the chemicals involved in the fluid phase, etc., are certainly affected by temperature, and therefore, from the point of view of the application of applied chemistry, this is a factor that has to be taken into account. At solar pilot-plant scale, the temperature inside the photochemical reactor will be hardly more than 50 °C, and that only in hot climates. This is very convenient, because it simplifies the construction of the reactor, and makes it

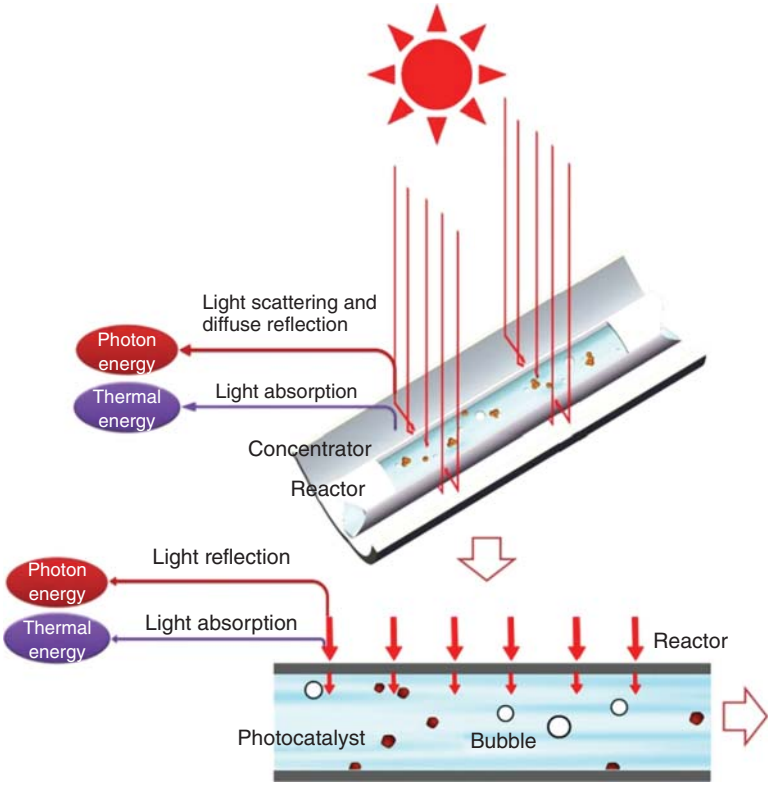

Figure 12.4 Energy losses in photocatalytic water splitting in a solar collector. Source: Guo et al. [51]/with permission of Elsevier.

possible to use cheap polymeric connections and pipelines between glass tubes. Interestingly, even in this narrow range of practical temperatures, there is a clearly beneficial effect of temperature on overall reaction efficiency. Kondarides [15] showed that using 0.5% Pt loaded TiO_2 with glycerol as the sacrificial agent for photocatalytic production of hydrogen, the gas production almost doubled when the temperature was raised from 40 to 60 °C, although at 80 °C, hydrogen production began to decay. Castedo et al. [54] also showed that irradiated Au/TiO_2 powder suspended in a 9 : 1 molar H_2O:ethanol solution provided an H_2 generation rate that doubled when the temperature was raised from 298 to 323 K, and was multiplied by more than 3 when the temperature increased to 348 K. These simple studies lead to the conclusion that moderate increases in temperature in a range that can be achieved by direct solar light radiation from the reactors can noticeably improve the hydrogen production process.

Li et al. [55] recently published an interesting study demonstrating that photocatalytic hydrogen production can be promoted at higher temperatures induced by the solar–thermal effect, while catalyst performance depends on the catalyst structure and solar light spectrum. In particular, pristine TiO_2 P25 and g-C_3N_4 have shown increased hydrogen evolution reaction (HER) performance at high temperatures.

Pt NP-decorated TiO_2 P25 and g-C_3N_4 presented varying HER efficiencies at higher temperatures, while Pt NP-modified g-C_3N_4 demonstrated enhanced HER performance from 25 to 65 °C under visible-light irradiation. These authors found that low electrical impedance, narrow bandgap, enhanced light absorption, and longer photoelectron lifetime with increasing temperature produce positive effects on these photocatalysts in temperature-based HER processes. The CB and VB become more negative with rising temperature and promote activity. However, agglomeration of Pt NPs can generate a significantly negative effect on the HER performance at higher temperatures. UV light can exacerbate the thermal agglomeration of Pt NPs, while visible light will minimize it. Finally, they suggest that, according to their results, visible-light responsive catalyst systems are more suitable for solar–thermal-induced HER for industrial applications.

12.2.4 pH

The pH of the aqueous solution also has a strong effect on the heterogeneous photocatalytic generation of hydrogen with the majority of the solid materials tested so far. Although the easiest reduction of protons at acid pH would suggest more hydrogen generation at those pH values, in general, a basic pH of around 10 provides much better hydrogen yields. There are many publications that illustrate this behavior. A good example is the study of Kondarides et al. on the production of hydrogen with simultaneous degradation of azo dyes using Pt/TiO_2 [15], or more recently, a study on the performance of different carbon nitride-metal ferrite (MFe_2O_4/mpg-CN; M: Mn, Fe, Co, and Ni) nanocomposites that show optimum photocatalytic performance for hydrogen production at pH = 9 [56]. The improved performance of catalysts at high pH is usually explained by the fact that the energy level of both VB and CB increases with increasing pH. The more energetic CB photoexcited electrons are then more effective for reducing protons. In any case, from the viewpoint of the application, the actual pH of the organic aqueous solutions used for hydrogen generation would be around pH = 7, with extreme pH rarely being used. Thus, for full-scale real application, the optimum pH for the reaction would be around 8, and at most, 9 in some extreme and unusual situations.

12.3 Current Photoreactors and Pilot Plants

Solar photocatalysis for hydrogen production is studied in three parts: (i) Evaluation of the incident solar radiation; (ii) Reactor design and reaction mechanism, and (iii) System evaluation and scale-up. Therefore, photoreactor design has an important role in photocatalytic hydrogen production. There is a plethora of studies, including critical reviews [57], on pilot-and commercial-scale solar reactor parameter design and performance for photocatalytic detoxification. However, photocatalytic hydrogen production has usually been evaluated at smaller volumes (4–300 ml) [58], and scaling up is challenging. A limited number of studies have

been done on pilot-scale photocatalytic hydrogen production, and therefore also, the design of pilot-plant scale photoreactors for this purpose.

Regardless of the process, the main role of a photoreactor is to provide solar radiation to the photocatalyst so it can absorb as many photons reaching the solid–liquid surface as possible. Depending on the nature of the catalyst, the system can be defined as heterogeneous (suspended or supported catalysts) or homogeneous (dissolved catalysts). Other hybrid systems combine a homogeneous catalyst with a heterogeneous photosensitizer [58]. Suspended heterogeneous systems must ensure correct suspension of the catalyst as well as uniform distribution of sunlight, which is disturbed by the catalyst, as it can absorb, reflect, or scatter photons, and too high a concentration can increase turbidity, reducing the penetration of solar radiation into the photoreactor. The optical-path length (OPL) is another design parameter that must be uniform for both radiation flow and its distribution. The liquid flow must be turbulent to avoid solid deposition without causing significant pressure loss, which would affect the maximum length of the photoreactor. Thus, to avoid undue pressure loss in the photoreactor and glass walls that are too thick, the optimal OPL is 20–50 mm [59]. With homogeneous catalysts, the proper concentration would depend on their molar absorptivity and would directly affect the light-path length of the photoreactor [57].

For solar radiation to be able to penetrate the reactor (absorber tube) wall material, it has to be transparent to solar UV radiation (>300 nm). In general, materials transparent to solar UV radiation are also transparent to higher wavelength photons in the rest of the solar spectrum. Commercial options include fluoropolymers, acrylate polymers, and different types of glass, however, the most commonly used is low-iron borosilicate glass of the type widely used in laboratory equipment (Pyrex and Duran glass) that has good transmittance at >300 nm. The iron content in conventional glass substantially reduces UV-light transmittance. Aluminum is the most widely used material for solar collector reflecting or concentrating surfaces, because of its high reflectivity at >300 nm and low cost. Usually, for a process based on water that does not require heating, the connections are made of conventional plastic polymers such as polypropylene or polyethylene, which are also resistant to solar degradation [57]. Thus, the most common solar photoreactor designs are based on: (i) Parabolic through collectors (PTCs), (ii) Non-concentrating collectors (NCCs), and (iii) Compound parabolic collectors (CPCs).

The first systems developed for photocatalytic applications were PTCs adapted from solar thermal collectors. Such solar photocatalytic collectors are made of a reflective concentrating parabolic surface and a support structure. The aperture plane of the collector must always be perpendicular to the sun's rays, so the structure has a motorized solar tracker to keep it aligned with the sun. This way, all the solar radiation on the aperture plane can be reflected and concentrated onto the absorber tube (photoreactor), located at the focus of the parabola. NCCs are usually stationary devices oriented towards the equator with an inclination determined by the site's latitude. Although this system has several advantages over PTCs, such as its ability to collect diffuse radiation and its easier and cheaper installation, it also has drawbacks, such as the need to withstand high pressures

because of the transparent photoreactor's larger surface, which must also be inert and resistant to chemicals, inclement weather, and solar UV rays. Finally, CPCs combine the advantages of PTCs and NCCs. This particular system can be designed for an acceptance angle of +90° to −90°, the concentration factor is equal to 1, and all the solar rays in the aperture of the CPC are collected and directed at the photoreactor. More details on general considerations for photoreactor design can be found in articles by Malato et al. [60]. CPCs are therefore the first choice for photocatalytic hydrogen production when the process is based on suspended photocatalysts illuminated at ambient temperature.

The general photoreactor requirements have been described above, however, photocatalytic hydrogen generation requires a series of additional characteristics due to the two-phase liquid and gas system requiring reductive conditions. This means that the system has to be airtight while enabling sampling of hydrogen for its measurement. Hydrogen formation from water raises the pressure within the system, so its design must be overpressure resistant and include a system outlet to extract the hydrogen. As mentioned above, there are very few studies on pilot-scale photocatalytic hydrogen production, so the main characteristics of the photocatalytic hydrogen production systems found in the literature are described below.

12.3.1 Pilot Solar Photoreactors for Photocatalytic Hydrogen Production: CPCs

CPCs are the photoreactors most used for this purpose. As mentioned, pilot-scale solar hydrogen production is not as well-developed as other photocatalytic applications, and there have been few attempts at pilot scale. One of the first approaches was installed at Xi'an Jiaotong University [61]. It consisted of a photoreactor made up of four non-truncated CPCs with adjustable angles connected in series and placed on a surface inclined 35° and a 35-l tank in which a turbulent solution was continuously recirculated by a hydraulic pump. The total irradiated volume was 20 l. The CPC Pyrex tubes were 1.6 m long with a 15 mm inner radius and an outer radius 1 mm more. The concentration factor was 4.76. N_2 gas was inserted at the bottom of the tank and H_2 collected at the top. H_2 was analyzed in situ by a thermal conductivity detector (TCD) in a gas chromatograph (GC) using N_2 as the carrier gas. The production of hydrogen using CdS (0.56 g l^{-1}) as photocatalyst and Na_2S/Na_2SO_3 (1.6/6.3 gl^{-1}) as sacrificial agent was 1.88 l h^{-1} (Figure 12.5a). The same approach was followed by researchers at the Plataforma Solar de Almeria (PSA) for the development of a pilot plant with similar characteristics [63], differing mainly in dimensions and CPC design. The PSA photoreactor consists of a tank (27 l) and 16 Pyrex tubes with an outer diameter of 32 mm and an irradiated length of 1.4 m. The total irradiated volume is 14.25 l. Unlike the system described above, the concentration factor of the CPCs is 1. The N_2 flow rate for reaching anoxic conditions and drawing H_2 produced for quantification (GC/TCD) is regulated by a mass flow controller. Various photocatalysts and sacrificial agents have been tested in this pilot system. Among them, Au/TiO_2 (0.5% Au, 0.2 g l^{-1}) with CH_2O_2 (2.3 g l^{-1}) as the sacrificial agent resulted in an H_2 production of $4{\cdot}10^{-4}$ l h^{-1} [64], while the use of a copper

(a) (b)

Figure 12.5 Pilot plants installed at: (a) Xi'an Jiaotong University. Source: Ren et al. [62]/with permission of Elsevier, (b) Plataforma Solar of Almeria (PSA).

cocatalyst and glycerol as the sacrificial agent increased the production from 0.14 to $0.37\,l\,h^{-1}$ [65]. (Figure 12.5b).

Other pilot plants have been designed for photocatalytic hydrogen production with some differences, such as the application of electricity, photoelectrocatalytic hydrogen generation, or the application of heat (temperatures higher than 100 °C) for photothermal catalytic hydrogen production. In particular, a hybrid system using natural solar radiation by day and artificial by night or on cloudy days was characterized for hydrogen production by the methods described above [66]. In the first configuration, the CPC was connected to a solar photovoltaic panel to generate electricity for electron donation through the electrode-solution interface. Two electrodes immersed in the solution function as the electron sacrificing agent. An anionic exchange membrane separates the hydrogen from the oxygen. Finally, the photoreactor is connected to the H_2 collection system for measurement and storage. In the photothermal catalytic hydrogen production system, electrodes and membranes are removed, and instead there is a heat exchanger and a separator to obtain the H_2 produced. The CPC is 4 m long in both cases with an aperture area of $10\,m^2$, supplying a maximum of 6 kW. The photoreactor has a 30-mm outer diameter and a length of 4.5 m. In the first method, the temperature is kept constant at 60 °C, while in photothermal catalytic hydrogen production, the temperature varies in a range of 150–300 °C (Figure 12.6).

Systems with more than one photoreactor , such as the pilot plant installed on the roof of the State Key Laboratory of Multiphase Flow in Power Engineering (Xi'an, China), have also been tested. The system consists of nine sets of CPC photoreactors, each of which is $9 \times 3.6\,m^2$ with a 23-l volume. Each photoreactor is mounted on an adjustable sun-tracking structure. The total volume is 23 l, of which 12.2 l are irradiated. The concentration factor is 4.12. [62]. Natural circulation is employed to avoid pumps, although high pressure H_2 or N_2 may be injected into the system to avoid sedimentation of the catalyst. Average hydrogen production is $10.3\,l\,h^{-1}$.

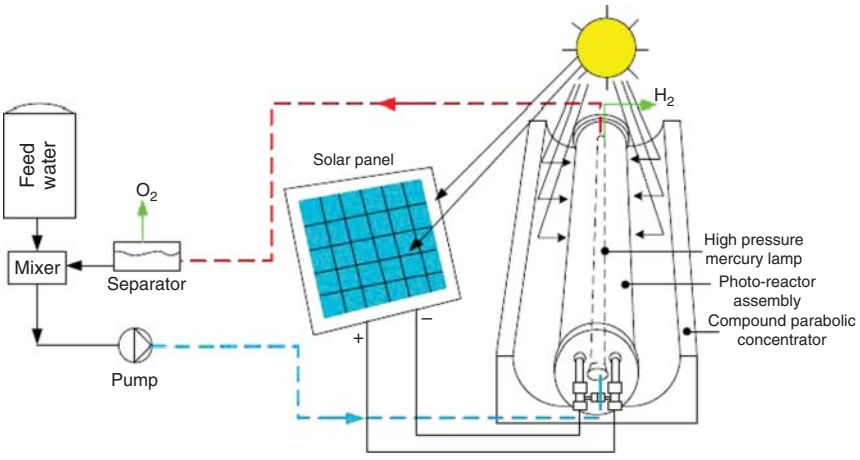

Figure 12.6 Pilot plant installed at University of Ontario Institute of Technology, Oshawa, Canada. Source: Baniasadi et al. [66]/with permission of Elsevier.

Figure 12.7 Pilot plants installed at (a) State Key Laboratory of Multiphase Flow in Power Engineering (Xian, China) Source: Cao et al. [67]/with permission of Elsevier and (b) near to Xian city. Source: Wei et al. [68]/with permission of Elsevier.

(Figure 12.7a) [67]. The same research group installed another larger CPC system with 4 rows and 76 units of truncated CPCs connected in parallel with single axis tracking, reaching a concentration factor of 4.22. The total irradiated area is 103.7 m^2 (Figure 12.7b). In this system, natural circulation and high-pressure gas (hydrogen or nitrogen) are combined. An average, hydrogen productivity was 7.14 l h^{-1} on a typical summer day (965.5 W m^2 irradiation intensity) [68].

In general, the little information available on the design of the photoreactors is mainly focused on the CPC dimensions and materials, system devices, but nothing about working pressure, inert gas used to create anoxic conditions or the flow rates.

12.3.2 Pilot Solar Photoreactors for Photocatalytic Hydrogen Production: Other Collectors

In addition to the CPCs, other photoreactor configurations have been developed. Among them, a tracking parabolic trough concentrator (PTC) with an aperture area of 10 m^2 and a concentration factor of 70 (5 kW with solar flux of 1000 W m^{-2}) designed for hydrogen production reached temperatures of 150–300 °C. The process was thermochemical, not photocatalytic [69], and is therefore out of the scope of this chapter. No other studies have described thermochemical processes in experimental-scale PTCs.

Figure 12.8 An overhead view of the 100-m^2 photocatalytic solar hydrogen plant based on NCCs installed at Kakioka Research Center (Japan). Source: Nishiyama et al. [70]/with permission of Springer Nature.

Finally, a 100 m^2 NCC photocatalytic hydrogen plant was designed and installed at Kakioka Research Center (Japan) using photocatalyst ($SrTiO_3$:Al) sheets installed in 1600 625-cm^2 units illuminated by sunlight through ultraviolet-transparent glass windows. It is by far the largest solar hydrogen production demonstration plant reported worldwide, delivering up to 27.2 mol H_2 per day. However, it reached a maximum STH of only 0.76%. While hydrogen production was inefficient and energy negative, it did demonstrate that large-scale photocatalytic water splitting is possible (Figure 12.8) [70].

12.4 Advances in Photoreactors

As discussed in the previous section, CPC and NCC photoreactors have been used for (solar) photocatalytic H_2 production in a few studies, however, the lack of photocatalytic H_2 reactor engineering studies should be emphasized. This growing area of research has a high potential impact on the feasibility of photocatalytic H_2 production. Three key factors determine photoreactor feasibility: (i) Radiation field distribution inside the system, (ii) Mass transfer limitations, and (iii) Catalyst area exposed to light [71]. Since the configuration of catalyst particles or sheets in the photoreactor critically influences these factors, this section is divided into two parts, slurry reactors and immobilized catalyst reactors. Figure 12.9 illustrates the fundamental mass transfer steps occurring during gas diffusion from the catalyst surface to the gas phase, which is largely dependent on reactor type.

12.4.1 Slurry Photoreactors

In this scheme, the catalyst is granular or a powder that remains suspended in the liquid. Its main advantage is the use of the entire illumination of the photocatalyst surface during the reaction. However, the energy needed for continuous mechanical stirring, the time and energy needed for recovery of the fine catalyst particles

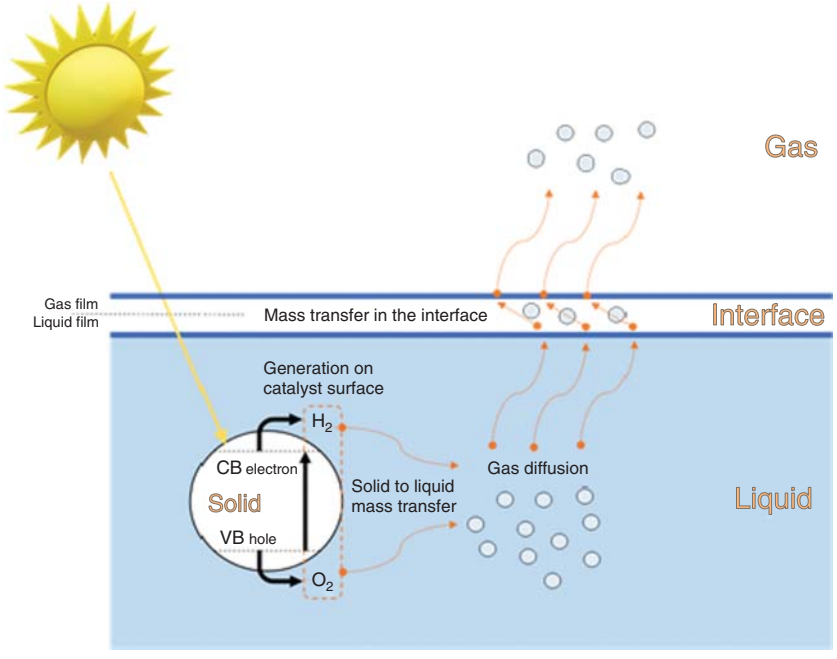

Figure 12.9 Steps in mass transfer during (solar) photocatalytic production of H_2.

afterwards, poor light penetration in the suspension due to light absorption and scattering, and the possibility of catalyst abrasion during stirring are all major drawbacks of slurry solutions [72]. While the most common design is the annular reactor, in which a lamp is either located at the center of the tubular reactor or outside of it [73], the simplest approach for solar H_2 photocatalytic production is probably a single-bed particle suspension reactor. This system was actually proposed by Pinaud et al. in 2013 for photoelectrochemical H_2 production, but it could also be used for photocatalytic production [74]. It consists of a plastic bag made of high-density polyethylene, a relatively cheap material with high optical transmission (90%) and very low hydrogen permeability. The bag is completely sealed by laminating a transparent sheet on top as the upper layer and a dark one at the bottom. The reactor is placed horizontally on the selected location. Once it is filled with the slurry suspension and the photocatalytic process starts, H_2 is accumulated in the extra volume (headspace) due to the freely moving upper layer. The main concern of the authors was the simultaneous H_2 and O_2 production and accumulation, which results in a highly risky combustible mixture. Nevertheless, this problem can be solved in a coupled wastewater treatment/photocatalytic H_2 production system, because an organic sacrificial agent is used, releasing mostly CO_2 instead of O_2. Obviously, the main advantage of this photoreactor is its technical simplicity, which would result in exceptionally low investment costs; however, its technical feasibility is unclear. Since this option is still mainly theoretical, key aspects of the process, such as mass transfer limitations or the best operating conditions (catalyst concentration, liquid depth, etc.) for an acceptable distribution of the solar radiation inside the system,

still need to be studied. Until then, process efficiency, and therefore, photoreactor feasibility are mostly conjectures.

Another interesting slurry photoreactor proposed for improving pure water splitting consists of a two-compartment ("H-shaped") reactor separated by a membrane that yields H_2 and O_2 separately [75]. This "twin reactor" was designed as a Z-scheme that mimics natural photosynthesis, using a dual system for water reduction and oxidation with one catalyst for producing H_2 and another for O_2 [76]. A Nafion membrane segregates the two photocatalysts in the twin reactor so that H_2 and O_2 are generated separately, avoiding the severe disadvantages associated with their coupled production (H_2 and O_2 recombination and combustion). Using $Pt/SrTiO_3$:Rh and WO_3 as photocatalysts and Fe^{2+}/Fe^{3+} as a reversible redox mediator to remove the unreacted electrons and holes in the photocatalysts, an average 1.59 μmol g^{-1} h^{-1} H_2 generation rate was achieved [75]. This system was also tested using $Pt/SrTiO_3$:Rh and $BiVO_4$ as H_2 and O_2 photocatalysts, respectively [77]. The results, obtained under visible light (500 W halogen lamp, 400–1100 nm), showed that H_2 generation is the rate-limiting step in this dual-approach.

Photocatalytic H_2 production has also been assessed in fluidized photoreactors. Fluidization is achieved when the gravitational force of the catalyst is equivalent to the aerodynamic drag. Process performance is improved with vigorous agitation, leading to improved mass transfer and good irradiation distribution, and the high catalyst surface area-to-volume ratio. Ref. [70] presented the concept of a UV-irradiated (annular) fluidized bed reactor for water splitting using a TiO_2 photocatalyst decorated with platinum nanodeposits for the first time, demonstrating better H_2 generation than slurry suspensions [78]. Skillen et al. 2016 also used a fluidized photoreactor, but in combination with sunlight provided by the George Ellery Hale Telescope [53]. Using 0.025 M oxalic acid and UV-vis light (4 × 36 W compact nonintegrated fluorescent lamps), the photocatalytic production of H_2 over $NaTaO_3La$, g-C_3M_4 and Pt-C_3N_4 was originally studied. Pt-C_3N_4 produced the highest H_2 production rate (89 μmol g^{-1} h^{-1}). Operating under sunlight at a power density of 800–900 W m^{-2} with $NaTaO_3La$, the H_2 production rate decreased to 5 μmol g^{-1} h^{-1}. The authors highlighted the importance of concentrating sunlight to improve process performance, which was achieved using the telescope. From our own experience, this is probably not necessary, as it has been widely demonstrated that non-concentrating (1 sun) photoreactors are the best option for wastewater treatment by heterogeneous photocatalysis [57].

12.4.2 Fixed Catalyst Photoreactors

Gopinath and Nalajala recently reviewed photocatalytic water splitting, highlighting the thin film photocatalyst approach instead of the slurry alternative [79]. Photocatalyst deposition on a fixed substrate, such as in the thin film approach, avoids the typical problems of slurry systems, such as poor light penetration and catalyst recovery. It is also worth mentioning that there is a lack of data about particulate catalyst activity after 100 hours, while several studies have reported good activity and high stability of thin films over long operating periods [80]. Nalajala et al. compared

H_2 production with powder and thin film TiO_2(P25) and TiO_2(P25)/Pd under natural solar radiation using methanol as the sacrificial agent [81]. H_2 production increased by a factor of 12 (104 mmol h^{-1} g^{-1} vs. 9 mmol h^{-1} g^{-1}) with the TiO_2/Pd catalyst thin film, which was made by depositing 1 mg of catalyst on a 4.7 cm^2 glass substrate. 25 mg of the catalyst was used in the powder suspension experiment. In both cases, the experiments were done in a 70 ml round-bottomed quartz flask with 40 ml of a 25% v/v methanol aqueous solution. It should be mentioned that the catalyst concentration selected for the powder suspension experiment (625 mg l^{-1}) was probably too high, negatively affecting performance. The optimum TiO_2 concentration suggested for solar photoreactors, which improves light distribution inside 3 to 5-cm diameter tubes, is ≈100–200 mg l^{-1} [59]. Schröder et al. reported H_2 production 7–15 times higher with an immobilized Pt@mp-gC_3N_4 thin film catalyst than the powder form with triethyl orthoacetate as the sacrificial agent (0.6 l m^{-2} h^{-1} vs. 0.04–0.08 l m^{-2} h^{-1}) [80]. Tudu et al. and Lin et al. found similar results with TiO_2/Cu–Ni and Cu_2O/WSe_2 photocatalysts, respectively, also including sacrificial agents [82, 83]. Therefore, in general, about one order of magnitude higher hydrogen yields can be expected for thin film configurations compared to powder suspensions. More efficient light absorption of catalyst films and enhanced mass transfer have been suggested as the main reasons for this improvement [79].

As structured photocatalytic configurations can improve photonic productivity, several options have attracted much attention for photocatalytic H_2 production. Of the various supports, the monolith photoreactor has shown promising results. A monolith block is essentially composed of an array of uniformly structured parallel channels that make it possible to increase the surface area of catalyst coating per unit of reactor volume more than other configurations such as plates and beads [84]. The monolith channels can be extruded into different shapes and sizes. In this context, the comparison between suspended 5% La/TiO_2 and 5% La/TiO_2 supported in a honeycomb monolithic structure for photocatalytic H_2 production was studied. In the Pyrex slurry reactor, 0.1 g of the catalyst was suspended in 80 ml of deionized water [85]. The resulting production rate was 18.0 ppm h^{-1}. The gas phase process was carried out in a monolith photoreactor, where a conical flask containing a mixture of a sacrificial agent and water was bubbled with N_2 gas and taken to the reactor immediately afterwards. The maximum production in the monolith photoreactor was 9.2 times higher (165.5 ppm h^{-1}) than the slurry alternative. The authors explained this improvement by the larger illuminated reactor volume, efficient mass transfer, larger illuminated catalyst area, and negligible sorption effects due to gas phase operation in the monolith reactor. The apparent quantum yield in the monolith reactor was also significantly higher (140%) than in the slurry reactor. Fajrina and Tahir compared performance using an Ag-pCN/TiO_2 composite as the photocatalyst in slurry, fixed-bed, and monolith reactors [86]. The slurry reactor experiment consisted of a quartz glass cylindrical reactor (150 ml) with 150 mg of the catalyst and 130 ml of a 5% glycerol–water mixture. In the fixed-bed reactor and monolith photoreactors, which were the same cylindrical reactors with the corresponding supported catalyst device, the experiments were carried out in the gas phase by inflowing N_2 gas previously bubbled in an alcohol–water mixture.

The monolith reactor boosted H_2 production (8230 μmol h^{-1}) with respect to the fixed-bed reactor (913 μmol h^{-1}) and the slurry reactor (667 μmol h^{-1}). Gaudiere et al. compared the catalytic activity of a Y_2O_3-doped ZrO_2 monolith infiltrated with Co to a powdered material with the same chemical characteristics using methanol as a sacrificial agent [87]. The results also showed improved performance of the monolith photoreactor. Tasleem and Tahir found that excessive length of the monolith channels and use of visible light lowers light penetration and consequently decreases process performance [88]. Although it has been demonstrated that this engineering approach is a promising system for photocatalytic water splitting and photoreforming, several issues, such as improving catalyst adhesion to the wall, still require further research.

Optical fiber reactors for water splitting have also been studied, since they present excellent light use efficiency, improving light distribution inside the photoreactor. In these systems, the optical fiber (usually fused SiO_2) is coated with a semiconductor (usually TiO_2). As the refractive index of the coating is higher than that of the optical fiber, part of the light is reflected inward and transmitted along the fiber, while the rest penetrates and excites the semiconductor layer at the interface [89]. Some disadvantages of optical fiber reactors are (i) relatively low surface area for chemical reactions, (ii) low reactor volume percentage available for photocatalysis, and (iii) low adhesive strength [73]. An optical fiber honeycomb reactor has been assessed to overcome the problems associated with the exponential decay of light intensity in the axial direction of the coated fiber and electron and hole recombination. In this design, the catalyst was immobilized on the monolith walls and the optical fibers were placed inside the channels, which improved H_2 production. Taboada et al. found that using Au/TiO_2 and ethanol–water mixtures, the optical fiber honeycomb photoreactor could increase slurry photoreactor H_2 production fivefold [90]. The same authors studied this process using various bio-derived alcohols with similar conclusions [91].

Finally, although most of these photoreactors have barely been explored under natural sunlight, this should not discourage their use. Today, lamps can be run efficiently by renewable energy, which is indeed a very similar concept to the direct use of sunlight in solar collectors. In this context, special attention should be given to the use of LED technology, and in fact, several H_2 photocatalytic production studies have recently integrated LED lamps in their photoreactors, such as Chang et al. [92].

12.5 Photocatalytic Wastewater Treatment with Simultaneous Hydrogen Production

In the last few years, research groups have focused on increasing STH efficiency using organic pollutants in wastewater as sacrificial agents [40, 93]. This strategy, i.e. simultaneous hydrogen generation and treatment of wastewater containing biorecalcitrant contaminants and/or pathogens, would clearly increase the societal interest in implementing such solar processes due to its huge positive impact

on environmental protection. However, other concepts have to be considered, as the process must be successful not only for H_2 production, but also for improving wastewater treatment, not just degrading contaminants, but also taking into account the two main concepts for safe disposal of any treated wastewater: biodegradability and toxicity [94]. Otherwise, wastewater used as a sacrificial agent to enhance STH could end up as solar photofuel production waste, raising process costs and hindering sustainability. As the process involves oxidation and reduction reactions, there are more possible pathways for contaminant transformation than with conventional use of photocatalysis as an advanced oxidation process, thereby increasing the diversity of byproducts formed from the parent contaminant and its possible toxicity, and impeding its biodegradability. Oxidation also usually produces more oxygenated byproducts, which are described as more easily biodegradable than reduced byproducts [42]. There have been many recent examples of simultaneous wastewater treatment and generation of H_2 in which wastewater decontamination evolution was not properly evaluated (only by basic analytical methods for one contaminant, COD, or BOD) or in which a purely contaminating substance is claimed to be found normally in wastewater. It must be taken into account that the water matrix always has a substantial effect on process efficiency and that organic contaminants are never found alone (other contaminants or byproducts of a parent contaminant are always present) in any wastewater [43, 95–99]. The majority of photoreforming research concentrates on photooxidation reactions, such as the oxidation of hydroxyl groups to carbonyls, while photoreduction research (beyond H_2 generation) is limited. Little attention is usually devoted to evaluating intermediates and oxidation or reduction products of the more structurally complex sacrificial agents; therefore, no information is provided about the need for further treatment before the final discharge of aqueous solutions. It is essential to assess the environmental aspects of photoreforming, since the wastewater generated could potentially harm the environment and human health. Indeed, much of the information about photocatalyst characteristics reports on high-resolution X-ray diffractometer (XRD), scanning electron microscope (SEM), energy dispersive X-ray spectrometry (EDS), UV-visible diffuse reflectance spectrum (DRS), optical bandgaps, optical emission spectroscopy, etc., but provides very little or poor information about aqueous solutions.

Contaminant treatment, in its strictest meaning, is mineralization of the contaminants, but photocatalytic processes only make sense for hazardous non-biodegradable pollutants. When feasible, biological treatment is the cheapest and also the most environmentally friendly. Therefore, biologically recalcitrant compounds could be treated with photocatalytic technologies until biodegradability and then discharged to a conventional biological plant. In future, simultaneous wastewater treatment and generation of H_2 efficiency should therefore be evaluated from this perspective, not only STH efficiency. Considering the complexity and recalcitrance of wastewater, to be more reliable, researchers should tackle these issues from a multidisciplinary point of view by effectively combining photocatalysis with already well-developed environmental chemistry. Wastewater pretreatment can also make it more susceptible to subsequent photoconversion. Many factors

strongly affect photoreforming for the valorization of wastewater. Similar samples might lead to widely diverging efficiency depending on the composition of each wastewater stream. No direct relationship has been found between the concentration of organic matter and photoreforming rate, but highly saline wastewater has been found to delay H_2 production [100].

In addition, the use of photoreforming as a pretreatment can be justified if the intermediates resulting from the reaction (more oxidized compounds, such as carboxylic acids and alcohols, but also reduced compounds) are readily degraded by microorganisms. Biotreatment and photocatalysis combination is at a very advanced stage, and there are many papers and reviews on the subject, from classical developments [94] to more modern approaches [101]. However, the choice of a suitable treatment option for complex wastewater treatment depends on its effectiveness, so the parameters selected must allow its control and monitorization. Physicochemical parameters, including dissolved oxygen, pH, dissolved organic carbon (DOC), chemical oxygen demand (COD), or total suspended solids (TSS), are generally considered fundamental criteria for defining the potential reuse of a treated effluent. However, this information is very often insufficient, and bioassays are a good complementary option for evaluating the toxic effects of complex mixtures commonly found in treated industrial effluents. The importance of the use of this strategy has been well documented in the literature [94]. As the partial oxidation or reduction of organic contaminants may result in the formation of intermediates more toxic than the parent compounds, toxicity tests have been used to evaluate whether the effluent has been detoxified [102]. The toxicity–biodegradability dichotomy when photocatalysis is used as a pretreatment to improve industrial wastewater biodegradability is a hot topic. Bioassays are a very useful tool for evaluating photoreforming efficiency, and setting the operating conditions, but bioassays must be chosen according to the final use of the treated wastewater. Acute toxicity tests may not be suitable to evaluate the toxicity of many target contaminants, so chronic effects should be further studied. Toxicity tests are not useful in evaluating potential biodegradability, so in this case, more suitable tests should be applied [103].

Since photoreforming would not always improve the biodegradability or reduce toxicity, another option, using photoreforming as a polishing step, should also be explored. The best option for remediation of a specific wastewater is not always so easy, and the combination of photoreforming and biotreatment, in this order, is not always the best approach. The water quality standards to be met affect the choice of the processes to be combined, along with overall costs.

Conventional treatment possibilities and capabilities are usually well-known. However, the efficiency of new and (photoreforming) conventional technologies very often is not. Therefore, scaled-up studies are useful when new wastewater treatment technologies are applied to industrial wastewater treatment. When photoreforming is applied, its effect may not be significant or even detrimental. Reasons for this could be the formation of stable byproducts, low selectivity for contaminants, catalysts difficult to remove from treated wastewater, increased toxicity, or slow kinetics. Therefore, a step-by-step research methodology is needed, applying advanced analytical tools and bioassays to infer the reaction steps,

kinetics, heteroatoms release (as cations and anions) in the wastewater matrix, biodegradability, toxicity, etc. [104].

Studies with model compounds cannot be applied to wastewater, as it contains different organics, inorganic salts, and natural organic matter. In their pioneer work, Scott and Ollis [105] identified different families of wastewater in which a combined strategy based on photoreforming/biological degradation could have an important impact: biorecalcitrant wastewater containing large, very persistent macromolecules, biodegradable wastewater containing contaminants in low concentrations, highly toxic wastewater able to inhibit biological cultures, and treated wastewater containing bioaccumulative microcontaminants and their metabolites.

12.6 Future Outlook

Apart from the choice of photocatalytic materials, light intensity, temperature, and pH clearly influence the performance of photocatalytic systems for hydrogen generation. Solar intensity above one sun and the use of concentrating reactors makes no sense, but hydrogen generation can be promoted by solar–thermal being visible-light responsive catalysts more sensible to this effect. In general, a basic pH of around 10 provides much better hydrogen yields but for full-scale real application, the optimum pH for the reaction would be around 8.

CPCs are the solar photoreactors most used for this purpose, with a concentration factor of 1. The absorber tube has to be transparent to solar UV radiation (>300 nm). Aluminum is the most widely used material for solar collector reflecting or concentrating surfaces. Special attention should be given to the use of LED technology run by renewable electricity, since it presents excellent light use efficiency, improving light distribution inside the photoreactor.

Simultaneous hydrogen generation and treatment of wastewater would clearly increase the implementation of such solar processes, taking into account that the ideal sacrificial agent would be compounds abundant and easily oxidized to innocuous reaction products, such as biomass-derived substrates or pollutants. It would provide added value to the overall process.

References

1 Verne, J. (1874). *The Mysterious Island*. Paris, France: Pierre-Jules Hetzel Publisher.
2 Fujishima, A. and Honda, K. (1972). Electrochemical photolysis of water at a semiconductor electrode. *Nature* 238: 37–38.
3 Wang, Q., Hisatomi, T., Jia, Q. et al. (2016). Scalable water splitting on particulate photocatalyst sheets with a solar-to-hydrogen energy conversion efficiency exceeding 1%. *Nat. Mater.* 15: 611–615.
4 Colón, G. (2016). Towards the hydrogen production by photocatalysis. *Appl. Catal., A* 518: 48–59.

5 Qian, R., Zong, H., Schneider, J. et al. (2019). Charge carrier trapping, recombination and transfer during TiO_2 photocatalysis: an overview. *Catal. Today* 335: 78–90.

6 Du, C., Yan, B., Lin, Z. et al. (2020). Enhanced carrier separation and increased electron density in 2D heavily N-doped $ZnIn_2S_4$ for photocatalytic hydrogen production. *J. Mater. Chem. A* 8: 207–217.

7 Liu, Y., Gu, X., Qi, W. et al. (2017). Enhancing the photocatalytic hydrogen evolution performance of a metal/semiconductor catalyst through modulation of the Schottky barrier height by controlling the orientation of the interface. *ACS Appl. Mater. Interfaces* 9: 12494–12500.

8 Liu, J., Wei, Z., and Shangguan, W. (2019). Defects engineering in photocatalytic water splitting materials. *ChemCatChem* 11: 6177–6189.

9 Tong, R., Ng, K.W., Wang, X. et al. (2020). Two-dimensional materials as novel co-catalysts for efficient solar-driven hydrogen production. *J. Mater. Chem. A* 8: 23202–23230.

10 Wang, X., Huang, J., Li, S. et al. (2021). Interfacial chemical bond and internal electric field modulated Z-scheme Sv-$ZnIn_2S_4$/$MoSe_2$ photocatalyst for efficient hydrogen evolution. *Nat. Commun.* 12: 4112.

11 Nagakawa, H. and Nagata, M. (2021). Photoreforming of lignocellulosic biomass into hydrogen under sunlight in the presence of thermally radiative CdS/SiC composite photocatalyst. *ACS Appl. Energy Mater.* 4: 1059–1062.

12 Ramis, G., Bahadori, E., and Rossetti, I. (2021). Design of efficient photocatalytic processes for the production of hydrogen from biomass derived substrates. *Int. J. Hydrogen Energy* 46: 12105–12116.

13 Uekert, T., Bajada, M.A., Schubert, T. et al. (2021). Scalable photocatalyst panels for photoreforming of plastic, biomass and mixed waste in flow. *ChemSusChem* 14: 4190–4197.

14 Kondarides, D.I., Daskalaki, V.M., Patsoura, A. et al. (2008). Hydrogen production by photo-induced reforming of biomass components and derivatives at ambient conditions. *Catal. Lett.* 122: 26–32.

15 Patsoura, A., Kondarides, D.I., and Verykios, X.E. (2006). Enhancement of photoinduced hydrogen production from irradiated Pt/TiO_2 suspensions with simultaneous degradation of azo-dyes. *Appl. Catal., B* 64: 171–179.

16 Patsoura, A., Kondarides, D.I., and Verykios, X.E. (2007). Photocatalytic degradation of organic pollutants with simultaneous production of hydrogen. *Catal. Today* 124: 94–102.

17 López, C.R., Pulido, M.E., Ortega Méndez, J.A. et al. (2015). Comparative study of alcohols as sacrificial agents in H_2 production by heterogeneous photocatalysis using Pt/TiO_2 catalysts. *J. Photochem. Photobiol., A* 312: 45–54.

18 Xing, C., Liu, Y., Zhang, Y. et al. (2021). A direct Z-scheme for the photocatalytic hydrogen production from a water ethanol mixture on $CoTiO_3$/TiO_2 heterostructures. *ACS Appl. Mater. Interfaces* 13: 449–457.

19 Yasuda, M., Matsumoto, T., and Yamashita, T. (2018). Sacrificial hydrogen production over TiO_2-based photocatalysts: polyols, carboxylic acids, and saccharides. *Renewable Sustainable Energy Rev.* 81: 1627–1635.

20 Kalamarasa, E. and Lianos, P. (2015). Current doubling effect revisited: current multiplication in a photo fuel cell. *J. Electroanal. Chem.* 751: 37–42.

21 Liu, R., Yoshida, H., Fujita, S. et al. (2014). Photocatalytic hydrogen production from glycerol and water with NiO_x/TiO_2 catalysts. *Appl. Catal., B* 144: 41–45.

22 Mallikarjuna, K., Kotesh, K.M., and Kim, H. (2021). Synthesis of oxygen-doped-g-C_3N_4/WO_3 porous structures for visible driven photocatalytic H_2 production. *Physica E* 126: 114428.

23 Toledo-Camacho, S.Y., Rey, A., Maldonado, M.I. et al. (2021). Photocatalytic hydrogen production from water-methanol and -glycerol mixtures using Pd/TiO_2(-WO_3) catalysts and validation in a solar pilot plant. *Int. J. Hydrogen Energy* 46: 36152–36166.

24 Lakshmana, R.N., Krishnan, C.K., Durga, K.V. et al. (2018). Photocatalytic reforming of biomass derived crude glycerol in water: a sustainable approach for improved hydrogen generation using $Ni(OH)_2$ decorated TiO_2 nanotubes under solar light irradiation. *ACS Sustainable Chem. Eng.* 6: 3754–3764.

25 Ribao, P., Esteves, M.A., Fernandes, V.R. et al. (2019). Challenges arising from the use of TiO_2/rGO/Pt photocatalysts to produce hydrogen from crude glycerol compared to synthetic glycerol. *Int. J. Hydrogen Energy* 44: 28494–28506.

26 Beasley, C., Gnanamani, M.K., Qian, D. et al. (2021). Photocatalytic reforming of sucrose and dextrose for hydrogen production on Pd/TiO_2. *Chem. Select* 6: 6512–65247.

27 Speltini, A., Gualco, F., Maraschi, F. et al. (2019). Photocatalytic hydrogen evolution assisted by aqueous (waste)biomass under simulated solar light: Oxidized g-C_3N_4 vs. P25 titanium dioxide. *Int. J. Hydrogen Energy* 44: 4072–4078.

28 Hamid, S., Dillert, R., and Bahnemann, D.W. (2018). Photocatalytic reforming of aqueous acetic acid into molecular hydrogen and hydrocarbons over co-catalyst-loaded TiO_2: shifting the product distribution. *J. Phys. Chem. C* 122: 12792–12809.

29 Chen, L., Xu, Y., and Chen, B. (2019). In situ photochemical fabrication of CdS/g-C_3N_4 nanocomposites with high performance for hydrogen evolution under visible light. *Appl. Catal., B* 256: 117848.

30 Jiang, X., Wang, L., Yu, F. et al. (2018). Photodegradation of organic pollutants coupled with simultaneous photocatalytic evolution of hydrogen using quantum-dot-modified g-C3N4 catalysts under visible-light irradiation. *ACS Sustainable Chem. Eng.* 6: 12695–12705.

31 Alkaima, F., Kandiel, T.A., Hussein, F.H. et al. (2013). Solvent-free hydrothermal synthesis of anatase TiO_2 nanoparticles with enhanced photocatalytic hydrogen production activity. *Appl. Catal., A* 466: 32–37.

32 Kuehnel, M.F. and Reisner, E. (2018). Solar hydrogen generation from lignocellulose. *Angew. Chem. Int. Ed.* 57: 3290–329619.

33 Nagakawa, H. and Nagata, M. (2021). Photoreforming of organic waste into hydrogen using a thermally radiative CdO_x/CdS/SiC photocatalyst. *ACS Appl. Mater. Interfaces* 13: 47511–47519.

34 Uekert, T., Pichler, C.M., Schubert, T. et al. (2021). Solar-driven reforming of solid waste for a sustainable future. *Nat. Sustainability* 4: 383–391.

35 Speltini, A., Sturini, M., Maraschi, F. et al. (2015). Evaluation of UV-A and solar light photocatalytic hydrogen gas evolution from olive mill wastewater. *Int. J. Hydrogen Energy* 40: 4303–4310.

36 Puga, A.V. (2016). Photocatalytic production of hydrogen from biomass-derived feedstocks. *Coord. Chem. Rev.* 315: 1–66.

37 Speltini, A., Sturini, M., Maraschi, F. et al. (2014). Swine sewage as sacrificial biomass for photocatalytic hydrogen gas production: explorative study. *Int. J. Hydrogen Energy* 39: 11433–11440.

38 Su, E., Huang, B., and Wey, M. (2017). Green route for hydrogen evolution from real electroplating waste liquids induced by a solar light responsive photocatalyst. *ACS Sustainable Chem. Eng.* 5: 2146–2153.

39 Kawai, T. and Sakata, T. (1980). Conversion of carbohydrate into hydrogen fuel by a photocatalytic process. *Nature* 286: 474–476.

40 Toe, C.Y., Tsounis, C., Zhang, J. et al. (2021). Advancing photoreforming of organics: highlights on photocatalyst and system designs for selective oxidation reactions. *Energy Environ. Sci.* 14: 1140–1175.

41 Khedr, T.M., El-Sheikh, S.M., Kowalska, E. et al. (2021). The synergistic effect of anatase and brookite for photocatalytic generation of hydrogen and diclofenac degradation. *J. Environ. Chem. Eng.* 9: 106566.

42 Saravanan, A., Kumar, P.S., Vo, D.V.N. et al. (2021). Photocatalysis for removal of environmental pollutants and fuel production: a review. *Environ. Chem. Lett.* 9: 441–446.

43 Munusamy, T.D., Chin, S.Y., Tarek, M. et al. (2021). Sustainable hydrogen production by CdO/exfoliated g-C_3N_4 via photoreforming of formaldehyde containing wastewater. *Int. J. Hydrogen Energy* 46: 30988–30999.

44 Hippargi, G., Mangrulkar, P., Chilkalwar, A. et al. (2018). Chloride ion: a promising hole scavenger for photocatalytic hydrogen generation. *Int. J. Hydrogen Energy* 43: 6815–6823.

45 Liu, W., Su, C., Liu, D. et al. (2021). Three-dimensional ordered macroporous materials with g-C_3N_4 and TiO_2 as pore walls for efficient photocatalytic hydrogen evolution. *Colloids Surf., A* 609: 125681.

46 Yao, Y., Gao, X., and Meng, X. (2021). Recent advances on electrocatalytic and photocatalytic seawater splitting for hydrogen evolution. *Int. J. Hydrogen Energy* 46: 9087–9100.

47 Kubacka, A., Barba-Nieto, I., Caudillo-Flores, U. et al. (2021). Interpreting quantum efficiency for energy and environmental applications of photocatalytic materials. *Curr. Opin. Chem. Eng.* 33: 100712.

48 Preethi, V. and Kanmani, S. (2014). Photocatalytic hydrogen production using Fe_2O_3-based core shell nano particles with ZnS and CdS. *Int. J. Hydrogen Energy* 39: 1613–1622.

49 Zhu, Y., Song, L., Song, N. et al. (2019). Bifunctional and efficient CoS_2–C@MoS_2 core–shell nanofiber electrocatalyst for water splitting. *ACS Sustainable Chem. Eng.* 7: 2899–2905.

50 Hou, Y., Abrams, B.L., Vesborg, P.C.K. et al. (2011). Bioinspired molecular co-catalysts bonded to a silicon photocathode for solar hydrogen evolution. *Nat. Mater.* 10: 434–438.

51 Guo, L., Chen, Y., Su, J. et al. (2019). Obstacles of solar-powered photocatalytic water splitting for hydrogen production: a perspective from energy flow and mass flow. *Energy* 172: 1079–1086.

52 Liang, Z., Liangliang, F., Dengwei, J. et al. (2012). Study on the radiation distribution in a fluidized tubular reactor for heterogeneous photocatalytic hydrogen production. *Procedia Environ. Sci.* 12: 285–292.

53 Skillen, N., Adams, M., McCullagh, C. et al. (2016). The application of a novel fluidised photo reactor under UV–Visible and natural solar irradiation in the photocatalytic generation of hydrogen. *Chem. Eng. J.* 286: 610–621.

54 Castedo, A., Casanovas, A., Angurell, I. et al. (2018). Effect of temperature on the gas-phase photocatalytic H_2 generation using microreactors under UVA and sunlight irradiation. *Fuel* 222: 327–333.

55 Li, X., Lin, J., Li, J. et al. (2021). Temperature-induced variations in photocatalyst properties and photocatalytic hydrogen evolution: differences in UV, visible, and infrared radiation. *ACS Sustainable Chem. Eng.* 9: 7277–7285.

56 Aksoy, M., Yanalak, G., Aslan, E. et al. (2020). Visible light-driven hydrogen evolution by using mesoporous carbon nitride-metal ferrite (MFe_2O_4/mpg-CN; M: Mn, Fe, Co and Ni) nanocomposites as catalysts. *Int. J. Hydrogen Energy* 45: 16509–16518.

57 Spasiano, D., Marotta, R., Malato, S. et al. (2015). Solar photocatalysis: materials, reactors, some commercial, and pre-industrialized applications. A comprehensive approach. *Appl. Catal., B* 170-171 (2015): 90–123.

58 Corredor, J., Rivero, M.J., Rangel, C.M. et al. (2019). Comprehensive review and future perspectives on the photocatalytic hydrogen production. *J. Chem. Technol. Biotechnol.* 94: 3049–3063.

59 Malato, S., Fernández-Ibáñez, P., Maldonado, M.I. et al. (2009). Decontamination and disinfection of water by solar photocatalysis: recent overview and trends. *Catal. Today* 147: 1–59.

60 Malato, S., Blanco, J., Vidal, A. et al. (2002). Photocatalysis with solar energy at a pilot-plant scale: an overview. *Appl. Catal., B* 37: 1–15.

61 Jing, D., Guo, L., Zhao, L. et al. (2010). Efficient solar hydrogen production by photocatalytic water splitting: from fundamental study to pilot demonstration. *Int. J. Hydrogen Energy* 35: 7087–7097.

62 Ren, Y., Zhao, L., Jing, D. et al. (2016). Investigation and modelling of CPC based tubular photocatalytic reactor for scaled-up hydrogen production. *Int. J. Hydrogen Energy* 41: 16019–16031.

63 Villa, K., Domènech, X., Malato, S. et al. (2013). Heterogeneous photocatalytic hydrogen generation in a solar pilot plant. *Int. J. Hydrogen Energy* 38: 12718–12724.

64 Arzate-Salgado, S.Y., Ramírez-Zamora, R.M., Zanella, R. et al. (2016). Photocatalytic hydrogen production in a solar pilot plant using Au/TiO_2 photocatalyst. *Int. J. Hydrogen Energy* 41: 11933–11940.

65 Maldonado, M.I., Saggioro, E., Peral, J. et al. (2019). Hydrogen generation by irradiation of commercial $CuO+TiO_2$ mixtures at solar pilot plant scale and in presence of organic electron donors. *Appl. Catal., B* 257: 117890.

66 Baniasadi, E., Dincer, I., and Naterer, G.F. (2012). Exergy and environmental impact assessment of solar photoreactors for catalytic hydrogen production. *Chem. Eng. J.* 213: 330–337.

67 Cao, F., Lin, H., Wei, Q. et al. (2018). Experimental study of direct solar photocatalytic water splitting for hydrogen production under natural circulation conditions. *Int. J. Hydrogen Energy* 43: 13727–13737.

68 Wei, Q., Yang, Y., Hou, J. et al. (2017). Direct solar photocatalytic hydrogen generation with CPC photoreactors: system development. *Sol. Energy* 153: 215–223.

69 Liu, Q., Hong, H., Yuan, J. et al. (2009). Experimental investigation of hydrogen production integrated methanol steam reforming with middle-temperature solar thermal energy. *Appl. Energy* 86 (2009): 155–162.

70 Nishiyama, H., Yamada, T., Nakabayashi, M. et al. (2021). Photocatalytic solar hydrogen production from water on a 100 m^2 scale. *Nature* 598: 304–307.

71 Nadeem, M., Khan, M., Ziani, A. et al. (2021). An overview of the photocatalytic water splitting over suspended particles. *Catalysts* 11 (1): 60.

72 Ola, O., Maroto-Valer, M., Liu, D. et al. (2012). Performance comparison of CO_2 conversion in slurry and monolith photoreactors using Pd and Rh-TiO_2 catalyst under ultraviolet irradiation. *Appl. Catal., B* 126: 172–179.

73 Fajrina, N. and Tahir, M. (2019). A critical review in strategies to improve photocatalytic water splitting towards hydrogen production. *Int. J. Hydrogen Energy* 44: 540–577.

74 Pinaud, B.A., Benck, J.D., Seitz, L.C. et al. (2013). Technical and economic feasibility of centralized facilities for solar hydrogen production via photocatalysis and photoelectrochemistry. *Energy Environ. Sci.* 6: 1983–2002.

75 Chen-Chia, L., Chao-Wei, H., Chi-Hung, L. et al. (2010). Novel twin reactor for separate evolution of hydrogen and oxygen in photocatalytic water splitting. *Int. J. Hydrogen Energy* 35: 1523–1529.

76 Nguyen, V.H. and Wu, J.C.S. (2018). Recent developments in the design of photoreactors for solar energy conversion from water splitting and CO_2 reduction. *Appl. Catal., A* 550: 122–141.

77 Yu, Y., Ren, J., and Meng, M. (2013). Photocatalytic hydrogen evolution on graphene quantum dots anchored TiO_2 nanotubes-array. *Int. J. Hydrogen Energy* 38: 12266–12272.

78 Reilly, K., Taghipour, F., and Wilkinson, D.P. (2012). Photocatalytic hydrogen production in a UV-irradiated fluidized bed reactor. *Energy Procedia* 29: 513–521.

79 Gopinath, C.S. and Nalajala, N. (2021). A scalable and thin film approach for solar hydrogen generation: a review on enhanced photocatalytic water splitting. *J. Mater. Chem. A* 9: 1353–1371.

80 Schröder, M., Kailasam, K., Borgmeyer, J. et al. (2015). Hydrogen evolution reaction in a large-scale reactor using a carbon nitride photocatalyst under natural sunlight irradiation. *Energy Technol.* 3: 1014–1017.

81 Nalajala, N., Patra, K.K., Bharad, P.A. et al. (2019). Why the thin film form of a photocatalyst is better than the particulate form for direct solar-to-hydrogen conversion: a poor man's approach. *RSC Adv.* 9: 6094–6100.

82 Lin, Z., Li, J., Zheng, Z. et al. (2016). A floating sheet for efficient photocatalytic water splitting. *Adv. Energy Mater.* 6: 1600510.

83 Tudu, B., Nalajala, N., Saikia, P. et al. (2020). Cu–Ni bimetal integrated TiO_2 thin film for enhanced solar hydrogen generation. *Sol. RRL* 4: 1900557.

84 Liu, H., Zhao, J., Li, C. et al. (2005). Conceptual design and CFD simulation of a novel metal-based monolith reactor with enhanced mass transfer. *Catal. Today* 105: 401–406.

85 Azam, M.U., Tahir, M., Umer, M. et al. (2019). Engineering approach to enhance photocatalytic water splitting for dynamic H_2 production using La_2O_3/TiO_2 nanocatalyst in a monolith photoreactor. *Appl. Surf. Sci.* 484: 1089–1101.

86 Fajrina, N. and Tahir, M. (2020). Monolithic Ag-Mt dispersed Z-scheme pCN-TiO_2 heterojunction for dynamic photocatalytic H_2 evolution using liquid and gas phase photoreactors. *Int. J. Hydrogen Energy* 45: 4355–4375.

87 Gaudillere, C., González, J.J., Chica, A. et al. (2017). YSZ monoliths promoted with Co as catalysts for the production of H_2 by steam reforming of ethanol. *Appl. Catal., A* 538: 165–173.

88 Tasleem, S. and Tahir, M. (2021). Investigating the performance of liquid and gas phase photoreactors for dynamic H_2 production over bimetallic TiO_2 and Ni_2P dispersed MAX Ti_3AlC_2 monolithic nanocomposite under UV and visible light. *J. Environ. Chem. Eng.* 9: 105351.

89 Tugaoen, H.O., Garcia-Segura, S., Hristovski, K. et al. (2018). Compact light-emitting diode optical fiber immobilized TiO_2 reactor for photocatalytic water treatment. *Sci. Total Environ.* 613–614: 1331–1338.

90 Taboada, E., Angurell, I., and Llorca, J. (2014a). Dynamic photocatalytic hydrogen production from ethanol–water mixtures in an optical fiber honeycomb reactor loaded with Au/TiO_2. *J. Catal.* 309: 460–467.

91 Taboada, E., Angurell, I., and Llorca, J. (2014b). Hydrogen photoproduction from bio-derived alcohols in an optical fiber honeycomb reactor loaded with Au/TiO_2. *J. Photochem. Photobiol., A* 281: 35–39.

92 Chang, Y.C., Tasi, C.L., and Ko, F.H. (2021). Construction of $ZnIn_2S_4/ZnO$ heterostructures with enhanced photocatalytic decomposition and hydrogen evolution under blue LED irradiation. *Int. J. Hydrogen Energy* 46: 10281–10292.

93 Nwosu, U., Wang, A., Palma, B. et al. (2021). Selective biomass photoreforming for valuable chemicals and fuels: a critical review. *Renewable Sustainable Energy Rev.* 148: 111266.

94 Oller, I., Malato, S., and Sánchez-Pérez, J.A. (2011). Combination of advanced oxidation processes and biological treatments for wastewater decontamination-a review. *Sci. Total Environ.* 409: 4141–4166.

95 Chung, K.H., Park, Y.K., Cho, E.B. et al. (2020). Simultaneous hydrogen production and pollutant degradation by photocatalysis of wastewater using liquid phase plasma. *Int. J. Hydrogen Energy* 45: 24028–24036.

96 Hippargi, G., Anjankar, S., Krupadam, R.J. et al. (2012). Simultaneous wastewater treatment and generation of blended fuel methane and hydrogen using Au-Pt/TiO_2 photo-reforming catalytic material. *Fuel* 291: 120113.

97 Lin, Z., Li, L., Yu, L. et al. (2017). Dual-functional photocatalysis for hydrogen evolution from industrial wastewaters. *Phys. Chem. Chem. Phys.* 19: 8356–8362.

98 Pansa-Ngat, P., Jedsukontorn, T., and Hunsom, M. (2017). Simultaneous H_2 production and pollutant removal from biodiesel wastewater by photocatalytic oxidation with different crystal structure TiO_2 photocatalysts. *J. Taiwan Inst. Chem. Eng.* 78: 386–394.

99 Vaiano, V. and Iervolino, G. (2019). Photocatalytic removal of methyl orange azo dye with simultaneous hydrogen production using Ru-modified ZnO photocatalyst. *Catalysts* 9: 964.

100 Imizcoz, M. and Puga, A.V. (2019). Assessment of photocatalytic hydrogen production from biomass or wastewaters depending on the metal co-catalyst and its deposition method on TiO_2. *Catalysts* 9: 584.

101 Zhang, C., Li, Y., Li, Y. et al. (2021). Simultaneous coupling of photocatalytic and biological processes: a promising synergistic alternative for enhancing decontamination of recalcitrant compounds in water. *Chem. Eng. J.* 403: 126365.

102 Rizzo, L. (2011). Bioassays as a tool for evaluating advanced oxidation processes in water and wastewater treatment. *Water Res.* 45: 4311–4340.

103 Sarria, V., Parra, S., Adler, N. et al. (2002). Recent developments in the coupling of photoassisted and aerobic biological processes for the treatment of biorecalcitrant compounds. *Catal. Today* 76: 301–315.

104 López, A., Di Iaconi, C., and Mascolo, G. (ed.) (2012). *Innovative and Integrated Technologies for the Treatment of Industrial Wastewater*. London, UK: IWA Publishing.

105 Scott, J.P. and Ollis, D.F. (1997). Integration of chemical and biological oxidation processes for water treatment: II Recent illustrations and experiences. *J. Adv. Oxid. Technol.* 2: 374.

Index

Photocatalytic Hydrogen Production for Sustainable Energy, First Edition. Edited by Alberto Puga.

i

t